

Proceedings of the 23rd Conference on Computational Mechanics ACME-UK 2015



Swansea, April 8-10, 2015



Swansea University
Prifysgol Abertawe

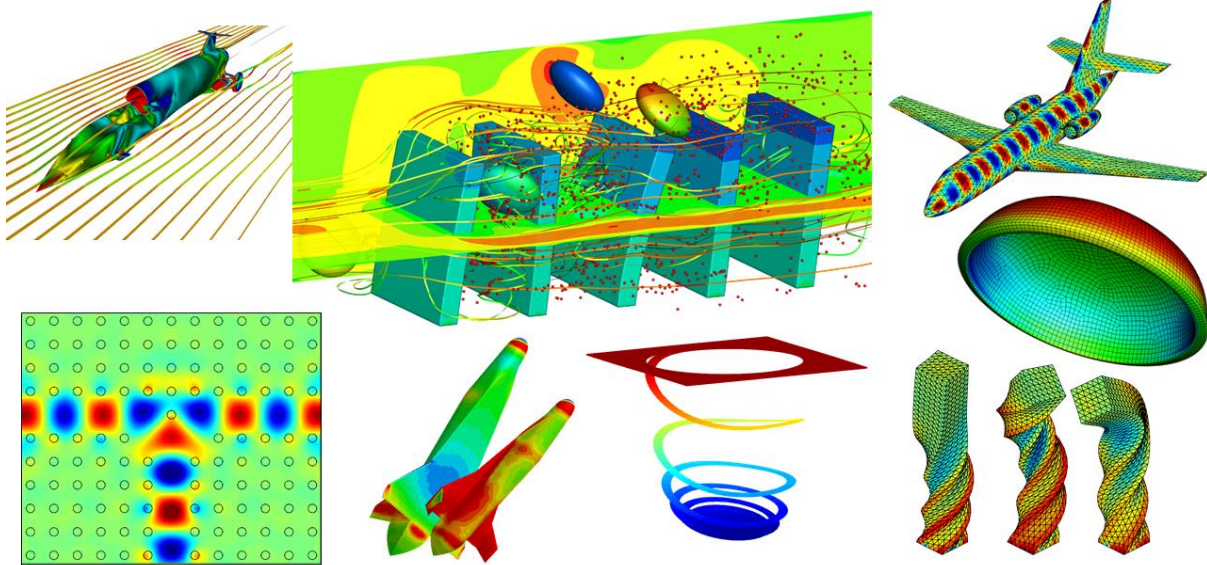
Edited by:
Antonio J. Gil
Rubén Sevilla



Association of Computational
Mechanics in Engineering - UK



Proceedings of the
23rd Conference on Computational Mechanics
ACME-UK 2015



8th-10th April 2015

College of Engineering, Swansea University, Wales, UK

Edited by:
Antonio J. Gil
Rubén Sevilla

Copyright © 2015 Swansea University. All rights reserved.

No parts of this publication may be produced, stored in a retrieval system, or transmitted in any form or by any means, electronic, mechanical, photocopying, recording or otherwise, without the prior written permission of Swansea University, Swansea, Wales, UK.

Contents

Contents	5
Acknowledgements	15
Preface	17
Programme	19
Conference Programme	21
Technical Sessions	22
4th ACME School	25
Plenary Lectures	29
Luca Formaggia - The challenge of complexity in sedimentary and reservoir simulations	33
Rainald Löhner - Recent CFD/FSI-based discoveries relevant to civil en- gineering	38
Jaime Peraire - Gaussian functional regression for state prediction using linear PDE models and observations	46
Advanced Applications 1	51
Konstantinos Krestenitis and Tomasz Koziara - Calculating the min- imum distance between two triangles on SIMD hardware	53
David James, Juergen Eckermann, Fawsi Belbidia and Johann SiENZ - Point cloud data from photogrammetry techniques to generate 3D geometry	57
Kulchamai Thienkarochanakul and Akbar Javadi - Finite element analysis on knee joint for knee OA patients	61
William G. Charles, Pooya Mahmoodi, Rajesh S. Ransing, Igor Sazonov and Michael I. Friswell - Comparison of the Lagrangian approach for modelling the heel-to-toe contact in passive dynamic walk- ers with the discrete pivot point method	65

Advanced Applications 2	69
Pooya Mahmoodi, Simon Annan and Nick Owen - A computational method of obtaining reliable measurement of periosteal cross-sectional area of human radii from laser scans	71
Marton Huszar, Patrick Wlodarski, Fawzi Belblidia, Sue Alston, Cris Arnold, Johann Sienz and David Bould - The influence of apparent-and true viscosity on injection pressure prediction	75
Moura Mehravar, Ouahid Harireche and Asaad Faramarzi - Evaluation of undrained bearing capacities of skirted foundations	79
Hocine Matallah, Nick Croft, Stephen Hardy and Johann Sienz - An investigation into problems associated with the overheating of air monitoring devices	83
Alireza Ahangar-Asr and Akbar Javadi - Effects of air permeability and perimeter area on air losses in compressed air tunnelling	87
Composites	91
Zahur Ullah, Lukasz Kaczmarczyk and Chris J. Pearce - Multiscale computational homogenisation to predict the long-term durability of composite structures	93
Shirin Yekrangian and Zhangjian Wu - Simulation of laminated composite plates under free vibration	97
Behrooz Tafazzolimoghaddam, Jose Luis Curiel-Sosa and Joaquín Navarro-Zafra - On the calculation of energy release rates in composite laminates by finite elements, boundary elements and analytical methods	101
Remi Caudoux and Karin de Borst - Mechanical modelling of nanocellulose composite	105
Coupled Problems 1	109
Maimouna Al Manthari and Perumal Nithiarasu - Vortex-induced vibration of a circular cylinder	111
Gede Pringgana, Lee S. Cunningham and Benedict D. Rogers - SPH modelling of tsunami-induced bore and structure interaction using DualSPHysics	115
Fawzi Belblidia, Shahid Mehmood, Chun Hean Lee, Hector U. Levatti, Johann Sienz, David T. Gethin and Cris Arnold - Numerical investigations into dynamic loading of rubber compound	119
Darong Jin, Paul D. Ledger and Antonio J. Gil - An hp-FEM framework for the simulation of stationary incompressible magnetohydrodynamics with magnetostrictive effects in three dimensions	123
Coupled Problems 2	127

Richard Evans, Igor Sazonov and Perumal Nithiarasu - A novel dual time stepping approach for fluid-structure-interaction problems	129
Chuansan Ma, Tony Jefferson, Diane Gardner and Robert Lark - A numerical model of the transportation of self-healing agent in and around concrete discrete cracks	133
Chennakesava Kadapa, Wulf Dettmer and Djordje Peric - Fluid-structure interaction with immersed boundary method based on hierarchical B-spline based Eulerian grid	137
Euan Richardson and Karin de Borst - Numerical modelling the sorption behaviour of wood cell walls	141
Coupled Problems 3	145
Hossein Madani, Jan Wissink and Hamid Bahai - Application of strip theory using 2D moving frame of reference and Euler Bernoulli beam theory to simulate oil riser problem	147
Min Wang, Yun Tian Feng and Chengyuan Wang - Coupled Problems bonded particle and lattice Boltzmann method for modelling fluid-solid interaction	151
Julien Vignollet, Stefan May and René de Borst - An isogeometric biphasic model for the dynamic rupture of geological faults	155
Scott Bagwell, Paul Ledger and Antonio Gil - A Newton Raphson scheme for Coupled Problems magneto-mechanical problems applied to MRI scanners	159
Coupled Problems 4	163
Chun Hean Lee, Antonio J. Gil, Javier Bonet and Rogelio Ortigosa - An entropy-based stabilised Petrov-Galerkin formulation for linear tetrahedral elements in compressible, nearly incompressible and truly incompressible fast solid dynamics	165
Susanne Claus, Erik Burman and Andre Massing - CutFEM: a stabilised Nitsche XFEM method for multi-physics problems	169
Rogelio Ortigosa, Antonio J. Gil and Javier Bonet - A variational framework for large strain polyconvex dielectric elastomers	173
Bruce Jones, Christopher Leonardi and John Williams - Numerical rheometry of dense particle suspensions using a Coupled Problems lattice Boltzmann and discrete element method	177
Roman Poya, Antonio J. Gil and Javier Bonet - A computational framework for linearised elasticity Coupled Problems with non-linear electro-magneto-statics	181
Fluid Dynamics 1	185

Adam Philo, Nicholas P. Lavery, Stephen G. R. Brown, John Cherry, Johann Sienz, Jason Joannou and Chris J. Sutcliffe - Comparison and validation of gas flow models in a powder bed selective laser melting process	187
Firas Badry, Bhushan Karihaloo and Sivakumar Kulasegaram - Simulation of the flow of non-Newtonian self-compacting concrete . . .	191
Violeta Moloney, Dominic Reeve and Harshinie Karunarathna - Investigation of stratified flows in Greenland fjords	195
Kenny W. Q. Low, Raoul van Loon, Sam Rolland and Johann Sienz - An efficient image-based framework for evaluating fluid flow of random fibrous porous media in oxygenators	199
Fluid Dynamics 2	203
Justin Prince and Joaquim Peiró - Application of a Lagrange multiplier approach for flow rate defective boundary conditions in a finite volume framework	205
Mahkame Sharbatdar, Alireza Jalali and Carl Ollivier-Gooch - A higher-order unstructured finite volume solver for generalized Newtonian Fluid Dynamics	209
Dirk Ekelschot, David Moxey, Joaquim Peiro and Spencer Sherwin - P-adaption for compressible laminar flow problems using a goal-based error estimator	213
Fluid Dynamics 3	217
Mohammed Hussain, Akbar Javadi and Reza Naseri-Karim-Vand - Control of seawater intrusion using aquifer storage and recovery (ASR) technique	219
Mai Abdul Latif and Yun Tian Feng - CFD analysis of high rise unconventional buildings subject to extreme wind loading	223
Alireza Jalali, Mahkame Sharbatdar and Carl Ollivier-Gooch - Exploiting a higher-order compressible flow solver for incompressible flows	227
David Jones, Oubay Hassan and Kenneth Morgan - A second order accurate Mach-uniform solver for the Euler and Navier-Stokes equations on pairs of mutually orthogonal unstructured grids	231
Fluid Dynamics 4	235
Farzaneh Hafezi, Sam Rolland, Diane McBride, Nick Croft, Mark Cross and Rob Ellis - A CFD case study of using turbulence models for evaluating the performance of a drag based vertical axis wind turbine	237
Soo-Hyeong Kim, Oubay Hassan, Kenneth Morgan and Nidal Hilal - Coupled Problems lattice Boltzmann and finite volume method for modelling crossflow microfiltration and nanofiltration	241

Michael Weberstadt, Antonio J. Gil and Rubén Sevilla - High fidelity methods for compressible flow problems on moving domains	245
Thomas Lake, Ian Masters and Nick Croft - Particles as porpoise - applying CFD results to environmental interactions	249
Fracture and Failure 1	253
Mohaddeseh Mousavi Nezhad, Elia Gironacci, Mohammad Reza-nia and Quentin J. Fisher - Computational modelling of crack propagation in shale-gas reservoir rocks	255
Luis Saucedo-Mora and Thomas James Marrow - FEMME: a multi-scale finite element microstructure meshfree fracture model for quasi-brittle materials with complex microstructures	259
Joaquín Navarro-Zafra, José Luis Curiel-Sosa and María Del Carmen Serna Moreno - 3D crack analysis of a CGRP cruciform under biaxial loading using two numerical approaches: XFEM and a progressive damage model	263
Hassan Al-Budairi, Lukasz Kaczmarczyk and Chris Pearce - Modelling of dynamic crack propagation in 3D elastic continuum using configurational mechanics	267
Fracture and Failure 2	271
Costy Kodsi, Lukasz Kaczmarczyk and Chris Pearce - Failure analysis of 3-D graphite bricks in an AGR core	273
Gabriel Hattori, Ibrahim A. Alatawi and Jon Trevelyan - A direct SIF approach for anisotropic materials using the boundary element method	277
Waled Alnaas and Anthony Jefferson - Nonlinear finite element analysis of quasi-brittle materials	281
Ibrahim Alatawi, Jon Trevelyan and Gabriel Hattori - Analysis of 3D crack problems by the extended boundary element method (XBEM)	285
Mesh Generation	289
Lucas Franceschi and Rubén Sevilla - A low-cost elasticity analogy approach to boundary motion of curved finite element meshes	291
Sean Walton, Oubay Hassan and Kenneth Morgan - Generating dual orthogonal meshes suitable for co-volume techniques	295
Luke Rees, Rubén Sevilla and Oubay Hassan - Meshes appropriate for use with NURBS-enhanced finite element method	299
Shahid Manzoor, Michael Edwards, Ali Dogru and Tareq Al-Shaalan - Boundary aligned PEBI-grid generation and CVD-MPFA discretization	303
Optimisation	307

Jennifer Thompson, Oubay Hassan, Sam Rolland and Johann Sienz - The use of computational techniques for the optimisation of metal powder particle size distribution (PSD) from gas atomisation (GA) process	309
H Alicia Kim, Joao Duro, Graham McShane and Peter Theobald - Topology optimisation of additively manufactured impact resistant structures	313
David Naumann and Ben J. Evans - A novel implementation of aerodynamic shape optimisation using modified cuckoo search	317
Sudip Dey, Tanmoy Mukhopadhyay, Hamed Haddad Khodaparast and Sondipon Adhikari - Reliability based optimization of composite spherical shells	321
Solids and Structures 1	325
Ansam Qsymah, Rajneesh Sharma, Zhenjun Yang and Lee Margetts - XCT image-based homogenisation of elastic properties of ultra high performance fibre reinforced concrete (UHPFRC)	327
Zheng Cui and Yun Tian Feng - Finite element analysis and optimal design of joints for concrete filled tubes in steel structure	331
Mt Rahmati, Hamid Bahai and Giulio Alfano - A comparison between periodic and fixed BC for structural analysis of flexible risers	335
Yao Xiao, Chengyuan Wang and Yun Tian Feng - Vibration behaviours of coated carbon nanotubes	339
Solids and Structures 2	343
Ramaseshan Kannan and Stephen Hendry - "The doctor will see you now!" Diagnosing models with ill conditioning problems and curing them	345
Andrew Evans, Nick Croft and Amit Das - An alternative method for beverage can parameter screening	349
Stefan May, Julien Vignollet and René de Borst - A Powell-Sabin B-spline method for Kirchhoff-Love plates	353
Raid Daud, Lee Cunningham and Yong Wang - Numerical study of effective bond length for externally bonded CFRP plate under cyclic loads	357
Solids and Structures 3	361
Charles Mortished, Johann Sienz and Peter Benzie - A comparison of response surface methodologies to represent crushing behaviour of thin-walled tubes	363
Moirangthem Dinachandra and Raju Sethuraman - Isogeometric based pseudo-elastic analysis of inelastic structures	367

Wenjun Tan, Matthew Profit and Yun Tian Feng - On the contact force and boundary treatment in smoothed particle hydrodynamics with Advanced Applications in glass forming	371
Martin Horak, Borek Patzak and Jan Novak - Preliminary outcomes on isogeometric Trefftz method	375
Solids and Structures 4	379
K.Adi Navaneetha Kumari and Raju Sethuraman - Evaluation of elasto-plastic stress and strain fields using pseudo-elastic finite element method for non proportional loading	381
Tanmoy Mukhopadhyay and Sondipon Adhikari - Prediction of equivalent elastic properties of irregular cellular solids	385
Shivani Srivastava and Raju Sethuraman - NURBS based differential quadrature method (N-DQM) for free vibration analysis of linearly tapered circular plate resting on Pasternak foundation	389
Giorgio Greto, Sivakumar Kulasegaram, Chun Hean Lee, Antonio J. Gil and Javier Bonet - A first order mixed formulation for fast solid dynamics using smooth particle hydrodynamics	393
Shahin Mehraban, E. Enticknap, J. Cullen, Cameron Pleydell-Pearce, D. Bould, Stephen G. R. Brown, Nicholas P. Lavery - Simulation of small punch test for rapid prototyping of alloys	397
Solids and Structures 5	401
Michael Cortis, Lukasz Kaczmarczyk and Chris Pearce - Finite element modelling of braided fibres subject to large deformations	403
Jibrán Haider, Antonio Gil, Javier Bonet and Chun Hean Lee - A first order conservation law formulation for lagrangian fast solid dynamics in OpenFoam	407
Tim Charlton, William Coombs and Charles Augarde - On the implicit implementation of the generalised interpolation material point method	411
Tien Long Nguyen, Carlo Sansour and Mohammed Hjiaj - Geometrically exact beams under impact: nonsmooth formulation and energy conserving scheme	415
Stochastics	419
Shaoqing Cui and Chenfeng Li - A comparison study of statistical reconstruction of heterogeneous materials	421
Yajun Li, Michael Hicks and Philip Vardon - High performance computing strategies for nonlinear finite element analysis of long heterogeneous soil slopes	425

Muhannad Aldosary, Chenfeng Li and Mohamed Benamer - A comparison study on stochastic finite element methods for structural reliability analysis	429
Elia Gironacci, Mohaddeseh Mousavi Nezhad and Mohammad Reza- nia - Modelling of crack propagation on brittle heterogeneous materials	433
Thermodynamics	437
Desmond Andrew Brennan, Ian Mabbett, Jon Elvins, Nicholas P. Lavery and David Worsley - Mathematical framework for predicting the thermal behaviour of spectrally selective coatings within industrial near infrared furnaces	439
Muhammad Iqbal, Heiko Gimperlein, Shadi Mohamed and Omar Laghrouche - A-posteriori error estimate for the partition of unity method for transient heat diffusion problems	443
Sergio Conde Martin, Juan Carlos García Orden and Peter Betsch - A temperature-based thermodynamically consistent time integration for discrete thermoelastodynamics	447
Adam Philo, Nicholas P. Lavery, Stephen Brown, John Cherry and Johann Sienz - Effects of Hatch pattern and laser parameters on the multi-scale thermal modelling of selective laser melting	451
Hichem Boulechfar and Mahfoud Djezzar - Numerical computation of heat and mass transfer by natural convection through a fluid-saturated porous medium in horizontal elliptical annulus	455
Wave Propagation 1	459
Fawzi Belblidia, Ian Cameron, Johann Sienz and Lintao Zhang - Characterization of the magnetic field in magnetic flux leakage type nondestructive testing at high specimen speed	461
Mar Giralt, Rubén Sevilla and Oubay Hassan - Numerical simulation of a geometrically parametrised electromagnetic problem	465
Alex Gansen, Mohamed El Hachemi, Oubay Hassan and Kenneth Morgan - Unstructured 3D leapfrog solver for electromagnetic modelling and simulation of arbitrary shaped anisotropic objects	469
Mark Dawson, Rubén Sevilla, Oubay Hassan and Kenneth Morgan - Computation of resonant modes in cavities with a discontinuous Galerkin time domain approach	473
Wave Propagation 2	477
Ross Kynch and Paul D. Ledger - Solving the magnetic induction tomography inverse problem using hp-finite elements	479

Konstantinos Christodoulou, Shadi Mohamed, Omar Laghrouche and Jon Trevelyan - Assessment of polynomial and non-polynomial based high order FEM for the solution of Helmholtz problems at high frequency	483
Mayank Drolia, M S Mohamed, Omar Laghrouche, Mohammed Seaid and Jon Trevelyan - Enriched finite elements for numerical solution of electromagnetic waves in the time domain	487
Robert Simpson, Michael Scott and Jon Trevelyan - A black-box fast multipole method for accelerated isogeometric boundary element analysis with T-splines	491
List of Authors	495

ACKNOWLEDGEMENTS

The conference organisers gratefully acknowledge the support given by the following organisations:

College of Engineering, Swansea University



Swansea University
Prifysgol Abertawe

Institute of Mathematics and its Applications (IMA)



National Research Network in Advanced Engineering and Materials



Society for Industrial and Applied Mathematics (SIAM)



Zienkiewicz Centre for Computational Engineering

PREFACE

This book of proceedings contains more than 100 four-page papers presented at the 23rd ACME Conference held in the College of Engineering, Swansea University, from the 9th to 10th April 2015.

The UK Association for Computational Mechanics in Engineering (ACME) was founded in March 1992 with the purpose of promoting research in computational mechanics in the UK and establishing formal links with similar organisations across Europe and worldwide. The Association is affiliated with the European Community of Computational Methods in Applied Sciences (ECCOMAS) and the International Association for Computational Mechanics (IACM).

The principal activity of ACME involves the organisation of an annual two day Conference focussed on the latest developments and research trends in the field of computational mechanics. The Conference is particularly orientated towards encouraging young scientists in the field to present their current research at both Doctoral and Post-Doctoral levels. The Conference is therefore a unique forum to foster ideas, enable new multidisciplinary research approaches and establish collaborative research links, helping to build strong research networks within the UK and at an international level.

The last ten editions of the Conference took place in the Universities of Exeter (2014), Durham (2013), Manchester (2012), Heriot-Watt (2011), Southampton (2010), Nottingham (2009), Newcastle (2008), Glasgow (2007), Belfast (2006) and Sheffield (2005). This year, the 23rd Edition of the ACME Conference returns to Swansea University, where it was inaugurated in 1993. The Conference is preceded by the 4th ACME School on the 8th of April, which focusses on the theme of low and high order methods for the next generation of computational engineering software. We would like to express our gratitude to the four invited keynote speakers, Professor Luca Formaggia (Politecnico di Milano), Professor Rainald Löhner (George Mason University), Professor Jaime Peraire (Massachusetts Institute of Technology) and Professor Jörg Schröder (Universität Duisburg Essen), for bringing their internationally recognised research expertise to this Conference to inspire the next generation of scientists in the

field of computational mechanics.

We would like to thank the many authors, coming from 32 different institutions and 12 different countries, whose papers are included in this book of proceedings, without whom this Conference would not take place. In addition, we would like to thank the many people who have contributed to the organisation of this Conference as part of the Local Scientific Committee and the Local Organising Committee. We gratefully acknowledge the support received from the College of Engineering at Swansea University, the Institute of Mathematics and Its Applications (IMA), the Zienkiewicz Centre for Computational Engineering (ZCCE), the National Research Network in Advanced Engineering and Materials (NRN) and the Society for Industrial and Applied Mathematics (SIAM). Finally, we would like to take this opportunity to thank Dr Chun Hean Lee, Dr Sean Walton and Dr Clare Wood for their dedication and hard work in the day-to-day organisation of the 23rd ACME Conference.

Antonio J. Gil and **Rubén Sevilla**

ACME-UK 2015 Chairmen

PROGRAMME

WEDNESDAY – 8th April 2015

13.00 – 14.00		REGISTRATION - Engineering Foyer	
4th ACME SCHOOL: Low or high-order: this is the question! (To p or not to p)			
14.00 – 14.40	Kenneth Morgan: Low order simulation methods for aerospace engineering		
14.40 – 15.20	Antonio J Gil: Bridging methodologies for the computational simulation of fluids and solids		
15.20 – 15.40	COFFEE BREAK		
15.40 – 16.20	Rubén Sevilla: High-order methods for the next generation of computational engineering software		
16.20 – 17.00	Paul D Ledger: High order <i>hp</i> -finite elements in electromagnetism and coupled problems		
18.00 – 20.00	CONFERENCE RECEPTION & REGISTRATION – National Waterfront Museum		

THURSDAY – 9th April 2015

08.30 – 09.00		LATE REGISTRATION - Engineering Foyer	
OPENING CEREMONY - Room A			
09.00 – 09.15	Room K	Room L	Room M
09.15 – 09.55	PLENARY SESSION 1 - Room A – JÖRG SCHRÖDER		
10.00 – 11.15	Solids & structures 1	Stochastics	Wave propagation 1 Composites
11.15 – 11.45	COFFEE BREAK		
11.45 – 13.00	Room A	Room K	Room L
13.00 – 13.45	Solids & structures 2	Optimisation	Wave propagation 2 Mesh generation
13.45 – 14.25	LUNCH - Fulton House Refectory (Building 17 on the Campus Map, First Floor)		
PLENARY SESSION 2 - Room A – LUCA FORMAGGIA			
14.30 – 15.45	Room A	Room K	Room L
15.45 – 16.15	Solids & structures 3	Fracture & failure 1	Coupled problems 1 Fluid dynamics 1
COFFEE BREAK			
16.15 – 17.45	Room A	Room K	Room L
19.00 –	Solids & structures 4	Fracture & failure 2	Coupled problems 2 Fluid dynamics 2
CONFERENCE DINNER – Swansca Marriott Hotel			

FRIDAY – 10th April 2015

PLENARY SESSION 3 - Room A – JAIME PERAIRE			
09.00 – 09.40	Room A	Room K	Room L
09.40 – 11.00	Solids & structures 5	Advanced applications 1	Coupled problems 3 Fluid dynamics 3
11.00 – 11.30	COFFEE BREAK		
11.30 – 13.00	Room A	Room K	Room L
13.00 – 13.45	Thermodynamics	Advanced applications 2	Coupled problems 4 Fluid dynamics 4
LUNCH - Fulton House Refectory (Building 17 on the Campus Map, First Floor)			
PLENARY SESSION 4 - Room A – RAINALD LÖHNER			
14.30 – 15.30	COFFEE BREAK – Award Deliberation		
15.30 – 16.00	AWARD CEREMONY		

THURSDAY – 9th April 2015

LATE REGISTRATION - Engineering Foyer

OPENING CEREMONY - Room A

PLENARY SESSION 1 - Room A – JÖRG SCHRÖDER

	Room A - Solids & structures 1	Room K - Stochastics	Room L - Wave propagation 1	Room M - Composites
08.30 – 09.00				
09.00 – 09.15				
09.15 – 09.55				
10.00 – 10.18	<u>A Qsymah</u> : XCT image-based homogenisation of elastic properties of ultra high performance fibre reinforced concrete (UHPRC)	<u>S Cui</u> : A comparison study of statistical reconstruction of heterogeneous materials	<u>L Zhang</u> : Characterization of the magnetic field in magnetic flux leakage type nondestructive testing at high specimen speed	<u>Z Ullah</u> : Multiscale computational homogenisation to predict the long-term durability of composite structures
10.18 – 10.36	<u>Z Cui</u> : Finite element analysis and optimal design of joints for concrete filled tubes in steel structure	<u>Y Li</u> : High performance computing strategies for nonlinear finite element analysis of long heterogeneous soil slopes	<u>M Giralt</u> : Numerical simulation of a geometrically parametrised electromagnetic problem	<u>S Yekrangian</u> : Simulation of laminated composite plates under free vibration
10.36 – 10.54	<u>Mt Rahmati</u> : A comparison between periodic and fixed BC for structural analysis of flexible risers	<u>M Aldosary</u> : A comparison study on stochastic finite element methods for structural reliability analysis	<u>A Gansen</u> : Unstructured 3D leapfrog solver for electromagnetic modelling and simulation of arbitrary shaped anisotropic objects	<u>B Tafazzolimoghaddam</u> : On the calculation of energy release rates in composite laminates by finite elements, boundary elements and analytical methods
10.54 – 11.12	<u>Y Xiang</u> : Vibration behaviours of coated carbon nanotubes	<u>E Gironacci</u> : Modelling of crack propagation on brittle heterogeneous materials	<u>M Dawson</u> : Computation of resonant modes in cavities with a discontinuous Galerkin time domain approach	<u>R Caudoux</u> : Mechanical modelling of nano-cellulose composite

COFFEE BREAK

	Room A - Solids & structures 2	Room K - Optimisation	Room L - Wave propagation 2	Room M - Mesh generation
11.15 – 11.45				
11.45 – 12.03	<u>R Kannan</u> : "The doctor will see you now!" Diagnosing models with ill conditioning problems and curing them	<u>J Thompson</u> : The use of computational techniques for the optimisation of metal powder particle size distribution (PSD) from gas atomisation (GA) process	<u>R Kyncl</u> : Solving the magnetic induction tomography inverse problem using <i>hp</i> -finite elements	<u>L Franceschi</u> : A low-cost elasticity analogy approach to boundary motion of curved finite element meshes
12.03 – 12.21	<u>A Evans</u> : An alternative method for beverage can parameter screening	<u>H A Kim</u> : Topology optimisation of additively manufactured impact resistant structures	<u>K Christodoulou</u> : Assessment of polynomial and non-polynomial based high order FEM for the solution of Helmholtz problems at high frequency	<u>S Walton</u> : Generating dual orthogonal meshes suitable for co-volume techniques
12.21 – 12.39	<u>S May</u> : A Powell-Sabin B-spline method for Kirchhoff-Love plates	<u>D Naumann</u> : A novel implementation of aerodynamic shape optimisation using modified cuckoo search	<u>M Drolia</u> : Enriched finite elements for numerical solution of electromagnetic waves in the time domain	<u>L Rees</u> : Meshes appropriate for use with NURBS-enhanced finite element method
12.39 – 12.57	<u>R Daudi</u> : Numerical study of effective bond length for externally bonded CFRP plate under cyclic loads	<u>S Dexy</u> : Reliability based optimization of composite spherical shells	<u>R Simpson</u> : A black-box fast multipole method for accelerated isogeometric boundary element analysis with T-splines	<u>S Manzoor</u> : Boundary aligned PEBI-grid generation and CVD-MPFA discretization

LUNCH - Fulton House Refectory (Building 17 on the Campus Map, First Floor)

13.00 – 13.45				
---------------	--	--	--	--

THURSDAY – 9th April 2015

PLENARY SESSION 2 - Room A – LUCA FORMAGGIA

	Room A - Solids & structures 3	Room K - Fracture & failure 1	Room L - Coupled problems 1	Room M - Fluid dynamics 1
13.45 – 14.25				
14.30 – 14.48	<u>C.Morishid</u> : A comparison of response surface methodologies to represent crushing behaviour of thin-walled tubes	<u>M.M.Nezhad</u> : Computational modelling of crack propagation in shale-gas reservoir rocks	<u>M.A.Manthari</u> : Vortex-induced vibration of a circular cylinder	<u>N.Lavery</u> : Comparison and validation of gas flow models in a powder bed selective laser melting process
14.48 – 15.06	<u>M.Dinachandra</u> : Isogeometric based pseudo-elastic analysis of inelastic structures	<u>L.Saucedo-Mora</u> : FEMME: a multi-scale finite element microstructure meshfree fracture model for quasi-brittle materials with complex microstructures	<u>G.Pringsang</u> : SPH modelling of tsunami-induced bore and structure interaction using DualSPHysics	<u>E.Badry</u> : Simulation of the flow of non-Newtonian self-compacting concrete
15.06 – 15.24	<u>W.Tan</u> : On the contact force and boundary treatment in smoothed particle hydrodynamics with applications in glass forming	<u>I.Navarro-Zafra</u> : 3D crack analysis of a CGRP cruciform under biaxial loading using two numerical approaches: XFEM and a progressive damage model	<u>H.U.Levairi</u> : Numerical investigations into dynamic loading of rubber compound	<u>V.Moloney</u> : Investigation of stratified flows in Greenland fjords
15.24 – 15.42	<u>I.Novak</u> : Preliminary outcomes on isogeometric Trefftz method	<u>H.Ai-Budairi</u> : Modelling of dynamic crack propagation in 3D elastic continuum using configurational mechanics	<u>D.Jin</u> : An <i>hp</i> -FEM framework for the simulation of stationary incompressible magnetohydrodynamics with magnetostrictive effects in three dimensions	<u>K.Low</u> : An efficient image-based framework for evaluating fluid flow of random fibrous porous media in oxygenators

COFFEE BREAK

	Room A - Solids & structures 4	Room K - Fracture & failure 2	Room L - Coupled problems 2	Room M - Fluid dynamics 2
15.45 – 16.15				
16.15 – 16.33	<u>K.A.N.Navaneetha</u> : Evaluation of elasto-plastic stress and strain fields using pseudo-elastic finite element method for non proportional loading	<u>C.Kodsi</u> : Failure analysis of 3-D graphite bricks in an AGR core	<u>R.Evans</u> : A novel dual time stepping approach for fluid-structure-interaction problems	<u>J.Prince</u> : Application of a Lagrange multiplier approach for flow rate defective boundary conditions in a finite volume framework
16.33 – 16.51	<u>T.Mukhopadhyay</u> : Prediction of equivalent elastic properties of irregular cellular solids	<u>G.Hattori</u> : A direct SIF approach for anisotropic materials using the boundary element method	<u>C.Ma</u> : A numerical model of the transportation of self-healing agent in and around concrete discrete cracks	<u>Y.Xie</u> : Higher resolution cell-centred finite-volume schemes for two-phase flow on unstructured grids
16.51 – 17.09	<u>S.Srivastava</u> : NURBS based differential quadrature method (N-DQM) for free vibration analysis of linearly tapered circular plate resting on Pasternak foundation	<u>W.Alhaas</u> : Nonlinear finite element analysis of quasi-brittle materials	<u>C.Kadapa</u> : Fluid-structure interaction with immersed boundary method based on hierarchical B-spline based Eulerian grid	<u>M.Sharbatdar</u> : A higher-order unstructured finite volume solver for generalized Newtonian fluids
17.09 – 17.27	<u>G.Greto</u> : A first order mixed formulation for fast solid dynamics using smooth particle hydrodynamics	<u>I.Alatawi</u> : Analysis of 3D crack problems by the extended boundary element method (XBEM)	<u>E.Richardson</u> : Numerical modelling the sorption behaviour of wood cell walls	<u>D.Ekelschot</u> : P-adaption for compressible laminar flow problems using a goal-based error estimator
17.27 – 17.45	<u>S.Mehraban</u> : Simulation of small punch test for rapid prototyping of alloys	<u>R.Ahmed</u> : CVD-MPPA scheme with full pressure support for discrete-fracture matrix simulations		

CONFERENCE DINNER – Swansea Marriott Hotel

19.00 –

FRIDAY – 10th April 2015

PLENARY SESSION 3 – Room A – JAIME PERAIRE

	Room A – Solids & structures 5	Room K – Advanced applications 1	Room L – Coupled problems 3	Room M – Fluid dynamics 3
09.00 – 09.40				
09.40 – 09.58	M Cortis: Finite element modelling of braided fibres subject to large deformations	K Krestenitis: Calculating the minimum distance between two triangles on SIMD hardware	H Madani: Application of strip theory using 2D moving frame of reference and Euler Bernoulli beam theory to simulate oil riser problem	M Hussain: Control of seawater intrusion using aquifer storage and recovery (ASR) technique
09.58 – 10.16	J Haider: A first order conservation law formulation for lagrangian fast solid dynamics in OpenFoam	D James: Point cloud data from photogrammetry techniques to generate 3D geometry	M Wang: Coupled bonded particle and lattice Boltzmann method for modelling fluid-solid interaction	M A Latif: CFD analysis of high rise unconventional buildings subject to extreme wind loading
10.16 – 10.34	T Charlton: On the implicit implementation of the generalised interpolation material point method	K Thienkaroachakul: Finite element analysis on knee joint for knee OA patients	J Vignoller: An isogeometric biphasic model for the dynamic rupture of geological faults	A Jalali: Exploiting a higher-order compressible flow solver for incompressible flows
10.34 – 10.52	C Sansour: Geometrically exact beams under impact: nonsmooth formulation and energy conserving scheme	W G Charles: Comparison of the Lagrangian approach for modelling the heel-to-toe contact in passive dynamic walkers with the discrete pivot point method	S Bagwell: A Newton Raphson scheme for coupled magneto-mechanical problems applied to MRI scanners	D Jones: A second order accurate Mach-uniform solver for the Euler and Navier-Stokes equations on pairs of mutually orthogonal unstructured grids

COFFEE BREAK

	Room A – Thermodynamics	Room K – Advanced applications 2	Room L – Coupled problems 4	Room M – Fluid dynamics 4
11.00 – 11.30				
11.30 – 11.48	D A Brennar: Mathematical framework for predicting the thermal behaviour of spectrally selective coatings within industrial near infrared furnaces	N Ower: A computational method of obtaining reliable measurement of perosteal cross-sectional area of human radii from laser scans	C H Lee: An entropy-based stabilised Petrov-Galerkin formulation for linear tetrahedral elements in compressible, nearly incompressible and truly incompressible fast solid dynamics	E Hafezi: A CFD case study of using turbulence models for evaluating the performance of a drag based vertical axis wind turbine
11.48 – 12.06	M Iqbal: A-posteriori error estimate for the partition of unity method for transient heat diffusion problems	M Huszar: The influence of apparent-and true viscosity on injection pressure prediction	S Claus: CurFEM: a stabilised Nitsche XFEM method for multi-physics problems	S Kim: Coupled lattice Boltzmann and finite volume method for modelling crossflow microfiltration and nanofiltration
12.06 – 12.24	S Conde: A temperature-based thermodynamically consistent time integration for discrete thermoelastodynamics	A Faramarzi: Evaluation of undrained bearing capacities of skirted foundations	R Ortigosa: A variational framework for large strain polyconvex dielectric elastomers	M Weberstadt: High fidelity methods for compressible flow problems on moving domains
12.24 – 12.42	A Philo: Effects of Hatch pattern and laser parameters on the multi-scale thermal modelling of selective laser melting	H Matallab: An investigation into problems associated with the overheating of air monitoring devices	B Jones: Numerical rheometry of dense particle suspensions using a coupled lattice Boltzmann and discrete element method	T Lake: Particles as porpoise - applying CFD results to environmental interactions
12.42 – 13.00	H Boulechfar: Numerical computation of heat and mass transfer by natural convection through a fluid-saturated porous medium in horizontal elliptical annulus	A Ahangar-Asl: Effects of air permeability and perimeter area on air losses in compressed air tunnelling	R Poya: A computational framework for linearised elasticity coupled with non-linear electro-magneto-static	

FRIDAY – 10th April 2015

LUNCH – Fulton House Refectory (Building 17 on the Campus Map, First Floor)

PLENARY SESSION 4 – Room A – RAINALD LÖHNER

COFFEE BREAK – Award Deliberation

AWARD CEREMONY

13.00 – 13.45

13.45 – 14.25

14.30 – 15.30

15.30 – 16.00

4th ACME SCHOOL

LOW OR HIGH-ORDER: THIS IS THE QUESTION!

To p OR NOT TO p

Antonio J. Gil

Bridging methodologies for the computational simulation of fluids and solids



Antonio J. Gil is an Associate Professor in the Zienkiewicz Centre for Computational Engineering at Swansea University. He graduated as Ingeniero de Caminos, Canales y Puertos from the University of Granada (Spain) and after completing his Masters, he moved to Swansea University where he completed a PhD in the field of computational analysis of nonlinear structural membranes.

His work covers the areas of computational simulation of nanomembranes, biomembranes (heart valves) and superplastic forming of medical prostheses, fluid-structure interaction using immersed methods, modelling of smart electro-magneto-mechanical devices and numerical analysis of fast transient solid dynamics. In 2012, he was awarded the prestigious Philip Leverhulme Prize for his achievements as young investigator in the field of computational mechanics in the United Kingdom.

Paul Ledger

High order hp-finite elements in electromagnetism and coupled problems



Paul Ledger is an Associate Professor in the Zienkiewicz Centre for Computational Engineering at Swansea University. He has a bachelors degree in Civil Engineering with Computational Mechanics from The University of Birmingham and a masters and PhD in Finite Elements in Engineering Mechanics and Computational Electromagnetics, respectively, from Swansea University. He has held post-doctoral positions in Swansea and

then at ETH Zurich, Switzerland, before returning to take up a lectureship in 2006. His research is focused on hp -version finite elements for applications in electromagnetics and coupled electro-mechanical-fluid systems. He has also recently expanded his interests to include the computational solution of electromagnetic inverse problems. For his work on hp -adaptivity he won the ECCOMAS prize for the best thesis of 2002.

Kenneth Morgan

Low order simulation methods for aerospace engineering



Kenneth Morgan is a Professor in the College of Engineering at Swansea University. He received his first degree and his PhD in the Department of Mathematics at the University of Bristol. He joined Swansea University following periods in the Mathematical Physics Department at AWRE, Aldermaston and in the Mathematics Department at the University of Exeter. He has also held the position of Zaharoff Professor of Aviation at Imperial College, London. For many years, his research interests have concentrated on the general area of unstructured grid methods, with applications in fluid mechanics and in electromagnetics.

Kenneth Morgan is the recipient of a NASA Special Achievement Award, the IACM Computational Mechanics Award and the ECCOMAS Prandtl Medal. He is a Fellow of the UK Royal Academy of Engineering and of the Learned Society of Wales.

Rubén Sevilla

High order methods for the next generation of computational engineering software



Rubén Sevilla is a Senior Lecturer in the Zienkiewicz Centre for Computational Engineering at Swansea University. He obtained his degree in Mathematics and the PhD in Applied Mathematics at the Universitat Politècnica de Catalunya. Then he moved to Swansea University where he was appointed as a research assistant in 2009. In 2012 he gained his lecturer position and was promoted to Senior Lecturer in 2015.

His main area of research is the development, analysis and application of high-order continuous and discontinuous Galerkin finite element methods, with applications to computational electromagnetics, computational fluid dynamics and solid mechanics. Of particular relevance is his work on finite element methods with an exact geometry representation, for which he was awarded several prizes, including the ECCOMAS prize to the best PhD thesis of 2009.

PLENARY LECTURES

LUCA FORMAGGIA
POLITECNICO DI MILANO, ITALY



Luca Formaggia is Professor of Numerical Analysis at Politecnico di Milano, Italy. He has obtained his PhD at University College of Swansea (UK) in 1990 with a work on finite elements for compressible fluid dynamics. He then joined Alenia Aeronautica, an Italian Aerospace Industry, where he collaborated on the development of numerical schemes for aerodynamic computations. In 1994 he moved to the CRS4 research center in Cagliari, where he became the head of the CFD unit. In 1998 he moved to the Mathematics Department of EPFL, Lausanne, as First Assistant to the Chair of Numerical Analysis directed by Prof. A. Quarteroni. Since 2002 he is at the Department of Mathematics of Politecnico.

His main research interests are: Numerical methods for PDE's; Engineering applications of numerical analysis; Flow in porous media Mesh adaptation for finite elements; Numerical modeling of the cardiovascular system.

He is Chief editor of the SEMA-SIMAI Springer Series on Applied and Industrial Mathematics, member of the editorial board of the SIAM Journal of Scientific Computing and the International Journal for Numerical Methods in Biomedical Engineering, and of the advisory board of the International Journal for Numerical Methods in Fluids. He is the Secretary of the Italian Society for Applied and Industrial Mathematics (SIMAI) and, since January 2014, responsible of the MOX Laboratory of the Department of Mathematics of Politecnico di Milano.

THE CHALLENGE OF COMPLEXITY IN SEDIMENTARY AND RESERVOIR SIMULATIONS

Luca Formaggia¹, Anna Scotti¹ and Alessio Fumagalli¹

¹MOX Laboratory, Department of Mathematics, Politecnico di Milano, Pza Leonardo da Vinci 32,
20133 Milan, Italy

luca.formaggia@polimi.it, anna.scotti@polimi.it, alessio.fumagalli@polimi.it

ABSTRACT

In this work we will present part of the activity of the `compgeo@mox` group on the numerical modeling and simulation of flow in sedimentary basins and reservoirs. We will focus on a particular aspect, namely geochemical compaction processes and flow in fractured media.

Key Words: *porous media flow; fractured media; geochemical compaction processes*

1. Introduction

Exploitation of oil and water resources, as well as the safe storage of nuclear waste or the sequestration of CO₂ calls for an accurate simulation of underground flows. The challenge is manifold. Properties of the underground rock and of its geometrical configuration are known with a very high level of uncertainty. Different coupled processes are involved: mono or multiphase-flow, chemical reactions, compaction phenomena, heat transfer. Material is usually heterogeneous with the presence of network of fractures and/or faults which typically act as preferential path for the flow (yet, sometimes, when filled with impervious material, they can act as flow barriers). In this presentation we will focus on two aspects, geochemical compaction phenomena and flow in fractured media.

Compaction processes occur in rock layers during sedimentation, and their study is relevant to assess possible over-pressures (i.e. areas where the pore pressure exceeds the hydrostatic value) and the variation of porosity and permeability. Together with the mechanical processes, the fluid ↔ solid conversion, induced by the degradation of solid organic matter or dissolution/precipitation of minerals, affects flow through two basic mechanisms. On the one hand fluid production/consumption by chemical reactions acts as a source/sink term and may cause changes in the fluid pressure and thus in the effective stress experienced by the rock matrix. On the other hand, dissolution/precipitation mechanisms alter the solid matrix porosity, and consequently permeability, in the areas where the reactions occur.

A numerical scheme for the solution of this complex coupled problem, outlined in Figure 1, has been developed [12], and it comprises chemical reactions, rock displacement and flow in the porous matrix, with permeability depending on porosity. It enables to treat, within the same framework, different geochemical processes such as dissolution/precipitation of minerals but also oil and gas generation from solid organic matter. We have used mixed finite elements for the Darcy equations and a mass preserving monotone scheme for the saturation equation. Figure 2 shows the result for the evolution of quartz mineral. The medium is subject to mechanical compaction and, at the same time, quartz may dissolve in water. The dissolution process produces extra porosity and therefore a stronger compaction in the corresponding portions of the domain.

Another challenging application is the simulation of underground flow in the presence of fractures. Fractures (and faults) may affect greatly the effective permeability and storage capacity of the medium and, since their distribution may presents preferential directions, they also introduce anisotropies. They usually display significant variations in connectivity and size over the formation. Large and strongly connected fractures are typically located near bedding planes and fault zones, while small and disconnected

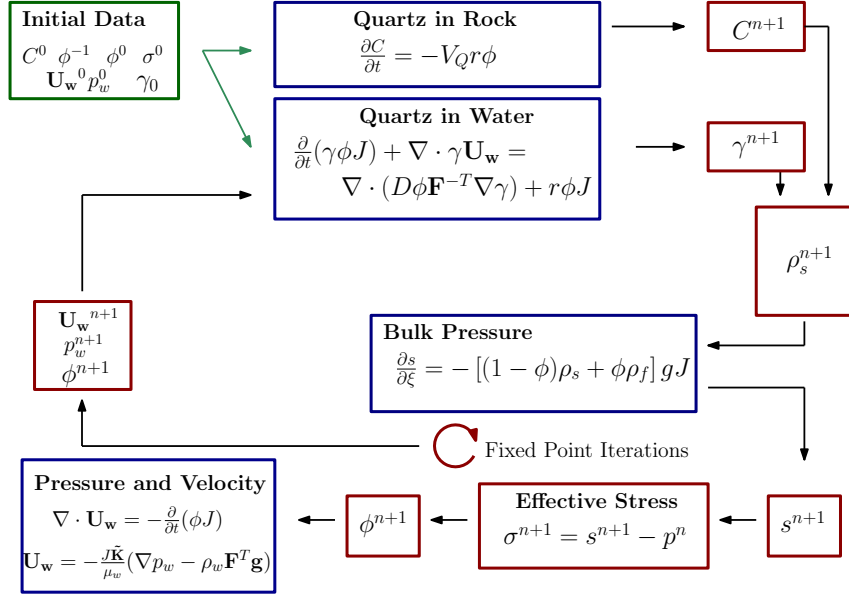


Figure 1: The coupled geochemical compaction problem in the case of mineral precipitation



Figure 2: Concentration of quartz in the rock at $t = 0$ My, $t = 15$ My, $t = 30$ My, $t = 45$ My, and $t = 60$ My during compaction.

fractures are usually located away from those regions. Traditional approaches based on heuristic modification of the permeability or semi-empirical transfer functions, see [18, 4, 3], are insufficient in the presence of a complex fracture distribution, making it impossible to compute transfer function analytically. Thus, numerical upscaling procedures based on realistic fracture characterization need to be applied to compute transfer functions accurately, for instance by solving local problems at grid blocks level [7, 14, 13, 15]. Due to their small aperture compared to the typical dimension of the computational domain it is unfeasible to use a grid capable of resolve fractures. Thus, fractures are modeled as a set of intersecting one co-dimensional manifolds immersed in the porous matrix, and reduced models are derived by projecting the differential equations on the tangent plane, while suitable conditions are imposed at the intersection among fractures [9].

In the presence of realistic fracture distribution the construction of a matching grid can be challenging. One possible strategy is to intersect a regular grid with the fracture network. This gives rise to a mesh of irregular polygons and finite volume or the mimetic finite difference (MFD) method can be used [5, 16, 1, 17, 8, 2]. An alternative, best suited for the study of single fractures or simple networks is to employ extended finite elements [6, 11]. In figure 3 we show an example of fractured media and the solutions obtained by the mimetic and the XFEM scheme described in [8], compared with a reference solution obtained by employing a finite volume scheme on an extremely refined mesh.

In figure 4 we show the result on a complex network of 3D fractures. The computation is part of the nu-

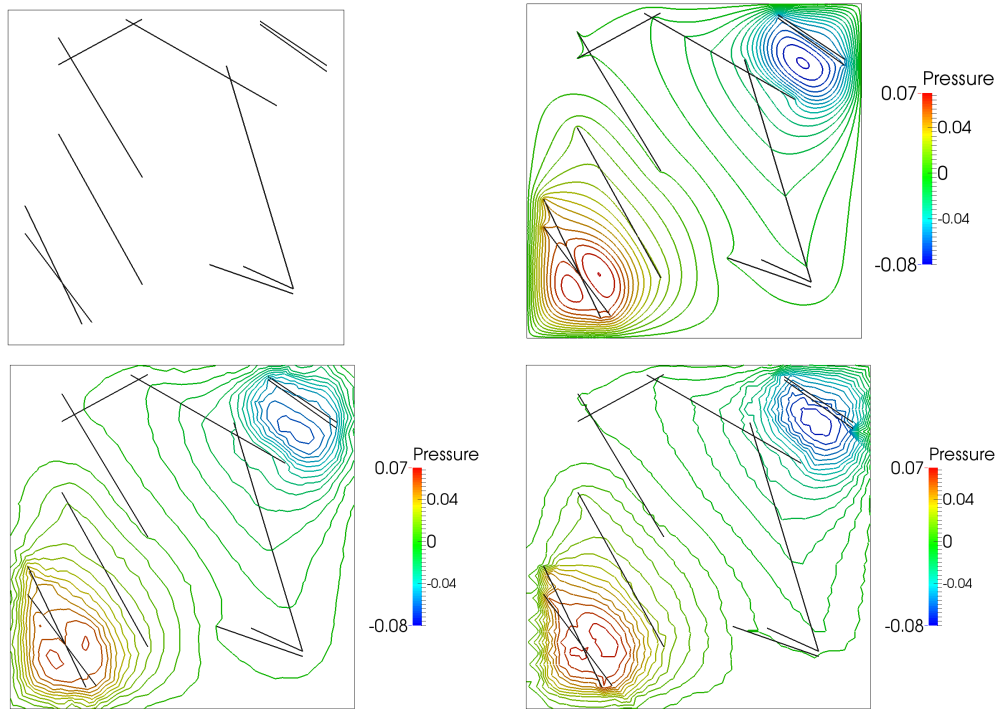


Figure 3: An example of 2D fractured porous media (top-left). Pressure field for a reference solution on a grid with more than 10^6 elements (top-right). Solution obtained by mimetic finite differences (bottom-left) and by the XFEM method (bottom-right). The latter two computations were carried out on a grid of approximately 2000 elements.

merical upscaling procedure described in [10], where equivalent upscaled transmissibilities are computed numerically by solving high resolution local problems.

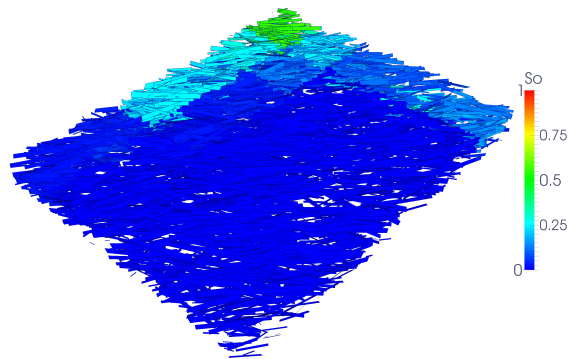


Figure 4: An example of simulation in a complex fracture network. Used within a numerical upscaling procedure to compute equivalent transmissibility.

Acknowledgements

The support of Eni SpA is gratefully acknowledged, as well as that of the Italian MIUR and Indam-GNCS. We also thank Paola Antonietti, Bianca Giovanardi, Nicola Verzotti, Stefano Zonca and all the other members of the compgeo@mox activity group.

References

- [1] F.O. Alpak. A mimetic finite volume discretization method for reservoir simulation. *SPE Journal*, 15(2):436–453, 2010.
- [2] P.F. Antonietti, L. Formaggia, A. Scotti, M. Verani, and N. Verzotti. Mimetic finite difference approximation of flow in fractured porous media. (submitted), 2015.
- [3] T. Arbogast, J. Douglas, Jr., and U. Hornung. Derivation of the double porosity model of single phase flow via homogenization theory. *SIAM J. Math. Anal.*, 21(4):823–836, 1990.

- [4] G.I. Barenblatt and Y.P. Zheltov. Fundamental equations of filtration of homogeneous liquids in fissured rocks. *Dokl. Akad. Nauk SSSR*, 13:545–548, 1960.
- [5] F. Brezzi, K. Lipnikov, and M. Shashkov. Convergence of the mimetic finite difference method for diffusion problems on polyhedral meshes. *SIAM J. Numer. Anal.*, 43(5):1872–1896 (electronic), 2005.
- [6] C. D’Angelo and A. Scotti. A mixed finite element method for Darcy flow in fractured porous media with non-matching grids. *ESAIM: Mathematical Modelling and Numerical Analysis*, 46(02):465–489, 2012.
- [7] L. Durlofsky. Upscaling of geocellular models for reservoir flow simulation: A review of recent progress. In *7th International Forum on Reservoir Simulation Bühl/Baden-Baden, Germany*, pages 23–27, 2003.
- [8] L Formaggia, P Antonietti, P Panfili, A Scotti, L Turconi, M Verani, and A Cominelli. Optimal techniques to simulate flow in fractured reservoir. In *ECMOR XIV-14th European conference on the mathematics of oil recovery*, 2014.
- [9] L. Formaggia, A. Fumagalli, A. Scotti, and P. Ruffo. A reduced model for Darcys problem in networks of fractures. *ESAIM: Mathematical Modelling and Numerical Analysis*, 48(04):1089–1116, 2014.
- [10] A. Fumagalli, L. Pasquale, S. Zonca, P. Panfili, and S. Micheletti. An upscaling procedure for disconnected fracture networks in multiple simulations and scenarios of reservoirs. (in preparation), 2015.
- [11] A. Fumagalli and A. Scotti. A numerical method for two-phase flow in fractured porous media with non-matching grids. *Advances in Water Resources*, 62:454–464, 2013.
- [12] B. Giovanardi, A. Scotti, L. Formaggia, and P. Ruffo. A general framework for the simulation of geochemical compaction. Technical Report MOX Report n. 07/2015, MOX, Department of Mathematics, Politecnico di Milano, 2015.
- [13] B Gong and L. Durlofsky. Upscaling discrete fracture characterizations to Dual-Porosity, Dual-Permeability models for efficient simulation of flow with strong gravitational effects. *SPE Journal*, 13(1):58–67, 2008.
- [14] M. Karimi-Fard, B. Gong, and L. Durlofsky. Generation of coarse-scale continuum flow models from detailed fracture characterizations. *Water Resources Research*, 42(10):1–13, October 2006.
- [15] K.T. Lim, M.H. Hui, and B. Mallison. A next-generation reservoir simulator as an enabling technology for a complex discrete fracture modeling workflow. *SPE Paper 124980*, 2009.
- [16] K. Lipnikov, J. D. Moulton, and D. Svyatskiy. A multilevel multiscale mimetic (M^3) method for two-phase flows in porous media. *J. Comput. Phys.*, 227(14):6727–6753, 2008.
- [17] H.M. Nielsen, J.R. Natvig, and K-T Lie. Accurate modeling of faults by multipoint, mimetic and mixed methods. *SPE Journal*, 17(2):568–579, 2012.
- [18] J.E. Warren and P.J. Root. The behaviour of naturally fractured reservoirs. *SPE J.*, 3(3):245–255, 1963.

RAINALD LÖHNER
GEORGE MASON UNIVERSITY, USA



Rainald Löhner is the head of the CFD center at the College of Sciences of George Mason University in Fairfax, VA, in the outskirts of Washington, D.C. He received a MSc in Mechanical Engineering from the Technische Universität Braunschweig, Germany, as well as a PhD and DSc in Civil Engineering from the University College of Swansea, Wales, where he studied under Profs. Ken Morgan and Olgierd Zienkiewicz. His areas of interest include numerical methods, solvers, grid generation, parallel computing, visualization, pre-processing, fluid-structure interaction as well as shape and process optimization. His codes and methods have been applied in many fields, including aerodynamics or airplanes, cars and trains, hydrodynamics of ships, submarines and UAVs, shock-structure interaction, dispersion analysis in urban areas and haemodynamics of vascular diseases. He is the author of more than 750 articles covering the fields enumerated above, as well as a textbook on Applied CFD Techniques.

RECENT CFD/FSI-BASED DISCOVERIES RELEVANT TO CIVIL ENGINEERING

***Rainald Löhner¹, Eberhard Haug², Alexander Michalski²,
Britto Muhammad², Atis Dreger², Ramakrishna Nanjundaiah² and Raham Zarfam²**

¹CFD Center, M.S. 6A2, College of Science, George Mason University, Fairfax, VA 22030-4444, USA

²SL Rasch GmbH, Kesslerweg 22, Oberaichen, Germany

*rlohner@gmu.edu

ABSTRACT

Two recent discoveries that originated from large-scale computational mechanics calculations are discussed. The first is butterfly effects in massively separated flows commonly encountered in wind calculations. The second is rogue loads for lightweight structures in complex windfields. Both of these discoveries have had a profound influence on the way calculations for such problems are performed.

Key Words: *Butterfly Effects; Rogue Loads; CFD; FSI*

1. Introduction

The analysis and design of lightweight structures exposed to windloads requires an accurate knowledge of the ensuing flowfields and their effect on structural loads and deformations. Time and again structures of this kind have failed catastrophically, highlighting the need to continuously improve the capabilities to calculate all relevant physical mechanisms involved.

All computational building blocks required: computational fluid dynamics (CFD), computational structural mechanics (CSM) and fluid-structure interaction techniques (FSI) have progressed rapidly over the last three decades. A number of excellent reviews summarize the state of the art in CFD [1,2,3]. The aim of the present paper is to report on two recent discoveries that are pertinent to the particular field of computing lightweight structures exposed to windloads: butterfly effects and rogue loads. Both imply much higher CPU demands than expected, highlighting the need to continuously improve field solvers.

2. Butterfly Effects

Flow solvers are widely used for the detailed simulation of natural wind flows in urban settings in order to determine the loads on structures or see how pollutants are dispersed. As far as the flow physics is concerned, most buildings are bluff bodies with sharp angles, leading to massive flow separation with complex wakes. In urban settings, the interplay of natural wind and the wakes of many buildings can lead to extremely complex flows and almost chaotic wind loads on the buildings.

Given the large size of the domains to be simulated (urban settings) the grids currently in use routinely exceed 10^8 elements. Grids of such magnitude make the use of parallel machines mandatory. During a routine benchmarking and scalability study, it was observed that the resulting loads for buildings varied considerably with the number of parallel processors employed. While the mean and maximum loads remained similar, the actual (deterministic) instantiations were completely different. Furthermore, the differences remained very small at the beginning of a typical run, and then grew progressively to a state of total dissimilitude.

Naturally, errors in the code(s) were suspected. The first series of tests checked the repeatability of results: indeed, running the same number of domains/cores yielded the same results. However, once the number of cores/domains was changed, the results became dissimilar after a while. Given the closeness of the results at the beginning of the runs, the suspicion was that perhaps this type of flow exhibits a 'butterfly

effect', whereby small differences can amplify to yield instantiations that are completely different (but statistically equivalent with same mean and maximum loads).

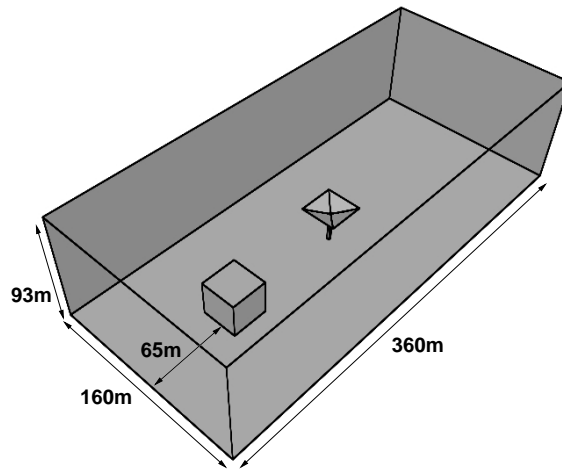


Figure 1a Cube With Umbrella: Problem Definition

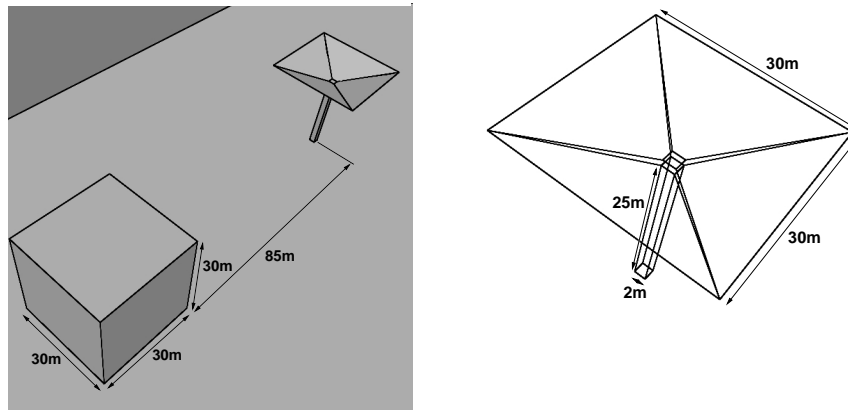


Figure 1b,c Cube With Umbrella: Problem Definition (Detail)

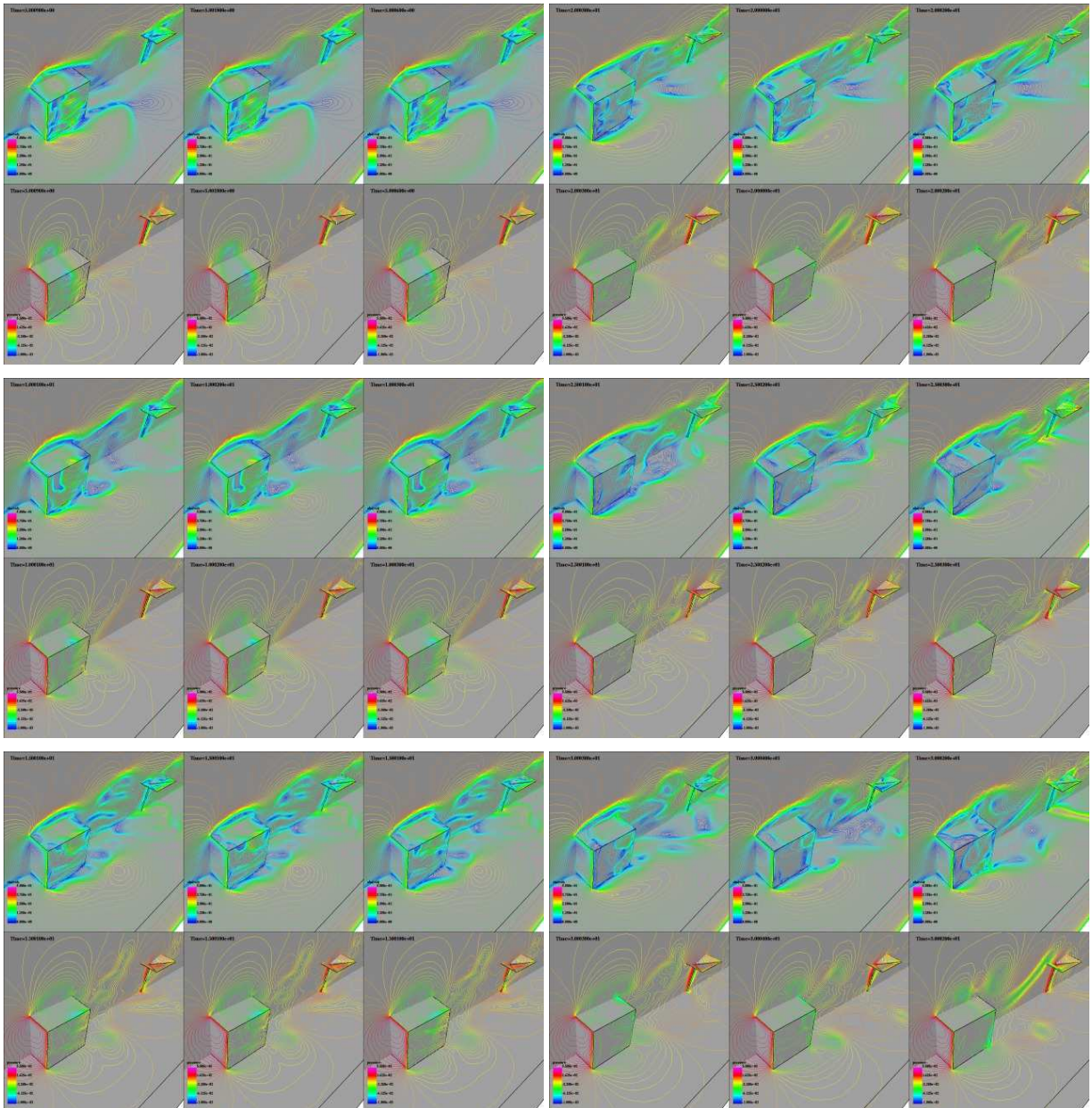
In order to test this hypothesis, a relatively simple geometry that exhibits the types of flows considered here was designed. The geometry is shown in Figures 1a-c. A cube of size $30\text{ m} \times 30\text{ m} \times 30\text{ m}$ is placed in front of an idealized umbrella of height $h = 30\text{ m}$. The flow separates from the cube, and the resulting shear layer impinges on the umbrella. Variations in the height of the shear layer lead to large changes in the loads seen by the umbrella. The flow was simulated using different flow codes (FEFLO, PAMFLOW, OpenFOAM), different settings for the numerical schemes in the codes (residual tolerances, upwind schemes, ...), different number of processors, different mesh types and mesh sizes, and (slightly) different inflow conditions. Surprisingly, all of these changes resulted in variations of similar magnitude [4]. Figure 2 shows a typical result. The code is FEFLO, all flow conditions, numerics and meshes are kept the same, but different (8, 16, 32) number of domains/cores are employed. The top figures are the velocity magnitude and the bottom figures the pressures on the surface and a plane cut through the middle of the domain. Note that initially all flows appear to be the same. However, after approximately the time the leading edge vortex hits the trailing edge, the flowfields diverge from each other until they become completely different instantiations. The resulting body forces, shown in Figures 2g-j, clearly reflect this behaviour. Roundoff errors were suspected as the principal reason for the discrepancy in the results when the number of domains/cores was changed. After all, if the resulting algebraic equation systems are solved iteratively (as is the case here), inner products of very long vectors that are distributed among domains/processors are required. Thus, for a domain-decomposed, distributed memory implementation the scalar product of two vectors, given by

$$s = \mathbf{a} \cdot \mathbf{b} \quad (1)$$

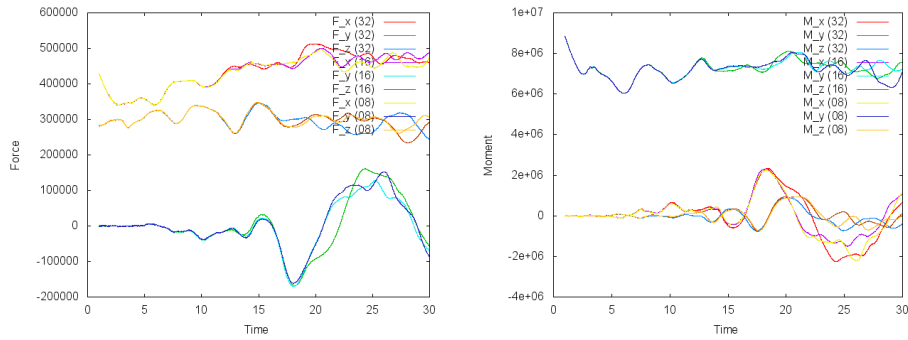
for a single processor becomes:

$$s = \sum_{i=1}^{N_p} s_i = \sum_{i=1}^{N_p} (\mathbf{a} \cdot \mathbf{b})_i, \quad (2)$$

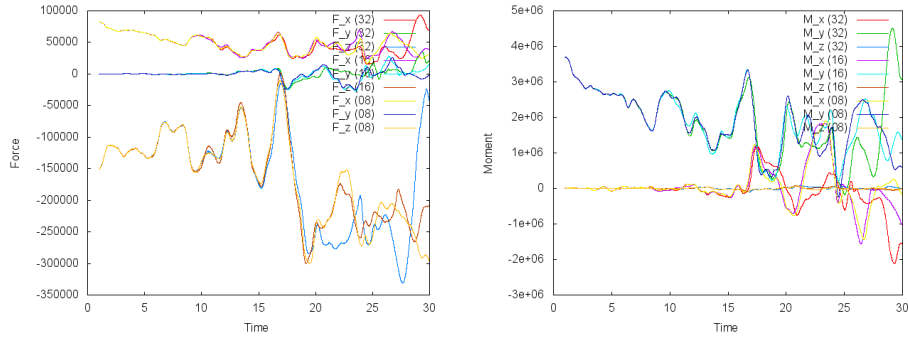
where N_p denotes the number of processors/domains. The order in which the required additions are carried in Eqns.(1,2) are different. This will affect the iterative solver, leading to different instantiations when changing the number of domains/ processors used to compute the flow. The same behaviour was also observed when increasing on a single multicore processor the number of cores used in shared-memory (i.e. OpenMP) mode. The explanation is the same as before, i.e. the order in which the additions are performed is different, leading to differences due to roundoff. In order to mitigate this effect, all entries after the 13th significant digit were set to zero for all inner products. It was surmised that given that we have 15-16 significant digits for double precision (64 bits) calculations, setting these last entries to zero would make the results independent of the number or processors/cores. To our surprise, the introduction of the change merely delayed the onset of the discrepancy in the results, but did not lead to results that were independent of the number of domains/cores. The same behaviour was observed when lowering the tolerances of the PISO solvers in OpenFOAM [4].



Figures 2a-f $T = 5/10/15/20/25/30$ sec:
FEFLO: Same Mesh, Same Inflow, Different Numbers of Domains/Cores (8/16/32)



Figures 2g,h Body Forces and Moments for Cube: FEFLO:
Same Mesh, Same Inflow, Different Numbers of Domains/Cores (8/16/32)



Figures 2i,j Body Forces and Moments for Umbrella: FEFLO:
Same Mesh, Same Inflow, Different Numbers of Domains/Cores (8/16/32)

Given that the same sensitivity of deterministic results is observed with respect to all other possible changes (slightly modified inflow, numerics, mesh, number of processors, ...), the important implications of this ‘butterfly effect’ is that analysts should use the statistically relevant measures of such flowfields instead of the deterministic results of a particular run.

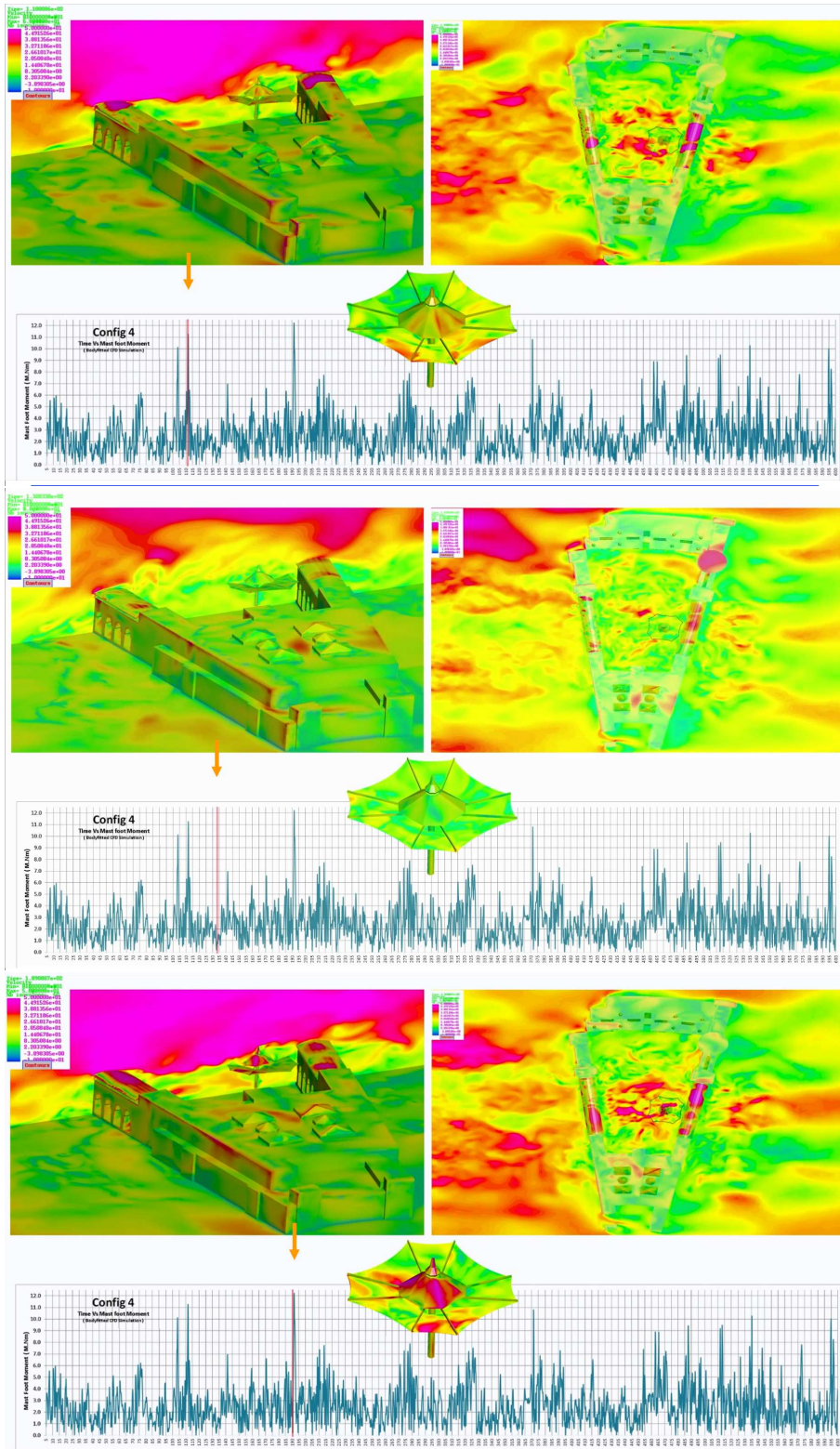
For practical calculations this in turn implies running to much larger times in order to reach statistically relevant ensembles, with the associated much higher CPU time requirements.

3. Rogue Loads

Parasols are often placed in courtyards, plazas or other urban settings. This leads to a very complex fluid-structure interaction problem. The **incoming wind** exhibits many length and timescales in its vortical structures. The possibly complex geometry of the surrounding buildings / city blocks will lead to massive flow separation (even for steady incoming wind), again with many length and timescales in its vortical structures. Furthermore, the parasols (or any lightweight structure for that matter) also have a large range of length and timescales in their eigenmodes (or stiffness, or response times). The interplay and superposition of all of these ‘modes’ can lead to so-called ‘rogue loads’. These are loads that appear in an aleatoric, unpredictable way every so often. They are much higher than the mean, ‘quasi-steady’ loads and their standard deviations [5]. Figure 3 shows a typical case. The upper part of the figures shows the velocity field, while the lower plot depicts the time-history of the mast moment. Note the high variability of all variables, as well as the sudden peaks that appear in the mast moment.

What is worrisome is that they appear to be much higher than the values allowed in building codes and norms (!). The rogue loads were discovered while performing large-scale simulations of (nonlinear) parasols exposed to unsteady wind profiles and/ or flowfield resulting from complex geometries. After the usual denial period (the mind can only see what it is prepared to see), these rogue loads were also seen in experiments. It is interesting to note that similar phenomena have been observed for waves in the ocean. A sudden, short-lived massive wave can appear aleatorically, and may not be seen for many days or years afterwards. Offshore platforms are at constant risk from such ‘rogue waves’.

For practical calculations the possibility of rogue loads implies running fluid-structure interaction calculations to much larger times in order to reach statistically relevant ensembles, with the associated much higher CPU time requirements.



Figures 3a-c Flow Field and Mast Moment for Umbrella (Coupled FSI Run)

4. Conclusions

Two recent discoveries that that originated from large-scale computational mechanics calculations were discussed.

The first of these discoveries are butterfly effects in massively separated flows commonly encountered in wind calculations. Massive flow separation is a chaotic phenomenon. It is therefore not surprising that small roundoff errors can lead to large deterministic differences as time progresses. This butterfly effect, which is also observed in other fields (e.g. crash analysis), implies that only statistical results are well defined. On the other hand, the possibility of butterfly effects also implies much higher CPU requirements in order to obtain statistically relevant data.

The second discovery was the appearance of rogue loads. These are loads that appear in an aleatoric, unpredictable way. They are much higher than the mean, ‘quasi-steady’ loads and their standard deviations. What is worrisome is that they appear to be much higher than the values allowed in building codes and norms (!). From a computational point of view the possibility of rogue loads implies much higher CPU demands than expected, highlighting the need to continuously improve field solvers.

Acknowledgements

It is a pleasure to acknowledge the many excellent collaborators we have been privileged to work with over the years: from the CFD Center at GMU Fernando Camelli, Juan Cebal, Chi Yang, Steve Hanna, Fernando Mut and John Keady, from the Univ. of Delaware Pablo Huq, and from the ESI Group Pierre de Kermel, Philippe Gelenne and David Mas.

References

- [1] B. Blocken - 50 Years of Computational Wind Engineering: Past, Present and Future; *J. Wind Engineering and Industrial Aerodynamics* (2014).
- [2] L. Cochran and R. Derickson - A Physical Modeler’s View of Computational Wind Engineering; *Proc. 5th Int. Symp. Computational Wind Engineering* , Chapel Hill, NC, USA, May 23-27 (2010).
- [3] R. Löhner, D. Britto, A. Michalski and E. Haug - Butterfly-Effect for Massively Separated Flows; *Engineering Computations* 31, 4, 742-757 (2014).
- [4] A. Michalski, P.D. Kermel, E. Haug, R. Löhner, R. Wüchner, K.-U. Bletzinger - Validation of the Computational FluidStructure Interaction Simulation at Real-Scale Tests of a Flexible 29 m Umbrella in Natural Wind Flow; *J. Wind Eng. Ind. Aerodyn.* 99, 400413 (2011).
- [5] T. Tamura - Application of LES-Based Model to Wind Engineering - Implementation of Meteorological Effects; *Proc. 5th Int. Symp. Computational Wind Engineering* , Chapel Hill, NC, USA, May 23-27 (2010).

JAIME PERAIRE
MASSACHUSETTS INSTITUTE OF TECHNOLOGY, USA



Jaime Peraire is the H.N. Slater Professor of Aeronautics and Astronautics and Head of the Department of Aeronautics and Astronautics at the Massachusetts Institute of Technology. He graduated in Civil Engineering from the Polytechnic University of Barcelona (Spain) in 1983 and obtained a PhD in 1986 from the University of Wales (UK). He taught as a lecturer at the University of Wales from 1985 to 1989. During 1989 and 1993, he was a Reader at the Department of Aeronautics at Imperial College, London, and in 1993, he joined the faculty at the Massachusetts Institute of Technology.

His areas of interest are computational aerodynamics as well as computational mechanics and optimization. His current interests include computational mechanics, flapping flight and the design of newly engineered materials. He is the author of over 200 technical papers and serves in the editorial board of several journals. In 2005 he established and co-directed a new MIT SM program in Computation for Design and Optimization (CDO). He is a fellow of the AIAA and IACM.

GAUSSIAN FUNCTIONAL REGRESSION FOR STATE PREDICTION USING LINEAR PDE MODELS AND OBSERVATIONS

N.C. Nguyen¹, H. Men¹, R. Freund² and *J. Peraire¹

¹MIT Department of Aeronautics and Astronautics, Cambridge, MA 02139, USA,

²MIT Sloan School of Management, Cambridge, MA 02139, USA

*peraire@mit.edu

ABSTRACT

Partial differential equations (PDEs) are commonly used to model a wide variety of physical phenomena. A PDE model of a physical problem is typically described by conservation laws, constitutive laws, material properties, boundary conditions, boundary data, and geometry. In most practical applications, however, the PDE model is only an approximation to the real physical problem due to both (i) the deliberate mathematical simplification of the model to keep it tractable, and (ii) the inherent uncertainty of the physical parameters. In such cases, the PDE model may not produce a good prediction of the true state of the underlying physical problem. We introduce a Gaussian functional regression method that incorporates observations into a deterministic linear PDE model to improve its prediction of the true state. Our method is devised as follows. First, we augment the PDE model with a random Gaussian functional which serves to represent various sources of uncertainty in the model. We next derive a linear regression model for the Gaussian functional by utilizing observations and adjoint states. We then apply the principle of Gaussian process to determine the posterior distribution of the Gaussian functional. This allows us to compute the posterior distribution for our estimate of the true state and provide a statistical measure of the prediction error. Furthermore, we consider the problem of experimental design in this setting, wherein we develop an algorithm for designing experiments to efficiently reduce the variance of our state estimate. We provide several examples from heat conduction, the convection-diffusion equation, and the reduced wave equation, all of which that demonstrate the performance of the proposed methodology.

JÖRG SCHRÖDER
UNIVERSITÄT DUISBURG-ESSEN, GERMANY



Jörg Schröder is a Professor of Mechanics and Vice-Rector for Research, Junior Academic Staff and Knowledge Transfer at the University of Duisburg-Essen. He graduated in Civil Engineering from the University of Applied Sciences (FH) Hildesheim/Holzminden (Germany) in 1988. He then obtained his Diplom-Ingenieur (U) and his Doktor-Ingenieur from the University of Hannover in 1992 and 1995, respectively. After holding a four year Research Assistantship position in Stuttgart University and completing his Habilitation thesis in 2000, he became Professor of Mechanics at TU Darmstadt. In 2001, he moved to the Department of Civil Engineering at the University of Duisburg-Essen, where he has stayed since then.

His areas of research interest are computational mechanics, continuum mechanics and constitutive modelling characterisation. Some of his latest work focusses on the computational treatment of polyconvexity for biological materials and the formulation and implementation of mixed finite elements. He is the author of over 200 technical papers and serves on the editorial board of several journals. Since 2009, he has been a member of the Directorate of the International Association of Applied Mathematics and Mechanics (GAMM).

ADVANCED APPLICATIONS 1

Calculating the Minimum Distance Between Two Triangles on SIMD Hardware

*Konstantinos Krestenitis, Tomasz Koziara

School of Engineering, University of Durham, Durham, DH1 3LE

*konstantinos.krestenitis@durham.ac.uk

ABSTRACT

This paper presents an investigation into calculating the minimum distance between two 3D triangles on SIMD hardware. We formulate the problem as constrained minimization and apply a quasi-Newton method to solve its multiple instances simultaneously on separate SIMD vector lanes. We test Intel's open-source ISPC compiler [2], which provides an explicit programming model for writing vectorized code for modern CPUs and GPUs. In the current communication we share our initial experience of producing an optimized ISPC implementation and show some preliminary numerical results.

Key Words: *Triangles, ISPC, SIMD, Minimum Distance*

1. Introduction

We try to find the minimum distance between two 3-dimensional triangles exploiting the Single Instruction Multiple Data (SIMD) parallelism of modern CPUs. The inspiration for this work comes from a paper by Kris Hauser [1], where a robust contact point generation method is proposed in the context of rigid body simulations on unstructured meshes. To avoid ill conditioned contact points that produce jitter and divergence, he introduce a virtual margin around the bodies and sought for pairwise distance between triangles of so expanded meshes. Our optimized subroutine can not only be used to speed up a framework like this, but also, it demonstrates a more general approach to optimizing computational primitives that may seem difficult to improve upon at first. As explicit SIMD-enabled programming models become more available now, it becomes more imperative to exploit this level of hardware parallelism. Consequently, we share our experience in the hope that it can be useful to others.

2. Finding The Shortest Distance Between Two Triangles

Our baseline method is the brute force one. Let v_{1i} , e_{1i} , v_{2i} , e_{2i} be the vertices and edges of triangles T_1 and T_2 . The brute force approach computes all fifteen distances v_{1i} -to- T_2 , v_{2i} -to- T_1 , e_{1i} -to- e_{2i} , and then selects the smallest. This approach is quite simple to implement. Optimization of this method can at most rely on reusing parts of the computation, but it is not possible to avoid a relatively complex branching and therefore it is hard to optimize this approach for SIMD hardware.

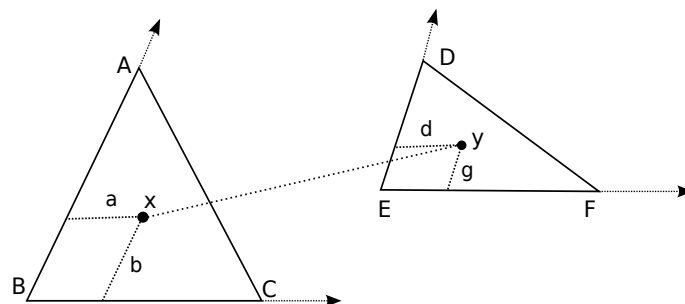


Figure 1: Barymetric Coordinates of a Triangle

Our optimized methods rely on an optimization based reformulation of the minimum distance problem. Triangles can be parameterized using barycentric coordinates. Let x and y be two points, belonging respectively to triangle T_1 and T_2 . Assuming that points A, B, C are vertices of T_1 and that points D, E, F are vertices of T_2 , x and y can be defined using the following equations: $T_1 : \vec{x}(a, b) = \vec{A} + (\vec{B} - \vec{A}) \cdot a + (\vec{C} - \vec{A}) \cdot b$, $T_2 : \vec{y}(g, d) = \vec{D} + (\vec{E} - \vec{D}) \cdot g + (\vec{F} - \vec{D}) \cdot d$. To find the minimum distance between T_1 and T_2 we minimize $f(a, b, c, d) = \|\vec{x}(a, b) - \vec{y}(c, d)\|^2$. What has to be noted is that for x and y to stay within the triangles, the four parameters of the function f have to comply with the six inequality constraints: find $\min f(a, b, g, d)$ such that $\{a \geq 0, b \geq 0, a + b \leq 1, d \geq 0, g \geq 0, g + d \leq 1\}$. This forms the basis of the optimization problem to be solved.

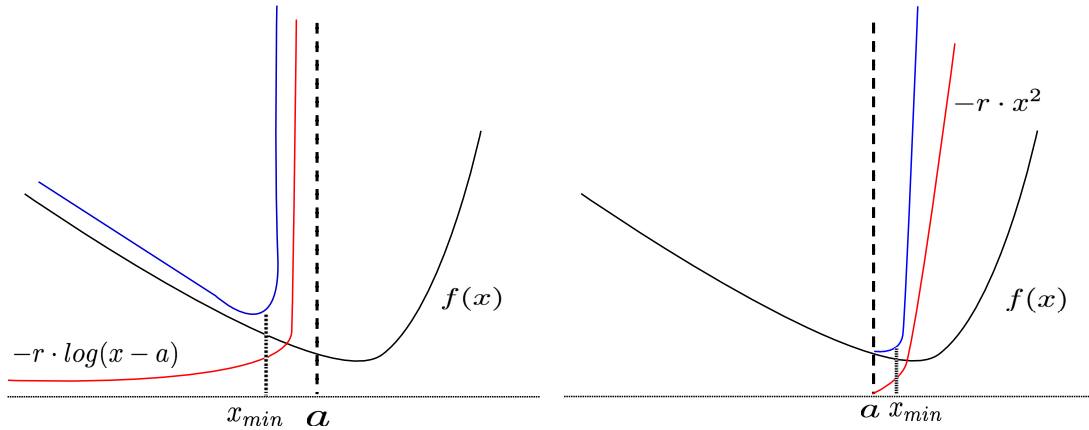


Figure 2: Illustration of: barrier method (left), penalty method (right)

In our exploration of suitable optimization approaches we began by testing the barrier method. The barrier method exploits a logarithmic function in order to incorporate the constraints into an extended objective function: $B(x) = f(x) + r \sum_{i=1..6} -\log(c(x_i))$, cf. Figure 2, left. The barrier method is characterized by its requirement to arrive at the solution from within the feasible region ($B(x)$ is not defined outside of the feasible region). In practice the barrier method has computational difficulties due to the fact that as the boundary of the feasible region is approached the log barrier function becomes infinite. An explicit check and re-positioning has to be made to guarantee that the search remains within the feasible region.

Our second method of choice, the penalty method, is on the other hand slightly different. This approach adds a penalty term to the objective function to penalize the solution when outside of the feasible region: $P(x) = f(x) + r \sum_{i=1..6} \max(c(x_i))^2$, cf. Figure 2, right. Unlike the barrier method, the penalty method doesn't require us to check whether the solution remains within the feasible region at each step. One aspect that needs extra care however, is the invertibility of the Hessian $\nabla^2 P$. Unlike the barrier method, where the log terms are nonzero inside of the feasible region and help to regularize $\nabla^2 B$, the penalty approach exposes the fact that f has multiple minima and $\nabla^2 f$ is singular. Consequently, $\nabla^2 P$ is also singular inside of the feasible region. To overcome that we resort ourselves to a quasi-Newton approach, where the Hessian is approximated by a perturbed operator $\nabla^2 P + \epsilon I$, where I is an identity matrix and ϵ is suitably small. This regularization, also akin to pseudo-transient continuation [3], allows as to avoid line search at the same time. This renders so formulated penalty approach specifically attractive. In the remaining part of the current paper we only focus on the penalty approach.

3. Implementation

For the prototype implementation, included in Algorithm 1, we use MATLAB. The non-optimized code follows a simple sequential pattern. It starts by initializing the edge vectors, the hessian of f , hf and the solution in lines 1-6. It then involves a loop section for the Newton steps, where X, Y are the evaluation of the points on the triangles T_1, T_2 respectively. In line 6 gf is the gradient of the objective function. The constraints h are specified in vector form and their derivatives in a six by four matrix dh . Due to the penalty function $p(x) = r \sum_{i=1..6} \max(c(x_i))^2$ we have to evaluate which constraints are active at each Newton step; we introduce a mask array for each of the six constraints and we use it to form a new matrix dmx that contains the active derivative constraints in line 11. The gradient gra and hessian hes is created to solve the Newton step dx by using the left slash operator. Finally the solution error is

calculated on real geometry in line 21 and the termination condition is checked based on the tolerance supplied by the user.

Algorithm 1 MATLAB version of the TTD test.

```

function x = ttd1(A, B, C, D, E, F, rho, tol)
1  BA = B-A; CA = C-A; ED = E-D; FD = F-D;
2  hf = [2*BA*BA', 2*CA*BA', -2*ED*BA', -2*FD*BA';
3        2*BA*CA', 2*CA*CA', -2*ED*CA', -2*FD*CA';
4        -2*BA*ED', -2*CA*ED', 2*ED*ED', 2*FD*ED';
5        -2*BA*FD', -2*CA*FD', 2*ED*FD', 2*FD*FD'];
6  x = [0.33; 0.33; 0.33; 0.33];
3  for i=1:99
4    X = A+BA*x(1) + CA*x(2);
5    Y = D+ED*x(3) + FD*x(4);
6    gf = [2*(X-Y)*BA'; 2*(X-Y)*CA'; -2*(X-Y)*ED'; -2*(X-Y)*FD'];
7    h = [-x(1); -x(2); x(1)+x(2)-1; -x(3); -x(4); x(3)+x(4)-1];
8    dh = [-1, 0, 1, 0, 0, 0; 0, -1, 1, 0, 0, 0;
9          0, 0, 0, -1, 0, 1; 0, 0, 0, 0, -1, 1];
10   mask = h' >= 0;
11   dmax = dh.* [mask; mask; mask; mask];
12   gra = gf + rho * dmax * max(0,h(:));
17   hes = hf + rho*dmax*dmax' + eye(4,4)/rho^2;
18   dx = hes\gra;
19   DX = BA*dx(1) + CA*dx(2);
20   DY = ED*dx(3) + FD*dx(4);
21   error = sqrt(DX*DX'+DY*DY');
22   if error < tol, break; end
23   x = x - dx;
24 end
25 end

```

The sequential MATLAB prototype forms the basis for the implementation of the optimized version of the algorithm. The optimized code uses the Intel SPMD Program Compiler (ISPC) [2]. ISPC is a C language extension for SIMD high performance CPU programming. It's designed to deliver very high performance on CPUs thanks to effective use of both multiple processor cores and SIMD vector units.

SIMD vector units allow to execute in parallel certain algebraic operations on data items with suitable memory alignment. Since our Newton method, cf. Algorithm 1, is relatively light, the key insight to optimizing it is in running multiple Newton methods (form multiple triangle pairs) in parallel on individual SIMD vector lanes. On each vector lane, we try to balance out the amount of computation and the amount of data movement (i.e. reads and writes) by suitably restructuring the algebra and the use of temporary variables. Hence, even though ISPC provides a suitable programming model, in order to take full advantage of the architecture of modern CPUs, it is still vital to hand craft the ISPC source code. We share the experience of optimizing Algorithm 1 below.

The optimized C version exploits matrix symmetries to reduce repetitions of calculations for matrix elements, e.g. hf in the above code is using symmetry for that reason. For the same reason X-Y is only calculated once and stored into a variable XY so that its value is accessed instead of being repetitively calculated. Inside of the Newton loop the optimized algorithm is totally different from the prototype. The derivatives of the constraints are stored in an array instead of the sparse matrix, so only the non-zeroes are used. Operator $\max(0, h(:))$ is calculated without the use of the std library function $\max()$ which is too generic for our code. We replace it with if statements and directly assign values to an array of active derivatives of constraints dmax, avoiding the masking operations in lines 10-11. The gradient gra is calculated so that any redundant operations are removed. The same techniques are used for the hessian matrix hes. The point here is to end up with as few assignments as possible. The most significant aspect of the optimized algorithm is the linear solution in line 18. Unlike MATLAB, which exploits a separate linear solver, in our implementation individual operations of a 4x4 Gaussian elimination have been

merged with the rest of the algorithm in a monolithic manner. This means that Gauss elimination, calculating of the gradient and calculation of the hessian are all fused together, still minimizing the number of necessary assignments to temporary variables. Operations like division are also limited because of their computational latency, operations like addition, subtraction and multiplication are preferred. Memory allocation is never done dynamically.

4. Performance

All methods were implemented in C in both sequential and SIMD code. The performance comparison comprises calculating the minimum distance between a pair of triangles replicated one thousand times and the average run-time is taken for both penalty and brute force approaches. As it can be observed

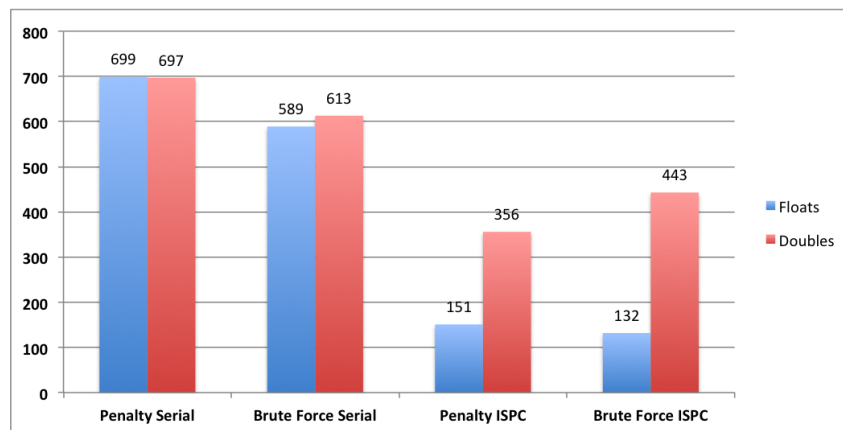


Figure 3: Illustration of run time comparison of the methods

in Figure 3 from the comparison of the serial codes for double precision, the penalty is slightly slower than the brute force approach. But when we compare the ISPC version of both methods, there is a gain in performance for penalty approach because it can exploit SIMD vectors more efficiently. The ISPC version of the penalty approach has nearly doubled or quadrupled its performance compared to its serial code for double and single precision versions respectively. Brute force method on the other hand behaves less consistently: its double precision ISPC version is outperformed by the penalty approach, while its single precision ISPC version outperforms the penalty method. We know that an ideal speedup for SIMD code is 8x in single and 4x in double precision, using the AVX instruction set on an Intel 2.3GHz i7 CPU that is used here. We think that achieving roughly half of this peak performance could be due to the throughput limit of the memory bus (1600 MHz DDR3 RAM), yet further checking is needed.

5. Conclusions

Tackling multiple small nonlinear problems is not uncommon in computational engineering. Our intention behind this study was to investigate whether such problems can still be optimized using SIMD hardware and ISPC. Our optimized penalty implementation shows that it is indeed possible to computationally gain from SIMD implementation and even outperform the brute force method (double precision). Further performance testing will be conducted for random sets of triangles. Furthermore a thorough performance profiling will be done in the hope of resolving the current computational bottleneck (i.e. the 2x and 4x speedup achieved versus the 4x and 8x speedups expected, based on SIMD vector width for AVX instruction sets used here).

References

- [1] Kris Hauser. Robust Contact Generation for Robot Simulation with Unstructured Meshes. *Intl. Symposium on Robotics Research*, 2013.
- [2] Matt Pharr, William R. Mark. ispc: A SPMD Compiler for High-Performance CPU Programming. Intel Corporation. *Innovative Parallel Computing (InPar)*, 1 - 13. 2012.
- [3] Todd S. Coffey, C. T. Kelley, David E. Keyes. Pseudo-transient continuation and differential-algebraic equations. *SIAM J. Sci. Comp*, Vol. 25, 553–569. 2013.

Point cloud data from Photogrammetry techniques to generate 3D Geometry

*David W. James, Juergen Eckermann, Fawsi Belblidia and Johann Sienz
School of Engineering, Swansea University, Singleton Park, Swansea, SA2 8BJ

[*d.w.james@swansea.ac.uk](mailto:d.w.james@swansea.ac.uk)

ABSTRACT

Most 3D modelling techniques require 3D CAD data. Often the subjects of modelling are real objects for which no 3D CAD data exists for. Photogrammetry is the practice of extracting 3D spatial dimensions from 2D two or more photographs taken at different locations. This information can then be used to produce CAD data via production of 3D point clouds. In this work we look at refining the photographic techniques used to capture the image to improve the consistency and accuracy of the generated point clouds. A model car (jaguar e-type) is the used as the object of this work and various methodologies were used to improve the quality of the extracted point cloud data. The improvements in methodology are related to factors in the extraction algorithm. The software packages 123D catch by Autodesk and Agisoft Photoscan are used to extract the point cloud data.

Keywords: *photogrammetry; 3D CAD; computer vision, geometry, 3D scanning*

1. Introduction

Computational modelling is a vital engineering tool and key to many industrial applications. There are many different 3D modelling techniques to look at areas such as stress analysis, fluid flow, impact testing etc and numerous numerical schemes to simulate the appropriate physics. In general these modelling techniques start with geometry of the part or system that requires modelling. Traditionally geometry is produced from 3D CAD. In some circumstances the object to be modelled has already been made and no CAD is in existence. This can include historical parts or natural parts. CAD of such parts can be produced from point clouds which give the location of many points on the surface of the object. Two main methods of extracting 3D point clouds exist: 3D scanning and photogrammetry. The 3D scanning techniques can be further sub-categorised into laser scanning and structured light scanning. Spatial data is obtained by moving the laser head or the structured light cameras relative to the object being scanned to obtain point clouds of the object, or sections of the object if it too large. With photogrammetry techniques 3D data is obtained by triangulation of the same feature in different spatially shifted 2D photographs. The resolution of 3D scanning techniques is generally higher than photogrammetry. The disadvantages of 3D scanning technologies have in common is the high cost of equipment, the generation of cloud point data that cannot be easily handled due to the number of cloud points, long processing time aligning point clouds and a great deal of expertise using in using scanning equipment. Also the time taken to collect the scans for large objects can be of the order of days [1]. With this in mind the benefits of photogrammetry over 3D scanning are:

- Much lower equipment expense. A consumer grade digital camera can be used to capture the images.
- Lower number of point data points allowing for easier processing. The number of data points to be calculated can be controlled by the user in photogrammetry software.
- Much reduced time obtaining photographs as opposed to 3D scans and much easier for a non-specialist to perform.

After 3D cloud point data is generated post processing is required to clean and smooth the cloud points using software such as Geomags studio. Triangular meshes are generated from the point cloud normally using Delaunay triangulation [2], then surfaces generated from the meshes and if required solid geometry generated. This stage requires a great deal of input from the user which cannot be avoided for either technique; however this is an area of continual improvement. In general photogrammetry will not capture the fine features of an object in the same way 3D scanning can. However this might actually prove an advantage to the modeller as CAD geometry usually has to be defeatured to minimise small elements which are not important to the problem and cause excessively high computation times. There are examples in the literature of photogrammetry techniques being used to obtain geometry for modelling applications [3] [4].

This work presents a case study on refining the process of taking photographs to produce the point cloud. A model jaguar e-type car is used as the subject and various improvements to the photography process are demonstrated. A set of images could easily be captured in less than one hour. The model used exhibits known problematic areas for photogrammetry such as shiny surfaces.

2. General steps of extracting point clouds from photos

The steps required to extract point cloud data from a series of photographs are:

- 1) Feature recognition – each photograph is analysed and key features which are invariant to scale and rotation that may be potentially used to align the photos. Generally variations of the SIFT algorithm developed by D. G. Lowe [5] [6] is used. A mathematical description of each feature is made and stored.
- 2) Feature matching – features have to be matched between photos. There are a range of algorithms available to perform this computation.
- 3) Alignment of cameras – the coordinates of the cameras relative to each other and the recognised features is calculated by minimising the error between distances on images and expected distances for all cameras. Minimisation is usually performed using Levenberg-Marquardt algorithm and is collectively known as bundle adjustment.
- 4) Construction of dense point cloud – once the cameras are aligned and distances between key features are known construction of the dense point cloud can begin. This step is the most computationally intensive.

3. Software

Two software packages were used to obtain point cloud data from photograph collections. Autodesk 123D catch which is a free cloud based software where images are uploaded to Autodesk's server for computation and a triangular mesh is returned. A commercial version is available for a small fee. The results returned by 123D catch are impressive but the amount of user control is limited. Agisoft's photoscan is a commercial photogrammetric software where computation of results is performed on the user's own hardware. The results are generally not as robust as 123D catch but the amount of control the user has over parameters such as size of the point cloud, export formats etc is much greater. Photoscan can produce a triangular mesh from the point cloud and add in the texture. The point cloud can also be exported directly which is useful for manipulations and mesh clean-up in other software. With 123D catch no point cloud is given, only the mesh with a texture applied to it.

4. Methods

Photos were taken with a Canon 550d camera a low to mid-range digital SLR camera which is commonly available at photographic retailers. Two lenses different lenses were used: i) canon 17-85mm EF-S zoom lens and ii) canon 50mm prime lens. Photographs were taken moving around the model in regular intervals in order to capture all of its features. The model was kept central and the camera was repositioned for each photograph in a series (see Figure 1). This was repeated at one or two additional heights.

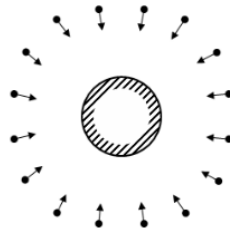


Figure 1 Circle represents object being photographed and arrows represent camera locations

A brief summary of some of the techniques used to improve the quality of the point cloud are described below:

Camera stability

To minimise image noise low ISO settings are used. The object is required to be in focus as much as possible and therefore good depth of field is required. To capture good depth of field a small aperture is required. In this work $f/11$ is used. The low ISO and small aperture require a low shutter speed in order that enough light enters the camera. To minimise blur due to the shutter speed a tripod is used and a remote trigger, so that the camera is as stable as possible and is not disturbed by the process of taking a photograph.

Small and consistent translations of the camera

Construction of point cloud data was found to be improved if small and consistent movements of the camera, with each point of the object visible in several images. Good results were found when the camera was kept a constant radius from the centre of the car and the camera was moved in 15° increments.

Shininess and lighting

The shininess of the model car resulted in specular reflections and reflections of other objects in the models surface. The reflections are in different locations in each picture as the camera moves. However they are particularly prevalent features and are identified by the feature recognition algorithm. As they are similar they may be matched during bundling giving false results. The windows of the model gave particularly poor results. It was found taking photos in areas where there was a constant light source and no spot light sources, such as light fittings helped. Coating the car with a matt powder gave the biggest improvements. This can be seen Figure 2 shows two photos at different locations from a range of images with and without the key features shown. The model has been coated with powder but it has been rubbed off the door. It can be seen that the reflection of the models wing mirror in the door is recognised in both images; however it has shifted relative to the rest of the model. Figure 3 shows the constructed point cloud. While for the majority of the model the dense cloud point is a good representation the door is badly reconstructed. This demonstrates the importance of minimising the shininess of the surface and the reasons that the shininess can cause problems for photogrammetry techniques.

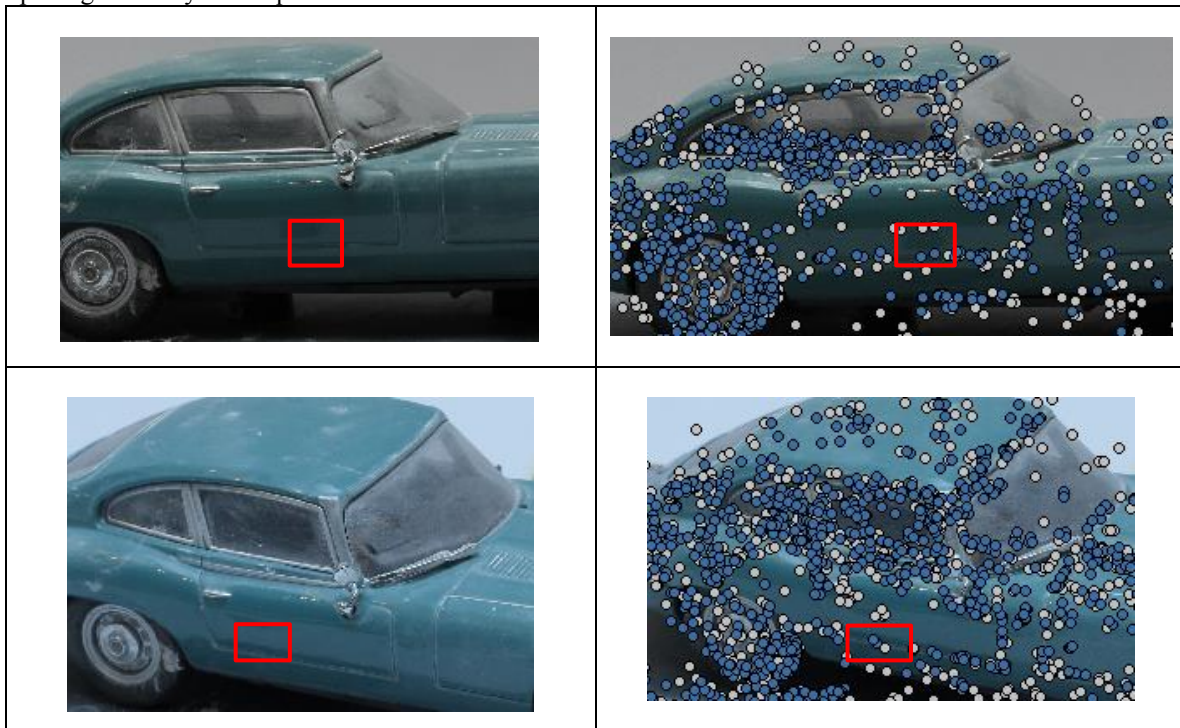


Figure 2 Movement of false recognised feature (reflection of wing mirror in door) due to shininess. Images on the right of the picture show key features that have been recognised. Wing mirror reflection in red boxes



Figure 3 Photoscan point cloud reconstruction of model from photos shown in Figure 2.

5. Final Results

Figure 4 shows 123D Catch results of photogrammetric construction of the car with a refined series of photos. It can be seen that most of main features are well represented. The time taken to achieve these results is less than two hours from start to finish and the equipment budget is less than £500. This represents a significant saving in both time and cost over 3D scanning techniques.

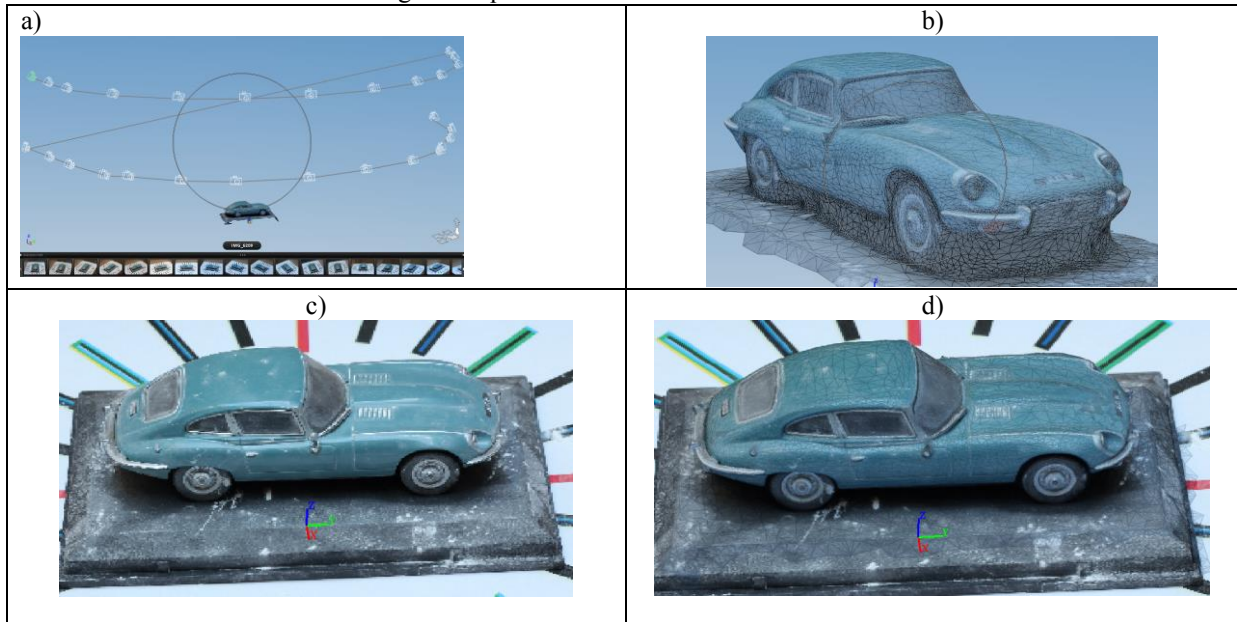


Figure 4 a) 123D Catch showing model with camera positions and photograph series b) textured mesh of model c) photograph from series d) photograph in 4c with mesh superimposed

6. Conclusions

Photogrammetry is a suitable technique for quickly and efficiently extracting 3D point cloud data which can then be used to create CAD models. It has many advantages over 3D scanning techniques for the modeller such as speed and cost. The algorithms used to extract the data are reasonably mature and robust. However care should be taken when capturing images to achieve good results. It is especially important to minimise the shininess of the surfaces being photographed as movement of specular reflections can lead to features being recognised that move relative to object being photographed.

7. References

- [1] S. Alai, "A Review of 3D Design Parameterization using Reverse Engineering," *International Journal of Emerging Technology and Advanced Engineering*, vol. 3, no. 10, 2013.
- [2] B. Delaunay, "Sur la sphère vide. A la mémoire de Georges Voronoï," *Sur la sphère vide. A la mémoire de Georges Voronoï, Bulletin de l'Académie des Sciences de l'URSS, Classe des sciences mathématiques et naturelles*, vol. 6, pp. 793-800, 1934.
- [3] S.P. Broderick, B.J. Doyleab, E.G. Kavanagh & M.T. Walsh, "Photogrammetry for use in biological surface acquisition: investigation of use, geometric accuracy and consequence on analysis," *Computer Methods in Biomechanics and Biomedical Engineering: Imaging & Visualization*, vol. 1, no. 4, 2013.
- [4] G. F Clauss and W. Heisen, "CFD analysis on the flying shape of modern yacht sails," in *Maritime Transportation and Exploitation of Ocean and Coastal Resources*, Berlin, Taylor and Francis Group, 2005, pp. 87-103.
- [5] D. G. Lowe, "Distinctive Image Features from Scale Invariant Keypoints," *International Journal of Computer Vision*, vol. 60, no. 2, pp. 91-110, 2004.
- [6] D. G. Lowe, "Object Recognition from local scale-invariant features," in *International Conference on computer vision*, Corfu, 1999.

Finite Element Analysis on Knee Joint for Knee OA Patients

K. THEEKAROCHANAKUL, A.A. JAVADI

College of Engineering, Mathematics and Physics Sciences, University of Exeter, Harrison Building, Streatham
Campus, University of Exeter, North Park Road, Exeter, EX4 4QF

*kt301@exeter.ac.uk

ABSTRACT

Osteoarthritis (OA) is a disease that influences the body joints. Knee OA is a degenerative, painful disease that can have crippling effects on those afflicted. Nearly every aging person develops knee OA to some extent. OA causes damage to the articular cartilage which results in severe pain in the joint. In order to design a system to help OA patients, a detailed understanding of the mechanical behaviour of knee joint is essential. This paper presents a study of the behaviour of knee joint using the finite element model. Axisymmetric condition and a relatively simple material behaviour are assumed in the first model. The results show that the developed model can be used to predict the stresses and strains in the knee joint. More realistic 3D geometry and a more accurate material model (especially for the cartilage) are needed to predict the distribution of stresses and strains more accurately. This will help to improve the understanding of the behaviour of knee joint system which in turn can be used to design remedial actions for OA patients and those with knee injuries.

Keywords: knee Osteoarthritis (knee OA); cartilage; orthosis; knee brace; FEA

1. Introduction

Knee anatomy and its functions

Human walking is a result of a complex process involving the brain, spinal cord, peripheral nerves, muscles, bones and joints [8]. Human walking requires the coordination of multiple muscles and joints to simultaneously move the legs in a periodic pattern, support body weight and maintain dynamic stability. Coordination may be simplified by taking advantage of the passive dynamics of the legs which can perform all of these functions automatically [8].

Knee diseases –OA

Osteoarthritis (OA) is a disease that influences the body joints. The most common affected joints are in the hands, spine, knees and hips. Knee OA is a degenerative, painful disease that if left untreated it can have crippling effects on those afflicted. Unfortunately, nearly every aging person develops knee OA to some extent [4]. OA causes damage to the articular cartilage (protective surface of the knee bone) and mild swelling of the tissues in and around the joints. OA is one of the most common causes of disability in the world. It is regarded as a whole joint disease with a multifactorial aetiology, including increased mechanical stress, ligament derangements, cartilage degradation, subchondral bone changes and muscular impairments [9]. However, not all knee pains are associated with OA, there are other diseases e.g. patella tendonitis, chondromalacia, Osgood-Schlatter disease or gout that can also cause pain to the knee, either acute or chronic [5]. In addition, obesity and lower limb misalignment have also been associated with increased risk for knee OA [7].

In OA patients, the cartilage (connective tissue) between their bones gradually degrades leading to painful rubbing of bone on bone in the joints. Sitting between the upper and lower leg bones at the knee joint are rubbery pads of tissue called menisci. These cushion the bones, acting as shock absorbers. The menisci can become worn as one gets older, and are commonly the reason for knee pain in middle-aged people. A meniscus can also be torn after suddenly twisting the knee joint, resulting in pain, swelling and, occasionally, locking of the knee. However, the illness caused by

muscle weakness, ligaments, nerves, degenerative bone disease or cerebrovascular disease can be treated, whether medical or surgical treatment including physiotherapy. The damage of these symptoms may cause tearing in the cartilage soft tissue due to the force of body weight, where activities such as walking, running or squatting cause great pain to the patient. In some cases, rehabilitation may be impossible and especially some older people with OA, who are not fit for surgery, will continue to suffer with pains.

There are a number of devices that assist in walking and knee pain relief, ranging from staff to robotic devices. Several knee braces are available in the market not only dealing with the OA but also with some other diseases or injuries. Some braces may not be comfortable to wear or slim enough to put under dress. Furthermore, when the device is more complicated, it is more expensive, which makes it unaffordable to some patients. The main focus of this research is on the design of a new knee bracing system which allows effective control of the transfer of forces through the knee joint. This can reduce the amount of force that is transferred through the joint and hence reduce the pain and improve mobility. The study of knee anatomy and the mechanical behaviour of knee are important part of this research

This paper presents a study of the mechanical behaviour of knee joint. The important knowledge is to understand the function and the behaviour of human knee. The understanding of how the force that applied by human body weight to the cartilage, the distribution of stress at the contacted surface of the cartilage and the deformation that occurred. This study is a part of the main research of the authors which leads to the creation of the new knee bracing system.

The first model of the knee joint is developed and used to study the mechanical behaviour of knee system using the finite element method. An axisymmetric model of knee joint is built by using ABAQUS 6.13-1. Pressure is applied on the top boundary of the model representing the weight of human body. There are two boundary conditions that are applied to this model. Axisymmetric boundary condition is assumed on the left boundary while the displacements are fixed on the bottom of the model in X and Y directions (Figure 1). The boundary condition and linear elastic material properties are applied based on published information (e.g., [1]). Different material properties are considered for bone and cartilage. The Young's moduli of bone and cartilage are considered as $E_{\text{Bone}} = 5\text{GPa}$, and $E_{\text{Cartilage}} = 5\text{MPa}$ and their Poisson's ratios as $\nu_{\text{Bone}} = 0.3$ and $\nu_{\text{Cartilage}} = 0.46$ respectively. Furthermore, the behaviour of the cartilage can be best represented by a pore elastic material model. The permeability of the cartilage is 4.7×10^{-12} mm/s and void ratio is assumed to be 1. The unit weight of the liquid in the cartilage is assumed to be 1×10^{-5} . The dimensions of the model are described in Figure 1. Contact condition is used in this model. A surface-to-surface contact interaction is applied to the sections 1 and 2 (Figure 1). The normal behaviour is set to hard contact and the tangential behaviour is set to frictionless. The small sliding setting is used in this model. 8-node quadratic quadrilateral elements with additional pore fluid pressure degree of freedom are used in the discretisation of the domain. Sections 1 and 2 have a slightly finer meshing than Femur and Tibia.

The system is subjected to a vertical pressure of 392 N, approximately 0.3 MPa, representing the weight in an average person that goes through a leg. The results of distribution of vertical stresses and vertical deformations of the knee joint are shown in Figure 2. Figure 2a shows the contours of distribution of vertical stresses and the distribution of the vertical deformations are shown in Figure 2b.

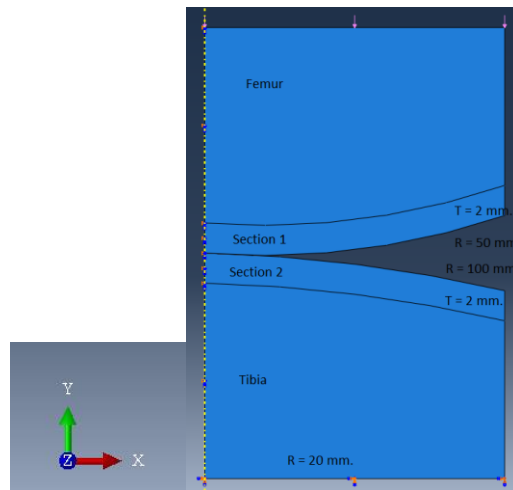
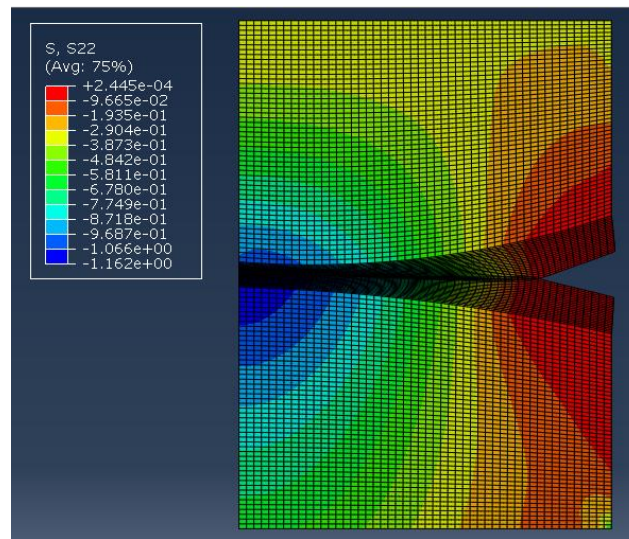
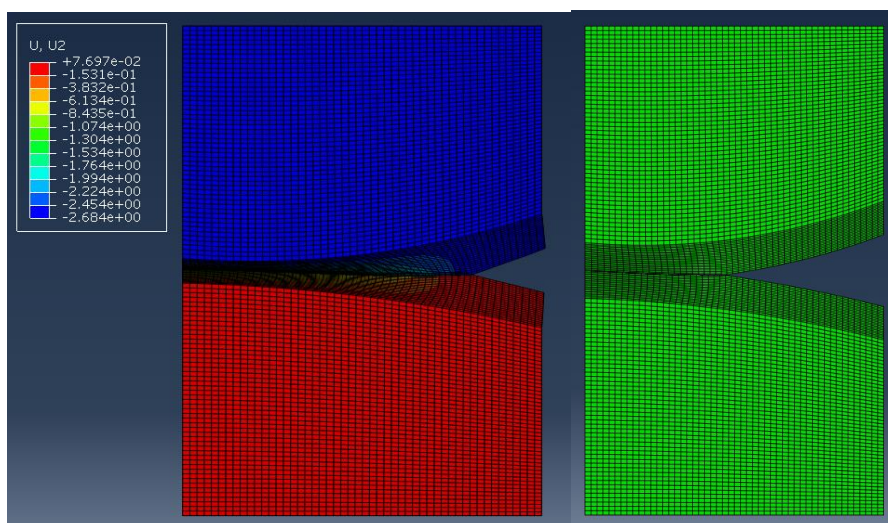


Figure 1 Geometry of the model, loading and boundary conditions



(A)



(B)

(C)

Figure 2 (a) Distribution of vertical stresses, (b) Distribution of vertical displacement, (c) unreformed shape

2. Result and Discussion

Figure 1 shows the geometry and the dimensions of the model before loading (undeformed). For simplicity, axial symmetry is assumed in the first model. Hence only a radial section of the model is analysed. The radii of bone and cartilage of femur and tibia are 50 mm and 100 mm respectively. Figure 2 shows the results of distributions of stresses and deformations in the knee joint. Figure 2A shows the distribution of vertical stresses in the knee while the distribution of vertical deformations is shown in Figure 2B. At the contact surface between the two cartilages there is a high stress concentration which leads to the deformation of the cartilage by about 1.16 mm. Figure 2B shows that largest deformation occurs in the contact surface of the cartilage.

Due to the page and time limitations further results and explanations will be presented at the conference.

3. Conclusions

Cartilage is an important part of a human body. It absorbs a large amount of force from body weight, preventing the pain in several joints. The damage that occurs to the cartilage causes pain and affects the normal life routine. To understand the behaviour of a knee joint and the mechanism of damage in the cartilage, a finite element model of the knee joint is developed. For simplicity, axisymmetric condition and a relatively simple material behaviour are assumed in the first model. The results show that the developed model can be used to predict the stresses and strains in the knee joint. More realistic geometry and a more accurate material model (especially for the cartilage) are needed to more accurately predict the distribution of stresses and strains. This will help to improve the understanding of the behaviour of knee joint system which in turn can be used to design remedial actions for OA patients and those with knee injuries.

This is a part of an ongoing research in the Computational Geomechanics Group at Exeter University involving development of a new knee bracing system. Further analysis and results, including the time-dependent behaviour of the knee joint system will be presented at the conference.

References

- [1] Bogatay, W., 2009. Finite Element Analysis of Knee Cartilage with an Osteochondral Graft.
- [2] Brouwer RW, van Raaij TM, Verhaar JA and Bierma-Zeinstra, S.M.A., 2009. Brace treatment for osteoarthritis of the knee: a prospective randomized multi-centre trial. *Osteoarthritis Cartilage* 2006; 14(8):777-83.
- [3] Dean, JC and Kuo, AD., 2008. Elastic coupling of limb joints enables faster bipedal walking. *Depts. Of Biomedical Engineering and Mechanical Engineering, University of Michigan*
- [4] Elliott, G.A., 2012. Design and Evaluation of a Quasi-Passive Robotic Knee Brace: on Human Running
- [5] Hutcheon, O. and Vhadra, R., 2013. Knee Pain Treatment. Patent application number: 20130012850
- [6] Ibrahim, B.S.K., 2011. Modelling and Control of Paraplegic's Knee Joint (Fes-Swinging). Thesis
- [7] Kirane, Y., Orth, D., Zifchock, R. and Hillstrom, H., 2010. Offloading strategies for knee osteoarthritis. Available at: <https://lowerextremityreview.com/article/offloading-strategies-for-knee-osteoarthritis>
- [8] Lee, G. and Pollo, F.E. 2001. Peer review: Technology Overview: The Gait Analysis Laboratory. *Journal of Clinical Engineering*.
- [9] Popa, D., Tarnita, D., Tarnita, D. and Lordachita, L., 2012. About the Simulation of the Human Knee Joint for Walking Locomotion.
- [10] Van Raaij TM, Reijman M, Brouwer RW et al. Medial Knee Osteoarthritis Treated by Insoles or Braces: A Randomized Trial. *Clin Orthop Relat Res* 2010.

Comparison of the Lagrangian approach for modelling the heel-to-toe contact in passive dynamic walkers with the discrete pivot point method

W.G. Charles, P. Mahmoodi, *R.S. Ransing, I. Sazonov and M.I. Friswell

College of Engineering, Swansea University, Swansea SA2 8PP, UK

*r.s.ransing@swansea.ac.uk

ABSTRACT

Traditional biped walkers based on passive dynamic walking usually have flat or circular feet. This foot contact may be modelled with an effective rocker - represented as a roll-over shape - to describe the function of the knee-ankle-foot complex in human ambulation. Mahmoodi et al. [1] has modelled this roll-over shape as a discretized set of pivot points. In this paper, Lagrangian mechanics are used to formulate non-discrete ordinary differential equations for the stance phase that conserve mechanical energy. Qualitative insight can be gained by studying the bifurcation diagrams of gait descriptors such as average velocity, step period, mechanical energy and inter-leg angle for different gain and length values for the feet, as well as different mass and length ratios. The results from both approaches are compared and discussed. This research is not only useful for understanding the stability of bipedal walking, but also for the design of prosthetic feet.

Key Words: *Passive walking; Gait analysis; Roll-over shape; Prosthetic foot; Bifurcation diagrams*

1. Introduction

An unpowered mechanical biped walker can walk down an inclined plane with a steady, symmetric gait comparable to human walking [2]. These 'compass-like' passive dynamic walkers are usually preferred because of their simplicity and may be used as a tool to analyse efficient bipedal locomotion. They are commonly modelled with flat or curved/circular feet; however it has been shown that foot kinematics have a direct influence on the stability of a bipedal robot [1]. This contact may be modelled using an effective rocker to describe the function of the knee-ankle-foot complex in human walking. This effective rocker can be obtained from the physiological roll-over shape defined as the trajectory of the centre of pressure in the local co-ordinate system aligned with the stance leg [3]. This roll-over shape can be determined experimentally from motion capture systems and ground reaction plates and does not change appreciably with walking speed [4], with shoe heel height [5] or when carrying extra weight [6]. Modelling the physiological knee-ankle-foot system can give a better understanding of its functions during able-bodied gait and can improve the stability of designs for ankle-foot prosthesis and orthoses.

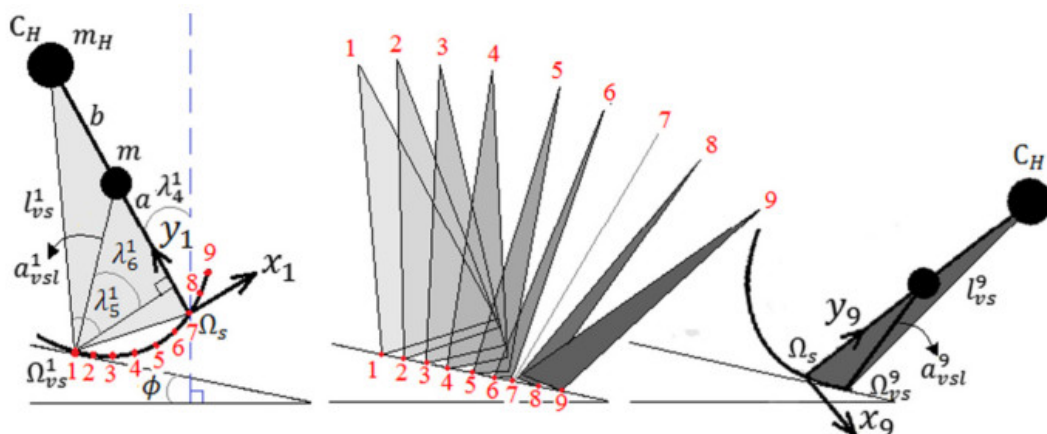


Figure 1: Discrete pivot point model

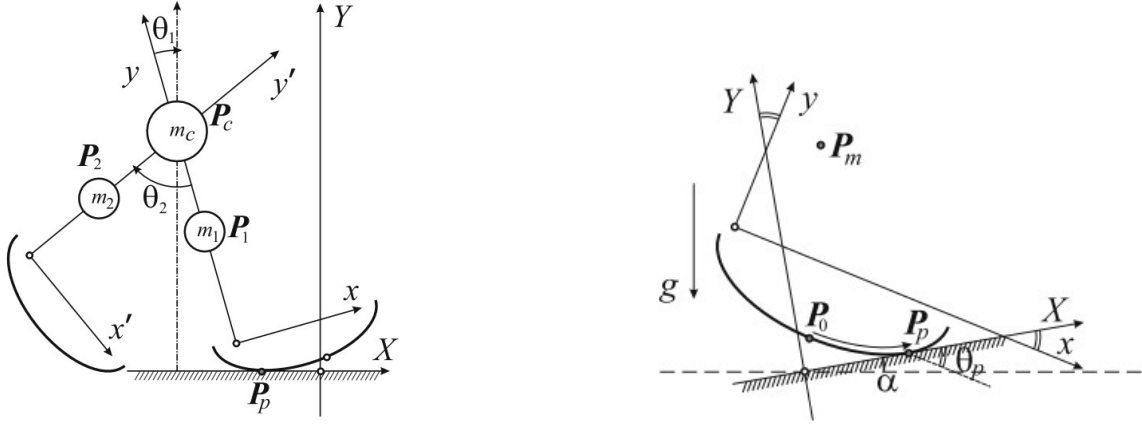


Figure 2: Modelling the rolling contact using the Lagrangian method

2. Implicit method for rolling contact

Mahmoodi et al. [1] modelled this rolling contact as a discretized set of pivot points as shown in Fig. 1. In this model the stance leg pivots about pivot point 1 with inverted pendulum dynamics until pivot point 2 makes contact with the floor. At this point a transition occurs that conserves the angular momentum of the walker using the initial conditions that consists of virtual leg lengths, initial angular velocities and initial angular displacements. This approach was done in order to overcome the inability to model the complex non-circular geometry of roll-over shapes. Before this, only point contact or curved/circular feet could be used. From this study, an interest was gained in the qualitative analysis using a complex roll-over shape in an inverted pendulum passive dynamic model. The drawbacks of using this model is that this approach is unable to conserve energy through the infinitesimal jumps that occur as the walker rolls over from one pivot point to another throughout the stance phase, as seen in Fig. 3. The approach proposed in this paper uses a Lagrangian method to model the roll-over contact of the stance leg. This provides more accurate results by conserving mechanical energy throughout the stance phase and hence gives a greater insight into the dynamics of bipedal locomotion.

3. Governing Equations

Further details of the equations of motion for the pivot point model are discussed in another publication [1]. Euler-Lagrange equations [7] are used in order to formulate the ordinary differential equations that determine the dynamics of the walker (see Fig. 2). The Lagrangian function $L = K - \Pi$ (the difference between kinetic and potential energies) can be determined in terms of angles θ_1 and θ_2 used here as the generalized co-ordinates,

$$L = \frac{1}{2}\Theta_1(\theta_i)\dot{\theta}_1^2 + \Theta_{12}(\theta_i)\dot{\theta}_1\dot{\theta}_2 + \frac{1}{2}\Theta_2(\theta_i)\dot{\theta}_2^2 - \Pi(\theta_i) \quad i = 1, 2.$$

Then from Lagrange's equations $\frac{d}{dt}\frac{\partial L}{\partial \dot{\theta}_i} - \frac{\partial L}{\partial \theta_i} = 0$ the following ODEs can be immediately obtained

$$\begin{aligned} \Theta_1\ddot{\theta}_1 + \Theta_{12}\ddot{\theta}_2 + \frac{1}{2}\frac{\partial\Theta_1}{\partial\theta_1}\dot{\theta}_1^2 + \frac{\partial\Theta_1}{\partial\theta_2}\dot{\theta}_1\dot{\theta}_2 + \left(\frac{\partial\Theta_{12}}{\partial\theta_2} - \frac{1}{2}\frac{\partial\Theta_2}{\partial\theta_1}\right)\dot{\theta}_2^2 &= -\frac{\partial\Pi}{\partial\theta_1} \\ \Theta_{12}\ddot{\theta}_1 + \Theta_2\ddot{\theta}_2 + \left(\frac{\partial\Theta_{12}}{\partial\theta_1} - \frac{1}{2}\frac{\partial\Theta_1}{\partial\theta_2}\right)\dot{\theta}_1^2 + \frac{\partial\Theta_1}{\partial\theta_2}\dot{\theta}_1\dot{\theta}_2 + \frac{1}{2}\frac{\partial\Theta_2}{\partial\theta_2}\dot{\theta}_2^2 &= -\frac{\partial\Pi}{\partial\theta_2}. \end{aligned}$$

Further details are being written as a journal publication [8].

4. Bifurcation diagrams

Bifurcation diagrams can be used to show gait factors such as inter-leg angle, step period and average velocity as a function of mass and leg length ratios. A mass ratio is defined as the ratio of hip mass, m_H to leg mass, m , while a length ratio is the ratio of upper leg length, b , to lower leg length, a . Refer to Fig. 1. Different curvatures for the feet can also be compared to see how this effects the dynamics of human locomotion. The curvature of the foot is characterised by the gain, where detailed definitions are explained in an earlier paper [1]. Figure 4 shows bifurcation diagrams as a function mass ratio and leg length ratio. Unless stated, the values for mass ratio, length ratio, slope angle, hindfoot length, forefoot length and roll-over gain are 2, 1, 2° , 16cm, 16cm and 0.8 respectively.

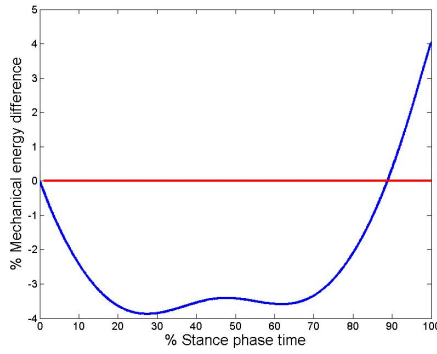
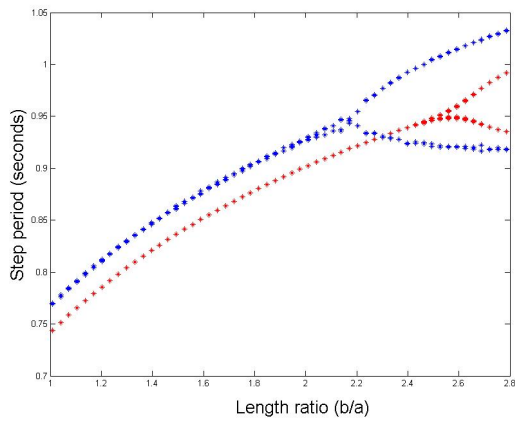
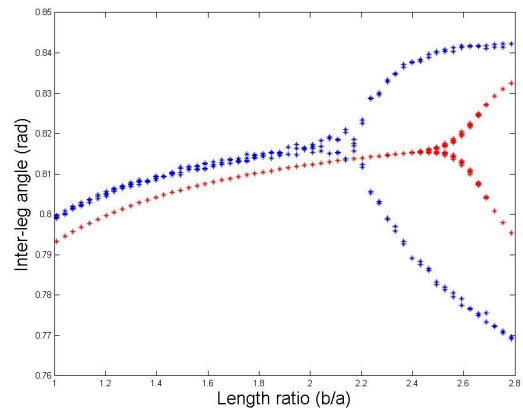


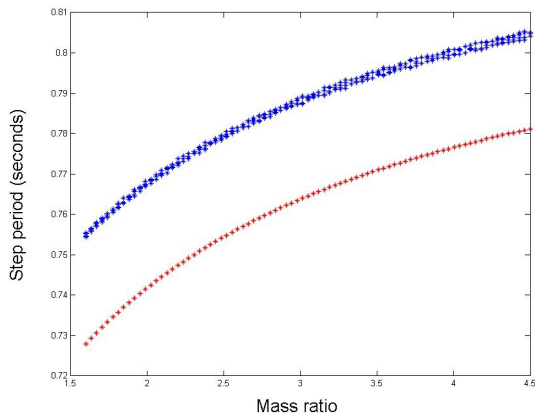
Figure 3: Mechanical energy difference in stance phase time. The blue line shows the mechanical energy difference in the pivot point model, while the red line shows that the analytical solution has constant mechanical energy throughout the stance phase.



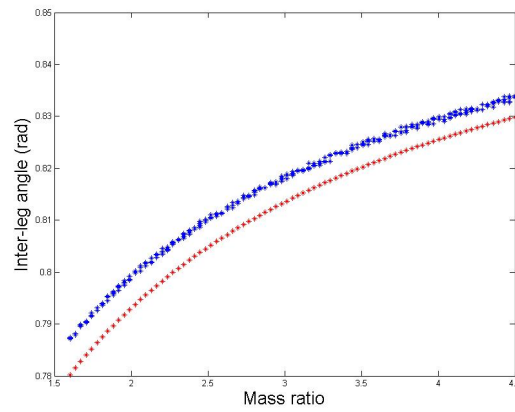
(a) length ratio step period



(b) length ratio inter-leg angle



(c) mass ratio step period



(d) mass ratio inter-leg angle

Figure 4: Bifurcation diagrams for inter-leg angle and step period at variations of mass ratio and length ratio. The pivot point model results are shown as blue dots, while the Lagrangian method is shown as red dots.

5. Discussion

By comparing the gait descriptors inter-leg angle and step period for each model, there can be seen to be a slight difference in values for the step period and inter-leg angle up until bifurcation occurs and the walker demonstrates two-period walking. The inter-leg angle in the pivot-point model was overpredicted by 0.66% and 0.70% for the length ratio and mass ratio respectively, while the step period was overpredicted by 3.51% and 3.39%. At bifurcation the walker displays asymmetric walking as one step takes longer than the next. Shown in Fig. 4a and Fig. 4b, bifurcation occurs earlier in the pivot point model at a length ratio of 2.17, while the Lagrangian approach it occurs at 2.53. The qualitative trends, however,

appear to be the same. The differences between these initial results is assumed to be because of the error in mechanical energy at the collisions at each pivot point in the rolling contact. In further work, it will be interesting to compare both models until the transition to a chaotic region, however, most decisions requiring optimisation of prosthetic feet are in the range before any bifurcation occurs as this is the region of symmetric walking. Hence within this range the accuracy of both models is comparable but computationally the Lagrangian model is approximately 100 times faster.

6. Conclusions

An analytical approach for modelling a rolling contact in a biped walker with a roll-over shape has been presented. This approach conserves mechanical energy throughout the stance phase and can be used to more accurately predict gait descriptors such as average velocity, step period, mechanical energy and inter-leg angle for different gain and length values for the feet, as well as different mass and length ratios. The next task is to compare results with unbalanced mass distributions in order to explore prosthetic design applications. Future work can also include adding a linear or torsional spring in order to emulate the muscle contractions in human walking and compare the ground reaction forces with experimental data. This research is not only useful in order to improve stability and correct gait for the design of prosthetic feet, but also for rehabilitative devices such as ankle-foot orthoses.

Acknowledgements

The Authors gratefully acknowledge the financial support provided by the Sêr Cymru National Research Network in Advanced Engineering and Materials.

References

- [1] Mahmoodi, P., Ransing, R. S., & Friswell, M. I. (2013). Modelling the effect of heel to toe roll-over contact on the walking dynamics of passive biped robots. *Applied Mathematical Modelling*, 37(12-13), 7352-7373.
- [2] McGeer, T. (1990). Passive Dynamic Walking. *The International Journal of Robotics Research*, 9(2), 62-82.
- [3] Miff, S. C., Hansen, A. H., Childress, D. S., Gard, S. A., & Meier, M. R. (2008). Roll-over shapes of the able-bodied knee-ankle-foot system during gait initiation, steady-state walking, and gait termination. *Gait & Posture*, 27(2008), 316-322.
- [4] Hansen, A. H., Childress, D. S., & Knox, E. H. (2004). Roll-over shapes of human locomotor systems: effects of walking speed. *Clinical Biomechanics (Bristol, Avon)*, 19(2004), 407-414.
- [5] Hansen, A. H., & Childress, D. S. (2004). Effects of shoe heel height on biologic rollover characteristics during walking. *Journal of Rehabilitation Research and Development*, 41, 547-554.
- [6] Hansen, A. H., & Childress, D. S. (2005). Effects of adding weight to the torso on roll-over characteristics of walking. *Journal of Rehabilitation Research and Development*, 42(3), 381-390.
- [7] David Morin. *Introduction to Classical Mechanics: With Problems and Solutions* (Chapter 6: The Lagrangian Method), Cambridge University Press, 2008.
- [8] Charles, W. G., Sazonov, I., Ransing, R. S., & Friswell, M. I. A Lagrangian approach for modelling the heel-to-toe contact in passive dynamic walkers, (Under preparation).

ADVANCED APPLICATIONS 2

A computational method of obtaining reliable measurement of periosteal cross-sectional area of human radii from laser scans

P. Mahmoodi, S. Annan and *N. Owen

College of Engineering, Swansea University, Singleton Park, Swansea, SA2 8PP

*n.j.owen@swansea.ac.uk

ABSTRACT

The accurate quantification of bones cross-sectional geometry provides valuable information about mechanical properties of bones such as rigidity to torsional, bending and compressive loading and also reveals insights into habitual activities of humans in the past. However, the use of current methods can produce large errors between measured and true cross-sectional areas. In this study the minimum cross sectional area was calculated at mid-shaft for a unique collection of laser scanned radii bones, recovered from Mary Rose warship, using a novel technique. A computational method was used to measure multiple cross-sectional areas for different orientations to then determine a minimum. This was then taken to represent a reliable mid-shaft cross-sectional area. The reliability of the process was tested using Bland and Altman plots to analyse the agreement between measurement trials. The systematic bias between the two measurement trials was 0.06mm^2 (0.04% of the average cross-sectional area measurement) with 95% limits of agreement of 1.69mm^2 (1.13%) and -1.57mm^2 (1.05%). Consequently this method can be used as a reliable measure of periosteal cross-sectional area. The possibility also exists to transfer the methods described here to other imaging technologies for example, micro CT and magnetic resonance imaging. This would augment existing methods of computational analysis and produce accurate models.

Keywords: *computational modelling, bone topology, osteology, biomechanics*

Introduction

The study of osteology and bone morphology refers to the detailed analysis of the form and structure of bone. The results of such analyses in human studies help science understand important areas of human development and health, such as habitual activities of humans in the past and evolutionary medicine [1,2]. The use of engineering theory, specifically beam analysis is increasingly used to analysis bones structurally. Recently the trend has been to use virtual bones derived from different imaging technologies for such studies [1]. The most common technologies used for creating dimensionally accurate virtual bones are laser scans [1], peripheral qualitative computed technology scan [2] and computed tomography scans [3]. However bones, when compared to manufactured objects, present certain challenges with regard to valid and reliable metrology. For example, it is common practice to align bones or limbs to be scanned with an external reference plane. Whilst this would provide a reliable position for repeated measurements of the same bone or limb, it would not necessarily allow reliable measurements of different bones due to inter-specimen/limb variation, that is, the same bone from different people vary considerably in shape and size. Consequently, the purpose of the current study is to develop a reliable method of measuring bone morphology, specifically mid-shaft cross-sectional area.

Materials and Methods

Human radii bones ($n = 10$), recovered from Mary Rose warship provided by the Mary Rose Trust, were used in this study

All radii were scanned on a FARO three dimensional (3-D) laser scanner (7 axis, 10 foot Fusion model; FARO Technologies Inc., Florida, USA). MeshLab (v1.3.1; Visual Computing Lab, Pisa, Italy) was used to input into MATLAB.

The minimum cross-sectional areas (at mid-shaft) of scanned bones, with arbitrary orientations, were measured in three steps. Reference bony landmarks were first defined from which orthogonal reference axis lines were determined. In the second step all the bones' reference axes were rotated to align them with the global reference frame. In the last step a computational method was used to find the minimum cross sectional area of the bone at the mid-shaft position.

Three reference bony landmarks were used to align the bones with the global reference frame to enhanced the performance of the method. Figure 1 shows the location of the bony landmarks used to define the reference axes, they were: a) the furthest point of the styloid process (point 1), b) the centre of the concaved surface on the proximal radial head (point 2) and c) the mid-point between the corners of the distal articulating surface above the ulnar notch and point 1 (point 3) . Orthogonal axes, \vec{V}_{31} and \vec{V}_{32} , were then defined based on the coordinates of the bony landmarks. The desired orientation of bones was defined such that a vector connecting points 3 and 2 (\vec{V}_{32}) is parallel to the global x-axis and \vec{V}_{31} is located on a plane parallel to (x-y), Figure 1. The procedure of alignment of bones to the desire orientation consists of three stages. In the first stage the point cloud rotates about the y-axis by the angle of θ . Stage two involved rotation of the point cloud about

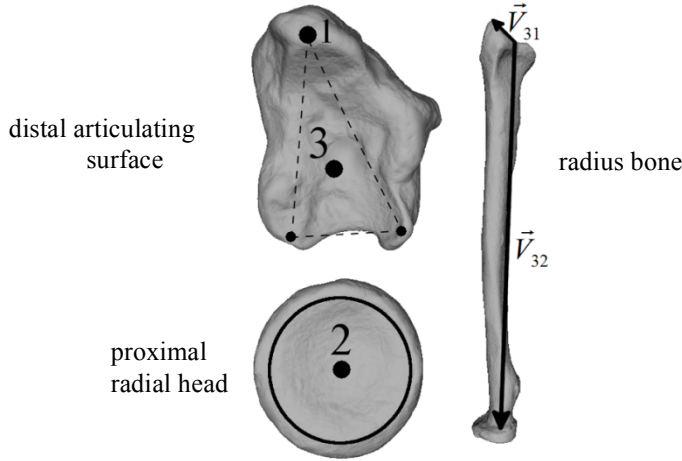


Figure 1: Position of reference bony landmarks and reference axes for each radius bone.

the z-axis by the angle of ϕ so that \vec{V}_{32} became parallel to the x-axis Figure 2. In the final stage new coordinates of the scanned bone rotate about its longitudinal vector (\vec{V}_{32}) by the angle of ψ so that \vec{V}_{31} is located on a plane parallel to (x-y) Figure 2. Thus, the point cloud at each stage is given by:

$$\begin{bmatrix} x_\theta \\ x_\phi \\ x_\psi \end{bmatrix} = \begin{bmatrix} x_1 + l_\theta \cos(\theta - \theta^*) \\ x_1 + l_\phi \cos(\phi - \phi^*) \\ x_\phi \end{bmatrix}, \quad \begin{bmatrix} y_\theta \\ y_\phi \\ y_\psi \end{bmatrix} = \begin{bmatrix} y_{initial} \\ y_1 + l_\phi \sin(\phi - \phi^*) \\ y_1 + l_\psi \cos(\psi - \psi^*) \end{bmatrix}, \quad \begin{bmatrix} z_\theta \\ z_\phi \\ z_\psi \end{bmatrix} = \begin{bmatrix} z_1 + l_\theta \sin(\theta - \theta^*) \\ z_\theta \\ z_1 + l_\psi \sin(\psi - \psi^*) \end{bmatrix}$$

Where l_θ , l_ϕ and l_ψ are the length of the projection of vectors connecting a point on the point cloud to the point3 on planes (x-z), (x-y) and (y-z) respectively at each stage. The angles θ^* , ϕ^* and ψ^* are the initial angles between the projections of \vec{V}_{32} on reference planes and axes.

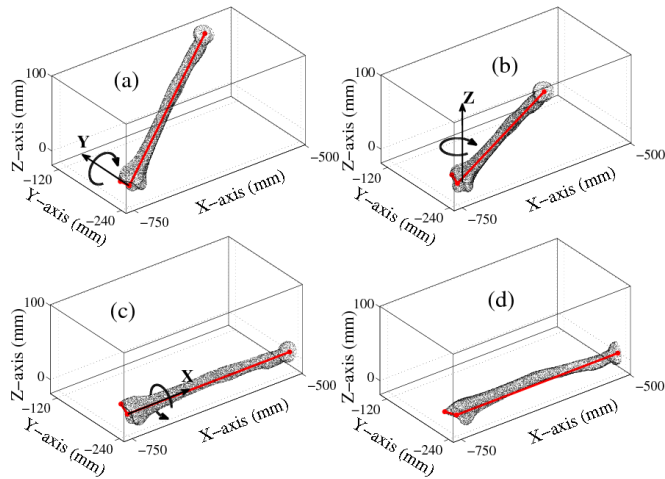


Figure 2: Rotation of the bone point cloud. a, b and c show the rotation of the bone with respect to y-axis, z-axis and x-axis or longitudinal reference line respectively. Final orientation of the bone is described in d.

In order to find a minimum cross-sectional area, an initial cross section is defined as the intersection of a plane parallel to (y-z) plane (local plane), Figure 3, and the bone at mid-point of the longitudinal

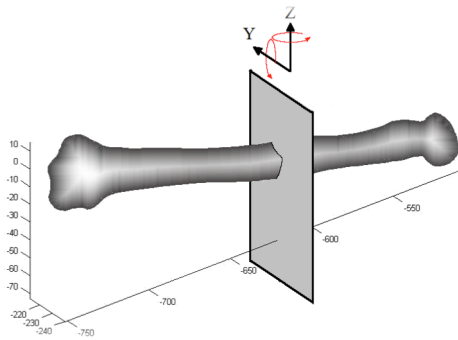


Figure 3. Local plane (y-z) used to define cross-sectional areas for different orientations

reference axes. In the second step a local coordinate system is defined such that its origin is located on the centre point of the initial cross section and its axes are parallel to the global coordinate system. In the next step, the minimum cross section area is determined by rotating the bone about the local y-axis and z-axis ($\pm 20^\circ$, 1° steps) and measuring the intersection of the bone and the local coordinate system at each orientation, thus producing 1600 cross-section measurements. The minimum cross-sectional area was then chosen. The minimum cross-sectional area of each bone was measured twice with measurements derived from separate laser scans. The pairs of measurements were then statistically assess for agreement.

Statistical Analysis

The aim of the statistical analysis was to assess reliability (repeatability) of the method of measuring mid-shaft cross-sectional area. The test described by Band and Altman [5], measures the systematic bias between paired measurements of the same object and quantifies the 95% confidence limits of agreement (LOA).

Results

The systematic bias between the paired measurements was 0.06 mm^2 with an upper LOA of

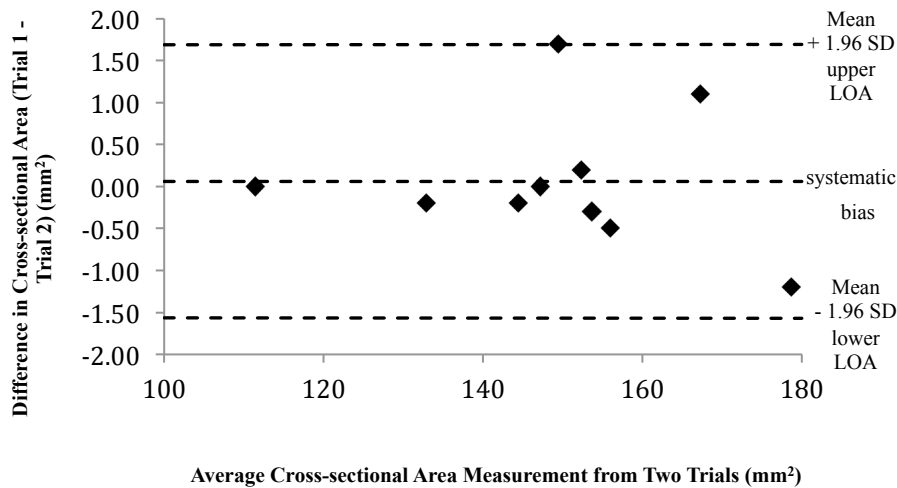


Figure 4. Bland and Altman plot of mid-shaft cross-sectional area

+1.69 mm² and a lower LOA of -1.57 mm², representing 0.04%, 1.13% and -1.05%, respectively, of the average cross-sectional area.

Conclusion and Discussion

The results of the study indicate that this method of assessing periosteal cross-sectional areas produces reliable and valid measurements within the range of the LOA. Analysis of bones for the assessment of occupational activity in humans increasingly uses engineering theory, specifically beam analysis. The current study provides quick and reliable method of providing metrics for such analyses. Future studies should increase the n number and determine the optimal orientation step and fan angle. Also, adaptation of this method for micro computed tomography and magnetic resonance imaging should be investigated, thus augmenting existing methodologies [6].

References

- [1] T.G. Davies, C.N. Shaw, J.T. Stock. A test of a new method and software for the rapid estimation of cross-sectional geometric properties of long bone diaphysis from 3D laser surface scans, *Archaeological and Anthropological Sciences*, 4, 277-290, 2012.
- [2] H. Sievänen, V. Koskue, A. Rauhio, P. Kannus, A. Heinonen, I. Vuori. Peripheral Quantitative Computed Tomography in Human Long Bones: Evaluation of In Vitro and In Vivo Precision. *Journal of Bone and Mineral Research*, 13, 871-882, 1998.
- [3] H. Haapsalo, S.Kontulainen, H. Sievänen, P. Kannus, M. Järvinen, & I. Vuori. Exercise-induced Bone Gain Is Due to Enlargement in Bone Size Without a Change in Volumetric Bone Density: A Peripheral Quantitative Computed Tomography Study of the Upper Arms of Male Tennis Players. *Bone*, 27 (3), 351-357, 2005
- [4] J.A.Rhodes and C.J. Knunsel Activity-Related Skeletal Change in Medieval Humeri: Cross-Sectional and Architectural Alterations. *American Journal of Physical Anthropology*, 128, 536-882, 2005.
- [5] J. M. Bland, & D. G. Altman, D.G. Statistical Methods for Assessing Agreement between Two Methods of Clinical Measurement. *The Lancet*, 327 (8476): 307-310, 1986.
- [6] P.Young, T. Beresford-West, S. Coward, B. Notarberardino, B. Walker, A. Abdul-Aziz, An efficient approach to converting three-dimensional image data into highly accurate computational models, *Philosophical transactions. Series A, Mathematical, physical, and engineering sciences*, 366, 3155-73, 2008

THE INFLUENCE OF APPARENT–AND TRUE VISCOSITY ON INJECTION PRESSURE PREDICTION

***Marton Huszar, Patrick Wlodarski, Fawzi Belblidia, Sue Alston, Cris Arnold, Johann Sienz
and David Bould**

College of Engineering, Swansea University, Singleton Park, Swansea, SA2 8PP

*m.huszar@swansea.ac.uk

ABSTRACT

An experimental–and computational case study to determine the injection moulding window of a rectangular ABS plate is presented. When apparent viscosity was adapted for computation, it was found that computed injection pressure was overestimated in contrast to experimental data. Shear rate–and stress corrections applied to apparent viscosity helped to achieve more accurate pressure estimation. More accurately predicted injection pressure utilised for mould–and process design purposes may help to generate less production waste and save costs, making a step towards sustainable manufacturing.

Keywords: *apparent viscosity; true viscosity; injection moulding simulation; injection pressure*

1. Introduction

Injection moulding has been a common processing technique to produce plastic components. The cycle starts with the injection or filling phase, during which the injection screw moves forward carrying molten material into the mould cavity. When the cavity is nearly filled, the packing phase commences by forcing further molten material into the cavity to compensate for the shrinkage of the part. When the packing is finished and the gate is solidified, the cooling phase starts. Within that time the remaining heat from the part is removed until it is sufficiently solid to be ejected from the mould [1]. The literature available in this subject is rich and it is beyond the scope of the paper to give a thorough insight into most of the work that has been undertaken. The purpose of this review is to present a few examples regarding injection moulding analyses which were based on utilising computer simulation packages, such as Moldflow. In one study, the cavity fill balancing was emphasized as being an important criterion during filling analyses to improve the quality of the moulded parts. If an unbalanced flow pattern existed, that would lead to packing difficulties [2]. Regarding packing analysis, it was reported that increased packing pressure would reduce the shrinkage of HDPE cups [3]. Specific to a warpage problem, it was shown that a longer cooling time and reduced melt temperature helped to improve the warpage of a box–like component [4]. Such simulations need the utilisation of accurate material properties, i.e. melt viscosity, pressure–volume–temperature data, coefficient of thermal expansion, mechanical properties, etc. For any analysis, the very first task is to fill the mould cavity. However, little information has been found that deals with the effect of the quality of material data input into injection moulding simulation packages. Among the many material properties, the viscosity may be a critical one, which will ultimately influence the reliability of injection pressure prediction. If inaccurate viscosity data is used, the injection pressure will be incorrectly estimated. It is therefore critical to utilise as accurate viscosity data as possible within the computational model. In this paper, the effect of apparent–and true viscosity of an amorphous thermoplastic material with respect to a filling analysis is considered. The details of experimental–and numerical analysis are presented below.

2. Aim and methodology

An experimental project was conducted to determine the mould processing window of a 3 mm thick rectangular plate (168 mm x 99 mm). This utilised a Haitian HTF120X moulding machine and a

generic grade of an ABS thermoplastic. The processing window, i.e. the injection pressure limits as a function of three melt temperatures (220–, 240–, 260 °C) and three injection times (1–, 2–, 3 s) were determined. This was accomplished by reducing the hydraulic pressure of the machine until complete cavity filling was just achieved. The cooling time was set to 30 s and the cycle–average mould (CAM) temperature of the Cu–mould was acquired based on the temperature readings of 12 thermocouples mounted in the mould. These temperature values [°C] at a given melt temperature [°C] and injection time (1–, 2–, 3 s) were found to be 220 (52, 48, 52), 240 (54, 56, 56) and 260 (57, 60, 61).

With reference to the viscosity measurement of the ABS grade, it was performed on a twin–bore (ϕ 15.5 mm) capillary rheometer with dies of 20 x ϕ 1 mm and 0.1 x ϕ 1 mm. The resulting P pressures measured above the die, corresponding to different Q volumetric flow rates, can be used to calculate the τ (wall) shear stress and γ (wall) shear rate [5]. To obtain the apparent shear stress of a Newtonian fluid, Equation 1 [5] can be used (where D and L are die diameter and length, respectively).

$$\tau_{\text{apparent}} = \frac{PD}{4L} \quad [\text{Pa}] \quad (1)$$

Having known the Q volumetric flow rate of the melt, the apparent or Newtonian shear rate can be determined. This correlation is described by Equation 2 [5].

$$\gamma_{\text{apparent}} = \frac{32Q}{\pi D^3} \quad [1/\text{s}] \quad (2)$$

Then, the apparent viscosity is defined as $\eta_{\text{apparent}} = \tau_{\text{apparent}} / \gamma_{\text{apparent}}$ [Pas]. However, the possession of apparent viscosity is yet not satisfactory. During the rheology measurements, the capillary entrance effects cause deviations from the ideally developed pressure profile. Due to the change in cross section from the larger diameter of the barrel to the small one of the die, Equation 1 yields a shear stress that is larger than that in the fully developed flow region of the die [6] [7]. According to Bagley's approach, this effect can be eliminated by conducting the measurement with (at least) two dies having the same diameter but different L/D ratio [5] [7]. By using Equation 3 [5], the true shear stress based on Bagley's approach can be obtained (where P_c is the pressure correction).

$$\tau_{\text{true}} = (P - P_c) \frac{D}{4L} \quad [\text{Pa}] \quad (3)$$

Since thermoplastic melts exhibit shear–thinning behaviour, the true shear rate is higher than the shear rate of Newtonian fluids [7]. To compensate this deviation, the Weissenberg–Rabinowitsch correction can be applied. Shown by Equation 4 [5], it is calculated by multiplying the apparent shear rate by the slope of apparent shear rate and true shear stress.

$$\gamma_{\text{true}} = \frac{\gamma_{\text{apparent}}}{4} \left(3 + \frac{d(\log \gamma_{\text{apparent}})}{d(\log \tau_{\text{true}})} \right) \quad [1/\text{s}] \quad (4)$$

Then, the true viscosity is obtained by $\eta_{\text{true}} = \tau_{\text{true}} / \gamma_{\text{true}}$ [Pas]. Both the apparent and true viscosities were data fitted separately into the Cross–WLF viscosity model based on the minimisation of the root–mean–square deviation (RMSD) [8] between the fitted and measured data. The model coefficients were imported into Moldflow to perform 3D, non–isothermal flow simulations. The melt (including the measured CAM) temperatures and injection times were set in Moldflow identical to those that were applied during the experimental. The rest of material data were adopted from Moldflow's materials database. Finally, the experimental–and numerically predicted injection pressure values were contrasted in light of apparent–and true viscosities.

3. Results and discussion

According to the measured data, the apparent viscosity of the ABS grade (on average) was 46% higher than the true viscosity. Similar findings were reported in literature (63%) [9], however with differences being dependent on the power–law index. The coefficients of the measured data fitted to the Cross–WLF model are summarised in Table 1. After performing the corrections according to Equation 3–4, it became clear that, $\tau_{\text{apparent}} > \tau_{\text{true}}$ and $\gamma_{\text{apparent}} < \gamma_{\text{true}}$, therefore $\eta_{\text{apparent}} > \eta_{\text{true}}$. In

addition, the measure of degree of the shear – thinning behaviour, $n_{\text{apparent}} > n_{\text{true}}$ yielded that the critical shear – stress was $\tau^*_{\text{apparent}} < \tau^*_{\text{true}}$.

Table 1: Cross-WLF model coefficients of apparent and true viscosity data

Coefficients		n [-]	τ^* [Pa]	D_1 [Pas]	A_1 [-]	A_2 [K]	T^* (T_g) [K]	RMSD
Viscosity	Apparent	0.30	55814	6.30E+10	22.80	51.6	379.15	0.11
	True	0.23	99253	1.37E+11	24.81	51.6	379.15	0.06

As a consequence of corrections applied to the apparent viscosity, slight discrepancies regarding flow profile can be noticed. The cross-sectional flows based on the apparent and true viscosity are illustrated in Figure 1.



Figure 1: The parabolic profiles of the apparent (left) and true (right) viscous flows

By looking at the figures in Table 2, working with the apparent viscosity led to overestimations from experimentally obtained (measured) injection pressures. However, the overestimation of pressure is attenuated by utilising the true viscosity for simulations. It can be claimed that more accurate injection pressure prediction can be achieved if the true viscosity is applied. Deviations however, are still present, although these become smaller compared to the results if apparent viscosity is considered. The average overestimation of injection pressure for the apparent viscosity was 14% and 6% for true viscosity, respectively. In some cases, large deviations were identified (~20–30%) which are likely to have occurred due to computational inaccuracies involved in the filling simulations.

Table 2: Differences between numerical–and experimental injection pressure

Viscosity utilised for simulations	(Numerical/experimental data [MPa]) and difference relative to experimental ones [%]			
	Injection time [s]	Melt temperature [°C]		
		220	240	260
Apparent	1	(99/90) 10	(81/79) 2	(68/64) 6
	2	(90/68) 32	(71/56) 26	(58/49) 18
	3	(84/78) 8	(67/58) 15	(53/48) 11
True	1	(91/90) 1	(75/79) –5	(60/64) –6
	2	(85/68) 25	(67/56) 20	(52/49) 7
	3	(82/78) 5	(63/58) 8	(49/48) 2

To give a physical insight into what the pressure difference may represent in reality, two samples at 210 °C melt temperature with injection time of 3 s were moulded. As seen in Figure 2 (including the numerical fill plot of the part), complete cavity filling was achieved at 85 MPa injection pressure and an incomplete filling at 83 MPa respectively.



Figure 2: Fill plot of the geometry (l) and the flow patterns of a complete (m) and incomplete (r) cavity filling

The injection pressure obtained by simulations is of great importance for mould design considerations. This value can give indication for geometrical constraints to be chosen for the gating system (through which the melt flows into the cavity). For a cylindrical gate, described by Equation 5 [10], the injection pressure is in direct proportion with the η viscosity, L flow length, Q volumetric flow rate and in inverse proportion with the R runner radius (where n is the melt's power-law index).

$$P_{\text{injection}} \sim \frac{\eta L Q^n}{R^{3n+1}} \quad [\text{Pa}] \quad (5)$$

Since the apparent viscosity overestimates the injection pressure, this misleading information would lead the designer to reduce the injection pressure and associated pressure loss by increasing the diameter of the feed system. However, increased gate radius increases the volume of the runner(s), yielding longer cooling time (i.e. longer cycle time) and more waste generated for cold runners [11]. In addition, the clamp force, which is required to maintain the mould halves closed, is also influenced by the injection pressure. However, to account for the peak pressure during the packing stage, higher clamp force is required. This is best captured by performing numerical simulations that are capable of calculating the clamp force during the whole moulding cycle. Clearly, if apparent viscosity is utilised for simulations, the injection pressure will be overestimated, so will the clamp force be. As a result, higher overall manufacturing costs may be involved with the inappropriate selection of an (unnecessarily) stronger clamping unit and/or when maintaining an unnecessarily high clamp force.

4. Conclusion

It has been shown that Bagley–and Weissenberg–Rabinowitsch corrections applied to the viscosity data have an impact on injection pressure prediction. If the apparent viscosity was used, the definition for the radius of the feed system and clamp force would be incorrectly interpreted. In order to achieve sustainable manufacturing, i.e. to reduce the excessive waste and costs associated with mould design, it is recommended to have the corrections performed. If the rheology measurements only permit the measurement of apparent viscosity, that may be used for quality assurance purposes or direct comparison of viscosity data.

Acknowledgement

The authors would like to acknowledge the support of the Advanced Sustainable Manufacturing Technologies (ASTUTE) project, which is part funded from the EU's European Regional Development Fund through the Welsh European Funding Office, in enabling the research upon which this paper is based. Further information on ASTUTE can be found at www.astutewales.com

References

- [1] P. Kennedy and R. Zheng, *Flow analysis of injection molds*, 2nd ed., Munich: Carl Hanser Verlag, ISBN 978-1-56990-512-8, 2013.
- [2] L. Seow and Y. Lam, "Optimizing flow in plastic injection molding," *Journal of Materials Processing Technology*, vol. 72, pp. 333-341, 1997.
- [3] T. Zhil'tsova, M. Oliveira and J. Ferreira, "Relative influence of injection molding processing conditions on HDPE acetabular cups dimensional stability," *Journal of Materials Processing Technology*, vol. 209, pp. 3894-3904, 2009.
- [4] R. Sánchez, J. Aisa, A. Martínez and D. Mercado, "On the relationship between cooling setup and warpage in injection molding," *Measurement*, vol. 45, pp. 1051-1056, 2012.
- [5] BS-ISO-11443, *Plastics - Determination of the fluidity of plastics using capillary and slit-die rheometers*, The BSI Standards Limited, 2014.
- [6] J. M. Dealy and J. Wang, *Melt rheology and its applications in the plastics industry*, 2nd ed., Dordrecht: Springer, ISBN 978-94-007-6394-4, 2013.
- [7] G. Potsch and W. Michaeli, *Injection molding, An introduction*, Munich: Carl Hanser Verlag, ISBN-13: 978-1-56990-419-0, 2008.
- [8] J. Aho and S. Syrjala, "On the measurement and modeling of viscosity of polymer at low temperatures," *Polymer Testing*, vol. 27, pp. 35-40, 2008.
- [9] G. Schramm, *A practical approach to rheology and rheometry*, 2nd ed., Karlsruhe: Gebrueder HAAKE GmbH., 2000.
- [10] J. Shoemaker, *Moldflow Design Guide*, Munich: Carl Hanser Verlag, ISBN-13: 978-1-56990-403-9, 2006.
- [11] R. A. Malloy, *Plastic part design for injection molding, an introduction*, 2nd ed., Munnich: Carl Hanser Verlag, ISBN-13: 978-1-56990-7, 2010.

Evaluation of Undrained Bearing Capacities of Skirted Foundations

Moura Mehravar¹, Ouahid Harireche¹ and *Asaad Faramarzi²

¹ Faculty of Engineering and Science, University of Greenwich, Chatham, Kent, ME4 4TB
² School of Civil Engineering, University of Birmingham, Edgbaston, Birmingham B15 2TT

*A.Faramarzi@bham.a.uk

ABSTRACT

Investigating the response of skirted foundations to uniaxial vertical, horizontal and moment loading as well as under the combinations of these loads is key feature in their designing procedure. Naturally the offshore loads take place under undrained conditions and the short term response of a foundation in undrained soil is most critical. Therefore investigating the foundation response in undrained condition is conservative. In this paper, a series of three-dimensional finite element analyses are performed to investigate the response of skirted foundations in undrained uniform soil under uniaxial vertical and horizontal loads. Uniaxial ultimate vertical and maximum horizontal bearing capacities are presented for different embedment ratios " $0 \leq L/D \leq 1$ ", where L is the embedment length and D is the caisson diameter. The maximum horizontal capacity corresponds to purely horizontal translation where the rotation degree of freedom is constrained. The results show a growing trend for uniaxial bearing capacities with an increasing embedment ratio; however this increasing trend dropped for roughly $L/D \geq 0.6$. Moreover, the accuracy of the obtained results is validated by comparing the uniaxial bearing capacity factors with other published data.

Keywords: Skirted foundation; Bearing capacity; Undrained loading; Three-dimensional finite element analysis.

1. Introduction

A suction caisson consists of a thin-walled upturned 'bucket' of cylindrical shape made from steel. This type of foundation has proven to be efficient and versatile as a support for offshore structures and appears to be a very attractive option for future use in offshore wind turbines [1]. The skirt can improve the foundation bearing capacity by trapping the soil between them during undrained loading. To predict the undrained bearing capacity factors of skirted foundations, various studies focused on plane-strain condition using finite element (FE) analyses and upper bound solution [2-3], while offshore foundations are three-dimensional, and embedded. Their bearing capacity should be considered as a three-dimensional problem. Only few studies were performed considering the skirted foundation using three-dimensional model, in which they have not comprehensively covered a wide range of practical embedment ratios [4]. Therefore, in this paper, a series of three-dimensional finite element analyses using ABAQUS [5] are performed to investigate the effect of the embedment depth on the bearing capacity of shallow foundations in homogenous undrained soil. Uniaxial vertical (V) and horizontal (H) bearing capacities are investigated to estimate the uniaxial ultimate vertical and maximum horizontal bearing capacity factors of skirted foundations.

2. Numerical modelling

2.1 Model geometry and mesh

The embedment length of the caisson foundation allows an additional mechanism of soil deformation. In order to obtain precise results, a series of three-dimensional finite element analyses were carried out for the practical range of embedment ratios, $L/D = 0$ (surface foundation), 0.25, 0.5, 0.75 and 1 in a homogenous undrained soil profile.

Taking advantage of the symmetrical nature of the problem, only half of the entire system was modelled. Figure 1 shows a semi-cylindrical section through a diametrical plane of a skirted foundation with $L/D=0.5$. This figure also represents the typical finite element mesh for caisson foundation, used in this study. A number of different mesh densities in which element sizes around

the caisson wall and tip are considerably refined were performed to obtain accurate results in a reasonable computational time. The mesh is extended $5D$ from the caisson foundation centre line and top of the soil, respectively so that the failure loads are not sensitive by their position or to the boundary conditions. The caisson thickness is considered $4 \times 10^{-3} D$. Displacements in all three coordinate directions (x , y and z) at the bottom of the base of the mesh were completely fixed, and also normal displacements on the lateral boundaries were prevented. The caisson foundation nomenclature and the sign convention which is adopted in this study are presented in **Error! Reference source not found.** In order to model the soil, first-order, eight-node linear brick, reduced integration continuum with hybrid formulation element (C3D8RH) is employed .

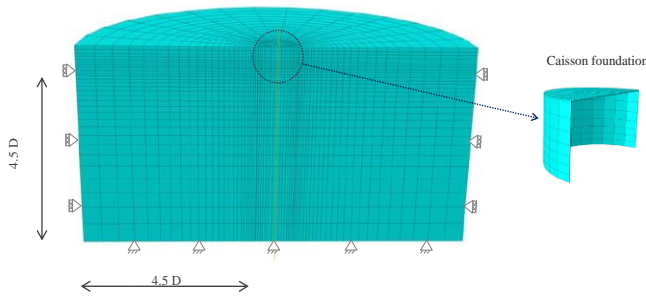


Figure 1: Finite element mesh and boundary conditions

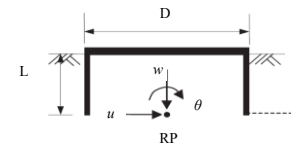


Figure 2: Foundation geometry

2.2 Material modelling and loading path

In this study the soil is modelled as a linear elastic-perfectly plastic material based on the Tresca failure criterion ($\phi = 0^\circ$) with an effective unit weight $\gamma' = 6 \text{ kN/m}^3$ and Poisson's ratio $\nu = 0.49$. The undrained shear strength of the clay are considered as $S_u = 5 \text{ kPa}$ with an undrained young's modulus to undrained shear strength ratio (E_u / S_u) of 500. The foundations are modelled physically as rigid bodies with a Young's modulus of $E = 10^9 E_u$. The interface between soil and foundation was fully bonded so that there is no detachment between the soil and the foundation. In this study the loading is applied using a displacement-controlled method by prescribing vertical (w), horizontal translation (u) or rotation (θ) at the reference point RP (Figure 2).

3. Finite element analysis results

3.1 Vertical bearing capacity

Figure 3 and **Error! Reference source not found.** show the predicted variation of normalised vertical load versus normalised vertical displacement (w/D) and the vertical bearing capacity factor ($N_{cv} = F_v / A \cdot S_u$) as a function of various embedment ratios (L/D), respectively. It is clear that the vertical bearing capacity increased non-linearly by increasing the embedment ratio. This confirms the effect of the skirt length in enhancing the vertical bearing capacity of caisson foundations. However, a smaller rate of the increasing trend is observed for $L/D \geq 0.6$. For comparison plane-strain finite element results for fully rough skirted foundations which have been obtained by [3] is presented in Figure 5. The comparison illustrates that using a plane-strain analysis for skirted foundation underestimates the vertical bearing capacity factor (e.g about 17% for $L/D = 1$). This difference can be explained by the fact that in a 2D analysis, the effects of foundation shape and soil-structure interaction are not considered properly. Meanwhile, a three-dimensional analysis allows the additional soil deformation mechanism to be taken into consideration.

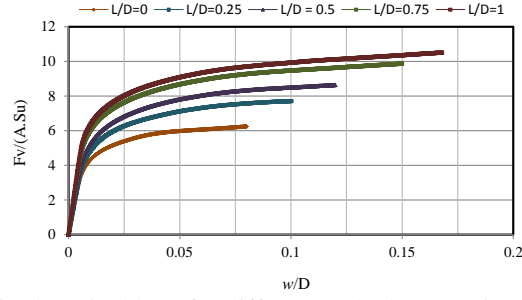


Figure 3: Normalised vertical load for different embedment ratios (L/D) vs normalised vertical displacement (w/D)

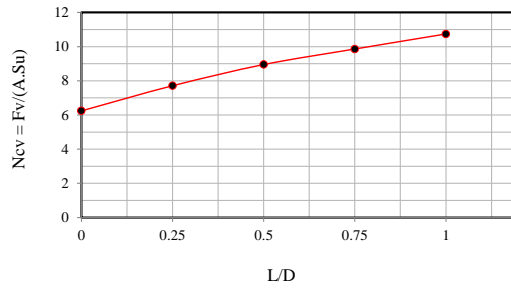


Figure 4: Vertical bearing capacity factors a function of embedment ratio

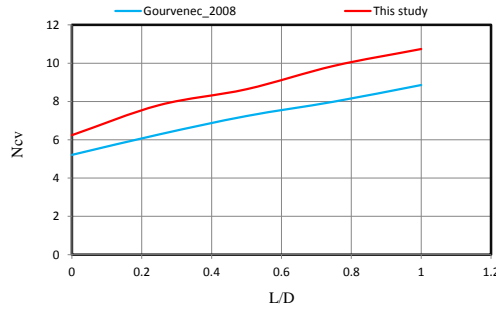


Figure 5: Comparison of vertical bearing capacity

3.2 Maximum horizontal bearing capacity

Figure 6 and Figure 7 present the normalised results of the variation of maximum horizontal load ($F_{h(max)}$) against horizontal displacement ratio (u/D) and the maximum horizontal bearing capacity factor ($N_{ch(max)} = F_{h(max)}/A.S_u$) as a function of various embedment ratios (L/D), respectively. In this section the maximum horizontal loads and bearing capacity correspond to pure horizontal translation ($u > 0$ and θ is constrained).

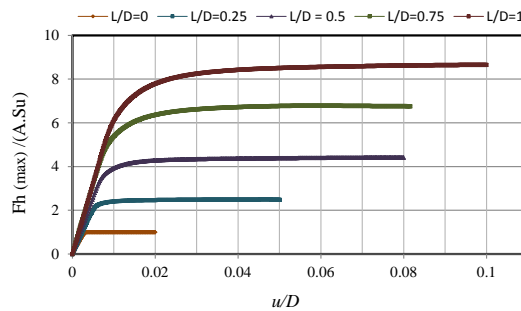


Figure 6: Normalised horizontal load for different embedment ratios (L/D) vs normalised horizontal displacement (u/D)

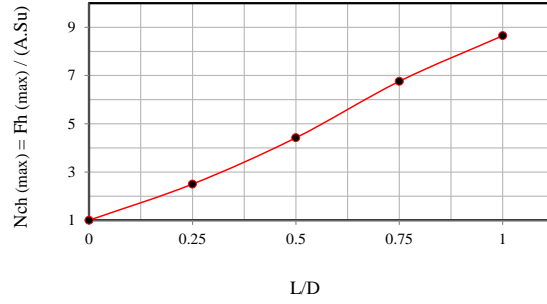


Figure 7: Maximum horizontal bearing capacity as a function of embedment ratio

The calculated results for maximum horizontal bearing capacity factor by [3] is shown in Figure 8, and compared with obtained results. Figure 8 indicates that both predictions for $N_{ch(max)}$ show a linear increasing trend for embedment ratios up to unity. However, prediction by [3] based on plane-strain model, underestimated the bearing capacity. The main reason is that in this case (plane-strain analysis); the problem was considered as two dimensional. Hence, the effect of foundation shape was not reflected.

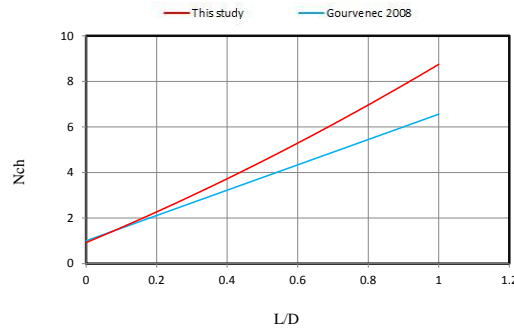


Figure 12: comparison of maximum horizontal bearing capacity predictions

4. Conclusions

In this paper a series of three-dimensional finite element analyses have been conducted with ABAQUS in order to investigate the ultimate vertical and maximum horizontal bearing capacity factors for skirted foundations at various embedment ratios ($L/D = 0, 0.25, 0.5, 0.75, 1$) in undrained condition. A nonlinear increasing trend was observed for ultimate vertical bearing capacity with an increasing embedment ratio. However, the results indicate that this increasing trend is less pronounced for $L/D \geq 0.6$. On the other hand, the maximum moment capacity is found to increase linearly for embedment ratios up to unity. Furthermore, the results of this study were compared with the obtained results by Gourvenec (2008), and indicated that plane-strain analyses underestimate the bearing capacity factors of skirted foundations due to the effects of foundation shape and soil-structure interaction which cannot be reflected properly in 2D analysis.

References:

- [1] B. W. Byrne and G. T. Houlsby, "Foundation for Offshore Wind Turbines," *Royal Society*, pp. 2909-2930, 2003.
- [2] C. Vulpe, S. Gourvenec and M. Power, "A generalised failure envelope for undrained capacity of circular shallow foundations under general loading," *Geotechnique letter*, vol. 4, pp. 187-196, 2014.
- [3] Simulia, ABAQUS user's manual. Dassault Systemes Simula Crop, 2012.
- [4] M. F. Bransby and M. F. Randolph, "The effect of embedment depth on the undrained response of skirted foundations to combined loading," *Soil and Foundations*, vol. 39, no. 4, pp. 19-33, 1999.
- [5] S. Gourvenec, "Effect of embedment on the undrained capacity of shallow foundations under general loading," *Geotechnique*, vol. 58, no. 3, pp. 177-185, 2008.

An investigation into problems associated with the overheating of air monitoring devices

***H. Matallah, N. Croft, S. J. Hardy and J. Sienz**

College of Engineering, Swansea University, SA2 8PP, UK

*h.matallah@swansea.ac.uk

ABSTRACT

An investigation was performed with the aim of understanding and simulating the overheating of devices that monitor air quality used in daily life. The investigation also examined a series of relatively minor changes to the design of the device. The changes were aimed at reducing the temperature in the device whilst maintaining the rate of air flow over the sensors. This will lead to a better performance of the IAQ monitor through durability, sustainability and accuracy. The flow and heat transfer within the device was predicted through simulation using Ansys-CFX solver. The first series of simulations was designed to obtain an estimate of the heat generated by each of the components of the device. The simulations assumed that the gas entering the device was air at 25 °C. Having established an estimation of the practical heat generation within the device, a range of simulations was performed under different redesign options in order to reduce the maximum temperature within the device. The option investigated was the inclusion of a baffle within the device to redirect air flow. This option reduced the maximum temperature in the device by about 12 °C.

Keywords: *Air-monitoring device; Heat Transfer; ANSYS CFX*

1. Introduction

We wish to give the conference proceedings a consistent, high-quality appearance. Therefore, we ask that authors to make their papers look exactly like this document. The easiest way to do this is simply to download a template from conference website and replace the content with your own material. Papers should clearly describe the background of the subject, the authors work, including the methods used, and concluding discussion on the importance of the work.

Every year, thousands of workers become ill due to hazardous substances, contracting lung disease such as asthma, cancer and skin disease. Under the Control of Substances Hazardous to Health Regulations 2002, employers are required to protect both employees and others who may be exposed to hazardous substances by ensuring that monitoring procedures are in place to ensure their safety.

As an example, formaldehyde resins used in many construction materials are one of the more common indoor air pollutants that can be toxic and allergenic [1-3]. A wide range of air monitoring devices may be used in any indoor environment, such as Hospitals, Laboratories, Offices, Public Buildings, Schools and Colleges, Recreational Areas, Hotels, Industrial Plants and Units [4].

In this paper, an internal air quality (IAQ) monitor widely used has been simulated. The issue that has been investigated in this paper is the overheating observed in these devices. The cooling process is an important factor in such devices as overheating in electronic components may lead to non-accurate estimation of the toxic gas in the surroundings. The heat generated by electronic devices and circuitry must be dissipated to improve reliability and prevent premature failure [5]. Many techniques exist to dissipate heat such as heat sinks and fans, as well as other forms such as liquid cooling. In this context, we are interested in cooling process using the air/gas which has passed over the sensors as the coolant. The Ansys-CFX solver [6] was used to get accurate simulations.

2. Air device simulation

The air device under consideration is a complex electronic device made from different materials and electronic components as displayed in Figure 1. The IAQ monitor is composed from six parts: sensors (part 1), part 2, part 3, part 4, LCD (part 5) and fan (part 6).

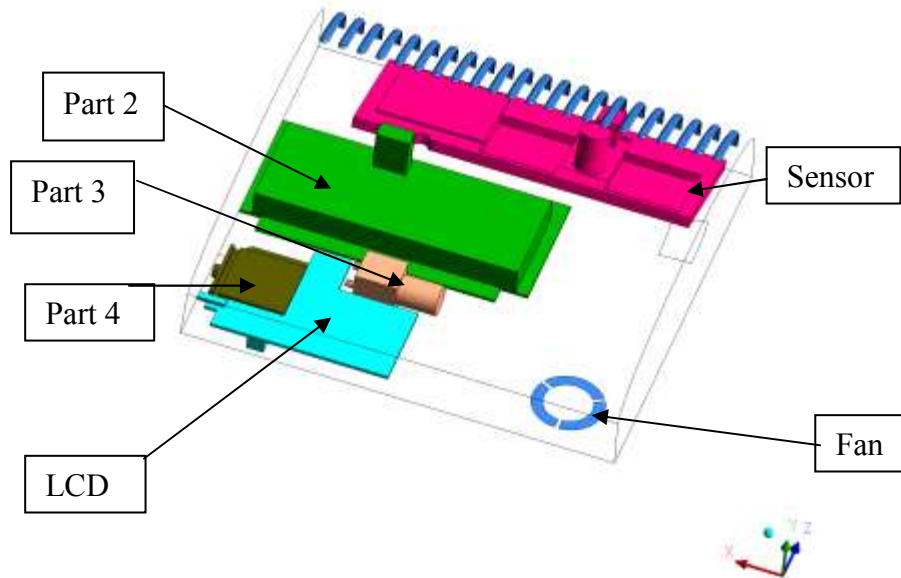


Figure 1: Air monitoring device schematic diagram

According to the power supply unit (PSU) specification, the maximum power supplied to the air device is about 18 W, where some of this energy will be converted to heat in the (PSU). The remaining is transferred to the internal components and the dissipating fan. This means that in one hour of continuous function, the energy consumed by the power supply (E) and transferred to the IAQ monitor will be around 64.8 kJ.

The fan used in the IAQ monitor is a D40SM-12A, with an output voltage and current as 12 V and 0.08 A, respectively. The maximum fan power will be 0.96 W. Most internal components, such as Low Offset Voltage Dual Comparators and Microcontrollers operate in temperature ranges of 0-70 °C [7]. Hence, to stop overheating, the targeted maximum temperature should be lower than 70 °C. A summary of the needed data is given in Table 1 at a temperature of 35 °C.

Table 1: Energy supplied and dissipated with exit velocity

Power supplied (W)	Energy supplied in 1 hour (kJ)	Fan power (W)	Fan flow rate (m ³ /s)	Air flow exit velocity (m/s)	Air mass exiting (g)	Energy dissipated in 1 hour (kJ)
18	64.8	0.96	2.596×10^{-3}	4.4	2.974	0.104

3. Simulation of the device

Using the Ansys-CFX simulation program [6], a number of simulations have been carried out in order to predict the air flow through and the temperature distribution inside the device. The CFX solver is based on a finite element scheme. In some of the tests, geometry redesign is applied to reduce the maximum temperature.

To conduct simulations, the domain is divided into small finite elements employing Hypermesh [8] to generate the mesh. The number of elements and nodes in the mesh used for the majority of the simulations are 121343 and 27015, respectively.

To model such device, some assumptions are made. The air enters the IAQ monitor through inlet and other openings, then driven out by the dissipating fan described above with a prescribed velocity of 4.4 m/s. The initial temperature around and inside the IAQ monitor is 25 °C, and the outer cover is considered as adiabatic. The pressure reference is set at inlet and at openings in the base of the monitor. In all simulations, the air at the ambient temperature of 25 °C is used.

The internal components are considered to be heated under different values of heat fluxes. Details of the choices made in this respect are explained in the next section. The first series of simulations was targeted at gaining an approximation of the heat being generated in each of the components. Once a

reasonable estimate of the heat fluxes in the components had been achieved it would then be possible to perform a number of comparative studies to identify the benefits of design alterations.

The total power consumption in the device (18 W) is dissipated into heat energy. The total heat rate is about 16.91 W added to the fan power (0.96 W) give a total power of 17.87 W. A remaining 0.13 W will be dissipated as heat for the external Power supply unit PSU.

Once the heat fluxes distribution on different components of the IAQ monitor have been established, attention is shifted to minimising the maximum temperature. In order to achieve this aim, a range of design changes were simulated to understand their potential for reducing the temperature. One of the main concerns with the existing design was that the air flow was largely over the sensors and then straight to the fan. Consequently there was very little air flow over the electronic components which resulted in stagnant regions in which the temperature was able to rise to potentially dangerous levels. Hence the design changes focussed on approaches that would change the route air travelled through the IAQ monitor in order to increase its interaction with the various components.

The design modification was investigated in the attempt to lower the temperature in the IAQ monitor. In this case, a baffle was positioned in the large open area in the IAQ monitor to direct the cooling incoming air (gas) towards other parts or components to reduce heat generated.

4. Results and Discussions

4.1. Current design simulations

A series of heat fluxes on the individual components have been tested for calibration as the real data from the components is not available. The main important issue is to get to a realistic temperature working range in the device through physical understanding of the individual components. Starting with guessed values for heat fluxes on the components, as 33 W/m² on the sensors, 200, 300, 250 and 800 W/m² for Part 2, Part 3, Part 4 and the LCD, respectively, a maximum temperature of 172 °C is observed in the LCD region. The temperature range for this test does not seem to be realistic; therefore more heat flux reduction is needed.

Through changing the heat fluxes for each component and evaluating the maximum temperature iteratively, a final heat flux set that replicates the working range temperature for the device has been achieved. The maximum temperature simulated is around 71 °C, as observed in Figure 2.

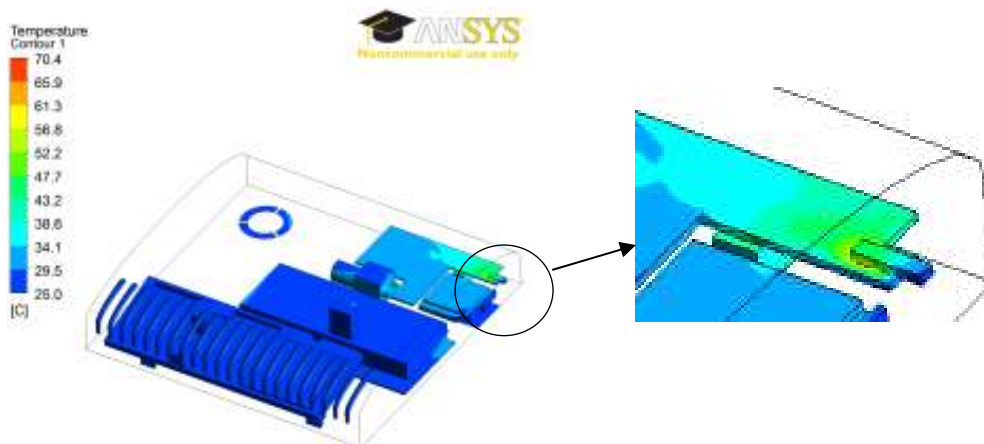


Figure 2: Temperature distribution on different components

As most integrated circuits in the electronic board have an operational range up to 70 °C, the simulated temperature with other factors, like sealing and dust, may lead to overheating. Whilst this test may not fully accurately predict the temperature distribution within the monitor, it does provide a suitable starting point for the investigation into what happens when the design is adjusted. Therefore, the heat flux values for this test were used as a standard case for the next redesign tests below.

4.2. Design optimisation

In this test, the air is diverted using an internal baffle. The heat flux settings are similar to those of the standard case above. In this case more air passes through the internal components allowing improved cooling. The maximum temperature is still in the LCD region but it has dropped significantly to

around 58.9 °C from 70.4 °C as in the standard design, see Figure 3. This design allows more cool air to flow through the sensors than for the standard case by an additional mass flow rate of 1.4 %.

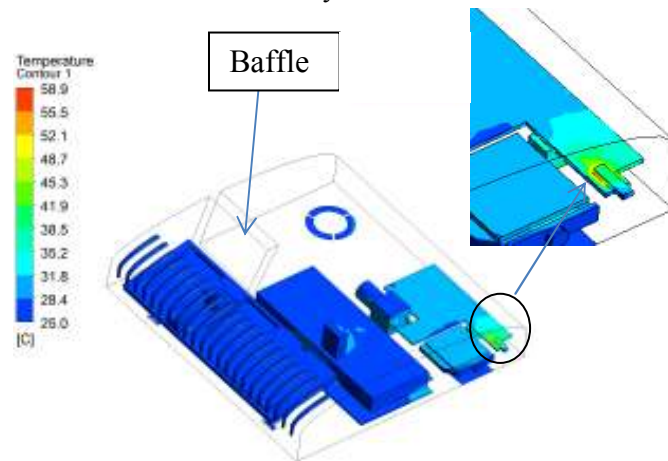


Figure 3: Baffle effect on temperature distribution

5. Conclusions

In this paper, it has been shown that the current design of the air monitor device is not an optimal one for heat distribution on components and may lead to significant overheating. The unwanted effect may be tackled by a geometry redesign in a number of ways. As the overheating process may be due to the air flow directions, and most of the cooled air enters through inlet sensors and exits through the fan passing by a large empty volume, one needs to redirect the air so that it flows over different electronic components or parts, and therefore cools them. Based on these ideas, the redesign of an obstacle in the large empty volume may be an appropriate alternative. This redesign has led to major beneficial temperature reduction inside the IAQ monitor. The maximum temperature was well below 70 °C, and it is reduced from 71 °C to 59 °C. As a consequence, a better performance of the IAQ monitor and durability and sustainability, alongside accuracy is achieved.

Acknowledgements

The authors wish to acknowledge the financial support of the European Union and of the Welsh Government is greatly acknowledged.

References

- [1] "Formaldehyde, 2-Butoxyethanol and 1-tert-Butoxypropan-2-ol". IARC Monographs on the Evaluation of Carcinogenic Risks to Humans 88. Lyon, France: International Agency for Research on Cancer. 2006. pp. 39–325. ISBN 92-832-1288-6
- [2] [2] "Formaldehyde (gas)", Report on Carcinogens, Eleventh Edition, U.S. Department of Health and Human Services, Public Health Service, National Toxicology Program, 2005
- [3] J.E. Rager, B.C. Moeller, S.K. Miller, D. Kracko, M. Doyle-Eisele, J.A. Swenberg, R.C. Fry., Formaldehyde-Associated Changes in microRNAs: Tissue and Temporal Specificity in the Rat Nose, White Blood Cells, and Bone Marrow, *Toxicol. Sci.*, 138 (1):36-46 (2014)
- [4] C. Arnold, M. Harms, J. Goschnick,, "Air quality monitoring and fire detection with the Karlsruhe electronic micronose KAMINA,,*Sensors Journal, IEEE*, vol.2, no.3, pp.179,188, (2002)
- [5] A. Kumar, H. Kim, G.P. Hancke, Environmental Monitoring Systems: A Review, *Sensors Journal, IEEE*, On page(s): 1329 - 1339 Volume: 13, Issue: 4, April 2013
- [6] Ansys.com
- [7] K. Kasten, N. Kordas, H. Kappert, W. Mokwa, Capacitive pressure sensor with monolithically integrated CMOS readout circuit for high temperature applications, *Sensors and Actuators A: Physical*, Volumes 97–98, 1 April 2002, pp. 83-87
- [8] Hypermesh.com

EFFECTS OF AIR PERMEABILITY AND PERIMETER AREA ON AIR LOSSES IN COMPRESSED AIR TUNNELLING

*A. Ahangar-Asr¹, A. A. Javadi²

¹School of Architecture, Computing and Engineering, University of East London, UK

²College of Engineering, Mathematics and Physical Sciences, University of Exeter, UK

*a.ahangar-asr@uel.ac.uk

ABSTRACT

Field measurement data obtained from a tunnel in Munich was used to develop a model to predict air losses in the process of compressed air tunnelling. In the implemented case study, compressed air was used to control the groundwater followed by placing a shotcrete lining as temporary support. Evolutionary polynomial regression was used as a data-driven method based on evolutionary computing aimed to search for polynomial structured model representing air losses. EPR uses a combination of the genetic algorithm (GA) and least square method to search for the most suitable structures. Data from different tunnel lengths were obtained to train/develop the model and also validate it with lines of data not used in the training phase. Comparisons made by the actual measurements represents robustness of the suggested models in learning and predicting the behaviour of the system. The sensitivity analysis conducted on the developed model further revealed the reliability of the models by presenting the expected effects from air permeability of the soil despite in non-homogeneous and layered nature of the geomaterials involved in this particular study.

Keywords: *air loss, tunnelling, evolutionary modelling*

1. Introduction

High ground pressures and also complicated and unpredictable soil and rock mix formations makes tunnelling a very challenging process. Tunnelling experts also have the responsibility to minimize the impact of the construction process on the surface environment and particularly settlement problems in densely populated cities which require expensive and time demanding protective measures to be taken for ground improvement that could lead to the project proving financially infeasible. Compressed air has been used as one of the tunnelling techniques that could help decrease some of these problems. In this approach the water in the ground is excluded using compressed air to help construction of the tunnel.

Applying compressed air as a way to assist tunnelling in under water table coarse soils has gained crucial importance with the construction of major transportation projects, particularly mass transit infrastructure projects and also water supply and sewage disposal systems in many European countries [1]. The open face tunnelling technique immediately followed by supporting the tunnel wall with a layer of sprayed concrete has proved, in many cases, to be an economical and effective measure to exclude water and minimize the ground settlement [1].

There are empirical and semi-empirical methods for calculating tunnel pressure and the quantity of air required [2]. The accuracy of these predictive methods was discussed by Hoad and Gittoes [3]. They showed that the empirical and semi-empirical methods could be appropriate for a first estimate of air losses, but do not account for real influences on air consumption like layered soil conditions, speed of tunnelling and surface conditions. Javadi [4] and Javadi and Snee [5] also developed a numerical model for predicting air losses in compressed air tunnelling. They implemented the model to study the effect of air flow in the partially saturated ground on volume change and subsequently the settlements [2], shear strength of the soil and also stability of the tunnel [6]. They also suggested a relationship to describe time-dependency of the air permeability of shotcrete lining in compressed air tunnelling. Javadi [7] also proposed a neural network approach for estimation of air losses from tunnels in compressed air tunnelling.

While neural networks have shown to be very efficient in modelling the behaviour of materials they do have shortcomings. One of the drawbacks of neural network is that the optimum structure of ANN (e.g., number of inputs, hidden layers, and transfer functions) must be identified a priori. This is usually done through a trial and error procedure. The other major shortcoming is the black box nature of ANN model and the fact that the relationship between input and output parameters of the system is described in terms of a weight matrix and biases that are not accessible to the user. In fact, the black box nature and lack of interpretability have prevented ANNs from achieving their full potential in engineering applications [8].

The total amount of air lost from a tunnel, Q_{total} , is the sum of three main sources; (a) Air loss from the tunnel face, Q_{face} , (b) Air loss from tunnel perimeter walls, Q_{wall} and (c) other losses (ventilation, etc.), Q_{other} .

In this paper EPR approach is implemented to develop a model to predict air losses from the tunnel in the compressed air tunnelling technique during the construction process. The proposed modelling methodology has previously been successfully implemented into modelling complicated behaviour of engineering materials and systems [9].

2. Evolutionary Polynomial Regression (EPR)

The implemented evolutionary technique, is a data-driven method based on evolutionary computing, aimed to search for polynomial structures representing a system. A general EPR expression can be presented as [10]:

$$y = \sum_{j=1}^n F(X, f(X), a_j) + a_0 \quad (1)$$

where y is the estimated vector of output of the process; a_j is a constant; F is a function constructed by the process; X is the matrix of input variables; f is a function defined by the user; and n is the number of terms of the target expression. The general functional structure represented by $F(X, f(X), a_j)$ is constructed from elementary functions by EPR using a Genetic Algorithm (GA) strategy. The GA is employed to select the useful input vectors from X to be combined. The building blocks (elements) of the structure of F are defined by the user based on understanding of the physical process. While the selection of feasible structures to be combined is done through an evolutionary process, the parameters a_j are estimated by the least square method. This technique uses a combination of the genetic algorithm to find feasible structures and the least square method to find the appropriate constants for those structures. In particular, the GA allows a global exploration of the error surface relevant to specifically defined objective functions. By using such objective (cost) functions some criteria can be selected to avoid the overfitting of models, push the models towards simpler structures and avoid unnecessary terms representative of the noise in the data. An interesting feature of EPR is in the possibility of getting more than one model for a complex phenomenon. The user physical insight can also be used to make hypotheses on the elements of the target function and on its structure. Selecting an appropriate objective function, assuming pre-selected elements based on engineering judgment, and working with dimensional information enable refinement of final models. The level of accuracy at each stage is evaluated based on the coefficient of determination (COD) i.e., the fitness function as:

$$COD = 1 - \frac{\sum_N (Y_a - Y_p)^2}{\sum_N \left(Y_a - \frac{1}{N} \sum_N Y_a \right)^2} \quad (2)$$

where Y_a is the actual output value; Y_p is the EPR predicted value and N is the number of data on which COD is computed. If the model fitness is not acceptable or the other termination criteria (in terms of maximum number of generations and maximum number of terms) are not satisfied, the

current model goes through another evolution in order to obtain a new model. Detailed explanation of the method can be found in [10].

3. Contributing parameters and modelling procedure

The Feldmoching tunnel in Munich, Germany, was used as the case study. The construction of the 635 m long Feldmoching tunnel was started in July 92 and finished in February 94. Detailed information about the tunnel can be found in [7].

Parameters used as input parameters in the model development process included, perimeter area of the tunnel (A_p), average horizontal permeability of the soil layers (K_h), average vertical permeability of the soil layers (K_v), the air pressure (P_a) required and face area of the tunnel (A_f). The output parameter was considered to be the air loss from the face and perimeter areas of the tunnel (Q_t).

Data was divided into training and testing sets. The training data set was used to develop the EPR model. The testing data was however kept unseen to EPR during the model development process and has been used to examine the generalization capabilities of the developed model in giving accurate predictions for the cases not previously experienced by the software.

Figures 1(a) and 1(b) show a comparison between the prediction results of the EPR model for training and validation data and the actual measurements which included 31 lines of measured data altogether. It can be easily seen that EPR had been able to capture the data patterns and underlying relations between input and output parameters to produce predictions to a high level of accuracy.

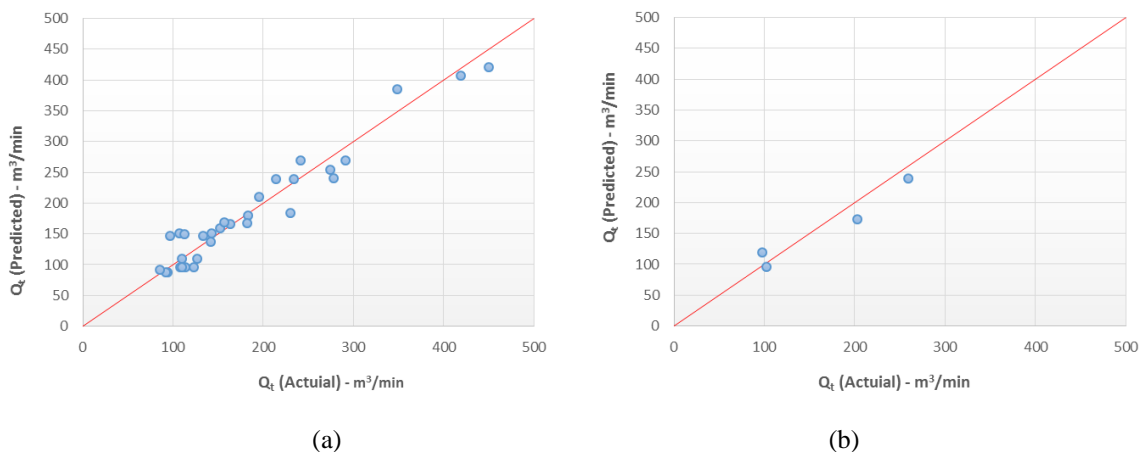


Figure 1: EPR predictions against field measurement values of total air loss for (a) training and (b) testing data

The coefficient of determination value for the model development data was 90.15%. The figures also show a very good correlation between the predictions of the EPR model and the actual data both for modelling and validation datasets.

4. Parametric study

A sensitivity analysis was also conducted on the developed EPR model to investigate into the level of impact from each contributing parameter on predicted air losses through the tunnel in construction. Figures 2a and 2b represent the combined sensitivity analysis results conducted on the effects of horizontal and vertical permeability as well as face and perimeter areas of the tunnel on the volume of air losses. It can be seen the increasing combined area and air permeability values in both horizontal and vertical directions lead to increase in air loss volumes.

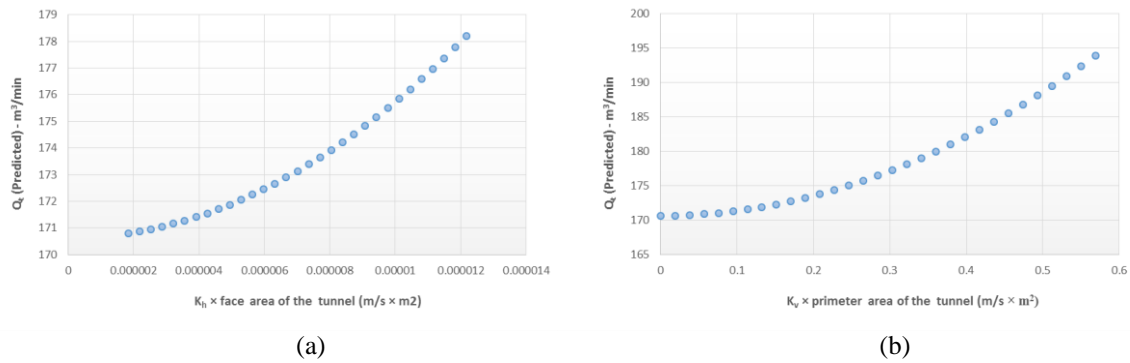


Figure 2: Combined sensitivity analysis results conducted to investigate the effects of (a) horizontal and (b) vertical permeability as well as face and perimeter areas of the tunnel on air loss volumes

5. Discussion and conclusions

An evolutionary-based model for predicting air losses in compressed air tunnelling was developed and validated using a field measurement database from literature. The model prediction results were compared to the actual measured data. Comparison of the results showed that the developed EPR model provides accurate predictions for total air losses from face and perimeter areas of the tunnel during the construction process. A parametric study results were conducted to evaluate the combined effects of the air permeability in both horizontal and vertical directions with the perimeter and face areas, on air loss volumes. The results revealed the high accuracy of the proposed modelling approach in correctly capturing and predicting the background relations between the contributing parameters to air loss volume in compressed air tunnelling.

References

- [1] Kammerer, G. & Semplich, S. 1999. Tunnelling under compressed air – the experience on site and a laboratory test. *In: Proceedings of the 12th European Conference on Soil Mechanics and Geotechnical Engineering*, 6–10 June, Amsterdam.
- [2] Javadi, A.A. & Snee, C.P.M. 1997 New method in predicting air losses in compressed air tunnelling. *In: Proceedings of the Tunnelling '97 Conference, Published by the Institution of Mining and Metallurgy*, London, 2–4 September, pp. 57–69.
- [3] Hoar, R.S. & Gittoes, G.P. 1992. Estimation of compressed air losses. *In: Proceedings of the Conference on Engineering and Health in Compressed Air Work, CIRIA*, 1992, pp. 157–17.
- [4] Javadi, A.A. 2003. Numerical and experimental study of compressed air tunnelling. A Chapter. *In: Bull, J.W. (Ed.), Numerical Analysis and Modelling in Geomechanics*. SPON Press.
- [5] Javadi, A.A. & Snee, C.P.M. 2002. Numerical modelling of compressed air tunnelling. *International Journal of Geomechanics* **2** (4), 399–417.
- [6] Javadi, A.A. & Snee, C.P.M. 2001. The effect of air pressure on the shear strength of soil as a consequence of compressed air tunnelling. *Canadian Geotechnical Journal* **38** (6), 1187–1200.
- [7] Javadi, A.A., 2006. Estimation of air losses in compressed air tunnelling using neural network. *Tunnelling and Underground Space Technology* **21**, 9–20.
- [8] Javadi A.A. Ahangar-Asr A. Johari A. Faramarzi A. & Toll D.G. 2012. Modelling Stress-Strain and Volume Change Behaviour of Unsaturated Soils using an Evolutionary Based Data Mining Technique, an Incremental Approach. *Engineering Applications of Artificial Intelligence Journal* **25**(5), 926-933.
- [9] Ahangar-Asr, A. Javadi, A. A. Johari, A. & Chen, Y. 2014. Lateral load bearing capacity modelling of piles in cohesive soils in undrained conditions; an intelligent evolutionary approach. *Applied Soft Computing; an international journal* **24**, 822-828.
- [10] O. Giustolisi and D. A. Savic. 2006. A Symbolic Data-driven Technique Based on Evolutionary Polynomial Regression. *Journal of Hydroinformatics* **8**(3), 207–22

COMPOSITES

MULTISCALE COMPUTATIONAL HOMOGENISATION TO PREDICT THE LONG-TERM DURABILITY OF COMPOSITE STRUCTURES

*Zahur Ullah, Łukasz Kaczmarczyk and Chris J. Pearce

School of Engineering, Rankine Building, The University of Glasgow, Glasgow, UK, G12 8LT

*Zahur.Ullah@glasgow.ac.uk

ABSTRACT

A fully coupled hygro-thermo-mechanical computational framework based on the multi-scale computational homogenisation is proposed for fibre reinforced polymers. At each macrostructure Gauss point, constitutive matrices for thermal, moisture transport and mechanical responses were calculated from the computational homogenisation of underlying representative volume element (RVE). A degradation model, developed from experimental data relating evolution of mechanical properties over time for a given exposure temperature and moisture concentration was also incorporated in the proposed computational framework. A unified approach is used to impose the RVE boundary conditions, which allows convenient switching between displacement, traction and periodic boundary conditions. A plain weave textile composite RVE consisting of matrix and yarns embedded in the matrix is considered in this case. Both matrix and yarns within the RVE were considered as isotropic materials. Furthermore, the computational framework utilises the flexibility of hierarchic basis functions and distributed memory parallel programming.

Key Words: Multiscale computational homogenisation; Hygro-thermo-mechanical analysis; Fibre reinforced polymer; Textile composites

1. Introduction

Fibre reinforced polymer (FRP) composites consist of mainly two constituents, i.e. glass, carbon or aramid fibres embedded in rigid polymer matrix. Due to their exceptional mechanical and chemical properties, FRP composites are commonly used in many engineering application including aerospace, ships, offshore platforms, automotive industry and civil structures [1]. Textile or woven composites is a class of FRP composites, in which interlaced fibres are used as reinforcement, which provides full flexibility of design and functionality due to the mature textile manufacturing industry [2]. On the other hand, during their service lives, FRP structures are exposed to harsh hygro-thermal environmental conditions in addition to mechanical loading, which leads to matrix plasticisation, hydrolysis and degradation of fibres/matrix interfaces [3]. These processes significantly reduce the mechanical properties of these structures. Therefore, fully coupled hygro-thermo-mechanical analysis based on multi-scale computational homogenisation strategy is vital for predicting the long-term durability of the FRPs structures, where microscopically heterogeneous representative volume element (RVE) is used to predict their macroscopic constitutive behaviour.

A plain weave textile composite RVE is considered here, consisting of matrix and yarns embedded in the matrix. These yarns are modeled with elliptical cross section and cubic spline paths. The multi-scale computational homogenisation framework is implemented in our group's FE software, MoFEM (Mesh Oriented Finite Element Method). A unified approach is used to impose the RVE boundary conditions, which allows convenient switching between displacement, traction and periodic boundary conditions [4]. Furthermore, the computational framework utilises the flexibility of hierarchic basis functions [5] and distributed memory parallel programming.

2. Model components

2.1. RVE boundary conditions

In computational homogenisation, an RVE is associated with each macroscopic Gauss point, the boundary conditions for which in case of thermal, moisture transport and mechanical problem are implemented using the generalised procedure proposed in [4]. The implementation of these boundary conditions are described here for the mechanical problem, which is straightforward to modify for the corresponding thermal and moisture transport cases. In matrix form these boundary conditions are given as

$$\mathbf{C}\mathbf{u} = \mathbf{D}\bar{\boldsymbol{\varepsilon}} = \mathbf{g}, \quad (1)$$

where $\bar{\boldsymbol{\varepsilon}} = \left[\bar{\varepsilon}_{xx} \quad \bar{\varepsilon}_{yy} \quad \bar{\varepsilon}_{zz} \quad 2\bar{\varepsilon}_{xy} \quad 2\bar{\varepsilon}_{xz} \quad 2\bar{\varepsilon}_{zy} \right]^T$ is the macro-strain associated with a Gauss point. \mathbf{g} is the constraints applied to enforce the boundary conditions, while matrices \mathbf{C} and \mathbf{D} are given as

$$\mathbf{C} = \int_{\Gamma} \mathbf{H}\mathbf{N}^T \mathbf{N} d\Gamma, \quad \mathbf{D} = \int_{\Gamma} \mathbf{H}\mathbf{N}^T \mathbf{X} d\Gamma. \quad (2)$$

In Equation (2), \mathbf{N} is a matrix of shape functions, \mathbf{X} is a matrix of Gauss point coordinates and \mathbf{H} is a matrix specific to the type of boundary conditions used (e.g. displacement, periodic, traction).

2.2. Unsteady field problems

Conduction and diffusion models are considered for the heat transfer and moisture transport analysis, both of which are represented by the same governing equation

$$\rho C_p \frac{\partial \psi}{\partial t} - K_\psi \nabla^2 \psi = 0, \quad (3)$$

where ∇^2 is Laplace operator, $\psi = T, c$ is scalar field (where T and c are temperature and moisture concentration respectively), t is time, ρ is density, C_p is specific heat capacity and K_ψ is thermal conductivity.

2.3. Degradation model

A fully generalised degradation model has been developed based on experimental data for the mechanical properties of FRP composites subjected to different hygro-thermal environmental conditions. The experimental data provided by our project partner at the University of Bath involves accelerated ageing, i.e. immersing of the FRP composites samples in hot distilled water with exposure temperatures of 25°C, 40°C, 60°C and 80°C, where different mechanical parameters (tensile strength, shear strength, young modulus and shear modulus) are recorded after 0, 28, 56 and 112 days. The proposed model can be used to predict the mechanical properties of the FRP composites with given histories of environmental exposure temperature and moisture concentration. The proposed model can be written in the rate form as

$$\frac{d}{dt} (1 - \omega) = -c\beta \ln \left(1 - \frac{T}{T_g} \right) (1 - \omega), \quad (4)$$

where ω is the isotropic damage parameter ($\omega = 0$ is equivalent to no degradation and $\omega = 1$ is fully degraded), T is the temperature, T_g the glass transition temperature, t is time and β is a material parameter and is estimated from the experimental data, c is moisture concentration ranges from 0 (dry) to 1 (fully saturated). The proposed degradation model is implemented using implicit Backward Euler Method.

2.4. Computational framework

The developed computational framework consists of series of micro and macro-level analysis, the detailed flow chart of which is shown in Figure 1(a). Both thermal and moisture transport problems are assumed as independent of each other and independent from mechanical problem. This assumption allow us to solve macro-level unsteady thermal and moisture transport problems independently, the conductivity matrices \mathbf{K}_T and \mathbf{K}_c for which are determined from the underlying RVEs. Both \mathbf{K}_T and \mathbf{K}_c are calculated only once and are used at each macro-level Gauss point. At each time step, temperature T and

moisture concentration c fields are saved to the macro-mesh, which are used subsequently in the calculation of degradation parameter $(1 - \omega)$. The damage parameter is approximated over the macro-mesh using

$$(1 - \omega)^h = \mathbf{N}\mathbf{q}_{(1-\omega)}, \quad (5)$$

where $(1 - \omega)^h$ is approximation of $(1 - \omega)$, \mathbf{N} is vector of shape functions and $\mathbf{q}_{(1-\omega)}$ is vector of nodal values of $(1 - \omega)$. At each time step, macro-mechanical problem consisting of linear elastic analysis is next solved using fully nested FE² algorithm, where at each macro-level Gauss point degradation parameter $(1 - \omega)$ is retrieved and pass onto the underlying RVE. Degradation of the form $\mathbf{D}_{matrix} = (1 - \omega)\mathbf{D}_{matrix}$ is considered only for the matrix part of the mechanical RVE, where \mathbf{D}_{matrix} is stiffness matrix of the matrix part. Homogenised matrix \mathbf{D} is calculated for each mechanical RVE and pass back to the macro-Gauss point to be used in the subsequent macro-level mechanical analysis.

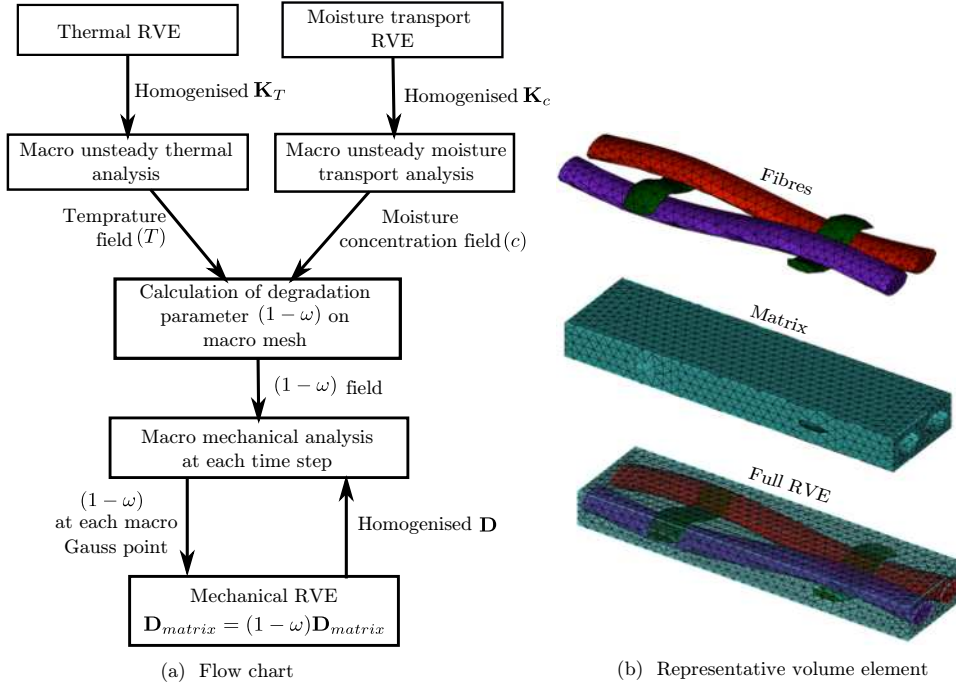


Figure 1: Flow chart of the computational framework and representative volume element

3. Numerical example

For the macro-level structure, a three-dimensional block of dimensions $5m \times 5m \times 1m$ is considered, geometry and corresponding mesh for which are shown in Figure 2(a) and Figure 2(b) respectively. The RVE used in this case is shown in Figure 1(b). Both macro-structure and RVE are discretised with tetrahedral elements with 542 elements and 172 nodes in the case of macro-structure and 10285 elements and 2364 nodes in the case of the RVE. For the macro-level thermal problem temperature of $80^\circ C$ is applied to the top surface and constant heat flux is applied to the bottom surface. Similarly, for the case of moisture transport problem, a constant concentration ($1=100\%$ RH) is applied to the top surface and constant moisture flux is applied to the bottom surface. For the mechanical problem, the bottom surface of the block is fully fixed, while a constant traction of 1000 MPa is applied to the top surface. For the matrix material, thermal conductivity, density, specific heat, moisture diffusivity, Young's modulus and Poisson's ratio are 0.19 W/mm^oC, 1.2 g/cm³, 805 J/kg ^oC, 2.8×10^{-6} mm²/s, 3.5GPa and 0.35 respectively are used, while the corresponding values used for the fibres materials with the same units are 1.03, 2.53, 1000, 1.46×10^{-7} , 230, 0.26. Both thermal and moisture transport problems are solved with time step of 10 days for total of 110 days. At the end of the simulation, temperature and moisture concentration fields are shown in Figures 2(c) and 2(d) respectively. Heat conduction is faster as compared to moisture transport due to its higher value of heat conductivity. Furthermore, at the same stage, distribution of field $(1 - \omega)$ and vertical displacement u_y are shown in Figure 2(e) and Figure 2(f) respectively. As expected, area near the top surface of the block degraded relatively faster due to the higher concentration of temperature and moisture concentration. u_y relative to the first time step for the four points A, B, C and D shown in

Figure 2(b), are shown in Figure 2(g), which shows increase in u_y for a constant top surface traction with degradation of the block stiffness.

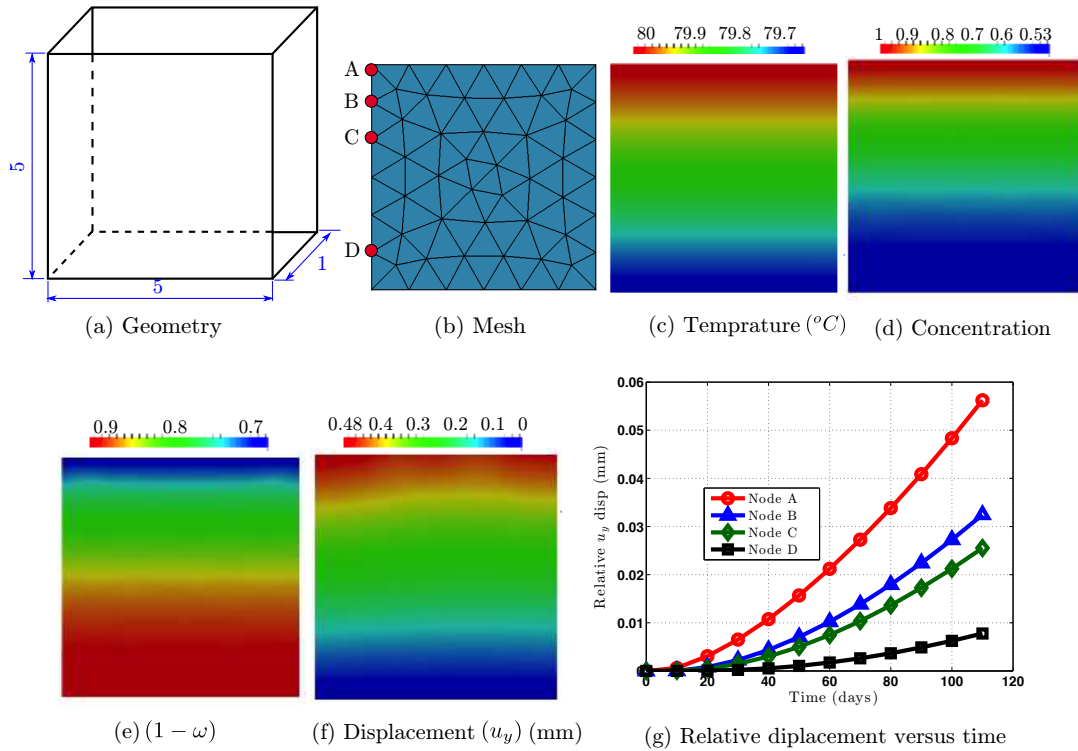


Figure 2: Numerical example geometry, mesh and results

4. Conclusions

A fully coupled hygro-thermo-mechanical computational framework based on multi-scale computational homogenisation is described for FRP composites. The proposed computational framework, which consists of a series of micro and macro analysis, is implemented in our group's FE code MoFEM. A parameterised geometry of the RVE is modelled with CUBIT using a python script, which gives us a flexible and automatic way to create an input file for MoFEM. A degradation model is developed from scratch from experimental data for the mechanical properties of the FRP composites. Finally, a numerical example is presented to demonstrate the correct implementation and performance of the proposed computational framework.

Acknowledgements

The authors gratefully acknowledge the support of the UK Engineering and Physical Sciences Research Council through the Providing Confidence in Durable Composites (DURACOMP) project (Grant Ref.: EP/K026925/1).

References

- [1] L. Tong, A. P. Mouritz, and M. K. Bannister. *3D Fibre Reinforced Polymer Composites*. Elsevier Science, Oxford, 2002.
- [2] A. C. Long, editor. *Design and manufacture of textile composites*. Woodhead Publishing Series in Textiles, Cambridge England, 2005.
- [3] X. Tang, J. D. Whitcomb, Y. Li, and H. J. Sue. Micromechanics modeling of moisture diffusion in woven composites. *Composites Science and Technology*, 65(6):817 – 826, 2005.
- [4] Ł. Kaczmarczyk, C. J. Pearce, and N. Bićanić. Scale transition and enforcement of RVE boundary conditions in second-order computational homogenization. *International Journal for Numerical Methods in Engineering*, 74(3):506–522, 2008.
- [5] M. Ainsworth and J. Coyle. Hierarchic finite element bases on unstructured tetrahedral meshes. *International Journal for Numerical Methods in Engineering*, 58(14):2103–2130, 2003.

SIMULATION OF LAMINATED COMPOSITE PLATES UNDER FREE VIBRATION

***S. Yekrangian and Z. J. Wu**

School of Mechanical, Aerospace and Civil Engineering, University of Manchester,
Sackville Street, Manchester M13 9PL, United Kingdom

*shirin.yekrangian@manchester.ac.uk

ABSTRACT

Laminated composite plates can offer great stiffness and high strength to weight ratio hence are widely used in various fields of industry such as aerospace, aviation, civil and mechanical engineering. Therefore studying their behaviour is of great interest. In this paper behaviour of laminated composite plates under free vibration has been investigated using ABAQUS finite element program. An 8-ply cantilever graphite/epoxy plate is simulated under free vibration using shell elements. The results are compared with experimental results and have shown good agreement. Then the model is used to study the effect of different ply orientations, boundary conditions and thickness to width ratios on the vibration behaviour of composite plates.

Keywords: *Laminated composite plate; Free vibration; Finite element method*

1. Introduction

Laminated composite plates with offering great stiffness and high strength to weight ratio are being more vastly used in various industries such as aerospace, marine, civil and mechanical engineering. In order to use them effectively, a good knowledge of their mechanical behaviour is needed [5,6]. This behaviour is affected by various factors such as material properties, thickness to width ratio and ply orientation of each lamina.

Many researchers have studied the vibration behaviour of laminated composite plates using numerical, analytical and experimental methods [2].

Ma and Lin (2005) [2] studied the vibration behaviour of piezoceramic plates using experimental and numerical methods; they investigated different boundary conditions and various element types however they didn't examine the effect of thickness to width ratio. Wu and Kamis (2012) [8] conducted a numerical study of laminated composite plates and they examined the effect of various element types on finite element modelling of composites under static loading. Kant and Swaminathan (2011) [6] investigated free vibration of laminated composite plates using analytical methods. They investigated the effect of various numbers of layers and different material properties. Kumar and Shrivastava (2005) [1] examined the behaviour of laminated plates with various young's modulus ratios and considered the effect of delamination. However they didn't investigate the effect of ply orientation on the behaviour of laminated composite plates.

In this study, firstly the free vibration of an 8-ply cantilever graphite/epoxy plate is simulated in ABAQUS program using shell elements. The numerical results are compared with experimental results and have been validated. After that the graphite/epoxy plate has been modelled and the effects of different boundary conditions, thickness to width ratios and ply orientations are studied.

2. Verification of the finite element modelling

In order to verify the finite element model, an experimental test for free vibration of an aluminium plate and an 8-ply cantilever graphite/epoxy plate conducted by Crawley (1979) [3] is simulated using ABAQUS program. Both aluminium plate and graphite/epoxy plate have the same geometry.

The geometry of the plate is shown in Figure 1. The specimen consists of a 76×76mm square plate with a total thickness of 1.04mm.

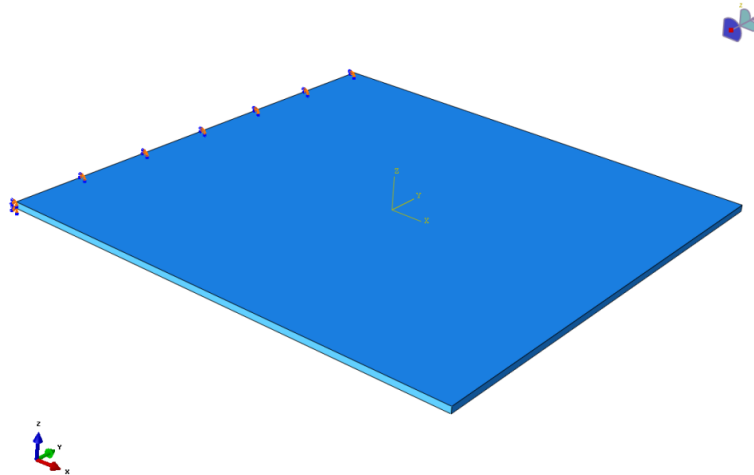


Figure 1: The plate geometry

Material Properties:

The material properties for Aluminium are [4]:

$$E = 68900\text{MPa}, \nu = 0.3, \rho = 2770 \text{ kg/m}^3$$

The material properties for graphite/epoxy are [4]:

$$E_L = 128000\text{MPa}, E_T = 11000\text{MPa}, \nu_{LT} = 0.25, G_{LT} = 4480\text{MPa}, G_{13} = 4480\text{MPa}, G_{23} = 1530\text{MPa}, \\ \rho = 1500 \text{ kg/m}^3, \text{ply thickness} = 0.13\text{mm}$$

Two different ply orientations are presented here for the graphite/epoxy plate that are:

$$[0_2 / \pm 30]_2 \text{ and } [\pm 45 / \mp 45]_2$$

Boundary Conditions: As it was mentioned earlier, the plate is a cantilever. As it is shown in Fig. 1, the left end of the plate has been clamped, restraining all movements and rotations on that edge. The rest of the plate is free for any movement or rotation.

Element Type: S8R shell elements are used to model the cantilever plate. A mesh sensitivity study has been carried out for the $[\pm 45 / \mp 45]_2$ plate. The results are shown in Table 1.

Table 1: The plate fundamental frequencies for the mesh sensitivity study

Mesh size (mm)	7.6mm	4mm	2mm	1mm
Fundamental frequency (Hz)	132.1 (-0.69%)*	132.05 (-0.65%)	132.03 (-0.63%)	132.02 (-0.625%)

*Numbers in the parentheses are the percentage difference with respect to experimental value.

As it is seen, mesh size 2mm shows a very small percentage difference comparing to experimental results and is very close to 1mm mesh size result. Hence the 2mm mesh size has been selected for the modelling. The meshed model is shown in Figure 2.

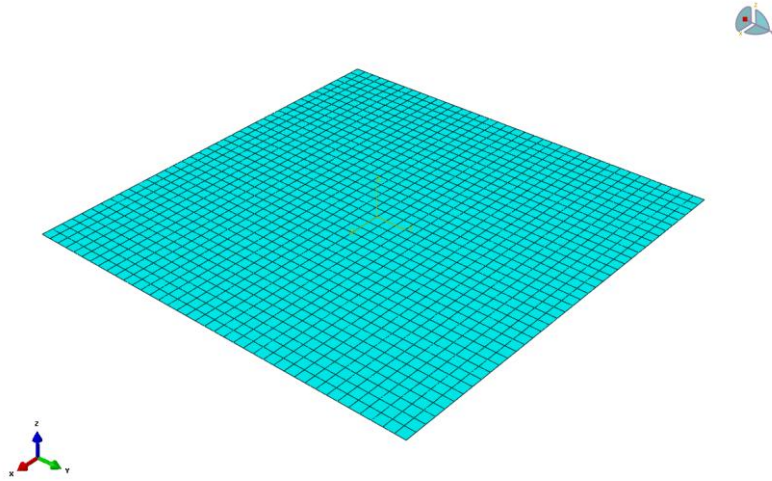


Figure 2: Meshed model

The results from the plates modelling are shown in Table 2. The fundamental frequencies of the plates from ABAQUS are compared with experimental results.

Table 2: Comparison of experimental and numerical fundamental frequencies

Plate Material	Experimental Results (Hz)	ABAQUS Results (Hz)
Aluminium	153	150.06 (2%)**
Graphite/epoxy [0 ₂ / ±30] ₂	234.2	224.94 (-4%)
Graphite/epoxy [±45 / ∓45] ₂	131.2	132.03 (-0.6%)

**Numbers in the parentheses are the percentage difference with respect to experimental values.

As it is shown in Table 2, the ABAQUS model shows good compatibility with experimental results.

3. Numerical Results

Now that the finite element model is validated, the graphite/epoxy square plate has been modelled subjected to various ply orientations, boundary conditions and thickness to width ratios (a/h). Tables 3-5 present fundamental frequencies of these laminated plates in Hz. Where a is the plate length and h is the thickness. Boundary conditions investigated are: CCCC, SSSS, SCSC and SFSF. Where: C stands for clamped, S for simply supported and F for free boundary conditions.

Table 3: Fundamental frequencies of the laminated composite plate with $a/h=5$

$a/h=5$	CCCC	SSSS	SCSC	SFSF
[0/90/0/90]	134270	109770	122510	75890
[0/90/90/0]	144096	111271	136156	86643
[45/-45/45/-45]	128779	109216	119340	53711
[45/-45/-45/45]	138362	110281	125008	54123

Table 4: Fundamental frequencies of the laminated composite plate with $a/h=10$

$a/h=10$	CCCC	SSSS	SCSC	SFSF
[0/90/0/90]	57221	37066	48180	24981
[0/90/90/0]	57993	38069	48819	31380
[45/-45/45/-45]	54216	39228	47432	16356
[45/-45/-45/45]	54811	39283	47715	16447

Table 5: Fundamental frequencies of the laminated composite plate with $a/h=100$

$a/h=100$	CCCC	SSSS	SCSC	SFSF
[0/90/0/90]	941.39	442.14	734.82	287.51
[0/90/90/0]	1004.3	470.83	612.32	393.79
[45/-45/45/-45]	910.48	560.3	753.16	193.86
[45/-45/-45/45]	915.83	548.52	751.49	199.01

4. Conclusions

From the current study, the following conclusions are observed:

In the finite element modelling of free vibration of both isotropic plate and composite plate, shell elements show good compatibility with experimental results.

For the laminated composite plates, it is seen that as thickness to width ratio gets higher, the frequency gets lower for all cases of boundary conditions and ply orientations.

When considering the same thickness to width ratio, it is seen that for all cases of ply orientations, the plate with fully clamped (CCCC) boundary conditions has the highest frequency comparing to other types of boundary conditions in this study, and the one with SFSF has the lowest frequency.

For the CCCC and SFSF boundary conditions in all cases of thickness to width ratios, the plate with ply orientation of [0/90/90/0] have the highest frequency and plates with [45/-45/45/-45] show the lowest frequency.

References

- [1] A. Kumar and R. P. Shrivastava. Free vibration of square laminates with delamination around a central cutout using HSDT. *Composite structures*, 70, 317-333, 2005.
- [2] C. C. Ma and H. Y. Lin. Experimental measurements on transverse vibration characteristics of piezoceramic rectangular plates by optical methods. *Journal of Sound and Vibration*, 286, 587-600, 2005.
- [3] E. F. Crawley. The natural modes of graphite/epoxy cantilever plates and shells. *Journal of Composite Materials*, 13, 195-205, 1979.
- [4] E. F. Crawley and J. Dugundji. Frequency determination and non-dimensionalization for composite cantilever plates. *Journal of Sound and Vibration*, 72(1), 1-10, 1980.
- [5] R. K. Khare, T. Kant and A. K. Garg. Free vibration of composite and sandwich laminates with a higher-order facet shell element. *Composite Structures*, 65, 405-418, 2004.
- [6] T. Kant and K. Swaminathan. Analytical solutions for free vibration of laminated composite and sandwich plates based on a higher-order refined theory. *Composite Structures*, 53, 73-85, 2001.
- [7] W. Q. Chen and C. F. Lue. 3D free vibration analysis of cross-ply laminated plates with one pair of opposite edges simply supported. *Composite Structures*, 69, 77-87, 2005.
- [8] Z. J. Wu and E. Kamis. Influence of element type on the simulation of laminated composite plates with clamped edges. *20th UK Conference on Computational Mechanics (ACME-UK)*, pp. 75-78, 2012.

On the calculation of energy release rates in composite laminates by Finite Elements, Boundary Elements and Analytical Methods

*****B. Tafazzolimoghaddam, J. L. Curiel-Sosa

Department of Mechanical Engineering, University of Sheffield, Sir Fredric Mappin Bld., Mappin St., Sheffield, S1 3JD, UK

*btafazzolimoghaddam1@sheffield.ac.uk

ABSTRACT

To characterise a transversal crack evolution in a cross-ply [0/90]_s fibre reinforced composite laminate, the associated energy release rate (ERR) was calculated by means of the J-integral embedded into the Finite Element Method (FEM). The ERR values computed for the propagation of the transversal crack were correlated to the ones obtained by using the Virtual Crack Closure Technique (VCCT) embedded within the Boundary Element Method (BEM). In addition, the results were compared with analytical values. The results correlated well except when the crack length was approximately 80% of the ply thickness. In such case, ERR values showed some discrepancies between FEM and BEM. The reason stems from the fact that in the VCCT used not all components of the stresses are considered, resulting in smaller ERR values. In addition, the results proved that transversal cracks can influence each other only in a limited distance.

Keywords: *J-Integral, Energy Release Rate, Finite Element Analysis, Boundary Element Method, Transversal Crack, Virtual Crack Closure Technique*

1. Introduction

Matrix cracks often appear prior to other damage modes in composite materials and Increasing the load can lead to their coalescence and formation of macro-transverse cracks [6],[8]. Researchers have attempted to predict different modes of failure in composite materials by using the energy release rate (ERR) as a fracture criterion. There are several methods used for ERR evaluation and comprehensive study on these methods can be found in reference [1].

Xie et al [14] used VCCT in order to calculate the ERR using finite element method. Similarly Zou et al [14] implemented VCCT using the laminate theory instead of linear elastic fracture mechanics to express the energy released in terms of stress-jumps and relative displacements for modes I, II, and III. The use of VCCT within a boundary element framework (BEM) is deemed more appropriate because the boundaries of the problem are directly related to the problem features such as fracture parameters (see Paris et al [6]). Paris and co-workers [6] considered different conditions (e.g. models with and without delamination) and calculated the ERR for different crack lengths. Their results were in good agreement with the analytical results by McCartney [12].

The J-integral approach as a measure of the energy release rate associated with crack propagation whereby a criterion can be introduced in terms of a bounding limit value [11], [10]. J-integral under quasi-static conditions is equal to the energy release rate G for linear elastic materials. In this paper, parametric studies by finite element analysis with different specimen and crack lengths are conducted and compared with results by VCCT-BEM and analytical means.

2. Background: J-integral

J. R. Rice in 1968 [10] formulated Eshelby's [9] contour integral for crack problems. For an edge crack in a nonlinear elastic body the J-integral equals the rate of change (with respect to crack growth, da) in potential energy U_p :

$$J = - \frac{\partial U_p}{\partial a} \quad (1)$$

By definition, J-integral is equal to ERR if the material behaviour is linear and elastic. The change in potential energy for infinitesimal crack extension is:

$$\frac{dU_p}{da} = \lim_{\Delta a \rightarrow 0} \frac{1}{\Delta a} \left(\int_{\Gamma} \bar{T}_i \Delta u_i ds - \int_A \Delta W dA \right) \quad (2)$$

Where Δa is the crack growth and A is the area encompassed by the contour, W is the elastic strain energy, u_i is the displacement, \bar{T} is the traction and ds is an infinitesimally small section of contour Γ enclosing the crack tip. Line integral form of Eq.2 is:

$$J = \oint \left(W dx_2 - \bar{T}_i \frac{\partial \bar{u}_i}{\partial x_1} ds \right) \quad \text{with} \quad T_i = \sigma_{ij} n_j \quad (3)$$

n_j is the normal vector to the integration path and σ is the stress on Γ and W is the density of energy. For linear elastic material elastic strain energy is related to stress and strain as $W = \sigma_{ij} \varepsilon_{ij} / 2$. Line integrals have difficulty of implementation in FE and domain integrals are preferred [3]. Li et al [4] showed that line integral can be transformed into an equivalent area integral around the crack tip. For linear elastic materials Atkinson and Eshelby [2] proposed the domain integral,

$$J = \int_{\Gamma} (W \delta_{1i} - \sigma_{ij} u_{j,1}) n_i ds \quad (4)$$

The process is assumed isothermal and body forces are neglected. Shih et al [3] implemented this integration within the FEM by means of Gaussian integration.

3. Modelling of Transverse Crack in [0/90]_s laminate

The laminate is composite HexPly8552 with the thickness of each lamina equal 0.55mm (1.1mm total thickness) and a defining the crack length. $2L$ is the distance between two transversal cracks. The interface between the two plies is modelled without potential discontinuity and, therefore, there is no possibility of replicating delamination. As the crack is assumed to be through the width, a two dimensional model is justified for analysis. The properties are from Hexeply8552 datasheet [7].

Table1. Material properties (Hexeply8552). All values in GPa. E_{11} represents fibre direction elastic module.

E_{11}	E_{22}	E_{33}	G_{12}	G_{23}	G_{13}	ν_{12}	ν_{13}	ν_{23}
141.3	9.85	9.58	5	3.5	5	0.3	0.3	0.32

The fibre tensile strength is 2207 MPa and the transversal –resin- strength is 81 MPa. The laminate thickness is much smaller than the other two dimensions, i.e. width and length. Therefore, the strain in perpendicular direction can be neglected and, hence, a plane strain state can be assumed. McCartney proposed the ERR analytical solution for the [0/90]_s laminae. In his work [6] the ERR is calculated as the infinitesimal variation of Gibbs Energy (G) in respect to the crack propagation (∂a):

$$ERR = \frac{1}{2} Lh \frac{\partial}{\partial a} \left(\frac{\sigma^2}{E} \right) \quad (5)$$

In McCartney's solution, σ , E and ε are axial components of stress, Young's modulus and strain in the first principal direction respectively. In this case, the principal direction is denoted as y-direction. Paris et al [6] calculate ERR by means of VCCT-BEM. VCCT calculates the ERR by multiplying the displacement of crack face nodes by the force required for crack closure at each node [6]. The interested reader is referred to reference [13] for further details.

4. 2D Cross-ply Laminate Model

The cross section of the laminate is modelled as two sections with separate material definition. The

model represents half of the specimen in both vertical and horizontal directions where symmetric boundary conditions can apply. In this case only one surface of the crack is drawn. The analysis is quasi static and ABAQUS standard solver is used. As the model dimension relatively large in to z direction, plain strain element is used. The crack length was varied between 0 and 0.55 mm at 0.1mm intervals for four different model lengths, L.

5. Results and Discussion

Fig.2a) shows the ERR calculated for L=2mm from three different methods (FEM, theoretical and BLM). FE solver considers transverse stresses which are not considered in VCCT. Therefore g higher value of ERR is achieved. The maximum value is observed approximately at $a=0.4\text{mm}$. For Hexply8552 G_c is equal to 0.3 KJ/m^2 for mode one crack opening [7]. For this load setting G_c is attained approximately $a=0.1\text{mm}$.

When this value is reached the crack extends until somewhere between the maximum ERR and the interface where ERR becomes zero [6]. Theoretically because the ERR decreases to very small amount near the interface the crack must stop just before reaching the 0° ply. In the stress analysis it is clearly visible that for cracks so close to the interface the normal tension at the interface is much larger than the material strength and delamination might happen prior to the crack reaching the interface. Fig.2b) shows the variation of J-integral at similar strain for different model lengths (L=0.5mm, 1mm, 2mm and 4 mm). At L=2 mm, which is twice as large as the model thickness, the neighbouring cracks do not have influence on each other and larger specimens have the same ERR curve.

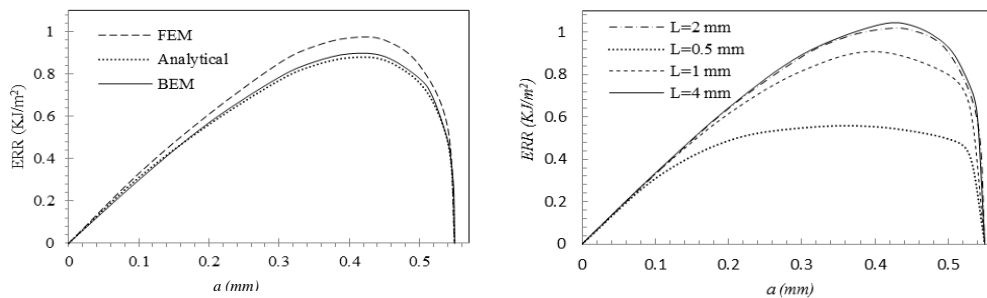


Fig.2 a) ERR for L=2 mm. The crack will extend unstably after $a = 0.1 \text{ mm}$ b) Different specimen length L

The stress distribution in transverse direction also shows large tensile stress in front of the crack tip near the interface. Based on the interface strength for this ply, the delamination must happen before crack reaches approximately 0.05mm to the interface.

6. Conclusion

ERR is a key factor in fracture analysis. The present study has compared three different methodologies for the calculation of the ERR associated to transversal crack in a $[0/90]_s$ laminate. Those are: 1-The J-integral embedded into FEM. 2-The VCCT embedded within BEM and, 3- Analytical means. The following remarks can be highlighted:

ERR values were well-correlated by all three methodologies except when the crack length was approximately 80% of the ply thickness, i.e. to a 20% distance of the interface between distinct plies. VCCT neglects the transversal stress in this implementation of BEM and also the analytical expression that is the possible reason for smaller value of ERR. Therefore, it results in a certain difference only at the aforementioned distance in which that neglected component is significant. No mesh dependence was observed with the FEM for the calculation of the J-integral, although the number of contours used can effect at some point.

The stress distribution at the interface was also presented. It was observed that the stress reaches the maximum allowable at the interface between distinct plies when the transverse crack is very close to the interface.

References

- [1] Banks-Sills and Leslie, "Application of the finite element method to linear elastic fracture mechanics," *Applied mechanics reviews*, pp. 44 (10), 447-461, 1991.
- [2] C. Atkinson and J. D. Eshelby, "The flow of energy into the tip of a moving crack," *International Journal of Fracture*, pp. 4, pp. 3-8., 1968.
- [3] C. F. Shih, B. Moran and T. Nakamura, "Energy release rate along a three-dimensional crack front in a thermally stressed body," *International Journal of Fracture*, pp. 30 (2), pp. 79-102, 1986.
- [4] F. Z. Li, C. F. Shih and A. Needleman, "A comparison of methods for calculating energy release rates," *Engineering Fracture Mechanics*, pp. 21 (1985) 405-421.
- [5] D. Xie, A. M. Waas, W. K. Shahwan, A. J. Schroeder and G. R. Boeman, "Computation of Energy Release Rates for Kinking Cracks based on Virtual Crack Closure Technique," Vols. CMES, vol.6, no.6, pp.515-524, 2004.
- [6] F. París, A. Blázquez, L. N. McCartney and V. Mantic̆, "Characterization and evolution of matrix and interface related damage in [0/90]S laminates under tension. part I: Numerical predictions," *Composites science and technology*, pp. 201. 70 (7), 1168-1175, 2010.
- [7] Hexcel Composites, "HexPly 8552," February 2013. [Online]. Available: http://www.hexcel.com/Resources/DataSheets/Prepreg-Data-Sheets/8552_eu.pdf. [Accessed 2013].
- [8] J. Berthelot, "Transverse cracking and delamination in cross-ply glass-fibre and carbon-fibre reinforced plastic laminates: static and fatigue loading," *Appl Mech Rev*, pp. 56:111-47, 2003.
- [9] J. D. Eshelby, "The Determination of the Elastic Field of an Ellipsoidal Inclusion and Related Problems", *Solid State Physics*, vol. Series:A. Vol. 241, p. Vol.3, 1957.
- [10] J. R. Rice, "A path independent integral and the approximate analysis of strain concentration by notches and cracks", *J. Appl. Mech*, pp. vol. 35, pp. 379-386, 1968.
- [11] L. J. Lee and D. W. Tu, "J-integral for delaminated composite laminates," *Composites Science and Technology*, pp. Volume 47, Issue 2, 1993, Pages 185-192, ISSN 0266-3538.
- [12] L. N. McCartney, "Predicting transverse crack formation in cross-ply laminates," *Composites science and technology*, pp. 58 (7), 1069-1081., 1998.
- [13] R. Krueger, "Virtual crack closure technique: History, approach, and applications," *Applied mechanics reviews*, pp. 57 (1-6), 109-143, 2004.
- [14] Z. Zou, S. R. Reid, S. Li and P. D. Soden, "General expressions for energy-release rates for delamination in composite laminates," *Proceedings of the Royal Society A: Mathematical, Physical and Engineering Sciences*, pp. 458(2019): p. 645-667, 2002.

MECHANICAL MODELLING OF NANO-CELLULOSE COMPOSITE

*CAUDOUX R., DE BORST K.

School of Engineering, University of Glasgow, Glasgow, G12 8QQ

*r.caudoux.1@research.gla.ac.uk

ABSTRACT

Crystalline cellulose is a promising material because of its excellent mechanical strength/weight performance. Current efforts to estimate the mechanical properties of nano-cellulose composites have mainly focused on analytical methods such as the models of Halpin-Tsai or Hashin. These methods have been shown to give good predictions of the overall elastic modulus. However, they only provide a global view of the composite and only consider overall parameters. In this paper, we propose a modelling approach which combine the Mori-Tanaka estimation with a numerical method (FEM) to estimate the dilute concentration strain tensor and the effective stiffness for inhomogeneities of non-ellipsoidal shape and non-homogeneous structure. Emphasis is placed on the interphase between the inclusion and the matrix as it takes a major role for nano-scaled reinforcements.

Key Words: FEM, Nano-cellulosic composites, inhomogeneities, interphase, effective stiffness

1. Introduction

Natural cellulose based material are considered promising due to their excellent mechanical strength/weight performance. The elastic modulus of cellulose is around 110-220 GPa, which is comparable to that of Kevlar (124-130 GPa), and its tensile strength is around 7.5-7.7 GPa, which is even higher than that of Kevlar (3.5 GPa) [3]. Its density of 1.6 is comparable to that of Kevlar (1.4) and of carbon (1.8). Moreover, it is an abundant natural material which is a great answer to the need of sustainable and biodegradable material.

Currently, efforts to estimate the mechanical properties of nano-cellulosic composites have mainly focused on analytical methods such as the models of Halpin-Tsai or Hashin. These methods have been shown to give good predictions of the overall elastic modulus [3]. However, these approaches only provide a global view of the composite and consider overall parameters, such as the volume fractions and the mechanical properties of its components. Therefore, these methods are limited to the elastic behavior and are not flexible enough to permit studying the effect of an interphase in between the fibre and the matrix.

For this reason, we use a combination of the Mori-Tanaka method with a numerical approach for estimating the stiffness of nano-cellulosic composites, the latter for determining the strain concentration tensor and the effective stiffness for inhomogeneities of non-ellipsoidal shape and non-homogeneous structure.

2. Materials and methods

2.1. Mori-Tanaka estimation

Based on mean strains in the individual phases (subdomains), the stiffness \mathbf{C}_{MT} of a composite material made up of inhomogeneities of stiffness \mathbf{C}_{inc} in a matrix of stiffness \mathbf{C}_m can be determined as [1]:

$$\mathbf{C}_{MT} = \mathbf{C}_m + \psi(\mathbf{C}_{inc} - \mathbf{C}_m)\mathbf{A}_{dil}[(1 - \psi)\mathbf{I} + \psi\mathbf{A}_{dil}]^{-1} \quad (1)$$

where ψ is the volume fraction of the inhomogeneities, \mathbf{I} is the unit tensor, and \mathbf{A}_{dil} is the dilute strain concentration tensor. The latter relates the average strain in a single inhomogeneity $\boldsymbol{\epsilon}_{inc}$ embedded into an infinite matrix to far field strain $\boldsymbol{\epsilon}_{\infty}$:

$$\boldsymbol{\epsilon}_{inc} = \mathbf{A}_{dil} : \boldsymbol{\epsilon}_{\infty} \quad (2)$$

The solution for this dilute strain concentration tensor can be obtained analytically for homogeneous inhomogeneities with a simple shape such as ellipsoid from the Eshelby solution [4]. To handle inhomogeneities with non-homogeneous properties (e.g. different materials arranged in different layers), a replacement tensor \mathbf{C}_{inc}^* for an effective inhomogeneity and an associated strain concentration tensor \mathbf{A}_{dil} can be computed numerically, the former using the inverted form of the Mori-Tanaka estimation [5]:

$$\mathbf{C}_{inc}^* = \mathbf{C}_m + 1/\psi_{dil}(\mathbf{C}_{dil}^* - \mathbf{C}_m)\mathbf{A}_{dil}^{-1} \quad (3)$$

where \mathbf{C}_{dil}^* is the overall stiffness tensor with the dilute inhomogeneity volume fraction ψ_{dil} . For this purpose, the elastic behaviour of a single inhomogeneity in an infinite matrix (dilute case) is examined by means of the finite element method. An estimate of the overall stiffness and the concentration strain tensor can be determined by subjecting the dilute model to 6 different displacement cases related to unit axial or shear strain in one direction and zero strain otherwise [2]. The replacement tensor for the inhomogeneity \mathbf{C}_{inc}^* and the concentration strain tensor \mathbf{A}_{dil} are then inserted into the Mori-Tanaka approximation (Eq. (1)).

2.2. Numerical approach

For nano-cellulose composites, the numerical model [Fig. 1] consists of a single, cylindrical particle, representing the cellulose reinforcement, and the surrounding matrix, big enough to behave as an infinitely extended medium. Moreover, a third phase, commonly denoted as interphase, is considered in between the particle and the matrix. The characteristics of this phase are known to lie between the ones of the particle and the matrix. We assumed in this model that the elastic modulus of the interphase is constant across its thickness. Because of the nano-size of the particles, the volume fraction of the interphase can become higher than the one of the particles, underlining the importance of this phase for the mechanical behavior of the composite. The model allows us to study the influence of the volume fraction or characteristics of the fibre, such as the aspect ratio, and the mechanical properties of fibre and interphase, on the overall composite behaviour. Emphasis is placed on the interphase in order to get a better understanding of its effects on the overall behavior.

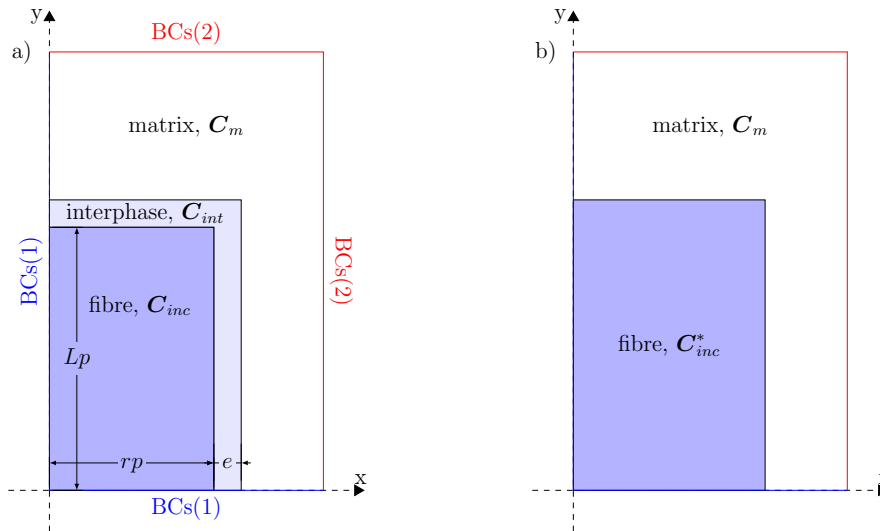


Figure 1: **a)** One eighth of the model representing an embedded inhomogeneity with an interphase in a matrix. **b)** One eighth of the model representing the replacement inhomogeneity, standing for the fibre and the interphase, embedded in a matrix.

Only one eighth of the model is investigated due to symmetries. As outlined before, six cases have been studied corresponding to unit values of strains ϵ_{xx} , ϵ_{yy} , ϵ_{zz} , $\epsilon_{xy/yx}$, $\epsilon_{xz/zx}$, $\epsilon_{yz/zy}$, with all other strains being zero. This allows us to compute the six columns of the dilute strain concentration tensor \mathbf{A}_{dil} and the dilute effective stiffness tensor \mathbf{C}_{dil} from the resulting strains and stresses in the model. The boundary conditions of the model depend on the case, since the deformation of the model can be symmetric or antisymmetric according to the load case (normal or shear stress).

For the strain concentration tensor of the effective inhomogeneity (including fibre and interphase), the averaged strain is obtained by summing the strain over all the elements of the considered volume. Because linear tetrahedrons are used to discretise the model, the averaged strain in one element is equal to its value at the Gauss point. Using the same method, the averaged stress in the entire model is determined. Its relation to the applied strain yields the components of the replacement stiffness tensor (\mathbf{C}_{inc}^* in Eq. (1)).

The mesh is refined in vicinity of the inhomogeneity in order to resolve stress and strain concentration in this region and to ensure that the results are mesh-independent. The volume fraction ψ_{dil} of the fibre has been fixed to 10^{-4} to simulate the far-field behavior of the matrix. The contact in between the three phases (fibre, interphase and matrix) is considered as perfect.

3. Results and discussion

All materials are assumed to be isotropic in a first step. The Young's moduli used for the simulation are for the matrix $E_m = 2$ GPa, the fibre $E_{inc} = 130$ GPa, and the interphase $E_{int} = 20$ GPa. The volume fraction of fibres is 0.05 when not specified differently. The radius of the fibre rp is $5e^{-6}$ mm, the aspect ratio of the fibre Lp/rp is 40, and the thickness of the interphase e is assumed to be $3e^{-6}$ mm. All Poisson's coefficients are assumed as 0.3. As mentioned before, the stiffness modulus of the interphase is assumed to be constant across the thickness. This assumption creates stress concentrations at the interfaces and does not represent the reality, where more gradual changes are expected. The volume fraction of the inhomogeneities is limited to low values because disturbance into the matrix due to short distance in between inhomogeneities is not considered.

The values obtained from the numerical method ('NUM') for a homogeneous inhomogeneity (same properties of fibre and interphase) for both cylindrical and ellipsoidal shapes have been compared to the analytical results ('ANA') for ellipsoidal shape obtained with the Eshelby solution (Fig. 2(a)). For the ellipsoidal cases, numerical and analytical results match well. However there is a difference of around 9% ('Err') between the results for the cylindrical and the ellipsoidal shapes for the value $A_{dil,y}$ related to the average axial strain $\epsilon_{inc,y}^*$ in the inhomogeneity in consequence of unit axial far-field strain $\epsilon_{\infty,y}$ as shown in Figure 2(a). Nevertheless in the literature the solution for the cylindrical shape is commonly approximated by the Eshelby solution (ellipsoidal shape) with one dimension much longer than the other ones. For all other directions, there is no significant difference in between analytical and numerical values. 'E_{voigt}' and 'E_{Reuss}' stand for the the Voigt and Reuss bounds (taking into consideration 3 phases: the inhomogeneity, the interphase and the matrix). These bounds are the same for all the directions because the materials have been assumed isotropic. This could be improved by assuming an orthotropic behaviour of the homogeneity as the mechanical characteristics are over-estimated in the transverse directions.

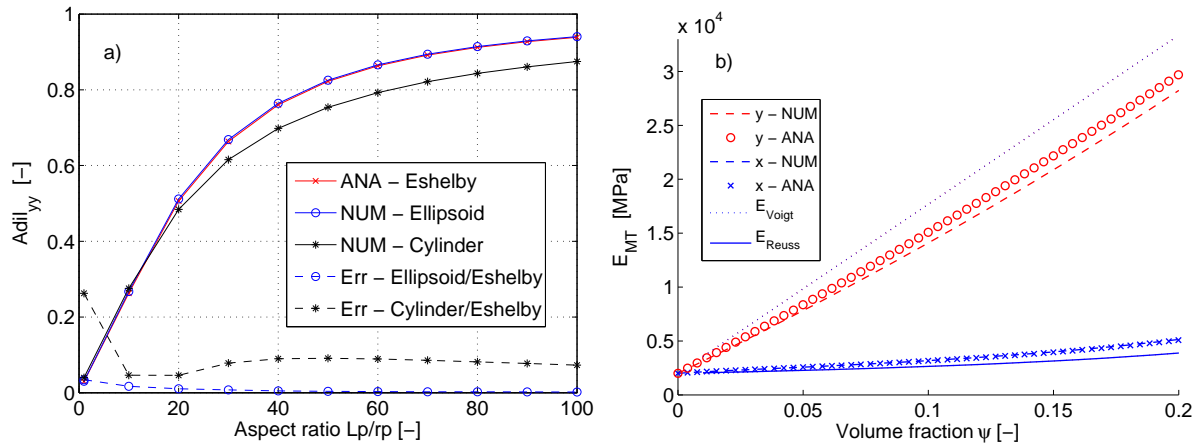


Figure 2: **a)** $A_{dil,y}$ with respect to the aspect ratio of the fibres. **b)** Effective elastic modulus of the nano-composite E_{MT} , with respect to the volume fraction of fibres ψ .

Figure 3(a) shows the evolution of the effective Young's modulus of the composite in the fibre direction with respect to the volume fraction of the fibres. Curves are plotted for different values of the Young's modulus of the interphase. Naturally, there is an increase of the effective stiffness as the stiffness of the interphase increases. Figure 3(b) shows the stiffness of a nano-cellulose composite with aligned fibres for

all directions (plotted on a circle with angles between 0° and 360° between loading and fibre direction). The results for random in-plane fibre orientation are plotted as well, resulting in a circle.

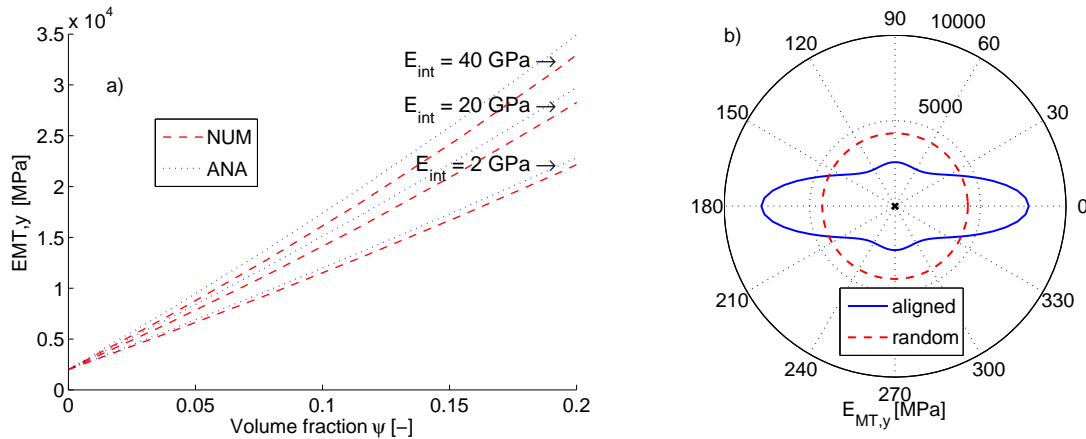


Figure 3: **a)** Effective elastic modulus of the nano-composite in fibre direction $E_{MT,y}$ with respect to the volume fraction of the fibres ψ , for different values of the elastic modulus of the interphase E_{int} . **b)** Effective elastic modulus of the nano-composite E_{MT} with respect to the load angle (0° to 360°).

4. Conclusions

By means of continuum micro-mechanics using a combination of the Mori-Tanaka estimation and a numerical method (FEM), we estimated the elastic modulus of cellulose nano-composites from their microstructural characteristics and the mechanical properties of their components. Contrary to analytical methods, numerical investigations offer more flexibility, which will allow us to go further and study non linear behaviour such as debonding in the future.

The modelling of the interphase plays a major role in the prediction of the overall elastic modulus, since its properties strongly affect the overall behaviour of the nano-composites. The results showed that the numerical solution for the dilute strain concentration tensor of a cylindrical shape gives different estimates of the overall behaviour in the fibre direction than the analytical and numerical approximations for an ellipsoidal shape although solutions for ellipsoidal shape are used to be approximated by the solutions for inhomogeneities with cylindrical shape in the literature.

In the future, a model based on numerical methods able to overpass the limits met by using analytic methods will be developed. We intend to use a numerical model also at macro-scale and develop scale-bridging methods to link the two models (nano-scale and macro-scale). This will enable to look at debonding and percolation effects and to take into consideration nano-composites with a higher volume fraction of the inhomogeneities.

Acknowledgements

I would like to thank Karin de Borst and the Glasgow university for giving me the opportunity work on that project.

References

- [1] Helmut J. Bohm. A short introduction to basic aspects of continuum micromechanics. 3.
- [2] R Bradshaw. Fiber waviness in nanotube-reinforced polymer compositesII: modeling via numerical approximation of the dilute strain concentration tensor. 63(11):1705–1722.
- [3] Robert J. Moon, Ashlie Martini, John Nairn, John Simonsen, and Jeff Youngblood. Cellulose nano-materials review: structure, properties and nanocomposites. 40(7):3941.
- [4] Toshio Mura. *Micromechanics of defects in solids*. Number 3 in Mechanics of elastic and inelastic solids. M. Nijhoff ; Distributors for the U.S. and Canada, Kluwer Academic Publishers, 2nd, rev. ed edition.
- [5] Sergio Nogales and Helmut J. Bohm. Modeling of the thermal conductivity and thermomechanical behavior of diamond reinforced composites. 46(6):606–619.

COUPLED PROBLEMS 1

Vortex-Induced Vibration of a Circular Cylinder

*M. Al Manthari and P. Nithiarasu

Zienkiewicz Centre of Computational Engineering, College of Engineering, Swansea University,
Swansea, SA2 8PP, United Kingdom

*683446@swansea.ac.uk

ABSTRACT

The topic of vortex-induced vibration (VIV) has been studied by a large number of researchers due its importance in the fields of energy generation, structural designs and biomedical engineering. The tool employed in the present work to study VIV of cylinders is OpenFOAM-2.2.2. The mathematical model employed is the two-dimensional Navier-Stokes equations. Initially, the VIV of rigid cylinder is studied in detail to benchmark the method. Both one and two degrees of freedom are used in the calculations. For all calculations presented in this work, the cylinder motion is represented by a spring stiffness and damping at a Reynolds number of 100. Two different types of vibration have been discussed, cross flow and in-line vibrations which are caused by drag and lift forces, respectively. The cylinder is allowed to oscillate naturally in cross flow direction (y -direction) in order to capture the cylinder displacement. The results obtained for a rigid cylinder shows that the drag (C_d) and the lift coefficients (C_l) are in good agreement with published data.

Keywords: vortex-induced vibration (VIV); rigid cylinder; OpenFOAM; lift coefficient; drag coefficient

1. Introduction

Vortex-induced vibration (VIV) for elastically or rigidly mounted circular cylinder in cross flow has been the subject of different investigations over a number of years. It is one of the major causes of engineering problems arising from fluid-structure interaction (FSI). The 1940 collapse of Tacoma-Narrow Bridge caused by wind-induced vibrations is the best example of severe structural limitations arising from Vortex-induced vibrations. The VIV phenomenon has since attracted extensive interest in both industry and academia for decades.

This phenomenon is commonly encountered in hydrodynamic systems where excitations occur due to vortex shedding from bluff bodies. The vortices excitations together with shedding process create asymmetric distribution of pressure around a circular cylinder, which eventually result in body motion. The body movement is inherently nonlinear and occurs over continuous and broad range of frequencies thus increasing the shedding strength.

To date, Xie and others [4, 5] denoted that there is massive body of literature on VIV covering both numerical and experimental investigations, single to multi-degree of freedom motion, VIV in air, flexible to rigid motions, water, etc. In addition, Anagnostopoulos studies [2, 3] used a numerical simulation method to investigate VIV. The author used a 2D circular cylinder in a two degrees of freedom under uniform flow at $Re=200$. The 2D incompressible Navier-Stokes equations were solved using space-time finite element approach, while cylinder motion equations are solved using explicit integral method. The study findings demonstrated as follows; at relatively low mass damping, the VIV exhibits different trends of drag and lift coefficients and analysis of cylinder displacements for the different oscillations is dependent of frequencies under lock-in.

2. Numerical Approaches

Although there are many existing methods and techniques in FSI applications, we have used OpenFOAM, an open source CFD tool, to perform flow simulations. The OpenFOAM CFD tool has in-built solver featuring a collections of C++ libraries specifically designed to solve continuum mechanics problems based on finite volume discretization approach. Finite volume is a necessary procedure in solving partial differential equations (PDE's) governing conservation of mass and

momentum. The dynamic mesh method in OpenFOAM is invoked to move the mesh. The pimpleDyMFOam solver, release 2.2.2 of OpenFOAM has been employed.

3. Governing Equations

The two dimensional, incompressible, Navier-Stokes equations are expressed in terms of Cartesian coordinate system as

$$\frac{\partial u_i}{\partial t} + u_j \frac{\partial u_i}{\partial x_j} = -\frac{\partial p}{\partial x_i} + \frac{1}{\text{Re}} \frac{\partial^2 u_i}{\partial x_j \partial x_j} \quad (1)$$

$$\frac{\partial u_i}{\partial x_i} = 0 \quad (2)$$

where u_i and u_j are the velocity components in x_i and x_j coordinate directions, respectively. P is the pressure. The dimensionless parameter, Reynolds number (Re), is based on the cylinder diameter, D , the free-stream velocity, U_∞ , and the kinematic viscosity of the fluid, ν ; $\text{Re} = U_\infty D / \nu$.

The dynamic equation of the body can be modelled via a mass-spring system as follows

$$\ddot{X} + 4\Pi \xi_x f_{nx} \dot{X} + 4\Pi^2 f_{nx}^2 X = \frac{C_D}{2M_{rx}} \quad (3)$$

$$\ddot{Y} + 4\Pi \xi_y f_{ny} \dot{Y} + 4\Pi^2 f_{ny}^2 Y = \frac{C_L}{2M_{ry}} \quad (4)$$

Here, \ddot{X} , \dot{X} and X represent the in-line acceleration, velocity and displacement of the cylinder, respectively; while the same quantities denote for the transverse motion by \ddot{Y} , \dot{Y} and Y . The natural frequencies of the cylinder along both directions are represented by f_{nx} and f_{ny} . $\xi_x = \xi_y = \xi$ are the structural damping ratios; $M_{rx} = M_{ry} = M_r = m/\rho D^2$ are the reduced masses of the body, where m is the mass of the cylinder per unit length. C_D and C_L are drag and lift coefficients, respectively. They are calculated as $C_D = 2F_D / \rho U_\infty^2 D$ and $C_L = 2F_L / \rho U_\infty^2 D$, where F_D and F_L are the in-line and cross-flow forces acting on the cylinder.

4. Description of the Problem and Simulation Parameters

In the present study both the one and two degrees-of-freedom are employed to predict vortex-induced vibration. In the case of one degree-of freedom, the cylinder is restricted from moving in the inline direction. On the other hand, the two-degrees-of-freedom case the cylinder is free to vibrate in both inline and transverse directions. All four springs shown in Figure 1 have the same stiffness and damping coefficients. The cylinder is not allowed to rotate. For both VIV cases, the results obtained are shown in Figures 2 to 4.

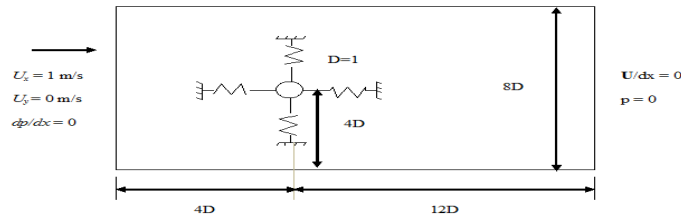


Figure 1: Geometry and Flow Conditions

5. Results and Discussions

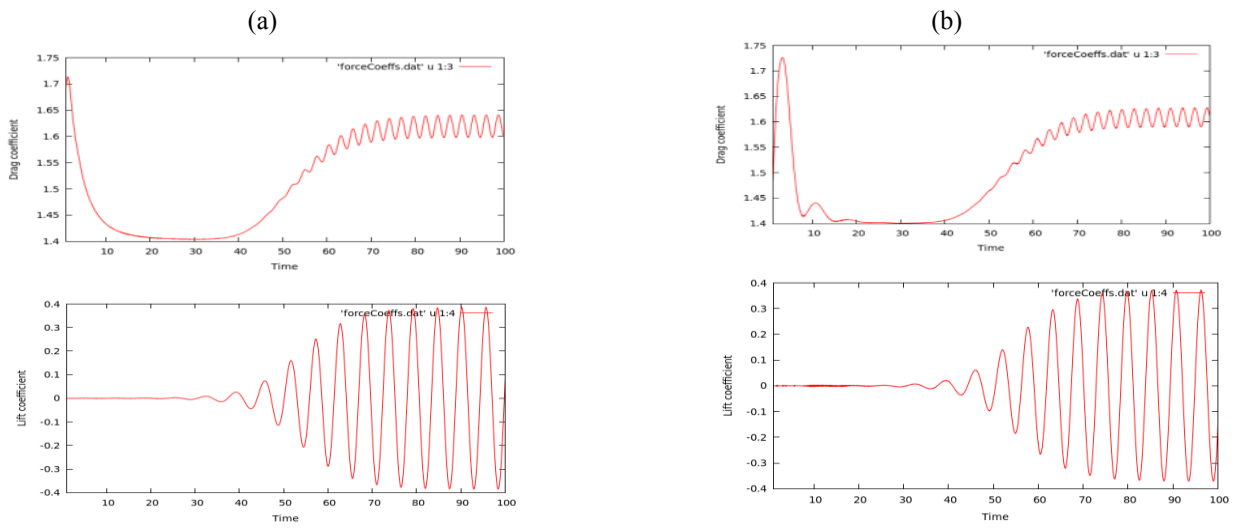


Figure 2: Vortex-Induced Vibration at $Re = 100$ of the Drag and Lift Coefficients of the Cylinder

(1) 1dof VIV, (b) 2dof VIV

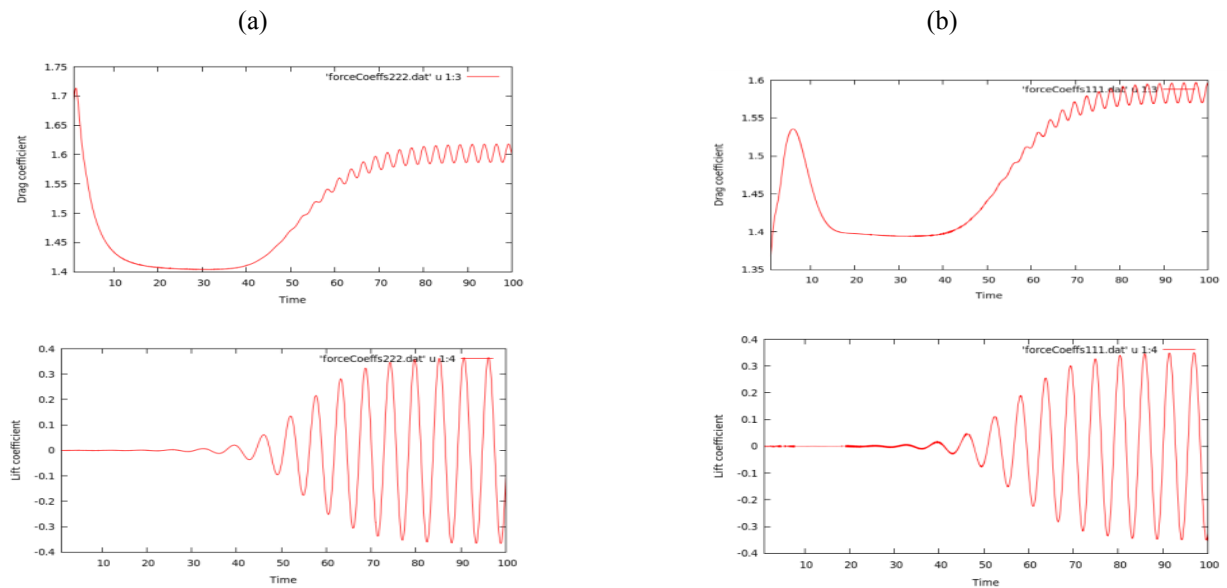
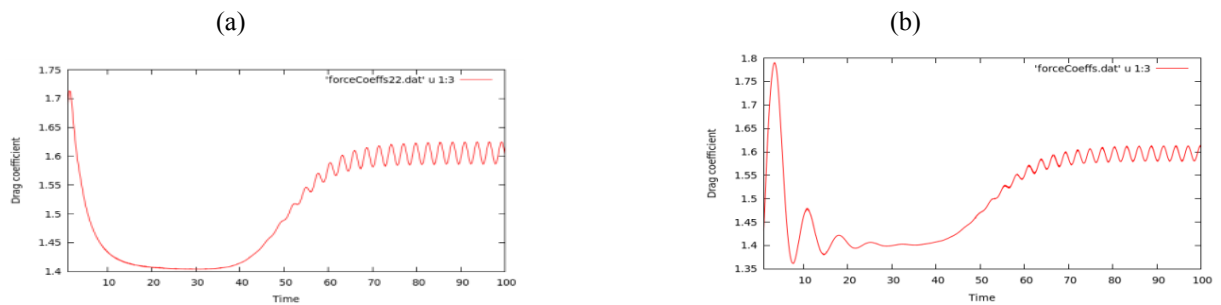


Figure 3: Vortex-Induced Vibration with Reduced Spring Stiffness at $Re = 100$ of the Drag and Lift Coefficients of the Cylinder. (a) 1dof VIV, (b) 2dof VIV



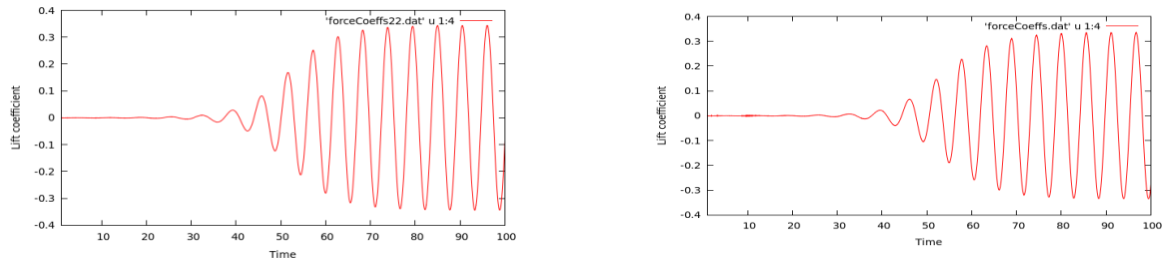


Figure 4: Vortex-Induced Vibration with Reduced damping at $Re = 100$ of the Drag and Lift Coefficients of the Cylinder. (a) 1dof VIV, (b) 2dof VIV

All calculations of one and two-degree-of-freedom of a cylinder are set for $Re = 100$, mass of the cylinder is set to be 9.97 kg, damping coefficient is 2, and spring stiffness is 4 for all four springs. Simulation results show that drag and lift coefficients of the naturally oscillating cylinder for 100 seconds flow time.

From Figures 2-4, it can be seen that the amplitude of lift coefficient of cylinder with one and two-degrees-of-freedom is higher than the amplitude results after reducing spring damping or stiffness. In reality, that shows oscillation becomes to vanish after some time because of forces affect on it.

6. Conclusion

In this work, vortex induced vibration (VIV) has been studied using OpenForm. As shown, this open source code is able to accurately model VIV of a circular cylinder. The drag and lift distributions obtained for freely vibrating cylinder are in good agreement with the published work.

References

- [1] P. Anagnostopoulos. Numerical investigation of response and wake characteristics of a vortex-excited cylinder in a uniform stream. *Journal of Fluids and Structures*, 8(4), 367-390, 1994.
- [2] P. Anagnostopoulos. Numerical study of the flow past a cylinder excited transversely to the incident stream. Part 1: lock-in zone, hydrodynamic forces and wake geometry. *Journal of Fluids and Structures*, 14(6), 819-851, 2000.
- [3] A. Khalak, and C. Williamson. Motions, forces and mode transitions in vortex induced vibrations at low mass-damping, *Journal of Fluids Structures*, 13,813–851, 1999.
- [4] F. Xie, J. Deng, Y. Zheng. Multi-mode of vortex-induced vibration of a flexible circular cylinder. *Journal of Hydrodynamics, Ser. B*, 23(4), 483-490, 2011.
- [5] F. Xie, J. Deng, Q. Xiao, Y. Zheng. A numerical simulation of VIV on a flexible circular cylinder. *Fluid Dynamics Research*, 44(4), 21-44, 2012.

SPH modelling of tsunami-induced bore and structure interaction using DualSPHysics

*Gede Pringgana, Lee S. Cunningham and Benedict D. Rogers

Modelling and Simulation Centre (MaSC)
School of Mechanical, Aerospace and Civil Engineering, The University of Manchester, Manchester, M13 9PL

*gede.pringgana@postgrad.manchester.ac.uk

ABSTRACT

A series of 3-D smoothed particle hydrodynamics (SPH) models with a domain in the form of a water tank were undertaken to simulate tsunami-induced bore impact on a discrete onshore structure on a dry bed. The tsunami-like waves were represented by solitary waves with different characteristics generated by the numerical paddle wavemaker. Numerical probes were uniformly distributed on the structure's vertical surface with spacing twice that of the diameter of particle, providing detailed measures of the pressure distribution across the structure. This allows the impact forces acting on certain areas to be derived directly from the pressures output. The peak impact location on the structure's surface can be specifically determined and the associated peak forces are compared with two existing design code predictions. The results show that the equations used to estimate the forces for design purposes can both over and under-predict the forces.

Keywords: SPH; tsunami; bore; wave-structure interaction

1. Introduction

At present, there is little, if any, detailed codified guidance specifically addressing the design of onshore structures situated in tsunami risk areas, Nistor et al. [1]. The work presented herein forms part of an investigation aiming to enhance current understanding of tsunami wave-structure interaction with a view to improving current design provisions. The numerical modelling technique of smoothed particle hydrodynamics (SPH) offers the potential for improved definition of wave characteristics and associated pressures on impacted structures. Previous studies have demonstrated the efficacy of the technique e.g. St-Germain et al. [2] where in addition to the laboratory experiments on tsunami wave impact on structures near shore, the associated numerical modelling study was conducted using SPH on the basis of analogies between tsunami bores and dam break waves. SPH is a meshless Lagrangian technique which is ideal for simulating highly nonlinear free-surface phenomena such as breaking waves. Furthermore, the SPH technique has also been used to model other violent wave behaviour such as storm wave impact on vertical walls near shore, Altomare et al. [3]. A study by the authors on tsunami wave and structure interaction showed the applicability of SPH in quantifying tsunami wave characteristics within acceptable levels of accuracy, Cunningham et al. [4].

Robertson et al. [5] stated that the main research on wave impact forces on structures can be categorized into the following three areas: (i) work related with storm wave impact on offshore platforms which is presently the most commonly studied; (ii) combining experimental and numerical research in order to develop design formulae for associated loads on structures; (iii) research on the forces and associated structural response resulting from tsunami bores impacting on land-based near shore structures. This last area, is least studied. Consequently, there is a need for better understanding of tsunami bore impact on onshore coastal structures due to the relatively limited available research. In the context of this work, a bore is a steep, rapidly moving broken wave with an onshore mass flux that can be very destructive [6]. In areas of vulnerability to tsunamis, designers of onshore structures need to have better guidance on quantifying tsunami induced loads that should be considered for building design and strengthening of existing structure. In conjunction with the numerical modelling described in the following sections, related studies needed to be reviewed and is part of ongoing work. For example, the propagation of bores on a dry bed and its impact on vertical walls were studied by Cross [7] who proposed the following equation to predict the bore impact force on the wall:

$$F = \frac{1}{2} \rho g h_b^2 + \rho h_b v_j^2 \quad (1)$$

in which ρ is the mass density of water, g is gravitational acceleration, h_b is the height of the bore, and v_j is the propagation speed. Alternatively, Fujima et al. [8] proposed two equations for a dry flat shoreline configuration based on the maximum water inundation level and the distance of the structure from the shoreline. The equation expresses the distance of structure from shoreline (D) in terms of (h_{im}/D) , where h_{im} is the maximum inundation depth. For the numerical model presented here the condition where $h_{im}/D > 0.05$ is satisfied, the structure is categorized as close to the shoreline, thus the equation that is applicable for an average estimation of force is:

$$F = 1.8 \rho g h_{im} B \quad (2)$$

in which B is the breadth of structure. As an appropriate safety factor, Fujima et al. [8] suggests the coefficient of 1.8 in Equation (2) be increased to 3.3. These equations have been based small-scale physical experiments for bores propagating over a dry bed.

2. Computational Domain

Numerical simulations using smoothed particle hydrodynamics (SPH) with open source software called DualSPHysics [9] were conducted to predict tsunami-like bores impacting on structures. The DualSPHysics code can use the acceleration provided by graphics processing units (GPUs) to run simulations involving large numbers of SPH particles in relatively short runtimes, for example, a few hours for 500,000 particles. A water tank for simulating near-shore and onshore areas was set as the model domain, see Figure 1. The dimensions of the numerical water tank are 15 m high, 3 m wide and 5 m high. The numerical domain consists of an offshore region containing water particles, an inclined sea bed and onshore region where the coastal structure is placed. The particles representing water and solid parts in the domain have initial spacing (d_p) equal to 1/20 of the still water level (h_0) that was in this case set to be 1 m leading to approximately 600,000 particles.

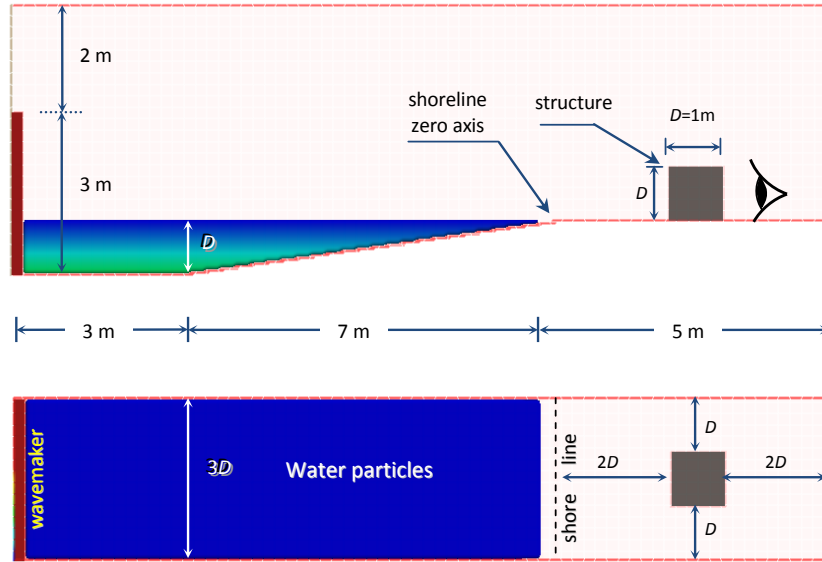


Figure 1 The side and top view of 3-D model (not to scale)

The paddle wavemaker was located at the left-hand side of the tank and partly submerged. The paddle generated solitary waves representing tsunami-like waves. The solitary wave travelled along the tank and produced a bore as it reached the shoreline before impacting the onshore structure at the opposite side of the tank. The solitary waves were designed to have different heights equal to $H/h_0 = 0.1, 0.3$ and 0.5 , hence, producing different bore characteristics. A separate simulation was performed for each different wave height. The paddle wavemaker motions were based on Goring's equation and related with wavemaker theory as explained by Dean and Dalrymple [10]. In accordance with this theory, for

example, a 1.63 m paddle stroke is needed for generating a solitary wave height equal to 50 cm or $H/h_0 = 0.5$.

The bore's characteristics for impact loading are velocity and height and both were measured by numerical probes situated in front of the onshore structure. The pressures caused by bore impact were measured by numerical probes mounted on the surface of the structure and from this pressure the acting force can then be derived. The pressure distribution on the structure's surface was also evaluated to determine the maximum impact occurrence location and time. The numerical probes were uniformly distributed on the structure's vertical surface, with spacing twice that of the diameter of particle, intended to be able to accurately measure pressure distribution. A numerical convergence study was conducted to identify the smallest resolution (particle size) such that simulations could be conducted in the shortest amount of time possible without compromising accuracy.

3. Results and Discussion

Figure 2 and Figure 3 show the 3-D simulation for the case with $H/h_0 = 0.5$. Figure 2a depicts snapshot of a propagating solitary wave which then followed by a bore impact on structure as shown by Figure 2b. Figure 3a shows the peak pressure impact that occurred at $t = 4.150$ sec and the peak pressure which took place at the lowest level of probes as indicated by the circle in the figure.

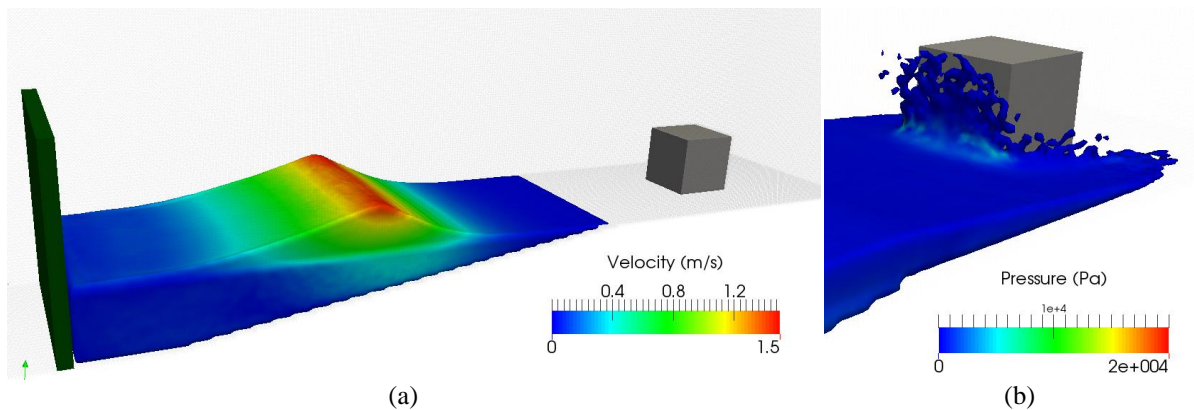


Figure 2 Side view of the 3-D simulation for case $H/h_0 = 0.5$; (a) solitary wave propagation at $t = 2.875$ sec., (b) bore impacting structure at $t = 4.325$ sec.

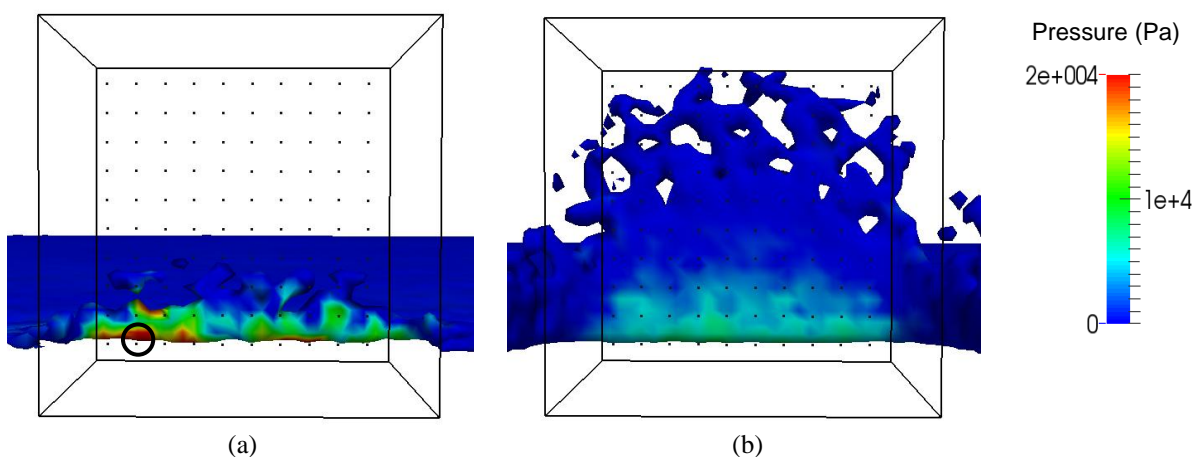


Figure 3 Pressure distribution on vertical surface for a model with $H/h_0 = 0.5$; (a) first impact at $t = 4.150$ sec, (b) peak impact occurred at probe in a circle at $t = 4.325$ sec.

In addition, Figure 3b shows the pressure distribution for the maximum bore runup on the surface of the structure that occurred at $t = 4.325$ sec and corresponding with Figure 2b. Pressure distributions in Figure 3 were seen from the rear of the structure (see illustration indicating direction of view in Figure 1) by assuming the cube structure is visually transparent.

The normalised peak pressures ($P/\rho gh$) for the simulation with wave height equal to $H/h_0 = 0.1, 0.3$ and 0.5 were $0.748, 18.165$ and 83.287 , respectively. The force (F) acting at a certain point in the 3-D model can be determined by multiplying the pressure (P) from SPH analysis output with the associated area (A). Hence, the total force (F) acting normal to a surface can be estimated by summing the total number of forces acting on the surface. The bore pressures for the case with $H/h_0 = 0.1$ were comparatively small, resulting in a correspondingly small impact force. Hence, the comparison of the predicted impact forces between the numerical and the empirical equation were made only for the case with $H/h_0 = 0.3$ and 0.5 . The maximum total forces (per m^2 area) for the case with wave height equal to $H/h_0 = 0.3$ and 0.5 were 1124.49 N, and 3915.46 N, respectively. The associated impact forces determined by Equation (1) were 2277.75 N and 4222.14 N for the case with $H/h_0 = 0.3$ and 0.5 , respectively. In addition, the impact forces predicted by Equation (2) were 1638.88 N and 3525.42 N, for the case with $H/h_0 = 0.3$ and 0.5 , respectively, which indicate potential non-conservatism in the design equation, even with the onerous factors of safety. However, this must be viewed within the context that in general design equations adopt a quasi-static approach to the wave pressures, whereas in reality the peak pressure occur over a very short time period.

Finally, it is important to note that one of the overall objectives of this work is to use the output from DualSPHysics SPH results presented here as an input to the structural analysis software ABAQUS to examine the structural response as already demonstrated in Cunningham et al. [4].

4. Conclusion

A realistic simulation of a tsunami-like wave induced bore impacting onshore structures on a dry bed is performed using SPH. The numerical results are based on varying solitary wave heights but with the same resolution and domain dimensions. The numerical predictions of the bore impact can offer greater insight into the resulting pressures than those predicted by current design equations. This level of detail in the wave-structure interaction can lead to improved resilience of onshore structures in tsunami risk areas of the world. The results from SPH show important differences from the forces predicted by the design equations and are the focus of ongoing research.

References

- [1] I. Nistor, D. Palermo, T. Al-Faesly, A. Cornett. Modelling of tsunami-induced hydrodynamic forces on buildings. *33rd IAHR Congress: Water Engineering for a sustainable environment*, pp.6766-6773, 2009.
- [2] P. St-Germain, I. Nistor, R. Townsend, T. Shibayama. Smoothed-Particle Hydrodynamics Numerical Modelling of Structures Impacted by Tsunami Bores. *Journal of Waterway, Port, Coastal, and Ocean Engineering*, 140, pp.66-81, 2014.
- [3] C. Altomare, A.J.C. Crespo, J.M. Dominguez, M. Gomez-Gesteira, T. Suzuki, T. Verwaest. Applicability of Smoothed Particle Hydrodynamics for estimation of sea wave impact on coastal structures, *Coastal Engineering*, 96, pp.1-12, 2015.
- [4] L.S. Cunningham, B.D. Rogers, G. Pringgana. Tsunami wave and structure interaction: an investigation with Smoothed Particle Hydrodynamics. *ICE Proceedings- Engineering and Computational Mechanics*, 167, Issue EM3, pp.126-138, 2014.
- [5] I.N. Robertson, H.R. Riggs, K. Paczkowski, A. Mohamed. Tsunami bore forces on walls. *Proc.30th Int. Conf. on Ocean, Offshore and Arctic Engineering*, June 19-24, Rotterdam, The Netherlands, 2011.
- [6] Intergovernmental Oceanographic Commission. Tsunami Glossary. *IOC Technical Series*, 85, Paris, France, UNESCO, 2008.
- [7] R.H. Cross. Tsunami surge force. *Journal of the Waterways and Harbors Division, Proceedings of the American Society of Civil Engineers*, November, pp. 201-231, 1967.
- [8] K. Fujima, F. Achmad, Y. Shigihara, N. Mizutani. Estimation of tsunami force acting on rectangular structures. *Journal of Disaster Research*, 4 (6), pp. 404-409, 2009.
- [9] A.J.C. Crespo, J.M. Dominguez, B.D. Rogers, M. Gomez-Gesteira, S.M. Longshaw, R. Canelas, R. Vacondio, A. Barreiro, O. Garcia-Feal. DualSPHysics: Open-source parallel CFD solver based on Smoothed Particle Hydrodynamics (SPH). *Computer Physics Communications*, Vol. 187, pp. 204-216, February, DOI: 10.1016/j.cpc.2014.10.004, 2015.
- [10] R.G. Dean and R.A. Dalrymple. Water wave mechanics for engineers and scientists. *World Scientific, Series on Ocean Engineering-Volume 2*, 1991.

NUMERICAL INVESTIGATIONS INTO DYNAMIC LOADING OF RUBBER COMPOUND

Fawzi Belblidia¹, Shahid Mehmood¹, Chun Hean Lee¹, *Hector U. Levatti¹ and Johann Sienz¹
David T. Gethin² and Cris Arnold²

¹ASTUTE, Advance Sustainable Manufacturing Technologies, Digital Technium,

^{1,2}College of Engineering, Swansea University, Swansea SA2 8PP, UK

*h.u.levatti@swansea.ac.uk

ABSTRACT

The present paper analyses the heat generation build-up in silicone rubber samples when subjected to dynamic cyclic loading. Material properties of the rubber were determined through thermal and mechanical experimental testing. These properties are necessary to set up the computational model. The model includes a fully coupled transient nonlinear thermo-mechanical finite element analysis. In order to validate this approach, numerical results are compared with those gathered experimentally. The numerical model developed and validated could be used to simulate various industrial applications, involving rubber parts, for efficient and sustainable design.

Keywords: rubber; heat build-up; cyclic load; dynamic; thermo-mechanical coupled model.

1. Introduction

Elastomers or rubbers are polymers comprised of long polymeric chains. Upon application of loads these chains are extended upto 200-800% [1], and the elastomer will recover its original form when these loads are removed. Heating of rubber in the presence of sulphur (vulcanization) creates the cross links between polymeric chains making the chains harder to pull apart [2] and hence stronger and more durable rubber is made.

In a dynamically loaded rubber structure, heat generated by hysteresis losses during cycling deformations causes aging and degradation of its physical and chemical properties [3], consequently increasing stiffness and loss of damping characteristics.

This paper presents a novel numerical model to simulate temperature rise within the silicone rubber during dynamic cyclic loading. This involves a direct fully coupled transient nonlinear thermo-mechanical finite element analysis, implemented within Ansys software platform. The model incorporates predictions of energy loss responsible of heat build-up and a hyper-elastic material model. The numerical model is validated by mean of a comparison with the experimental data gathered during a dynamic cyclic test. The model could be used in simulating various industrial applications, such as roller coating, pneumatics, joints, etc..., to design rubber parts for efficiency and sustainability.

2. Dynamic Mechanical Analysis

Dynamic Mechanical Analysis (DMA) is a standard test to evaluate hysteresis and, hence heat generation rate, within a rubber. To achieve this, recall first that the hysteresis H is typically described by:

$$H = \frac{E_L}{E_T} = \frac{E_L}{E_S + E_L} \quad (1)$$

Notice that the total modulus E_T can be additively decomposed into the summation of a storage modulus E_S and a loss modulus E_L . Here, the storage modulus measures the stored energy representing the elastic portion. The loss modulus, on the other hand, measures the energy dissipation

through heat representing the viscous portion. Therefore, it is possible to obtain the heat generation rate as:

$$Q = E_L \times f = H \times E_T \times f \quad (2)$$

where f represents the frequency of the loading. It is crucial to point out that the temperature build-up within a rubber is strongly dependent on the calculation of heat generation rate Q .

3. Ogden Hyper-elastic Constitutive Law

Rubber elastomers are characterized by a low elastic modulus and a high yield strain. They undergo large deformation when stretched and are able to recover their initial shape reversibly. They exhibit a nonlinear hyper-elastic behaviour that can be described through Ogden material model. This model uses the strain energy density function from which stress–strain relationship can be derived.

In this paper, the strain energy density per unit volume is expressed as a function of the three principal stretch ratio λ_j in the j^{th} direction, and material constants μ_i and α_i as:

$$W = \sum_{i=1}^N \frac{\mu_i}{\alpha_i} \left(\lambda_1^{\alpha_j} + \lambda_2^{\alpha_j} + \lambda_3^{\alpha_j} - 3 \right); \forall j = \{1, 2, 3\} \quad (3)$$

4. Curve Fitting 3rd Order Ogden Model

Under dynamic cyclic loading, rubber material will generate internal heat build-up due to energy loss that results in a temperature rise, and subsequently higher stresses. Here, stress-strain curves corresponding to a medium test speed of 50 mm/minute and five different temperatures in the range 25-125 °C are used for curve fitting based on a 3rd order Ogden model. Material parameters (of Equation 3) derived after curve fitting are shown in the Table 1. With these values the constitutive equations were calibrated achieving good agreement with the experimental data.

Table 1 - Ogden material parameters (according to Equation 3) between 25 and 125 °C at the crosshead speed of 50 mm/min

Temp °C	Material parameters for Ogden model					
	μ_1	μ_2	μ_3	α_1	α_2	α_3
25	-41.037	46.134	231.382	0.645	0.626	0.003
50	-44.329	48.653	230.425	0.268	0.278	0.007
75	-52.614	40.305	230.968	0.610	0.671	0.035
100	-50.489	54.473	232.021	0.225	0.066	0.049
125	-72.853	71.120	204.775	0.253	0.081	0.079

5. Computational Model with Experimental Validation (2Hz, 15%)

Dynamic tests in compression mode were conducted to study the temperature build-up inside the cylindrical rubber of 25 mm diameter x 25 mm thickness. The tests were conducted on servo-hydraulic Phoenix universal testing machine at room temperature (25 °C). A cyclic displacement of 3.75 mm (i.e. compressions of 15 %) is imposed on the top plate, whilst the bottom plate is fixed (see Figure 1). In this paper, a loading frequency of 2 Hz is assumed. The main objective of this testing is to illustrate the performance of the numerical approach in silicone rubber experiencing large deformation. For comparison purposes, a K-type thermocouple is inserted into the specimen centre, through a small drilled hole, so as to measure the exact temperature inside the rubber under loading.

A transient nonlinear direct coupled structural-thermal analysis in ANSYS Workbench is developed to perform the numerical calculations. An axisymmetric quadrilateral finite element (Plane 223 – selected using APDL command) is used, with the aim of avoiding volumetric locking [4] and pressure

instabilities [5]. The mechanical and thermal material data for the plates is assumed to be stainless steel, whilst the rubber material is fully characterised through the various experimental tests performed in the present work. Thermal and structural boundary conditions are assumed. The bottom-plate lower face is fully constraint where the temperature is also set to 25 °C. Free convection on external faces is considered respective to each material (with no radiation).

Bounded contact between rubber sample and plates is also considered. For each cycle (2Hz), four loading steps of 0.25s each are considered [2 x (loading/unloading)]. In our study, we allow the simulation to run for a minimum of 12min.

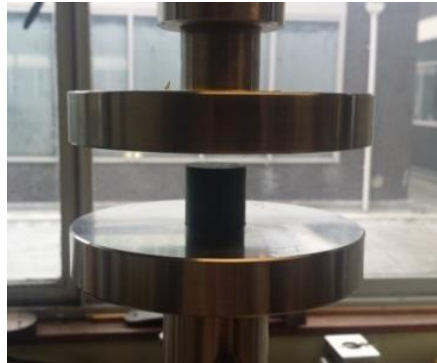


Figure 1: Test setup used for dynamic testing of silicone rubber

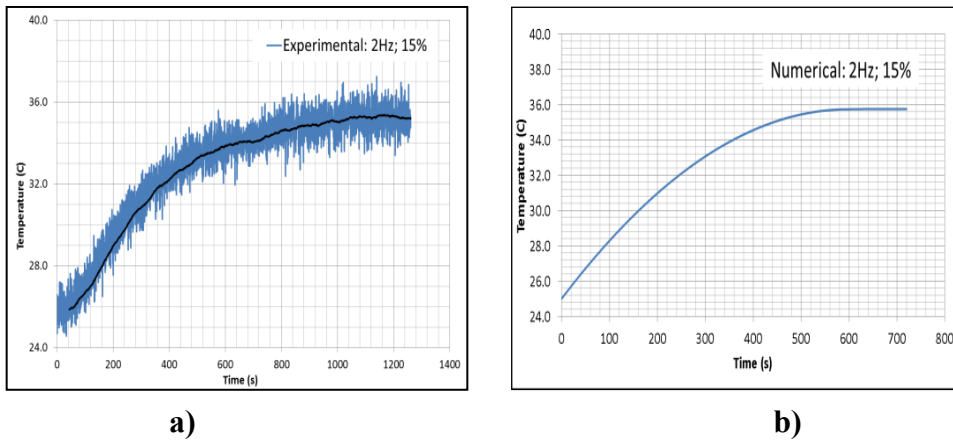


Figure 2: Temperature evolution at the silicone rubber centre at 2 Hz and 15% displacement based upon: (a) Experiment; and (b) Numerical findings

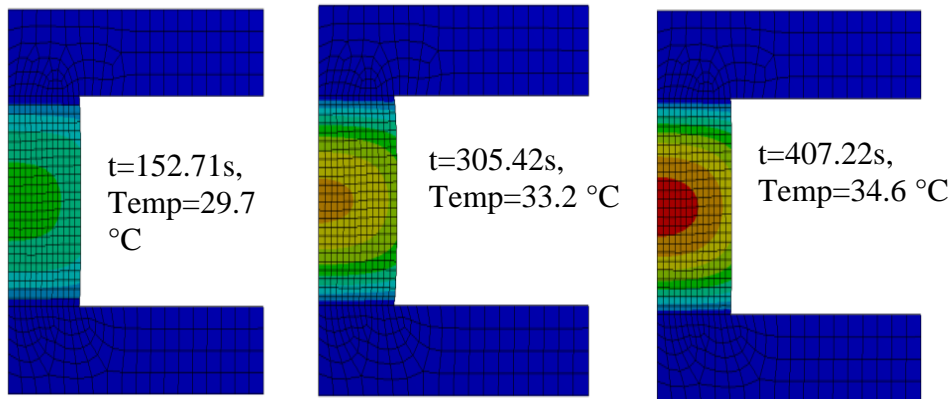


Figure 3: Simulation of temperature build-up within silicone rubber at various times; 2Hz & 15%

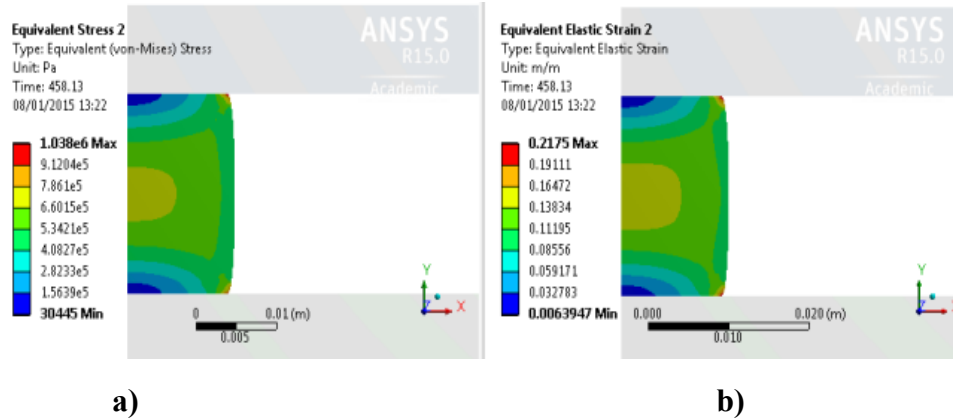


Figure 4: Equivalent stress (a) and equivalent strain (b) contours at 458.13 sec; 2Hz & 15%

Experimental time-temperature variation is shown in Figure 2a. Oscillations in the data are mainly due to thermocouple being cyclically compressed and uncompressed within the rubber specimen. The ‘black’ line represents an average of this data. The simulation results of this test are presented in Figure 2b and it shows a good agreement with the experimental data. After 10 minutes, a stabilised temperature of 37 °C is observed.

Temperature contours within the rubber at various time stations calculated numerically are shown in Figure 3. The maximum temperature is observed at the centre of rubber sample. The numerical model predicts the stress and strain evolution in the rubber. This is depicted in Figure 4. Apart from the discretisation issue at the contact region, stress and strain are higher at the specimen centre.

6. Conclusions

In this study, a silicone rubber compound has been characterised for evaluating important thermal and mechanical properties, to be used in a transient nonlinear direct coupled thermo-mechanical simulations. When compared against experimental trials, the proposed computational model was able to predict the temperature rise at the centre of the rubber as occurs in practice. This was made possible by considering a temperature dependent hyper-elastic material model and the computation of the hysteresis due to energy loss within the rubber under consideration. The numerical model presented could be used in designing rubber parts for efficiency and sustainability within complex industrial applications.

Acknowledgements

ASTUTE authors acknowledged the European Regional Development Fund (ERDF) through the Welsh Government financial contribution to undertake this study.

References

- [1] J. R. Davis, Tensile testing, ASM International, 2004.
- [2] Y.-J. Lin and S.-J. Hwang, "Temperature prediction of rolling tires by computer simulation," *Mathematics and Computers in Simulation*, vol. 67, pp. 235-249, 2004.
- [3] R. K. Luo, W. J. Mortel and X. P. Wu, "Investigation on rubber failure due to heat generation under dynamic loading," *Proc IMechE Part L: J Materials: Design and Applications*, 2013.
- [4] C. H. Lee, A. J. Gil and J. Bonet, "Development of a cell centred upwind finite volume algorithm for a new conservation law formulation in structural dynamics," *Computers and Structures*, vol. 118, pp. 13-38, 2014.
- [5] C. H. Lee, A. J. Gil and J. Bonet, "Development of a stabilised Petrov–Galerkin formulation for conservation laws in Lagrangian fast solid dynamics," *Computer Methods in Applied Mechanics and Engineering*, vol. 268, pp. 40-64, 2014.

AN HP-FEM FRAMEWORK FOR THE SIMULATION OF STATIONARY INCOMPRESSIBLE MAGNETOHYDRODYNAMICS WITH MAGNETOSTRICTIVE EFFECTS IN THREE DIMENSIONS

D. Jin, P.D. Ledger and A.J. Gil

Zienkiewicz Centre for Computational Engineering, College of Engineering, Swansea University,
Swansea, SA2 8PP, Wales, UK

{536040; p.d.ledger; a.j.gil } @swansea.ac.uk

ABSTRACT

Magnetohydrodynamics (MHD) applications play a crucial role in both industry and science (e.g. fusion reactor, solar wind simulation). To cost-effectively understand the mechanisms behind MHD, a computational approach must be applied. In this paper, we provide a novel three-dimensional *hp*-finite element method (FEM) framework for the simulation of stationary incompressible MHD problems including magnetostrictive effects. The fully coupled non-linear system is solved via a consistent linearisation Newton-Raphson strategy. A series of benchmark results, as well as an investigation of multiphase MHD problem are presented.

Key Words: *Magnetohydrodynamics; hp-Finite element method; Newton-Raphson; Magnetostriction*

1. Introduction

Magnetohydrodynamics involves the behaviour of electrically conducting fluids (such as plasmas, salt waters, etc.) in the presence of electromagnetic fields. An electromagnetic field exerts a body force on the fluid and, in turn, the fluid flow may alter the magnetic properties of the conducting fluid. Furthermore, this may influence the final distribution of the magnetic field. Amongst the contributions to the body force, the Lorentz force is often considered as dominant to the coupling mechanism in previous research. However when considering applications with different fluid phases (such as fusion reactor and metallurgy processes), the magnetostrictive effect, which depends on the gradient of the permeability, becomes important and needs to be included to accomplish further improvements of accuracy [1].

In the present research, we extend our previous two-dimensional *hp*-FEM framework for the stationary incompressible MHD discussed in [2] to three-dimensions. The magnetostrictive effect is also included, which allows our scheme to simulate more complex and accurate MHD phenomena than previously considered. The finite element method is employed to discretise the problem and the resulting fully coupled non-linear equation system is linearised by the Newton-Raphson strategy. The complexity of the equations requires the spatial discretisation of the velocity, pressure and magnetic field by different element types in order to satisfy the LBB constraint. High order (or *hp*-) version of the elements are used in order to achieve high accuracy and allows us to capture the resulting singularities that may develop in the fields.

The three-dimensional scheme is verified with the Hartmann flow benchmark problem with different Hartmann numbers denoted as *Ha* in the following. In each case the quadratic convergence for the Newton-Raphson scheme is obtained. The multiphase MHD problem are simulated with the verified scheme to provide an interesting investigation of a complex MHD flow in three dimensions.

2. The Basic Formulations and The Coupling Mechanism

The equations, which describe MHD, are made up of a coupled equation system, composing of the Navier-Stokes equations for incompressible fluids and Maxwell's equations for electromagnetism, as

Table 1: The stationary Navier-Stokes equations and Maxwell's equations and the corresponding constitutive laws.

Navier-Stokes equations	Maxwell's equations
$\rho (\nabla \mathbf{v}) \mathbf{v} - \nabla \cdot [\sigma_F] = \rho \mathbf{f}$ $\nabla \cdot \mathbf{v} = 0$	$\nabla \times \mathbf{E} = \mathbf{0}$ $\nabla \times \mathbf{H} = \mathbf{J}$ $\nabla \cdot \mathbf{D} = \rho_e$ $\nabla \cdot \mathbf{B} = 0$
$[\sigma_F] = -\hat{p} [\mathbb{I}] + 2\hat{\mu} [d(\mathbf{v})]$	$\mathbf{B} = [\mu_r] \mathbf{H}$ $\mathbf{D} = [\epsilon_r] \mathbf{E}$

shown in Table 1. The corresponding constitutive relations are also shown in the table. Here, ρ is the fluid density, \mathbf{v} is the fluid velocity, $[\sigma_F]$ is the fluid stress tensor, \mathbf{f} is the total body force, \hat{p} is the pressure, $\hat{\mu}$ is the viscosity, $[\mathbb{I}]$ is the identity tensor and $[d(\mathbf{v})]$ is the strain rate tensor. \mathbf{E} and \mathbf{H} are the scaled electric and magnetic field intensity vectors, respectively. The vectors \mathbf{D} and \mathbf{B} are the scaled electric and magnetic flux intensities, respectively. The scaled electric current density is denoted by \mathbf{J} and ρ_e denotes the scaled volume charge density. The relative permittivity and permeability tensors are denoted by $[\epsilon_r]$ and $[\mu_r]$, respectively. For the scaling approach see [1]. Note that our concern lies purely on the magnetic field, the equations related to electric field (shown in red) can be neglected.

In order to couple those two physics together, a two-way coupling mechanism will be introduced. Firstly, the existence of a magnetic field exerts a stress field $[\sigma_H]$ on the fluid, the divergence of which contributes to the total body force. Secondly, the relative magnetic permeability $[\mu_r]$ is altered by the fluid strain rate. In order to complete the derivation of coupled system of equation, the scaled electric current must be further specified. It consists of three parts, the Ohmic current, the Lorentz current and the external current. We summarise the coupling mechanism in equation (1), and the coupling terms are expressed in blue for easy of recognition.

$$\begin{aligned}
 [\sigma_H] &= \sigma(\mathbf{H} \otimes \mathbf{H}, \mathbf{H} \cdot \mathbf{H}), & \mathbf{f} &= \nabla \cdot [\sigma_H] + \tilde{\mathbf{f}}, \\
 [\mu_r] &= \mu_r([d(\mathbf{v})]), & \mathbf{J} &= [s]\mathbf{E} + [s](\mathbf{v} \times \mathbf{B}) + \mathbf{J}_{ex},
 \end{aligned} \tag{1}$$

where $[s]$ indicates the scaled conductivity, \mathbf{J}_{ex} is the external current which will result in sourcing term $\mathbf{g} = \nabla \times [s]^{-1} \mathbf{J}_{ex}$, and $\tilde{\mathbf{f}}$ is the fluid body force. The governing equations then become

$$\rho (\nabla \mathbf{v}) \mathbf{v} - \nabla \cdot ([\sigma_H] + [\sigma_F]) = \rho \tilde{\mathbf{f}}, \tag{2a}$$

$$\nabla \cdot \mathbf{v} = 0, \tag{2b}$$

$$\nabla \cdot ([\mu_r] \mathbf{H}) = 0, \tag{2c}$$

$$\nabla \times [s]^{-1} \nabla \times \mathbf{H} + \nabla r - \nabla \times (\mathbf{v} \times [\mu_r] \mathbf{H}) = \mathbf{g}. \tag{2d}$$

With this strong formulation, we can derive the weak formulation which leads to a fully coupled non-

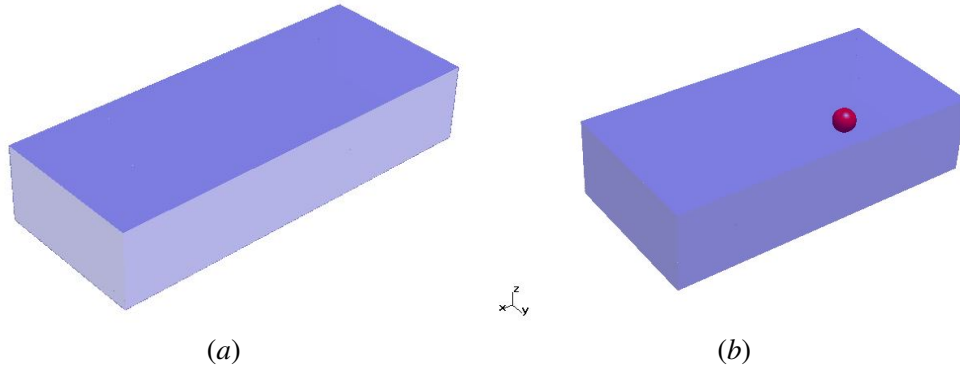


Figure 1: The geometries of the Hartmann flow problem and the multi-phase MHD problem

linear system of equations. The weak formulation will then linearised via a Newton-Raphson algorithm for the further discretisation. The procedure will be fully described in [3].

3. Numerical Discretisation

To ensure accuracy, the hp -finite element discretisation of Schöberl and Zaglmayr [4] is used for the simplicial triangulation of Ω in three-dimensions, with suitable hierarchic conforming finite element spaces for each of the variables. The magnetic field \mathbf{H} must be described by $\mathbf{H}(\text{curl}, \Omega)$ conforming edge elements, and the Lagrangian multiplier r must be described by $H^1(\Omega)$. The fluid velocity and the pressure is described by the pair of $\mathbf{H}^1(\Omega)$ and $L^2(\Omega)$, respectively. The polynomial degree must be chosen as $P_{p-1}, P_p, P_p, P_{p-3}$ for $\mathbf{H}, r, \mathbf{v}$ and \hat{p} to satisfy the LBB condition [5].

4. Numerical Examples

The three dimensional hp -FEM framework will be benchmarked with the classical three dimensional Hartmann flow problem. In order to adapt to the dimensionless problem, we regard ρ^{-1} as the coupling number, $[s]^{-1}$ as the magnetic Reynolds number and $\hat{\mu}/\rho$ as the Reynolds number. The specific parameters for the following problem can be found in [3]. The geometry is shown in Figure 1 (a), which is a rectangular duct given by $\Omega = (0, L) \times (-y_0, y_0) \times (-z_0, z_0)$ with the dimensionless coordinates $y_0 = 2, z_0 = 1, L = 10$. The source terms $\tilde{\mathbf{f}} = \mathbf{g} = \mathbf{0}$ and the analytical solutions is in the form of $\mathbf{v} = [v_x, 0, 0], \mathbf{H} = [H_x, 1, 0]$ and the detail expressions can be found in [6]. The Neumann boundary condition is applied at the face $x = 10$ and the Dirichlet boundary condition is applied to the other faces. The benchmark solution obtained on an unstructured grid of 125 elements by performing p -refinement to reach convergence with $p = 6$ is shown in Figure 2. The quadratic convergence shows the correct implementation of the Newton-Raphson algorithm and the comparison of the centre line profile shows the accuracy of the hp -FEM framework. However, we also deduce that for strong coupling, we can not capture the singularity by only using p -refinements and h -refinements is also required.

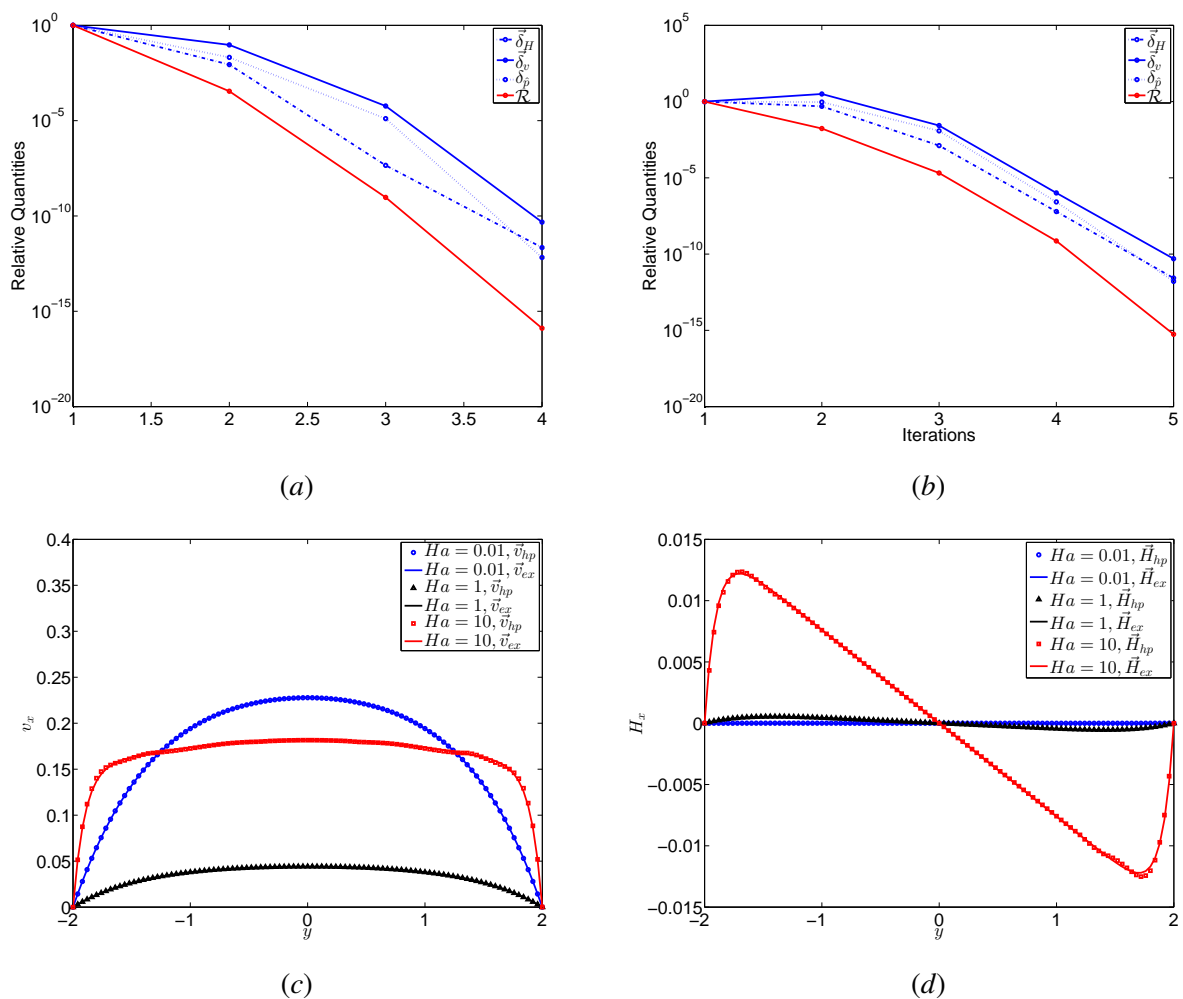


Figure 2: The benchmark results from the Hartmann flow problem with 125 tetrahedra elements and order $p = 6$, (a) and (b) are the quadratic convergence for the Newton-Raphson scheme for $Ha = 1$ and $Ha = 10$, (c) and (d) are the analytical and numerical comparison for centre line profile for v_x and H_x for $Ha = 0.01, 1, 10$. (The definition of Ha is found in [3, 6]).

The now verified hp -FEM framework is further applied to the multi-phase MHD problem to investigate the coupling behaviour. The geometry is shown in Figure 1 (b), which is a rectangular duct given by $\Omega = (0, L) \times (-y_0, y_0) \times (-z_0, z_0)$ with dimensionless coordinate $y_0 = 2, z_0 = 1, L = 8$ containing a sphere with radius 0.3 at the point of $(2, 0, 0)$. The source terms $\tilde{\mathbf{f}} = \mathbf{g} = \mathbf{0}$ and the Neumann boundary condition is applied at the face $x = 8$ and Dirichlet boundary conditions are applied to all the other boundaries based on the analytical solution $\mathbf{v} = [0.001(2 + y)(2 - y), 0, 0]$, $\mathbf{H} = [0, 1, 0]$. The parameters are also the same as the previous problem, except we assign the background fluid such that $Ha = 1$ and the fluid in the sphere such that $Ha = 10\sqrt{10}$. We also obtained the quadratic convergence for our implementation of Newton-Raphson scheme for this problem. Here only a few results are shown, but already the influence of the permeability in and outside of the sphere on Poiseuille flow pattern can be observed.

5. Conclusions

The hp -FEM framework, including magnetostriction, for the MHD has been implemented in three-dimensions. The coupling mechanism and the numerical discretisation are briefly introduced. The three-dimensional implementation has been benchmarked and applied to investigate the multi-phase MHD problem. The p -refinement resulted in exponential convergence when the coupling was weak, however, h - and p -refinement must be combined in order to achieve the same convergence speed with strong coupling. The important factors influencing the multi-phase MHD behaviour have also been described.

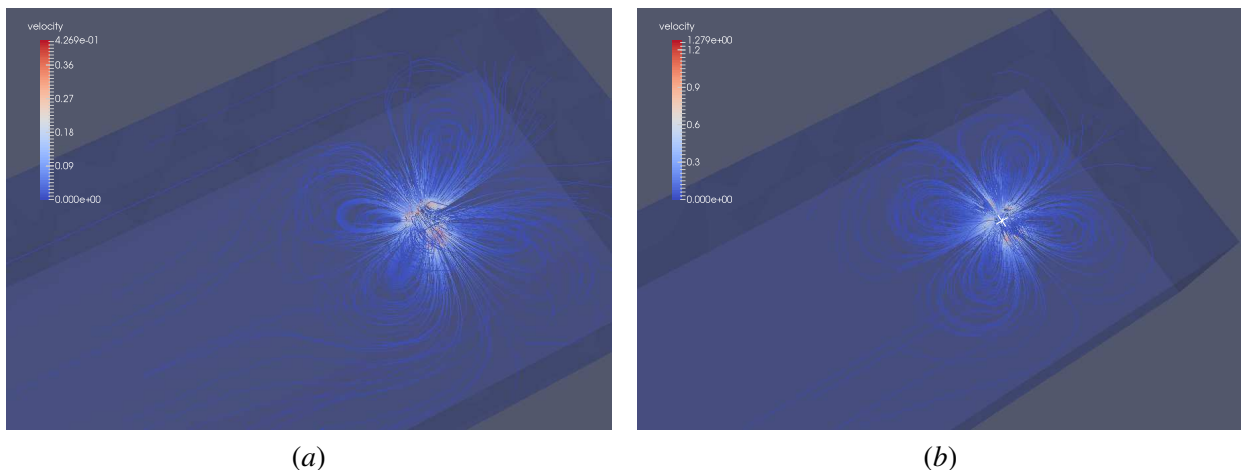


Figure 3: Solutions of a multi-phase MHD problem using 1765 tetrahedral elements and $p = 4$. (a) and (b) are the Streamlines for different material properties for inside sphere $\mu_{rin} = 0.1, 10$.

Acknowledgements

The first author gratefully acknowledges financial support in the form of the Zienkiewicz Scholarship awarded by the College of Engineering, Swansea University.

References

- [1] D. Jin, P.D. Ledger, A.J. Gil. An hp -FEM framework for the simulation of electrostrictive and magnetostrictive materials. *Computers and Structures*, 133, 131–148, 2014.
- [2] D. Jin, P.D. Ledger, A.J. Gil, An hp -FEM framework for the simulation of coupled magneto-fluid effects. *Proceedings of the 22nd UK conference of the ACME*, pp.222–225, 2014, Exeter.
- [3] P.D. Ledger, D. Jin, A.J. Gil, hp -Finite element solution approaches to the coupled stationary Magneto-hydrodynamic Equations including Magnetostrictive Effects, In preparation.
- [4] J. Schöberl and S. Zaglmayr. High order Nédélec elements with local complete sequence properties. *COMPEL*, 24, 374-384, 2005.
- [5] L. Demkowicz et al. Computing with hp -Adaptive Finite Elements: Volume 2:Frontiers: Three Dimensional Elliptic and Maxwell Problems with Applications. *Chapman and Hall, USA*, 2005.
- [6] C. Greif, D. Li, D. Schötzau, X. Wei. A mixed finite element method with exactly divergence-free velocities for incompressible magnetohydrodynamics. *Computer Methods in Applied Mechanics And Engineering*, 99, 2840-2855, 2010.

COUPLED PROBLEMS 2

A Novel Dual Time Stepping Approach for Fluid-Structure-Interaction Problems

R. Evans, I. Sazonov and P. Nithiarasu

Zienkiewicz centre for Computational Engineering, College Of Engineering, Swansea University, Singleton Park, Swansea, SA2 8PP

{R.A.Evans.551274 , I.Sazonov, P.Nithiarasu}@swan.ac.uk

ABSTRACT

The numerical simulation used for this paper utilises a partitioned approach for the FSI which is implemented via a strongly coupled Fixed Point Iteration scheme. For temporal integration a previously developed scheme is used; the Characteristic-Based Split algorithm for fluid dynamics and the Newmark-Beta Method for solid dynamics. The fluid and solid are implemented on two completely separate meshes and the Fixed Point Iteration scheme utilises the boundary data from both the fluid and solid meshes to pass information back and forth through an interface boundary. The validity of this FSI implementation has been confirmed by a benchmark case which consists of 2D flow past a thin elastic beam attached to a fixed, rigid square block.

Keywords: FSI; Fixed Point Iteration; CBS Algorithm; Newmark-beta Method

1. Introduction.

A large part of modern day computational mechanics is Fluid-structure interaction (FSI) which involves the intimate coupling of both fluid and solid domains. Depending on the problem to be solved (Aeroelasticity [4], Civil Engineering [10], Hemodynamics [1], etc) different approaches are required. One of the most commonly use FSI approaches is the sequentially staggered coupling scheme [3] which utilises subsequent solutions of both the fluid and the structure sub-problems, thus enabling existing fluid and structure solvers to be reused.

The sequentially staggered coupling scheme can be loosely coupled where only one solution per timestep is obtained which is very appealing in terms of efficiency and has been successfully employed in aeroelasticity problems [3]. However loosely coupled schemes have an inherent instability when applied to FSI problems which have a comparable density of the fluid and structure [2]. This instability can be overcome by employing an iterative or strongly coupled scheme which utilises multiple iterations per timestep to converge to the monolithic solution.

The aim of this work is to develop a robust and efficient sequentially staggered coupling scheme for FSI problems. To do this the Characteristic-based split algorithm [6,7] for solving the fluid domain, has been coupled with the Newmark-beta method [8] for solving the structural domain, via a fixed point iteration scheme[9].

2. Fluid Dynamics.

The fluid dynamics solver implements the fully explicit form of the characteristic based split algorithm for incompressible flows which employs artificial compressibility [6, 7], and utilises linear triangular finite elements to discretise the special domain.

3. Structural Dynamics.

The structural dynamics solver implements standard Galerkin finite element method for the spatial discretisation and for this work uses the 4 node bi-linear isoparametric quadrilateral. For the temporal

discretisation the Newmark-beta method [8] is employed.

4. Fluid-Structure Interface.

The intimate coupling between the fluid and structural domain can be described as follows: the flow of the fluid generates a traction which acts upon the structure. This traction on the structure results in a deformation which alters the geometry of the fluid domain and thus also alters the fluid flow. An intimately coupled system like this requires certain coupling conditions to be employed in order to be solved, they are:

$$t_i^s = t_i^f = Pn_i - \sigma_{ij}^f n_j \quad (1)$$

$$x_i^s = x_i^f \quad (2)$$

The tractions are calculated at the fluid nodes and are then projected to the structural nodes (Figure 1) so that even for an interface which has non-coinciding nodes, equation can be used to integrate the tractions in the structural domain (3):

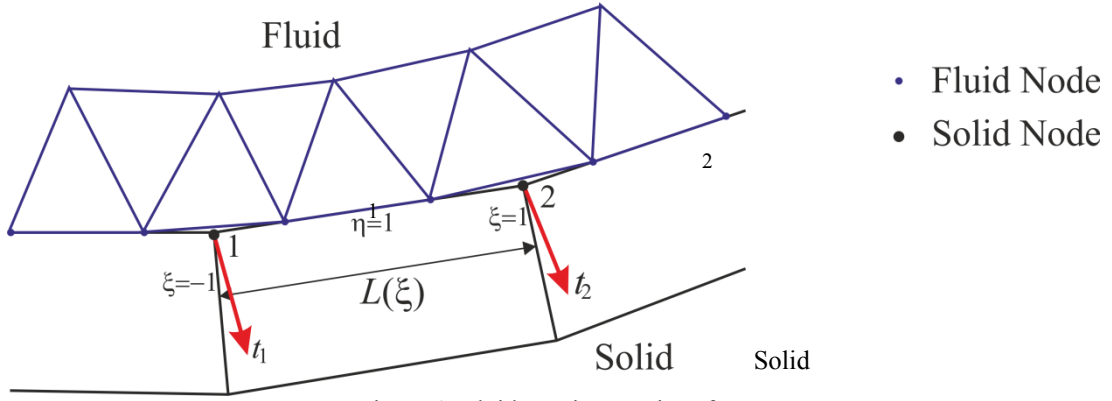


Figure 1: Fluid tractions on interface

$$\{F\} = b \int_0^L [N]^T t dL \quad (3)$$

Where b is the element depth, $[N]$ is the element nodal shape functions along the interface edge and L is the length of the edge.

$$\begin{Bmatrix} F_{1x} \\ F_{1y} \\ F_{2x} \\ F_{2y} \end{Bmatrix} = b \int_{-1}^1 \begin{bmatrix} N_1 & 0 \\ 0 & N_1 \\ N_2 & 0 \\ 0 & N_2 \end{bmatrix} \left[S_1 \begin{Bmatrix} t_{1x} \\ t_{1y} \end{Bmatrix} + S_2 \begin{Bmatrix} t_{2x} \\ t_{2y} \end{Bmatrix} \right] \frac{dL}{d\xi} d\xi \quad (4)$$

Where S_1 and S_2 are assumed linear shape functions associated with the tractions (which is suitable due to the linear elements used in the fluid domain):

$$S_1 = \frac{1}{2}(1 - \xi), \quad S_2 = \frac{1}{2}(1 + \xi) \quad (5)$$

Since the Bi-linear quadrilateral elements are used for the solid, the shape functions associated with the nodes along edge are:

$$N_1 = \frac{1}{2}(1 - \xi), \quad N_2 = \frac{1}{2}(1 + \xi) \quad (6)$$

The edge length can be expressed in natural coordinates as:

$$L(\xi) = N_1 x_1 + N_2 x_2 \quad (7)$$

And its derivative with respect to ξ :

$$\frac{dL}{d\xi} = \frac{dN_1}{d\xi} x_1 + \frac{dN_2}{d\xi} x_2 = \frac{(x_2 - x_1)}{2} \quad (8)$$

Substituting equations (5), (6) and (8) into equation (4) and integrating gives the closed form expressions:

$$\begin{Bmatrix} F_{1x} \\ F_{1y} \\ F_{2x} \\ F_{2y} \end{Bmatrix} = \begin{Bmatrix} 2t_{1x} + t_{2x} \\ 2t_{1y} + t_{2y} \\ t_{1x} + 2t_{2x} \\ t_{1y} + 2t_{2y} \end{Bmatrix} \frac{(x_2 - x_1)}{6} \quad (9)$$

The solution procedure for the coupled FSI problem requires that the fluid and structural domains are solved separately and that the mesh is updated in an iterative manner as follows:

1. The fluid domain is iteratively solved (using pseudo time-steps) until convergence is obtained for one time-step.
2. The tractions are calculated at the fluid interface nodes and projected to the structural interface nodes and integrated.
3. The structural domain is solved for one time-step.
4. Both the fluid and structural meshes are moved based on the structural domains solution.
5. Steps 1-4 are repeated until convergence is achieved, i.e. the change in displacement of the FSI interface between consecutive iterations must be lower than a specified tolerance.

5. Results.

To verify the validity of the FSI implementation the following problem (Figure 2) proposed by Wall [9] was used:

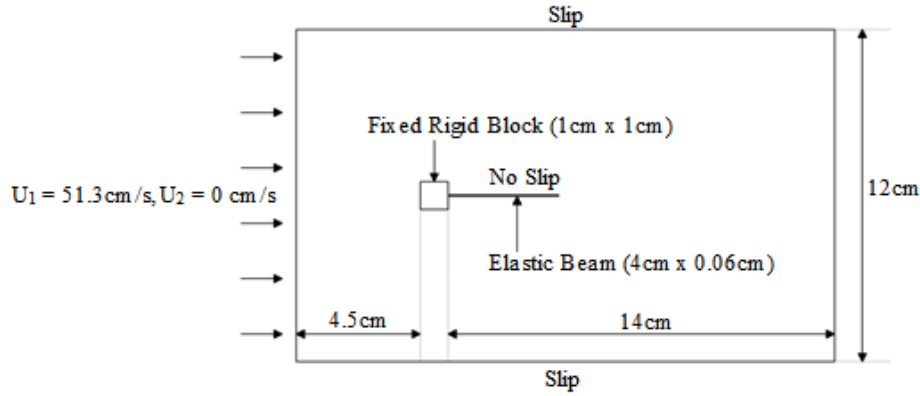


Figure 2: Problem setup for 2D flow past an elastic beam attached to a fixed rigid block.

For this problem the fluid density and viscosity used were $1.18 \times 10^{-3} \text{g/cm}^3$ and $1.82 \times 10^{-4} \text{g/cm s}$ respectively. The elastic beam has a density, Youngs modulus and Poissons Ratio of 0.1^3g/cm^3 , $2.5 \times 10^6 \text{g/cm s}^2$ and 0.35 respectively. To obtain the results the structural domain was kept fixed until stable vortex shedding had established of the rear of the fixed rigid block. At which point the structural domain was released and left to deform under the actions of the fluid. The vortex shedding of the fluid resulted in a gradual increase in the amplitude of structures oscillations.

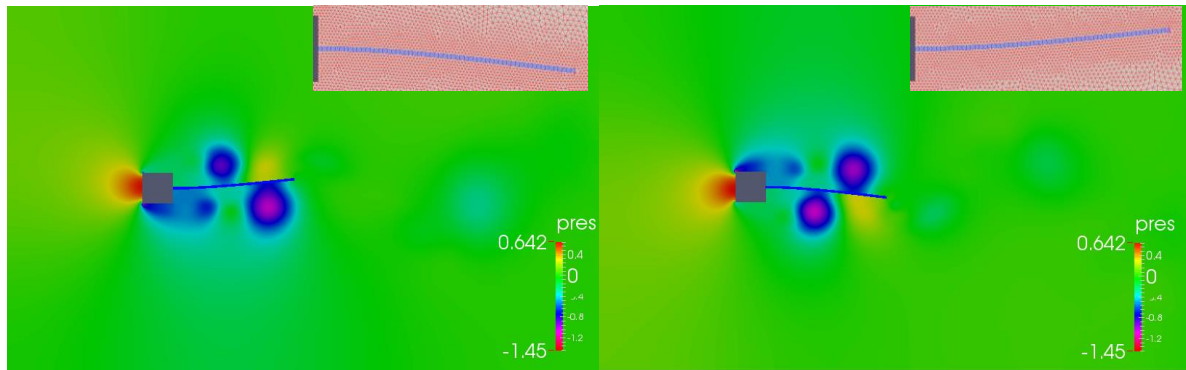


Figure 3: 2D fluid flow past an elastic beam attached to a fixed rigid block. Larger frames: Fluid pressure field. Smaller frames: Deformed mesh.

References

- [1] Bazilevs Y, Calo VM, Zhang Y, Hughes TJR, “Isogeometric Fluid-Structure Interaction Analysis With Applications to Arterial Blood Flow,” *Computational Mechanics*, vol 38, pp 310-322, Sept 2006.
- [2] Causin P, Gerbeau JF, Nobile F, “Added-mass effect in the design of partitioned algorithms for fluid-structure problems”, *Computer Methods in Applied Mechanics And Engineering*, vol 194, pp 4506-4527, Oct 2005.
- [3] Dettmer W, Perić D, “ A computational framework for fluid-structure interaction: Finite element formulation and applications,” *Computer Methods in Applied Mechanics And Engineering*, vol 195, pp 5754-5779, Aug 2006.
- [4] Farhat C, van der Zee KG, Geuzaine P, “ Provably second-order time-accurate loosely-coupled solution algorithms for transient nonlinear computational aeroelasticity.” *Computer Methods in Applied Mechanics And Engineering*, vol 195, pp 1973-2001, Mar 2006.
- [5] Karlo V, Tezduyar TE, “A parallel 3D computational method for fluid-structure interactions in parachute systems,” *Computer Methods in Applied Mechanics And Engineering*, vol 190, pp 321-332, Oct 2000.
- [6] Nithiarasu P, “An efficient artificial compressibility (AC) scheme based on the characteristic based split (CBS) method for incompressible flows.” *Numerical Methods in Engineering*, vol 56, pp 1815-1845, April 2003.
- [7] O.C. Zienkiewicz, R.L. Taylor and P. Nithiarasu, “The characteristic-based split (CBS) algorithm. A general procedure for compressible and incompressible flow,” *The Finite Element Method For Fluid Dynamics*, 6th Edition, 2005.
- [8] Thomas J.R. Hughes, “Algorithms for Hyperbolic and Parabolic-Hyperbolic Problems,” *The finite element method Linear Static And Dynamic Finite Element Analysis*, Dover Edition, 2000.
- [9] Ulrich Küttler and Wolfgang A. Wall, “Fixed-Point Fluid-Structure Interaction solvers with dynamic relaxation,” *Computational Mechanics*, vol 43, pp 61-72, Dec 2008.
- [10] Wall W.A. “Fluid-Struktur-Interaktion mit stabilisierten Finiten Elementen,” *Dissertation, Institut für Baustatik, Universität Stuttgart*, 1991.
- [11] Wüchner R, Kupzok A, Bletzinger K-U, “A framework for stabilized partitioned analysis of thin membrane-wind interaction.” *International Journal for Numerical Methods In Fluids*, vol 54, pp 945-963, Jun-Jul 2007.

A Numerical Model of the Transportation of Self-healing Agent in and around Concrete Discrete Cracks

*Chuanan Ma, Tony Jefferson, Diane Gardner, Robert Lark

School of Engineering, Cardiff University, the Parade, Cardiff, CF24 3AA

*mac1@cardiff.ac.uk

ABSTRACT

A vascular self-healing system for cementitious materials comprises the following functions: storage, delivery, release, dissipation and curing. Among them, the dissipation of the healing agent in and around the cracks after being released from the delivering system is critical to the effectiveness of the system, because it affects both the ongoing flow in the delivery networks and the healing process. A coupled numerical model was developed in this study to simulate the dissipation process assuming the source is provided at the crack opening. The model predicts the flow rate and total discharge into the cracks and also the change of moisture conditions in the surrounding concrete matrix.

The flow in the discrete crack is modelled by a modified Lucas-Washburn (L-W) equation [1], where an additional flow term Q has been introduced to take account of the mass being absorbed by the surrounding matrix. This flow term is determined by a 2D finite element continuum model of the surrounding matrix and is based on isothermal unsaturated flow theories. These two models are coupled by adding a mass balance equation for the interflow between the discrete crack and the matrix. This is achieved by treating the crack as an internal boundary within the matrix and computing the flow across this boundary. The individual models, for discrete and matrix flow, as well as the coupled flow model was firstly calibrated and then validated using a range of experimental data.

Keywords: concrete, finite element model, moisture transportation, capillary movement, self-healing

1. Introduction

Self-healing construction materials and structures have the potential to improve the infrastructures' service life and reduce maintenance cost, leading to a more sustainable and greener construction industry. Recently there have been development of various types of self-healing systems in cementitious material, among which is the vascular based self-healing system. Figure 1 shows an example of the most basic vascular self-healing system investigated in [2], which comprises an embedded brittle capillary tube filled with liquid self-healing materials. Upon the mechanical crack propagating into the level above the brittle tube, the tube will break and the enclosed self-healing materials will be passively released into the discrete crack. Previous studies [3, 4] have assessed visually the release and dissipation of the healing agents into the crack, but none has revealed quantitatively the discharge and rate of the outflow of the healing agent. This is achieved in the present study, where a coupled numerical model is developed to simulate the dissipation process in a discrete crack. This paper presents the modelling schemes of a case where the liquid is freely available at the crack mouth and is not constrained by the delivery system.

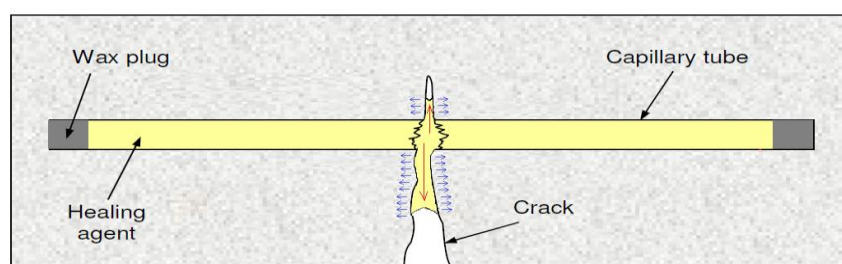


Figure 1: The basic form of vascular self-healing system

As indicated in Figure 1, two distinct flow processes will be happening simultaneously after the system is triggered: the capillary flow in the macro-crack domain which is represented by the red arrows; and the imbibition flow into the surrounding matrix domain represented by the blue arrows. For a typical self-healing flow problem, the influence of the imbibition flow on the dissipation process in the discrete crack could be particularly important because the matrix around the macro-scale cracks has much higher permeability due to the developed micro-crack zones.

2. The matrix flow model

An isothermal-hygral finite element model is developed in MATLAB to simulate the imbibition flow into the matrix continuum. The governing equation for this microscopic flow is based on the mass balance equation of the water content in the domain [5, 6], as shown in equation 1.

$$\dot{\rho}_v + \dot{\rho}_l + \nabla \mathbf{q}_v + \nabla \mathbf{q}_l + \dot{\rho}_{vl} + \dot{\rho}_{lv} = 0 \quad (1)$$

Where $\dot{\rho}_v$ and $\dot{\rho}_l$ are the time differentiation of vapour mass and water mass in the domain; $\nabla \mathbf{q}_v$ and $\nabla \mathbf{q}_l$ are the mass flux of vapour and water out of the domain; because the mass balance equation of water content includes both liquid and vapour water, the phase change between the liquid water and water vapour $\dot{\rho}_{vl}$ and $\dot{\rho}_{lv}$ could be cancelled.

The movement of the water content is driven separately by the capillary pressure gradient and vapour concentration gradient. Darcy's law and Fick's law are used to determine the capillary absorption flow term and the vapour diffusion term respectively. Different flow properties have been applied to elements at different locations to account for the larger permeability in micro-crack zones and surface zones. Capillary pressure p_c is the primary variable for the modelling and the van Genuchten equation is used to establish the relationship between saturation degree and capillary pressure. The relative permeability and vapour diffusion coefficient are functions of the water content; therefore the problem is nonlinear. Newton-Raphson iteration is adopted for nonlinear approximation and the element averaged capillary pressure and the flow properties is updated within each iteration for a new cycle of calculation until the p_c converges for this time step.

A primary target of this finite element model is to quantify the flux rate at the wetted boundary of the flow domain. A fixed boundary condition of $S_w=1$, i.e. fully saturated, is applied at the wetted boundary. The oscillation of results near the sharp front (abrupt water front) has been eliminated by using mass lumped scheme for the formulation of mass matrix [7]. The flux through the wetted boundary at a certain time step is calculated by substituting the solved capillary pressure field back into the governing equation at the end of this time step.

This 2D finite element model is validated by a series of experiments where the absorption of water through the bottom surface of concrete cubes was monitored by the relative humidity probes planted at two locations in the sample. The mass of water absorbed by the sample was also recorded over time. The simulation has shown good agreement with the experimental results in both the relative humidity value and the absorbed mass as shown in Figure 2.

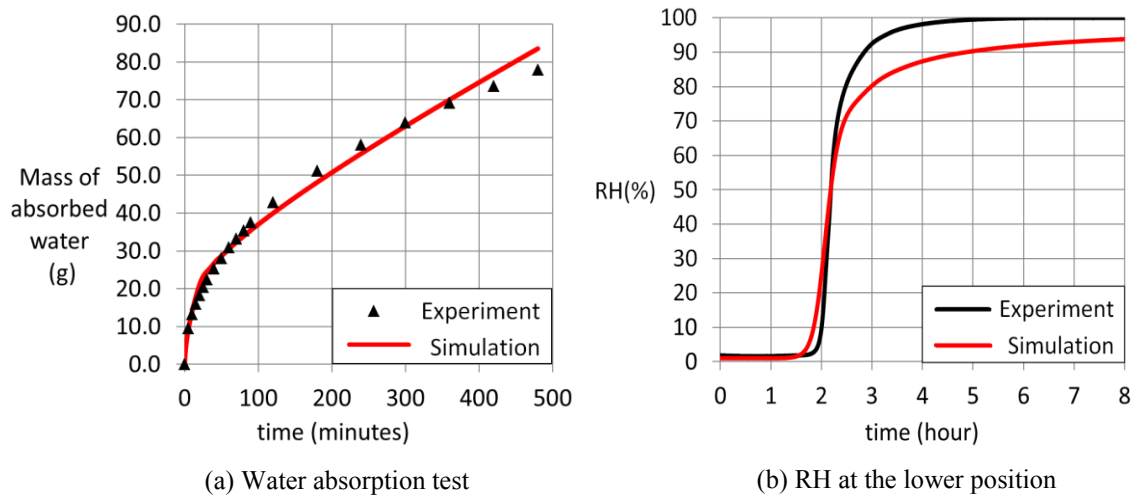


Figure 2: The experiment validation of the matrix flow model

3. The crack flow model

The capillary flow in the discrete crack is described by a modified Lucas-Washburn Equation as shown in equation 2.

$$p_{c0}(z)(1 - \beta_s) - \frac{2\beta_m \dot{z}}{b(z)} - \rho g z \sin(\phi) - \int_0^z \frac{\bar{v}(x)}{\frac{k(x)}{\mu} + \frac{\beta_w b(x)}{2}} dx = 0 \quad (2)$$

Where p_{c0} is the surface tension at the meniscus; b is the crack width for a planer water channel; z is the present rise height of the meniscus and \dot{z} is the velocity of the meniscus; μ is the viscosity of the flow agent and $k(x)$ is the effective permeability term that accounts for the shape of the flow cross-section and may vary along the profile of the flow channel. The inclusion of the factors to account for stick-slip (β_s), friction dissipation at meniscus (β_m), and wall slip (β_w) has been proved to be able to achieve a better agreement with experiment results [1].

However, previous studies have not considered the influence of the imbibition flow through the crack faces. Assume a general imbibition flow field $q(x')$ along the crack faces. Based on the mass conservation law, the relationship between the moving velocity of the meniscus and the velocity at any point within the flow section is expressed in equation 3.

$$\bar{v}(z)A(z) = \bar{v}(x)A(x) - \int_x^z q(x') dx' \quad (3)$$

Substituting equation 3 into equation 2 and rearranging leads to the modified governing equation of the crack flow, which is as follows:

$$p_{c0}(z)(1 - \beta_s) - \frac{2\beta_m \dot{z}}{b(z)} - \rho g z \sin(\phi) - \int_0^z \frac{\bar{v}(x)}{\frac{k(x)}{\mu} + \frac{\beta_w b(x)}{2}} dx - Q = 0 \quad (4)$$

Where:

$$Q = \int_0^z \frac{(\int_x^z q(x') dx')}{A(x) \left(\frac{k(x)}{\mu} + \frac{\beta_w b(x)}{2} \right)} dx \quad (5)$$

Compared with the original L-W equation, there is an additional double integration term Q which accounts for the influence of the total imbibition flow at a certain instant of time. Some numerical tests based on an assumed uniform and constant imbibition flow has shown that the imbibition flow has non-negligible influence on the capillary movement in the crack, and the magnitude of such influence is a function of the imbibition flow rate as well as the crack width.

4. The coupled model and current results

In reality, this imbibition flow into the porous crack face $q(x')$ is neither uniform nor constant. It varies along the length of the wetted cracked face and changes as the moisture condition changes in the surround matrix. A coupled model which combines the capillary flow in the discrete crack and the imbibition flow in the surrounding matrix is therefore required to simulate this problem.

The two models are linked in the following manner: within each time step, the height of the capillary rise in the crack is firstly calculated by the L-W equation. Then in the finite element matrix flow model, any nodes on the crack face boundaries below the meniscus height are assigned a fixed value of capillary pressure that is equivalent to the fully saturated condition. Given this updated boundary condition, the capillary pressure field in the matrix domain and the flux through the saturated boundary can be solved. The imbibition flow profile along the crack faces is then approximated by a step function based on the solved point flux value at the wetted nodes. Then for the next time step,

this imbibition flow profile is numerically integrated to obtain the imbibition flow term Q in the governing L-W equation.

Experiments were carried out where the capillary rise in a discrete crack was recorded by a high speed camera. The crack of a width of 0.1mm and a height of 0.08m is formed between two dry concrete samples and is kept uniform by metal spacers. Figure 3(a) compares the capillary rise calculated by the original crack flow model and the coupled model. The coupled model has shown better agreement with the experiment results. Figure 3(b) illustrates the capability of the coupled model to simulate the change of moisture conditions in the surrounding matrix, which has huge implications on the design of vascular system to facilitate different self-healing techniques.

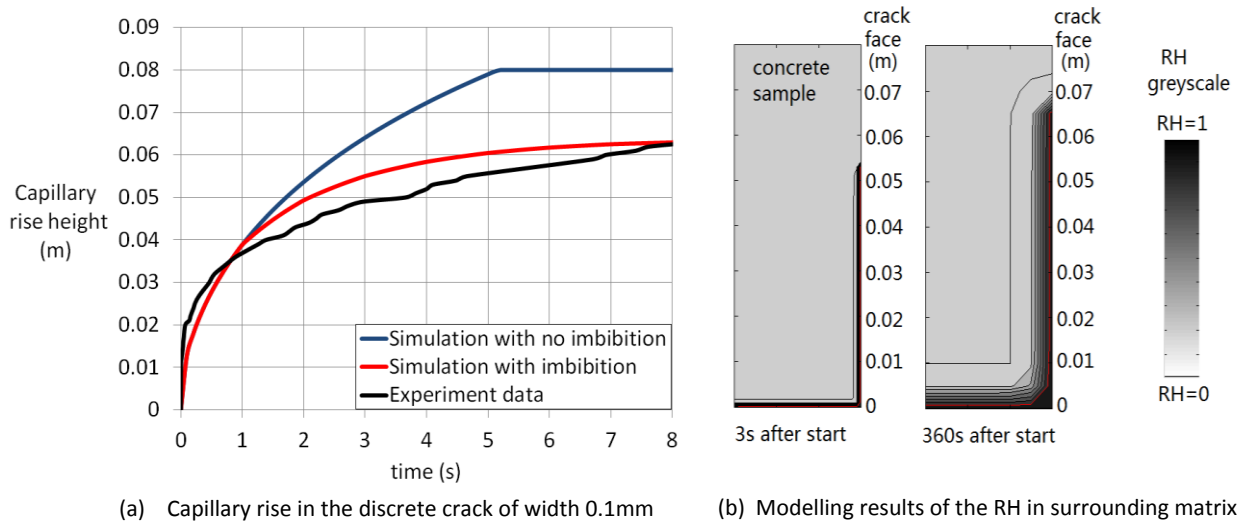


Figure 3: An example results of the coupled model

Acknowledgements

Financial support from EPSRC project Materials for Life (M4L) for this study is gratefully acknowledged by the author.

References

- [1] Gardner, D., A. Jefferson, and A. Hoffman, *Investigation of capillary flow in discrete cracks in cementitious materials*. Cement and Concrete Research, 2012. 42(7): p. 972-981.
- [2] Joseph, C., et al., *Self-healing cementitious materials: a review of recent work*. Concrete Materials, 2010. 164(CM1).
- [3] Dry, C., Matrix cracking repair and filling using active and passive modes for smart timed release of chemicals from fibers into cement matrices. Smart Materials and Structures, 1994. 3(2): p. 118.
- [4] Sangadji, S. and E. Schlangen, Mimicking Bone Healing Process to Self Repair Concrete Structure Novel Approach Using Porous Network Concrete. Procedia Engineering, 2013. 54(0): p. 315-326.
- [5] Schrefler, B.A., Mechanics and thermodynamics of saturated/unsaturated porous materials and quantitative solutions*. 2002. 55(4): p. 351-388.
- [6] Gawin, D., C. Majorana, and B. Schrefler, Numerical analysis of hygro-thermal behaviour and damage of concrete at high temperature. Mechanics of Cohesive-Frictional Materials, 1999. 4(1): p. 37-74.
- [7] Pan, L., A.W. Warrick, and P.J. Wierenga, Finite element methods for modeling water flow in variably saturated porous media: Numerical oscillation and mass-distributed schemes. Water Resources Research, 1996. 32(6): p. 1883-1889.

Fluid-structure interaction with immersed boundary method based on hierarchical B-Spline based Eulerian grid

*Chennakesava Kadapa, Wulf Dettmer, Djordje Perić

Zienkiewicz Centre for Computational Engineering,
Swansea University, Swansea SA2 8PP, UK.

*c.kadapa@swansea.ac.uk

ABSTRACT

Fluid-Structure interaction (FSI) is a complex phenomenon and developing robust numerical schemes for studying FSI is a challenging task. The most widely used approach to simulate FSI is to use body-fitted meshes with Arbitrary Lagrangian-Eulerian (ALE) formulation. However, fluid-mesh distortions due to the movement of solids limit the applicability of ALE formulation and also require efficient re-meshing algorithms. Creating good quality body-fitted meshes also adds to the difficulties associated with the ALE formulation. Immersed-boundary methods (IBMs) have proved to be efficient alternatives in such scenarios involving large movements of solid bodies. In IBM fluid is solved on a regular cartesian grid on which the solid is free to move and as fluid mesh is independent of the movement of the solid there is no need for re-meshing algorithms.

In the present work we propose IBM based on hierarchical B-Spline cartesian grid. One of the main motivating factors behind using hierarchical B-Splines for the background fluid grid is their local refinement capability. The solution space, at the locations of steep gradients, can be enriched by the use of hierarchical B-Splines thereby eliminating the need to refine the whole grid. The immersed solid is represented by a set of Lagrangian points. The standard Galerkin formulation is used to discretise the governing equations and the unconditionally stable and second-order accurate generalised- α method is used for time-integration. Performance of the proposed formulation is demonstrated by studying several benchmark problems and comparing the parameters of interest with the reference values. Without the need for any re-meshing algorithms and with the capability to perform local refinement the proposed formulation proves to be efficient and robust for simulating fluid-structure interaction phenomenon.

Key words: Hierarchical B-Splines, Navier-Stokes, Immersed-boundary method, Fluid-Structure interaction.

1. Introduction to immersed boundary method

The fundamental idea behind the immersed boundary method is that a solid-body, which is free to move, is overlaid on top the fluid mesh as shown in Figure 1. The fluid mesh need not coincide with the boundary of the solid and hence there is no need for the body-fitted meshes used with ALE formulations. The methodology employed in the present work relies on the fictitious domain approach [1, 4, 5] within the original immersed boundary method developed by Peskin and co-workers [6].

The Eulerian fluid grid is discretised with the hierarchical B-Splines because of their smoothness and local-refinement properties. The boundary of the immersed solid body is represented by a set of Lagrange points.

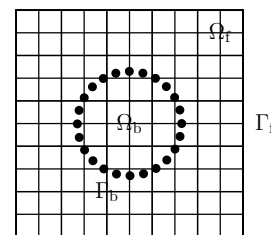


Figure 1: A solid body immersed on a fluid grid.

2. Hierarchical B-Splines

B-Splines are piecewise-continuous polynomial functions which can be evaluated, for a given knot vector $\Xi = \{\xi_0, \dots, \xi_{n+a+1}\}$ and degree of polynomial a , by the relations,

$$N_{i,0}(\xi) = \begin{cases} 1 & \text{if } \xi_i \leq \xi \leq \xi_{i+1} \\ 0 & \text{otherwise} \end{cases} \quad (1)$$

$$N_{i,p}(\xi) = \frac{\xi - \xi_i}{\xi_{i+p} - \xi_i} N_{i,p-1}(\xi) + \frac{\xi_{i+p+1} - \xi}{\xi_{i+p+1} - \xi_{i+1}} N_{i+1,p-1}(\xi) \quad (2)$$

One of the important properties of the B-Spline functions is that a B-Spline function on a knot vector with knot span h can be evaluated as a linear combination of B-Spline functions defined on a knot vector with knot span $h/2$, as illustrated in Fig. 2. This hierarchical property of B-Spline functions is utilised to *locally* refine the areas of the fluid grid where steep gradients in the solution variables occur i.e., near immersed bodies.

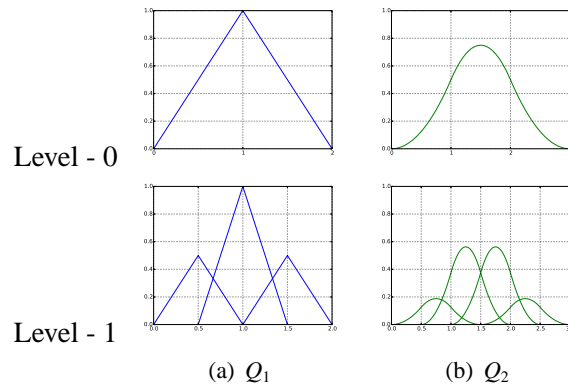


Figure 2: Two-scale relation of the B-Spline functions.

3. Formulation for FSI

Governing (Navier-Stokes) equations for the fluid:

$$\rho \frac{\partial \mathbf{u}}{\partial t} + \rho(\mathbf{u} \cdot \nabla) \mathbf{u} - \mu \Delta \mathbf{u} + \nabla p = \mathbf{f} \quad \text{in } \Omega \quad (3a)$$

$$\nabla \cdot \mathbf{u} = 0 \quad \text{in } \Omega \quad (3b)$$

Governing equations for the rigid body:

$$\mathbf{M} \mathbf{a} + \mathbf{C} \mathbf{v} + \mathbf{K} \mathbf{d} = \mathbf{F} \quad (4)$$

Kinematic conditions at the interface:

$$\mathbf{u} = \mathbf{v} \quad (5)$$

where, ρ , μ , \mathbf{u} and p are the density, dynamic viscosity, velocity, and pressure of the fluid, respectively, and \mathbf{d} , \mathbf{v} , \mathbf{a} , \mathbf{M} , \mathbf{C} and \mathbf{K} are the displacement, velocity, acceleration, mass matrix, damping matrix and stiffness matrix of the rigid-body, respectively.

Using a time-stepping scheme and after applying the weak form and Newton-Raphson method to solve the set of nonlinear equations (3), (4) and (5), yields the following the matrix system,

$$\begin{bmatrix} \mathbf{K}_{uu} & \mathbf{K}_{up} & \mathbf{K}_{u\lambda} & \mathbf{0} \\ \mathbf{K}_{pu} & \mathbf{0} & \mathbf{0} & \mathbf{0} \\ \mathbf{K}_{\lambda u} & \mathbf{0} & \mathbf{0} & \mathbf{K}_{\lambda v} \\ \mathbf{0} & \mathbf{0} & \mathbf{K}_{v\lambda} & \mathbf{K}_{vv} \end{bmatrix} \begin{Bmatrix} d\bar{\mathbf{u}} \\ d\bar{\mathbf{p}} \\ d\bar{\lambda} \\ d\bar{\mathbf{v}} \end{Bmatrix} = - \begin{Bmatrix} \mathbf{R}_u \\ \mathbf{R}_p \\ \mathbf{R}_\lambda \\ \mathbf{R}_v \end{Bmatrix} \quad (6)$$

where, λ are the Lagrange multipliers to impose the kinematic interface condition (5) at the immersed points.

4. Numerical examples

4.1. Flow over an elastically mounted square - galloping

Galloping is aerodynamically unstable phenomenon involving oscillations of high amplitudes. The fluid domain, boundary conditions and hierarchical mesh composed of quadratic B-Splines are as shown in Fig. 3. A rigid square body supported on a spring-mass-damper system is exposed to fluid flow. The properties of the spring-mass-damper system are: $\mathbf{K} = [3.08425]$, $\mathbf{C} = [0.0581195]$ and $\mathbf{M} = [20.0]$. The density and viscosity of the fluid are $\rho = 1.0$ and $\mu = 0.01$, respectively. The side of square is $D = 1$. The problem is studied with a staggered scheme for Reynolds numbers upto $Re = \rho Du_1/\mu = 250$, by varying the inflow velocity. The amplitudes of oscillation of the the rigid-body for different Reynolds numbers are shown in Fig. 3(c) along with the reference values obtained with body-fitted meshes with ALE formulation [3]. The graph illustrates that the phenomenon of galloping is captured very well.

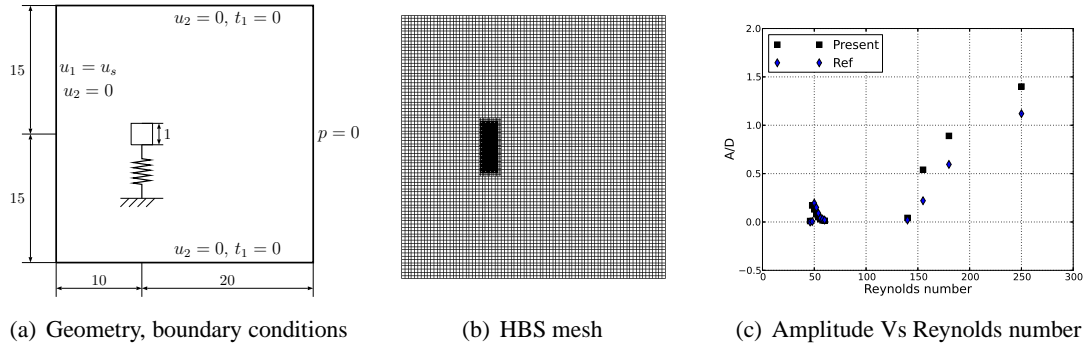


Figure 3: Galloping of a square. DOF = 34314 (fluid) + 160 (points) = 34474.

4.2. Simulation of a check-valve in operation

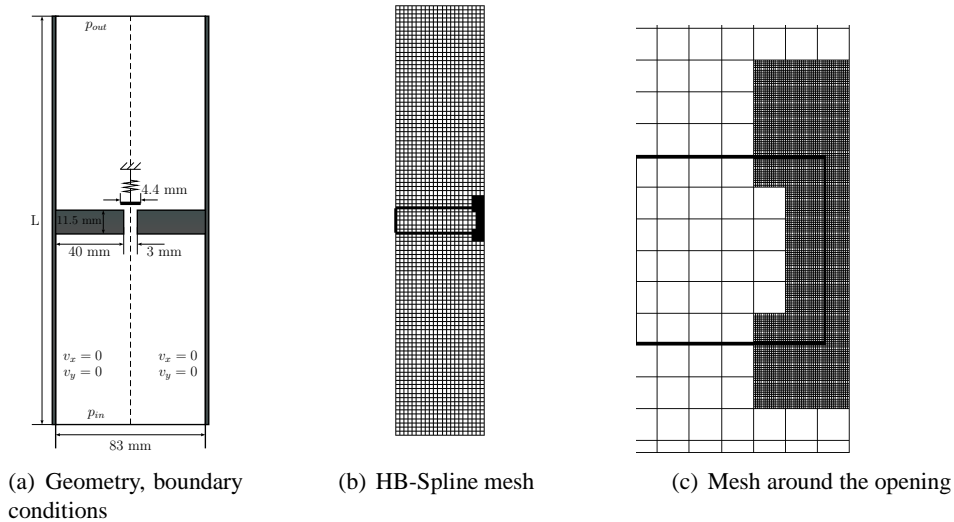


Figure 4: Check-valve simulation: Symmetric boundary is considered on the right edge. DOF = 29001 + 48 + 2 = 29051.

In this example we demonstrate the performance of a check-valve under varying inflow conditions. The geometry, boundary conditions and the hierarchical B-Spline mesh used for the simulation are as shown in Fig. 4. The length of the domain is taken as $L = 200$ mm. Because of the symmetry only a half portion is modelled. The density and viscosity of the fluid are considered to be $\rho_f = 792$ kg/m³ and $\mu_f = 0.008$ Ns/m², respectively. The valve is assumed to be a rigid-body supported by a spring-mass system and is modelled as a line. The mass and stiffness of the spring-mass system are $m = 3.52 \times 10^{-5}$ kg and $k = 380.0$ N/m, respectively. The inlet pressure varies sinusoidally given by the relation $p_{in} = p \sin(2\pi ft)$ and the outlet pressure is $p_{out} = 0$. The contact between the two rigid bodies is modelled using the Lagrange multiplier approach.

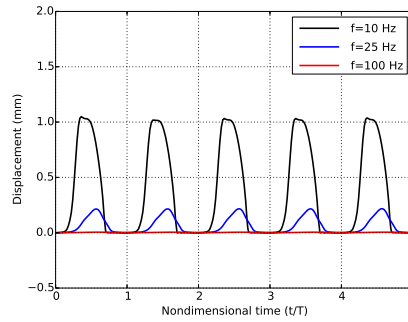


Figure 5: Check-valve simulation: Response of the valve for inlet pressure, $p_{in} = 6 \sin(2\pi ft)$.

The problem is solved using the monolithic scheme and 100 time-steps per time period is used. The displacement of the valve in response to the varying inlet pressure shown in Fig. 5 illustrates that opening and closing of the valve are captured extremely well. It can also be observed that, for the given magnitude of inlet pressure, the valve ceases to operate as the frequency of the inflow is increased. This is in line with the expected behaviour.

5. Conclusions

We presented an efficient immersed boundary method based on hierarchical B-Spline cartesian grid for the numerical simulation of fluid-structure interaction problems. The numerical examples presented demonstrate the robustness of the proposed method. The local refinement capability of the hierarchical B-Splines makes the proposed method extremely efficient by reducing significantly the scale of the problem, while maintaining the high accuracy of the solution.

References

- [1] Baaijens, F. P. T., *A fictitious domain/mortar element method for fluid-structure interaction*, International Journal for Numerical Methods in Fluids, Vol.35, pp. 743761, 2001.
- [2] Cottrell, J. A. and Bazilevs, Y. and Hughes, T. J. R., *Isogeometric Analysis: Toward Integration of CAD and FEA*, John Wiley & Sons, Chichester, England, 2009.
- [3] Dettmer, W. G., *Finite Element Modelling of Fluid Flow with Moving Free Surfaces and Interfaces Including Fluid-Solid Interaction*, PhD thesis, Swansea University, 2004.
- [4] Diaz-Goano, C. and Mineev, P. D. and Nandakumar, K., *A fictitious domain/finite element method for particulate flows*, Journal of Computational Physics, Vol.192, pp. 105123, 2003.
- [5] Glowinski, R. and Pan, T. -W. and Hesla, T. I. and Joseph, D. D., *A distributed Lagrange multiplier/fictitious domain method for particulate flows*, International Journal of Multiphase Flow, Vol.25, pp. 755-794, 1999.
- [6] Peskin, C. S., *The immersed boundary method*, Acta Numerica, Vol.11, pp. 479-517, 2002.

NUMERICAL MODELLING THE SORPTION BEHAVIOUR OF WOOD CELL WALLS

*Euan Richardson, Karin de Borst

School of Engineering, University of Glasgow, Rankine Building, Glasgow, G12 8QQ

*e.richardson.1@research.gla.ac.uk

ABSTRACT

Timber is a naturally occurring material, with properties adapted to its local environment. Moisture has a pronounced effect on the strength, stiffness and dimensional stability of timber. One particular concern is moisture induced warping, both during the drying process and during construction and the lifespan of any building. Recent research into sorption kinetics has determined that the rate limiting step in moisture sorption in timber could be due to substrate swelling rather than the process being diffusion limited, or could be a more complex interplay of the various processes. In order to better understand the sorption behaviour and to elucidate the role of the individual processes, we develop a thermodynamically consistent model for the hygro-mechanical response of timber in reaction to a change of humidity. We formulate the sorption model in terms of the conservation of mass, the kinetics of deformation and solvent migration, and the balance of forces. Constitutive assumptions are introduced to resolve the mechanical, chemical and diffusive behaviour, including a Zener model for the viscoelastic behaviour, the Flory-Huggins theory for the heat of mixing, and Ficks law for the moisture transport. The model is solved numerically using a Finite Difference scheme to obtain sorption curves. The current model will serve as the starting point in an attempt to create a multi-scale model to create an accurate set of hygro-mechanical properties for softwood.

Key Words: *Timber; Sorption; Viscoelastic; Finite Difference*

1. Introduction

Wood is a highly complex heterogeneous material with a multi-scale hierarchical structure, incorporating properties over many length scales. It is naturally occurring and thus the structure is adapted to its local environment. This makes timber an inherently unpredictable material to work with. A major issue that arises from the unpredictable properties is moisture induced distortion. During the drying process (or after), changes in moisture content can lead to changes in water uptake of the timber. This in turn leads to dimensional changes that can be observed on the macroscopic scale. The key to mitigating the issue of moisture induced distortion is to understand and predict how moisture interacts on each of the length scales within timber. As a first step we aim at deriving the moisture sorption behaviour of the cell wall from the hygro-mechanical behaviour of the various cell wall polymers contained within. We consider moisture transport by diffusion, viscoelastic effects of stress relaxation and creep which occur over time and their relationship with varying moisture content, and the heat of mixing of water with the cell wall polymers. The resulting model will shed light on the rate determining factor in sorption kinetics within the wood i.e. whether solvent migration is diffusion or mechanically limited at any given time. This information will be related to the macroscale deformation effects by multiscale modelling in the future.

2. Cell Wall Structure

The wood cell wall is a multilayer composite structure (containing cellulose, hemicelluloses and lignin) and consists of a primary cell wall and a 3 layer secondary cell wall [6]. In the secondary cell wall the cellulose chains form fibres which are embedded in a non-cellulosic polymer matrix. The cellulose is split into both crystalline and semi-crystalline (amorphous) components, and it is the amorphous component

which interacts most strongly with water. This hygroscopic water is bound to the cell wall by forming hydrogen bonds with the hydroxyl groups within amorphous cellulose, hemicelluloses and a small amount of hydroxyl groups within the lignin matrix. The amount of hygroscopic water within the cell wall is limited both by the number of sorption sites and the number of water molecules that can be held per sorption site. When water enters the cell wall it causes a swelling of the cell wall material. The water then occupies the space between the microfibrils, forcing them apart and thereby opening up new sorption sites [4].

3. Sorption Model

3.1. Model Outline

The developed sorption model of the wood cell wall describes the interaction between wood and water and the hygro-mechanical behaviour of the cell wall. In a simplified manner a 1-D model is formulated which resolves the moisture flow across the wood cell wall. The model initially focuses on the S2 layer, as this makes up around 80 percent of the mass of a wood fibre. We formulate the sorption model in terms of the conservation of mass, the kinetics of deformation and solvent migration, and the balance of forces. The cellulose contains both crystalline sections and less ordered amorphous sections which contribute to the swelling behaviour. It is assumed that the crystalline sections are rigid and inaccessible to water. The mechanical, chemical and diffusive behaviour of the amorphous parts is resolved by the introduction of constitutive assumptions detailed below.

To begin with, before modelling the wood cell wall, the model focuses on cellulosic plant/natural fibres (such as cotton or flax). This is simpler to model than the wood cell wall initially, as there are no contributions from any lignins or hemicelluloses to the amorphous material component. There is also a large amount of experimental material available which can be used to compare results and to validate the model.

3.2. Constitutive Equations

Constitutive assumptions are introduced to describe the mechanical, chemical and diffusive behaviour of the cell wall. Firstly a zener spring-dashpot model is implemented, in a similar approach that has been used for poroelastic gels [8], to describe the mechanical behaviour. This also covers the time dependent relaxation behaviour. The Zener model is coupled with Fick's 2nd law of diffusion to describe the solvent migration. Finally, the interaction between water and the wood polymers in terms of the heat of mixing is described through the Flory-Huggins theory, taking into account both entropy and enthalpy changes. It is a statistical mechanical theory which is used as a starting point and will be replaced by more elaborate theories in the future. Although it was actually formulated for polymer solutions with low polymer contents, it has proven suitable for describing the swelling of polymers also at low solvent contents.

A finite difference scheme is used to obtain numerical solutions of the sorption model. An implicit Euler (backwards time centred) scheme is used which gives better performance than an explicit scheme in this case due to the slow rate of diffusion and the relatively long relaxation times making the time steps relatively large.

4. Input Parameters

4.1. Mechanical Behaviour

The rate of diffusion for a cellulosic fibre is taken as $1.19 \times 10^{-6} \text{mm}^2/\text{s}$ [1]. The chemical potential is related to the relative humidity of the air (RH) surrounding the sample by

$$\mu = \mu_0 + RT \ln(\text{RH}) \quad (1)$$

where we have assumed equality of the chemical activity and relative humidity.

The mechanical behaviour of amorphous cellulose is strongly dependent on the moisture content. This is a consequence of the dominant influence of hydrogen bonds on the mechanical behaviour and the breakage and re-organization of hydrogen bonds upon moisture uptake. Using an approach presented by Nissan [2], the change of the Young's modulus on wetting can be related to the change of the number

of hydrogen bonds, and this, in turn, to the change of moisture content of cellulose. At low moisture contents, each water molecule is assumed to break one hydrogen bond when it attaches to a hydroxyl group. Considering the molecular weights of cellulose and water, this yields:

$$\ln(N/N_0) = -1/3(w/W) \quad (2)$$

where N , denotes the number of hydrogen bonds at moisture content w , N_0 is the initial number of bonds in the dry state, and W is the moisture content at which all hydroxyl groups carry one water molecule, which is close to $1/3$ for cellulose. The number of hydrogen bonds can be related to the Young's modulus, E , as follows:

$$N = (E/k)^{1/3} \quad (3)$$

where the proportionality coefficient, k , has been identified as 8×10^3 . Therefore the Young's modulus, E , in the low moisture regime (regime 1) is given by:

$$\ln(E/E_0)_1 = -w \quad (4)$$

where E_0 is the initial Young's modulus.

Above a critical moisture content w_c (regime 2), there is an abundance of water and, thus, the breakdown of intramolecular hydrogen bonding happens cooperatively, i.e. one bond breaking down will trigger others in the vicinity. The degree to which this happens is described by the cooperative index ($C.I.$). The ($C.I.$) can be identified as a function of the moisture content [2] ranging from 0.1 at 0% moisture content to 70 at over 90% content. Thus the change in Young's Modulus above w_c can then be described by:

$$\ln(E/E_0)_2 = (w_c/W)[(C.I) - 1] - (C.I)(w/W) \quad (5)$$

According to Nissan [2], stress relaxation can be described by the cooperative breaking of hydrogen bonds under stress, which allows small units of the cellulose chains to move. The change in the number of hydrogen bonds over time is given as:

$$\frac{-d(N/N_0)}{dt} = k(N/N_0)^\alpha \quad (6)$$

where α is the cooperative index in the case of relaxation where the reaction is of order α and not uni-molecular as in the case of stiffness. Relating the number of hydrogen bonds to the Young's modulus according to equation 8, yields the change of stiffness over time. The influence of moisture on the relaxation process can be introduced by adjusting the ratio N/N_0 on the right-hand side of equation 6. Moreover, hysteresis can be induced by setting the cooperative index, α , to a different value in adsorption and desorption. This is due to the trapped moisture within the cellulose matrix in the desorption path, leading to an increased internal moisture content compared to adsorption and, thus, to a lower number of hydrogen bonds. Accordingly, the number of bonds that has to break for the movement of a unit under stress is smaller, and so is the cooperative index α . This relationship of rate of relaxation with RH is used to set the dashpot modulus within the model, as it describes the time dependent behaviour within the cellulose.

There is little information available on the Poissons ratio of amorphous cellulose, however a value of the Poisson's ratio of microcrystalline cellulose of 0.30 has been determined from independent measurements of the elastic modulus and the shear modulus, which can serve as an initial estimate for this parameter [7]. It is assumed that this is remains unchanged with different moisture contents. The initial Young's modulus, E_0 , of the amorphous cellulose is set to a value of 5.6GPa [5].

5. Results

The model has been used to obtain a sorption isotherm for a sample of cellulosic material, 50 microns thick. The material is placed in an environment of increasing relative humidity from 0% to 90%. The water content within the sample increases upon exposure to a higher external relative humidity until equilibrium between the internal moisture content and external relative humidity is reached. The model was allowed to run for 400 minutes for each humidity step of 2.5%. This allowed enough time for the equilibrium moisture content (EMC) to be reached in each case. The results in the figure 1 compare favourably to experimentally obtained sorption isotherms [3].

Future studies will incorporate hysteresis effects during the desorption phase and the model will later be extended to model the cell wall of a softwood sample.

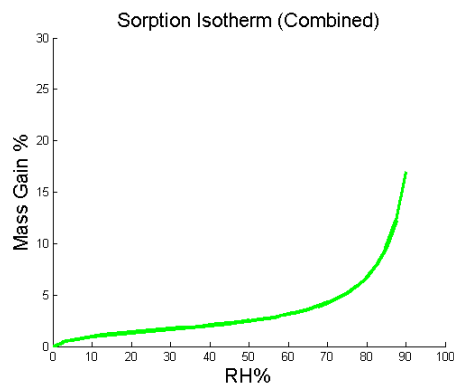


Figure 1: : Sorption Isotherm

References

- [1] A. Clino, S. Frouf, F. Jacquemin, and P. Casari. Characterization and modeling of the moisture diffusion behavior of natural fibers. *Journal of Applied Polymer Science* 130(1) 297-306, 2013.
- [2] A. H. Nissan. H-bond dissociation in hydrogen bond dominated solids. *Macromolecules*, 9(5) 840-850, 1976.
- [3] C. AS. Hill, A. Norton, and G. Newman. Analysis of the water vapour sorption behaviour of sitka spruce [picea sitchensis (bongard) carr.] based on the parallel exponential kinetics model. *Holz-forschung*, 64(4) 469-473, 2010.
- [4] E. T. Englund, L. G. Thygesen, S. Svensson, and C. AS. Hill. A critical discussion of the physics of wood water interactions. *Wood science and technology*, 47(1) 141-161, 2013.
- [5] K. Kulasinski, S. Keten, S. V. Churakov, D. Derome and J. A. Carmeliet. Comparative molecular dynamics study of crystalline, paracrystalline and amorphous states of cellulose. *Cellulose*, 21(3) 1103-1116, 2014
- [6] R. C. Neagu, E. K. Gamstedt, S. L. Bardage, and M. Lindstrom. Ultrastructural features affecting mechanical properties of wood fibres. *Wood Material Science and Engineering*, 1(3-4) 146-170, 2006.
- [7] R. J. Roberts, R. C. Rowe and P. York. The Poisson's ratio of microcrystalline cellulose. *International journal of pharmaceutics*, 105(2) 177-180, 1994
- [8] Y. Hu and Z. Suo. Viscoelasticity and poroelasticity in elastomeric gels. *Acta Mechanica Sinica*, 25(5), 441-458, 2012

COUPLED PROBLEMS 3

APPLICATION OF STRIP THEORY USING 2D MOVING FRAME OF REFERENCE AND EULER BERNOULLI BEAM THEORY TO SIMULATE OIL RISERS PROBLEM

SEYED HOSSEIN MADANI, JAN WISSINK, HAMID BAHAI

College of Engineering, Design and Physical study - Brunel University London

Email: Hossein.Madani@brunel.ac.uk

ABSTRACT

The numerical simulation of the multi-mode response of a flexible long riser to vortex induced vibration received significant attention in the recent decade. For applications with large physical domains and large body displacements it is of vital importance to use an accurate and computationally affordable numerical model [1], and a fully 3D simulation of the interaction of the flow and the riser is not feasible due to the high computational power demand. Hence, simulations rely (and for the foreseeable future will continue to rely) on simplifying assumptions [2]. In this study, various models which have been used to solve the riser problem are investigated. A strip theory model is consequently selected to solve the riser problem. The strip theory methods are typically many orders of magnitude cheaper than fully three dimensional simulations [3]. In this approach, fluid flow is simulated in multiple two dimensional planes and the hydrodynamic forces are coupled through structure responses.

Key words: *Vortex shedding, FSI, Moving frame of reference, cylindrical coordinates, Euler Bernoulli beam.*

1. Introduction

Marine risers are typically flexible, long pipes with a circular cross section. These pipes are used in the offshore industry to transfer flow from the bottom of the sea to the platforms and vice versa. Top Tensioned Risers (TTRs) and Steel Catenary Risers (SCRs) are among the most common flexible risers. The former is normally vertical while the latter is highly curved and flexible in a catenary shape connecting a sub-sea pipeline to a floating production structure. SCR lines are commonly subjected to fatigue loads, particularly in the touchdown zone, due to platform motions, waves and current [4]. Riser pipes normally have a length, L , of about a few hundred meters with an outer diameter less than a meter which gives a L/D ratio on the order of $O(10^3)$. Risers are normally exposed to a current speed with a maximum of 2m/s and a current profile that can vary with depth. The Reynolds number of the flow typically is on the order of $O(10^5)$ to $O(10^6)$. At very high depth, the riser pipes become longer and more flexible and can be exposed to a higher vibrational mode (say above 40th) [3]. Especially when the frequency of the vortex shedding of the flow behind the riser coincides with the natural frequency of the structure a phenomenon occurs that is known as Vortex-Induced Vibration (VIV) in the literature.

Simulations are necessary to reduce the cost and scope of expensive testing programs. CFD analysis of off-shore engineering applications is becoming increasingly popular [5,6,7,8]. Despite the considerable research on VIV during the last decades, the whole process for predicting the load and response is still subject to a considerable amount of uncertainty. Therefore, high safety factors between 10 and 20 are required in the design process [4].

One of the main issues which make the VIV simulation of the flexible riser a challenging task is the size of the problem. In spite of significant increases in computational power in the recent years a full simulation of the riser is still impossible. Therefore some kind of modelling and/or simplification is necessary. There are three main approaches to overcome this issue. In the first approach experimental data have been interpolated to represent the hydrodynamic forces from the fluid flow instead of solving the flow equations while still solving the structural equations. An example of this method is VICOmo Code [9]. In an alternative way, semi-empirical data from Morrison's equation is used to predict the hydrodynamic forces [10]. The SHEAR7 code, which is mainly used in the industry, is based on this method. In the third approach a CFD based model is coupled with the structural

equations to simultaneously simulate the Fluid-Structure-interaction [3]. Chaplin has made a remarkable effort to compare 11 codes based on these models with experimental data [2].

In this research, the main approaches from literature in which hydrodynamic forces are calculated using CFD methods to model the flexible riser problem are studied. Also a model based on 2D strip theory is suggested which has the potential for further development into 3D strip model. The simulation results will be presented in a separate paper.

2. Various CFD based approaches

Schulz & Meling [11] and Willden & Graham [3] introduced a strip-theory numerical method to model long, flexible risers. The hydrodynamic forces at each 2D strip are summed to obtain the overall loading along the span of each riser. This loading is then used to integrate forward a single time-step in the riser equations of motion to obtain an updated riser displacement profile. Closure of the coupled flow-structure method is achieved by updating the riser displacements for each of the corresponding hydrodynamic strips in the next time-step integration.

Holmes [12] presented a fully three dimensional CFD model combined with a structural model of a tensioned riser to predict VIV of the riser using a finite element method with high element aspect ratio in the axial direction of the structure which allows the simulation of large fluid domain using limited computational power. They reported that it was possible to capture the large fluid vortical structures which drive the pipe in the axial direction.

Constantinides et al. [7] developed a scaled three-dimensional fluid flow simulation with a simple structural model to simulate long riser pipes. They showed that their model was able to simulate properly the effects of three-dimensional structures such as strakes, buoyancy modules and catenary riser shapes. Their method is benchmarked against laboratory and offshore experiments.

Huang et al. [13] proposed a scaled riser model in order to compare the results with the VIVs experimental data performed by Marintek, Trondheim, Norway, and donated by ExxonMobil URC, Houston, TX, USA. They were able to predict similar dominant modes and amplitudes as observed in the experiment. It is also shown that the cross flow VIV in the riser top section is not symmetric to that of the bottom section. One end has considerably higher cross flow vibrations than the other end. It is concluded that the present CFD approach is able to provide reasonable results and is suitable for 3D riser VIV analysis in deep water and complex current conditions.

Wu [14] used a scaled 3D model to analyse the loads and response of flexible riser in a wave-current environment. The loads and responses are calculated through the CFD module System Coupling in the software package ANSYS14.5. The results show that the vibration equilibrium position of riser offsets in the direction of the current when wave and current are in the same direction, the response of the riser is larger than in the case of having only a wave, the vibration amplitude increases with the current and the results are opposite to the above when wave and current have opposite directions.

Table 1: CFD based model presented in the literature to model the flexible riser problem

Researcher	Model	Riser L/D	Riser Type	Other important aspects
Schulz & Meling 2004	Strip Theory	2D strip, FVM, RANS, loose coupling, time domain, uniform and shear current, single and multiple bare risers. Sensitivity study to the number of the strip
Willden & Graham 2005	Strip Theory	1435	TTR,SCR	2D strip, LES, velocity vortices model, uniform and stepped current profile. Suggest 6 to 7 strip per half wave length. Euler-Bernoulli Beam model.
Holms et a. 2006	Full 3D CFD	1400	TTR	high element aspect ratio in riser axial direction
Constantinides et al. 2007	3D CFD Scaled model	4000	SCR	Simple structural model, include the effects of Strakes, buoyancy modules.
Huang et al. 2010	3D CFD scaled model	482	TTR 817N	RANS, Chimera domain over lapping approach, Pinned supports riser, 250 structural elements.
Wu 2015	3D CFD	a pipe	FVM, RANS, Wave-current, Structure: 3D FEM, using commercial software, ANSYS 14.5

In this research a computational affordable model based on strip theory is developed to simulate the behaviour of a flexible riser which is exposed to unsteady hydrodynamic forces caused by vortex

shedding. Primitive parameters are used to solve the two dimensional Navier-Stokes equations using cylindrical coordinates [15]. The moving frame of reference [16] is attached to the riser at each 2D plane to be able to use an efficient fixed mesh to simulate the Fluid structure interaction with large displacement. The dynamic response of the riser is computed in the time domain with a finite element structural model based on the Euler–Bernoulli beam theory [17].

3. Numerical model and algorithm

The flexural rigidity, EI , and the mass per unit length of riser, m are taken to be constant, however the axial tension, T , in the riser is not constant and is changing according to the height of the riser. Therefore the equation of the transverse motion for a point on the riser reads:

$$EI \frac{\partial^4 u}{\partial y^4} - \frac{\partial}{\partial y} \left(T \frac{\partial u}{\partial y} \right) + m \frac{\partial^2 u}{\partial t^2} = F_{transverse} \quad (1)$$

In this equation u is the displacement in the transverse direction, y , (to the flow direction) and z is the coordinate in the axial direction of the riser (Figure 1, left). T , the axial tension at each point along the axial direction, z , can be formulated based on the height of the riser, H , the top initial tension, T_{top} , the riser mass and buoyancy forces. In the axial direction, by neglecting shear deformation and assuming linear material, the equation of motion for a point on the riser becomes.

$$-EA \frac{\partial^2 w}{\partial z^2} + m \frac{\partial^2 w}{\partial t^2} = F_{axial} \quad (2)$$

The governing equation for an unsteady, incompressible fluid flow in vector form is given by the Navier–Stokes equation which reads:

$$\rho \left(\frac{\partial \mathbf{V}}{\partial t} + \mathbf{V} \cdot \nabla \mathbf{V} \right) = -\nabla p + \mu \nabla^2 \mathbf{V} + \mathbf{f} \quad (3)$$

$$\nabla \cdot \mathbf{V} = 0 \quad (4)$$

The governing equation is rewritten in cylindrical coordinates and has been discretised in the staggered arrangement to guarantee the coupling between the velocity and pressure. The fractional step method is used to solve the Navier-Stokes equations and the Pressure Poisson Equation is solved to preserve conservation of mass. The origin of each 2D fluid plane is attached to the riser cross section for each 2D strip and the Navier-Stokes equations are derived in the moving frame of references to be able to simulate structure displacement without using mesh deformation. In order to couple the equations of structural motion to the fluid governing equations, all equations are non-dimensionalised using the same parameters.

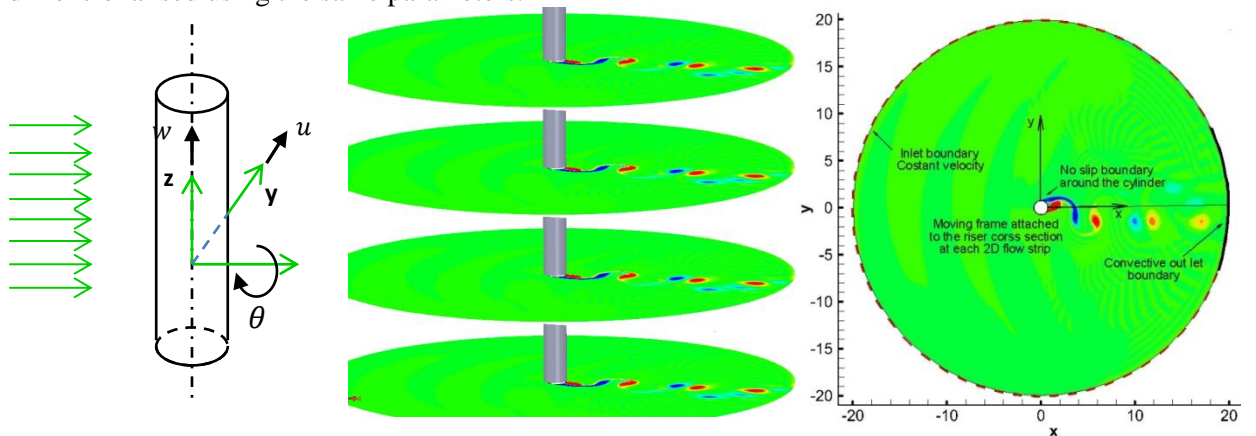


Figure 1: left) element of structure with three degrees of freedom at each node. Right) definition of the fluid domain for each 2D flow strip. Middle) schematic of a strip theory model for a Top Tensioned Riser.

When starting the code the axis of the structure coincides with the centres of each 2D flow strip. The solution at $t = t^n$ is used to initialize the flow velocity, pressure fields and also the structure location, velocity and acceleration at the first iteration step $l = 0$. The flow governing equations are solved for each 2D strip to advance the flow field to the $l = l + 1$ level. Hydrodynamic forces at each 2D strips

are interpolated (using a cubic spline approach) to calculate the overall load distribution over the riser pipe. The structural governing equation is integrated to $l + 1$ to calculate the new structural position. The structural displacement, velocity and acceleration are subsequently distributed to each 2D flow plane. The convergence of the results at l and $l + 1$ is checked before going to the next physical time step.

4. Summery and conclusion

In this study various approaches which have been presented in last decade to solve the flexible riser problem are classified and the methods which are mostly based on CFD method were compared. Three main approaches were found: 1) using 2D flows calculated in several strips in which hydrodynamic forces were coupled through the structure, 2) applying scale models in which case there might be some serious problems how to extend this to simulate a full scale model. 3) The application of large-sized elements with a very high aspect ratio in the axial riser direction to be able to decrease the computational time which might have an adverse effect on the accuracy of the results especially near the riser wall. In addition, a strip theory model was introduced with the potential to consider 3D strips and deformation of the structure cross-section.

5. References

- [1]. Mittal, R., and Iaccarino, G., "Immersed Boundary Methods," Annual Review of Fluid Mechanics, Vol. 37, 2005, pp. 239–261. doi:10.1146/annurev.fluid.37.061903.175743
- [2]. Chaplin, J. R., Bearman, P. W., Cheng, Y., Fontaine, E., Graham, J. M. R., Herfjord, K., ... & Willden, R. H. J., 2005, Blind predictions of laboratory measurements of vortex-induced vibrations of a tension riser, *Journal of fluids and structures*, 21(1), 25-40.
- [3]. Willden, R. H., & Graham, J. M. R. (2005, January). CFD simulations of the vortex-induced vibrations of model riser pipes. In *ASME 2005 24th International Conference on Offshore Mechanics and Arctic Engineering* (pp. 837-846). American Society of Mechanical Engineers.
- [4]. Wang, J., Fu, S., Baarholm, R., Wu, J., & Larsen, C. M. (2015). Fatigue damage induced by vortex-induced vibrations in oscillatory flow. *Marine Structures*, 40, 73-91.
- [5]. Oakley, O. 2005. Modeling Vortex Induced Motions of Spars in Uniform and Stratified Flows. *Offshore Mechanics and Arctic Engineering OMAE2005-67238*,
- [6]. Constantinides, Y. and Oakley, O. 2006. Numerical Prediction of Bare and Straked Cylinder VIV. *Offshore Mechanics and Arctic Engineering OMAE2006-92334*.
- [7]. Constantinides, Y., Oakley, O. H., & Holmes, S. (2007, January). CFD high L/D riser modeling study. In *ASME 2007 26th International Conference on Offshore Mechanics and Arctic Engineering* pp. 715-722.
- [8]. Holmes, S. 2008. Using CFD to study the effects of staggered buoyancy on drilling riser VIV. *Offshore Mechanics and Arctic Engineering OMAE2008-57434 CP*.
- [9]. Gopalkrishnan, R., 1993. Vortex-Induced forces on oscillating bluff cylinders. Ph.D. Thesis, Department of Ocean Engineering, Massachusetts Institute of Technology, Cambridge, MA, USA.
- [10]. Lyons G.J., Vandiver J.K., Larsen C.M., Ashcombe G.T., 2003, Vortex induced vibrations measured in service in the Foinaven dynamic umbilical, and lessons from prediction *Journal of Fluids and Structures*, 17, 1079–1094
- [11]. Schulz, K. W., & Meling, T. S. (2004, January). Multi-strip numerical analysis for flexible riser response. In *ASME 2004 23rd International Conference on Offshore Mechanics and Arctic Engineering* (pp. 379-384). American Society of Mechanical Engineers.
- [12]. Holmes, S., Oakley, O. H., & Constantinides, Y. (2006, January). Simulation of riser VIV using fully three dimensional CFD simulations. In *25th International Conference on Offshore Mechanics and Arctic Engineering* (pp. 563-570). American Society of Mechanical Engineers.
- [13]. Huang, K., Chen, H. C., & Chen, C. R. (2010). Vertical riser VIV simulation in uniform current. *Journal of Offshore Mechanics and Arctic Engineering*, 132(3), 031101.
- [14]. Wu, Z. X., Zhu, R. Q., Gu, S. Q., Xia, Z. P., Luo, Y., Li, H. Y., & Wang, L. (2015, March). Analysis of Loads and Response on Flexible Riser under the Combined Effects of Wave and Current. In *Applied Mechanics and Materials* (Vol. 723, pp. 120-124).
- [15]. Verzicco, R., & Orlandi, P. A finite-difference scheme for three-dimensional incompressible flows in cylindrical coordinates. *Journal of Computational Physics*, 123(2) (1996), 402-414.
- [16]. Li, L., Sherwin, S. J., & Bearman, P. W., 2002, A moving frame of reference algorithm for fluid/structure interaction of rotating and translating bodies, *International journal for numerical methods in fluids*, 38(2), 187
- [17]. Patel, M. H., & Witz, J. A., 1991, *Compliant offshore structures*, Oxford: Butterworth-Heinemann, pp. 353-398.

COUPLED BONDED PARTICLE AND LATTICE BOLTZMANN METHOD FOR MODELLING FLUID-SOLID INTERACTION

* Min Wang, Y.T. Feng and C.Y. Wang

Zienkiewicz Centre for Computational Engineering, College of Engineering, Swansea University, Singleton
Park, Swansea, SA2 8PP

* sacewangmin@gmail.com

ABSTRACT

This paper presents a coupled Bonded Particle and Lattice Boltzmann Method (BPLBM) for modelling the fluid-solid interactions in e.g. geomechanics. In this new technique, the Bonded Particle model is employed to describe the inter-particle movement and forces, and the bonds between contacting particles are assumed to break when the tension force and/or tangential force reach a certain critical value. While the fluid phase is modelled by using the Lattice Boltzmann method, the Immersed Moving Boundary scheme is utilized to characterize the fluid-solid interactions. Based on the novel technique, case studies have been conducted, which show that the coupled BPLBM enjoys substantially improved accuracy and enlarged range of applications in characterizing the mechanics responses of the fluid-solid systems.

Keywords: LBM; DEM; BPM; Immersed Moving Boundary; Fluid-solid Interaction; Hydraulic fracture

1. Introduction

Dynamics of particle-fluid systems has attracted considerable attention from the community of computational mechanics. The current interest is due to its broad range of applications in petroleum engineering, geotechnical engineering, chemical engineering and biomechanical engineering. In solving the problems the complexity of particle-fluid interactions remains a major challenge that cannot be easily resolved via experiments with high cost and limited resolution. As a result computational simulation has been employed as an alternative technique in characterizing the coupling between solid mechanics and fluid dynamics. This work aims to largely improve the accuracy in simulating fluid-particle systems by coupling the Bonded Particle method and Lattice Boltzmann Method (BPLBM). Key computational issues, including the algorithm of BPM and the fluid-solid coupling, will be addressed in detail.

2. Bonded Particle Method

It has been noted that the bonds existing between adjacent particles can resist both traction and shear forces and will break due to excessive traction and/or shear forces [1, 2]. Therefore, the bonds play a vital role in determining the critical strength and force-displacement behaviour of geomaterials. Nowadays BPM is being extensively used for simulating construction materials i.e. soil, rock and concrete. The concept of BPM is firstly proposed for rock by Potyondy and Cundall [3]. It originates from the Discrete Element Method which has been proved to be an effective numerical tool for modelling problems consisting of granular particles. In BPM, the bond model mimicking cementation can be implemented between the particles in contact, and the bonds are able to carry normal forces, tangential forces and moment. When the bond force exceeds its critical value, the contact bond will break. In this case, only the particle-particle contact forces (independent of the bond) need to be considered. The Newton's second law is utilised to determine the translation and rotation of each particle arising from the contact forces, e.g., externally applied forces and body forces as well as cohesive forces, while the force-displacement law is used to update the contact forces that keep changing due to the relative motion of particles at each contact.

The Newton's second law governing the motion of a particle is given by

$$ma + cv = F_c + F_f + mg \quad (1)$$

$$I\ddot{\theta} = T_c + T_f \quad (2)$$

where m and I are respectively the mass and the moment of inertia of particles, c is a damping coefficient, a and $\ddot{\theta}$ are acceleration and angular acceleration, F_c and T_c are, respectively, contact forces and corresponding torques, F_f and T_f are hydrodynamic forces and their torques. It should be emphasized that F_c can be either particle-particle contact forces for granular particles or cohesion forces F_b existing between bonded particles.

The contact bond is characterized by two parameters, i.e., normal bond strength (F_{bn}) and shear bond strength (F_{bs}). If the tensile contact force equals or exceeds the normal contact bond strength, the bond breaks, and both the normal and shear contact forces are set to be zero. Differently, when the shear contact force is equal or greater than the shear contact bond strength, the bond breaks, but the contact forces do not change. The normal and tangential contact bond model are, respectively, described by

$$F_n^b = \begin{cases} K_n^b \delta; & F_n^b \leq F_{\max} \\ 0, & F_n^b > F_{\max} \end{cases} \quad (3)$$

$$F_t^b = -\frac{\dot{\delta}_t}{|\dot{\delta}_t|} \begin{cases} K_t^b |\delta_t|; & |K_t^b \delta_t| \leq \mu F_n^b \\ \mu F_n^b; & |K_t^b \delta_t| > \mu F_n^b \end{cases} \quad (4)$$

where K_n^b and K_t^b are the normal stiffness and tangential stiffness for the cement, F_{\max} is the critical tensile force.

The computational procedures of the Bonded Particle Method is given as follows:

- 1). A particle packing with a specified size distribution will be generated first. Then, the first contact detection will be performed to build up a contact list for bonded particles and install bond models into bonded particles;
- 2). Relax the sample until the balance state is reached. After that, the boundary conditions will be applied for the first time-step calculation;
- 3). Carry out the global contact detection and work out the overlap between contact particles for the subsequent contact force calculation;
- 4). Then check whether these contact pairs are on the bond contact list, if yes, use the contact bond model to calculate the cohesion forces between bonded particles, otherwise calculate contact forces between no bonded pairs using the particle-particle contact models;
- 5). Check the calculated bond forces, if the tensile force or shear force exceeds its critical value, remove these contact pairs from the bond contact list;
- 6). Use Newton's Second law to update the position and velocity of each particle;
- 7). Repeat Steps 3-6 till the specific time interval is exceeded and output the useful data for postprocess.

3. Lattice Boltzmann Method

The Lattice Boltzmann Method (LBM) is a kind of microscopic or mesoscopic fluid dynamics approach. In the LBM, the fluid domain is divided into regular lattices. The fluid phase is treated as a group of fluid particles which are allowed to move to the adjacent lattice nodes or stay at rest. During each discrete time step of the simulation, fluid particles at each lattice node move to their immediate neighbouring lattice nodes along given directions. At each node, the fluid particles from neighbouring nodes collide, which is controlled by solving the Lattice Boltzmann equation. Finally, the macro fluid behaviour can be obtained through the statistics of the motion of fluid particles [4].

The Lattice Bhatnagar-Gross-Krook (LBGK) Model is one kind of popular Lattice Boltzmann Model. It can be characterised by the following Lattice Boltzmann Equation

$$f_i(\mathbf{x} + \mathbf{e}_i \Delta t, t + \Delta t) - f_i(\mathbf{x}, t) = \Omega \quad (5)$$

Where f_i is the primary variables in the LB formulation (so-called fluid density distribution functions), Ω is the collision operator.

In the LBGK Model, Ω is characterised by a relaxation time τ and the equilibrium distribution function $f_i^{eq}(\mathbf{x}, t)$

$$\Omega = -\frac{\Delta t}{\tau} [f_i(\mathbf{x}, t) - f_i^{eq}(\mathbf{x}, t)] \quad (6)$$

4. Fluid-Solid Coupling

Since the 1990s, a number of fluid-solid coupling schemes have been proposed for LBM. In this work the commonly used Immersed Moving Boundary [5, 6] is adopted. An additional collision term, Ω_i^s , for nodes covered partially or fully by the solid is introduced into the collision operator. Then the collision term in the LB equation including body force becomes

$$\Omega = -\frac{\Delta t}{\tau} (1 - B) [f_i(\mathbf{x}, t) - f_i^{eq}(\mathbf{x}, t)] + (1 - B) \Delta t F_i + B \Omega_i^s \quad (7)$$

Where B is a weighting function that depends on the local solid ratio ε , defined as the fraction of the node area (see Fig. 1).

$$B = \frac{\varepsilon (\tau - 0.5)}{(1 - \varepsilon) + (\tau - 0.5)} \quad (8)$$

The additional collision term is based on the bounce-rule for nonequilibrium part and is given by

$$\Omega_i^s = f_{-i}(\mathbf{x}, t) - f_i(\mathbf{x}, t) + f_i^{eq}(\rho, U_s) - f_{-i}^{eq}(\rho, \mathbf{u}) \quad (9)$$

Where U_s is the velocity of the solid node.

The resultant hydrodynamic force and torque exerted on the solid can be calculated by summing the momentum change of solid nodes:

$$F_f = Ch \left[\sum_n (B_n \sum_i \Omega_i^s \mathbf{e}_i) \right] \quad (10)$$

$$T_f = Ch \left\{ \sum_n [(\mathbf{x} - \mathbf{x}_c) \times (B_n \sum_i \Omega_i^s \mathbf{e}_i)] \right\} \quad (11)$$

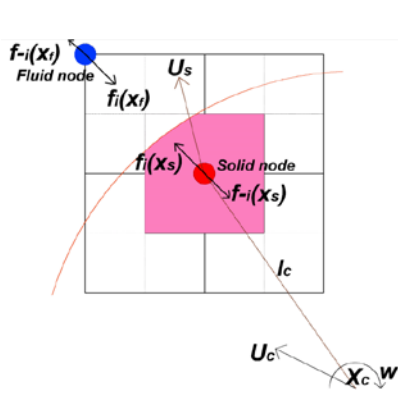


Fig. 1 Immersed moving boundary including rotation

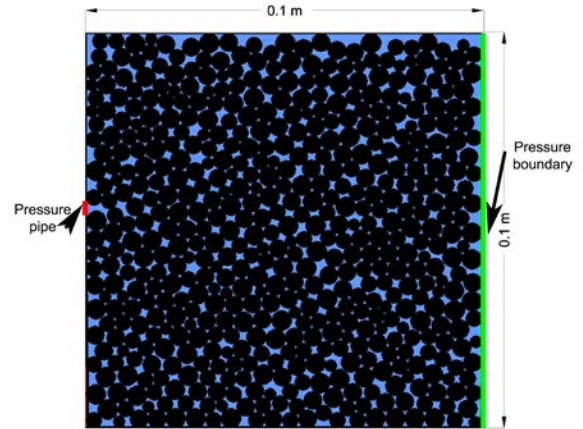


Fig. 2 Hydraulic fracture: problem setup

5. Numerical Example

A hydraulic fracture process triggered by the horizontal directional drilling in underground construction was investigated. The model with sides $0.1\text{ m} \times 0.1\text{ m}$ is shown in Fig. 2 and it is comprised of 488 bonded particles of different sizes. The fluid domain is divided into 200×200 lattices with spacing $h = 0.5\text{ mm}$. The parameters of the fluid and solid particles are the same in the previous erosion simulation. A pressure pipe ($\rho_{in} = 1005\text{ kg/m}^3$) is applied in the middle of the left vertical wall. At the right boundary, a solid wall which is only effective for solid particles and a pressure boundary ($\rho_{out} = 1000\text{ kg/m}^3$) for the fluid are implemented. The other boundaries are stationary walls. At the meantime, a corresponding numerical test with 488 granular particles is conducted for comparison.

Fig. 3 gives the states of simulation at several different time steps. It can be found that the onset of fracture is captured in Fig. 3b, which is achieved by breaking the bond model between particles undergoing too large forces. At the beginning small cavity is formed near the pressure pipe. Then a

horizontal hydraulic fracture is formed due to high fluid pressure. With the progress of excavation, the hydraulic fracture grows gradually. In the granular soil test, a cavity is easily formed and it grows up quickly. Finally, a big hole can be seen near the pipe and no fracture appears. The bond effect is apparent through the comparison of the simulations with and without the bond model. The preliminary result demonstrates that this coupled BPLBM is promising for hydraulic fracture study in shale oil exploitation where the experiments and conventional numerical methods have limited resolutions.

6. Conclusions

This paper introduces a coupled Bonded Particle and Lattice Boltzmann Method for the simulation of fluid-solid interactions in fluid-particle systems. Numerical tests confirm that the coupled BPLBM technique is promising and efficient in handling hydraulic fracture. Compared to DEM-LBM, it enjoys substantially improved accuracy and enlarged range of applicability in characterizing the mechanics responses of geomaterials in which cohesion forces play an important role. Furthermore, BPLBM is a mesoscopic or microscopic method, which can process fluid-particle issues at the grain-level which commonly ranges from hundreds of microns to several centimetres. This characteristic is difficult to achieve in continuum method. Due to the explicit time-stepping scheme and nature to parallelize, BPLBM is promising for modelling large-scale even field problems using parallel computing.

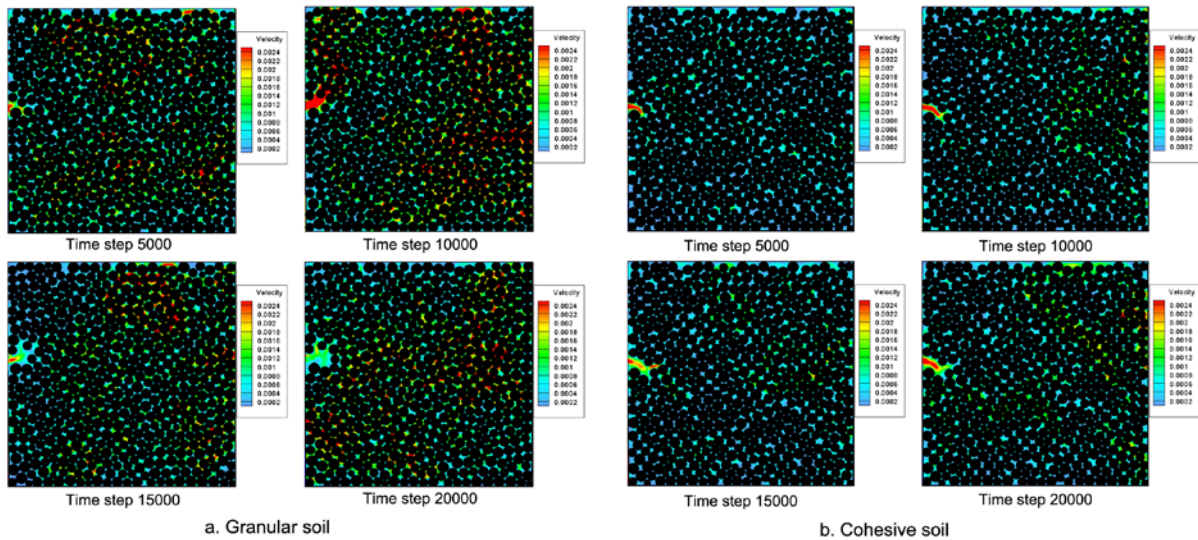


Fig. 3 Lattice velocity contour of hydraulic fracture without (a) and with (b) bonds

References

- [1] J.Y. Delenne, M. S. El Youssoufi, F. Cherblanc and J.C. Bénet. Mechanical behaviour and failure of cohesive granular materials. *International Journal for Numerical and Analytical Methods in Geomechanics*, 28, 1577-1594, 2004.
- [2] M.J. Jiang, Y.G. Sun, L.Q. Li and H.H. Zhu. Contact behavior of idealized granules bonded in two different interparticle distances: An experimental investigation. *Mechanics of Materials*, 55, 1-15, 2012.
- [3] D.O. Potyondy and P.A. Cundall. A bonded-particle model for rock. *International Journal of Rock Mechanics and Mining Sciences*, 41, 1329-1364, 2004.
- [4] Y.T. Feng, K. Han, and D.R.J. Owen. Coupled lattice Boltzmann method and discrete element modelling of particle transport in turbulent fluid flows: Computational issues. *International Journal for Numerical Methods in Engineering*, 72, 1111-1134, 2007.
- [5] D.R. Noble and J.R. Torczynski. A lattice-Boltzmann method for partially saturated computational cells. *International Journal of Modern Physics*, 9, 1-13, 1998.
- [6] M. Wang, Y.T. Feng and G.N. Pande, Coupled discrete element and lattice Boltzmann scheme for simulating soil erosion, in: O. Laghrouche, A. Javadi, M.S. Hussain (Eds.), *22nd UK Conference on Computational Mechanics (ACME-UK)*, pp.65–68, 2014.

AN ISOGEOMETRIC BIPHASIC MODEL FOR THE DYNAMIC RUPTURE OF GEOLOGICAL FAULTS

*Julien Vignollet, Stefan May and René de Borst

School of Engineering, University of Glasgow, Oakfield Avenue, Rankine Building, Glasgow G12 8LT

Julien.Vignollet@Glasgow.ac.uk

ABSTRACT

An implicit fluid-saturated model is developed to assess the performance of isogeometric analysis in the context of dynamic fault rupture. We take advantage of a number of attributes inherent to NURBS-based approximation functions, including a flexible control of the continuity of the shape functions across elements, the utilisation of high order shape functions and an exact representation of complex geometries of arbitrary shapes. An increased knot multiplicity is used to locally introduce a discontinuity across the considered geometries in order to represent the geological fault. Particular attention is given to the integration method along the resulting interface to handle traction oscillations for relatively high dummy stiffnesses. For stability reasons, biphasic models require that functions approximating displacements are of one degree higher than those approximating the pressure field. In addition, as second order derivatives of the pressure field are required to characterise the fluid flow within the fault, a mixed formulation with a quadratic pressure interpolation and a cubic displacement interpolation is employed.

Key Words: *Isogeometric analysis, biphasic, slip-weakening, absorbing boundary conditions*

1. Introduction

Seismic events are particularly complex phenomenon, overlapping a number of branches in mechanics such as dynamics, fracture, poro-elasticity and plasticity. Although the holy grail of earthquake prediction, with regard to both time and location, seems out of reach today [1], computational models can provide valuable insight to describe earthquake processes such as initiation and propagation. This work represents a first step toward the modelling of fault rupture dynamics. The double objective is to participate to the current and active exploration of the performances of IGA, but also to provide an alternative framework to existing models, which tend to use finite differences or boundary integral element methods.

2. Theory

2.1. Balance of momentum

We consider a body Ω shown in Fig. 1, with Dirichlet boundary conditions at Γ_u and Neumann boundary conditions at Γ_t . An interface Γ_d divides the domain into two parts Ω^+ and Ω^- , such that $\Omega = \Omega^+ \cup \Omega^-$. It is equipped with a local coordinate system $(\mathbf{n}, \mathbf{s}, \mathbf{t})$, where \mathbf{n} is the vector normal to the interface, while \mathbf{s} and \mathbf{t} define the directions tangential to the interface.

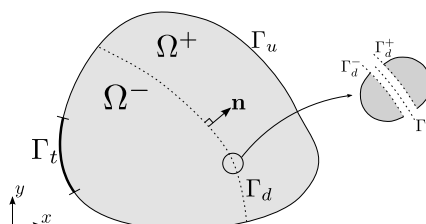


Figure 1: Schematic representation of a body Ω crossed by a discontinuity Γ_d

The balance of linear momentum, closed by imposing boundary conditions at the external boundaries Γ_u and Γ_t , and on the discontinuity Γ_d , reads:

$$\nabla \cdot \boldsymbol{\sigma} = \rho \ddot{\mathbf{u}} \quad \mathbf{x} \in \Omega, \quad (1a)$$

$$\mathbf{u} = \bar{\mathbf{u}} \quad \mathbf{x} \in \Gamma_u, \quad (1b)$$

$$\mathbf{n} \cdot \boldsymbol{\sigma} = \bar{\mathbf{t}} \quad \mathbf{x} \in \Gamma_t, \quad (1c)$$

$$\mathbf{n} \cdot \boldsymbol{\sigma} = \mathbf{t}_d(\llbracket \mathbf{u} \rrbracket, p) \quad \mathbf{x} \in \Gamma_d, \quad (1d)$$

where $\boldsymbol{\sigma}$ denotes the total stress, ρ the bulk density and $\ddot{\mathbf{u}}$ the acceleration at a material point $\mathbf{x} \in \Omega$. The total stress can be expressed as a function of the stress in the skeleton $\boldsymbol{\sigma}'$ and the pore pressure p :

$$\boldsymbol{\sigma} = \boldsymbol{\sigma}' - p\mathbf{I}, \quad (2)$$

The displacement jump $\llbracket \mathbf{u} \rrbracket$ at the interface is defined with the convention $\llbracket \bullet \rrbracket = (\bullet)^+ - (\bullet)^-$, where $(\bullet)^+$ and $(\bullet)^-$ are evaluated at Γ_d^+ and Γ_d^- respectively. According to Eqs. 2 and 1d, the total traction \mathbf{t}_d is a function of the displacement jump and the pressure at the interface:

$$\mathbf{t}_d(\llbracket \mathbf{u} \rrbracket, p) = \tilde{\mathbf{t}}_d(\llbracket \mathbf{u} \rrbracket) - p\mathbf{n}_{\Gamma_d}, \quad (3)$$

where the term $\tilde{\mathbf{t}}_d$ defines the bond in the solid skeleton across the interface; it must be defined constitutively. When interface elements are used to model cracks that nucleate in a hitherto intact medium, the interface compliance is zero till the onset of cracking, which is usually approximated by assigning high values to the 'dummy' stiffness k_i . It is noted that the value of the dummy stiffness is problem and length-scale dependent, but must be chosen as high as possible. Prior to the onset of cracking the interface stiffness matrix \mathbf{D}_i in the local coordinate system then attains the format $\mathbf{D}_i = k_i\mathbf{I}$, and the traction in the solid phase is defined as:

$$\tilde{\mathbf{t}}_d = \mathbf{D}_i \llbracket \mathbf{u} \rrbracket. \quad (4)$$

The weak form is derived in a standard fashion by multiplying Eq. 1 by a virtual displacement and applying the divergence theorem. It is important to note that the total traction, as well as the pressure field, are required to be continuous across this interface Γ_d . It is assumed that only displacements can be discontinuous. After discretisation, this results in the following elemental internal force vector:

$$\mathbf{f}_U^{\text{int}} = \int_{\Omega} \mathbf{B}_u^T \mathbf{D}_b \mathbf{B}_u \mathbf{u}^e \, dV - \int_{\Omega} \mathbf{B}_u^T \mathbf{N}_p \mathbf{p}^e \, dV - \int_{\Gamma_d} \mathbf{M}_u^T \mathbf{D}_i \mathbf{M}_u \mathbf{u}_i^e \, dA + \int_{\Gamma_d} \mathbf{M}_u^T \mathbf{N}_p \mathbf{p}_i^e \, dA \quad (5)$$

In Eq. 5, the vectors \mathbf{u}^e and \mathbf{p}^e respectively contain nodal displacements and pressures in the bulk, while their counterparts \mathbf{u}_i^e and \mathbf{p}_i^e are defined at the interface. The other operators are designed as to evaluate, at each integration point, the stresses ($\mathbf{B}_u \mathbf{u}^e$), the pressure ($\mathbf{N}_p \mathbf{p}^e$) and the displacement jump $\mathbf{M}_u \mathbf{u}_i^e$.

2.2. Balance of mass

Assuming a Biot coefficient $\alpha = 1$, the balance of mass in the strong form is (the derivation can for example be found in [2]):

$$\nabla \cdot \mathbf{v} + \frac{1}{M} \frac{\partial p}{\partial t} + \nabla \cdot \mathbf{q} = 0 \quad \mathbf{x} \in \Omega, \quad (6a)$$

$$\mathbf{q} = \bar{\mathbf{q}} \quad \mathbf{x} \in \Gamma_q, \quad (6b)$$

$$p = \bar{p} \quad \mathbf{x} \in \Gamma_p, \quad (6c)$$

$$\mathbf{q} = \mathbf{q}_d \quad \mathbf{x} \in \Gamma_d. \quad (6d)$$

In the above, \mathbf{v} is the time derivative of the displacements, $(1/M)$ the compressibility modulus, and Γ_p and Γ_q are respectively the Dirichlet and Neumann boundaries. The weak form Eq. 6 is derived under the assumption that the flux \mathbf{q} is proportional with the permeability k to the pressure gradient, i.e. using

Darcy's law: $\mathbf{q} = -k\nabla p$. Similarly to the linear momentum, the pressure is assumed to remain continuous across the thin interface, while the flux can experience a jump due to the potential tangential flux in the formed cavity. This allows to derive the internal force vector of the mass balance in its discretised form:

$$\mathbf{f}_p^{\text{int}} = \int_{\Omega} \mathbf{N}_p^T \mathbf{B}_u \dot{\mathbf{u}}^e dV + \int_{\Omega} \frac{1}{M} \mathbf{N}_p^T \mathbf{N}_p \dot{\mathbf{p}}^e dV + \int_{\Omega} k \mathbf{B}_p^T \mathbf{B}_p \mathbf{p}^e dV + \int_{\Gamma_d} \mathbf{N}_p^T \mathbf{q}_d dA \quad (7)$$

The last term in Eq. 7 describes the fluid flow through the interface. If the interface opens, i.e. $\llbracket u_n \rrbracket > 0$, a cavity has formed. Under the assumption of a one-dimensional flow along the cavity, the following term can be derived (see [2] for detailed derivation):

$$\mathbf{n}_{\Gamma_d}^T \mathbf{q}_d = \frac{n_f}{12\mu} \frac{\partial^2 p}{\partial x^2} \llbracket u \rrbracket^3 + \frac{n_f}{4\mu} \frac{\partial p}{\partial x} \frac{\partial \llbracket u \rrbracket}{\partial x} \llbracket u \rrbracket^2 - \llbracket u \rrbracket \left(n_f \frac{\partial v_s}{\partial x} - k_f \frac{\partial^2 p}{\partial x^2} \right) - n_f \frac{\partial \llbracket u \rrbracket}{\partial t} \quad (8)$$

3. Results

Extending the model presented in [3], an increased knot multiplicity is employed to locally introduce discontinuities across the considered geometries to represent geological faults. It is well known that the dummy stiffness k_i introduces oscillations in the traction profile when using Gauss quadrature for the interface elements. A standard remedy is the utilisation of a Newton-Cotes quadrature at the interface. It was illustrated in [4] that this outcome is aggravated for interface elements that use B-splines or NURBS as basis functions, but also that these oscillations cannot be removed when resorting to a Newton-Cotes integration scheme. Amongst other findings regarding the nature of these oscillations, it was demonstrated in [4] the use of lumped integration at the control points removes the spurious oscillations.

The propagation of elastic waves in unbounded domains raises the problem of wave reflection at the fictitious numerical boundaries back into the domain. The literature abounds with models to tackle this issue. These are usually either over simplified and perform well only for normal incident waves, or very complex and difficult to implement for the general case. In the present work, we choose to implement the simple method presented in [5]. It is based on a variation of Rayleigh damping, and provides an acceptable level of energy absorption for a wide range of incident angles. An example of the performance of this method is shown in Fig. 2, where over 70% of the total energy was absorbed by the boundary. Time integration was performed using a Newmark scheme.

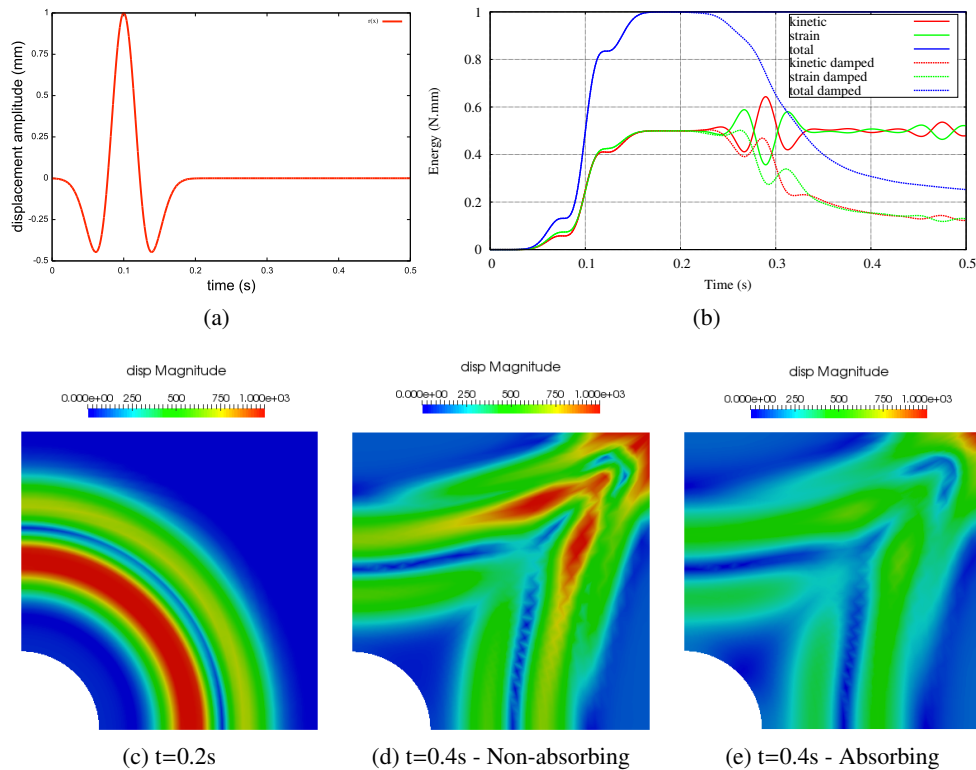


Figure 2: (a) Rickler wavelet. (b) Energy in the system. (c)-(e) Norm of displacements at various times

In order to avoid instabilities, biphasic models require the approximation of the displacement field to be one degree higher than that of the pressure field. This is due to the definition of the total stress Eq. 2. In addition, Eq. 8 contains second order derivatives of the pressure field. Therefore, a mixed formulation with a quadratic pressure interpolation and a cubic displacement interpolation is employed. In order to generate matching quadratic and cubic meshes, the p-refinement algorithm presented in [6] was used. As an example in Fig. 3, we revisit an example presented in [7], where a square plate with a slit at its centre is loaded on its sides with a constant velocity \bar{v} (see [7] for simulation parameters).

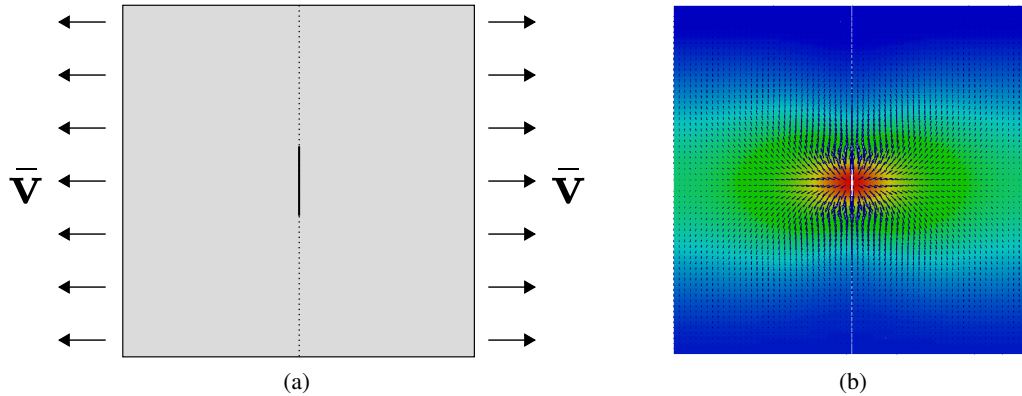


Figure 3: Pressure profile and fluid flow direction in plate with a slit

4. Conclusions

In this paper, a set of "tools" was presented in order to pave the way toward the numerical modelling of geological fault using IGA: an oscillation-free interface element, absorbing boundary conditions to model an unbounded domain and cavity flow were introduced, all in a fully implicit setting. Although not presented here, a plastic slip-weakening model was also implemented, enhancing Eq. 3, to describe the relative motion between both sides of the fault.

References

- [1] Scholz C. *The Mechanics of Earthquakes and Faulting*. Cambridge University Press, 2002.
- [2] Réthoré J, de Borst R, Abellan MA. A two-scale approach for fluid flow in fractured porous media. *International Journal for Numerical Methods in Engineering* 2007; **71**(7):780–800.
- [3] Verhoosel CV, Scott MA, de Borst R, Hughes TJR. An isogeometric approach to cohesive zone modeling. *International Journal for Numerical Methods in Engineering* 2011; **87**(1-5):336–360.
- [4] Vignollet J, May S, Borst R. On the numerical integration of isogeometric interface elements. *International Journal for Numerical Methods in Engineering* 2015; :Accepted for publication.
- [5] Semblat JF, Lenti L, Gandomzadeh A. A simple multi-directional absorbing layer method to simulate elastic wave propagation in unbounded domains. *International Journal for Numerical Methods in Engineering* 2011; **85**(12):1543–1563.
- [6] Thomas D, Scott M, Evans J, Tew K, Evans E. Bézier projection: A unified approach for local projection and quadrature-free refinement and coarsening of NURBS and T-splines with particular application to isogeometric design and analysis. *Computer Methods in Applied Mechanics and Engineering* Feb 2015; **284**(0):55–105.
- [7] Irzal F, Remmers J, Verhoosel C, de Borst R. An isogeometric analysis Bézier interface element for mechanical and poromechanical fracture problems. *International Journal for Numerical Methods in Engineering* 2014; **97**(8):608–628.

A NEWTON RAPHSON SCHEME FOR COUPLED MAGNETO-MECHANICAL PROBLEMS APPLIED TO MRI SCANNERS

S.G. Bagwell, P.D. Ledger and A.J. Gil

College of Engineering, Swansea University, Swansea SA2 8PP, UK

{638988, p.d.ledger, a.j.gil}@swansea.ac.uk

ABSTRACT

This paper presents a linearised axisymmetric hp -finite element formulation to the solution of coupled Magneto-mechanical problems applied to MRI scanners. We focus on the set up of a fast analysis tool for determining the vibration and deformation in the conducting components of an MRI scanner. In order to facilitate the design stage and reduce computation time, a series of assumptions are included, which involve neglecting the displacement currents in the Maxwell equations and using time harmonic rather than pulsed gradient fields. We then linearise the resulting non-linear equations using a Newton-Raphson procedure and adopt an axisymmetric formulation of the full "three" dimensional problem. We also utilise a stress tensor approach for the electromagnetic forces, previously employed in [3, 4, 5]. This formulation allows the use of H^1 conforming hp finite elements for the computational solution of the weak variational statements and gives the possibility of accurate solutions. The fully discretised scheme is solved by a Newton-Raphson procedure, in continuation of the work of D. Jin, P.D. Ledger, A.J. Gil in [4]. We also present a numerical example used to benchmark the analysis tool and formulation.

Key Words: Magneto-mechanical Coupling; hp -Finite Elements; Axisymmetric geometry; MRI Scanners; Newton-Raphson

1. Introduction

Since the first body scan in July 3, 1977 [1], Magnetic Resonance Imaging (MRI) scanners have become a popular tool in the medical industry. Their non-intrusive imaging capability of the human body makes them desirable for identifying certain medical ailments of a patient, such as tumours, damaged cartilage and internal bleeding [2].

The primary components of an MRI scanner are the main magnet, which produces a strong uniform, stationary magnetic field across the radial cross section of the scanner and a set of secondary (gradient) coils, which produce pulsed field gradients required to generate an image. The most common type of magnet used in MRI scanners are superconducting magnets, consisting of superconducting wire cooled by liquid helium contained with a vessel known as a cryostat. The cryostat consists of a set of nested metallic vessels of a toroidal topology. The presence of eddy currents in these conducting (metallic) vessels can be caused by changing magnetic fields, such as those generated by the pulsed gradient fields. These eddy currents can cause perturbations in the magnetic field. They also give rise to Lorentz forces and exert electro-mechanical stresses in the conducting components which cause them to vibrate and deform. These deformations cause the magnetic fields to further perturb thus generating more eddy currents. These phenomena can have undesired effects causing imaging artefacts (ghosting), decreased component life and uncomfortable conditions for the patient, due to the noise from mechanical vibrations.

The need to accurately simulate these vibrations and deformations in the cryostat is essential in designing an efficient MRI scanner with increased component life and comfortable conditions for the patient. There exists great motivation in quantifying these mechanical deformations, eddy currents and Lorentz forces in order to improve the design of the current MRI scanners.

2. Governing Equations

The aim of this work is to develop a computational analysis tool to aid in the design of the coils by providing a better understanding of the induced mechanical vibrations. These are described by solving the coupled set of time harmonic Maxwell and linear elasticity equations presented in equation (1). In the following notation ρ denotes the density of the material, μ the electromagnetic permeability, ϵ dielectric permittivity, γ the electric conductivity, $\mathring{\mathbf{E}}$ the electric field vector, $\mathring{\mathbf{H}}$ the magnetic field vector and $\mathring{\mathbf{u}}$ the displacement field vector and $\mathring{\sigma}^m$ is the cauchy stress tensor, where the $\mathring{\circ}$ symbol denotes a time varying quantity.

$$\nabla \times \mathring{\mathbf{E}} = \mu \frac{\partial \mathring{\mathbf{H}}}{\partial t} \quad \nabla \cdot \epsilon \mathring{\mathbf{E}} = \mathbf{0} \quad (1a)$$

$$\nabla \times \mathring{\mathbf{H}} = \mathring{\mathbf{J}}(\mathring{\mathbf{u}}, \mathring{\mathbf{E}}) \quad \nabla \cdot \mu \mathring{\mathbf{H}} = \mathbf{0} \quad (1b)$$

$$\nabla \cdot \mathring{\sigma}^m(\mathring{\mathbf{u}}) + \mathring{\mathbf{b}}(\mathring{\mathbf{H}}) = \rho \frac{\partial^2 \mathring{\mathbf{u}}}{\partial t^2} \quad (1c)$$

The current term consists of $\mathring{\mathbf{J}}(\mathring{\mathbf{u}}, \mathring{\mathbf{E}}) = \mathring{\mathbf{J}}^s + \mathring{\mathbf{J}}^l(\mathring{\mathbf{u}}, \mathring{\mathbf{E}}) + \gamma \mathring{\mathbf{E}}$, the source, Lorentz and ohmic, or eddy currents. The coupling is caused by the presence of this Lorentz current, which depends non-linearly upon the electric field and mechanical displacement of the conducting components, in the Maxwell system and the presence of the body force $\mathring{\mathbf{b}} = \mathring{\mathbf{b}}(\mathring{\mathbf{H}})$ in the linear elastic equations. It can be shown that this body force can be rewritten in terms of a stress tensor that depends non-linearly upon the magnetic field [3].

3. The problem and simplifying assumptions

In order to better understand the coupled physical system between the displacement caused by eddy currents and the Lorentz currents generated in the conducting components of the cryostat in MRI scanners a suitably scaled experiment was proposed by Siemens Magnet Technology, Siemens plc, as described in [3]. This experiment suggests a simplified geometry of the MRI scanner in which only one gradient coil is considered, the Z-gradient coil. It also includes the main coil, and the three metallic shields, all being modelled as solid cylinders. The geometry in this problem, illustrated in Figure 1 is constant across the bore section of the cylinder. We can therefore formulate our problem in terms of an axisymmetric representation by considering the geometry in cylindrical coordinates. This allows us to express our 3D problem on a 2D domain whilst computing the 3D contribution of the fields. For this formulation our domain is considered on the r, z plane, as opposed to the standard x, y plane from the Cartesian coordinate system. Whilst this modification reduces the order of the geometry, it requires a more complex weak formulation of the equation system, solution vector and the basis functions due to the complexity of the differential operator in cylindrical coordinates. But all the fields can be described by H^1 conforming elements.

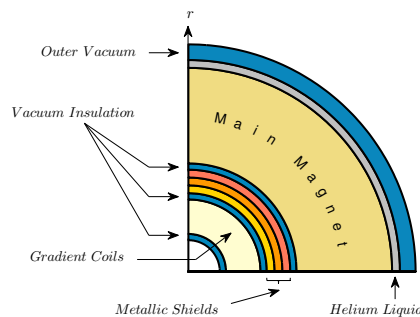


Figure 1: Radial cross section of the simplified MRI scanner

The two separate sets of coils of the simplified scanner each give rise to a different electromagnetic field type, stationary or DC field for the main coil and pulsed or AC field in the gradient coil. By considering the sourcing terms in different sub domains we are able to split the electromagnetic field into both DC and AC parts, where the static DC field is independent of the time dependent AC and displacement fields and so can be solved separately without frequency dependency.

In designing the MRI scanner, one would prefer to solve the equation set in the frequency domain as opposed to the time domain as it is better suited to give the desired computational speed. It also allows for the designer to sweep quickly over the sourcing frequencies of the Z gradient coil and obtain the dissipated power as a function of the frequency. We have therefore chosen to adopt the approach taken in [3] of assuming a time harmonic, rather than pulsed, sourcing current in the gradient coil so that we can formulate the equations in the frequency domain.

4. Newton-Raphson Scheme

The work previously carried out in [3] involved the implementation of a fixed point iteration scheme in order to solve the coupled set of non-linear equations presented in Section 2. In this paper we now employ a Newton-Raphson procedure to solve the non linear discretised form of the coupled equations that results from their *hp*-discretisation and axisymmetric formulation of the problem. The benefits of this procedure over the fixed point scheme is that quadratic as opposed to linear convergence is achieved provided the initial guess is sufficiently close to the solution. It is generally more robust as the fixed point scheme is not always guaranteed to converge, and requires more iterations to converge.

The generalised Newton-Raphson procedure is an iterative numerical approach that involves computing a matrix of derivative terms \mathbf{K} , also known as a Jacobian or tangent stiffness matrix. Setting the product of this and a vector of updates equal to some residual vector $\mathbf{R}(\mathbf{x}_k) = [\mathbf{R}_{DC} \mathbf{R}_{AC} \mathbf{R}_U]^T$ for a given solution produces the linearised equation system. Given some initial guess \mathbf{x}_0 the equation system

$$[\mathbf{K}]\delta = -\mathbf{R}(\mathbf{x}_k) \quad \text{with} \quad \mathbf{x}_{k+1} = \mathbf{x}_k + \delta \quad (2)$$

can be solved iteratively to obtain $\delta = [\delta_{DC} \delta_{AC} \delta_U]^T$, the incremental solution vector. The updated solution vector is then computed using the identity in equation 2. We omit the details for the full linearisation, which follows the procedure described in [6], but will present the actual terms at the conference.

5. Numerical Examples

A simplified numerical example has been considered here to test the behaviour and performance of the Newton-Raphson scheme within the adopted *hp*-finite element scheme. The benchmark problem involves a spherical shell (conducting region, $\gamma = 1e7 S/m$) placed inside an alternating magnetic field with a frequency $\omega = 314.2 rad/s$. The shell is deformed by an external pressure on the outer surface, $p_0 = 1e4 Pa$. The two problems are independent and so decouple from one another and have analytical solutions. Fixing a mesh of 1292 elements and uniformly increasing the polynomial degree (p) of the elemental basis functions we plot the L^2 , H^1 and Energy norms of the error for both the eddy current (AC) and mechanical problem in Figure 3. We observe that uniformly increasing p results in a dramatically decreasing error norm. The corresponding solution fields for the two problems are illustrated in Figure 2.

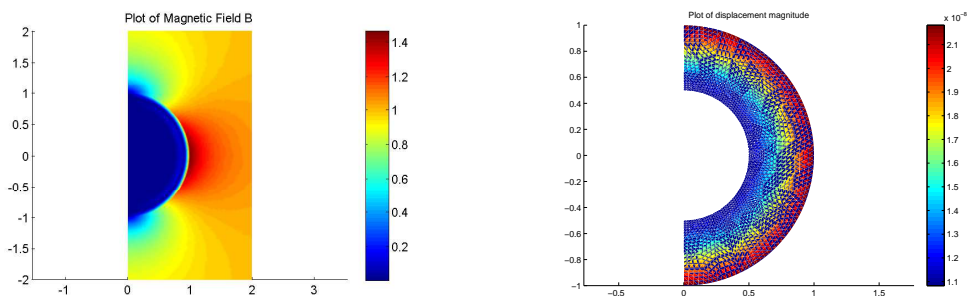


Figure 2: electromagnetic (left) and displacement (right) vector fields

The same problem was also used to test the behaviour of the Newton-Raphson scheme against the previously implemented fixed point scheme. The problem was set-up with the same conditions as for the previous case but with coupling effects added. The result for the mechanical displacement is shown in Figure 4. The mechanical displacement is clearly larger, seen by comparing the colour scales of Figures 4

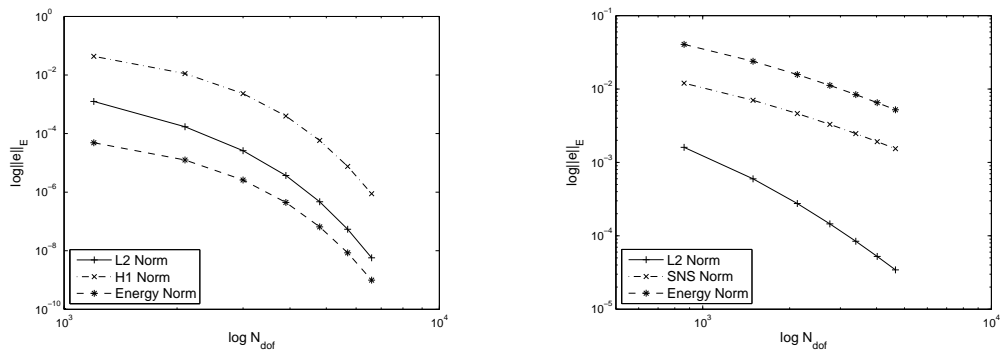


Figure 3: electromagnetic (left) and mechanical (right) p -convergence for the uncoupled problems

and 2, both of which are solutions at $p = 7$. Figure 4 also shows the comparison between the convergence rates of the Newton-Raphson scheme and the fixed point. The Newton-Raphson scheme converges far quicker, requiring only 2 iterations to the fixed point's 7.

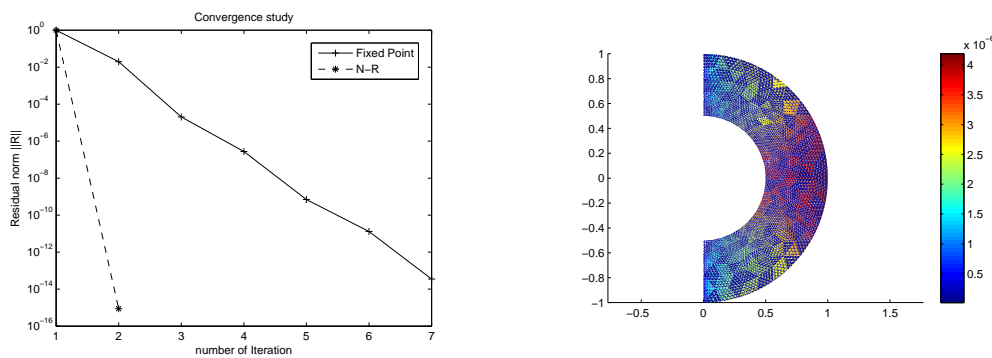


Figure 4: Convergence of two schemes (left) and mechanical displacements of coupled problem (right)

6. Conclusions

The results presented here provide a validation to the set up of an tool for the prediction of deformation and vibration in the conducting regions of the simplified MRI scanner proposed by Siemens. The presentation of the full coupled results on the benchmark problem will be presented at the ACME conference.

Acknowledgements

The authors would like to acknowledge the funding recieved from EPSRC and Siemens Magnet Technology, Siemens plc

References

- [1] Damadian R., Goldsmith M., Minkoff L. NMR in cancer: XVI. Fonar image of the live human body, *Physiol Chem Phys*, 9, 97-100, 1977
- [2] Pope J. Medical Physics: Imaging, Heinemann advanced science, *Pearson Education*, 72-96, 1999
- [3] Ledger P.D., Gil A.J., Poya R., Wilkinson I., Kruij M., Bagwell S.G. Solution of an industrially relevant coupled magneto-mechanical problem set on an axisymmetric domain, *Submitted 2014*
- [4] Jin D., Ledger P.D., Gil A.J. An hp -fem framework for the simulation of electrostrictive and magnetostrictive materials, *Computers and Structures vol. 133*, 131-148, 2014
- [5] A.J. Gil and P.D. Ledger, A coupled hp -finite element scheme for the solution of two-dimensional electrostrictive materials, *International Journal for Numerical Methods in Engineering*, Vol. 91, Issue 11, 1158-1183, 2012
- [6] J. Bonet and R.D.Wood, Nonlinear Continuum Mechanics for Finite Element Analysis, *Cambridge University Press*, ISBN 978-0-521-83870-2, 1997

COUPLED PROBLEMS 4

An entropy-based stabilised Petrov-Galerkin formulation for linear tetrahedral elements in compressible, nearly incompressible and truly incompressible fast solid dynamics

*Chun Hean Lee, Antonio J. Gil, Javier Bonet and Rogelio Ortigosa

Zienkiewicz Centre for Computational Engineering, College of Engineering, Swansea University,
Singleton Park, SA2 8PP, United Kingdom

*c.h.lee@swansea.ac.uk

ABSTRACT

Modern displacement-based linear tetrahedral element technology in solid mechanics (e.g. ANSYS AUTODYN, LS-DYNA, ABAQUS, Altair HyperCrash) possesses several distinct disadvantages, namely: (1) Reduced order of convergence for strains and stresses; (2) High frequency noise in the vicinity of shocks; (3) Stability issues associated with shear locking, volumetric locking and pressure checkerboard instabilities.

To address the shortcomings mentioned above, a novel mixed momentum/strains formulation as a set of first order conservation laws, fulfilling numerical involutions, has been recently developed by the authors [1–6]. In this paper, an alternative version of entropy-based conservation laws, aligned with the classical framework of hydrodynamics, by using a mixed velocity/stresses formulation, is introduced. Crucially, the use of nearly incompressible polyconvex constitutive laws [5] ensures the physical existence of wave speeds. One of the key novelties, upon the work of Gil et al. [4], is to extend a conservation-based Petrov-Galerkin fractional step method to polyconvex entropy system.

A series of numerical examples are presented in order to assess the robustness of the proposed methodology [7]. The overall scheme shows excellent behaviour in compressible, nearly incompressible and truly incompressible scenarios without any spurious hydrostatic oscillations and locking phenomena, yielding equal second order of convergence for velocities and stresses.

Key Words: *Conservation laws; Entropy; Petrov Galerkin; Incompressibility; Polyconvexity*

1. Introduction

Traditional displacement-based linear tetrahedral finite element formulations, along with Newmark-type time integrators, are typically employed when simulating large strain complex engineering problems. However, this approach presents a number of well-known shortcomings, namely, a reduced order of convergence for strains and stresses, inefficient in nearly and truly incompressible bending dominated scenarios [3], numerical instabilities in the form of shear and volumetric locking, non-physical hydrostatic pressure fluctuations and high frequency noise in the vicinity of sharp spatial gradients.

To overcome all the shortcomings mentioned above, a mixed velocity/strains methodology was first introduced where the linear momentum \mathbf{p} and the deformation gradient \mathbf{F} were treated as primary variables of a new mixed approach in the form of a system of first order conservation laws [1–3]. The two-field formulation was then augmented by incorporating a new conservation law for the Jacobian of the deformation J to effectively solve nearly incompressible deformations [4, 6]. Moreover, the formulation was also extended to account for truly incompressible materials utilising a fractional step approach to circumvent the volumetric wave speed constraint. Further enhancement of the framework has recently been reported by the authors [5], when considering compressible materials governed by a polyconvex constitutive law.

In this paper, an alternative set of entropy-based conservation laws by means of velocity/stresses methodology is introduced. The main objective is to introduce an efficient Petrov-Galerkin methodology [4] for

linear tetrahedral elements in polyconvex entropy system, extending the range of applications towards incompressibility limit. An extensive set of numerical examples will be assessed to illustrate the robustness and capabilities of the hydrodynamic-like mixed algorithm.

2. Entropy-based System for Reversible Elastodynamics

Recently, a complete set of first order conservation laws for conservation-based momentum/strains elastodynamics [5] was established with a vector of variables \mathcal{U} , flux vector \mathcal{F}_I and source term \mathcal{S} given by:

$$\frac{\partial \mathcal{U}}{\partial t} + \frac{\partial \mathcal{F}_I}{\partial X_I} = \mathcal{S}; \quad \forall I = 1, 2, 3, \quad (1)$$

where

$$\mathcal{U} = \begin{bmatrix} \mathbf{p} \\ \mathbf{F} \\ \mathbf{H} \\ J \end{bmatrix}; \quad \mathcal{F}_I = - \begin{bmatrix} \mathbf{P} \mathbf{E}_I \\ \frac{1}{\rho_0} \mathbf{p} \otimes \mathbf{E}_I \\ \mathbf{F} \times \left(\frac{1}{\rho_0} \mathbf{p} \otimes \mathbf{E}_I \right) \\ \mathbf{H} : \left(\frac{1}{\rho_0} \mathbf{p} \otimes \mathbf{E}_I \right) \end{bmatrix}; \quad \mathcal{S} = \begin{bmatrix} f_0 \\ \mathbf{0} \\ \mathbf{0} \\ 0 \end{bmatrix}; \quad \mathbf{E}_1 = \begin{bmatrix} 1 \\ 0 \\ 0 \end{bmatrix}; \quad \mathbf{E}_2 = \begin{bmatrix} 0 \\ 1 \\ 0 \end{bmatrix}; \quad \mathbf{E}_3 = \begin{bmatrix} 0 \\ 0 \\ 1 \end{bmatrix}. \quad (2)$$

Here, \mathbf{p} represents the linear momentum, ρ_0 is the material density, f_0 is the body force per unit undeformed volume, \mathbf{F} is the deformation gradient, \mathbf{H} is the cofactor of the deformation gradient, J the Jacobian of the deformation gradient, \mathbf{P} the first Piola-Kirchhoff stress and the notation \times represents the tensor cross product [5]. Essentially, for closure of the system (2), a constitutive relationship fulfilling polyconvexity can be established where the first Piola \mathbf{P} is expressed in terms of the minors of deformations, namely, \mathbf{F} , \mathbf{H} and J .

It is now possible to define a new set of conjugate entropy variables by applying chain rule on the left hand side of equation (1) via $[\mathbb{H}_{S\mathcal{U}}] = \frac{\partial \mathcal{V}}{\partial \mathcal{U}}$, for which the entropy system becomes:

$$\frac{\partial \mathcal{V}}{\partial t} = -[\mathbb{H}_{S\mathcal{U}}] \frac{\partial \mathcal{F}_I}{\partial X_I} + [\mathbb{H}_{S\mathcal{U}}] \mathcal{S}. \quad (3)$$

To obtain the Hessian operator $[\mathbb{H}_{S\mathcal{U}}]$, consider the following convex entropy function defined by:

$$S_{\mathcal{U}}(\mathbf{p}, \mathbf{F}, \mathbf{H}, J) = \frac{1}{2\rho_0} \mathbf{p} \cdot \mathbf{p} + W(\mathbf{F}, \mathbf{H}, J), \quad W = \hat{W}(\mathbf{F}, \mathbf{H}, J) + U(J) \quad (4)$$

which clearly represents the kinetic and elastic energy W (which can be decomposed into the summation of a deviatoric energy \hat{W} and a volumetric energy U) per unit undeformed volume. Note that the conjugate entropy variables \mathcal{V} are given by the derivatives of $S_{\mathcal{U}}$ as: $\mathcal{V} = \frac{\partial S_{\mathcal{U}}}{\partial \mathcal{U}} = [\mathbf{v}, \Sigma_{\mathbf{F}}, \Sigma_{\mathbf{H}}, \Sigma_J]^T$. Differentiating the above expression \mathcal{V} , which contains second derivatives of \mathcal{U} , can now be followed:

$$[\mathbb{H}_{S\mathcal{U}}] = \frac{\partial \mathcal{V}}{\partial \mathcal{U}} = \frac{\partial^2 S_{\mathcal{U}}}{\partial \mathcal{U} \partial \mathcal{U}} = \begin{bmatrix} \frac{1}{\rho_0} \mathbf{I} & \mathbf{0} \\ \mathbf{0} & [\mathbb{H}_W] \end{bmatrix} = \begin{bmatrix} \frac{1}{\rho_0} \mathbf{I} & \mathbf{0} & \mathbf{0} \\ \mathbf{0} & \frac{\partial^2 \hat{W}}{\partial \mathbf{F} \partial \mathbf{F}} & \frac{\partial^2 \hat{W}}{\partial \mathbf{F} \partial \mathbf{H}} & \frac{\partial^2 \hat{W}}{\partial \mathbf{F} \partial J} \\ \mathbf{0} & \frac{\partial^2 \hat{W}}{\partial \mathbf{H} \partial \mathbf{F}} & \frac{\partial^2 \hat{W}}{\partial \mathbf{H} \partial \mathbf{H}} & \frac{\partial^2 \hat{W}}{\partial \mathbf{H} \partial J} \\ \mathbf{0} & \frac{\partial^2 \hat{W}}{\partial J \partial \mathbf{F}} & \frac{\partial^2 \hat{W}}{\partial J \partial \mathbf{H}} & \frac{\partial^2 \hat{W}}{\partial J \partial J} + \frac{d^2 U}{dJ^2} \end{bmatrix} = \begin{bmatrix} \frac{1}{\rho_0} \mathbf{I} & \mathbf{0} \\ \mathbf{0} & \mathbb{H}_{\mathbf{FF}} & \mathbb{H}_{\mathbf{FH}} & \mathbb{H}_{\mathbf{FJ}} \\ \mathbf{0} & \mathbb{H}_{\mathbf{HF}} & \mathbb{H}_{\mathbf{HH}} & \mathbb{H}_{\mathbf{HJ}} \\ \mathbf{0} & \mathbb{H}_{\mathbf{JF}} & \mathbb{H}_{\mathbf{JH}} & \hat{\mathbb{H}}_{\mathbf{JJ}} + \mathbb{H}_{\mathbf{JJ}} \end{bmatrix}. \quad (5)$$

Combining equation (5) into (3) for $[\mathbb{H}_{S\mathcal{U}}]$, a set of entropy conservation laws particularising for the case of velocity and stresses become:

$$\begin{aligned} \frac{\partial \mathbf{v}}{\partial t} &= \frac{1}{\rho_0} \text{DIV} \mathbf{P} + \frac{1}{\rho_0} \mathbf{f}_0; & \frac{\partial \Sigma_{\mathbf{F}}}{\partial t} &= (\mathbb{H}_{\mathbf{FF}} + \mathbb{H}_{\mathbf{FH}} \times \mathbf{F}_{\Sigma} + \mathbb{H}_{\mathbf{FJ}} \otimes \mathbf{H}_{\Sigma}) : \nabla_0 \mathbf{v}; \\ \frac{\partial \Sigma_{\mathbf{H}}}{\partial t} &= (\mathbb{H}_{\mathbf{HF}} + \mathbb{H}_{\mathbf{HH}} \times \mathbf{F}_{\Sigma} + \mathbb{H}_{\mathbf{HJ}} \otimes \mathbf{H}_{\Sigma}) : \nabla_0 \mathbf{v}; & \frac{\partial \Sigma_J}{\partial t} &= (\mathbb{H}_{\mathbf{JF}} + \mathbb{H}_{\mathbf{JH}} \times \mathbf{F}_{\Sigma} + \hat{\mathbb{H}}_{\mathbf{JJ}} \mathbf{H}_{\Sigma}) : \nabla_0 \mathbf{v}; \\ \frac{\partial p}{\partial t} &= \mathbb{H}_{\mathbf{JJ}} (\mathbf{H}_{\Sigma} : \nabla_0 \mathbf{v}). \end{aligned} \quad (6)$$

Note that the strain measures $\{\mathbf{F}_{\Sigma}, \mathbf{H}_{\Sigma}, \mathbf{J}_{\Sigma}\}$ are obtained using reverse constitutive relationships.

3. Stabilised Petrov Galerkin Methodology

It is well known that the resulting standard Bubnov-Galerkin variational formulation requires extra numerical stabilisation, which is usually introduced by means of a Petrov-Galerkin approach [5] whereby the conjugate weighting functions $\delta\mathcal{U}$ are augmented as $\delta\mathcal{U}^{st} = \delta\mathcal{U} + \tau\mathcal{A}_I \frac{\partial\delta\mathcal{U}}{\partial X_I}$. Note that \mathcal{A}_I is the flux Jacobian matrix in the material direction I and τ denotes a matrix of stabilisation parameters to be described below.

In the case of a diagonal stabilisation matrix τ , the individual components of $\delta\mathcal{U}^{st}$ are easily obtained with the help of equation (2) to give:

$$\delta\mathbf{p}^{st} = \delta\mathbf{p} - \tau_{pF} \left(\frac{\partial(\mathbf{PE}_I)}{\partial\mathbf{F}} : \frac{\partial\delta\mathbf{F}}{\partial X_I} \right) - \tau_{pH} \left(\frac{\partial(\mathbf{PE}_I)}{\partial\mathbf{H}} : \frac{\partial\delta\mathbf{H}}{\partial X_I} \right) - \tau_{pJ} \left(\frac{\partial\mathbf{P}^{dev}}{\partial J} \nabla_0 \delta J \right) - \tau_{pp} \left(\frac{\partial\mathbf{P}^{vol}}{\partial J} \nabla_0 \delta J \right) \quad (7a)$$

$$\delta\mathbf{F}^{st} = \delta\mathbf{F} - \frac{\tau_{Fp}}{\rho_0} (\nabla_0 \delta\mathbf{p}); \quad \delta\mathbf{H}^{st} = \delta\mathbf{H} - \frac{\tau_{Hp}}{\rho_0} (\mathbf{F}_\Sigma \times \nabla_0 \delta\mathbf{p}); \quad \delta J^{st} = \delta J - \frac{\tau_{Jp}}{\rho_0} (\mathbf{H}_\Sigma : \nabla_0 \delta\mathbf{p}). \quad (7b)$$

Observe that τ_{pF} , τ_{pH} , τ_{pJ} , τ_{pp} , τ_{Fp} , τ_{Hp} and τ_{Jp} are appropriate numerical stabilising parameters and their units are those of time.

It is now possible to derive the stabilised weak statement by multiplying appropriate conjugate virtual fields $\delta\mathcal{U}^{st}$ with the corresponding residuals \mathcal{R}_ν and integrating over the initial volume V , to give

$$\int_V \delta\mathcal{U}^{st} \cdot \mathcal{R}_\nu dV = \int_V \left[\delta\mathbf{p}^{st} \cdot \mathcal{R}_\nu + \delta\mathbf{F}^{st} : \mathcal{R}_{\Sigma_F} + \delta\mathbf{H}^{st} : \mathcal{R}_{\Sigma_H} + \delta J^{st} (\mathcal{R}_{\Sigma_J} + \mathcal{R}_p) \right] dV = 0 \quad (8)$$

for all $\delta\mathcal{U} = [\delta\mathbf{p}, \delta\mathbf{F}, \delta\mathbf{H}, \delta J]^T$ compatible with the boundary conditions. Following a C_0 linear finite element spatial discretisation strategy, as well integration by parts, the rate of change of velocity at each node a is given as:

$$\sum_b M_{ab} \dot{\mathbf{v}}_b = \int_V \frac{1}{\rho_0} f_0 N_a dV + \int_{\partial V} \frac{1}{\rho_0} \mathbf{t}_B N_a dA - \int_V \frac{1}{\rho_0} \mathbf{P}^{st} \nabla_0 N_a dV. \quad (9)$$

The stabilised first Piola \mathbf{P}^{st} is in the form of

$$\mathbf{P}^{st} = \Sigma_F^{st} + \Sigma_H^{st} \times \mathbf{F} + (\Sigma_J^{dev,st} + p^{st}) \mathbf{H} \quad (10)$$

and the stabilised stresses are defined by

$$\Sigma_F^{st} = \Sigma_F + \tau_{Fp} \mathcal{R}_{\Sigma_F}; \quad \Sigma_H^{st} = \Sigma_H + \tau_{Hp} \mathcal{R}_{\Sigma_H}; \quad \Sigma_J^{dev,st} = \Sigma_J^{dev} + \tau_{Jp} \mathcal{R}_{\Sigma_J}; \quad p^{st} = p + \tau_{pp} \mathcal{R}_p. \quad (11)$$

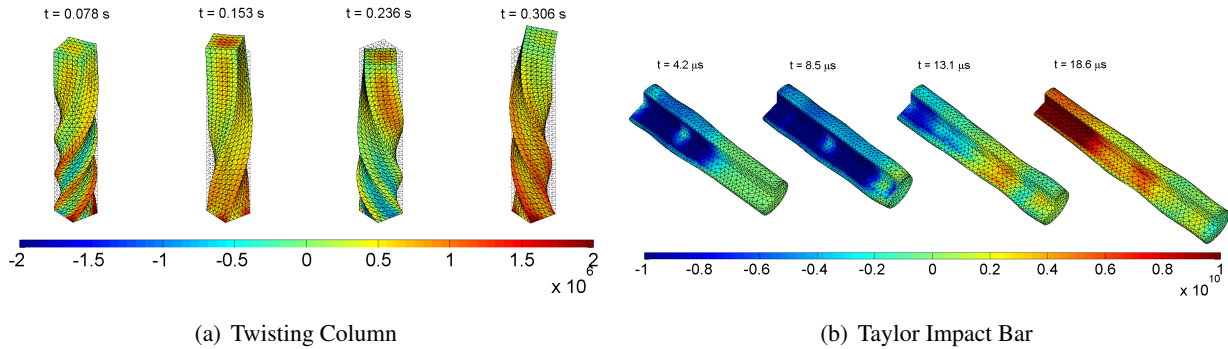
Finally, introducing the linear interpolation equations for the stress variables and their conjugate strains gives a full set of equations for the nodal stress values as:

$$\begin{aligned} \sum_b M_{ab} \dot{\Sigma}_F^b &= \int_V N_a (\mathbb{H}_{FF} + \mathbb{H}_{FJ} \otimes \mathbf{H}_\Sigma) : \nabla_0 \mathbf{v} dV; & \sum_b M_{ab} \dot{\Sigma}_H^b &= \int_V N_a (\mathbb{H}_{HH} \times \mathbf{F}_\Sigma + \mathbb{H}_{HJ} \otimes \mathbf{H}_\Sigma) : \nabla_0 \mathbf{v} dV \\ \sum_b M_{ab} \dot{\Sigma}_J^{dev,b} &= \int_V N_a (\mathbb{H}_{JF} + \mathbb{H}_{JH} \times \mathbf{F}_\Sigma + \hat{\mathbb{H}}_{JJ} \mathbf{H}_\Sigma) : \nabla_0 \mathbf{v} dV; \\ \sum_b M_{ab} \dot{p}^b &= \int_{\partial V} N_a \mathbb{H}_{JJ} \mathbf{v}_B \cdot (\mathbf{H}_\Sigma \mathbf{N}) dA - \int_V \mathbb{H}_{JJ} \mathbf{v}^{st} \cdot (\mathbf{H}_\Sigma \nabla_0 N_a) dV, \end{aligned} \quad (12)$$

where the stabilised velocity $\mathbf{v}^{st} = \mathbf{v} + \tau_{pp} \mathcal{R}_\nu$. The set of equations (9) and (12) represents a stabilised system of differential equations in time for the entropy variables $\{\mathbf{v}, \Sigma_F, \Sigma_H, \hat{\Sigma}_J, p\}$ that satisfy numerical involutions. These semi-discrete expressions (9) and (12) may then be integrated in time by employing the explicit two-stage Total Variation Diminishing Runge-Kutta (TVD-RK) time stepping procedure due to its excellent TVD qualities.

4. Numerical Examples

A column with a unit square cross section initially loaded with a prescribed angular velocity is first examined (see Figure a). Its objective is to illustrate the applicability and robustness of the proposed algorithm in extremely high nonlinear nearly incompressible scenarios. Moreover, Figure b shows that the velocity/stresses mixed methodology performs extremely well in truly incompressible impact problems without any spurious pressure modes.



5. Conclusions

A stabilised computational framework, aligned with the classical framework of hydrodynamics, is proposed for the numerical analysis of fast transient phenomena within the context of large deformations. The mixed velocity/stresses formulation performs extremely well in nearly and truly incompressible bending dominated scenarios. Both velocities (or displacements) and stresses display the same rate of convergence, which proves ideal in the case of linear finite element interpolation oftenly used in industry. The proposed formulation overcomes excessive artificial stiffness and pressure checkerboard modes, and provides a good balance between accuracy and speed of computation.

6. Acknowledgements

The authors gratefully acknowledge the financial support provided by the Sêr Cymru National Research Network for Advanced Engineering and Materials, United Kingdom.

References

- [1] C. H. Lee, A. J. Gil and J. Bonet. Development of a cell centred upwind finite volume algorithm for a new conservation law formulation in structural dynamics. *Computers and Structures*, 118, 13–38, 2013.
- [2] I. A. Karim, C. H. Lee, A. J. Gil and J. Bonet. A Two-Step Taylor Galerkin formulation for fast dynamics. *Engineering Computations*, 31, 366–387, 2014.
- [3] C. H. Lee, A. J. Gil and J. Bonet. Development of a stabilised Petrov-Galerkin formulation for conservation laws in Lagrangian fast solid dynamics. *CMAME*, 268, 40–64, 2014.
- [4] A. J. Gil, C. H. Lee, J. Bonet and M. Aguirre. A stabilised Petrov-Galerkin formulation for linear tetrahedral elements in compressible, nearly incompressible and truly incompressible fast dynamics. *CMAME*, 276, 659–690, 2014.
- [5] J. Bonet, A. J. Gil, C. H. Lee, M. Aguirre and R. Ortigosa. A first order hyperbolic framework for large strain computational solid dynamics. Part I: Total Lagrangian isothermal elasticity. *CMAME*, 283, 689–732, 2015.
- [6] M. Aguirre, A. J. Gil, J. Bonet and C. H. Lee. An upwind vertex centred finite volume solver for Lagrangian solid dynamics. *JCP*, Under Review.
- [7] C. H. Lee, A. J. Gil, J. Bonet and R. Ortigosa. An entropy-based stabilised Petrov-Galerkin formulation for linear tetrahedral elements in compressible, nearly incompressible and truly incompressible Lagrangian fast solid dynamics. *CMAME*, Submitted.

CutFEM: a stabilised Nitsche XFEM method for multi-physics problems

*S. Claus¹, E. Burman¹, A. Massing²

¹ Department of Mathematics, University College London, London, UK–WC1E 6BT, United Kingdom

² Department of Mathematics and Mathematical Statistics, Umeå University, SE–901 87 Umeå, Sweden

*Presenter: susanne.claus@ucl.ac.uk

ABSTRACT

In this communication, we will give an overview over CutFEM, a new stabilised XFEM technique. Here, different PDEs are coupled across an interface, that intersects a fixed background mesh in an arbitrary manner. The boundary conditions on the interface are enforced using Nitsche-type coupling conditions [1]. Nitsche’s method offers a flexible approach to design XFEM methods that is amenable to analysis. Classically, XFEM methods suffer from ill-conditioning if the interface intersects elements close to element nodes leaving only small parts of the element covered by the physical domain. In our method, we overcome this major difficulty, by adding ghost-penalty terms to the variational formulation over the band of elements that are cut by the interface [3, 4]. In this contribution, we will illustrate the usage of CutFEM on the three field Stokes problem.

Key Words: *Nitsche’s method, XFEM, multi-physics problems, ghost penalty, three field Stokes.*

1. Introduction

The simulation of multi-physics problems involves the discretisation of a set of partial differential equation in complex or evolving geometries. Classically, these geometries are discretised by fitting the edges of a mesh to the boundary or interface between different physical domains. However, if the physical domains undergo large deformations or are extremely complex, fitting meshes to the interface can be prohibitively expensive. Here, a description of the interface location independent of the background mesh by using implicit functions such as level set functions is computationally efficient and advantageous. However, to retain the same accuracy as fitted finite element methods, interface conditions between the physical domains need to be enforced inside elements and sub-integration over the resulting physical parts of the elements need to be performed (see Figure 1). This geometric discretisation has to be stabilised in the interface region to avoid ill-conditioning when the interface intersects elements close to edges or facets leaving only very small parts of the elements covered by one physical domain. This is because the integration over these small physical parts leads to small element matrix entries and therefore to ill-conditioned system matrices.

Using a-priori finite element analysis, we have developed a finite element framework that guarantees the stability and accuracy of unfitted interface descriptions independent of how the interface cuts the mesh. In our novel framework, called CutFEM [4], we employ Nitsche’s method to enforce interface conditions inside the elements [1] combined with so-called ghost-penalties in the interface region to regularise the solution [3].

Nitsche’s method offers a flexible approach to design unfitted finite element methods that is amenable to analysis. It has several advantages over alternative methods that can be used to enforce weak interface coupling conditions, such as Lagrange multiplier or penalty methods. In contrast to classical Lagrange multiplier methods no other unknown is introduced in the Nitsche method and no discrete inf-sup condition needs to be satisfied. And conversely to standard penalty parameter techniques, the resulting Nitsche method is consistent [1].

The ghost penalty term, that we add in the interface region [3] extends the coercivity of the discrete

system to the whole elements in the interface region. This penalty term is carefully designed to add sufficient stability, while remaining weakly convergent for smooth solutions. In this contribution, we will illustrate the usage of CutFEM on the three field Stokes problem. The multi-physics formulation of the three field Stokes problem detailed below is an extension of the cut finite element formulation described in [6], which contains the detailed analysis for one three field Stokes fluid in a fictitious domain.

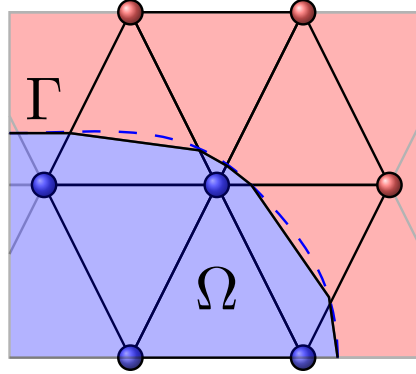


Figure 1: Multi-physics finite element method in which the interface between physical domains intersects arbitrarily through a fixed background mesh. Interface conditions are enforced inside elements and integration of the weak formulation of the underlying partial differential equation is performed over sub-elements covered by the respective physical domains.

2. Stabilised Finite Element Discretisation of The Three Field Stokes Problem

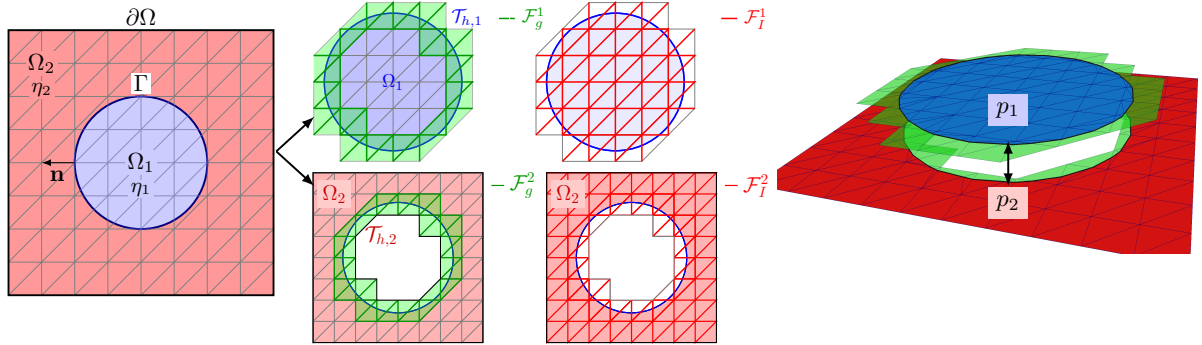


Figure 2: Three field Stokes multi-domain discretisation. The cells that are intersected by the interface are doubled allowing for arbitrary discontinuities inside elements. The middle figure illustrates the definition of interior \mathcal{F}_g^i and ghost penalty facets \mathcal{F}_g^i as well as the domain triangulations $\mathcal{T}_{h,1}$ and $\mathcal{T}_{h,2}$.

Let Ω be a domain in \mathbb{R}^d ($d = 2$ or 3) with a polyhedral boundary $\partial\Omega$. We assume that two immiscible incompressible three field Stokes fluids occupy subdomains $\Omega_i \subset \Omega$, $i = 1, 2$, with $\Omega = \Omega_1 \cap \Omega_2$ and that Γ denotes the smooth interface between them. Then, the three field Stokes problems reads: Find the extra-stress tensor $\boldsymbol{\sigma} : \Omega \rightarrow \mathbb{R}^{d \times d}$, the velocity $\mathbf{u} : \Omega \rightarrow \mathbb{R}^d$ and the pressure $p : \Omega \rightarrow \mathbb{R}$, such that

$$\begin{aligned} \boldsymbol{\sigma} - 2\eta\boldsymbol{\varepsilon}(\mathbf{u}) &= 0 && \text{in } \Omega, \\ -\nabla \cdot \boldsymbol{\sigma} + \nabla p &= \mathbf{f} && \text{in } \Omega, \\ \nabla \cdot \mathbf{u} &= 0 && \text{in } \Omega, \end{aligned} \tag{1}$$

$$\begin{aligned} \mathbf{u} &= \mathbf{g} && \text{on } \partial\Omega, \\ \llbracket \mathbf{u} \rrbracket &= 0 && \text{on } \Gamma, \\ \llbracket (\boldsymbol{\sigma} - p\mathbf{I}) \cdot \mathbf{n} \rrbracket &= \gamma\kappa\mathbf{n} && \text{on } \Gamma, \end{aligned} \tag{2}$$

where $\boldsymbol{\varepsilon}(\mathbf{u}) = \frac{1}{2}(\nabla\mathbf{u} + \nabla\mathbf{u}^T)$ is the rate of deformation tensor, $\eta|_{\Omega_i} = \eta_i$, $i = 1, 2$, is the constant fluid viscosity on Ω_i , respectively and $\mathbf{f} \in [L^2(\Omega)]^d$ is a given function. At the fluid interface, we enforce a zero jump condition on the velocity, $\llbracket \mathbf{u} \rrbracket = (\mathbf{u}_1 - \mathbf{u}_2)|_{\Gamma} = 0$, $\mathbf{u}_i = \mathbf{u}|_{\Omega_i}$, $i = 1, 2$, and the jump in the traction vector over the interface is given by the surface tension. Here, γ is the surface tension coefficient, κ is the

curvature of the interface and \mathbf{n} is the outward unit normal on the interface pointing from Ω_1 to Ω_2 .

Let $\{\mathcal{T}_h\}_{0 < h \leq 1}$ be a shape-regular family of triangulations of the domain $\Omega = \Omega_1 \cup \Omega_2$ independent of the location of the interface. Define meshes on the subdomains Ω_i as

$$\mathcal{T}_{h,i} = \{K \in \mathcal{T}_h : K \cap \Omega_i \neq \emptyset\}. \quad (3)$$

Note that elements intersected by the interface are both in $\mathcal{T}_{h,1}$ and $\mathcal{T}_{h,2}$. Let \mathcal{V}_h denote the space of piecewise linear polynomials on \mathcal{T}_h and we let

$$\mathcal{V}_h = \mathcal{V}_{h,1} \oplus \mathcal{V}_{h,2} \quad \text{with } \mathcal{V}_{h,i} = \mathcal{V}_h|_{\mathcal{T}_{h,i}}, i = 1, 2. \quad (4)$$

This means, for example, p_h consists of a pair $(p_{h,1}, p_{h,2})$, with $p_{h,i} \in \mathcal{V}_{h,i}$, and $p_h \in \mathcal{V}_h$ is double valued for elements that are intersected by the interface. This allows p_h to be discontinuous at the interface (see Figure 2) similar to XFEM methods [2]. Analogously, we define vector, \mathcal{V}_h^d , and tensor valued, $\mathcal{V}_h^{d \times d}$, linear finite element spaces for the velocity and the extra stress tensor.

Let's denote

$$(\mathbf{u}, \mathbf{v})_\Omega = \sum_i (\mathbf{u}_i, \mathbf{v}_i)_{\Omega_i}, \quad i = 1, 2. \quad (5)$$

Introducing the notation

$$a_h(\boldsymbol{\sigma}_h, \mathbf{v}_h) = (\boldsymbol{\sigma}_h, \boldsymbol{\epsilon}(\mathbf{v}_h))_\Omega - (\{\boldsymbol{\sigma} \cdot \mathbf{n}\}, \llbracket \mathbf{v} \rrbracket)_\Gamma - (\boldsymbol{\sigma} \cdot \mathbf{n}_\Omega, \mathbf{v})_{\partial\Omega}, \quad (6)$$

$$b_h(p_h, \mathbf{v}_h) = -(p_h, \nabla \cdot \mathbf{v}_h)_\Omega + (\{p \cdot \mathbf{n}\}, \llbracket \mathbf{v} \rrbracket)_\Gamma + (p \cdot \mathbf{n}_\Omega, \mathbf{v})_{\partial\Omega}, \quad (7)$$

the stabilised finite element formulation of the three-field Stokes problem reads: find $U_h := (\boldsymbol{\sigma}_h, \mathbf{u}_h, p_h) \in \mathcal{V}_h^{d \times d} \times \mathcal{V}_h^d \times \mathcal{V}_h$ such that for all $V_h := (\boldsymbol{\tau}_h, \mathbf{v}_h, q_h) \in \mathcal{V}_h^{d \times d} \times \mathcal{V}_h^d \times \mathcal{V}_h$

$$A_h(U_h, V_h) + S_h(U_h, V_h) = L(V_h), \quad (8)$$

where

$$\begin{aligned} A_h(U_h, V_h) &= \frac{1}{2\eta} (\boldsymbol{\sigma}_h, \boldsymbol{\tau}_h)_\Omega + a_h(\boldsymbol{\sigma}_h, \mathbf{v}_h) - a_h(\boldsymbol{\tau}_h, \mathbf{u}_h) \\ &\quad + b_h(p_h, \mathbf{v}_h) - b_h(q_h, \mathbf{u}_h), \\ &\quad + \lambda_\Gamma (\llbracket \mathbf{u} \rrbracket, \llbracket \mathbf{v} \rrbracket)_\Gamma + \lambda_\Omega (\mathbf{u}, \mathbf{v})_{\partial\Omega}, \end{aligned} \quad (9)$$

$$L_h(V_h) = (\mathbf{f}, \mathbf{v}_h)_\Omega + (\gamma \boldsymbol{\kappa}, \langle \mathbf{v} \cdot \mathbf{n} \rangle)_\Gamma + (\boldsymbol{\tau}_h \cdot \mathbf{n}, \mathbf{g})_{\partial\Omega} - (q_h \cdot \mathbf{n}, \mathbf{g})_{\partial\Omega} + \lambda_\Omega (\mathbf{g}, \mathbf{v}_h)_{\partial\Omega}, \quad (10)$$

$$S_h(U_h, V_h) := s_u(\mathbf{u}_h, \mathbf{v}_h) + s_p(p_h, q_h) + s_\sigma(\boldsymbol{\sigma}_h, \boldsymbol{\tau}_h). \quad (11)$$

Here, λ_Γ and $\lambda_{\partial\Omega}$ are penalty parameters arising from Nitsche's method to enforce the Dirichlet boundary conditions (2) weakly. These penalty parameters have to be chosen large enough to guarantee the coercitivity of the weak formulation. The interface terms contain jumps and weighted averages, defined as

$$w_1 + w_2 = 1, 0 \leq w_i \leq 1, i = 1, 2 :$$

$$\{\mathbf{v}\} := w_1 \mathbf{v}_1 + w_2 \mathbf{v}_2, \quad (12)$$

$$\langle \mathbf{v} \rangle := w_2 \mathbf{v}_1 + w_1 \mathbf{v}_2. \quad (13)$$

The method is stabilised using penalties on the gradient jumps across interior edges ($\mathcal{F}_i^I \in \mathcal{T}_{h,i}, i = 1, 2$) for the velocity and the pressure and across edges in the interface layer ($\mathcal{F}_i^S \in \mathcal{T}_{h,i}, i = 1, 2$) for the extra stress tensor (see Figure 2). The stabilisation terms are given by

$$s_p(p_h, q_h) = \frac{\gamma_p}{2\eta} \sum_{i=1}^2 \sum_{F \in \mathcal{F}_i^I} h^3 (\llbracket \nabla p \rrbracket_n, \llbracket \nabla q \rrbracket_n)_F, \quad (14)$$

$$s_u(\mathbf{v}_h, \mathbf{u}_h) = 2\eta\gamma_u \sum_{i=1}^2 \sum_{F \in \mathcal{F}_i^I} h^1 (\llbracket \nabla \mathbf{v} \rrbracket_n, \llbracket \nabla \mathbf{u} \rrbracket_n)_F, \quad (15)$$

$$s_\sigma(\boldsymbol{\sigma}_h, \boldsymbol{\tau}_h) = \frac{\gamma_\sigma}{2\eta} \sum_{i=1}^2 \sum_{F \in \mathcal{F}_i^S} h^3 (\llbracket \nabla \boldsymbol{\sigma} \rrbracket_n, \llbracket \nabla \boldsymbol{\tau}_h \rrbracket_n)_F. \quad (16)$$

Here, $[[\nabla x]]_n$ denotes the normal jump of the quantity x over the facet, F , defined as $[[\nabla x]]_n = \nabla x|_{K_F^+} \mathbf{n}_F - \nabla x|_{K_F^-} \mathbf{n}_F$, where \mathbf{n}_F denotes a unit normal to the facet F with fixed but arbitrary orientation. The stabilisation parameters $\gamma_p, \gamma_u, \gamma_\sigma$ have to be chosen large enough.

The stabilisation terms on the velocity and the pressure ensure the inf-sup stability of the equal order approximation scheme across the entire mesh domains $\mathcal{T}_{h,i}$ and the penalty term on the stress tensor ensures H^1 control of the stress tensor in the entire elements in the interface region. The penalty terms added to intersected edges prevent ill conditioning of the discretised system matrices. We refer to these penalty terms as ghost-penalties. Note that, the jump gradient penalty terms vanish with optimal order with mesh refinement and therefore the stabilised scheme retains optimal convergence rates ([4],[?]).

3. Numerical Results

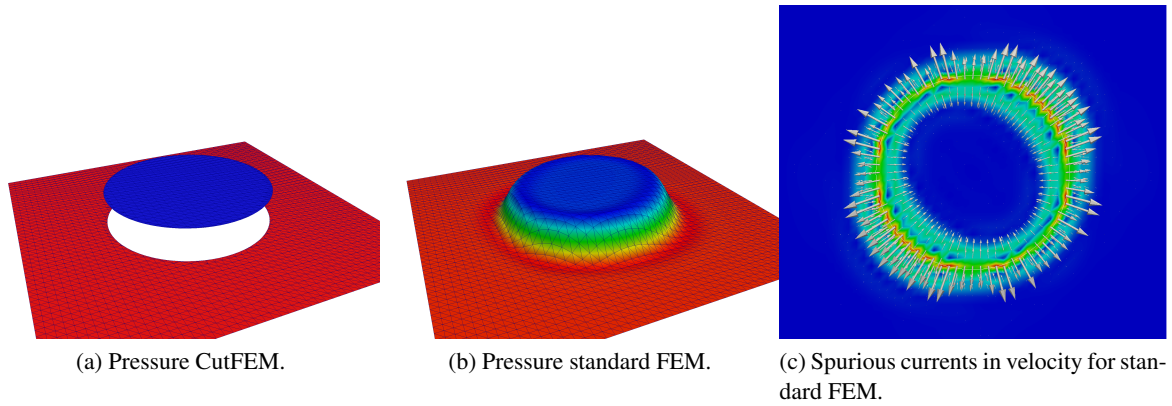


Figure 3: Static drop pressure and velocity solution of CutFEM versus standard FEM.

Consider a circular interface Γ of radius R in equilibrium in the interior of a domain in two dimensions with $\eta_i = 2$ and surface tension $\gamma = 1$ and vanishing \mathbf{u} on $\partial\Omega$. The exact solution is $\boldsymbol{\sigma} = \mathbf{0}, \mathbf{u} = \mathbf{0}, p_1 = 0, p_2 = \frac{\gamma}{R}$ and therefore features a jump in the pressure. We prescribe the exact curvature $\kappa = \frac{1}{R}$ and choose a regular background mesh as depicted in Figure 2. The penalty parameters are chosen as $\lambda_\Gamma = \lambda_{\partial\Omega} = 10, \gamma_u = 0.1, \gamma_p = 0.1, \gamma_\sigma = 0.1$. Figure 3 shows the comparison of the stabilised CutFEM scheme with a standard finite element method. The standard finite element method is not capable of representing the jump in the pressure solution, which leads to a poor solution of the pressure and Gibbs oscillations in the interface region. These Gibbs oscillations in the pressure cause large spurious velocities, which may lead to unphysical movements of the interface in case of multi-phase flows. The CutFEM approach is able to represent the sharp jump in the pressure and there are no spurious oscillations in the velocity.

References

- [1] P. Hansbo. Nitsche’s method for interface problems in computational mechanics. *GAMM-Mitt.*, Vol. **28**(2), 183–206, 2005.
- [2] Goangseup, Z. and Belytschko, T. New cracktip elements for XFEM and applications to cohesive cracks. *International Journal for Numerical Methods in Engineering*, Vol. 57 (2221-2240), (2003).
- [3] E. Burman. Ghost penalty. *Comptes Rendus Mathematique*, Vol. **348** (21-22), 1217 – 1220, 2010.
- [4] E. Burman, S. Claus, P. Hansbo, M. G. Larson, and A. Massing. CutFEM: discretizing geometry and partial differential equations. *International Journal for Numerical Methods in Engineering*, 2014.
- [5] E. Burman and P. Hansbo. Fictitious domain finite element methods using cut elements: II. A stabilized Nitsche method. *Applied Numerical Mathematics*, Vol. **64** (328–341), 2011.
- [6] E Burman, S Claus, A Massing. A Stabilized Cut Finite Element Method for the Three Field Stokes Problem. *SIAM Journal on Scientific Computing*, to appear (preprint at arXiv:1408.5165) 2015.
- [7] A. Bonito and E. Burman. A Continuous Interior Penalty Method for Viscoelastic Flows. *SIAM Journal on Scientific Computing*, Vol. 30 (1156–1177), 2008.

A variational framework for large strain polyconvex dielectric elastomers

R. Ortigosa, A. J. Gil and J. Bonet

Civil & Computational Engineering Centre, College of Engineering, Swansea University, Swansea
SA2 8PP, UK

{577350; a.j.gil; j.bonet}@swansea.ac.uk

ABSTRACT

In this paper, a new variational framework is presented for the analysis of large strain electromechanics. The framework is applicable to the wide spectrum of electro active materials but it is specially suitable for Electro Active Polymers (EAPs) which are known for their outstanding electrically induced deformation capabilities. In nonlinear elasticity, the condition of polyconvexity characterises admissible strain energy functionals in the large strain regime. The objective of this work is the extension of this condition to the field of electromechanics, where a new energy functional is introduced as a polyconvex combination of both strain and electric field variables. A series of valid variational mixed formulations will be presented and discretised in space with the Finite Element Method, where the resulting system of nonlinear algebraic equations is solved via the Newton-Raphson method after consistent linearisation. Finally, a series of numerical examples are presented in order to assess the capabilities of the new formulation.

Key Words: Energy harvesting; Dielectric elastomers; Polyconvexity; Large deformations; Electromechanics; Finite Element Method

1. Introduction

The numerical simulation of smart materials is pushing the limits of the current computational mechanics techniques. The present work focusses on the simulation of EAPs. EAPs can be classified into two large groups: Electronic Electroactive Polymers (or field activated) and Ionic Electroactive Polymers. Within the first group, Dielectric Elastomers (DEs) form a very attractive subgroup of polymeric materials, which have drawn the attention of scientists over the last two decades. Their fast dynamic response, large electrically induced deformations and lightness surpass those of the highly rigid piezoelectric polymers, initially thought of for actuation purposes. Moreover, the versatility of DEs enables their use in sensor and energy harvesting applications.

The initial linearised variational framework developed for rigid ceramics and piezoelectric polymers is no longer applicable for the numerical simulation of these new materials, which tend to exhibit large deformations whilst subjected to giant electric fields. For instance, a voltage induced area expansion of 1962% in a thin DE film material called 3MTMVHBTM4910 has been recently reported [1]. In this specific case, electro-mechanical instability is harnessed as a means for obtaining these electrically induced massive deformations. Hence, special attention needs to be paid when defining appropriate constitutive laws, since the introduction of non-physical instabilities, such as loss of ellipticity of the model, might lead to a polluted numerical solution.

In this paper, appropriate constitutive laws for nonlinear electro-elasticity are proposed based upon the extension of the concept of polyconvexity proposed by Ball [2] for nonlinear elasticity. The new definition of polyconvexity introduces an extended set of variables and requires convexity of the internal energy with respect to the entire set. This new electro-kineto variable set leads to new work conjugates and enables the introduction of new Hu-Washizu type [5, 3] of mixed variational principles. For the purpose of numerical simulation, the Finite Element Method is preferred for discretisation and a series of numerical examples are presented in order to assess the capabilities of the new formulation.

2. Mathematical requirements: Polyconvexity.

Polyconvexity is nowadays well accepted as a fundamental mathematical requirement that must be satisfied by admissible strain energy functionals used to describe elastic materials in the large strain regime. Essentially, the strain energy Ψ per unit of undeformed volume must be a function of the deformation gradient \mathbf{F} via a convex multi-valued function U of \mathbf{F} , its cofactor \mathbf{H} and its determinant J as

$$\Psi(\nabla_0 \mathbf{x}) = U(\mathbf{F}, \mathbf{H}, J), \quad (1)$$

where $\nabla_0 \mathbf{x}$ is the gradient operator of the spatial configuration with respect to the initial undeformed configuration. The three strain measures \mathbf{F} , \mathbf{H} and J have work conjugate stresses $\boldsymbol{\Sigma}_F$, $\boldsymbol{\Sigma}_H$ and Σ_J , respectively, defined by

$$\boldsymbol{\Sigma}_F = \frac{\partial U}{\partial \mathbf{F}}, \quad \boldsymbol{\Sigma}_H = \frac{\partial U}{\partial \mathbf{H}}, \quad \Sigma_J = \frac{\partial U}{\partial J}. \quad (2)$$

In electro-mechanics, above expression (1) must be extended in order to account for electric field variables. An enhanced energy density functional Ψ is defined as a function of the deformation gradient \mathbf{F} and the material gradient of the electrical potential φ via a convex multi-valued function U of \mathbf{F} , \mathbf{H} , J , the electric displacement vector \mathbf{D}_0 and an additional vector $\mathbf{V} = \mathbf{F}\mathbf{D}_0$ defined as

$$\Psi(\nabla_0 \mathbf{x}, \nabla_0 \varphi) = U(\mathbf{F}, \mathbf{H}, J, \mathbf{D}_0, \mathbf{V}). \quad (3)$$

The new electric variables \mathbf{D}_0 and \mathbf{V} have new work conjugate variables $\boldsymbol{\Sigma}_{D_0}$ and $\boldsymbol{\Sigma}_V$ respectively, which can be defined as

$$\boldsymbol{\Sigma}_{D_0} = \frac{\partial U}{\partial \mathbf{D}_0}, \quad \boldsymbol{\Sigma}_V = \frac{\partial U}{\partial \mathbf{V}}. \quad (4)$$

3. Variational principles in nonlinear electromechanics.

Numerous authors have previously incorporated the concept of polyconvexity for solid mechanics into computational models for both isotropic and non-isotropic materials for a variety of applications [4]. The standard approach consists of ensuring that the strain energy density satisfies first the polyconvexity condition and then proceed towards a computational solution by re-expressing the energy density in terms of the deformation gradient alone.

A mixed formulation can be derived in which the deformation gradient, its cofactor and its determinant are retained as fundamental problem variables by means of a Hu-Washizu mixed variational principle [5]. Moreover, we can generalise this concept to the electromechanical problem by including the electric displacement as a new variable in the variational principle. The resulting formulation opens up new interesting possibilities in terms of using various interpolation spaces for different variables, leading to enhanced formulations.

A possible variational principle can be introduced in terms of the total potential energy Π_U as follows,

$$\begin{aligned} \Pi_U(\mathbf{x}^*, \mathbf{F}^*, \mathbf{H}^*, J^*, \boldsymbol{\Sigma}_F^*, \boldsymbol{\Sigma}_H^*, \Sigma_J^*, \phi^*, \mathbf{D}_0^*, \mathbf{V}^*, \boldsymbol{\Sigma}_V^*) = & \min_{\mathbf{x}, \mathbf{F}, \mathbf{H}, J, \mathbf{D}_0, \mathbf{V}} \left\{ \max_{\boldsymbol{\Sigma}_F, \boldsymbol{\Sigma}_H, \Sigma_J, \phi, \boldsymbol{\Sigma}_V} \left\{ \int_V W(\mathbf{F}, \mathbf{H}, J, \mathbf{D}_0, \mathbf{V}) dV \right. \right. \\ & \left. \left. + \int_V [\boldsymbol{\Sigma}_F : (\mathbf{F}_x - \mathbf{F}) + \boldsymbol{\Sigma}_H : (\mathbf{H}_x - \mathbf{H}) + \Sigma_J (J_x - J) + \mathbf{D}_0 \cdot \nabla_0 \phi + \boldsymbol{\Sigma}_V \cdot (\mathbf{F}_x \mathbf{D}_0 - \mathbf{V})] dV - \Pi_{ext}(\mathbf{x}, \phi) \right\} \right\} \end{aligned} \quad (5)$$

where \mathbf{F}_x , \mathbf{H}_x and J_x represent the deformation gradient, the cofactor and the determinant of the spatial configuration \mathbf{x} . In addition, $\Pi^{ext}(\mathbf{x}, \varphi)$ represents the external work generated from mechanical and electrical body and surface effects. Alternatively, a different ordering in equation (6) leads to the following variational principle,

$$\begin{aligned} \Pi_\Phi(\mathbf{x}^*, \mathbf{F}^*, \mathbf{H}^*, J^*, \boldsymbol{\Sigma}_F^*, \boldsymbol{\Sigma}_H^*, \Sigma_J^*, \phi^*, \mathbf{D}_0^*, \boldsymbol{\Sigma}_{D_0}^*, \boldsymbol{\Sigma}_V^*) = & \min_{\mathbf{x}, \mathbf{F}, \mathbf{H}, J, \mathbf{D}_0} \left\{ \max_{\boldsymbol{\Sigma}_F, \boldsymbol{\Sigma}_H, \Sigma_J, \phi, \boldsymbol{\Sigma}_{D_0}, \boldsymbol{\Sigma}_V} \left\{ \int_V \Phi(\mathbf{F}, \mathbf{H}, J, \boldsymbol{\Sigma}_{D_0}, \boldsymbol{\Sigma}_V) dV \right. \right. \\ & \left. \left. + \int_V [\boldsymbol{\Sigma}_F : (\mathbf{F}_x - \mathbf{F}) + \boldsymbol{\Sigma}_H : (\mathbf{H}_x - \mathbf{H}) + \Sigma_J (J_x - J) + \mathbf{D}_0 \cdot (\boldsymbol{\Sigma}_{D_0} + \nabla_0 \phi) + \boldsymbol{\Sigma}_V \cdot \mathbf{F}_x \mathbf{D}_0] dV - \Pi_{ext}(\mathbf{x}, \phi) \right\} \right\} \end{aligned} \quad (6)$$

where the energy density functional Φ is defined by means of the Legendre transform as

$$\Phi(\mathbf{F}, \mathbf{H}, J, \Sigma_{D_0}, \Sigma_V) = -\max_{D_0, V} \{U^e - U(\mathbf{F}, \mathbf{H}, J, D_0, V)\}; \quad U^e = \Sigma_{D_0} \cdot D_0 + \Sigma_V \cdot V. \quad (7)$$

4. Constitutive models for piezo-hyperelastic materials.

The convex nature of the internal energy density $U(\mathbf{F}, \mathbf{H}, J, D_0, V)$ makes this energy the most suitable for the definition of constitutive laws. More specifically, in the purely elastic case, polyconvexity of the internal energy is equivalent to ellipticity and hence, rank-one convexity. This implies that the acoustic tensor is always positive definite. Hence, hyperbolicity of the dynamic and linearised governing equations is never compromised. In other words, it is possible to guarantee wave-like solutions (characterised by the direction of propagation vector N) in the neighbourhood of an equilibrium configuration. In the context of electro-elasticity, a generalised electromechanical acoustic tensor emerges analogous to that of the elastic problem. In this case, the new definition of polyconvexity proposed in equation (3) ensures the positive definiteness of the new generalised electromechanical acoustic tensor. Therefore, the existence of wave-like solutions for the linearised version of the new extended set of governing equations (Gauss law and conservation of linear momentum) is guaranteed. Figure 1 shows the evolution of the least minor¹ of the generalised electromechanical acoustic tensor for a polyconvex material according to equation (3) and a non polyconvex material. This representation corresponds to a biaxial stretch state in the plane of a thin layer of a representative DE subject to an electric potential gradient across the thickness. Clearly, in the case of the non polyconvex material, at least one of the minors becomes negative, compromising the existence of real wave speeds.

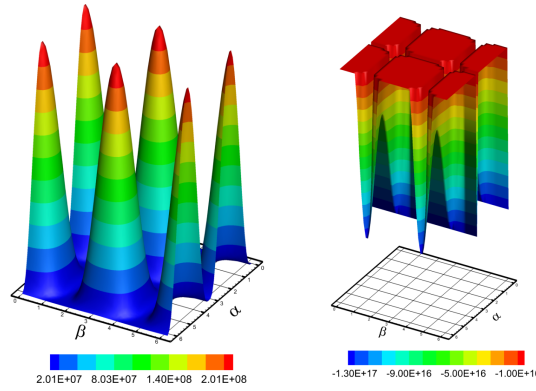


Figure 1: Graphical representation of the least value of the three leading minors of the generalised electro-mechanical acoustic tensor for a biaxial stretch in the plane of the DE subject to an electric potential gradient across the thickness. Figures (a) and (b) correspond to a polyconvex and a non polyconvex constitutive model, respectively, for the same applied electric field. The parameters α and β correspond to a spherical parametrisation of the direction of propagation vector N .

A simple polyconvex constitutive model satisfying equation (3) can be expressed as

$$U(\mathbf{F}, \mathbf{H}, J, D_0, V) = \mu_1(\mathbf{F} : \mathbf{F}) + \mu_2(\mathbf{H} : \mathbf{H}) - (2\mu_1 + 4\mu_2) \ln J + \frac{\kappa}{2}(J - 1)^2 + \frac{1}{2\varepsilon_1} \mathbf{V} \cdot \mathbf{V} + \frac{1}{\varepsilon_2} \mathbf{D}_0 \cdot \mathbf{D}_0 \quad (8)$$

where μ_1 , μ_2 , κ , ε_1 and ε_2 are representative material parameters. Non polyconvex invariants as for example $(\mathbf{H}D_0 \cdot \mathbf{H}D_0)$ can be included in (8) via a simple regularisation technique proposed in [3].

5. Numerical results.

The resulting variational formulations are discretised in space with the help of the Finite Element Method, where the resulting system of nonlinear algebraic equations are solved via the Newton-Raphson method after consistent linearisation. A series of numerical examples will be presented in order to demonstrate the robustness and applicability of the formulation. Figure 2 shows an example in which an electric field applied across the thickness of a composite shell leads to an electrically induced deformation. Figure 3 shows an example in which the twisting of a piezoelectric polymer leads to a distribution of electric field in the material.

¹The Sylvester's criterion is used to check the positive definiteness of the generalised electromechanical acoustic tensor

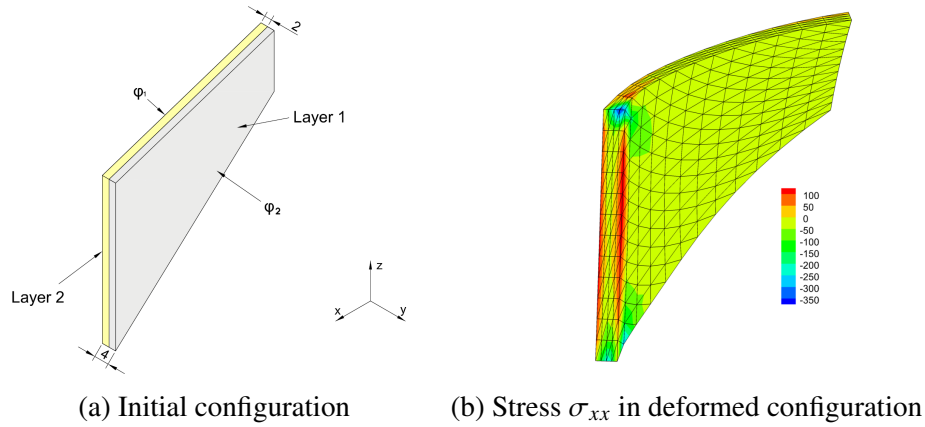


Figure 2: Composite DE actuator: electrically induced deformation.

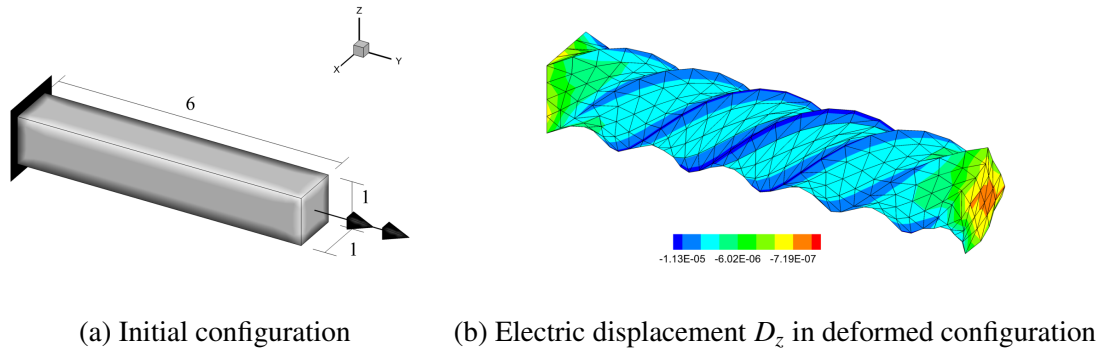


Figure 3: Twisting of transversely anisotropic piezoelectric polymer: deformation induced electric field

6. Conclusions and further research.

A nonlinear variational framework for the numerical simulation of electro active materials has been presented. An extended energy density functional has been introduced satisfying the physical and mathematical requirements established by polyconvexity. A mixed variational formulation has been implemented in which the deformation gradient, its cofactor, its determinant and the electric displacement field are retained as fundamental problem variables by means of a Hu-Washizu type variational principle. Application of the Legendre transform on the internal energy or, equivalently, rearrangement of the terms in the variational principle allows to derive alternative mixed variational formulations. The resulting different formulations are resolved numerically with the aid of the Finite Element Method, using suitable interpolations for the newly introduced variables.

References

- [1] T. Li, C. Keplinger, R. Baumgartner, S. Bauer, W. Yang, Z. Suo. Giant voltage-induced deformation in dielectric elastomers near the verge of snap-through instability. *Journal of the Mechanics and Physics of Solids*, 61, pp. 611-628, 2013.
- [2] J.M. Ball, Convexity conditions and existence theorems in nonlinear elasticity. *Archive of Rational Mechanics Analysis*, 63, pp. 337-403, 1977.
- [3] A.J. Gil, R. Ortigosa and J. Bonet. A computational framework for polyconvex large strain electromechanics. *In preparation*.
- [4] J. Schröder, Anisotropic Polyconvex Energies on the Basis of Crystallographic Motivated Structural Tensors. *Journal of the Mechanics and Physics of Solids*, 56, 3486–3506, 2008.
- [5] J. Bonet, A.J. Gil and R. Ortigosa. A computational framework for polyconvex large strain elasticity. *Computer Methods in Applied Mechanics and Engineering*, 238, pp. 1061-1094, 2015.

NUMERICAL RHEOMETRY OF DENSE PARTICLE SUSPENSIONS USING A COUPLED LATTICE BOLTZMANN AND DISCRETE ELEMENT METHOD

*Bruce D. Jones¹, Christopher R. Leonardi², John R. Williams¹

¹Department of Civil and Environmental Engineering, Massachusetts Institute of Technology,
77 Massachusetts Ave., Cambridge, MA 02139, USA

²School of Mechanical and Mining Engineering, University of Queensland, St. Lucia, QLD 4072,
Australia

*bdjones@mit.edu

ABSTRACT

Transport of dense particle suspensions is of interest in a broad variety of industries from drug development to oil recovery. However the rheology of such suspensions is often characterised by semi-empirical models [1] which may lack flexibility when flow through complex geometries is of interest.

Using a coupled lattice Boltzmann and discrete element method [2], we have developed a new tool for the numerical characterisation of dense suspension rheology. This approach has been implemented using a shared memory, multicore, parallel architecture which allows for rapid and inexpensive evaluation of model results. Where model capabilities include non-Newtonian rheology, turbulence, fluid-solid interactions, and lubricated solid-solid interactions. Through consideration of the fundamental phenomena of flow and contact mechanics this model is able to accurately capture the suspension rheology.

A numerical couette flow rheometer has been implemented in which discrete element particles are packed into a cubic lattice Boltzmann domain. Using either shear stress control this model then simulates the shearing of the particulate suspension. Upon steady state the resultant strain rate, hydrodynamic forces, and mechanical forces, on the shearing plane are recovered. These results are used to characterize a frictional rheology which is compared with experimentally calibrated published expressions.

1. Introduction

A number of constitutive models exist to describe the rheology of particle suspensions as a function of solid volume fraction. Such models are often based on a frictional rheology, where the resultant shear stress, τ , due to shear strain, $\dot{\gamma}$, is related by a fluid and suspension viscosity,

$$\tau = \eta_f \eta_s \dot{\gamma} \quad (1)$$

In which the suspension viscosity is characterised as a dimensionless ratio of a friction coefficient, μ , and viscous number, I ,

$$\eta_s = \frac{\mu}{I} \quad (2)$$

Where the viscous number is the ratio of fluid shear stress and particle pressure, p' ,

$$I = \frac{\eta_f \dot{\gamma}}{p'} \quad (3)$$

In the works of Morris & Boulay [3], and Boyer *et al.*[4], the friction coefficient is decomposed into individual hydrodynamic, μ^{hydro} , and particulate contact, μ^{cont} , contributions.

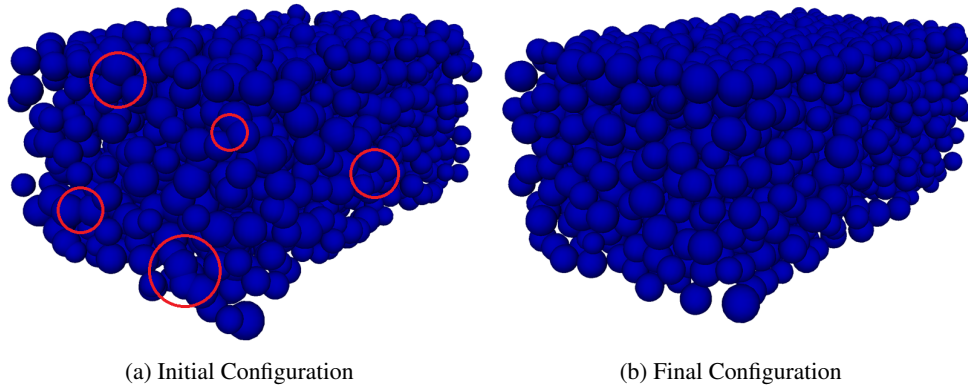


Figure 1: A typical numerical rheometer packing before and after relaxation, some overlaps highlighted by red circles

$$\mu = \mu^{hydro} + \mu^{cont} \quad (4)$$

Both [3] and [4] applied a semi-empirical methodology to propose a form for μ^{hydro} and μ^{cont} , where their expressions include a number of coefficients which were calibrated experimentally. However, a typical load cell can not discern the proportion of force exerted by the individual fluid and particle phases. So it was not possible for [3] and [4] to confirm the accuracy of the individual contributions to friction coefficient, only the accuracy of the sum.

We therefore use a coupled LBM-DEM model of a couette flow rheometer to investigate the frictional rheology of particle suspensions at a variety of particle packing densities and applied shear stresses. By using such a model, we are able to separate hydrodynamic and mechanical contributions to the friction coefficient, and draw a comparison with the expressions of [3] and [4].

2. Methodology

The couette flow rheometer model employed uses the immersed boundary method proposed by Nobel & Torczynski [5] to couple the LBM model to the DEM model. This boundary condition was chosen as it is simple and efficient, its accuracy has been validated for force on particles in previous work by Leonardi *et al.*

Since we are interested in a range of packing densities which includes those approaching the random close packing limit of ≈ 0.63 , we had to define a methodology for packing none overlapping spheres in cubic domains. To do this we used a simplified DEM model with no friction or rotation. Particles are initially placed at random, the system is then allowed to relax to a non overlapping state by using a simple spring contact model. The input and result of this process is seen in figure 1.

The model is bounded by two Z-normal planar surfaces. The bottom surface is kept static, where the top surface is allowed to move. A shear stress is applied to the top surface and the model is executed until the top surface achieves a steady state velocity, as seen in figure 2. Once steady state is achieved we compute the normal and shear forces on the top surface due to particle contact, and the viscous shear stress exerted by the fluid. Knowledge of these stresses subsequently leads to computation of hydrodynamic and particle contact contributions to the friction coefficient.

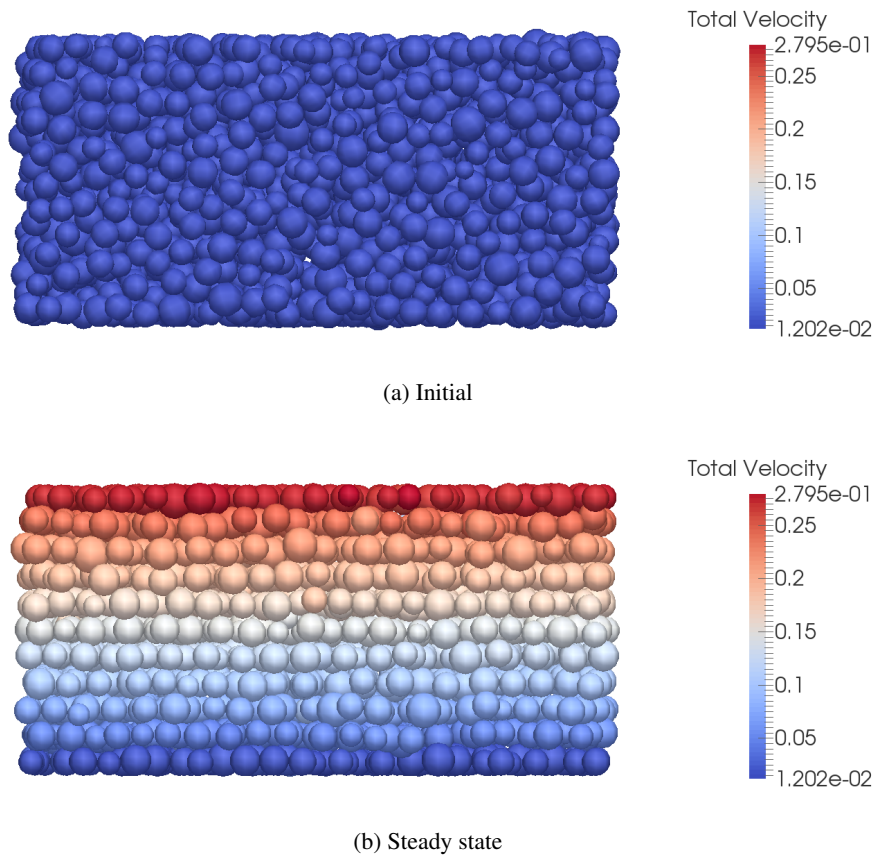


Figure 2: Particle packing configuration of a suspensions with 40% solid volume fraction

3. Results

The simulation was carried out for solid volume fractions in a range $0.05 \leq \phi \leq 0.65$, with a shear stress of $\tau = 15 \text{ Nm}^{-2}$ applied to the top surface. Particle were on average $100\mu\text{m}$ in diameter, with a standard deviation of $10\mu\text{m}$. The width between rheometer surfaces was $1000\mu\text{m}$, this width was chosen to be well above the limit at which surface contact effects dominated the rheology. Hydrodynamic and contact contributions to the friction coefficient were computed, and a comparison with [3] and [4] is shown in figure 3.

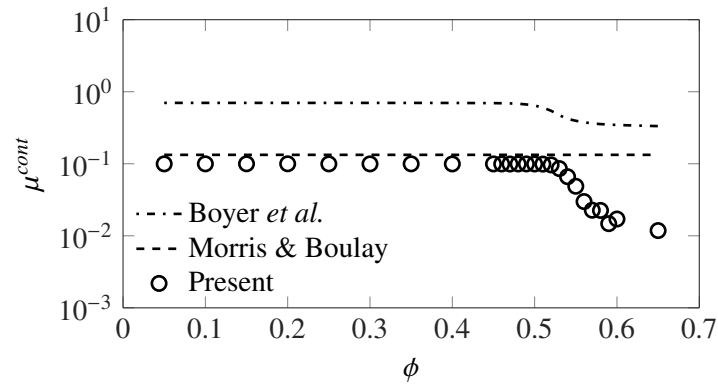
It is seen in the figure that whilst there is good general agreement on μ^{hydro} between the expressions of [3] and [4], they differ significantly on μ^{cont} . This is attributed to the geometry of the rheometer surfaces used in the experimental calibration of their expressions. In [3] the surfaces were smooth, where in [4] the rheometer surfaces were rough, with steel bars of equivalent size and spacing to the particle diameters.

Comparing with the simulation, the computed hydrodynamic contribution is in good agreement with [3] and [4] up to a solid volume fraction of $\phi = 0.53$. With respect to the contact contribution, quantitative agreement is closes with [3], however qualitatively the model is closer to [4].

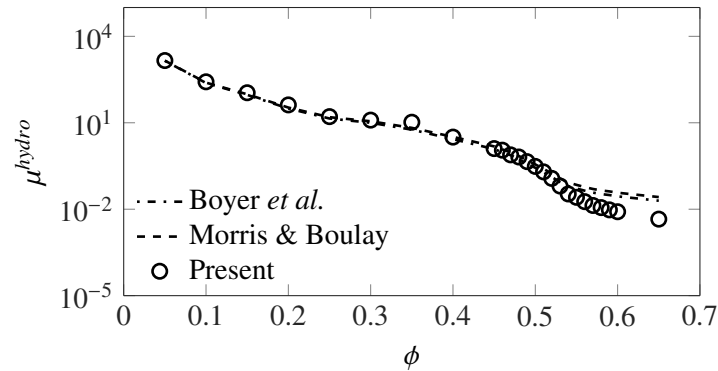
Since [4] set out to improve the form of [3], it makes sense that the shape of the curve of particle contribution is in agreement with [4]. The discrepancy in magnitude is likely explained by the difference in rheometer surface geometry, where the model rheometer surfaces were smooth as in [3].

4. Conclusion

We have applied a coupled LBM-DEM model to rheometry of particle suspensions. Using this model it is possible to accurately determine the contribution of mechanical and hydrodynamic factors to the overall rheology of particle suspensions, which is not possible experimentally. The results of this investigation have been compared with semi-empirical expressions for hydrodynamic and particle contact contributions to a frictional rheology, where favourable agreement is observed.



(a) Contact Contribution



(b) Hydrodynamic Contribution

Figure 3: Hydrodynamic and contact contributions to friction coefficient with an applied shear stress of $\tau = 15 \text{ Nm}^{-2}$

References

- [1] J. Adachi, E. Siebrits, A. Peirce, and J. Desroches. Computer simulation of hydraulic fractures. *International Journal of Rock Mechanics and Mining Sciences*, 44(5):739–757, July 2007.
- [2] C.R. Leonardi, D.R.J. Owen, and Y.T. Feng. Numerical rheometry of bulk materials using a power law fluid and the lattice Boltzmann method. *Journal of Non-Newtonian Fluid Mechanics*, 166(12-13):628–638, July 2011.
- [3] J. F. Morris and F. Boulay. Curvilinear flows of noncolloidal suspensions: The role of normal stresses. *Journal of Rheology*, 43(5):1213, 1999.
- [4] F. Boyer, E. Guazzelli, and O. Pouliquen. Unifying Suspension and Granular Rheology. *Physical Review Letters*, 107(18):188301, October 2011.
- [5] D. R. Noble and J. R. Torczynski. A Lattice-Boltzmann Method for Partially Saturated Computational Cells. *International Journal of Modern Physics C*, 09(08):1189–1201, December 1998.

A COMPUTATIONAL FRAMEWORK FOR LINEARISED ELASTICITY COUPLED WITH NON-LINEAR ELECTRO-MAGNETO-STATICS

*Roman Poya, Antonio J. Gil and Javier Bonet

Zienkiewicz Centre for Computational Engineering, College of Engineering, Swansea University,
Singleton Park, SA2 8PP, United Kingdom

{*r.poya; a.j.gil; j.bonet; p.d.ledger}@swansea.ac.uk

ABSTRACT

This paper presents a new computational framework for coupled electromechanical systems which is linear in strain and non-linear in electric field. Starting from a postulated stored energy functional defined in terms of the right Cauchy-Green tensor \mathbf{C} and the Lagrangian electric displacement vector \mathbf{D}_0 , an internal energy is introduced by performing a Taylor series expansion of up to second order around a small variation of \mathbf{C} evaluated at the origin, which is then readily particularised for the case of small strains. By performing consistent linearisation of the latter energy, aside from recovering the constitutive equations of linear elasticity, the electrostatic terms also naturally arise in the definition of stress tensor. This is in contrast with other available models in which a Maxwell-like stress is added as an *add-on* to the Cauchy stress tensor, which are energetically inconsistent. We present a *hp*-finite element implementation of the proposed model at a continuum level as well as at a beam level. For linear problems, we also show the exponential *hp*-convergence of the numerical scheme using available or derived closed-form solutions. Numerical examples showing the performance of the scheme under various loading scenarios are presented.

Key Words: *Coupled electromechanics; linearised elasticity; non-linear electrostatics*

1. Introduction

In recent years, piezoceramics, piezomagnets, electro-active polymers and materials of similar nature inhibiting more than one physics, have been numerically modelled and investigated using various continuum theories and axioms [1, 2, 3]. Traditionally, when coupling mechanics with electrostatics, strains and electric fields are assumed to be either both linear [4, 5, 6] or non-linear [1, 3]. Similar coupling techniques have been utilised in magneto-mechanics.

A different class of coupling in electromechanics which has recently attained considerable research focus due to its practical applicabilities is the equations of linear elasticity coupled to those of electrostatics through the addition of a *symmetrised Maxwell-like* stress tensor to the Cauchy stress tensor [7, 8]. Theoretical aspects of these formulations were first introduced in Landau and Lifshitz [9]. There have been numerous studies on the objectivity of such stresses and the fact that in situations they can even lead to a non-realistic physical response, see for instance [7]. Starting from an energy principle, it becomes evident that for a conservative system under isothermal conditions, the addition of these stresses essentially imposes restrictions on the constitutive and the coupling tensors (e.g. piezoelectric tensor), which are often neglected. Based on the works in [1, 2, 3, 8], it is equivalently possible to introduce energy functionals for an electromechanical system which satisfy objectivity and consistency in the constitutive relations, without the need for an additive decomposition and or symmetrisation of the stress tensor.

Although the formulations developed in [1, 2, 3] are primarily for large strains, particularisation for the case of small strains is also feasible. From a practical point of view, systems with small deformations and non-linear electrostatic behaviour is particularly of interest in the smaller length scales. One such application is in studying the behaviour of flexoelectric materials [10, 11] where the electric forces are

too feeble to trigger large deformations but nevertheless the electrostatic response can be a non-linear function of the electric field [10].

In this work, we present a computational framework for a coupled electromechanical system based on the equations of linear elasticity and non-linear electrostatics. The point of departure is the stored energy of an electro-hyperelastic system defined in terms of the right Cauchy-Green tensor \mathbf{C} and the Lagrangian electric displacement vector \mathbf{D}_0 . For small deformations, it is possible to approximate this energy by performing a Taylor series expansion of it for a small variation of \mathbf{C} in the origin, i.e. around $\mathbf{C} = \mathbf{I}$. This yields the classical equations of linear elasticity coupled with non-linear electrostatics. One can then formulate a variational principle to facilitate numerical implementation.

In the next sections, we present the theoretical framework and the subsequent *hp*-finite element implementation of the proposed model. To benchmark the numerical scheme, for linear problems, we show the exponential *hp*-convergence of error using available closed-form solutions [6] at a continuum as well as at a beam level.

2. Theoretical Framework

Consider a body possessing the volume Ω in the \mathbb{R}^3 Euclidean space. The equations governing the quasi-static behaviour of the coupled electromechanical system at small deformations are given by

$$\begin{array}{ll} \boldsymbol{\varepsilon} = \nabla^{\text{sym}} \mathbf{u} & \text{in } \Omega, \\ \nabla \cdot \boldsymbol{\sigma} + \mathbf{b} = \mathbf{0} & \text{in } \Omega, \\ \mathbf{u} = \bar{\mathbf{u}} & \text{on } \partial\Omega_{Dm}, \\ \underbrace{\boldsymbol{\sigma} \cdot \mathbf{n} = \mathbf{t}}_{\text{mechanics}} & \text{on } \partial\Omega_{Nm}, \end{array} \quad \begin{array}{ll} \mathbf{E} = \nabla\varphi & \text{in } \Omega, \\ \nabla \cdot \mathbf{D} - \rho = 0 & \text{in } \Omega, \\ \varphi = \bar{\varphi} & \text{on } \partial\Omega_{De}, \\ \underbrace{\mathbf{D} \cdot \mathbf{n} = -\omega}_{\text{electrostatics}} & \text{on } \partial\Omega_{Ne}. \end{array}$$

where ∇ and $\nabla \cdot$ are the gradient and divergence operators, respectively with ∇^{sym} representing the symmetric part of the gradient. \mathbf{u} is the displacement vector, φ the electric potential, \mathbf{E} the electric field vector and $\boldsymbol{\varepsilon}$ is the infinitesimal strain tensor. The *total* stress tensor is denoted by $\boldsymbol{\sigma}$ and the electric displacement vector is \mathbf{D} . Notice that in small deformation no distinction is made between material and spatial settings. To obtain the constitutive equations for the linearised electroelastic problem, we postulate an internal energy for the electro-hyperelastic system in the following form

$$W(\mathbf{C}, \mathbf{D}_0) = \frac{\mu}{2} I_C - \mu C^{1/2} + \frac{\kappa}{2} (C^{1/2} - 1)^2 + \frac{C^{-1/2}}{2\varepsilon_1} \mathbf{D}_0 \cdot \mathbf{C} \mathbf{D}_0, \quad (1)$$

where μ and κ are the Lamé parameters and ε_1 is permittivity of the material. The right Cauchy-Green tensor itself is defined as $\mathbf{C} = \mathbf{F}^T \mathbf{F}$, where $\mathbf{F} = \partial\boldsymbol{\phi}/\partial\mathbf{X}$ is the deformation gradient tensor with $\boldsymbol{\phi}$ representing the motion map between reference and current configurations, in large deformation setting. The third invariant of \mathbf{C} is denoted by $C = \det \mathbf{C} = III_C$. The mathematical requirements of the energy functional defined in (1) such as polyconvexity and objectivity are discussed in detail in [1, 2]. In (1), notice that in the absence of electrostatic forces the Neo-Hookean model is recovered. In the case of small displacements, equation (1) can be approximated via a Taylor series expansion of up to second order around small variation of \mathbf{C} as

$$W(\mathbf{C} + DC[\mathbf{u}], \mathbf{D}_0) \approx W(\mathbf{C}, \mathbf{D}_0) \Big|_{\mathbf{C}=\mathbf{I}} + \left(2 \frac{\partial W}{\partial \mathbf{C}} \right) \Big|_{\mathbf{C}=\mathbf{I}} : \left(\frac{1}{2} DC[\mathbf{u}] \right) + \frac{1}{2} \left[\left(\frac{1}{2} DC[\mathbf{u}] \right) : 4 \frac{\partial^2 W}{\partial \mathbf{C} \partial \mathbf{C}} \Big|_{\mathbf{C}=\mathbf{I}} : \left(\frac{1}{2} DC[\mathbf{u}] \right) \right] \quad (2)$$

After evaluating the gradient and the hessian terms and noting that for small strains the deformation gradient tensor \mathbf{F} is the identity tensor, such that we have $J = \det \mathbf{F} = 1$ and

$$DC[\mathbf{u}] \Big|_{\mathbf{F}=\mathbf{I}} = 2\mathbf{F}^T \boldsymbol{\varepsilon} \mathbf{F} \Big|_{\mathbf{F}=\mathbf{I}} = 2\boldsymbol{\varepsilon}, \quad \mathbf{D}_0 \Big|_{\mathbf{F}=\mathbf{I}} = J\mathbf{F}^{-1} \mathbf{D} \Big|_{\mathbf{F}=\mathbf{I}} = \mathbf{D}.$$

After some algebra we obtain the linearised internal energy W_{lin} as

$$W_{lin}(\boldsymbol{\varepsilon}, \mathbf{D}) = \mu \text{tr} \boldsymbol{\varepsilon} \boldsymbol{\varepsilon} + \frac{\kappa}{2} (\text{tr} \boldsymbol{\varepsilon})^2 + \frac{1}{2\varepsilon_1} (\mathbf{D} \cdot \mathbf{D}) + \frac{1}{\varepsilon_1} \left[\mathbf{D} \cdot \boldsymbol{\varepsilon} \mathbf{D} - \frac{1}{2} (\mathbf{D} \cdot \mathbf{D}) \text{tr} \boldsymbol{\varepsilon} \right] (1 - \text{tr} \boldsymbol{\varepsilon}). \quad (3)$$

We can observe that the the first two terms in the linearised internal energy (3) correspond to the classical constitutive equation of linear elasticity with (3) being a non-linear function of electric displacement. From a numerical implementation point of view, it is more convenient to work with the enthalpy of the system $H = H(\boldsymbol{\varepsilon}, \mathbf{E})$, which for the present model becomes

$$\begin{aligned} H(\boldsymbol{\varepsilon}, \mathbf{E}) &= W_{lin}(\boldsymbol{\varepsilon}, \mathbf{D}(\boldsymbol{\varepsilon}, \mathbf{E})) - \mathbf{E} \cdot \mathbf{D}(\boldsymbol{\varepsilon}, \mathbf{E}) \\ &= \text{tr} \boldsymbol{\varepsilon} \boldsymbol{\varepsilon} + \frac{\kappa}{2} (\text{tr} \boldsymbol{\varepsilon})^2 + \frac{\varepsilon_1}{2} (\mathbf{A}^{-1} \mathbf{E} \cdot \mathbf{A}^{-1} \mathbf{E}) + \varepsilon_1 \left[(\mathbf{A}^{-1} \mathbf{E}) \cdot \boldsymbol{\varepsilon} (\mathbf{A}^{-1} \mathbf{E}) - \frac{1}{2} (\mathbf{A}^{-1} \mathbf{E} \cdot \mathbf{A}^{-1} \mathbf{E}) \text{tr} \boldsymbol{\varepsilon} \right] (1 - \text{tr} \boldsymbol{\varepsilon}), \end{aligned} \quad (4)$$

where

$$\mathbf{A} = \left(1 - \text{tr}\boldsymbol{\varepsilon} + (\text{tr}\boldsymbol{\varepsilon})^2\right)\mathbf{I} + 2(1 - \text{tr}\boldsymbol{\varepsilon})\boldsymbol{\varepsilon}.$$

Finally the constitutive equations of the proposed model can be obtained as

$$\begin{aligned} \boldsymbol{\sigma} &= \frac{\partial H}{\partial \boldsymbol{\varepsilon}}, & \mathbf{D} &= -\frac{\partial H}{\partial \mathbf{E}}, \\ \mathbb{C} &= \frac{\partial^2 H}{\partial \boldsymbol{\varepsilon} \partial \boldsymbol{\varepsilon}}, & \mathbf{e} &= \frac{\partial^2 H}{\partial \boldsymbol{\varepsilon} \partial \mathbf{E}}, & \boldsymbol{\epsilon} &= \frac{\partial^2 H}{\partial \mathbf{E} \partial \mathbf{E}}, \end{aligned}$$

where \mathbb{C} , \mathbf{e} and $\boldsymbol{\epsilon}$ are the fourth order elasticity tensor, the third order coupling (piezoelectric tensor) and the second order dielectric tensor, respectively. The variational form of the linearised electroelastic problem can now be written as

$$D\delta H(\delta\tilde{\mathbf{u}})[\Delta\tilde{\mathbf{v}}] = \int_{\Omega} \delta\tilde{\mathbf{u}} \cdot \mathbb{H} \Delta\tilde{\mathbf{v}} \, dV - \int_{\Omega} \tilde{\mathbf{b}} \cdot \Delta\tilde{\mathbf{v}} \, dV - \int_{\partial\Omega} \tilde{\mathbf{t}} \cdot \Delta\tilde{\mathbf{v}} \, dA = \mathbf{0}, \quad (5)$$

with

$$\delta\tilde{\mathbf{u}} = \begin{bmatrix} \delta\mathbf{u} \\ \delta\varphi \end{bmatrix}, \quad \Delta\tilde{\mathbf{v}} = \begin{bmatrix} \Delta\mathbf{v} \\ \Delta\psi \end{bmatrix}, \quad \tilde{\mathbf{b}} = \begin{bmatrix} \mathbf{b} \\ \rho \end{bmatrix}, \quad \tilde{\mathbf{t}} = \begin{bmatrix} \mathbf{t} \\ -\omega \end{bmatrix}, \quad \text{and} \quad \mathbb{H} = \begin{bmatrix} \mathbb{C} & \mathbf{e} \\ \mathbf{e}^T & \boldsymbol{\epsilon} \end{bmatrix}.$$

Equation (5) is discretised using a hp interpolation space for both displacements and electric potential; see [6, 4] for details.

3. Numerical Examples

To benchmark the numerical scheme developed for the coupled electromechanical system and specifically to show the hp -convergence of the error, here we report two benchmark problems for a linear piezoelectric model one at a continuum level and the other at the beam level [6]; the first one a hollow circle with Dirichlet boundary conditions applied at inner and outer radii $u_r(r_i = 1\text{mm}) = 0$, $\phi(r_i = 1\text{mm}) = 50\text{V}$ and $u_r(r_o = 2\text{mm}) = 0.1\text{mm}$, $\phi(r_o = 2\text{mm}) = 100\text{V}$.

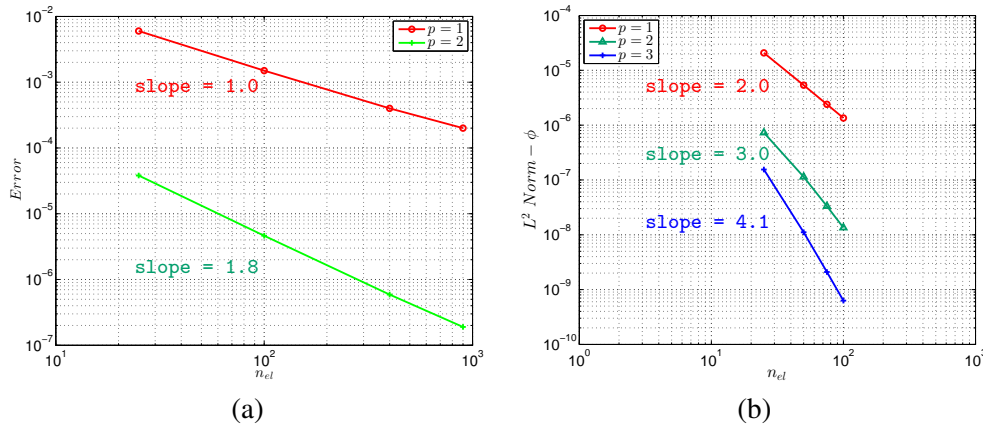


Figure 1: a) h -convergence of energy norm for hollow circle, b) h -convergence of L^2 norm of electric potential for cantilever beam

The second example is a planar cantilever beam, of height 1mm and length 10mm , under the action of a unit tip load $\bar{Q}^m = 1\text{N}$. In both the examples the material used is PZT-5H; see [6] for material properties. The h convergence of the error for both problems is shown in Figure 1. The convergence of the error is in good agreement with the theoretical predictions. Note that for the case of hollow circle a set of blending interpolation functions have been used to represent the circular geometry exactly. Having benchmarked the numerical scheme, we present an example of non-linear problem (in strains and electric field) based on (1). We consider a cube of $(2 \times 2 \times 2)\text{mm}^3$, with all the degrees of freedom are fixed at the base ($z = 0$) and a traction force $P_z = 25\text{kN/mm}^2$ and an electric displacement of $(\mathbf{D} \cdot \mathbf{n} = 1\text{e} - 06\text{C/mm}^2)$ is applied at the upper surface ($z = 2$). The material properties are kept the same. The displacement and electric potential distribution are shown in Figure 2.

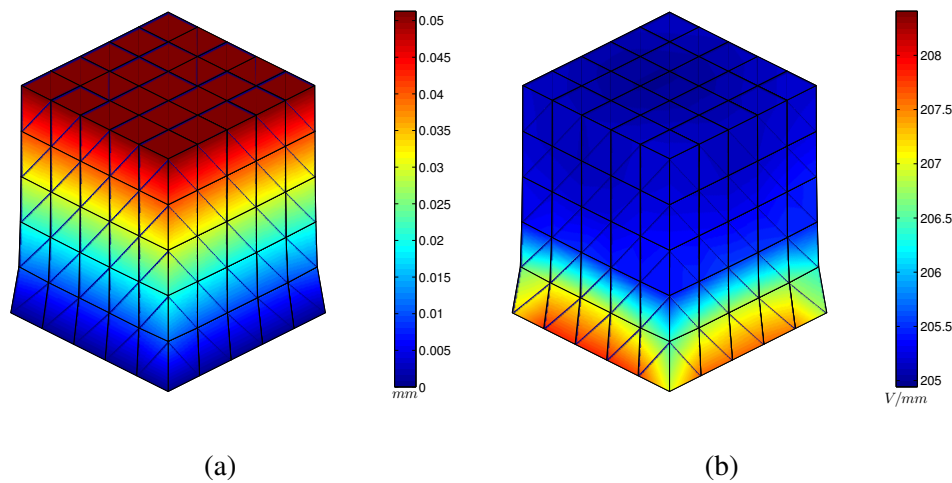


Figure 2: a) Displacement u_z , b) Electric field E_z

4. Conclusions

In this paper a computational framework for coupled electromechanics based on linear mechanics and non-linear electrostatics is proposed. The model is derived through a Taylor series approximation of an underlying electro-hyperelastic model which is well-defined in the literature. The theoretical framework is laid out from the governing equations to the constitutive relations of the proposed model in a procedural manner. We have reported the hp -convergence of the scheme for two problems in a small deformation regime, where theoretically predicted convergence rate is achieved.

Acknowledgements

The second author acknowledges the financial support received through “The Leverhulme Prize” awarded by “The Leverhulme Trust”, United Kingdom.

References

- [1] A. L. Dorfmann, R. W. Ogden, [Nonlinear Theory of Electroelastic and Magnetoelastic Interactions](#), Springer, Dordrecht, Heidelberg, London, New York, 2014.
- [2] D. K. Vu, P. Steinmann, [Nonlinear electro- and magneto-elastostatics: Material and spatial settings](#), International Journal of Solids and Structures 44 (2007) 7891–7905.
- [3] A. J. Gil, R. Ortigosa, J. Bonet, A computational framework for polyconvex large strain electromechanics, In preparation for submission.
- [4] A. J. Gil, P. D. Ledger, [A coupled \$hp\$ -finite element scheme for the solution of two-dimensional electrostrictive materials](#), International Journal for Numerical Methods in Engineering 91 (11) (2012) 1158–1183.
- [5] D. Jin, P. D. Ledger, A. J. Gil, [An \$hp\$ -fem framework for the simulation of electrostrictive and magnetostrictive materials](#), Computers and Structures 133 (2014) 131–148.
- [6] R. Poya, A. J. Gil, P. D. Ledger, [A computational framework for the analysis of linear piezoelectric beams using \$hp\$ -FEM](#), Computers and Structures, Accepted.
- [7] C. Rinaldi, H. Brenner, [Body versus surface forces in continuum mechanics: is the Maxwell stress tensor a physically objective Cauchy stress?](#), Physical Review E 65 (2002) 036615.
- [8] R. M. McMeeking, C. M. Landis, [Electrostatic forces and stored energy for deformable dielectric materials](#), Journal of Applied Mechanics 72 (2005) 581–590.
- [9] L. D. Landau, E. M. Lifshitz, [Electrodynamics of Continuous Media](#), Pergamon, Oxford, 1960.
- [10] P. V. Yudin, A. K. Tagantsev, [Fundamentals of flexoelectricity in solids](#), Nanotechnology 24 (2013) 432001.
- [11] J. Chen, [Micropolar theory of flexoelectricity](#), Journal of Advanced Mathematics and Applications 1 (2012) 269–274.

FLUID DYNAMICS 1

Comparison and Validation of Gas Flow Models in a Powder Bed Selective Laser Melting Process

Adam Philo¹, *N.P. Lavery¹, S.G.R. Brown¹, J. Cherry¹, J. Sienz¹, J. Joannou², C. J. Sutcliffe²

¹College of Engineering, Swansea University, Singleton Park, Swansea, SA2 8PP

²Renishaw Plc, Additive Manufacturing Products Division, Whitebridge Park, Stone, Staffordshire ST15 8LQ

*Corresponding author: N.P.Lavery@Swansea.ac.uk

ABSTRACT

Previous work has demonstrated that the flow of argon gas within a powder bed system can have a significant impact on the porosity and the strength of as-built parts, [1]. Argon is used as the inert environment of choice within powder bed systems, often in conjunction with prior chamber evacuation, to impede the formation of oxides which would hinder the melting of the powder metal and result in poor properties, to suppress vapourisation of the alloy, and transport condensate away from the laser path minimising scattering of the available beam power [1-3].

There is a difficult balance to be reached between a uniform velocity distribution across the build platform which is relatively tranquil to minimise disruption of the metal powder and with sufficient flow rate to remove the condensate effectively. Previous Computational Fluid Dynamics (CFD) using ANSYS FLUENT, [1] has been used as a manufacturing design guide iteration resulting in improved flow uniformity and better parts.

In the current work, CFD models are developed in FLUENT, and validated against hot-wire anemometry test data taken from a real-scale physical model of a powder-bed build chamber. The emphasis of the work described in this paper is in comparing turbulence models valid at a relatively low Reynolds number/transitional regime and in distinguishing between numerical- and physically- based flow differences. Current results demonstrate that the particular methodology adopted is a quick, efficient and powerful tool which can be utilised for the design of a new gas flow system instead of undertaking extensive and time consuming simulations or experimentations.

The outcome of the work will enable models which can be used both qualitatively and quantitatively in the design of new gas flow systems. The models will help gain a better understanding of interfacial heat transfer between the gas and the heated metal powder, which will then be incorporated into melt-pool and residual stress models.

Keywords: Powder Bed; Selective Laser Melting; Gas Flow Modelling;

1. Introduction

Additive Layer Manufacturing (ALM) is a rapidly developing manufacturing process with its origins in rapid prototyping, which has been attracting interest from end-users in the aerospace, automotive and medical sectors. More specifically powder-bed Selective Laser Melting (SLM) provides a useful tool to produce superior fully dense metal parts, across a range of materials. Modelling is being used extensively across a range of physics to understand all aspects of powder bed SLM, from the melt-pool, through to powder deposition, through to predicting material properties [1-3]. To a lesser extent, CFD has been used to look at locally improving the gas flow of argon, which is thought to be important in the final component properties, [1]. A uniform flow is required across the base plate to ensure removal of condensate material and particulates formed at the level of the melt pool. These particulates are transported with the gas through the outlet, and then collected in a filtration system, and then the gas is re-circulated.

CFD is now being used extensively as part of the design cycle primarily as a guide in design configurations. This work aims to be a benchmark for future computational results, providing a higher level of confidence on more quantitative applications of the computational results.

2. Experimental Methodology

In an SLM process, metal powder is delivered from a hopper at the rear of the machine into the build chamber in front of a wiper which then rolls across the powder bed build plate depositing a layer of about 50 microns of powder. A 200W Ytterbium fibre laser is focussed to a 70 micron spot size through a theta lens onto the layer of powder to melt the sectioned component on a layer by layer basis. After drawing a vacuum, oxygen levels below 50ppm can be achieved. High purity argon is then delivered through an inlet manifold on the right hand side of the build chamber directly from an argon tank, and subsequently recirculated through the chamber using a pump passing through the outlet and coming back through the inlet at about 20 m³/hr.

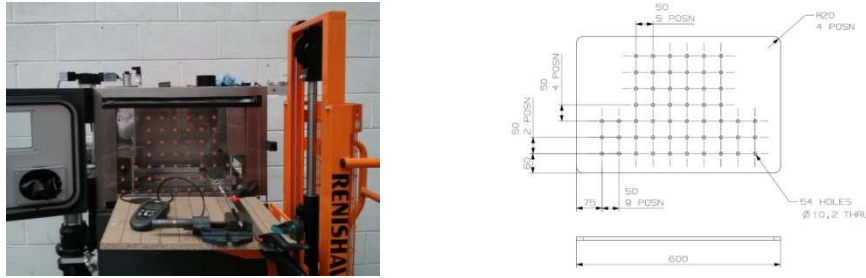


Figure 1: Renishaw Test Rig (left) Hot-wire Anemometer Reading Positions (right)

A gas-flow rig has been set-up by Renishaw to take hot-wire anemometer measurements of the gas velocity as shown in Figure 1. HWA results were taken at the centre plane to the inlet.

3. Computational Methodology and Results

The properties of the Argon gas were taken from default values in the FLUENT database, and are given in Table 1. For a mass-flow of argon of 20 m³/hr, a single jet velocity was estimated to be in the order of 3.7m/s, for which the resulting Reynolds number was calculated at 3462. This would place the flow firmly in a transitional turbulent regime as it enters the build chamber.

Table 1: Properties of argon and derived Reynolds number as used for the computational models

Property	Symbol	Value	Units	Source
Density	ρ	1.6228	kgm^{-3}	[Fluent]
Dynamic viscosity	μ	2.125e-05	$kgm^{-1}s^{-1}$	[Fluent]
Diameter of single jet	D	0.012	m	Measured
Estimated maximum velocity for single jet	V	3.77	ms^{-1}	Calculated
Reynolds number based on single jet	Re	3462	N/A	Calculated

Several viscous flow models have been simulated namely laminar and Reynolds Average Navier Stokes (RANS) turbulence models, namely the Spalart-Allmaras, k-omega and k-epsilon. Preliminary models were tested with different mesh configurations – combined tetragonal/structured hexagonal meshes were used where possible in the domain, as well as completely unstructured tetrahedral meshes. In domains discretised using combined elements, residual convergence difficulties were encountered, particularly the convergence of the continuity equation stagnated at 10E-02 even after a large number of iterations. Possible causes include discontinuities at the interface between element types, and/or large differences in scales between the sudden expansions of small jets into the relatively large cavity of the build chamber.

To solve this problem, a completely tetragonal mesh was used as shown in Figure 2 (a) with smoothly varying element size distribution. This discretisation was combined with a modification to the standard non-linear iterative approach SIMPLE (Semi-Implicit Method for Pressure Linked Equations) in which the momentum under-relaxation parameter was ramped down from 0.9 to 0.1, whilst maintaining the sum of the pressure and momentum parameters equal to 1. This forced the convergence of the continuity residual to below $1E-03$ and the other of residuals to below $5E-04$, as shown in Figure 2 (b), all within a relatively small number of iterations. The resulting effect on the convergence of velocities at specific points is shown in Figure 2 (c).

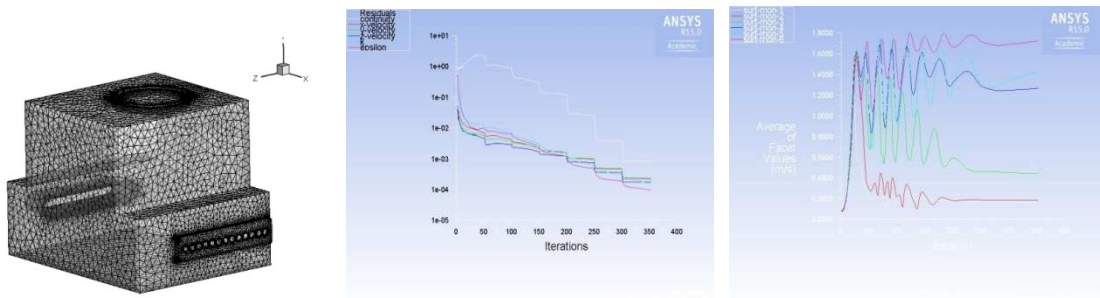


Figure 2: Tetrahedral Mesh (a) Plot of Residuals (b) Surface Monitor Plots (c)

Comparing Figure 4 (c) and (d), the realizable $\kappa - \epsilon$ model was found to most closely resemble the experimental data.

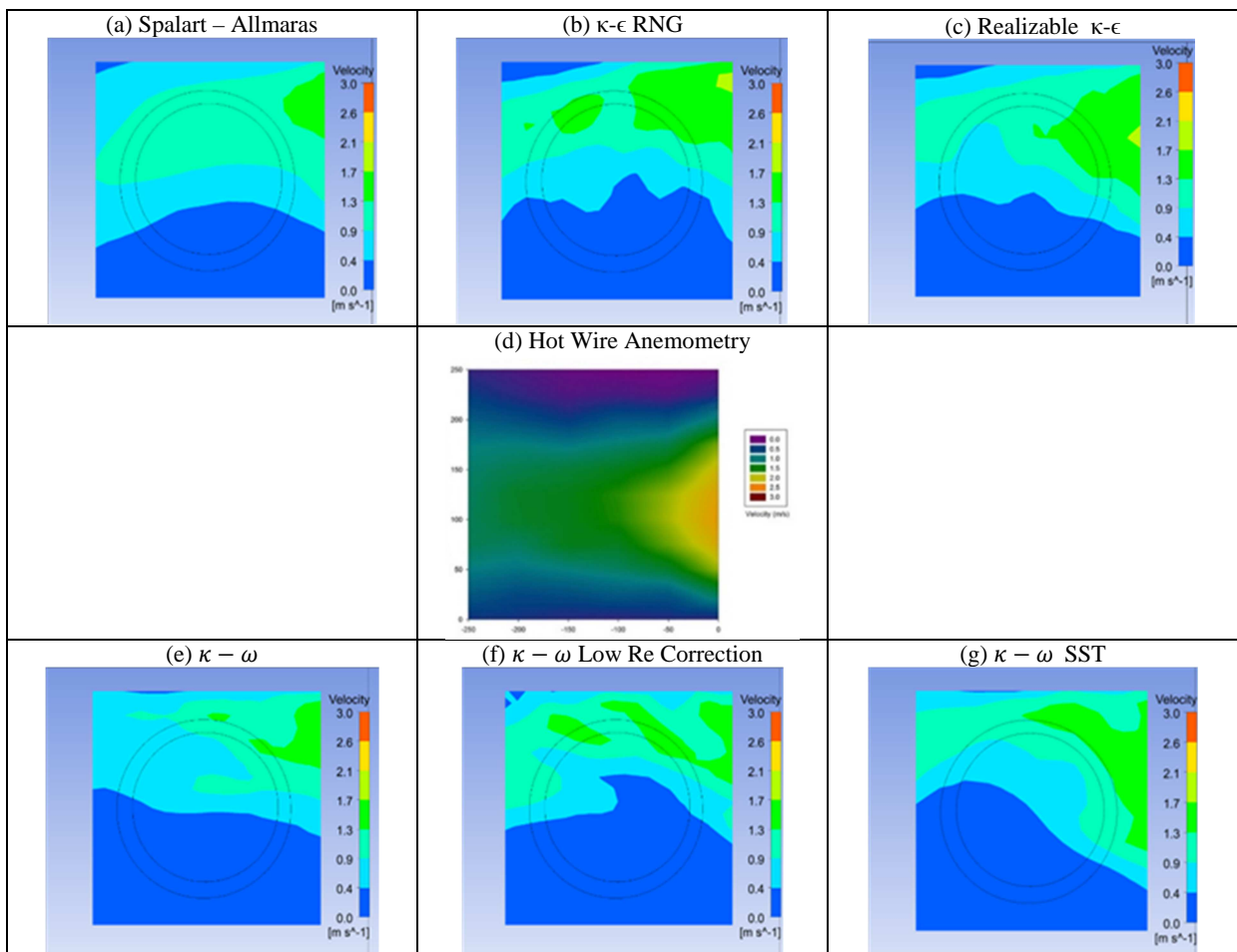


Figure 4: Comparison of Turbulence Models against HWA Experimental Results

The sensitivity of the method to both mesh size and increasing iterations between under-relaxation increments is shown in Figure 5, showing that finer mesh results tend more towards the HWA results.

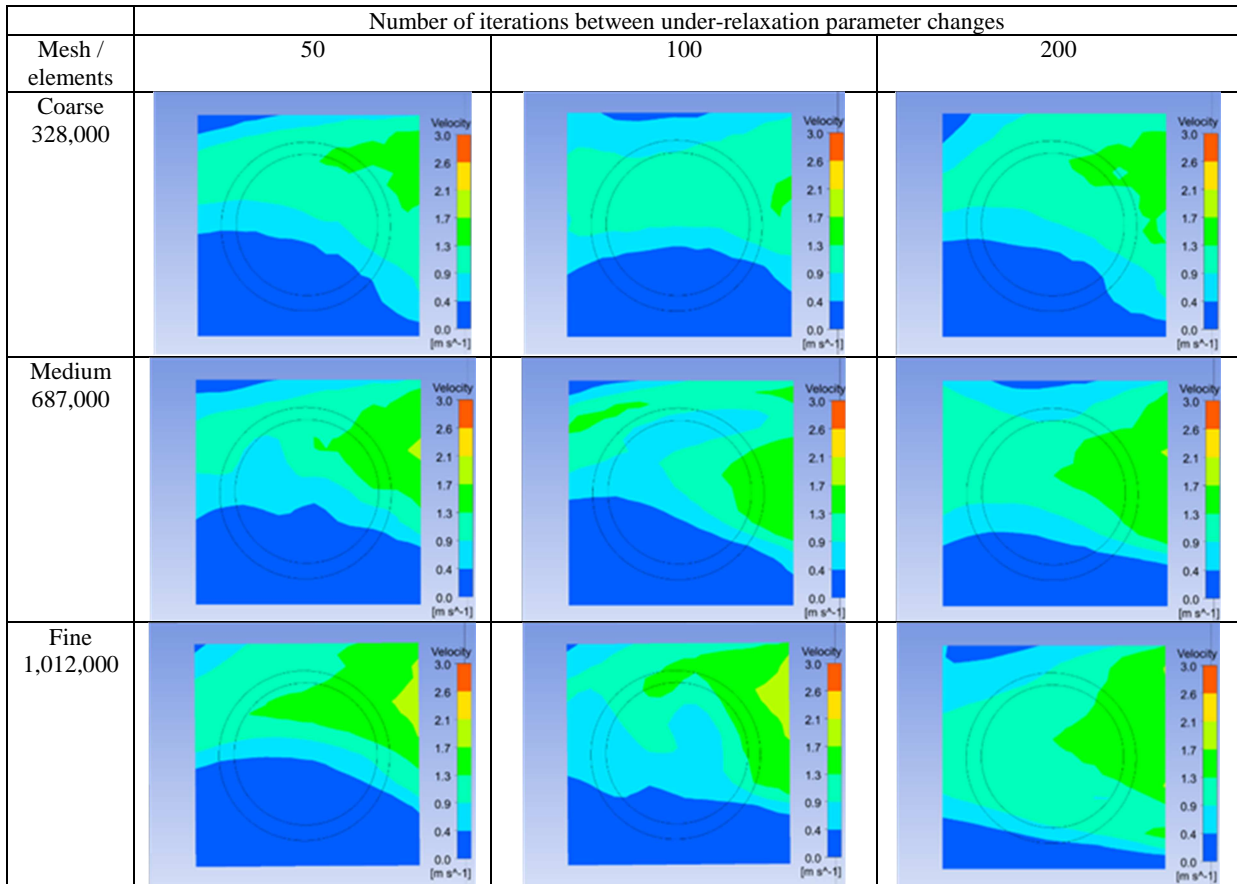


Figure 5: Velocity Comparison of Various Staggered Approached Methods

4. Conclusions

While the staggered relaxation parameter approach may be considered unconventional, the bulk characteristics of the flow are clearly captured with a computationally low-cost mesh, so solution methodology and turbulence models can be used with more confidence in future design modifications with similar flow configurations. However, work in the short term will focus on more detailed comparisons of velocity profiles to establish a more quantitative comparison.

Acknowledgements

The authors would like to acknowledge the contribution of the Advanced Sustainable Manufacturing Technologies (ASTUTE) project, part-funded by the European Regional Development Fund, as well as the MACH1 centre for Advanced Materials Characterisation funded by Welsh Government's A4B scheme. Finally, the authors would like to thank Renishaw, specifically Dr Chris Sutcliffe, Jason Joannou and Ben Robinson for ongoing discussions on the laser powder-bed process.

References

- [1] B. Ferrar, L. Mullena, E. Jones, R. Stamp and C.J. Sutcliffe, Gas flow effects on selective laser melting (SLM) manufacturing performance. *Journal of Materials Processing Technology* 212, 355–364, 2012.
- [2] C. Hauser, T.H.C. Childs, K.W. Dalgarno, R.B. Eane, Atmospheric Control during Direct Selective Laser Sintering of Stainless Steel 314S powder, *In proceedings of the 10th Solid Freeform Fabrication Symposium (SFFS)*, The University of Texas at Austin, pp.265–272, 1999.
- [3] S. Das, On Some Physical Aspects of Process Control in Direct Selective Laser Sintering of Metals – Part I, *In proceedings of the 12th Solid Freeform Fabrication Symposium (SFFS)*, The University of Texas at Austin, pp.94–101, 2001.

SIMULATION OF THE FLOW OF NON-NEWTONIAN SELF- COMPACTING CONCRETE

Firas F Badry*, Bhushan L Karihaloo and Sivakumar Kulasegaram

School of Engineering, Cardiff University

*BadryFF@Cardiff.ac.uk

ABSTRACT

A wide range of normal strength self-compacting concrete (SCC) mixes ranging in compressive strength from 30 to 80 MPa with a maximum aggregate size of 20 mm were prepared in the laboratory, and for each mix the time taken by the flow to reach the spread diameter of 500 mm (t_{500}) and to stop (t_{stop}) were recorded in the slump cone flow test. The entire test was then numerically simulated from the instant the cone was lifted until the flow stopped, using a three-dimensional smoothed particle hydrodynamics (SPH) computational approach, treating the SCC mix as a non-Newtonian Bingham fluid. Flow characteristics of SCC mixes have been studied by comparing the numerical results with the corresponding experimental observations. The key findings of these investigations are presented in this article.

Keywords: *Self-compacting concrete (SCC); Smooth particle hydrodynamics (SPH); yield stress (τ_y); coarse aggregate distribution; Cone lift Rate (CLR).*

1. Introduction

SCC was first pioneered in Japan where most structures often contain a large percentage of steel reinforcement to withstand earthquakes which presents an issue with the on-site vibratory compaction of regular concrete. With such a large amount of reinforcement it is difficult to ensure that the formwork is correctly filled. SCC was designed for this purpose. Being able to flow into sections with congested reinforcement and not segregate means a much easier cast without the need for any vibration. The flow-ability of SCC is characterized by its fluidity and cohesion, and is often assessed using the slump flow test. This test is inexpensive, and has been advocated as a more useful test for self-compacting concrete. The slump flow test is used to assess the horizontal flow of SCC and self-compacting fibre-reinforced concrete (SCFRC) mainly when there are no obstacles. In the current work, an effort is made to numerically simulate the slump flow test and to use the numerical tests and corresponding experimental observations to estimate the vital parameters that characterise the flow of SCC. Due to its simplicity and robustness, a Lagrangian SPH computational approach is used for numerical simulations of the aforementioned SCC mixes.

2. Numerical implementations

SCC is treated as a non-Newtonian fluid best described by a Bingham-type constitutive model [1]. From a practical computational point of view, it is expedient to approximate the bi-linear Bingham constitutive model with a kink at $\dot{\gamma} = 0$ by a smooth continuous function. In which m is a very large number (e.g. $m = 10^5$) [2].

$$\boldsymbol{\tau} = \eta \dot{\boldsymbol{\gamma}} + \tau_y (1 - e^{-m \dot{\boldsymbol{\gamma}}}) \quad (1)$$

The basic equations solved in the SPH are the incompressible mass and momentum conservation equations, together with the constitutive relation given as,

$$\frac{1}{\rho} \frac{D\rho}{Dt} + \nabla \cdot \mathbf{v} = 0, \quad \frac{D\mathbf{v}}{Dt} = -\frac{1}{\rho} \nabla P + \frac{1}{\rho} \nabla \cdot \boldsymbol{\tau} + \mathbf{g} \quad (2), (3)$$

where ρ , t , \mathbf{v} , P , \mathbf{g} and $\boldsymbol{\tau}$ represent the fluid particle density, time, particle velocity, pressure, gravitational acceleration, and shear stress tensor, respectively. As the flows considered here can be assumed to have constant density, the first term in Equation (2) vanishes.

The solution procedure uses prediction-correction fractional steps with the temporal velocity field is integrated forward in time without enforcing incompressibility in the prediction step. Only the viscous stress and gravity terms are considered in the momentum Equation (3) and an intermediate particle velocity \mathbf{v}_{n+1}^* is obtained as:

$$\mathbf{v}_{n+1}^* = \mathbf{v}_n + \left(\mathbf{g} + \frac{1}{\rho} \nabla \cdot \boldsymbol{\tau} \right) \Delta t \quad (4)$$

Here, \mathbf{v}_n and \mathbf{v}_{n+1}^* are the particle velocity and intermediate particle velocity at time t_n and t_{n+1} respectively. Then the correction step is applied to enforce the incompressibility condition. This step is performed by considering the pressure term in Equation (3),

$$\frac{\mathbf{v}_{n+1} - \mathbf{v}_{n+1}^*}{\Delta t} = - \left(\frac{1}{\rho} \nabla P_{n+1} \right) \quad (5)$$

Rearranging Equation (5) gives,

$$\mathbf{v}_{n+1} = \mathbf{v}_{n+1}^* - \left(\frac{1}{\rho} \nabla P_{n+1} \right) \Delta t \quad (6)$$

where \mathbf{v}_{n+1} is the corrected particle velocity at the time step $n+1$. The pressure P_{n+1} in equation (6) will be obtained by imposing the incompressibility condition in the mass conservation Equation (2). As the particle density remains constant during the flow, the velocity \mathbf{v}_{n+1} is divergence-free. Enforcing the incompressibility condition as Equation (2) yields,

$$\nabla \cdot \mathbf{v}_{n+1} = 0 \quad , \quad \nabla \cdot \left(\frac{1}{\rho} \nabla P_{n+1} \right) = \frac{\nabla \cdot \mathbf{v}_{n+1}^*}{\Delta t} \quad (7), (8)$$

Since the density of particles remains constant in the present simulations, Equation (8) can be rewritten as:

$$\nabla^2 P_{n+1} = \frac{\rho}{\Delta t} \nabla \cdot \mathbf{v}_{n+1}^* \quad (9)$$

where ∇^2 is the Laplacian operator. Once the pressure is obtained from the Poisson Equation (9) the particle velocity is updated by equation (6). And finally, the instantaneous particle position is updated using the corrected velocity:

$$\mathbf{x}_{n+1} = \mathbf{x}_n + \mathbf{v}_{n+1} \Delta t \quad (10)$$

Where \mathbf{x}_{n+1} and \mathbf{x}_n is the particle position at t_{n+1} and t_n respectively.

The above numerical procedure incorporating an efficient technique for locating large coarse aggregate particles [2] of various sizes was implemented to investigate the SCC flows.

3. Simulation results

The simulation of the mixes (30 to 80 MPa) had a number of aims. Firstly, to investigate whether the yield stress τ_y of an SCC mix could be accurately estimated from its measured t_{500} time and spread in a cone flow test knowing its plastic viscosity. The latter was estimated by a micromechanical procedure from the known plastic viscosity of the paste [3]. The yield stress τ_y in the Bingham fluid model is the minimum shear stress that an SCC mix has to overcome to start flowing. Conversely, a flowing SCC mix will stop, when the shear stress due to external forces, e.g. gravity, driving the flow is about to

fall below the yield stress value. This nature of Bingham fluid was exploited to numerically estimate τ_y of the mixes from the t_{500} and t_{stop} measured in the cone flow test. The estimation of τ_y required a trial-and-error approach and the results obtained are listed in Table 1.

Table 1: Numerically estimated yield stress of mixes 1–6.

	Mix 1 30 MPa	Mix 2 40 MPa	Mix 3 50 MPa	Mix 4 60 MPa	Mix 5 70 MPa	Mix 6 80 MPa
Spread (mm); experimental	700	700	715	735	720	730
Spread (mm); numerical	700	704	720	733	720	739
t_{500} (s); experimental	1.0	1.1	1.3	1.6	1.6	2.0
t_{500} (s); numerical	1.0	1.1	1.3	1.6	1.6	2.0
t_{stop} (s); experimental	15.7	16.4	17.2	20.3	17.9	20.4
t_{stop} (s); numerical	15.7	16.4	17.2	20.0	18.0	20.5
Viscosity (Pa s)	6.57	7.31	7.60	9.31	9.36	10.62
τ_y (Pa); estimated	175	175	178	180	180	190

Secondly, to compare the statistical distribution of coarse aggregate particles larger than or equal to 8 mm in the cone spread after it stopped to flow as revealed by the numerical simulation (Figure 1) with the distribution of the aggregate particles of the corresponding sizes in the cut sections (along A-A and B-B) of the cured test cone spread. For this, the large coarse aggregate particles in the size ranges ($8 \leq g < 12$, $12 \leq g < 16$, $16 \leq g < 20$ and $g \geq 20$ mm) of the test SCC mixes were colour coded with non-toxic non-water soluble paints so that the outlines of the aggregate particles could be clearly distinguished in the cut sections of the hardened cone spread and compared with the numerical simulations for two mixes (30 and 50 MPa). It can be noted from Table 2, that the aim of the investigation was successfully attained.

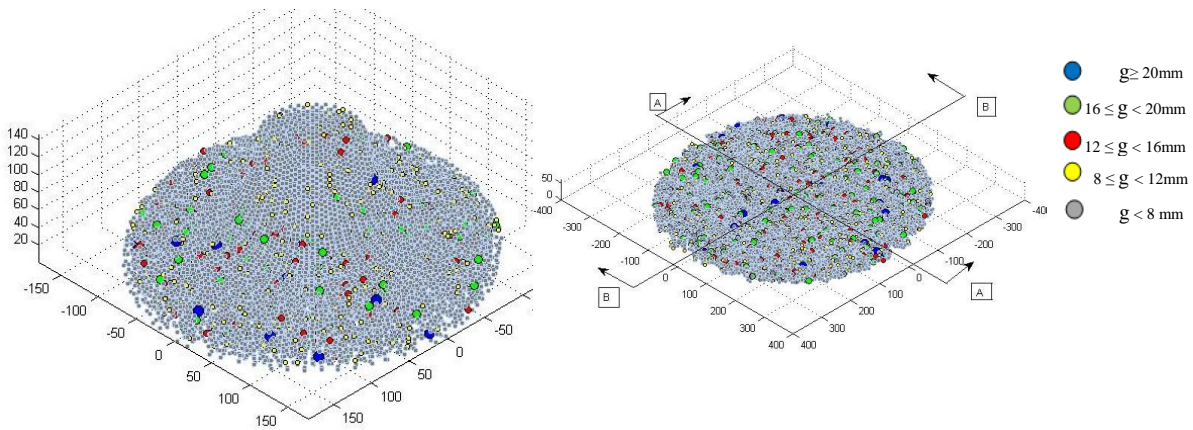


Figure 1: Slump flow pattern of SCC mix 3 after 0.2 s and 15.7 s in 3D configuration

Finally, the third aim of the simulation was to investigate the effect of the cone lift rate on the flow pattern and t_{500} . The results demonstrated that an increase in the cone lift rate from 0.1m/s to 0.5m/s (i.e. cone raised to a height of 300 mm in 3 to 0.6 s) leads to a significant reduction in t_{500} , but the rate of reduction slows considerably when the cone lift rate is increased beyond 0.5 m/s (i.e. cone raised to 300 mm in under 0.6 s) (Figure 3). This bilinear reduction in t_{500} with the increase in the cone lift rate was observed in mixes with cube compressive strength between 30 MPa and 70 MPa. This result has profound implications for the cone flow test procedures outlined in the current European and American testing standards.

Table 2: Average number of coarse aggregates along two perpendicular sections of two mixes

Mix	Size range (mm)	Average Number in experiment	Average number in simulation	Ratio of Average Number in Experiment to average number of 20 mm	Ratio of Average Number in Simulation to average number of 20 mm
	$g \geq 20$	5.0	2.0	1	1
Mix 1	$16 \leq g < 20$	12.5	4.5	2.50	2.25
	$12 \leq g < 16$	12.0	5.0	2.40	2.50
	$8 \leq g < 12$	27.0	12.5	5.40	6.25
	$g \geq 20$	4.0	2.0	1	1
Mix 3	$16 \leq g < 20$	13.0	6.5	3.33	3.25
	$12 \leq g < 16$	12.5	6.5	3.12	3.25
	$8 \leq g < 12$	26.5	14.0	6.62	7.00

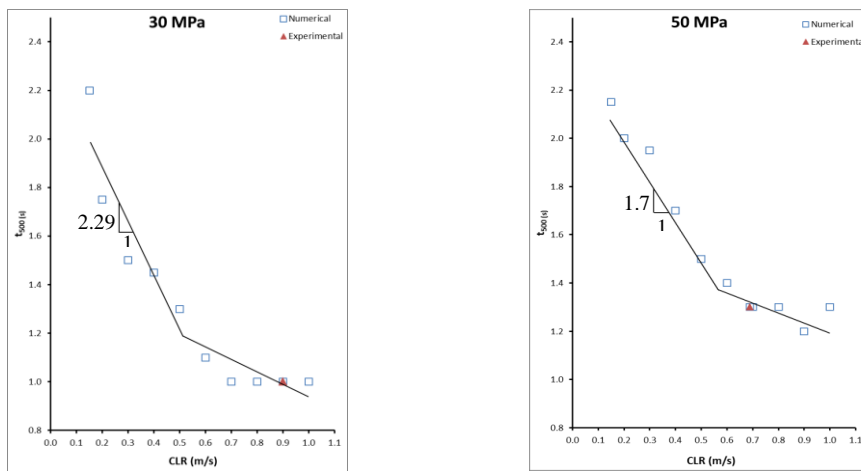


Figure 3: Variation of t_{500} with CLR for mix 1 and 3

4. Conclusions

Three main flow characteristics of SCC have been studied in this paper. Firstly, the yield stress of an SCC mixes has been predicted in an inverse manner using the SPH simulation methodology, and comparing the measured and simulated t_{500} and t_{stop} . The yield stress of SCC mixes varied only slightly with an increase in the characteristic compressive strength of the mix. The plastic viscosity, on the other hand, shows a marked increase. Secondly, the SPH simulations of SCC mixes was used to observe the distribution of large coarse aggregates in the simulated cone spread, this distribution is indeed very similar to that revealed in the cut sections of the hardened test cone spread. Finally, the effect of cone lift rate on the measured t_{500} was investigated. It was noted that t_{500} decreased as the cone lift rate (CLR) was increased from 0.1 to 1 m/s. The corresponding effect on the spread (i.e. t_{stop}) was however insignificant.

References

1. Kulasegaram, S., Karihaloo, B.L., and Ghanbari, A., *Modelling the flow of self-compacting concrete*. International Journal for Numerical and Analytical Methods in Geomechanics, 35(6): p. 713-723, 2011.
2. Deeb, R., Kulasegaram, S., and Karihaloo, B., *3D modelling of the flow of self-compacting concrete with or without steel fibres. Part I: slump flow test*. Computational Particle Mechanics, p. 1-17, 2014.
3. Ghanbari, A. and Karihaloo, B.L., *Prediction of the plastic viscosity of self-compacting steel fibre reinforced concrete*. Cement and Concrete Research, 39(12): p. 1209-1216, 2009.

Investigation of Stratified Flows in Greenland Fjords

*Violeta Moloney, Prof Dominic Reeve and Dr Harshinie Karunarathna

College of Engineering, Swansea University, Singleton Park, Swansea, SA2 8PP, UK

*716469@swansea.ac.uk

ABSTRACT

Greenland is the world's largest island and most of it is covered by ice. It has a large system of fjords where glaciers are terminated and the change in the volume of ice gives the rise to the sea level. For the last twenty years there has been a noticeable increase in the mass loss of the Greenland ice sheet [5]. The glacier/fjord/ocean system is complicated and its relationship is a very sensitive to any changes in regional and global climate system. The subject of discussion and analysis here is the physical processes in Greenland Fjord. Many researchers analysed the wind affect on fjord dynamics by using two-dimensional numerical models [3,4]. In this paper, I would like to investigate the influence of the wind and tidal forces on the fjord circulation as a whole, by using the three-dimensional numerical model. The transport-diffusion equations are the governing equations in the model that represents the tracer evolution in time and space. The CFD Model TELEMAC3D, a three-dimensional physical coastal ocean model, is implemented in order to analyse the effects of varying intrusions of warm saline Atlantic Water into the fjord. Firstly, the matching conditions for temperature and salinity between coastal and fjord domains had to be found before the other forces as wind and tide, independently, were applied. The real wind data for 2011 has been used to analyse both summer and winter case scenarios.

Keywords: stratification; horizontal pressure gradients; Coriolis force; buoyancy force; fjord circulation; double diffusion.

1. INTRODUCTION

Due to the global climate change the South East Greenland glaciers have started to accelerate and retreat, and as a result, the situation has become alarming as there are big volumes of fresh water being added to the fjord domain on a constant basis. Also the frequency of glacier calving events has been increased, and such violent events produce more icebergs which are terminated in waters of the North Atlantic Ocean. It is of great importance to study and analyse the current situation, as we need to understand the scale of impact on global ocean circulation and what changes it may bring to the future climate of the whole planet. The study area is Sermilik fjord that is located in south-east part of Greenland (Fig 1). Sermilik fjord is approximately 100km long, 8km wide and 600-900m deep with steep and mountainous coastline. Its geographical coordinates are: latitude 65°N and longitude 38°W. Compared with other fjords, like Storfjorden (Svalbard), Scoresby Sund (Greenland), Sermilik Fjord does not have a sill [5]. The fact, that Sermilik is a sill free fjord, makes it more vulnerable to any changes in adjacent waters, as it allows for direct exchange between the cold and fresh fjord waters and warm and saline North Atlantic waters at a shelf.

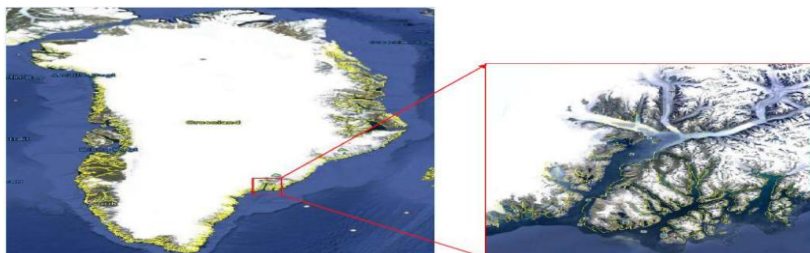


Figure1: Sermilik Fjord, Southeast coast of Greenland. <http://www.google.com/earth>

2. COMPUTATIONAL MODEL

The computational fluid dynamics model TELEMAC3D is an open source software that solves hydrodynamic problems by using the finite element method on unstructured triangular grid. The code solves the three-dimensional hydrodynamic equations with the following assumptions: three-dimensional hydrostatic and non-hydrostatic Navier-Stokes equations, and Boussinesq approximation. The cases have been run in parallel on the Swansea University HPC Cluster supercomputer on 8 processors, a multiple number of nodes, in order to speed up the time of the simulation run. The code is written in Fortran90 and has been run under a Linux operating system. The visualisation and animation program Delft3D-QUICKPLOT, written in Matlab, has been used to analyse the simulation results [6]. The Matlab toolbox, “t_tide”, has been used to perform the tidal harmonic analysis of the simulated flow in the fjord [7].

Firstly, the model has been run by using a simple geometrical shape representing the scale of the real size fjord, to make sure that the model produces the expected results that are in agreement with the work of other researchers [1,3,4], and then by using the real fjord bathymetry. The model domain has dimensions of 120 x 8 x 0.9km. The mesh was constructed on an unstructured triangular grid on horizontal plane, that later was developed vertically into prismatic shape elements. The size of the elements on the horizontal plane is 1km, and on the vertical grid is 25m, with evenly spaced layers, with exception of the bottom layer where the vertical grid is 200m.

The main parameters that characterise the state of the fjord water are temperature and salinity. The governing equation that describes the evolution of these parameters in time and space may be written as:

$$\frac{\partial T}{\partial t} + U \frac{\partial T}{\partial x} + V \frac{\partial T}{\partial y} + W \frac{\partial T}{\partial z} = \frac{\partial}{\partial x} (v_T \frac{\partial T}{\partial x}) + \frac{\partial}{\partial y} (v_T \frac{\partial T}{\partial y}) + \frac{\partial}{\partial z} (v_T \frac{\partial T}{\partial z}) + Q \quad (1)$$

where T is a tracer (Salinity or Temperature), v_T is a tracer diffusion coefficient, t is time and Q is tracer source or sink [2].

As was shown by Cottier [1], the wind plays a very important role in the fjord mixing and establishing the circulation. The wind forcing is represented in TELEMAC3D by the following equation:

$$\nu \frac{\partial \vec{u}_H}{\partial n} = \frac{\rho_{air}}{\rho} a_{wind} \vec{W} \parallel \vec{W} \parallel \quad (2)$$

where $\rho_{air} = 1.29 \text{ kg/m}^3$, \vec{u}_H is the horizontal velocity at a surface, $\nu \frac{\partial \vec{u}_H}{\partial n}$ is stress and \vec{W} is the wind velocity 10m above the water surface with a_{wind} wind coefficient [2].

TELEMAC3D offers various friction laws. These were tested by running the model with a range of friction coefficients lying within ranges and compared with observations. The best result, with the lowest RMSE (= 0.08m) for the tidal model, was achieved using the Nikuradse Friction Law with its bottom and lateral wall coefficients as $K_s = 0.01$. The Nikuradse Friction Law is implemented in TELEMAC3D with the following equation

$$C_d = 2 \left[\frac{K}{\log\left(\frac{12h}{K_s}\right)} \right]^2 \quad (3)$$

where C_d is the friction coefficient, K_s is the Nikuradse bed roughness, K is the *VonKármán* constant (set to 0.41) and h is an average water depth.

One of the main challenges was to create the tracers vertical profile so that conditions matched between domain and an open boundary. Having set the initial water properties, and run for one month in model time, without any other forces applied, except the non-linear processes due to the double

diffusion, the resulting tracers profile was used to prescribe the value of the tracers at the open boundary. This was done, in order to avoid large density differences between domain and open boundary water masses that can cause numerical instabilities. The goal was to reach an equilibrium state between the fjord and adjacent waters as closely as possible.

3. RESULTS

Wind forcing. The effect of the wind forcing on the fjord circulation was investigated. Firstly, using a constant, uniform wind. Secondly, using the measured seasonal winds taken to be uniform over the model domain but time varying. When alongshore winds were applied, the surface elevation shows the *flooding* or *emptying* results at the head of the fjord, as the Ekman transport pushes water into or out of the fjord, depending on whether the wind is westward or eastward. The resulting plot of

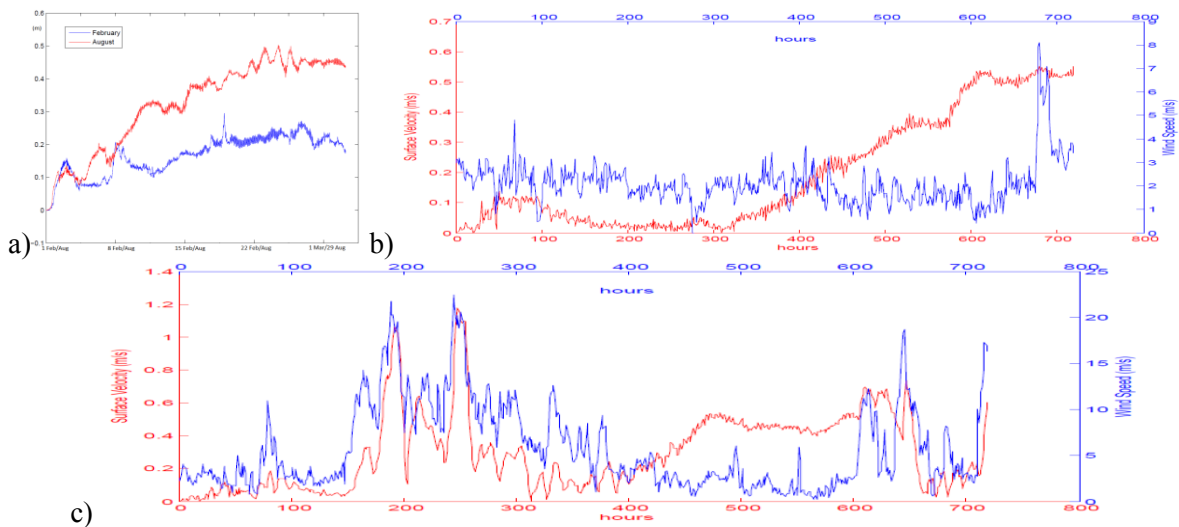


Figure 2: Wind forcing results a) Surface elevation; b) Surface velocity Vs August wind speed; c) Surface velocity Vs February wind speed.

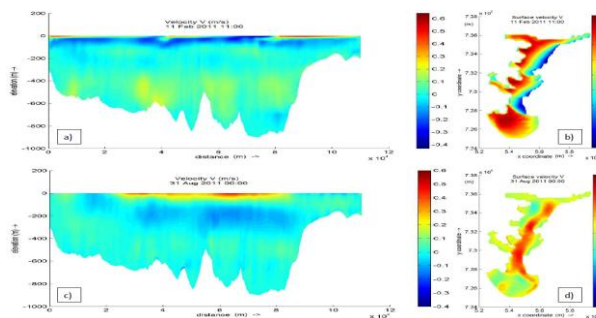


Figure 3: Up-fjord (red) and down-fjord (blue) velocities for February and August at a full length fjord vertical cross section (a and c), and at a surface (b and d).

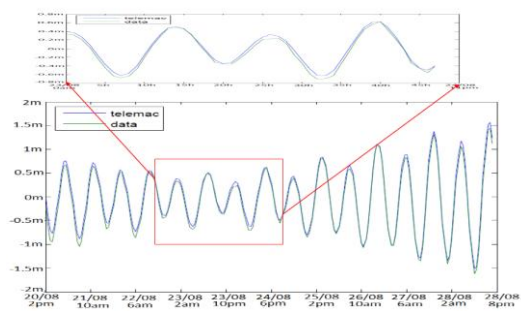


Figure 4: Model tidal amplitude Vs data for period 20/08-28/08/ 2011.

flooding is shown in Figure 2a. In terms of the February winds, the dominant direction was offshore north-easterly winds and that fact does not change the surface elevation dramatically as net water mass transport is directed partially towards the shoreline. These conclusions are in agreement with those presented in [3]. The wind forcing has an almost instant affect on the surface velocities. The correlation between the wind speed and surface velocity is presented in Figures 2 (b and c) for both scenarios. The velocity profiles are shown in Figure 3.

Tidal forcing. The TPXO tidal data were used to specify tidal conditions at the open boundary. This provides the amplitudes and phases of 11 tidal harmonic constituents. Tidal harmonic analysis was

performed with the Matlab toolbox, “t_tide” [7], and the comparison of data with model amplitudes of the fjord five most important constituents is shown in Table 1. It can be noticed that the most significant constituent is M_2 . Also, the validation results of the tidal simulation against measurements, with RMSE = 0.08m, are shown in Figure 4. The model tidal amplitude is in good agreement with data, that is also supported by the small RMSE. The pressure measurements were taken for period 20/08/2011 - 23/08/2013 from a seabird microcat deployed around 14 m, located in the bay to the west of the island in the upper part of the fjord, at geographical point: Lat 66.178, Long -37.864. Also the correlation between the model and predicted tidal amplitudes is shown in Figure 5. The simulation does not include the wind forcing, when it is done so, the better match shall be expected.

Table 1: Amplitude (in metres) from the data, model results and their difference.

	M_2	S_2	N_2	K_1	K_2	O_1
Data Amp	1.07	0.43	0.22	0.16	0.12	0.06
Model Amp	1.08	0.46	0.21	0.13	0.13	0.06
Difference	-0.01	-0.03	0.01	0.03	-0.01	0.00

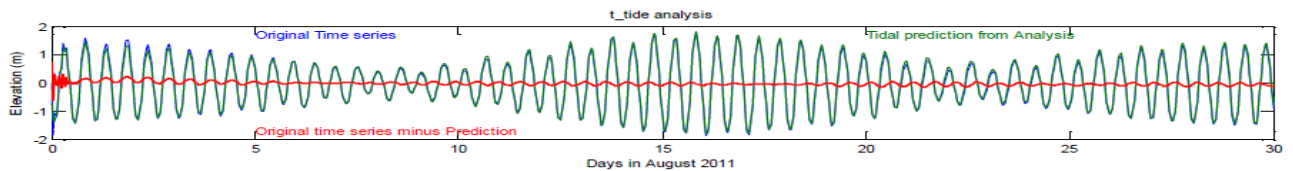


Figure 5: Tidal Amplitudes: Predicted (green) Vs Model (blue).

4. CONCLUSIONS AND FUTURE WORK

Earlier work has shown that the wind forcing is a major driver for the fjord circulation. Our research shows this is the case but that tidal forcing can be as important as wind, as a mixing force, especially in summer time when the wind speeds are much lower. Both of these factors are very important and need to be included in fjord modelling. Further work is underway to recreate a more “realistic scenario”, that includes the under glacier water discharge. This plays a big role in fjord circulation dynamics [5], especially in summer time, when the ice melting rate is at its highest. The analysis of the final “realistic scenario” results will help us to understand the dynamics of the complicated fjord system, what affect it has on the shrinking Greenland Ice Sheet, and as a result of this, the global sea level rise and what future it brings to us.

Acknowledgements

The pressure data was kindly provided by Fiamma Straneo, Woods Hole Oceanographic Institution.

References

- [1] F.R. Cottier, F. Nilsen, R. Skogseth, V. Tverberg, J. Skardhamar, H. Svendsen. Arctic fjord: a review of the oceanographic environment and dominant physical processes. *Geological Society*, 344, 35-50, 2010.
- [2] J.-M. Hervouet. Hydrodynamics of free-surface flows modelling with the FEM. *Wiley*, 2007.
- [3] J.M. Klinck, J.J. O’Brien, H. Svendsen. A simple Model of Fjord and Coastal Circulation Interaction. *Journal of Physical Oceanography*, 11, 1612-26, 1981.
- [4] R. Sciascia, C. Cenedese, D. Nicoli, P. Heimbach, F. Straneo. Impact of periodic intermediary flows on submarine melting of a Greenland glacier. *Journal of Geophysical Research: Oceans*, 119, 7078-98, 2014.
- [5] T. Murray, K. Scharrer, T.D. James, S.R. Dye, E. Hanna, A.D. Booth, N. Selmes, A. Luckman, A.L.C. Hughes, S. Cook, P. Huybrechts. Ocean regulation hypothesis for glacier dynamics in southeast Greenland and implications for ice sheet mass changes. *Journal of Geophysical Research*, 115, F03026, 2010.
- [6] <http://www.deltaressystems.com/>
- [7] http://www.eos.ubc.ca/~rich/t_tide/

AN EFFICIENT IMAGE-BASED FRAMEWORK FOR EVALUATING FLUID FLOW OF RANDOM FIBROUS POROUS MEDIA IN OXYGENATORS

*Kenny W. Q. Low¹, Raoul van Loon², Samuel A. Rolland¹ and Johann Sienz¹

¹Advanced Sustainable Manufacturing Technologies (ASTUTE) Project, College of Engineering,
Swansea University, Swansea, SA2 8PP, United Kingdom

²Zienkiewicz Centre for Computational Engineering, College of Engineering, Swansea University,
Swansea, SA2 8PP, United Kingdom

*K.W.Q.Low@swansea.ac.uk

ABSTRACT

In this current work, an alternative efficient framework to evaluate the behaviour of flow in random fibrous porous media of oxygenators is proposed. This methodology aims improve the iterative nature of oxygenator design without the effort of remeshing. The geometry of the oxygenator is extracted from a micro-CT image and their fibre coordinates are determined. A fictitious domain approach is adopted whereby a structured Cartesian mesh is embedded onto the physical domain which contains sub-domains of fluid and solid. The identification of fluid and solid regions are controlled with an additional Darcy viscous loss term added to the Navier–Stokes equations. The governing equations are solved using ANSYS Fluent[®]. Two examples using this methodology are performed and compared against boundary-fitted method.

Key Words: *Image-based; micro-CT; fictitious domain; random fibrous porous media; oxygenator.*

1. Introduction

Patients' lives are maintained during open heart surgery and other cardiopulmonary procedures by oxygenating their blood in oxygenators. These devices employ mass transfer through gas permeable hollow fibres to provide blood with oxygen and remove carbon dioxide. Several types of oxygenators have been developed throughout the years such as film, bubble and hollow fibre membrane oxygenators. Hollow fibre membrane oxygenators are the most common type of oxygenators but they can only support low levels of patient activity and are bulky equipment. These limitations of the current designs motivates research to design better performing solutions to improve patients' quality of life. The use of Computational Fluid Dynamics (CFD) for investigating the flow characteristic through a random pack of fibres deemed to be an attractive tool for iterative design improvements. Nonetheless, this repetitive procedure to some extent considered to be laborious and time consuming.

In this current work, an efficient framework is proposed to investigate the flow behaviour through random arrays of fibres without the effort of remeshing. Similar approach have been employed previously to the incompressible Navier-Stokes equations [1], arterial media [2] and dual scale fibrous porous media [3] have been performed but not particularly in oxygenators.

The framework begins with the use of micro-CT where several image cross-sections of the physical oxygenator are obtained. Based on these images, fibre coordinates are then established. Next, a fictitious domain approach is adopted in which a structured Cartesian mesh is embedded onto the physical domain. The fluid and solid regions are identified through an additional Darcy viscous loss term introduced in the classical Navier–Stokes equations. The governing equations are solved using a commercial finite volume software package ANSYS Fluent[®] [4]. Finally, the proposed framework is validated against boundary-fitted method.

2. Methodology

2.1. Geometry extraction

A series of cross-sectional images of the physical oxygenator were obtained using micro-CT. An image sample of a micro-CT scan can be seen in Figure 1(a). Based on these snapshots, no displacement of fibres were observed. Therefore, the fibres are treated as perfectly straight and circular in shape. The fibre centres of the image are determined via a built-in MATLAB[®] function. Additional refinement in position is performed for fibres which are conflicted or touching each other. A gap of 10 micron between fibres are achieved for refinement. The final form of the fibre arrangements is illustrated in Figure 1(b).

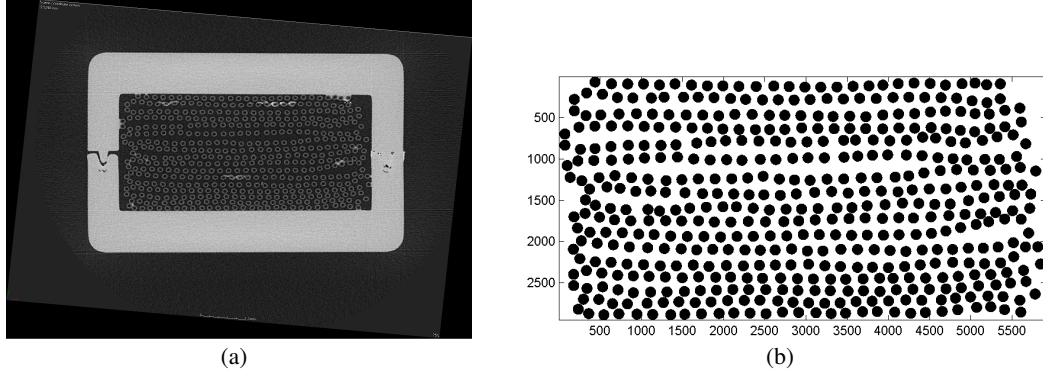


Figure 1: Visualisation of (a) Image and (b) Final form of the geometry extraction process.

2.2. Image–computational grid mapping

A fictitious domain approach is adopted whereby a structured Cartesian mesh is embedded onto Figure 1(b). The fictitious domain (Ω) can be seen as a heterogeneous medium consisting of sub-domains of fluid and solid ($\Omega_f \cup \Omega_s$) which can be illustrated in Figure. The handling of fluid and solid regions are done through an additional Darcy viscous loss term in the incompressible Navier–Stokes equations which treats the Ω as a porous medium. Creeping and lower end of the laminar regimes are only considered in this present context. The single set of governing equations over Ω can be expressed as

$$\nabla \cdot (\varepsilon \mathbf{u}) = 0 \quad (1)$$

$$\nabla \cdot (\varepsilon \rho \mathbf{u} \otimes \mathbf{u}) = -\varepsilon \nabla p + \nabla \cdot \left[\mu (\nabla \varepsilon \mathbf{u} + \{\nabla \varepsilon \mathbf{u}\}^T) \right] - \frac{\mu}{K} \varepsilon^2 \mathbf{u} \quad (2)$$

where ε , ρ , \mathbf{u} , p , μ and K are the porosity, density, physical velocity vector, static pressure, dynamic viscosity and permeability. The two parameters ε and K are both strongly related, numerous studies (numerical and experimental) have been carried out to investigate their relationship [5, 6, 7]. In this current work, $\varepsilon(\mathbf{x})$ is computed based on the ratio of white and total grayscale pixels (N_W/N_T) occupying each cell. The calculation of parameter K is based on the value of ε . A ratio of 0.5 and above is considered to be in Ω_f ; otherwise in Ω_s . The values for each sub-domain is defined as

$$\varepsilon(\mathbf{x}) = \begin{cases} \varepsilon_f \rightarrow 1 & \text{when } \mathbf{x} \in \Omega_f \\ \varepsilon_s \rightarrow 0 & \text{when } \mathbf{x} \in \Omega_s \end{cases} ; \quad K(\mathbf{x}) = \begin{cases} K_f = 10^{10} & \text{when } \mathbf{x} \in \Omega_f \\ K_s = 10^{-12} & \text{when } \mathbf{x} \in \Omega_s \end{cases}$$

where the subscript f and s denote to the fluid and solid regions. The α value is known as the ratio of solid and fluid permeabilities. The governing equations are solved using a commercial software package ANSYS Fluent[®]. Fluent[®] utilises a cell-centered finite volume approach in which all flow variables are stored in the centroid of each cell. PISO scheme is employed for pressure-velocity coupling whereby a pressure correction equation is being reformatted to satisfy both continuity and momentum equations. The linear system of equations are solved in a segregated manner using Gauss-Seidel in conjunction with an algebraic multigrid method. Convergence criterion by default is set to 10^{-10} for global scaled residuals of all flow variables.

3. Results and Discussions

3.1. Method validation

To demonstrate this methodology, flow around a circular object is simulated and compared against boundary-fitted meshing method (reference method). The domain under consideration is a square block with a length $l = 1$ and a circular object situated at the centre with a diameter $d = 0.8$ – giving a porosity $\varepsilon \approx 0.5$. The fluid studied is water ($\rho = 1000 \text{ kg/m}^3$ and $\mu = 0.001 \text{ Pa}\cdot\text{s}$). A periodic mass flow rate of Reynolds number (Re) 1 is imposed between the inlet (left) and outlet (right) of the domain. The top and bottom surfaces of the domain is treated as symmetrical. For the reference method, the geometry is discretised using 21,000 quadrilateral mesh. For the fictitious domain approach, a structured Cartesian grid of 3,600 elements is used. Figure 2 illustrates the periodic pressure and velocity magnitude distribution. Both pressure and velocity are in good agreement. In Figure 2(a), it is worth noting that Fluent® provides a contour of the periodic components but also reports a linear pressure gradient value in the stream-wise direction when the periodic boundary condition is used. The velocity magnitude (see Figure 2(b)) in the solid region of the fictitious approach reduces to a value that is near zero ($\approx 10^{-6}$).

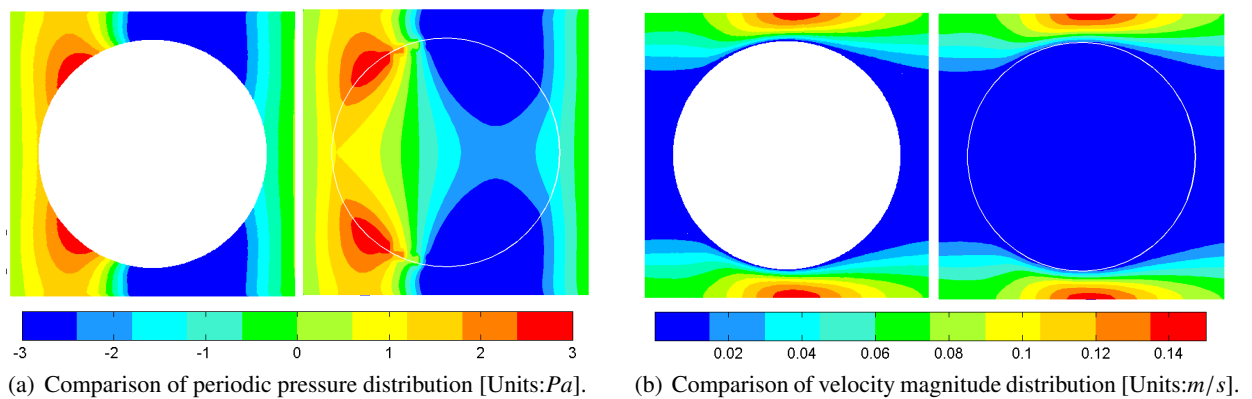


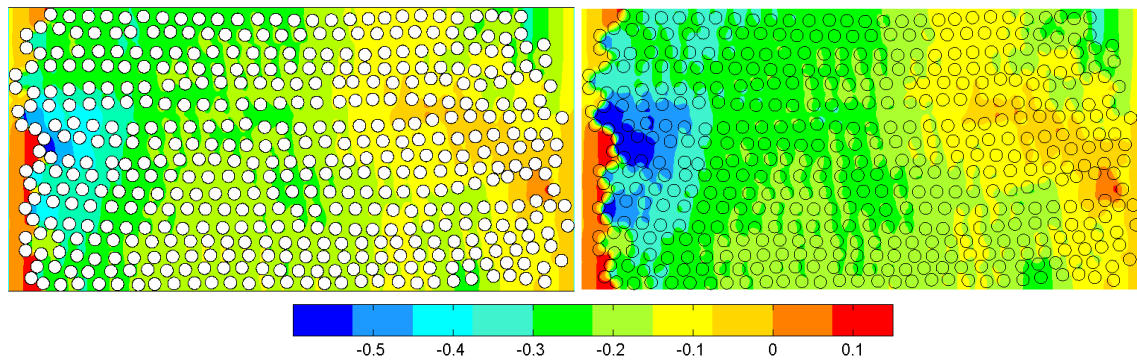
Figure 2: Comparison of (a) periodic pressure and (b) velocity magnitude components for boundary fitted (left) and fictitious (right) methods. White line denotes the outline of fibre.

3.2. Oxygenator

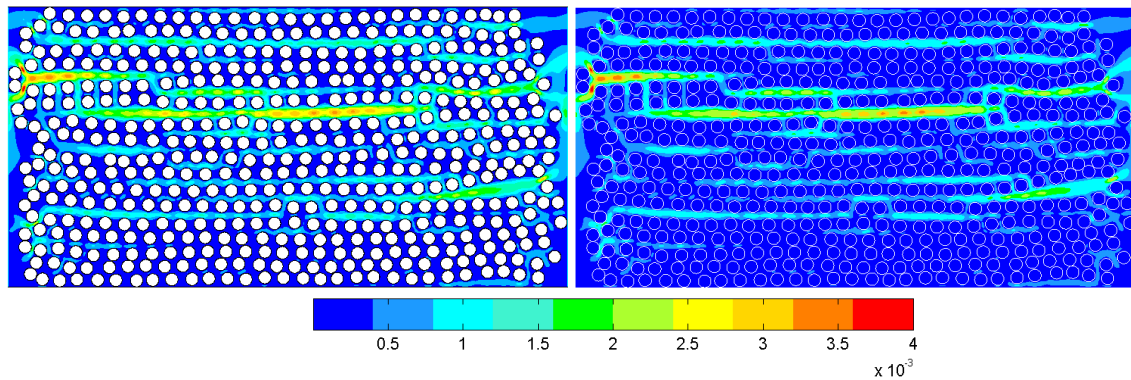
Next, this methodology is being applied to a notional oxygenator fibre bundle prototype. The geometrical extraction is being discussed in Section 2.1. The physical oxygenator is 8.5 mm by 17.5 mm in height and width respectively. The fibre diameter is 380 microns. The fluid studied remains the same. A periodic mass flow rate of Reynolds number (Re) 0.1 is imposed between the inlet (left) and outlet (right) of the domain. The top and bottom surfaces of the domain is treated to be symmetry. For the reference method, the geometry is discretised using 2,100,000 unstructured tetrahedral elements. For the fictitious domain approach, a structured Cartesian grid of 300 by 600 is used. Furthermore, similar parameter settings of ε and K are applied for the treatment of solid and fluid regions. The results are compared against the reference method and illustrated in Figure 3. It can be seen that the fictitious domain approach is in good agreement with some slight variations in the periodic pressure distribution (see Figure 3(a)).

4. Conclusions and Future Work

An alternative framework for evaluating fluid flow behaviour through random fibrous porous media in oxygenators is presented. The method mainly utilises a fictitious domain approach in which a structured Cartesian mesh is embedded onto the physical domain and an additional Darcy source term to control the fluid and solid regions. The results demonstrated that this approach seems promising and could be potentially extended further. Future work includes extending to a proper three-dimensional oxygenator and non-Newtonian blood flow.



(a) Comparison of periodic pressure distribution [Units:Pa].



(b) Comparison of velocity magnitude distribution [Units:m/s].

Figure 3: Comparison of (a) periodic pressure and (b) velocity magnitude components for boundary fitted (left) and fictitious (right) methods. Black and white lines represent the outline of fibres for pressure and velocity respectively.

Acknowledgements

The authors would like to acknowledge the financial support received from the Welsh Government and the European Regional Development Fund (ERDF). They would like to thank HaemAir Ltd. in providing the oxygenator prototypes. Finally, they would like also to express their gratitude to Dr. Richard Johnston and Claudio D’Onofrio for providing the micro-CT technology and scan images.

References

- [1] K. Khadra, P. Angot, S. Parneix and J.-P. Caltagirone. Fictitious domain approach for numerical modelling of Navier-Stokes equations. *International Journal for Numerical Methods in Fluids*, 34, 651–684, 2000.
- [2] A. Comerford, K.Y. Chooi, M. Nowak, P.D. Weinberg and S.J. Sherwin. A combined numerical and experimental framework for determining permeability properties of the arterial media. *Biomechanics and Modeling in Mechanobiology*, 1–17, 2014.
- [3] W.R. Hwang and S.G. Advani. Numerical simulation of Stokes–Brinkman equations for permeability prediction of dual scale fibrous porous media. *Physics of Fluids*, 22, 1–14, 2010.
- [4] ANSYS Inc., *ANSYS Fluent User’s Guide*, release 14.0 Edition, 2011.
- [5] X.M. Chen and T.D. Papathanasiou. The transverse permeability of disordered fiber arrays: a statistical correlation in terms of the mean nearest interfiber spacing. *Transport in Porous Media*, 71, 233–251, 2008.
- [6] K. Yazdchi, S. Srivastava and S. Lusing. Micro–macro relations for flow through random arrays of cylinders. *Composites: Part A*, 43, 2007–2020, 2012.
- [7] Y. Matsumura and T.L. Jackson. Numerical simulation of fluid flow through random packs of cylinders using immersed boundary method. *Physics of Fluids*, 26, 1–22, 2014.

FLUID DYNAMICS 2

Application of a Lagrange multiplier approach for flow rate defective boundary conditions in a finite volume framework

*J. Prince¹ and J. Peiro¹

¹ Department of Aeronautics, Imperial College, London

*j.prince11@imperial.ac.uk

ABSTRACT

Defective boundary conditions occur when only average quantities are available at boundaries being modelled in 2D/3D, which require pointwise data. This is usually solved by applying an arbitrary boundary profile that is consistent with the average quantities, which can lead to inaccuracies. More sophisticated methods to treat defective boundary conditions have been developed, which are reviewed in [4]. Here the Lagrange multiplier approach for flow rate defective boundary conditions [3, 5] is considered for the application of modelling flow in a network of tunnels, using OpenFOAM. Previous implementations of the Lagrange multiplier approach were in the context of the finite-element method [4, 5], therefore the formulation is adapted for the cell-centred finite volume discretisation in OpenFOAM. This approach is verified using an analytic solution.

Key Words: *Lagrange multiplier; Incompressible Navier-Stokes; Finite-volume-method; OpenFOAM; Tunnel ventilation*

1. Introduction

When modelling airflow in a large network of tunnels 1D area-averaged models are often used, as they are computationally cheap. At junctions such as bends and flow-splits empirical data can be used to predict pressure losses. However in areas of complex flow, such as in a subway station, 1D models are not able to capture the flow accurately. In these circumstances 3D models can be used to provide an accurate representation of the flow-field, although their computational cost is too high to be able to model the entire network. Geometrical multiscale modelling, which has previously been used for modelling tunnel networks in [1] and for cardiovascular modelling in [2] amongst many others, is a tool that has been developed to combine the best features of 1D and 3D models. This is achieved by decomposing the network into sub-sections that can be modelled in 1D, and those that require 3D modelling. An iterative exchange of boundary conditions is required to achieve a smooth solution over the whole domain, however only scalar quantities are available to pass from 1D to 3D. These are known as defective boundary conditions. For modelling a 3D domain such as that in figure 1, the following sections address the problem of having defective flow-rate boundary conditions (BC's) on $\Gamma_0, \dots, \Gamma_4$.

2. The Lagrange multiplier method for solving defective flow-rate boundary conditions

The 3D simulations require the solution of the incompressible Navier-Stokes (NS) equations, which are given as

$$\begin{aligned} \frac{\partial \mathbf{u}}{\partial t} + \nabla \cdot (\mathbf{u}\mathbf{u}) - \nu \nabla^2 \mathbf{u} &= \mathbf{f} - \frac{1}{\rho} \nabla p \\ \nabla \cdot \mathbf{u} &= 0 \end{aligned} \quad (1)$$

where \mathbf{u} is the velocity, p is the pressure, ν is the kinematic viscosity and \mathbf{f} is a forcing term. This problem also has an initial condition of $\mathbf{u} = \mathbf{u}_0$ at time $t = 0$. To complete the problem description a set of well posed boundary conditions is required. Referring to the domain in figure 1, homogeneous Dirichlet BC's

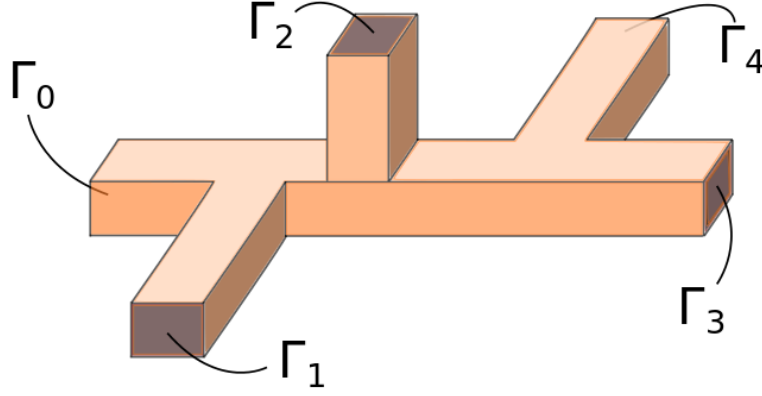


Figure 1: Reference 3D domain Ω that requires pointwise boundary conditions on $\Gamma_0, \dots, \Gamma_4$.

are applied on the wall $\Gamma_w = 0$ and $M + 1$ further BC's are required on the artificial boundaries $\Gamma_0, \dots, \Gamma_M$. For the flow rate problem the boundary conditions available are

$$\int_{\Gamma_m} \mathbf{u} \cdot \mathbf{n} d\Gamma = Q_m \quad \text{for } m = 0, \dots, M \quad (2)$$

where one of the flow-rate conditions has to be left free in order to satisfy mass conservation, for example if Γ_0 is chosen $Q_0 = -\sum_{m=1}^M Q_m$. The conditions (2) are not well posed from a mathematical point of view since a single value is available to apply where the NS equations require pointwise conditions. To make the NS equations (1) with defective flow-rate BC's (2) well posed a Lagrange multiplier approach was used in [4]. This gives a constrained weak form of the incompressible NS equations, which is

$$\begin{aligned} \int_{\Omega} \frac{\partial \mathbf{u}}{\partial t} \cdot \mathbf{v} d\Omega + \int_{\Omega} \nabla \cdot (\mathbf{u}\mathbf{u}) \cdot \mathbf{v} d\Omega - \int_{\Omega} \nu \nabla \mathbf{u} : \nabla \mathbf{v} d\Omega &= \int_{\Omega} \mathbf{f} \cdot \mathbf{v} d\Omega \\ - \int_{\Omega} p \nabla \mathbf{v} d\Omega + \sum_{m=1}^M \lambda_m \int_{\Gamma_m} \mathbf{v} \cdot \mathbf{n} d\Gamma & \\ \int_{\Omega} \nabla \cdot \mathbf{u} q d\Omega &= 0 \\ \int_{\Gamma_m} \mathbf{u} \cdot \mathbf{n} d\Gamma &= Q_m \quad \text{for } m = 1, \dots, M \end{aligned} \quad (3)$$

where \mathbf{v} are the test functions and $\lambda_1, \dots, \lambda_M$ are the Lagrange multipliers. It was shown in [3] that in addition to satisfying the flow-rate constraints (2) system (3) also satisfies the incompressible NS equations (1), a homogeneous natural boundary condition on Γ_0 and on $\Gamma_1, \dots, \Gamma_4$ the heterogeneous Neumann BC's

$$\left(\nu \frac{\partial \mathbf{u}}{\partial \mathbf{n}} - p \mathbf{n} \right) \Big|_{\Gamma_m} = -\lambda_m \mathbf{n} \quad \text{for } m = 1, \dots, M \quad (4)$$

which shows that the Lagrange multipliers are equivalent to the normal stress on the boundary.

3. Finite-volume method implementation

System (3) is typically discretised using the finite-element-method (FEM) [3, 5], however in this work commercial finite-volume-method (FVM) codes are considered for solving defective flow-rate BC's. A brief overview of the OpenFOAM FVM discretisation will allow a consideration of the differences between the discretisations so that a modified version of the the LM approach can be derived.

The cell-centred finite-volume-method discretisation in OpenFOAM [6] integrates the incompressible NS equations (1) over a control volume Ω_p , giving

$$\begin{aligned} \int_{\Omega_p} \frac{\partial \mathbf{u}}{\partial t} d\Omega + \int_{\Omega_p} (\mathbf{u} \nabla \mathbf{u})_f d\Omega - \int_{\Omega_p} \nu \nabla^2 \mathbf{u} d\Omega + \int_{\Omega_p} \nabla p \mathbf{n} d\Omega &= \int_{\Omega_p} \mathbf{f} d\Omega \\ \int_{\Omega_p} \nabla \cdot \mathbf{u} &= 0 \end{aligned} \quad (5)$$

Now, linearising the convective term and applying Gauss theorem to the viscous stress terms and the convective term so that

$$\int_{\Omega_P} \frac{\partial \mathbf{u}}{\partial t} d\Omega + \int_{\Gamma_P} (\beta \nabla \mathbf{u}) d\Gamma = \int_{\Omega_P} \mathbf{f} d\Omega + \int_{\Gamma_P} \left(\nu \frac{\partial \mathbf{u}}{\partial \mathbf{n}} - p \mathbf{n} \right)_f d\Gamma \quad (6)$$

$$\int_{\Gamma_P} (\mathbf{u})_f \mathbf{n} = 0$$

where β is the linearised part of the convective term. Also note that the stress terms have been grouped on the right hand side so that the imposition Lagrange multipliers and natural BC's can be considered when a boundary of the cell Ω_P lies on a boundary Γ_m . The boundary integrals are evaluated as a sum over the faces of the control volume to give

$$\Omega_P \frac{\partial \mathbf{u}_P}{\partial t} + \sum_f S_f (\beta \nabla \mathbf{u})_f = \Omega_P \mathbf{f} + \sum_f S_f \left(\nu \frac{\partial \mathbf{u}}{\partial \mathbf{n}} - p \mathbf{n} \right)_f \quad (7)$$

$$\sum_f S_f (\mathbf{u})_f \mathbf{n} = 0$$

where f are the boundary faces and S_f are the magnitudes of the face areas. For control volumes that lie on a boundary, the velocity, pressure and their gradients can be imposed as BC's in OpenFOAM.

With this basic description of the FVM discretisation, modifications can be considered to the formulation of (3) so that the Lagrange multiplier approach can be solved in OpenFOAM. A key difference between the FEM discretisation and the FVM discretisation is the domain over which the governing equations are discretised. The FEM weak statement is defined over the domain Ω and then discretised over the control volumes. Whereas in the FVM the discretisation is defined on a single control volume Ω_P and a system of equations is formed by combining contributions over the whole domain. Therefore when Gauss theorem is applied to the governing equations, as in equation (6), there is a boundary integral for each control volume rather than over the whole domain. This means that a direct conversion from the weak statement (3) to a FVM discretisation cannot be considered. However, from a physical point of view, equation (4) shows that the Lagrange multiplier adjusts the stresses on the boundary of the domain to achieve the correct flow-rate. Therefore imposing the Lagrange multipliers through natural BC's in the FVM code is considered.

The OpenFOAM BC's are set separately for each variable and therefore cannot form the natural boundary conditions which are required to satisfy equation (4). However, following [3], the Lagrange multiplier definition (4) can be decomposed into two components which on a section m are

$$\left(\nu \frac{\partial u_n}{\partial \mathbf{n}} - p \right) \Big|_{\Gamma_m} = -\lambda_m \quad \text{and} \quad \frac{\partial \mathbf{u}_\tau}{\partial \mathbf{n}} \Big|_{\Gamma_m} = 0 \quad (8)$$

where $u_n = \mathbf{u} \cdot \mathbf{n}$ is the normal velocity and $\mathbf{u}_\tau = \mathbf{u} - u_n \mathbf{n}$ are the tangential velocities. As pointed out in [3] condition (8)₂ also implies that $\frac{\partial u_n}{\partial \mathbf{n}} = 0$ in the case that the section Γ_m is perpendicular to the axial direction of the pipe. In order to implement this technique using the FVM it has to be ensured that this is the case, which it would be for sections being coupled with 1D models. Applying this assumption allows a FVM system that is equivalent to system (3), which solves the incompressible NS equations (7) with the boundary conditions

$$\frac{\partial \mathbf{u}}{\partial \mathbf{n}} \Big|_{\Gamma_m} = 0 \quad \text{for } m = 0, \dots, M \quad (9)$$

$$p|_{\Gamma_m} = \lambda_m \quad \text{for } m = 1, \dots, M \quad (10)$$

$$p|_{\Gamma_0} = 0 \quad (11)$$

Now a way to impose the Lagrange multiplier using a FVM discretisation has been formulated, a suitable solution algorithm is required. In its current form the Lagrange multiplier approach cannot be solved without modifying the source code of a FVM commercial software, since there are additional variables and constraints. In [5], solution techniques for solving system (3) that treat the solver as a "black box" were considered. Of those methods the "continuous splitting-based scheme" and the "inexact splitting" are suitable for implementation in OpenFOAM.

4. Numerical results

The analytic Womersley solution for oscillating flow is now shown in comparison with the numerical solution to the flow-rate problem. This was implemented in OpenFOAM using the "continuous splitting" algorithm from [5]. Figure 2 shows that the profile of the numerical solution is slightly different to

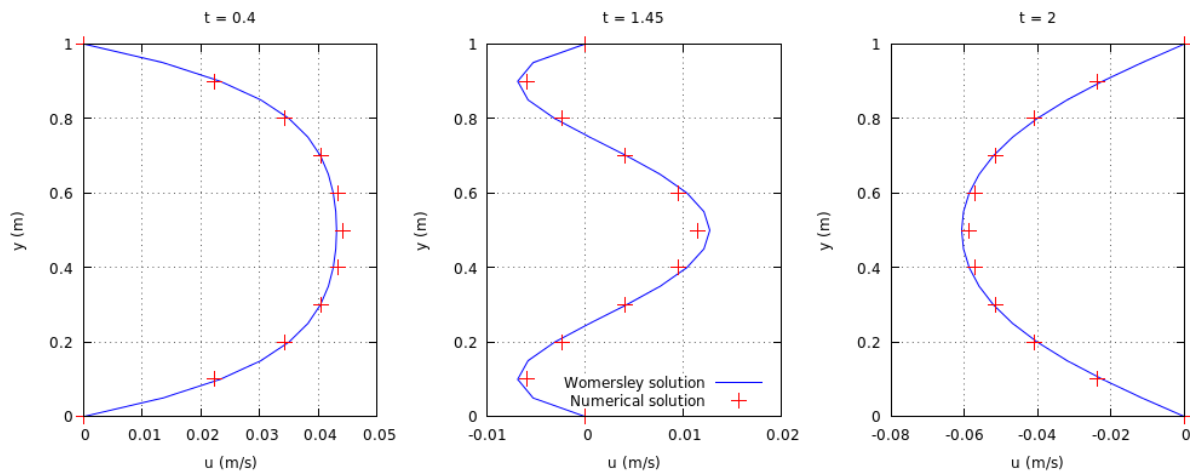


Figure 2: Unsteady Womersley solution with $\frac{dp}{dx} = \mu \sin(2\pi t)$, where the blue line is the analytic solution, and the red markers are from the OpenFOAM numerical solution.

that of the Womersley solution. This is due to the semi-implicit discretisation of the convective term in OpenFOAM.

5. Conclusions

The Lagrange multiplier technique for solving defective flow-rate boundary conditions has been implemented in the commercial finite-volume-method software OpenFOAM. Natural boundary conditions that are part of the weak formulation have been imitated by the BC's that are available in OpenFOAM, under the specific circumstance of the tube axis being perpendicular to the artificial boundary. A modular solution to the Lagrange multiplier technique for flow-rate BC's has given a good comparison with the analytic solution.

Acknowledgements

The author would like to thank the EPSRC and Arup Ltd. for funding this PhD project.

References

- [1] F. Colella. PhD thesis: Multiscale Modelling of Tunnel Ventilation Flows and Fires. *Politecnico di Torino, Dipartimento di Energetica*, 2010.
- [2] L. Formaggia and J.F. Gerbeau and F. Nobile and A. Quarteroni. On the coupling of 3D and 1D Navier–Stokes equations for flow problems in compliant vessels. *Computer Methods in Applied Mechanics and Engineering*, 191, 561-582, 2001.
- [3] L. Formaggia and J.F. Gerbeau and F. Nobile and A. Quarteroni. Numerical treatment of defective boundary conditions for the Navier-Stokes equations. *SIAM J. Numer. Anal.*, 40, 376-401, 2002.
- [4] L. Formaggia and C. Vergara. Prescription of General Defective Boundary Conditions in Fluid Dynamics. *Milan J. Math.*, 80, 333-350, 2012.
- [5] C. Vergara. PhD thesis: Numerical Modelling of Defective Boundary Problems in Incompressible Fluid-Dynamics. *Politecnico di Milano, Dipartimento di Matematica*, 2006.
- [6] The OpenFOAM team: *OpenFOAM*, www.openfoam.org.

A HIGHER-ORDER UNSTRUCTURED FINITE VOLUME SOLVER FOR GENERALIZED NEWTONIAN FLUIDS

*Mahkame Sharbatdar, Alireza Jalali, and Carl Ollivier-Gooch

Department of Mechanical Engineering, University of British Columbia, Vancouver, BC, V6T 1Z4,
 Canada

*mahkame@interchange.ubc.ca

ABSTRACT

The development of a higher-order finite volume solver for power-law non-Newtonian fluids is described. This flow solver works based on a higher-order least-squares solution reconstruction for primitive variables. Also, implicit time advance scheme with global time-stepping is used to obtain a fast and efficient convergence to the steady-state solutions. The higher-order accuracy of our flow solver is verified and the effects of flow variables such as Reynolds number and power-law index on convergence speed are investigated.

Key Words: *higher-order; finite-volume; unstructured; non-Newtonian; power-law*

1. Introduction

Non-Newtonian fluids have a wide range of applications in biology, industrial and manufacturing processes. One way to investigate the flow features of non-Newtonian fluids is Computational Fluid Dynamics (CFD) in which the governing equations of the flow fields are solved by a numerical method.

Finite volume approach has been very successful in the simulation of complex flows and forms the basis of many commercial softwares. Therefore, the development of robust finite volume solvers for non-Newtonian fluids has become an active research area in the field of CFD. However, these flow solvers are typically second-order accurate and for structured meshes. The examples are the flow solver of Oliveira *et al.* [1] for viscoelastic fluids in which a non-staggered grid arrangement was used to simplify the adoption of curvilinear coordinates for general structured meshes and the implicit flow solver of Nejat *et al.* [2] for power-law fluids on structured meshes.

Considering that the numerical errors can be as large as physical modeling errors, high-order methods are motivated. Moreover, the use of unstructured meshes is essential for complex geometries due to their flexibility in refinement and adaptation.

In this paper, we describe the development of a higher-order unstructured flow solver for the generalized Newtonian fluids, where the shear stress tensor is a non-linear function of shear rate tensor. In particular, we investigate the power-law model, which describes the behavior of many industrial or biological fluids under special circumstances.

2. Governing Equations

To simulate the generalized Newtonian fluid flows, we need to solve the continuity and Navier-Stokes equations. Assuming incompressible flows, these equations can be written in the conservative form as:

$$\frac{\partial u}{\partial x} + \frac{\partial v}{\partial y} = 0 \quad (1)$$

$$\frac{\partial u}{\partial t} + \frac{\partial u^2}{\partial x} + \frac{\partial uv}{\partial y} = -\frac{\partial P}{\partial x} + \frac{1}{Re} \left(\frac{\partial \tau_{xx}}{\partial x} + \frac{\partial \tau_{yx}}{\partial y} \right) \quad (2)$$

$$\frac{\partial v}{\partial t} + \frac{\partial uv}{\partial x} + \frac{\partial v^2}{\partial y} = -\frac{\partial P}{\partial y} + \frac{1}{Re} \left(\frac{\partial \tau_{xy}}{\partial x} + \frac{\partial \tau_{yy}}{\partial y} \right)$$

where τ_{ij} are the stress tensor components and found based on fluid constitutive relations. For a power-law fluid, the shear stress is defined as:

$$\tau_{ij} = \eta \dot{\gamma}_{ij}, \quad \dot{\gamma}_{ij} = \frac{\partial V_i}{\partial X_j} + \frac{\partial V_j}{\partial X_i}, \quad \eta = \left(\frac{\dot{\gamma} : \dot{\gamma}}{2} \right)^{\frac{n-1}{2}} \quad (3)$$

To couple the continuity and the momentum equations, the pseudo-compressibility technique is used where an unphysical time derivative of pressure is added to the continuity equation in the form of:

$$\beta \frac{\partial P}{\partial t} + \frac{\partial u}{\partial x} + \frac{\partial v}{\partial y} = 0 \quad (4)$$

3. Spatial Discretization

To discretize the flow equations using the finite volume methods, the governing equations should be recast in fully conservative form as:

$$\frac{\partial U}{\partial t} + \nabla \cdot (\vec{F}_c - \vec{F}_v) = 0 \quad (5)$$

Integrating Equation 5 over an arbitrary control volume and using the divergence theorem, the finite volume formulation of the governing equation is written as:

$$\frac{d\bar{U}_i}{dt} + \frac{1}{A_i} \oint_{CS_i} (\vec{F}_c^n - \vec{F}_v^n) ds = 0 \quad (6)$$

where

$$\vec{U} = \begin{pmatrix} P \\ u \\ v \end{pmatrix}, \quad \vec{F}_c^n = \begin{pmatrix} (u\hat{n}_x + v\hat{n}_y)/\beta \\ (u^2 + p)\hat{n}_x + uv\hat{n}_y \\ uv\hat{n}_x + (v^2 + p)\hat{n}_y \end{pmatrix}, \quad \vec{F}_v^n = \frac{1}{Re} \begin{pmatrix} 0 \\ \tau_{xx}\hat{n}_x + \tau_{yx}\hat{n}_y \\ \tau_{xy}\hat{n}_x + \tau_{yy}\hat{n}_y \end{pmatrix} \quad (7)$$

The flux integral can be evaluated by numerical integration over the faces of each control volume. To have a higher-order estimate of the normal fluxes, the primitive variables are reconstructed by a piecewise polynomial about the control volume's reference point. The polynomial is obtained by solving a least-squares system such that the conservation of mean is satisfied within a control volume and the error in predicting the mean values of the neighboring control volumes is minimized [3]. Boundary conditions can be also be enforced as extra constraints in the LS system. Ultimately, the flux vectors are computed by applying a flux function to the two fluxes computed on each side of an interface. We use central flux function for convective fluxes and add a solution jump term to the averaged components of the gradients for the viscous fluxes [4].

4. Solution Method

To obtain the steady-state solution, we use the backward implicit time-stepping:

$$\frac{\bar{U}^{n+1} - \bar{U}^n}{\Delta t} = -R(\bar{U}^{n+1}) \quad (8)$$

where $R(\bar{U})$ is the flux integral in Equation 6. The right hand-side can be linearized about the state \bar{U}^n :

$$\left(\frac{I}{\Delta t} + \frac{\partial R}{\partial U} \right) \delta \bar{U} = -R(\bar{U}^n), \quad \bar{U}^{n+1} = \bar{U}^n + \delta \bar{U} \quad (9)$$

where I is the identity matrix, Δt is the global time-step and $\frac{\partial R}{\partial U}$ is the global Jacobian matrix.

Also, we use the successive evolution-relaxation to find the global CFL number:

$$CFL^{n+1} = c_2 \cdot CFL^n \cdot \frac{\|R(\bar{U}^{n-1})\|_2}{\|R(\bar{U}^n)\|_2}, \quad c_2 = 1.1, \quad CFL^0 = 1.0 \quad (10)$$

Table 1: Error norms for power-law fluid in a channel

Nominal order	670 CVs			2624 CVs			Actual order		
	L_1	L_2	L_∞	L_1	L_2	L_∞	L_1	L_2	L_∞
2	0.0179	0.223	0.0903	0.00372	0.00486	0.0195	2.27	2.20	2.21
4	0.00127	0.00196	0.00907	0.000081	0.000142	0.000761	3.96	3.79	3.56

Having the global CFL number, we can derive a local time-step for each control volume:

$$\Delta t_i^{n+1} = CFL^{n+1} \cdot \frac{h_i}{speed_i^n} \quad (11)$$

where $speed_i$ is the largest characteristic speed in the control volume and h_i is a characteristic size. The global time-step, Δt in Equation 9, is obtained by selecting the smallest time-step, computed using Equation 11, amongst all control volumes. Using the pseudo-compressibility method, the system of equations are transformed into a hyperbolic system in which the characteristic speeds are the eigenvalues of the normal convective flux Jacobian, $\frac{\partial F_c^n}{\partial U}$:

$$\lambda_1 = \vec{V} \cdot \hat{n} - \sqrt{(\vec{V} \cdot \hat{n})^2 + 1/\beta} \quad \lambda_2 = \vec{V} \cdot \hat{n} \quad \lambda_3 = \vec{V} \cdot \hat{n} + \sqrt{(\vec{V} \cdot \hat{n})^2 + 1/\beta} \quad (12)$$

The above eigenvalues are calculated on the quadrature points located on the interfaces of a control volume and the one with the largest magnitude (λ_1 or λ_3) is selected as $speed_i$ in Equation 11.

5. Results

To verify the nominal accuracy of our spatial discretization for generalized Newtonian fluids, we consider the fully-developed pressure-driven flow of power-law fluids in a rectangular channel. The exact solution for u -velocity

$$u_e(x, y) = U_{max} \left(1 - \left(1 - \frac{2y^*}{D} \right)^{\frac{n+1}{n}} \right), \quad y^* = \min(y, D - y) \quad (13)$$

where U_{max} is the maximum velocity at the centerline, $y = D/2$. Having the exact solution of Equation 13, it is possible to calculate the numerical error in each control volume. Table 1 shows the norms of error for u -velocity on two meshes for $Re = 100$, $n = 0.5$, $U_{max} = 1.5$, $L = 3$ and $D = 1$. As expected, the fourth-order method results in smaller error values and the asymptotic orders of error convergence are close enough to the nominal orders in all norms.

Now, we turn our attention to the performance of our flow solver for the convergence to the steady-state solution of power-law fluids in a lid-driven cavity. The simulations are performed on a unit-square cavity tessellated with 3132 triangular cells for a wide range of power-law indices, $0.6 \leq n \leq 1.4$, at $Re = 10, 300$. For all cases, the initial conditions are the same so that the pressure and v -velocity are zero everywhere and u -velocity changes linearly with vertical position, i.e. $u = y$. Table 2 shows the number of non-linear iterations for dropping the L_2 -norm of residual vector by 8 orders of magnitude from the initial flux integral, the L_2 -norms of the absolute residual after those iterations and the simulation time on a single core of i7-3820 (3.60 GHz) CPU for second-order discretizations. The GMRES method preconditioned with ILU-2 is used to solve the linear system in each iteration where the Krylov size is 100 and the relative norm for the linear solve is 0.001. Furthermore, we set $\beta = 0.5$ for all shear-thinning fluids ($n < 1$) and $\beta = 1$ for others. Similarly, Table 3 summarizes the convergence properties for fourth-order discretization with the same settings. The number of non-linear iterations are comparable to second-order; however, the simulation times are longer due to the additional cost of higher-order discretizations in each step.

6. Conclusions

A higher-order unstructured finite volume solver was developed for power-law fluids. The primitive variables were approximated with least-squares reconstruction. The pseudo-compressibility method was employed to couple the governing equations and backward implicit time-stepping was used for obtaining the steady-state solution. Our results verified the higher-order accuracy of velocity fields for a channel flow. Also, fast and efficient convergence was shown for both second- and fourth-order schemes.

Table 2: Convergence properties for second-order discretization

Index	$Re = 10$			$Re = 300$		
	Iteration	Time (sec)	Residual	Iteration	Time (sec)	Residual
$n = 0.6$	28	3.555	4.93×10^{-6}	46	6.074	1.97×10^{-6}
$n = 0.8$	23	2.655	6.92×10^{-6}	36	4.244	1.73×10^{-6}
$n = 1.0$	16	2.011	7.98×10^{-6}	34	3.840	5.53×10^{-7}
$n = 1.2$	21	2.593	6.47×10^{-6}	27	3.383	7.96×10^{-7}
$n = 1.4$	23	2.812	1.04×10^{-5}	19	2.538	3.38×10^{-6}

Table 3: Convergence properties for fourth-order discretization

Index	$Re = 10$			$Re = 300$		
	Iteration	Time (sec)	Residual	Iteration	Time (sec)	Residual
$n = 0.6$	26	12.753	3.98×10^{-6}	43	20.722	1.41×10^{-6}
$n = 0.8$	18	8.972	4.43×10^{-6}	39	18.049	2.53×10^{-6}
$n = 1.0$	16	7.827	2.82×10^{-6}	33	15.402	2.45×10^{-6}
$n = 1.2$	18	9.011	5.67×10^{-6}	21	10.456	1.73×10^{-6}
$n = 1.4$	21	10.399	1.38×10^{-5}	18	9.576	8.35×10^{-6}

References

- [1] P.J. Oliveira, F.T. Pinho, G.A. Pinto. Numerical simulation of non-linear elastic flows with a general collocated finite-volume method. *Journal of Non-Newtonian Fluid Mechanics*, 79, 1–43, 1998.
- [2] A. Nejat, A. Jalali, M. Sharbatdar. A Newton-Krylov finite volume algorithm for the power-law non-Newtonian fluid flow using pseudo-compressibility technique. *Journal of Non-Newtonian Fluid Mechanics*, 166, 1158–1172, 2011.
- [3] C. Ollivier-Gooch, M. van Altena. A High-order Accurate Unstructured Mesh Finite-Volume Scheme for the Advection-Diffusion Equation. *Journal of Computational Physics*, 181, 729–752, 2002.
- [4] A. Jalali, M. Sharbatdar, C. Ollivier-Gooch. Accuracy analysis of unstructured finite volume discretization schemes for diffusive fluxes. *Computers and Fluids*, 101, 220–232, 2002.

P-ADAPTION FOR COMPRESSIBLE LAMINAR FLOW PROBLEMS USING A GOAL-BASED ERROR ESTIMATOR

D. Ekelschot*, D. Moxey, J. Peiró and S.J. Sherwin

Imperial College London, Department of Aeronautics, South Kensington Campus, London SW7 2AZ

*d.ekelschot12@imperial.ac.uk

ABSTRACT

High-order spectral/ hp element methods are known to be computationally expensive and ongoing research is performed to lower the computational cost. Goal-based error estimation is a technique that is used to drive mesh adaption to reduce the computational cost while preserving high accuracy in a pre-defined target quantity. This technique relies on the concept of duality in which an adjoint problem is derived from the governing equations. The solution to the adjoint problem represents the sensitivity to an infinitesimal perturbation on the target quantity and has been applied for the first time to typical computation fluid dynamics problems by [2]. A local error indicator is defined by taking the inner product of the residual and the corresponding adjoint variable. In this way, the residual is weighted and its contribution to the error in the target quantity is determined. Based on this error indicator, the mesh is refined by increasing the local polynomial order.

Key Words: *High-order spectral/ hp element methods, p -adaption, goal-based error estimation, compressible flow, adjoint methods*

1. Introduction

In this work, a continuous adjoint formulation for the compressible Navier-Stokes equations is presented that is used to perform goal-based error estimation and mesh refinement in the framework of high-order spectral/ hp element methods. Goal-based error estimators are interesting mesh refinement tools since they incorporate the underlying physics of the problem that is solved. The adjoint problem prescribes the sensitivity of the domain with respect to the quantity of interest and the local residual is weighted with the adjoint solution. In this way, we obtain an error indicator that can be used to adapt the mesh such that the target is approximated more accurately.

Adjoint-based mesh refinement techniques are particularly interesting for compressible flow problems due to the hyperbolic nature of the compressible Euler or Navier-Stokes equations. The flow field upstream has a domain of dependence and independence which is governed by the characteristics and their related invariants. Hence the quality of the solution at a given point is dependent on the quality of the solution in its corresponding domain of dependence which can be seen as a form of solution sensitivity. The adjoint solution allows us to subtract this sensitivity information to perform mesh refinement.

The adjoint solver and the p -refinement technique are implemented in Nektar++ which is a high-order spectral/ hp element library. Both the governing and adjoint problem are solved using a discontinuous Galerkin (DG) scheme. In this case, the solution at the interface between two elements is determined using a flux function and mapped back onto the local element which makes the handling of different polynomial orders within different elements relatively easy. For smooth enough solutions, adapting the polynomial order within the domain leads to an exponential rate of convergence rather than a linear rate when we would adapt in h .

2. Goal-based error estimation

Goal-based error estimation is a technique that relates the error in a pre-defined target functional to the local residual in the domain by using the concept of duality. The sensitivity of the state variables with respect to a given target functional follows from the solution to the derived adjoint problem.

The sensitivity, also referred to as the adjoint solution, tells us then how the value of the target functional will change when a small perturbation is added to the state solution at an arbitrary point in the domain. The solution to the adjoint problem is then used to weigh the local residual and determine a local error indicator which is used to drive a mesh refinement algorithm.

For aerodynamic problems a typical quantity of interest is the lift (C_l) or drag (C_d) coefficient. These coefficients are determined by integrating the pressure and shear forces over the surface of the body. This allows us to define the following target quantity,

$$j(\mathbf{u}) = \int_{\partial\Gamma_w} (p(\mathbf{u}) - \tau(\mathbf{u})) \mathbf{n} \cdot \boldsymbol{\theta} ds \quad (1)$$

where $\boldsymbol{\theta}$ is a force projection vector and when interested in drag or lift, this depends on the angle of attack and the side slip angle. The idea of goal-based error estimation is to determine the error in the target functional given in equation 1.

$$\epsilon = |j(\mathbf{u}) - j(\mathbf{u}_\delta)| \quad (2)$$

where $\mathbf{u} \in \Omega$ represents the exact solution to the governing equations. The discrete solution is defined as $\mathbf{u}_\delta \in \Omega_\delta$ where the subscript δ indicates the fineness of discretisation and incorporates both the mesh size and the approximation order within the element. Furthermore holds that $\Omega_\delta \subset \Omega$. Equation (2) represents a perturbation in the defined target quantity due to the discretisation of the problem. The aim is to relate the local residual or discretisation error in the domain to the error in target quantity defined in equation (2). For a discrete system this is written in the following way

$$\begin{aligned} \delta j &= j(\mathbf{u}) - j(\mathbf{u}_\delta) \\ &= \mathbf{z}_{\delta_e}^t \mathcal{R}(\mathbf{u}) - \mathbf{z}_{\delta_e}^t \mathcal{R}(\mathbf{u}_\delta) \\ &= \mathbf{z}_{\delta_e}^t \mathcal{R}(\mathbf{u}_\delta) \end{aligned} \quad (3)$$

Where $\mathcal{R}(\mathbf{u})$ represents the conservation laws that we are interested in, which in this case are the compressible Navier-Stokes equations. For the exact solution to Navier-Stokes equations holds $\mathcal{R}(\mathbf{u}) = 0$. The exact and approximate target functional are represented by $j(\mathbf{u})$ and $j(\mathbf{u}_\delta)$ respectively. The vector \mathbf{z}_{δ_e} represents the weights that are given to the local residual and serves as an indication of the impact of the local solution on the target quantity. Hence, based on the analogy given in equation (3), a set of continuous equations is sought that prescribe \mathbf{z} which is done using the concept of duality.

The continuous adjoint equations

A continuous form of the relation given in equation (3) is found by linearising both the Navier-Stokes equations and the target function around \mathbf{u} . Assuming that $j(\mathbf{u})$ and $\mathcal{R}(\mathbf{u})$ are differentiable

$$j_{\mathbf{u}}(\mathbf{u}') = - \int_{\Omega} \mathbf{z}^t \mathcal{R}_{\mathbf{u}}(\mathbf{u}') d\Omega \quad (4)$$

where the subscript \mathbf{u} represents the linearisation with respect to \mathbf{u} and \mathbf{u}' represents a small perturbation \mathbf{u} . Equation (4) corresponds to what is given in equation (3) where the linearised target functional is given by

$$j_{\mathbf{u}}(\mathbf{u}') = \int_{\Gamma_w} \mathbf{u}' \{ (p_{\mathbf{u}} - \tau_{\mathbf{u}}) \mathbf{n} \cdot \boldsymbol{\theta} \} ds \quad (5)$$

where \mathbf{u}' represents the small perturbation on \mathbf{u} . and $\mathcal{R}_{\mathbf{u}}(\mathbf{u}')$ represents the linearised steady Navier-Stokes operator.

$$\mathcal{R}_{\mathbf{u}}(\mathbf{u}') = \nabla \cdot \left((\mathbf{A}_c - \mathbf{A}_v) \mathbf{u}' - \tilde{\mathbf{A}}_v \nabla \mathbf{u}' \right) \quad (6)$$

where the jacobian matrices of the convective and viscous fluxes corresponding the direction i are given by

$$\mathbf{A}_{c_i} = \frac{\partial \mathbf{f}_i^c}{\partial \mathbf{u}}, \quad \mathbf{A}_{v_i} = \frac{\partial \mathbf{f}_i^v}{\partial \mathbf{u}}, \quad \tilde{\mathbf{A}}_{v_{i,j}} = \frac{\partial \mathbf{f}_i^v}{\partial (\partial_j \mathbf{u})}, \quad i, j = 1, 2, 3 \quad (7)$$

Applying integration by parts on the right hand side term of equation 4 results in a set of equations dependent on \mathbf{z} instead of \mathbf{u} . Using the definition of the adjoint operator

$$\int_{\Omega} \mathbf{z}^t \mathcal{R}_{\mathbf{u}}(\mathbf{u}') d\Omega = \int_{\Omega} (\mathbf{u}')^t \mathcal{R}_{\mathbf{u}}^*(\mathbf{z}) d\Omega \quad (8)$$

we find the adjoint operator $\mathcal{R}_{\mathbf{u}}^*(\mathbf{z})$ for the linearised Navier-Stokes operator $\mathcal{R}_{\mathbf{u}}(\mathbf{u})$ that is dependent on \mathbf{z} instead of \mathbf{u} . The volumetric and boundary integrals are matched and the following dual problem is determined. The target functional is only defined at the wall, hence the volume integral of the adjoint equations will be equal to zero. The continuous adjoint equations are given by

$$-(\mathbf{A}_c^t - \mathbf{A}_v^t) \cdot \nabla \mathbf{z} - \nabla \cdot (\tilde{\mathbf{A}}_v^t \nabla \mathbf{z}) = 0 \quad \text{on } \Omega \quad (9)$$

The adjoint problem is driven by the wall boundary term, hence the adjoint wall boundary conditions become

$$\begin{aligned} \tilde{\mathbf{A}}_v^t \nabla \mathbf{z} \cdot \mathbf{n} + ((\mathbf{A}_c^t - \mathbf{A}_v^t) \cdot \mathbf{n}) \mathbf{z} &= (p_{\mathbf{u}} - \tau_{\mathbf{u}}) \mathbf{n} \cdot \boldsymbol{\theta} \quad \text{on } \Gamma_w \\ (\tilde{\mathbf{A}}_v^t \cdot \mathbf{n}) \mathbf{z} &= 0 \quad \text{on } \Gamma_w \end{aligned} \quad (10)$$

for any other boundary we have

$$\begin{aligned} \tilde{\mathbf{A}}_v^t \nabla \mathbf{z} \cdot \mathbf{n} + ((\mathbf{A}_c^t - \mathbf{A}_v^t) \cdot \mathbf{n}) \mathbf{z} &= 0 \quad \text{on } \Gamma \neq \Gamma_w \\ (\tilde{\mathbf{A}}_v^t \cdot \mathbf{n}) \mathbf{z} &= 0 \quad \text{on } \Gamma \neq \Gamma_w \end{aligned} \quad (11)$$

By expressing the equations in terms of the primitive variable $\tilde{\mathbf{u}} = [\rho, u, v, w, p]^t$, the linearisation process of the diffusive fluxes becomes more straightforward. The adjoint solver that obtains the solution to the adjoint problem stated above has been successfully implemented in the Nektar++ library for both the compressible Euler and Navier-Stokes equations.

Numerical example

As an initial test case, we consider 2D subsonic ($M=0.4$) inviscid flow past a NACA0012 wing profile at an angle of incidence of 5° . We are interested in the sensitivity of the domain with respect to the lift, hence the lift coefficient is the target quantity in this example. The goal-based error estimation procedure will give us an indication of the error in C_l and this information can be used to define a local element wise error indicator which drives the p -adaptive algorithm. In figure 1 an example is shown of the x -momentum adjoint solution and a new p -distribution based on the goal-based error estimator. Using this procedure we were able to reduce the error in C_l by one order of magnitude with an addition of 10% in degrees of freedom.

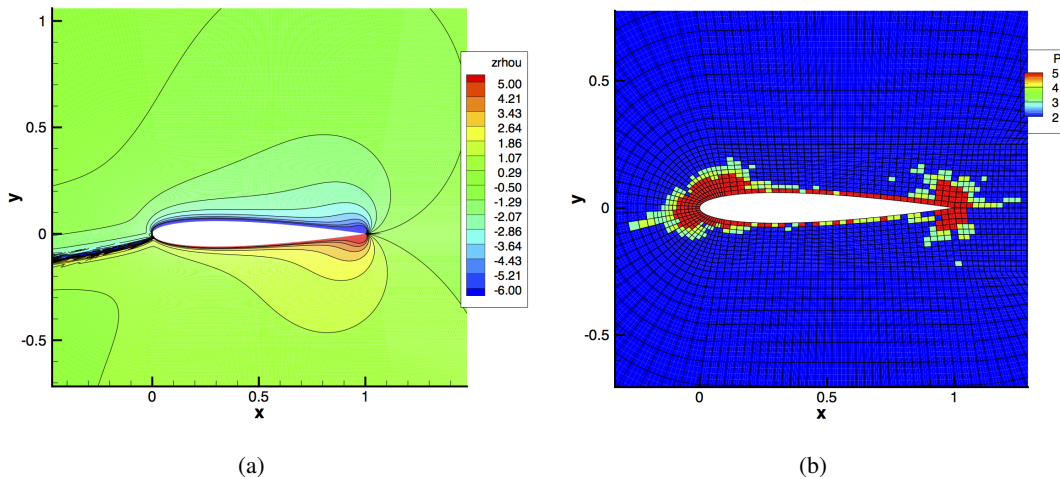


Figure 1: **a** The adjoint solution corresponding the x -momentum. **b** An example of the new p -distribution based on the goal-based error estimator.

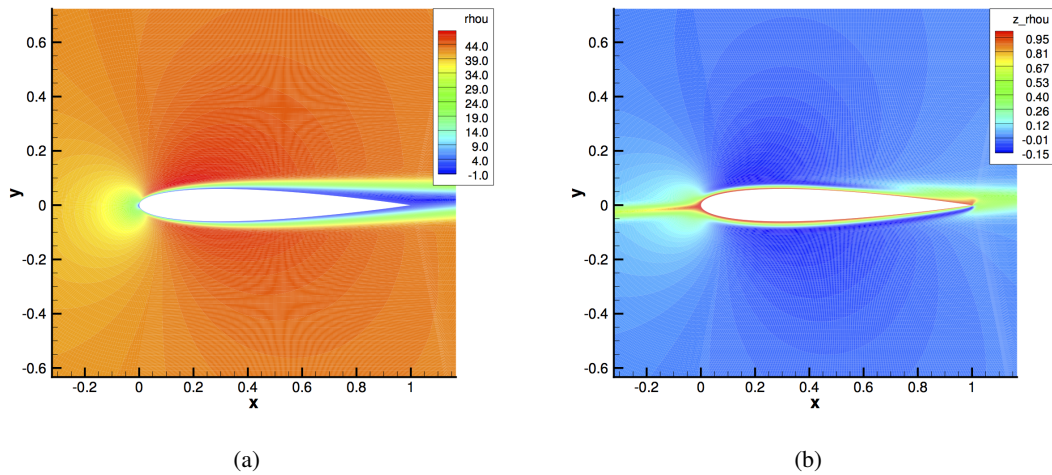


Figure 2: **a** The x-momentum solution for the governing equations. **b** The adjoint solution for the x-momentum variable

The adjoint solver for the compressible Navier-Stokes equations has been successfully implemented and we are expecting to obtain similar results. As a numerical example, we will present the test case of subsonic laminar flow ($M = 0.1$, $Re = 5000$) past a NACA0012 wing profile at an angle of incidence of 2° . For this particular test case, the quantity of interest is the drag coefficient, C_d , and the application of the goal-based error estimator driving the p -adaptive algorithm is demonstrated. In figure 2, the solution to the governing and adjoint equations is given for this particular test case.

Conclusions

The application of goal-based error estimation for p -adaptation has been successfully applied to compressible inviscid flow problems. Furthermore, the adjoint solver is now able to solve for compressible laminar flow problems as well which enables us to apply the same p -adaptive algorithm as shown in the numerical example of the inviscid test case and results will be presented during the conference. Nektar++ is able to deal with unstructured 2D and 3D meshes and therefore the aim for the future is to extend and test the adjoint solver in 3D and to apply this technique to a complex three-dimensional geometry.

Acknowledgements

This work has been carried out in the framework of the Advances in Numerical and Analytical tools for DETached (ANADE) project which is funded under the European Commission' Seventh Framework Programme (FP7) within People work programme (Marie Curie actions).

References

- [1] K.J. Fidkowski and D.L. Darmofal. Review of Output-Based Error Estimation and Mesh Adaptation in Computational Fluid Dynamics *AIAA Journal*, 49(4), pp 573-694, 2011.
- [2] M.B. Giles and N.A. Pierce. Adjoint equations in CFD: duality, boundary conditions and solution behaviour. *AIAA Paper 97-1850*, 1997.
- [3] G.E. Karniadakis and S.J. Sherwin. Spectral/hp Element Methods for CFD. *Oxford University Press*, 1999.

FLUID DYNAMICS 3

CONTROL OF SEAWATER INTRUSION USING AQUIFER STORAGE AND RECOVERY (ASR) TECHNIQUE

*Mohammed S. Hussain, Akbar A. Javadi and Reza Naseri-Karim-Vand

Department of Engineering, University of Exeter, Exeter, EX4 4QF, UK

*msh218@exeter.ac.uk

ABSTRACT

In this paper the Aquifer Storage and Recovery (ASR) is used to control saltwater intrusion in coastal aquifer systems. The study is conducted on Wadi Ham aquifer in the UAE simulated numerically with SUTRA-finite element code in 3D. The aquifer is under continuous pumping of water from an available production well located close to the coastline that intensifies the inland encroachment of saltwater. The transient responses of saltwater intrusion are simulated over a ten year period in two different scenarios with and without management actions. The proposed management measure (ASR) is implemented in repeated cycles of artificial recharge, storage and recovery using an additional set of wells defined in the model. The results show that ASR is a reliable method in controlling saltwater intrusion in coastal aquifer systems besides its conventional role in subsurface water banking.

Keywords: seawater intrusion; coastal aquifer; artificial recharge; groundwater; ASR

1. Introduction

Aquifer storage recovery is a technique introduced by Cederstrom [3] and has been widely used in developed countries for management of water resources as an alternative to surface storage of water such as dams and reservoirs. The methodology involves continuous storage of excess water by deep injection through recharge wells into deep aquifer or other water-bearing formations, when water is available or during the wet and low demand season of the year. The stored water is then recovered when needed using the same wells to meet the water demand of the community and during the next dry or high demand season of the year [7]. Depending on quality and level of contamination of the native groundwater in the aquifer and also the quality of the recharge water, the recovered water may be required to pass a short treatment process before use.

The ASR process is repeated continuously during the years depending on the levels of water scarcity. These repeated cycles of recharge and abstraction also contribute to improvement of water quality [4]. Typically, the volume of the extracted water is less than injected water and the buffer zone with marginal quality created by unrecoverable fraction amount of water helps controlling the inland advancement of saltwater wedge [6]. Therefore, ASR can be considered as one of management options to control seawater intrusion rather than its other positive role in water production/demand issues and maintaining the seasonal fluctuation in groundwater storage. Misut and Voss [6] investigated the beneficial aspects of ASR in controlling seawater intrusion by defining a series of ASR wells in different confined/unconfined aquifers of regional case study in USA.

Recovery efficiency is another specific term in ASR process. It is defined as total volume of recovered water as percentage of volume stored in each of this operating cycle while satisfying a target water quality criterion in the abstracted water [7]. The enhancement of recovery efficiency achieved by ASR in Wadi Ham aquifer in the UAE has been reported by Sherif and Shetty [4] using a numerical experiment approach. The impacts of different hydrological factors on recovery efficiency also have been assessed by Lowry and Anderson [2] through a set of parametric studies.

The objective of the current research was to numerically investigate the effects of ASR on controlling of seawater intrusion progress in Wadi Ham aquifer (in UAE). This study presents a 3D simulation of this aquifer that helps to illustrate the growth pattern of dispersive intruded saltwater wedge.

2. Study Area and Simulation Model

The study area is the lower alluvial plain of Wadi Ham catchment located in Fujairah emirate in the UAE. The area generally consists of recent Pleistocene Wadi gravels underlined by the fractured ophiolite rocks (Semail ophiolite). Figure 1 shows the domain of Wadi Ham aquifer with the total area of 80.26 km² and the available hydrological/natural features and also the boundary conditions used in its numerical modelling. Hydrostatic pressure boundary condition with a constant head at the mean seawater level is used to define the coastline of gulf of Oman. The model is calibrated based the available groundwater-level measurements in 8 observation boreholes (marked on figure 1) for two different stress periods from year 1988 to year 1993 and from year 1993 to year 2005. By considering the data of the year 1988 as initial condition, and by defining an appropriate permeability field obtained by trails as parameter calibration, a good match between the calculated and the observed water levels are obtained for the years 1993 and 2005. Further details about the hydrogeological setting of the study area can be found in Sherif et al. [5].

The system was simulated using the finite element-based model called SUTRA (Saturated-Unsaturated TRAnsport [1]).The numerical mesh was discretized into 48160 elements and 55990 nodes. 65m and 6.5m are used for longitudinal dispersivity [m] in horizontal and vertical directions of flow respectively with 0.65m for transverse dispersivity. Moreover, the total dissolved solids (TDS) of groundwater and inflow water is 250 mg/l. 35700 mg/l and 100 mg/l are assigned to be the salinity seawater and rainwater respectively.

By maintaining the boundary conditions and also the pumping rates, from Sharaah and Kalbha wellfields, for the next 10 years of simulation period, the current condition of the flow and salinity for the year 2015 is obtained. In order to assess and compare the future advancement of the saltwater in year 2025, the current model has been subjected to two different scenarios. In the first scenario the all boundary conditions and pumping rates are kept unchanged during the simulation period. And, in the second scenario a hypothetical ASR system (using five wells ASR#1, ASR#2,...and ASR#5) is defined in southern part of the model as an additional feature to countermeasure and control saltwater intrusion (Figure 1).

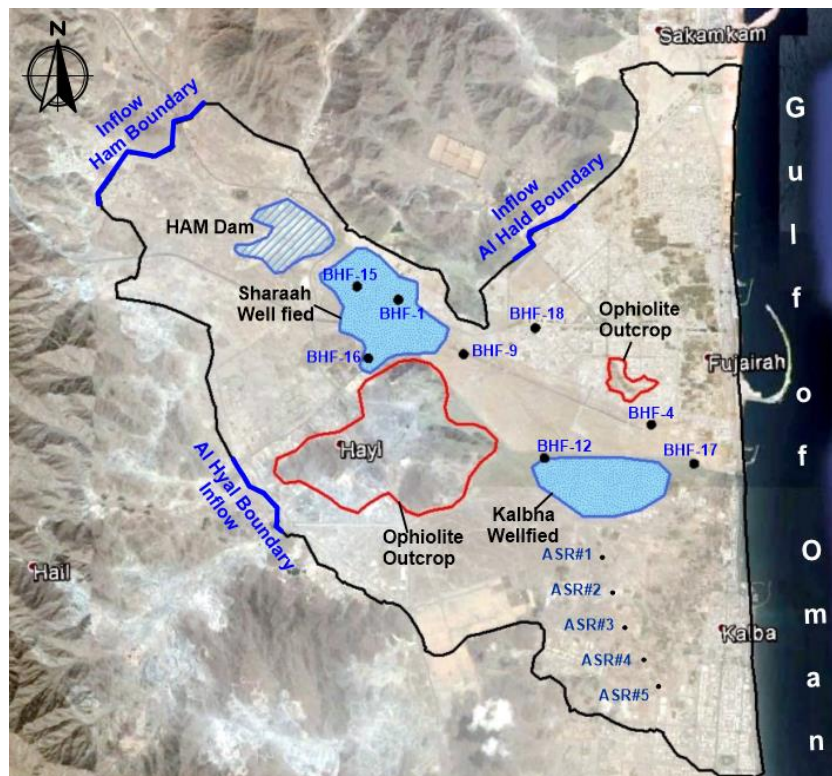


Figure 1: Study area and the used boundary conditions.

3. Results and Discussion

In year 2015, the inland advance of 50% isochlor measured at the aquifer bottom floor from the seaside, is 1650m. The value is calculated along an arbitrary horizontal section passing through Kalbha pumping field at UTM-Northing coordinate 2776000 m. In the first scenario, the flow and salinity distribution of the year 2025 is obtained by maintaining the current hydrological settings for the next 10 years, indicating a further inland progression of saltwater. In the second scenario, the ASR system involving five hypothetical wells is considered in front of the current intruded saltwater wedge. Each of these recharge/recovery wells has been subjected to two full cycles of recharge, pause (storage) and recovery per year; with a time span of the 75 days for each of recharge and abstraction stages and 32 days for storage stage. Injection and recovery rates of 2000 m³/day are applied in each of ASR wells to guarantee the 100% recovery efficiency. The TDS of the injected water is assumed to be 150 mg/l.

The 10%, 50% and 90% iso-salinity contours of these two scenarios along the base layer of the model are illustrated in Figure 2. The projections of ASR wells' locations are also presented on this XY plane. In the “no management” scenario (first scenario), the system experiences a further intrusion of 100 m of 50% iso-concentration line compared to the results of the year 2015, measured on x-x section. The positive role of ASR system to control saltwater intrusion is more pronounced in the second scenario by recording about 170 m push back effect on the horizontal location of 50% isochlor measured with respect to the simulated value in the first scenario and on same x-x section. Generally, the low concentration lines (less than 10%) are more sensitive to recharge and abstraction events of ASR process.

The raising and lowering of the hydraulic head in each cycles of ASR is followed by the variations of salinity (TDS) in the location of the inserted wells and consequently in the entire aquifer. Figure 3 shows the overall progress of these repeated cycles during the simulation period in ASR#1 and ASR#5 wells. By recharging the aquifer in the first cycle the amount of salinity in the location of wells are significantly reduced due to mixing of the injected water with the ambient water, implying the improvement of water quality. In contrast, during the storage and abstraction phases of the process, the solute starts to progress toward the wells and therefore the salinity levels are partially reversed. The bandwidths of the corresponding repeated cycles decrease with the time and almost become equilibrium at the end.

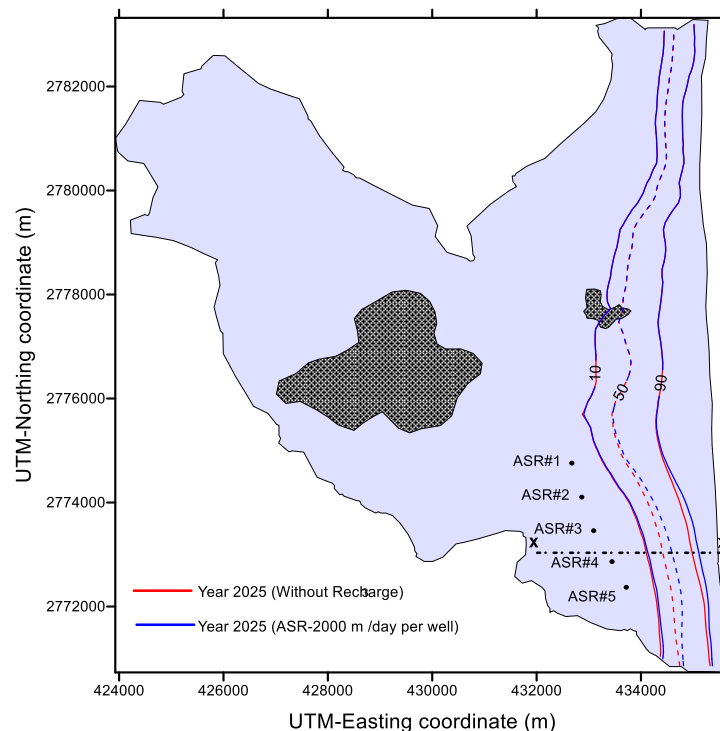


Figure 2: Inland progress of iso-concentration lines across the base of aquifer in XY plane

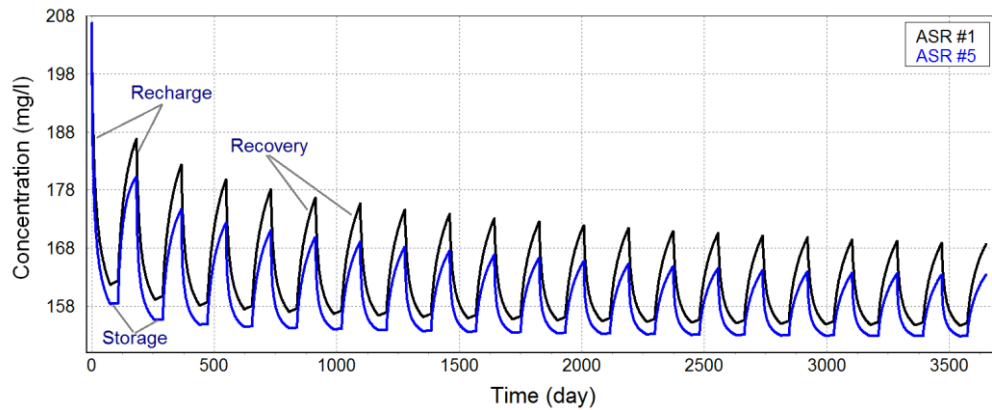


Figure 3: Variation of TDS level during ASR cycles

In large scale assessments, these repeating cycles of ASR process are simultaneously associated with seaward landward advancements of intruded saltwater wedge. And, the overall response of Wadi Ham aquifer to the mentioned gradual enhancement of water quality is positive. Where, and even though the system is under continues pumping from the two local wellfields, the ASR succeeds to control the seawater intrusion by keeping the freshwater/saltwater interface back to the seaward direction. However, the ASR, and like any other management strategy, has some limitation and its implementation needs further attention. For instance, the high rates of mixing of injected water with the poor native groundwater quality tend to reduce the total recoverable volume of freshwater (recovery efficiency).

4. Conclusions

A numerical simulation was performed to outline the effects of ASR system, as a management policy, on inland advancement of saline water in the Wadi Ham aquifer (in UAE). It has been shown that a considerable reduction in salinity levels occurs in areas surrounding the system owing to application of ASR-management scenario. The deep confined or unconfined aquifers have been typically documented to be used for long term underground storage of the injected water. However, and in order to benefit from excess surface water presence during the intense rain events in the study area, ASR system can be followed to control saltwater intrusion in this unconfined aquifer with a relatively shallow hydrogeological setting (Wadi Ham aquifer).

References

- [1] C.I. Voss and A.M. Provost. SUTRA-A model for saturated-unsaturated variable-density ground-water flow with solute or energy transport. *U.S. Geological Survey (USGS), Water Resources Investigation*, p. 300, 2010.
- [2] C.S. Lowry and M.P. Anderson. An assessment of aquifer storage recovery using ground water flow models. *Ground Water*, **44**(5), 661–667, 2006.
- [3] D.J. Cederstrom. Artificial recharge of a brackish water well. *The Commonwealth, Virginia Chamber Commerce*, **14**(12), 71-73, 1947.
- [4] M.M. Sherif and A. Shetty. Freshwater storage in brackish aquifers, *Proceedings of World Environmental and Water Resources Congress, EWRI, Cincinnati, Ohio*, 2013.
- [5] M. Sherif, A. Kacimov, A. Javadi and A. Ebraheem. Modeling Groundwater Flow and Seawater Intrusion in the Coastal Aquifer of Wadi Ham, UAE. *Water Resour Manage*, **26**(3),751-774,2012.
- [6] P.E., Misut and C.I. Voss. Freshwater–saltwater transition zone movement during aquifer storage and recovery cycles in Brooklyn and Queens, New York City, USA. *Journal of Hydrology*, **337**, 87-103,2007.
- [7] R.D.G. Pyne. *Groundwater recharge and wells: a guide to aquifer storage recovery*. Lewis Publishers, Boca Raton, Florida, 375 pp, 1995.

CFD Analysis of High Rise Unconventional Buildings Subject to Extreme Wind Loading

*M. Abdul Latif, Y. T. Feng

Zienkiewicz Centre for Computational Engineering, Swansea University, Singleton Park, Swansea, SA2 8PP
*744973@swansea.ac.uk , y.feng@swansea.ac.uk

ABSTRACT

The current work aims to establish a CFD based computational simulation framework for modelling a group of irregular shaped high rise buildings subject to extreme wind loading conditions, in order to replace the demand and code requirements on wind tunnel testing in design of high rise buildings. At this stage, a series of 2D CFD models, corresponding to the plan views of the model buildings at different heights but under the same scale and loading conditions as used for a wind tunnel test, are analysed first. In particular, the applicability and limitations of the layered 2D models are assessed in terms of computational costs and solution accuracy. At the next stage, the validated numerical model and procedure are applied to the full scale of the buildings under real scenarios. Finally, the simulated worst wind pressures exerted to the buildings will be utilised as the static loading for the stress analysis of the buildings.

Keywords: Computational fluid dynamics; High rise buildings; Extreme wind load

1. Introduction

In the design process of almost every high rise structure, or structure with an unconventional (irregular) shape, a wind tunnel test must be performed in order to analyse wind behaviour on the structure in a way that cannot be determined using conventional structural engineering software and building codes (Eurocode and ASCE). Building codes cannot accommodate all shapes, sizes and topography of structures [1]; therefore, as per the ASCE, wind tunnel tests are required if:

1. The building is not regularly shaped;
2. The building is subject to either across wind loading, vortex shedding, and instability due to galloping or flutter or has a site location which channels effects of buffeting in the wake of upwind obstructions.

It is apparent that any high rise structure will undergo at least one of the mentioned wind phenomena, and therefore a wind tunnel test is required for the design of high rise structures.



Figure 1: Wind tunnel test [1]

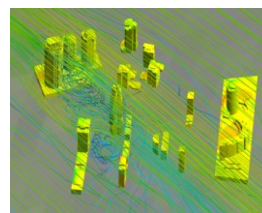
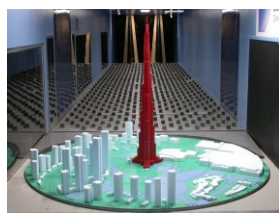
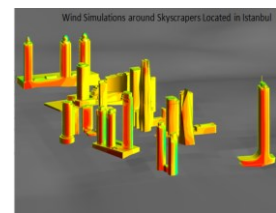


Figure 2: CFD modelling of wind flow fields and pressure distributions on the buildings [2]



With the development of advanced computational techniques, computational fluid dynamics (CFD) can provide results almost as accurate as or even better than wind tunnel tests. Some of the advantages of using CFD over wind tunnel testing include [3]:

1. Full domain analysis - wind tunnel tests require instruments to record the wind speed at each discrete point, while CFD computes these variables throughout the whole domain.
2. Easy alternative analysis – the structure can be easily modified in the CFD domain and remodelled. Physical models require more effort for adjustments.
3. Cost efficiency – CFD have same or lower costs
4. Better visualization of results – CFD results are displayed in a user friendly graphical output, unlike wind tunnel photographs

2. Flow past a circular cylinder

The flow past a circular cylinder will be analysed under different values for the Reynolds number. A circular domain is used for this simulation. The outer boundary is set to 64 times as large as the diameter of the cylinder, since the effects that the cylinder has on the flow extend far. The left half of the outer boundary is set as a velocity inlet. The right half of the outer boundary is set as a pressure outlet with a gauge pressure of 0 Pa. Finally, the cylinder wall is set as a wall, with a no slip boundary condition. Figure 3 is a representation of the boundary conditions and the mesh used to model the structure. The total number of elements in the mesh is approximately 18,400.

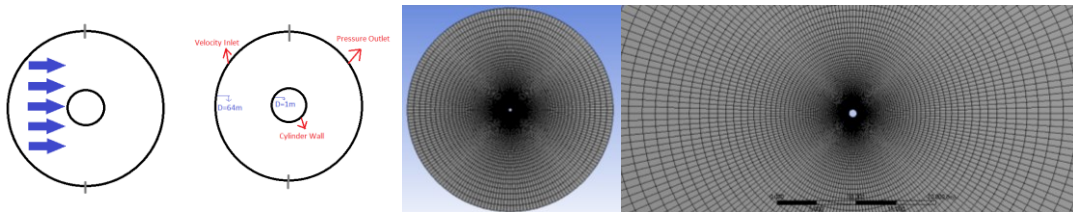


Figure 3: Mesh for circular cylinder

The velocity and vorticity magnitude is analysed for different Reynolds numbers in order to display the behaviour of the fluid flow past the cylinder. From the analysis it was apparent that the flow goes through a number of transitions; ideal, separated, laminar and turbulent.

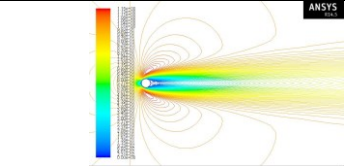
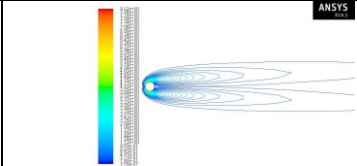
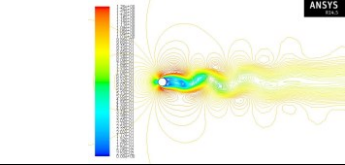
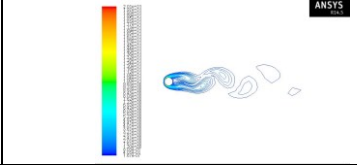
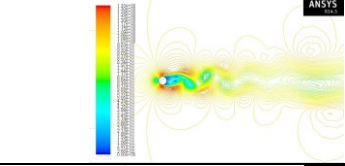
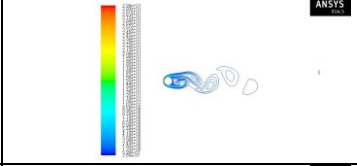
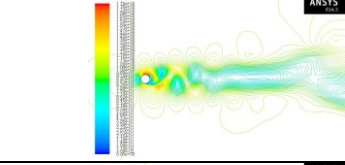
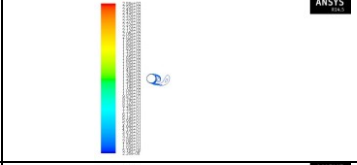
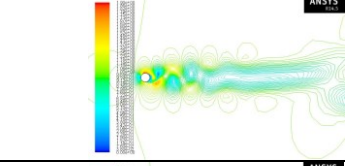
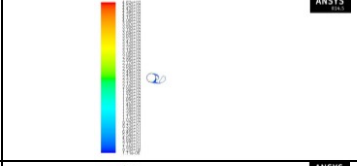
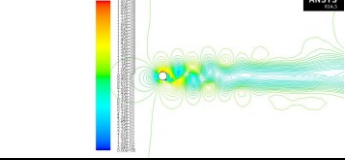
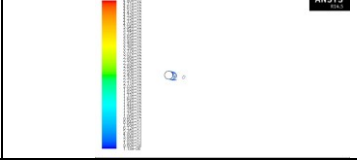
Table 1 displays the velocity magnitude and the vorticity magnitude of the flow past the cylinder for different Reynolds numbers. The phenomenon described for the different behaviour is clearly apparent for the flow. Firstly, for Reynolds number less than 5, the flow is ideal, where there is completely attached flow (no separation) and no viscous wake downstream of the cylinder. Secondly, when Reynolds number is between 5 and 40, the flow is separated, but steady. A pair of vortices is formed on the downside of the cylinder. When Reynolds number is between 40 and 150, a vortex street is formed with laminar properties. As Reynolds number increases to 300, it was found that the flow is a separated laminar flow. In other words, the flow on the leeward side of the cylinder is laminar, and on the windward side there is a chaotic wake. For Reynolds number greater than 300,000 it was found that the flow is turbulent and the vortices are shed in a turbulent wake form of the body.

Next, the drag coefficient for the different Reynolds numbers is obtained and plotted. The results are compared to the results obtained by Lindsey [4], for the flow past a cylinder. The results displayed showed similarity for low Reynolds number; however, for higher Reynolds number, there was an apparent difference in the empirical results by W Lindsey, and from the results obtained using the model on Fluent. It was found for Reynolds number between 1,000 and 10,000, the drag coefficient is approximately 1.2. At higher Reynolds number, the behaviour of the drag coefficient is similar to the empirical results but numerically different. These results validate the model and therefore, the same model is used to simulate the behaviour of flow past a rectangular cylinder. The drag coefficient for the rectangular cylinder is found to be higher than the drag coefficient for the circular cylinder, for all values of Reynolds number. Figure 4 is a plot of the drag coefficient for different Reynolds number for the flow past a circular cylinder, flow past a rectangular cylinder, and the results obtained from Lindsey [4].

3. Flow past structures

Since the models for the flow past cylinders were validated, the flow past structures can be analysed under different wind loading conditions, using the same models. Table 2 is a representation of a high rise structure in 2D subject to the design wind speed of 45 m/s and extreme wind speed of 200 m/s. the vortices and wind velocity magnitude are displayed. A top view representation of the flow around a dense medium of structures is also displayed.

Table 1: Flow past cylinder for different Reynolds number

Reynolds Number	Velocity magnitude	Vorticity magnitude
$5 < R_d < 40$		
$40 < R_d < 150$		
$150 < R_d < 300$		
$300 < R_d < 3 \cdot 10^5$		
$3 \cdot 10^5 < R_d < 3.5 \cdot 10^6$		
$3.5 \cdot 10^6 < R_d$		

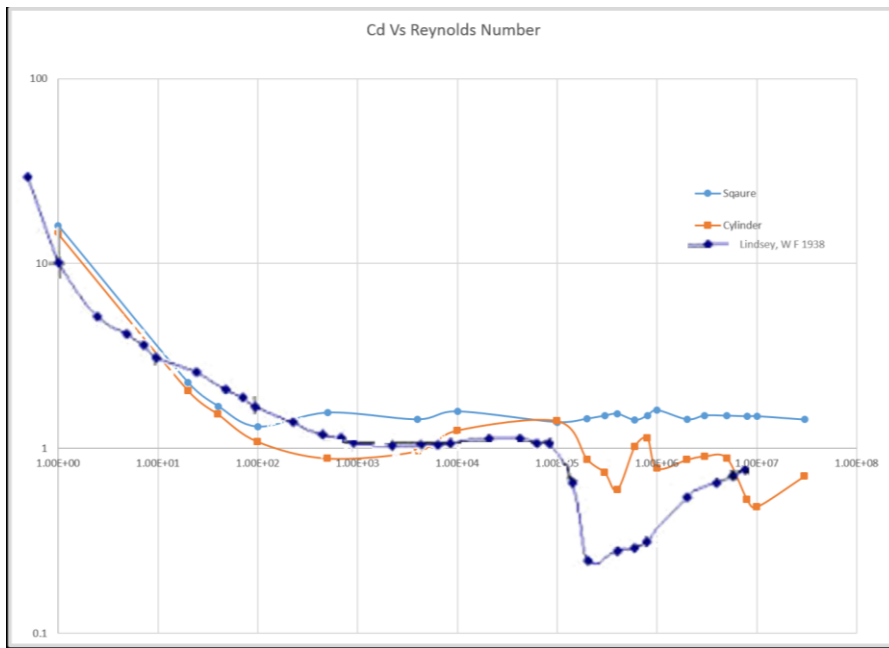
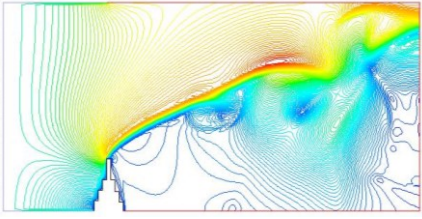
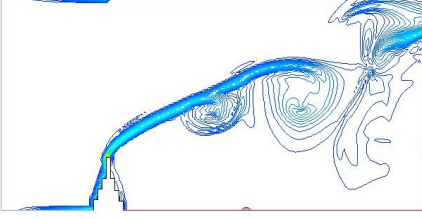
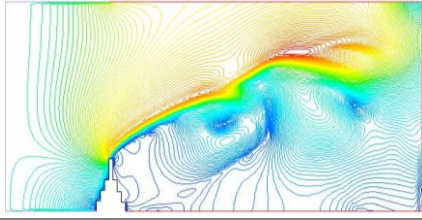
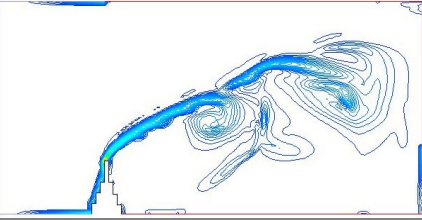
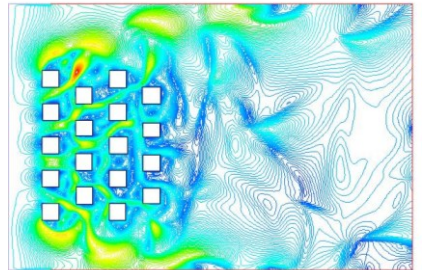
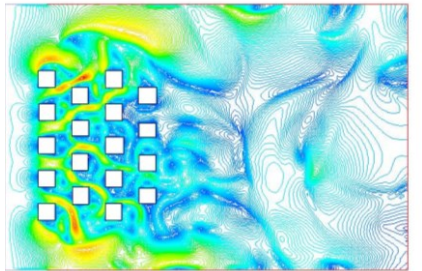
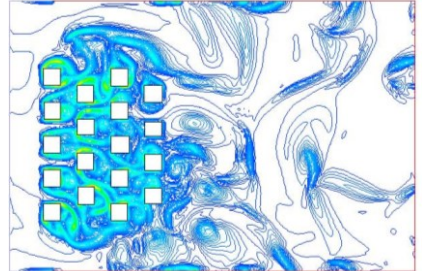


Figure 4: Cd vs Reynolds Number

Table 2: Flow past structures

		Velocity Magnitude	Vorticity Magnitude
High rise irregular structure	45 m/s		
	200 m/s		
Dense group of buildings	45 m/s		
	200 m/s		

4. Conclusion

The current work aims to establish a CFD based computational simulation framework. Initially, the flow past a circular cylinder is modelled, since the flow past structures are modelled in the same way. The drag coefficient for the flow past the cylinder for a series of different Reynolds number is obtained and compared to empirical results previously conducted. This is done as a benchmark test to validate the model. Once the model is validated, the flow past a 2D irregular high rise structure is analysed under two different loading conditions. Also, the flow past an urban dense group of buildings, in the plan view, is analysed.

References

- [1] <http://www.sefindia.org/forum/viewtopic.php?p=53531>
- [2] "Finite Element Analysis (FEA) Services & Consultancy." *Finite Element Analysis FEA Services Consultancy*. Web. 5 Dec. 2014. <<http://www.nodeng.co.uk/building-aerodynamics/>>.
- [3] Lindsey, W. F. "Drag of Cylinders of Simple Shapes." Report NO. 619 (1937). National Advisory Committee for Aeronautics. Web. <<http://naca.central.cranfield.ac.uk/reports/1938/naca-report-619.pdf>>.
- [4] McAlpine, J.D. "Computational Fluid Dynamics or Wind Tunnel Modelling?" *Envirometrics, Inc.* Web.

EXPLOITING A HIGHER-ORDER COMPRESSIBLE FLOW SOLVER FOR INCOMPRESSIBLE FLOWS

*Alireza Jalali, Mahkame Sharbatdar and Carl Ollivier-Gooch

Department of Mechanical Engineering, University of British Columbia, Vancouver, BC, V6T 1Z4,
 Canada

*arjalali@interchange.ubc.ca

ABSTRACT

In this paper, we present the steps required for exploiting a higher-order compressible flow solver for incompressible fluids. This flow solver works based on a higher-order least-squares solution reconstruction for primitive variables. Also, implicit time advance scheme with local time-stepping is used to obtain a fast and efficient convergence to the steady-state solutions. Our results demonstrate the effectiveness of higher-order methods.

Key Words: higher-order; finite-volume; unstructured; incompressible fluids; pseudo-compressibility

1. Introduction

Computational Fluid Dynamics (CFD) is a practical tool in the analysis of flow fields with complex geometries. The accuracy of a numerical solution is mainly dependent on mesh size and the order by which PDEs are discretized. One route to improve the numerical accuracy of CFD simulations is increasing the order of accuracy. The development of accurate and efficient higher-order solvers is a common practice in the context of compressible flows and has a long history within that framework. Ollivier-Gooch *et al.* [1] described the process of constructing a higher-order finite volume solver for compressible flows. In this paper, we present the steps required for exploiting such a flow solver for incompressible fluids. Considering that nearly all commercial CFD solvers use second-order finite volume methods, the development of a higher-order finite volume solver provides an easier transition to the world of higher-order for existing software and preserves the effort that has been put into developing previous solvers. In particular, we are interested in unstructured meshes, which offer more flexibility in refinement and adaptation for complex geometries.

2. Governing Equations

To simulate the incompressible fluid flows, we need to solve the continuity and Navier-Stokes equations. Assuming incompressible flows, these equations can be written in the conservative form as:

$$\begin{aligned} \frac{\partial u}{\partial x} + \frac{\partial v}{\partial y} &= 0 \\ \frac{\partial u}{\partial t} + \frac{\partial u^2}{\partial x} + \frac{\partial uv}{\partial y} &= -\frac{\partial P}{\partial x} + \frac{1}{Re} \left(\frac{\partial}{\partial x} \left(2 \frac{\partial u}{\partial x} \right) + \frac{\partial}{\partial y} \left(\frac{\partial u}{\partial y} + \frac{\partial v}{\partial x} \right) \right) \\ \frac{\partial v}{\partial t} + \frac{\partial uv}{\partial x} + \frac{\partial v^2}{\partial y} &= -\frac{\partial P}{\partial y} + \frac{1}{Re} \left(\frac{\partial}{\partial x} \left(\frac{\partial u}{\partial y} + \frac{\partial v}{\partial x} \right) + \frac{\partial}{\partial y} \left(2 \frac{\partial v}{\partial y} \right) \right) \end{aligned} \quad (1)$$

As opposed to compressible flows, the continuity and the momentum equations are decoupled for an incompressible fluid since the time derivative of density is not present in the continuity equation. One way to deal with this issue is the use of staggered grids; however, this requires a high level of sophistications for unstructured meshes. On the other hand, we can use the pseudo-compressibility technique [2] to add an unphysical time derivative of pressure to the continuity equation in the form of:

$$\beta \frac{\partial P}{\partial t} + \frac{\partial u}{\partial x} + \frac{\partial v}{\partial y} = 0 \quad (2)$$

where β is the pseudo-compressibility factor.

3. Spatial Discretization

To discretize the flow equations using the finite volume methods, the governing equations should be recast in fully conservative form as:

$$\frac{\partial U}{\partial t} + \nabla \cdot (\vec{F}_c - \vec{F}_v) = 0 \quad (3)$$

Integrating Equation 3 over an arbitrary control volume and using the divergence theorem, the finite volume formulation of the governing equation is written as:

$$\frac{d\bar{U}_i}{dt} + \frac{1}{A_i} \oint_{CS_i} (\vec{F}_c^n - \vec{F}_v^n) ds = 0 \quad (4)$$

where

$$\vec{U} = \begin{pmatrix} P \\ u \\ v \end{pmatrix}, \quad \vec{F}_c^n = \begin{pmatrix} (u\hat{n}_x + v\hat{n}_y)/\beta \\ (u^2 + p)\hat{n}_x + uv\hat{n}_y \\ uv\hat{n}_x + (v^2 + p)\hat{n}_y \end{pmatrix}, \quad \vec{F}_v^n = \frac{1}{Re} \begin{pmatrix} 0 \\ 2\frac{\partial u}{\partial x}\hat{n}_x + \left(\frac{\partial u}{\partial y} + \frac{\partial v}{\partial x}\right)\hat{n}_y \\ \left(\frac{\partial u}{\partial y} + \frac{\partial v}{\partial x}\right)\hat{n}_x + 2\frac{\partial v}{\partial y}\hat{n}_y \end{pmatrix} \quad (5)$$

The flux integral can be evaluated by numerical integration over the faces of each control volume. To have a higher-order estimate of the normal fluxes, the primitive variables are reconstructed by a piecewise polynomial about the control volume's reference point. The polynomial is obtained by solving a least-squares system such that the conservation of mean is satisfied within a control volume and the error in predicting the mean values of the neighboring control volumes is minimized [3]. Boundary conditions can be also be enforced as extra constraints in the LS system. Ultimately, the flux vectors are computed by applying a flux function to the two fluxes computed on each side of an interface. We use central flux function for convective fluxes and add a solution jump term to the averaged components of the gradients for the viscous fluxes [4].

4. Solution Method

To obtain the steady-state solution, we use the backward implicit time-stepping:

$$\frac{\bar{U}^{n+1} - \bar{U}^n}{\Delta t} = -R(\bar{U}^{n+1}) \quad (6)$$

where $R(\bar{U})$ is the flux integral in Equation 4. The right hand-side can be linearized about the state \bar{U}^n :

$$\left(\frac{I}{\Delta t_i} + \frac{\partial R}{\partial U}\right)\delta\bar{U} = -R(\bar{U}^n), \quad \bar{U}^{n+1} = \bar{U}^n + \alpha\delta\bar{U} \quad (7)$$

where I is the identity matrix, Δt_i is the time-step associated with each control volume and $\frac{\partial R}{\partial U}$ is the global Jacobian matrix. To add more robustness, we apply a single iteration of a line search algorithm at any iteration, which has been successfully used for our compressible flow solvers [5]. Note that the convergence to the steady-state solution can be posed as an optimization problem in which we seek to minimize the norm of the residual vector at each iteration. The line search algorithm is employed to find the value of α that satisfies the sufficient decrease condition from one iteration to another. If the initial guess $\alpha = 1$ does not satisfy this condition, a quadratic backtracking line search algorithm is used to find a value α which does.

Also, we use the successive evolution-relaxation to find the global CFL number:

$$CFL^{n+1} = c_2 \cdot CFL^n \cdot \frac{\|R(\bar{U}^{n-1})\|_2}{\|R(\bar{U}^n)\|_2}, \quad c_2 = 1.1, \quad CFL^0 = 1.0 \quad (8)$$

Since we do not seek a time-accurate solution, we have the choice of deriving a local time-step from the global CFL number:

$$\Delta t_i^{n+1} = CFL^{n+1} \cdot \frac{h_i}{speed_i^n} \quad (9)$$

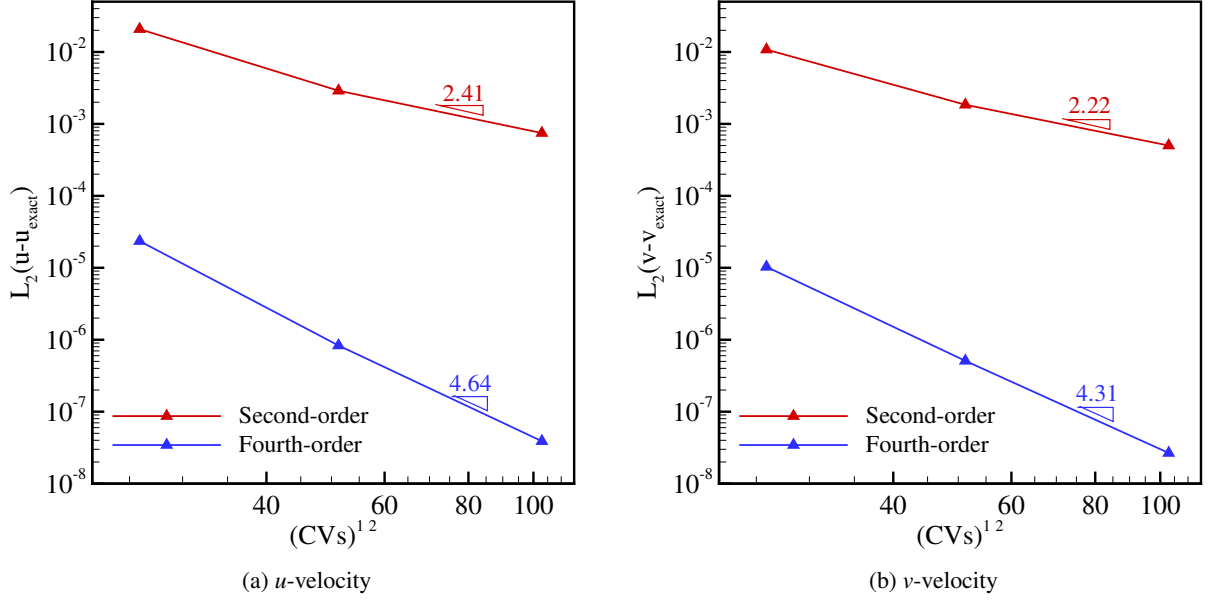


Figure 1: Error in velocity components for fully developed channel flow

where $speed_i$ is the largest characteristic speed in the control volume, h_i is a characteristic size. Using the pseudo-compressibility method, the system of equations are transformed into a hyperbolic system in which the characteristic speeds are the eigenvalues of the normal convective flux Jacobian, $\frac{\partial F_c^n}{\partial U}$:

$$\lambda_1 = \vec{V} \cdot \hat{n} - \sqrt{(\vec{V} \cdot \hat{n})^2 + 1/\beta} \quad \lambda_2 = \vec{V} \cdot \hat{n} \quad \lambda_3 = \vec{V} \cdot \hat{n} + \sqrt{(\vec{V} \cdot \hat{n})^2 + 1/\beta} \quad (10)$$

The above eigenvalues are calculated on the quadrature points located on the interfaces of a control volume and the one with the largest magnitude (λ_1 or λ_3) is selected as $speed_i$ in Equation 9.

5. Results

To verify the nominal accuracy of our spatial discretization, we consider the fully-developed pressure-driven flow of an incompressible fluid in a rectangular channel. The exact solution for the velocity components of this flow are :

$$u_e(x, y) = 4U_{max} \frac{y}{D} \left(1 - \frac{y}{D}\right), \quad v_e(x, y) = 0 \quad (11)$$

where U_{max} is the maximum velocity at the centerline, $y = D/2$. Having the exact solution of Equation 11 for u and v , it is possible to calculate the numerical error in each control volume. Figure 1 shows the L_2 norms of error in the computation of velocity components on a sequence of systematically refined meshes for $Re = 100$, $U_{max} = 1.5$, $L = 3$ and $D = 1$. As expected, the fourth-order method results in considerably smaller error values compared to second-order. Also, the asymptotic orders of error convergence are even better than nominal orders.

As a second test case, we consider flow in a unit square lid-driven cavity at $Re = 100$. Figure 2a shows the v -velocity magnitudes at cavity mid-line, i.e. $y = 0.5$ ($0 \leq x \leq 0.5$) for second- and fourth-order methods on a coarse mesh with 778 triangular control volumes and second-order method on two level finer mesh, with 12766 triangular control volumes. Note that the coarse mesh length scale is almost four times larger. Clearly, the fourth-order solution on the coarse grid is comparable with the second-order solution on the fine mesh. However, comparing the simulation time reveals the advantage of higher-order schemes. Figure 2b shows the convergence history for the second-order solution on the fine mesh and fourth-order solution on the coarse grid. The number of non-linear iterations and simulation time are considerably smaller for the fourth-order solution. Note that we have set the same initial conditions for all cases such that pressure and v -velocity are zero everywhere and u -velocity changes linearly with vertical position, i.e. $u = y$. Also, the GMRES method preconditioned with ILU-2 is used to solve the

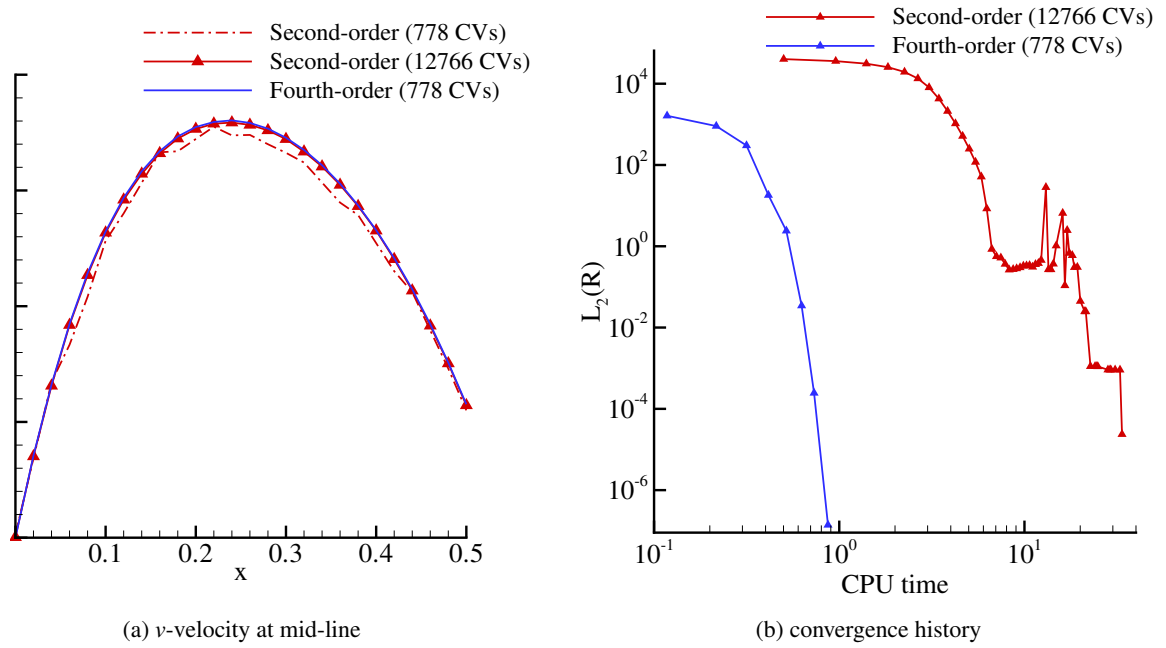


Figure 2: Comparison of second- and fourth-order results for lid-driven cavity

linear system in each iteration where the Krylov size is 100 and the relative norm for the linear solve is 0.001. These results prove the effectiveness of the fourth-order scheme on the coarse mesh compared to the second-order solution on the fine mesh.

6. Conclusions

The steps for extending our higher-order unstructured compressible flow solver to incompressible flows were described. The pseudo-compressibility technique was employed to couple the continuity equation to the momentum equations. In this way, the system of equations exhibits hyperbolic behaviors and thus the eigenvalues of flux Jacobian can be used to tune the local time steps. Implicit time stepping with line search algorithm was used to accelerate the convergence to steady-state. Our results proved the effectiveness of higher-order methods over second-order.

References

- [1] C. Ollivier-Gooch, A. Nejat, and K. Michalak. Obtaining and Verifying High-Order Unstructured Finite Volume Solutions to the Euler Equations. *AIAA Journal*, 47, 2105–2120, 2009.
- [2] D. Kwak, C. Kiris, C.S. Kim. Computational challenges of viscous incompressible flows. *Computers and Fluids*, 34, 283–299, 2005.
- [3] C. Ollivier-Gooch, M. van Altena. A High-order Accurate Unstructured Mesh Finite-Volume Scheme for the Advection-Diffusion Equation. *Journal of Computational Physics*, 181, 729–752, 2002.
- [4] A. Jalali, M. Sharbatdar, C. Ollivier-Gooch. Accuracy analysis of unstructured finite volume discretization schemes for diffusive fluxes. *Computers and Fluids*, 101, 220–232, 2002.
- [5] C. Michalak, C. Ollivier-Gooch. Globalized matrix-explicit Newton-GMRES for the high-order accurate solution of the Euler equations. *Computers and Fluids*, 39, 1156–1167, 2010.

A Second-Order Accurate Mach-Uniform Solver for the Euler and Navier-Stokes Equations on Pairs of Mutually Orthogonal Unstructured Grids

*D. Jones, O. Hassan and K. Morgan

College of Engineering, Swansea University, Swansea, SA2 8PP

*D.A.Jones@swansea.ac.uk

ABSTRACT

A second-order accurate Mach uniform solver for the Euler and Navier-Stokes equations on pairs of mutually orthogonal grids is presented and discussed. In subsonic flow regions, the use of mutually orthogonal grid pairs allows second-order accurate solutions to be obtained using scalar interpolation stencils of just two grid points, and the solver is highly efficient as a result. Numerical solutions are presented, which demonstrate the accuracy and Mach-uniform applicability of the solver.

Keywords: Co-volume methods; Mach-uniform; higher-order methods; mutually orthogonal grid pairs

1. Introduction

Many solvers for the Euler and Navier-Stokes equations are capable of predicting either incompressible flows or compressible flows, but not both [1]. Mach-uniform solvers are an attempt to unify these into a single solver, which is able to accurately and efficiently predict fluid flows over the whole range of Mach numbers, from zero to hypersonic.

A Mach-uniform co-volume solver is being developed for the Euler and Navier-Stokes equations. In the co-volume method, systems of partial differential equations are solved on pairs of grids, rather than a single grid. Here, we employ Delaunay-Voronoi grid pairs, as they lead to significant efficiency improvements, which are discussed in Section 4. Historically, it been difficult to generate suitable grid pairs of this type, preventing widespread use of co-volume methods in CFD. However, recent advances in grid generation and optimisation have made good quality unstructured, mutually orthogonal grid pairs available for complex 2D and 3D geometries [4].

2. Grid Requirements

The solver is used with Delaunay-Voronoi grid pairs. These pairs have the property that the Voronoi edges are perpendicular bisectors of the Delaunay edges they intersect, and vice-versa. In our solver, scalars, and their directional derivatives, are evaluated at the Delaunay edge centres using the stored values of the scalar at the adjacent Voronoi vertices. Short Voronoi edges, therefore, negatively influence the stability and accuracy of the solver, and impose a strict upper limit on the time step. In the worst case, Voronoi edges can be zero-length, or very close to it, and this can prevent solution convergence altogether. A grid optimisation step is therefore included in pre-processing, to remove short Voronoi edges. This is done through a combination of moving “bad” Voronoi points to more suitable positions, and by merging “bad” Delaunay elements, to form quadrilaterals. The former is done whilst strictly maintaining orthogonality, and so the grid loses (locally) the mutual bisection property of intersecting Delaunay and Voronoi edges. The latter imposes the requirement that the solver be applicable to the case where the Delaunay grid is mixed. It is important to note here that only a very small percentage (typically $< 1-2\%$) of the Voronoi edges in a grid pair require this treatment. A more detailed discussion of mesh optimisation is presented in [4]. An example of an optimised Delaunay-Voronoi grid pair is shown in Figure 1.

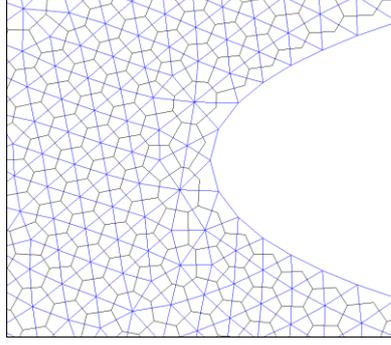


Figure 1: An example of an optimised Delaunay-Voronoi grid pair used by the solver – a detail near the leading edge of a NACA 0012 aerofoil. The blue lines are the Delaunay edges, the black lines are the Voronoi edges.

3. Solution Procedure

Our solver is based on the Mach-uniform solver presented in [3]. The solver is both segregated and staggered. The scalar primary flow variables (density and pressure) are stored at the Voronoi vertices, and the normal momentum is stored at the Delaunay edge centres. The choice of a segregated approach provides good performance in incompressible flow regions, without noticeably affecting performance in compressible regions. The solver proceeds as follows:

- (i) The density at the Voronoi vertices is updated by applying the continuity equation. The control volume for a Voronoi vertex is taken as the Delaunay element which contains it.
- (ii) Normal momentum predictions at the Delaunay edge centres are calculated by applying the normal momentum equation. The control volume for a Delaunay edge centre is taken as the adjacent Delaunay elements.
- (iii) Pressure corrections at the Voronoi vertices are calculated by applying the pressure correction equation. The control volumes are the same as for (i).
- (iv) The pressure corrections which were calculated in (iii) are used to update the pressures at the Voronoi vertices, as well as the normal momentums at the Delaunay edge centres.

The procedure is repeated iteratively, until some convergence criterion is met. The equations themselves can be found in [3], and are not reproduced here. The discretisation of the equations is fully implicit, which is required due to the form of the pressure correction equation. However, the density and normal momentum equations could be treated explicitly or semi-implicitly if desired.

4. Interpolation of Scalar Flow Variables and Evaluation of Scalar Gradients

During the solution process, the scalar primary flow variables must be evaluated at the centres of the Delaunay edges. This can be accomplished to first-order accuracy, regardless of grid type, by setting the value at the Delaunay edge centre equal to the value at the Voronoi vertex which is immediately upwind of it. To achieve a second-order accurate solver, however, linear interpolation is required, and this is significantly more complex. In [3], the authors used a piecewise linear reconstruction of the scalar gradient in the vicinity of the upwind cell centre. Depending on the local grid geometry, this typically results in a stencil of 5-6 points. When these are inserted into the continuity and pressure correction equations, the resulting stencils can include up to 25 points when solving on a mixed grid.

We can, however, use the properties of Delaunay-Voronoi grid pairs to greatly reduce the size of these stencils. Consider a typical Delaunay edge, d , and its adjacent Voronoi vertices, a and b . We need to evaluate a scalar, φ , at the centre of d , and its gradient normal to d . Because of the mutual orthogonality of Voronoi edges with Delaunay edges, the gradient of φ normal to d can be evaluated using a simple finite-difference approximation:

$$(\nabla\varphi \cdot \hat{n})_d \approx \frac{\varphi_b - \varphi_a}{\|\vec{x}_b - \vec{x}_a\|_2} \quad (1)$$

where \vec{x} is the position of a point. We can then evaluate φ_d using $(\nabla\varphi \cdot \hat{n})_d$ (calculated as in equation 1) and the value of the scalar at the Voronoi vertex upwind of d . We obtain the expression:

$$\varphi_d \approx \eta_a \varphi_a + \eta_b \varphi_b \quad (2)$$

The coefficients η_a and η_b depend only on the ratios of the distances from the Voronoi points a and b to the Delaunay edge centre d . At Delaunay edges where mutual bisection with the intersecting Voronoi edge has been maintained (typically $> 98\%$ of Delaunay edges in a grid pair), the coefficients are both equal to 0.5. The interpolation stencil uses only two points – a significant efficiency improvement over the piecewise linear reconstruction. We use this method of scalar interpolation in subsonic regions of the flow, and switch to a piecewise linear reconstruction in supersonic regions, where only upwind flow information can be used, due to the hyperbolic nature of the governing equations.

5. Numerical Results

To demonstrate the accuracy and Mach-uniform applicability of the solver, two test cases are presented. We chose to use inviscid test cases for this purpose, as they allow us to investigate the characteristics of the solver, whilst minimising unnecessary complexity.

(i) Inviscid, Incompressible Flow Over A Right Circular Cylinder:

The first test case considered was inviscid, incompressible flow over a right circular cylinder. This test case was especially useful, as an exact potential flow solution is available, allowing the accuracy of the solver to be assessed in absolute terms. Both first-order accurate and second-order accurate solutions were obtained at a Mach number of 0.05. Figure 2 shows the obtained pressure coefficient distributions on the surface of the cylinder, as well the exact potential flow solution. Both of the presented numerical solutions show good agreement with the exact solution, although the second-order solution is clearly considerably more accurate. In both numerical solutions, there is some undershoot near the 0° , 90° , 180° , and 270° positions. This is likely due to a combination of grid coarseness and some numerical diffusion inherent in the solver.

(ii) Inviscid Channel Flow Over A Circular Arc Bump:

The second test case considered was inviscid channel flow over a circular arc bump, a common test case for inviscid flow solvers. We obtained numerical solutions for flows at Mach numbers of 0.5 over a 10% circular arc bump and 1.65 over a 4% circular arc bump. The resulting pressure fields are shown in Figure 3, and show good agreement with existing numerical solutions, such as those found in [2], apart from a small discrepancy between the angles at which the shock is reflected from the top wall of the channel in the supersonic case. This could be caused by differences in flux limiting, wall treatment, or grid fineness or distortion. For the subsonic case, the fact that the flow is inviscid means it is also isentropic, and therefore there will be no diffusion of total energy. As a result, the flow will be symmetric about a vertical line passing through the centre of the circular arc bump. The presented numerical solution shows very close agreement with this, indicating that the numerical diffusion of our solver is small.

6. Conclusions

A new second-order accurate solver for the Euler and Navier-Stokes equations has been presented. Numerical results demonstrate that the solver is both accurate and applicable across a wide range of Mach numbers, from incompressible to hypersonic, and has low numerical diffusion. The solver shows good agreement with both exact flow solutions and other available numerical solutions. In addition, a significant improvement in solver efficiency is obtained over existing solvers, by utilising the geometric characteristics of Delaunay-Voronoi grid pairs.

During the lecture, the discretisation of the flow equations, grid refinement studies demonstrating the second-order accuracy of the solver, and further test cases, including lifting and viscous flows, will be presented, and intended future extensions of the solver will be discussed.

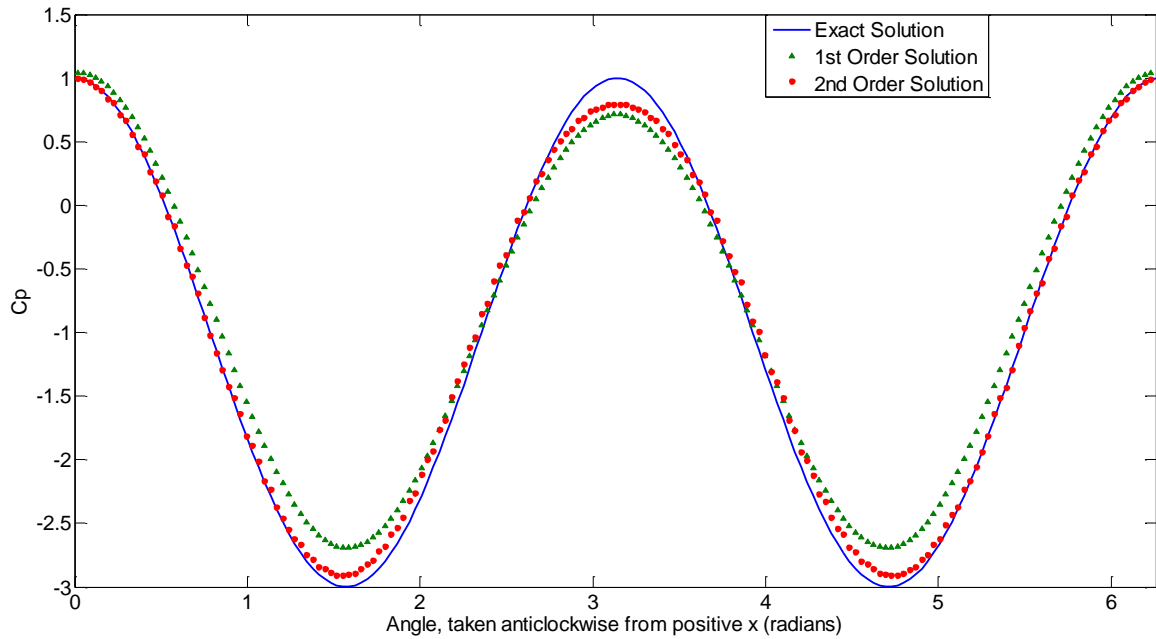


Figure 2: Exact and predicted surface pressure coefficient distributions for a circular cylinder at Mach 0.05.

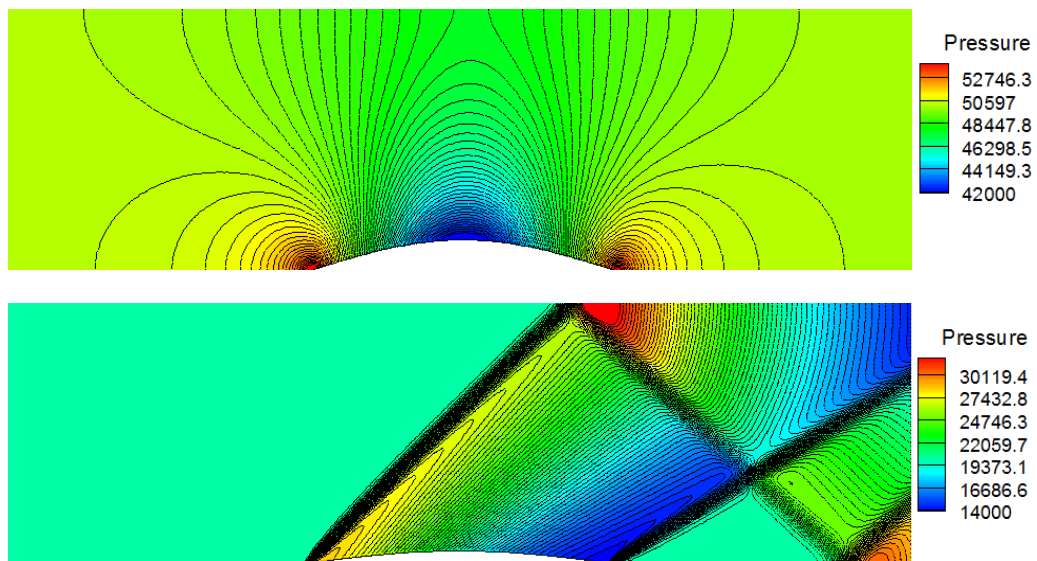


Figure 3: Obtained numerical solutions of channel flow over circular arc bumps. Top: flow at Mach 0.5 over a 10% circular arc bump; bottom: flow at Mach 1.65 over a 4% circular arc bump.

References

- [1] J. Blazek, *Computational Fluid Dynamics: Principles and Applications*, 1st Edition, Elsevier, 2001.
- [2] I Demirdžić, Ž Lilek, M. Perić, 1993. A collocated finite volume method for predicting flows at all speeds. *International Journal for Numerical Methods in Fluids* 16, p1029-1050.
- [3] D. Vidović, A. Segal, P. Wesseling, 2006. A superlinearly convergent Mach-uniform finite volume method for the Euler equations on staggered unstructured grids. *Journal of Computational Physics* 217, p277-294,
- [4] S. Walton, O. Hassan, K. Morgan, 2012. Reduced order mesh optimisation using proper orthogonal decomposition and a modified cuckoo search. *International Journal for Numerical Methods in Engineering*, DOI:10.1002/nme.4400.

FLUID DYNAMICS 4

A CFD CASE STUDY OF USING TURBULENCE MODELS FOR EVALUATING THE PERFORMANCE OF A DRAG BASED VERTICAL AXIS WIND TURBINE

*F. Hafezi¹, S. Rolland¹, D. McBride¹, T.N. Croft¹, M. Cross¹ and R. Ellis²

¹College of Engineering, Swansea University, SA28PP, Swansea, UK

²C-FEC Ltd, Singleton park, Swansea SA2 8PP

*F.Hafezi@swansea.ac.uk

ABSTRACT

The goal of this research is to use CFD tools to assess the performance of vertical axis wind turbines. Although experiments can cover wide range of operational parameter, a CFD based computational model would have an advantage of predicting the effect of different design changes on the final efficiency and power of the device.

The C-feg is a drag based vertical axis wind turbine (VAWT), it is characterised by a design tip speed ratio (TSR) design of 0 – 2, which is substantially lower than the typical values of 5 and 9 seen for lift-driven darrieus VAWT and a horizontal axis wind turbines respectively[1].

This study compares $k-\omega$, $k-\omega$ SST and LES turbulence models and an enhanced laminar flow model for simulating the C-feg wind turbine in order to study whether turbulence models provide any useful insight that can be converted into an actionable information for the design process. In this research a conventional pressure correction procedure using a finite volume unstructured mesh code, PHYSICA [2] has been used to simulate turbulent flows for turbine size 1.6m diameter, TSRs 0.4, wind velocities 8(m/s) and yaw 30°.

The enhanced laminar simulation results are compared against the experimental results for 1.6m diameter turbine which was tested in a wind tunnel [3]. In this paper the turbulence simulations are compared against the experimental data published earlier [4] and results discussed.

Keywords: Vertical axis wind turbine, Turbulence models, Experimental validation

1. Introduction

Wind energy is one of the most environmentally friendly sources of energy and has the potential to become a real solution for areas with poor energy sources. The Global Wind Energy Council (GWEC) reports wind power is already exploited in 90 countries with a total installed capacity of 318 gigawatts at the end of 2013 and this capacity could increase by 2030 and reaching a total of more than 2,000 gigawatts, meeting almost 20 percent of electricity demand [5]. This growth means that the wind turbine industry is now a key point for research and investment. In this study, a novel wind turbine (C-feg device, <http://www.c-fec.com/>) device has been investigated in two different sizes: the first case is 1.6m diameter with 8 blades and without the pylon [3] Figure 1 and the second case is 8m diameter with ten blades and pylon.

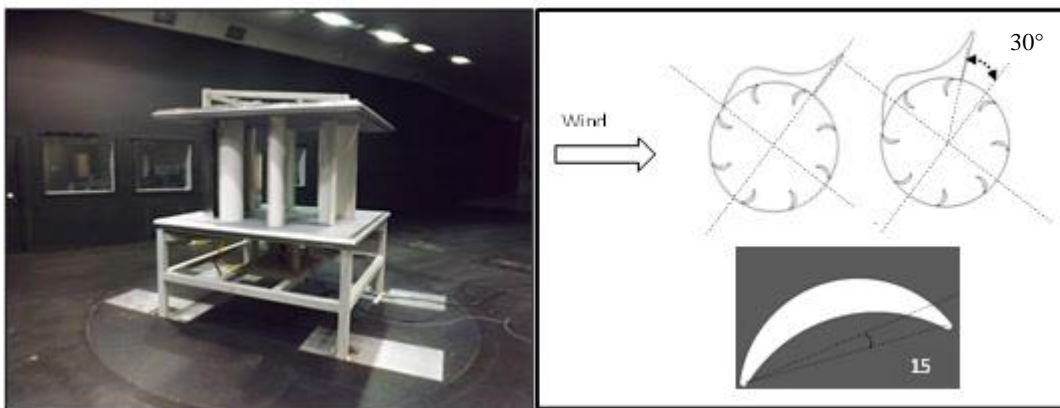


Figure 1: Experimental wind turbine setup in a wind tunnel. The corresponding model geometry is shown on the right.

In a previous study Rolland et al [3] used an enhanced laminar model (by adjusting viscosity to 200 times air viscosity) to generate realistic performance predictions that can be compared with experimental results. It is found in this research that the adjusted value is mesh sensitive as can be expected. The current study focuses on understanding the effect of using different turbulence models with the actual air viscosity value. For this study the same values for the yaw angle and blade pitch angle are fixed to 30° and 15° . However, the coarse mesh used for the enhanced laminar model (number of elements not more than 100,000) does not meet the criteria for use with more advanced turbulence models. A mesh sensitivity study confirms that mesh adequacy is achieved with 350,000 elements and $y^+ \approx 1$ around the blade, a similar mesh was used for the 8m diameter turbine model and element count increases to 500,000 elements to account for open flow.

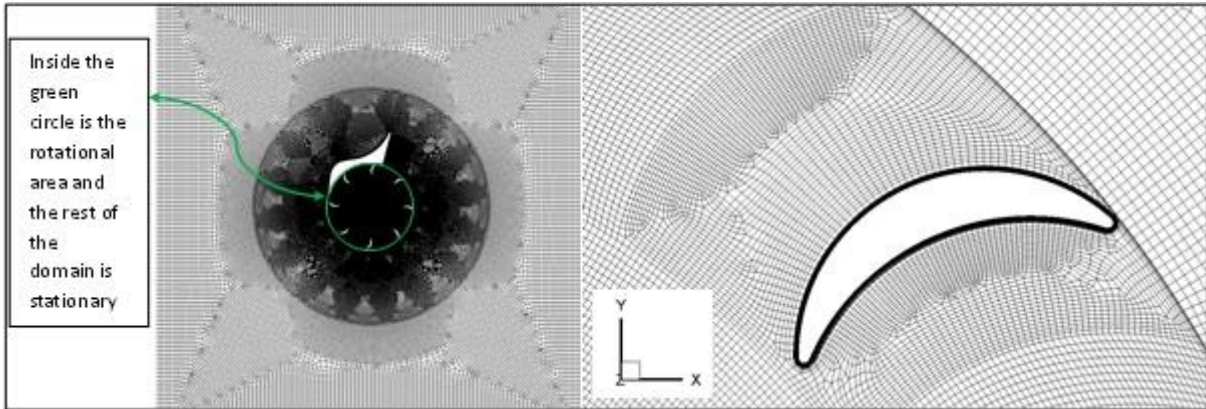


Figure 2: The cut section of the mesh for the model is shown at the top. The bottom left section shows the rotating blades and the stationary housing. The corresponding blade geometry along with the mesh is shown at bottom right.

In this paper results are simulated at TSR value of 0.4 and wind velocity value of 8m/s and compared to experiment has been done in Wind tunnel, MacNaughton et al[6] they used two version of RANS model: (i) the $k-\omega$ SST in its standard form, and (ii) correction for low Reynolds number ($k-\omega$ SST LRE) effects on a 3 blades vertical axis turbine, The standard $k-\omega$ SST model is shown to over-predict the maximum value of the power coefficient, compared to the experimentally reported value, although the mesh refinement study has shown a reasonable convergence. However, the $k-\omega$ SST LRE, low-Reynolds number version predicts the laminar separation which allows the correct reproduction of the flow structure characterising a dynamic stall: a main leading edge vortex forming before stall, coupled with a secondary vortex later appearing next to the former, as well as a trailing edge vortex. The maximum power coefficient returned by this model matches the experimental data. Mitre et al [7] performed a series of 2D CFD studies using FLUENT with the $k-\omega$ SST turbulence model. They compared their results with experimental data from a 3 bladed HAWT employing a NACA 0018 aerofoil shape in a marine context. These authors were very careful about their mesh densities and particularly the y^+ values in the neighbourhood of the blades. Their results also showed over estimation of power coefficients by a factor of 2 across a range of TSRs from 1 to 3 for wind speeds up to 2.8 m/s. Dobrev and Massouh [8] showed experiments for a simple Savonius design which has blade shape similarities to C-feg that is essentially a drag device. They employed FLUENT and used the $k-$ SST in 2D and 3D and in 3D they also used the DES/ $k-\omega$ SST model. They appeared to have paid attention to the detail and the quality of the mesh in the neighbourhood of the blades. They found 2D $k-\omega$ SST simulations over predict the efficiency vary between 3%-24% depend on TSRs and 3D $k-\omega$ SST simulations are under predict the efficiency vary between 13%-20% depend on TSRs (the percentages are related on experimental value). Many other experimental and numerical studies also reviewed the different turbulence models for a horizontal or vertical axis wind turbines such as [6, 7, 9-11 with varying accuracy,]

2. Turbulence modelling

The choice of turbulence models influences the computational results and the required computation resource. The RANS models are widely used in turbulence modelling with fair accuracy and

efficiency [12]. Among the various RANS models, the $k-\omega$ model is the first model employed in the present study and then $k-\omega$ SST with LRE correction which is combining the $k-\omega$ and $k-\epsilon$ models and is considered a promising approach for simulating flow. Figure 3 shows velocity contours for TSR 0.4 and wind velocity of 8 m/s for different turbulence models. The flow structure, wake and vortex shading effects are observed. The results show correlation between a short wake and good match with experiment which are realistic [13]. Even though the efficiency is overestimated by each turbulent models $k-\omega$ SST LRE model shows shorter wake as compare to other, the corresponding velocity profiles over blades are shown in Figure 4.

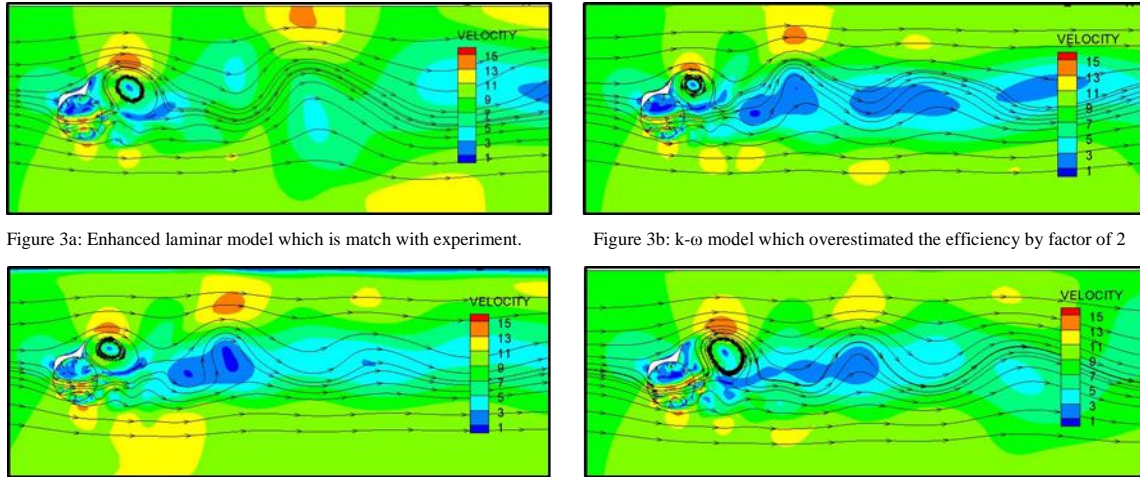


Figure 3a: Enhanced laminar model which is match with experiment.

Figure 3b: $k-\omega$ model which overestimated the efficiency by factor of 2

Figure 3c: LES model which overestimated the efficiency by factor of 1.6.

Figure 3d: $k-\omega$ SST LRE model which overestimated the efficiency by factor of 1.

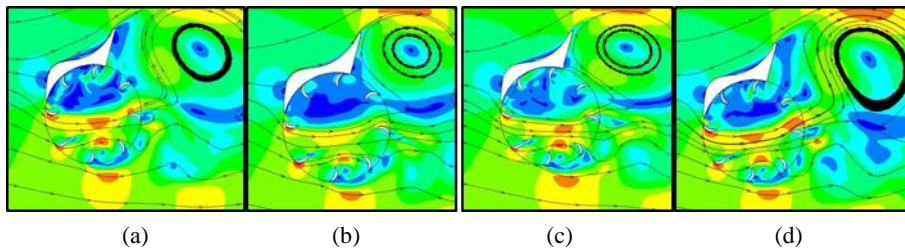


Figure 4: velocity contours for (a) Enhanced Laminar, (b) $k-\omega$, (c) LES and (d) $k-\omega$ SST LRE models

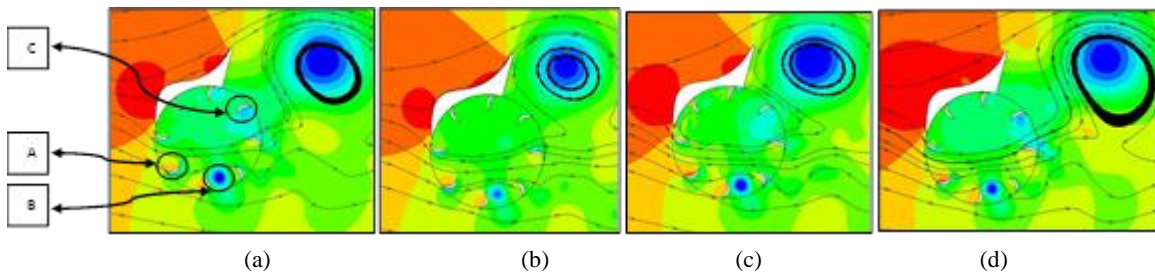


Figure 5: Pressure contours for (a) Enhanced Laminar, (b) $k-\omega$, (c) LES and (d) $k-\omega$ SST LRE models

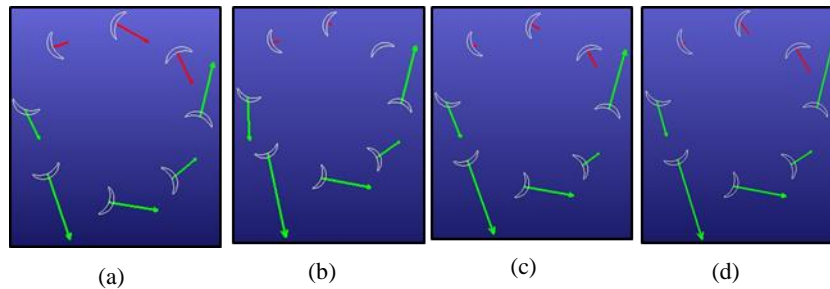


Figure 6: Total force on the blades for (a) Enhanced Laminar, (b) $k-\omega$, (c) LES and (d) $k-\omega$ SST LRE models

The pressure contours are shown in Figure 5 and corresponding resultant force vectors shown in Figure 6. The low pressure area between two blades (position B, Figure 5) and the high pressure area

(position A) are predicted by all models. However, it is interesting to note that k- ω SST LRE model has predicted a low pressure area (position C) that is not captured by other models. However it is seen in Figure 5a and d that the enhanced laminar flow model given a similar profile to the k- ω SST LRE model. The corresponding force vector in Figure 6d is negative. It is this variation of forces that gives rise to a dynamic stall situation. There is a noticeable difference in Force vector plots Figure 6, the magnitude of return stroke (red vectors) are much higher in enhanced laminar model as compare to turbulence models which could be one of the reasons for lower efficiency.

3. Conclusions

In this study, the sensitivity of using different turbulence models to predict wind turbine performance is demonstrated. After undertaking a mesh refinement study an optimal mesh was chosen for the study. The pressure and velocity contours were plotted by modelling, at the real size scale, the rotating part of the turbine as well as the stationary housing. In order to optimise the performance of the wind turbine, blade design including its shape, numbers and orientation are important. The study shows the variation in results by using different turbulence models. It is shown that k- ω SST LRE turbulence model gives realistic pressure and velocity contours. The work confirmed the research that turbulence models do over predict the efficiency values. Enhanced laminar models can adjust air viscosity values to align results with real efficiency values. However, results in this research have shown that these models are sensitive to prediction of pressure and velocity profiles around the blades. This prediction is important in order to optimise the direction and magnitude of resultant forces across all blades under various operating conditions. The enhanced laminar flow model is computationally efficient and hence can be used to undertake initial designs that can later assessed by a comprehensive k- ω SST LRE model. The next step in this research is to instrument a real sized turbine and measure pressures and forces across all blades for under various operating conditions and compare results with the numerical prediction. However, the research undertaken in this study has given us the confidence to proceed to the experimental programme.

References

- [1] Jamieson, P., Innovation in wind turbine design. 2011: John Wiley & Sons Ltd.
- [2] Croft, T.N., K. Pericleous, and M. Cross, PHYSICA: a multiphysics environment for complex flow processes. Numer Methods Lamin Turb Flow, 1995. 3: p. 1269-1280.
- [3] Rolland, S., et al., Simulations technique for the design of a vertical axis wind turbine device with experimental validation. Applied Energy, 2013. 111: p. 1195-1203.
- [4] Rolland, S.A., et al., Benchmark experiments for simulations of a vertical axis wind turbine. Applied Energy, 2013. 111: p. 1183-1194.
- [5] GLOBAL WIND ENERGY OUTLOOK 2014.
- [6] McNaughton, J., F. Billard, and A. Revell, Turbulence modelling of low Reynolds number flow effects around a vertical axis turbine at a range of tip-speed ratios. Journal of Fluids and Structures, 2014. 47: p. 124-138.
- [7] Maître, T., E. Amet, and C. Pellone, Modeling of the flow in a Darrieus water turbine: Wall grid refinement analysis and comparison with experiments. Renewable Energy, 2013. 51: p. 497-512.
- [8] Dobrev, I. and F. Massouh, CFD and PIV investigation of unsteady flow through Savonius wind turbine. Energy Procedia, 2011. 6: p. 711-720.
- [9] Lanzafame, R., S. Mauro, and M. Messina, 2D CFD Modeling of H-Darrieus Wind Turbines Using a Transition Turbulence Model. Energy Procedia, 2014. 45: p. 131-140.
- [10] McLaren, K., S. Tullis, and S. Ziada, Measurement of high solidity vertical axis wind turbine aerodynamic loads under high vibration response conditions. Journal of Fluids and Structures, 2012. 32: p. 12-26.
- [11] Wang, S., et al., Numerical investigations on dynamic stall of low Reynolds number flow around oscillating airfoils. Computers & Fluids, 2010. 39(9): p. 1529-1541.
- [12] Li, C., et al., 2.5D large eddy simulation of vertical axis wind turbine in consideration of high angle of attack flow. Renewable Energy, 2013. 51: p. 317-330.
- [13] Kinzel, M., Q. Mulligan, and J.O. Dabiri, Energy exchange in an array of vertical-axis wind turbines. Journal of Turbulence, 2012. 13: p. N38

Coupled Lattice Boltzmann and Finite Volume Method for Modelling Crossflow Microfiltration and Nanofiltration.

*Soo-hyeong. Kim, Oubay Hassan, Ken Morgan and Nidal Hilal

College of Engineering, Swansea University, Singleton Park, Swansea, SA2 8PP

*669279@swansea.ac.uk

ABSTRACT

A new computer modelling tool has been developed to simulate concentration polarisation and cake layer formation during a crossflow microfiltration (MF) and nanofiltration (NF). MF and NF processes are applied in a variety of industrial sectors to separate solute from a solution. To improve efficiency of the filtration process, a predictive tool is required to model the dynamic behaviour of the solute suspension and fluid solution governed by convection-diffusion (C-D) equation and the Navier-Stokes (NS) equation.

A decline in permeate flux over a duration of a filtration process is caused by membrane pore blocking and cake layer formation on the surface of a membrane. Unlike the dead-end filtration which reaches an equilibrium at a zero permeate flux, a crossflow filtration reaches an equilibrium at a non-zero permeate flux determined by a range of variables such as transmembrane pressure (TMP), suspended particle size and concentration, and crossflow velocity.

The MF modelling techniques is based on the use of the Lattice Boltzmann method(LBM) for hydrodynamics and convection-diffusion processes. The advantages of using the Lattice Boltzmann technique are; its simplicity compared to other more conventional finite difference methods, ability to solve fluid and solute dynamics simultaneously, capabilities of modelling porous materials and its ability to model complex geometries [1]. For NF problems [2] [3], the LBM for hydrodynamics is coupled with finite volume method (FVM) for C-D equation to remove the restriction on the time step limit that arises from the small value of the diffusion.

The presented results from the simulation of concentration polarisation and cake layer formation of MF and NF problems will be compared to experimental data at a various operating conditions.

Key Words: *Crossflow filtration; Microfiltration; Nanofiltration; Lattice Boltzmann method; Finite volume method*

1. Method

1.1. Lattice Boltzmann method for fluid flow

The Navier-Stokes equation of fluid flow can be solved using a lattice Boltzmann equation with a multiple relaxation collision operator

$$f_{\alpha}(\mathbf{x} + \mathbf{e}_{\alpha}\Delta t, t) - f_{\alpha}(\mathbf{x}, t) = M^{-1}S [f_{\alpha}^{M(eq)}(\mathbf{x}, t) - Mf_{\alpha}(\mathbf{x}, t)] \quad (1)$$

in which f_{α} is the particle distribution function, $f_{\alpha}^{M(eq)}$ is the local equilibrium distribution function in the moment space relaxed by a diagonal relaxation matrix S over a time step Δt in discrete velocities \mathbf{e}_{α} according to the directional index α to solve for the macroscopic velocity \mathbf{u} and density ρ .

$$\rho = \sum_{\alpha} f_{\alpha}, \quad \mathbf{u} = \sum_{\alpha} \mathbf{e}_{\alpha} f_{\alpha} \quad (2)$$

The transformation matrix M and inverse matrix M^{-1} converts the particle distribution function between velocity and moment spaces such that $f = M^{-1}f^M$ and $f^M = Mf = (\rho, e, \epsilon, j_x, q_x, j_y, q_y, p_{xx}, p_{xy})$. Where ρ is the density, e is a function of kinetic energy, ϵ is a function of energy squared. The terms j_x, j_y, q_x and q_y are the x and y components of the momentum energy and energy flux respectively. The last two terms p_{xx} and p_{xy} are functions of diagonal and off-diagonal components of the viscous stress tensor. To conserve density, ρ and momentum j_x and j_y , the diagonal relaxation matrix is simplified to $S = \text{diag}(0, s_2, s_3, 0, s_5, 0, s_7, s_8, s_9)$. For all simulations for this paper the relaxation terms were fixed to $s_2 = 1.64, s_3 = 1.54, s_5 = s_7 = 1.9$ and $s_8 = s_9 = 1/\tau_f$ where $\tau_f = 3\nu + 0.5$ is a relaxation term calculated from the fluid viscosity ν .

To create fluid flow, pressure boundary condition is applied at inlet, outlet and permeate side of a model using boundary conditions proposed by Zou and He [4]. The pressure gradient across the membrane causes the fluid to pass through the membrane which is a porous medium with a hydraulic resistance modelled using the modification proposed by Freed [5].

1.2. Modelling Microfiltration

To solve the convection-diffusion equation for macroscopic particle migration, a lattice Boltzmann equation with the Bhatnagar-Gross-Krook(BGK) collision operator is applied

$$g_\alpha(\mathbf{x} + \mathbf{e}_\alpha \Delta t, t + \Delta t) - g_\alpha(\mathbf{x}, t) = \frac{1}{\tau_g} [g_\alpha^{(eq)}(\mathbf{x}, t) - g_\alpha(\mathbf{x}, t)]. \quad (3)$$

Similar to the lattice Boltzmann equation for the fluid flow, g_α is the particle distribution function, $g_\alpha^{(eq)}$ is the local equilibrium distribution function relaxed by a single relaxation $\tau_g = 3D + 0.5$ over a time step Δt in discrete velocities \mathbf{e}_α to solve for a scalar value for concentration,

$$\phi = \sum_{\alpha} g_\alpha. \quad (4)$$

Over time, a lattice cell may reach a maximum concentration limit $\phi_{max} = 0.64$ for rigid spherical particles. At this point, the lattice cell is considered to be a cake layer with fluid passing through it rather than particles being transported within a fluid. The hydraulic resistance of a cake layer is modelled the same way as the membrane resistance. For concentrations below ϕ_{max} , the viscous property of the fluid is modified and the local effective relative viscosity of rigid spherical suspensions is defined in terms of solute free fluid viscosity μ_0 defined by Davis [7]:

$$\mu(\phi) = \mu_0 \left[1 + 1.5 \frac{\phi}{(1 - \frac{\phi}{0.58})} \right]^2. \quad (5)$$

Due to the unique behaviour of particles in a crossflow microfiltration, shear-induced hydrodynamic diffusion model by Leighton and Acrivos [6] is applied:

$$D(\phi) = 0.33\gamma a^2 \phi^2 (1 + 0.5e^{8.8\phi}) \quad (6)$$

where γ is the local shear rate. Both the effective viscosity $\mu(\phi)$ and shear induced diffusion coefficient $D(\phi)$ are time and space dependent and are required to be computed at each lattice points at all time steps.

1.2.1. Pore block

Another cause of flux decline during filtration is pore block in which the particles block membrane pores thus increasing membrane resistance which can be described by:

$$R_m^* = R_m + R_p = \frac{8\tau\delta_m A_m}{\pi N_p^t a_{pore}^4} \quad (7)$$

where N_p^t is a number of pores available at time t with pore radius of a_{pore} and pore tortuosity τ over a membrane area of A_m which has a membrane thickness δ_m . The number of pores available at a time t is a product of a number of pores available at a previous time step N_p^{t-1} and the probability P of a pore being free $N_p^t = PN_p^{t-1}$ and the probability can be calculated by $P = 1 - [\beta r_p N_p^{t-1} A_p]$, where β is a probability coefficient of rate of particles $r_p = -u_y N_{pl}$ arriving at a free pore area $N_p^{t-1} A_p$ at a velocity u_y and N_{pl} describes the number of particles perpendicular to the membrane $N_{pl} = \sqrt[3]{\frac{3\phi}{4\pi a^3}}$.

1.3. Modelling Nanofiltration

To model nanofiltration using the lattice Boltzmann method would require large grids to accurately capture a cake layer and be stable to model small diffusion coefficient. Due to the scaling issues, this would result in high computational cost due to increase in grid size and number of time steps required to solve the problem. Therefore a hybrid differencing finite volume method is applied as a grid refinement at lattice points where a cake would form to eradicate both issues of large grid and small time steps.

2. Results

Shown in fig1, is the comparison of effect of transmembrane pressure on permeate flux decline of a problem previously modelled by Kromkamp [1] also using the lattice Boltzmann method during microfiltration. The model shows capability of predicting flux decline over time and the different rates of decrease in flux depending on the transmembrane pressure. As expected, at high transmembrane pressure there is high convection of fluid towards the membrane surface thus transporting the particles faster and eventually create a thicker cake layer.

To model a pore block dominant microfiltration problem, a priori experiment is required to compute the probability coefficient β . For the results shown in fig2, coefficient $\beta = 8000$ is used for all transmembrane pressures. This indicates that β is not a function of transmembrane pressure as the results from a single β value shows good agreement with experimental results. Similar to the cake dominant problem, the overall flux decline is greater for higher transmembrane pressure.

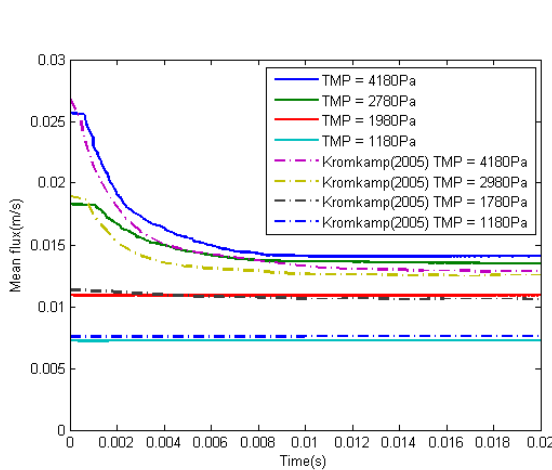


Figure 1: Comparison of effect of transmembrane pressure on permeate flux decline in a cake dominant crossflow microfiltration with previous work done [1] operating with $a = 2.5\mu\text{m}$, $\phi_0 = 0.05$ volume fraction, $\gamma = 54000\text{s}^{-1}$ and $R_m = 1.62 \times 10^8 \text{m}^{-1}$.

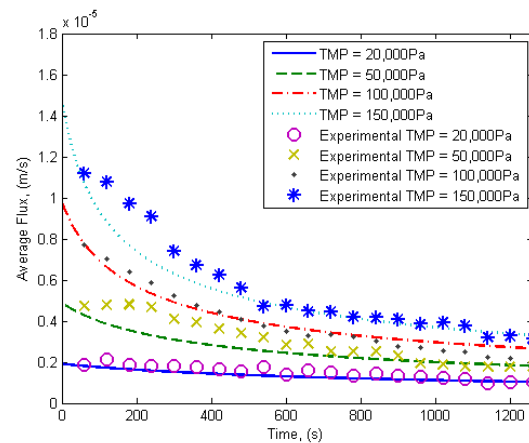


Figure 2: Comparison of effect of transmembrane pressure on permeate flux decline in a pore block dominant microcrossflow filtration with experimental results operating with $a = 20\mu\text{m}$, $\phi_0 = 0.0015$ volume fraction, $u_0 = 0.015\text{m/s}$ and $R_m = 4.5 \times 10^{12} \text{m}^{-1}$.

The nanofiltration experiments carried out by Hong et al [3] are simulated in fig3 and fig4. The effect of three different feed particle concentrations are compared in fig3. The results show greater rate of flux decline at higher feed concentration which is caused by the increase in number of particles convected. Comparison of permeate flux decline between particles of diameter 100nm and 300nm is shown in fig4. It is evident that the rate of flux decline is much greater for the smaller particle due to the lower porosity when compacted into a cake.

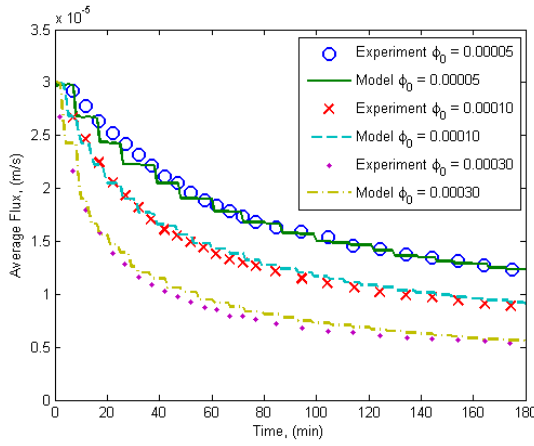


Figure 3: Comparison of effect of particle concentration on permeate flux decline in a cake dominant crossflow nanofiltration with experimental results [3] operating with $a = 50\text{nm}$, $\text{TMP} = 41.4\text{kPa}$, $\gamma = 280\text{s}^{-1}$ and $R_m = 1.39 \times 10^{12}\text{m}^{-1}$.

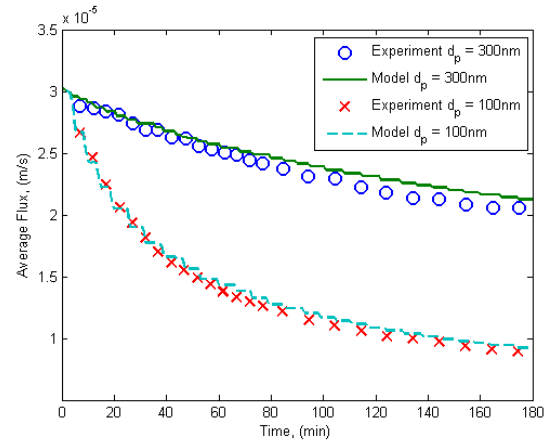


Figure 4: Comparison of effect of particle size on permeate flux decline in a cake dominant crossflow nanofiltration with experimental results [3] operating with $\text{TMP} = 41.4\text{kPa}$, $\phi_0 = 0.0001$ volume fraction, $\gamma = 280\text{s}^{-1}$ and $R_m = 1.39 \times 10^{12}\text{m}^{-1}$.

3. Conclusion

In this work we have developed a computational tool to simulate cake and pore block dominant problems for crossflow microfiltration and nanofiltration using lattice Boltzmann method to solve Navier-Stokes for hydrodynamic fluid flow and convection-diffusion equation for particle migration. Finite volume method is applied as a grid refinement coupled with the lattice Boltzmann method to provide another method to solve the convection-diffusion equation. The computational tool is tested on different cake and pore block dominant cases exploring varying effects of transmembrane pressure, feed concentration and particle size. Results were shown to be in good agreement with previous simulations [1] and experiments [3] indicating a capability of solving variety of problems in microfiltration and also nanofiltration.

Acknowledgements

The author would like to acknowledge Swansea University and the supervisors for funding and supporting this research.

References

- [1] J. Kromkamp et al. A suspension flow model for hydrodynamics and concentration polarisation in crossflow microfiltration. *Journal of Membrane Science*, 253, 69-79, 2005.
- [2] S. Kim et al. Crossflow membrane filtration of interacting nanoparticle suspension. *Journal of Membrane Science*, 284, 361-372, 2006.
- [3] S. Hong et al. Kinetics of permeate flux decline in crossflow membrane filtration of colloidal suspensions. *Journal of Colloid and Interface Science*, 196, 267-277, 1997.
- [4] Q. Zou, X. He. On pressure and velocity flow boundary conditions for the lattice Boltzmann BGK model. *Phys. Fluids*, 9, 1591-1598, 1997.
- [5] D. Freed. Lattice-Boltzmann method for macroscopic porous media modelling. *International Journal of Modern Physics*, 9, 1491-1503, 1998.
- [6] D. Leighton, A. Acrivos. Viscous resuspension. *Chemical Engineering Science*, 41, 1377-1384, 1986.
- [7] R. Davis. Shear-induced transport of a particle layer along a porous wall. *Chemical Engineering Science*, 42, 275-281, 1987.

High fidelity methods for compressible flow problems on moving domains

*Michael Weberstadt, Antonio J. Gil and Ruben Sevilla

Zienkiewicz Centre for Computational Engineering, College of Engineering, Swansea University,
 Singleton Park, SA2 8PP, United Kingdom

{439409, a.j.gil, r.sevilla}@swansea.ac.uk

ABSTRACT

This paper examines the properties of high-fidelity finite element simulations for inviscid compressible flows on moving domains by extending the SUPG method to higher order approximations. A non-conservative total Arbitrary Lagrangian Eulerian (ALE) formulation is adopted allowing a de-coupling of the so-called geometric conservation law from the flow variables. The high-order spatial approximation is combined with the implicit alpha-method temporal integrator resulting in a high-fidelity solver. The advantages of high-order approximations are illustrated by using numerical examples that involve the Burgers' and Euler flow equations for static and moving domains.

Key Words: stabilised finite elements; arbitrary Lagrangian Eulerian formulation; compressible flow; inviscid flow; high fidelity.

1. Introduction

Stabilised finite element methods, such as the Streamlined/Upwind Petrov Galerkin (SUPG), have been extensively used in the solution of flow [1] and Fluid-Structure Interaction (FSI) problems [2]. This paper presents the extension of SUPG to higher order approximations on moving domains. The ALE form of the Euler equations is revisited alongside a local geometric conservation law [3]. Several numerical examples are presented to demonstrate the applicability and advantages of the proposed approach.

2. The ALE form of the Euler equations

The ALE form of any conservation law mathematically accounts for the motion of the domain on which the equations are formulated, allowing a non-Newtonian frame of reference to be adopted. This is particularly useful for simulation of FSI problems, where the fluid domain is required to stay congruent to a deforming solid domain.

The physical laws governing the flow of an inviscid fluid are collectively known as the Euler equations. Considering a mapping $\mathbf{x} = \Phi(\chi, t)$, relating a moving spatial domain Ω_x and static referential domain Ω_χ , H_{ij} is component (i, j) of the cofactor $\mathbf{H} = \det(\partial\mathbf{x}/\partial\chi)(\partial\mathbf{x}/\partial\chi)^{-T}$ and g is the Jacobian field. In an ALE formulation for a 2D domain the Euler equations can be written, with accompanying geometric involution, as,

$$\frac{\partial \mathbf{U}}{\partial t} + \mathcal{A}_J \frac{\partial \mathbf{U}}{\partial \chi_J} - \mathbf{S} = \mathbf{0} \quad (1a)$$

$$\frac{\partial g}{\partial t} - \frac{\partial v_i}{\partial \chi_J} H_{iJ} = 0, \quad (1b)$$

where $\mathbf{U} = (\rho, \rho u_1, \rho u_2, \rho E)^T$ is the vector of conservation variables, ρ is the density, $\mathbf{u} \equiv (u_1, u_2)^T$ is the velocity vector, E is the total energy density, P is the pressure, \mathbf{S} is the source vector, $\mathcal{A}_J = (\mathbf{A}_i - \mathbf{I}v_i) H_{iJ} g^{-1}$ is the referential flux jacobian matrix, $\mathbf{A}_i = \frac{\partial \mathbf{F}_i}{\partial \mathbf{U}}$ is the spatial flux jacobian matrix, \mathbf{I} is the identity matrix, $\mathbf{F}_i = (\rho u_i, \rho u_1 u_i + \delta_{i1} P, \rho u_2 u_i + \delta_{i2} P, u_i (\rho E + P))^T$ is the inviscid flux vector, $v_i = \frac{\partial x_i}{\partial t} \Big|_\chi$ is the mesh velocity. δ_{ij} is the Kronecker delta and the summation convention is adopted for repeated indexes. Furthermore, ideal gas law is assumed, coupling pressure P to the conservation variables \mathbf{U} , and closing the system of equations. Note that under this solution formulation, the Jacobian field is an unknown to be solved for rather than computed directly from the mapping. That is $g \neq \det(\partial\mathbf{x}/\partial\chi)$.

Equations (1) constitute a multi-component non-conservative total ALE hyperbolic partial differential equation (1a) and a local geometric involution ordinary differential equation (1b).

3. SUPG for discrete ALE formulations

The SUPG method is used to discretise (1), where the stabilisation term depends upon the referential flux jacobian matrices in order to maintain invariance between SUPG applied for a static spatial formulation and a dynamic ALE formulation,

$$\int_{\Omega_\chi} \left(\underbrace{N_a}_{\text{Galerkin}} + \underbrace{\tau \mathcal{A}_J^T \frac{\partial N_a}{\partial \chi_J}}_{\text{SUPG}} \right) \cdot \left(\frac{\partial \mathbf{U}}{\partial t} + \mathcal{A}_J \frac{\partial \mathbf{U}}{\partial \chi_J} - \mathbf{S} \right) d\Omega_\chi = 0. \quad (2)$$

where N_a is the Galerkin shape function belonging to node a and τ is the stabilisation matrix. Gauss' theorem is applied to the Galerkin contributions to give a suitable boundary term before (2) is combined with the alpha method temporal integrator, to give the residual for discrete node a ,

$$\begin{aligned} \mathbf{R}_a = & \int_{\Omega_\chi} \left(N_a \cdot N_b \left(\frac{\partial \mathbf{U}}{\partial t} \right)_b^{(m)} g^{(f)} - \frac{\partial N_a}{\partial \chi_J} \cdot (\mathbf{F}_i H_{ij})^{(f)} - N_a \cdot \frac{\partial N_b}{\partial \chi_J} (\mathbf{U}_b v_i H_{ij})^{(f)} - N_a \cdot (g \mathbf{S})^{(f)} \right) d\Omega_\chi + \\ & \int_{\Gamma_\chi} (N_a \cdot (\mathbf{F}_i H_{ij})^{(f)} n_J) d\Gamma_\chi + \int_{\Omega_\chi} \left(\tau \mathcal{A}_J^T \frac{\partial N_a}{\partial \chi_J} \right)^{(n)} \cdot \left(N_b \left(\frac{\partial \mathbf{U}}{\partial t} \right)_b^{(m)} + \frac{\partial N_b}{\partial \chi_J} (\mathcal{A}_J \mathbf{U}_b)^{(f)} - \mathbf{S}^{(f)} \right) d\Omega_\chi. \quad (3) \end{aligned}$$

Bracketed () superscripts indicate the relative time of evaluation, $m \equiv n + \alpha_m$ and $f \equiv n + \alpha_f$, and α_m and α_f are parameters of the alpha method temporal integrator. Linearisation is performed by using (2), with respect to $\mathbf{U}^{(n+1)}$. These are used under a Newton-Raphson platform in order to converge to the solution.

4. Numerical examples

Numerical examples involving the inviscid Burgers' equation are considered first to demonstrate the optimal convergence of the proposed method. To guarantee that the solution of the problem is smooth the final time is chosen such that the final solution does not present a shock. The results (figure 1) show optimal temporal convergence for all values of the alpha-method parameter ρ_∞ for a static mesh. However, choices of $\rho_\infty \neq 1$ for moving meshes result in a loss of temporal accuracy. This loss arises due to a violation of GCL that is caused uniquely by the combination of the alpha method temporal integration scheme and the decoupled GCL (1a). Optimal spatial convergence is observed for both static and moving domains for a range of degrees of approximation p . The constant is greater for the cases of the moving mesh due to varying resolution of the physics, as a result of the mapping.

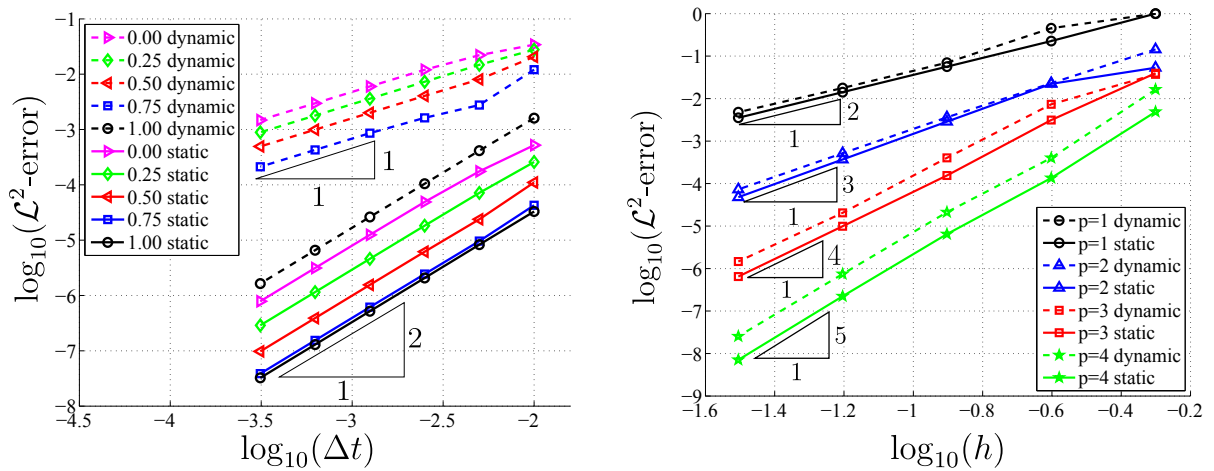


Figure 1: Temporal (left) and spatial (right) convergence study for the inviscid Burgers' equation.

The 2D formulation of the Euler equations was benchmarked against the analytical solutions for the so-called *Euler vortex* problem [4] on both static and dynamic meshes. Propagation of the vortex from a physical and referential frame of reference can be seen in figure 2. The physical (Newtonian) domain is

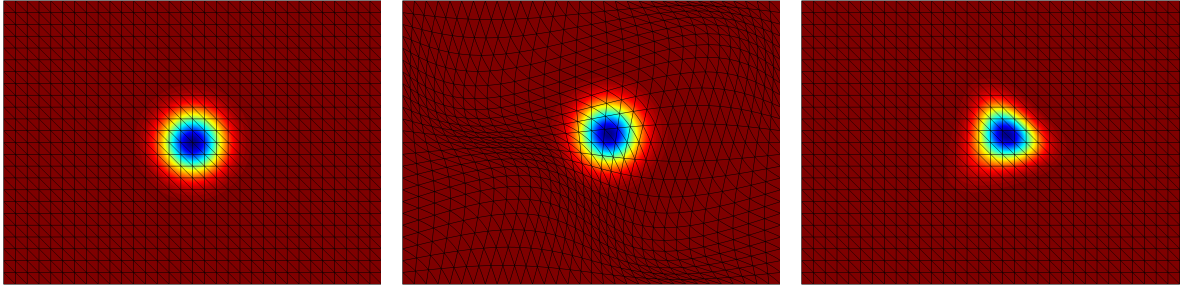


Figure 2: Density field plots of a propagating Euler vortex at $t = 0$ (left) and $t = 1$ for the physical domain (centre) and the referential domain (right) for a moving mesh.

used for visualisation of the flow fields, whereas calculations are made on the static referential domain, to which the physics are pulled back for computational efficiency.

Optimal temporal (for $\rho_\infty = 1$) and spatial accuracy were observed in all cases (figure 3). The constant of numerical convergence is consistently greater for moving meshes. Moving meshes have a greater critical rate of convection due to the velocity of the mesh. The result of this is an increased CFL number in moving meshes when compared with the equivalent static mesh for a fixed time-step Δt . Since large CFL numbers are associated with reduced accuracy, the temporal error is increased by the velocity of the mesh in the dynamic-mesh case. This is consistent with the results obtained for the Burgers' problem.

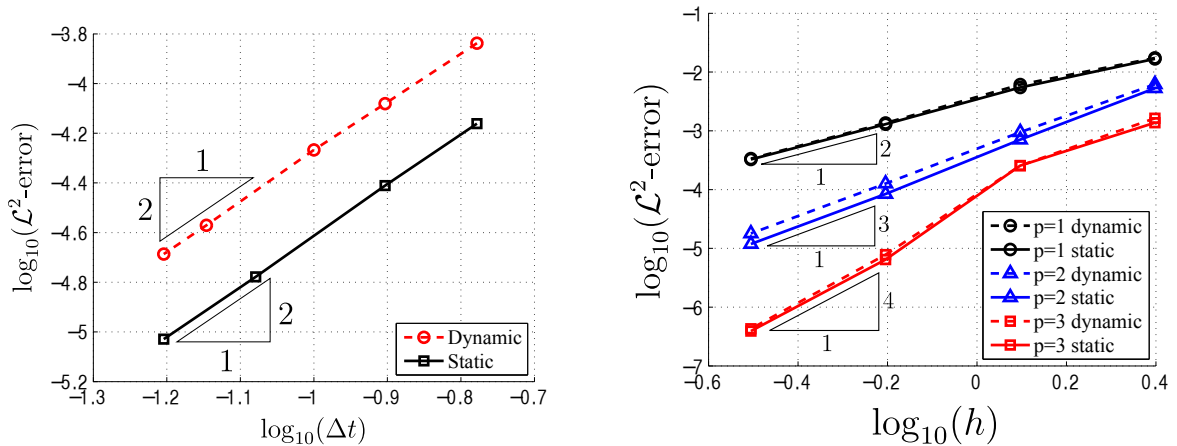


Figure 3: Temporal (left) and spatial (right) convergence study results for the propagation of an Euler vortex.

Spatial convergence rates are observed as the optimal $(p + 1)$ for all orders of approximation p . As with the Burgers' simulation, the increased constant of convergence is attributed to a varying resolution of the physics on the referential domain due to the mapping Φ , a phenomenon easily observed in figure 2.

High-fidelity methods are known to possess superior flow-effect representation due to reduced numerical diffusion [1]. Simulation of the propagation of time-harmonic gusts (figure 4) [5] was used in order to determine the computational efficiency of high-fidelity methods. Gusts were introduced by means of the source term S , and propagated a distance of approximately 7 wavelengths at which point the amplitude was evaluated against the initial, unconvected amplitude. Compared to the initial amplitude, figure 5 shows the cost to maintain 95% amplitude.

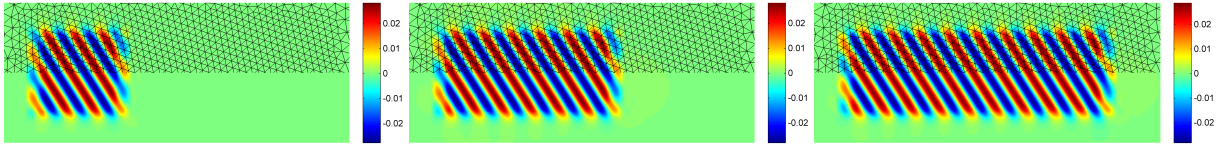


Figure 4: Vertical velocity component field solution snapshots in time (left to right) of a propagating time-harmonic gust for a cubic mesh of 2894 elements.

Number of Elements	Elements per wavelength	$p = 1$	$p = 2$	$p = 3$
876	≈ 2	1.3% (0.003)	48.4% (0.020)	80.9% (0.100)
2894	≈ 4	6.8% (0.012)	92.7% (0.074)	97.5% (0.391)
5330	≈ 8	93.1% (0.077)	96.4% (0.650)	–
20421	≈ 16	95.4% (1.000)	–	–

Figure 5: Table showing the percent of gust amplitude maintained after propagation of approximately 7 wavelengths distance. Factored CPU time is shown in brackets ().

Clearly, as the order of approximation p increases, the cost to compute the solution to a given accuracy is reduced, for the case of cubic $p = 3$ elements, a time-saving of more than 60% is achieved over linear elements. Memory requirements are also reduced, with cubic elements requiring 36% fewer degrees of freedom to capture the solution to the specified accuracy.

5. Conclusions

A new high-fidelity formulation has been presented along with a local method for enforcing GCL. Test problems for both the Burgers’ and Euler equations were employed to evaluate the properties of the formulation. Optimal temporal convergence was demonstrated for both the inviscid Burgers’ equation and Euler flow equations on both static and moving meshes. Spatial convergence was also demonstrated to be optimal for all orders of approximation p , on both static and moving meshes. A propagating time-harmonic gusts example was used to demonstrate the computational superiority of higher-order methods. Superiority was demonstrated by evaluating the relative efficiencies of high and low order methods against their ability to preserve flow effects over large distances.

Acknowledgements

The authors would like to greatly acknowledge the financial support provided by the EPSRC.

References

- [1] R. Sevilla, O. Hassan and K. Morgan, “An analysis of the performance of a high-order stabilised finite element method for simulating compressible flows”, *Computer Methods in Applied Mechanics and Engineering* 253 (2013) 15–27.
- [2] W. Dettmer and D. Perić, “A computational framework for fluid-structure interaction: Finite element formulation and applications”, *Computer Methods in Applied Mechanics and Engineering* 195 (2005) 5754–5779.
- [3] A. J. Gil, J. Bonet, J. Silla and O. Hassan, “A discrete geometric conservation law (DGCL) for a cell vertex finite-volume algorithm on moving domains”, *International Journal for Numerical Methods in Biomedical Engineering* 26 (2010) 770–779.
- [4] P.-O. Persson, J. Bonet and J. Peraire, “Discontinuous galerkin solution of the navier-stokes equation on deformable domains”, *Computer Methods in Applied Mechanics and Engineering* 198 (2009) 1585–1595.
- [5] V. Golubev and M. Visbal, “Unsteady viscous analysis of low-re gust-airfoil interaction”, in: *ECCOMAS CFD 2010*, 2010.

Particles as Porpoise - Applying CFD Results to Environmental Interactions

*Thomas Lake, Ian Masters and T. Nick Croft

Marine Energy Research Group, College of Engineering, Swansea University, SA2 8PP

*527562@swansea.ac.uk

ABSTRACT

Individual Based Models (IBMs) provide a way of taking simple rules and principles and simulating the movement and interaction of living creatures with each other and/or the environment around them. These models have been used to investigate habitat use and movements of a variety of animals, including both marine and terrestrial mammals, fish and birds, over a range of timescales and degrees of sophistication. An advantage of this type of model is the potential to allow changes to the environment to be simulated, and potential effects of these changes to be investigated before they take place. This could include potential impacts of marine energy devices on local marine mammals.

This model uses meshes and tidal flow data from an openTELEMAC model, with the 3D mesh being composed of linear, wedge shaped elements with nodes fixed in x, y but with time varying z coordinates. Data values (such as x, y and z flow velocities, prey density or noise levels) are specified at each node and are interpolated spatially using mean value coordinates and interpolated linearly with respect to time in order to obtain values at the location of each individual animal, or boid, within the simulation. The movement of the mesh, including the changing heights of the elements, leads to a variety of issues when tracking the location of the boids within the mesh.

Key Words: *Individual Based Model, Marine Energy, Environmental Impact, Harbour Porpoise, Phocoena Phocoena*

1. Introduction

1.1. Marine Energy

The UK has access to the best wind, wave and tidal energy resources in Europe, and has a well developed renewable electricity sector[6]. In 2013, 14.9% of electricity generated in the UK came from renewable sources, with 32% of that coming from onshore wind and a further 21% from offshore wind[5]. Electricity generation from wave and tidal resources is a smaller contributor to the UK's energy needs, with current supply being limited to a small number of testing and demonstration sites, which were predicted to reach a total of 300MW of installed capacity by 2020, but with a total theoretical resource of 69TWh/year for wave energy, 95TWh/year for tidal stream devices, 25TWh/year from tidal lagoons and 96TWh/year from tidal barrages[10].

1.2. Environmental Impacts

The environmental impact of any construction or engineering project is something that should always be taken into consideration, and in many cases is a regulatory requirement. In the context of marine energy developments, an environmental impact assessment (EIA) is a legal obligation in almost all cases within the EU and the UK[2]. In part, this is due to the number of protected species and habitats that are part of the marine habitat and need to be conserved. It is also a requirement to consider the impact of a development on other people and groups using the area, which can also be investigated using the methods described below.

A typical EIA will include details on the effect of the proposed development on physical processes, including currents, changes to tidal flows, ranges and the local wave climate, sediment transport and

other changes to the local water quality. These aspects of the assessment can be covered using existing, well established numerical modelling techniques combined with detailed site observations to validate the models used. Other aspects that need to be investigated cover the potential impacts on marine life in the area, such as fish, birds and marine mammals. The latter group includes both cetaceans such as dolphins and porpoise that live exclusively in water and animals such as seals, which spend time on the shoreline as well as at sea.

2. Individual Based Modelling

2.1. Introduction

An individual based model is designed to independently simulate the movements and/or states of a number of individual objects or creatures. These simulated objects, referred to as agents or boids, are designed to mimic a subset of the natural behaviour of the real objects or creatures they represent. It has previously been shown (and previously discussed in [8]) that plausible looking behaviour can be obtained from comparatively simple rules and behaviours. This has been extended by a range of other works to show that these simulated behaviours can be representative of real world animal behaviours, rather than just being visibly plausible.

A simple IBM can be described as an iterative process - At each timestep every boid acquires details about it's surroundings, applies its list of behavioural rules to that data and its position, velocity and other properties are updated accordingly. The information available to each boid during this process can be limited to restrict the simulated sensory range of each creature.

2.2. Previous Examples

It has been shown that plausible behaviours can be achieved with a small selection of rules. An early application of this technique came from work aimed at creating believable computer animations for a flock of birds. Three simple rules were implemented, and ranked in importance:[9]

1. Avoid collisions with nearby boids
2. Match velocity with neighbouring boids
3. Aim to stay close to centre of the flock¹

While the exact rules used vary between different simulations, they serve to illustrate that reasonably simple rules can give rise to otherwise complex behaviours and patterns. Individual Based Models have been used to predict the movement of a range of animals, from larvae in complex tidal environments[11] to panthers[4]. These (and many other) examples compare favourably to field measurements of the species in question.

3. Building a Harbour Porpoise IBM

One species of interest for marine energy developers in Wales is the Harbour Porpoise (*Phocoena Phocoena*) - a small cetacean found in many coastal areas[3]. Harbour Porpoise are protected under the EU Habitats directive[1], which makes it illegal to capture, kill or disturb these animals - the potential for disturbance is one of the aspects that developers must investigate as part of their Environmental Impact Assessment, as mentioned above.

3.1. Simulated seas

In this model, boids representing Harbour Porpoise will be placed into a simulated tidal environment. This environment will be based on the output of a model in openTELEMAC - a set of simulation tools commonly used for a range of hydrodynamic simulations, including large tidal areas. The 3D meshes used by openTELEMAC consist of layers of a 2D triangular mesh, forming prismatic elements as shown in figure 1. These nodes forming these elements move vertically over time, with the uppermost layer of the mesh representing the free surface of the water. This means that elements are free to grow, shrink and move in the z -axis, but are constrained in x and y . This requires the vertical coordinates of every node to be updated at the start of each timestep and the position and/or enclosing element of each boid altered accordingly.

¹Or the portions of the flock within the perceptual range of that boid

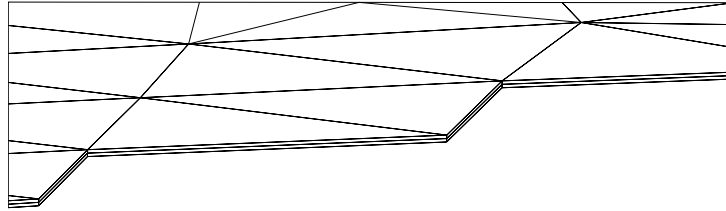


Figure 1: Slice of an example mesh, showing how the triangular faces of the 2D mesh form prismatic elements

The elements in the openTELEMAC models used have edges in the x, y plane ranging in length from 50m to 1700m, with vertical edges ranging from 0m to 40m. This presents two problems - elements with zero height and large distances between nodes and the potential locations of boids within the simulation. Dry/zero height elements are handled at the start of each timestep - the smallest vertical separation between points is calculated once the z -coordinates have been updated and stored in the element for future use. This minimum element height is then taken as the input for one of the behavioural rules, as described below.

The distances between boids and their adjacent nodes, and the potential variation in local variables that this allows, are handled using mean value coordinate interpolation. This interpolation technique takes the values of input variables at each node of an element and calculates a value at the location of our boid or test point. The technique generates smooth, continuous values for any closed polygon and any planar polyhedron[7], and allows a suitable linearly interpolated value to be calculated for the interior of any element.

3.2. Example behaviour: Responding to water depth

In order to illustrate the response of the simulated boids to changing environmental conditions, a sample set of results is presented below. These results incorporate 3 simple rules:

- Is height of element $< 5\text{m}$?
 - Yes: Head for deeper water
 - Otherwise:
 - * Head towards greater concentrations of food
 - * Minimise drag

The direction to deeper water is determined by the local elevation gradient (precomputed), and takes precedence over other behaviours. The general behaviour is subject to further work, but was implemented as a weighted average of the two conflicting aims with an additional noise term. The addition of noise to the orientation and velocity terms of the model is a common component of similar environmental models, the resulting paths are referred to as Correlated Random Walks² (CRWs).

The output of this example is shown in figure 2. The background mesh represents a snapshot at the end of the simulation - the depths change over the course of the simulation. It can be seen that the porpoise stay within the deeper channel when searching for deeper areas (white trails), remaining in an area to feed when those deeper areas are encountered (black trails). A small number of areas are crossed by both black and white trails - this is due to the changing water depth throughout the simulation - while some boids may enter an area when it is deeper than the threshold (5m in this instance), others may enter the area at a shallower time and continue searching for deeper water.

4. Conclusions

Although brief, the example illustrates that relatively complex behaviours can be simulated with comparatively simple rules and inputs. It also touches upon some of the additional complication encountered when applying CFD and numerical models to a realistic environment.

²Although porpoise swim rather than walk, the term is retained for ease of reference

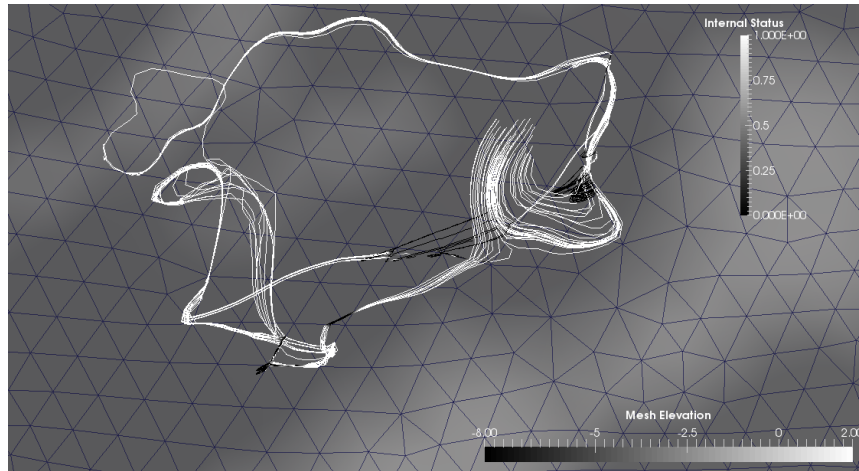


Figure 2: Example output, showing paths taken by boids representing Harbour Porpoise

Acknowledgements

The authors would like to acknowledge the support of EPSRC through grant EP/I027912/1, which funds the UKCMER project

References

- [1] Council Directive 92/43/EEC of 21 May 1992 on the conservation of natural habitats and of wild fauna and flora, as amended.
- [2] Directive 2011/92/EU of the European Parliament and of the Council of 13 December 2011 on the assessment of the effects of certain public and private projects on the environment, o.J. L. 26, 28.1.2012.
- [3] P. Berggren, P. Wade, J. Carlström, A. Read, Potential limits to anthropogenic mortality for harbour porpoises in the Baltic region, *Biological Conservation* 103 (3) (2002) 313 – 322. doi:[http://dx.doi.org/10.1016/S0006-3207\(01\)00142-2](http://dx.doi.org/10.1016/S0006-3207(01)00142-2). URL <http://www.sciencedirect.com/science/article/pii/S0006320701001422>
- [4] P. C. Cramer, K. M. Portier, Modeling Florida panther movements in response to human attributes of the landscape and ecological settings, *Ecological Modelling* 140 (2001) 51–80. doi:10.1016/S0304-3800(01)00268-X.
- [5] Department of Energy & Climate Change, Digest of United Kingdom Energy Statistics 2014, TSO, London, 2014, Ch. 6, pp. 157–194. URL <https://www.gov.uk/government/collections/digest-of-uk-energy-statistics-dukes>
- [6] HM Government, UK Renewable Energy Roadmap, Tech. rep., Department of Energy and Climate Change (Jul. 2011).
- [7] T. Ju, S. Schaefer, J. Warren, Mean value coordinates for closed triangular meshes, *ACM Transactions on Graphics* 24 (3) (2005) 561–566. doi:10.1145/1073204.1073229.
- [8] T. Lake, T. N. Croft, I. Masters, Methods for Individual Based Modelling of Harbour Porpoise, in: *Proceedings of the 10th European Wave and Tidal Energy Conference*, 2013.
- [9] C. W. Reynolds, Flocks, herds and schools: A distributed behavioral model, *ACM SIGGRAPH Computer Graphics* 21 (4) (1987) 25–34. URL <http://www.red3d.com/cwr/boids/>
- [10] The Crown Estate, UK Wave and Tidal Key Resource Areas Project, Tech. rep., The Crown Estate (Oct. 2012).
- [11] J. Willis, Modelling swimming aquatic animals in hydrodynamic models, *Ecological Modelling* 222 (2324) (2011) 3869–3887. doi:10.1016/j.ecolmodel.2011.10.004. URL <http://www.sciencedirect.com/science/article/pii/S0304380011004893>

FRACTURE AND FAILURE 1

Computational modelling of crack propagation in shale-gas reservoir rocks

*M. Mousavi-Nezhad¹, E. Gironacci¹, M. Rezaia² and Q. J. Fisher³

¹Computational Mechanic, Civil Research Group, School of Engineering, University of Warwick, Coventry,
CV4 7AL, UK

²Nottingham Centre for Geomechanics, Department of Civil Engineering, Faculty of Engineering, University of
Nottingham, Nottingham, NG7 2 RD, UK

³School of Earth and Environment, University of Leeds, Leeds, LS2 9JT, UK

*M.Mousavi-Nezhad@warwick.ac.uk

ABSTRACT

This paper presents a computational modelling framework for simulation of crack propagation in brittle materials. The framework is on the basis of a variational approach, consistent with Griffith's theory. The modelling framework is used to reproduce the fracture propagation process in a shale rock sample under standard laboratory Brazilian Disc test. To incorporate the effects of shale formation heterogeneity in simulation of crack paths, fracture properties of the sample are defined as spatially random fields. A parametric study has been carried out to better understand how anisotropy and heterogeneity of the mechanical properties affect both direction of cracks and rock strength.

Key Words: *fracking; crack propagation; heterogeneous shale rock*

1. Introduction

Hydraulic fracturing, commonly known as “fracking”, is important in extracting gas from shale formations, but accurate prediction of the direction and extent of fractures is required to conduct gas production operations in safe and economically viable manner. Fracture toughness, the resistance of the rock to crack propagation, is considered to be a significant factor in determining the pattern of artificially created fracture network.

Fractures tend to propagate along the direction of the least resistance path. The direction and extent of this path is a complex function of *in-situ* stress condition, anisotropic mechanical properties of the rock, and pore and fracture fluid pressures [1]. It is possible to evaluate the influence of the *in-situ* stress condition and pore-pressure variations on the evolution of fracture networks. This could be done using a hydraulic fracture test, deep borehole data from the field, and coupled fluid-solid computational codes. However, the role of spatial variability and anisotropy of mechanical properties on crack propagation remains poorly understood.

In the context of numerical modelling, strategies for characterising the random heterogeneity in materials can be categorized as either multi-scale homogenization or spatially-varying random fields. The former is attractive from the point of view that the different phases in a material such as the matrix, inclusions, and the interfaces are explicitly modelled. However, the applicability of the method is limited to the cases that a closed-form macroscopic equation can be driven to describe the relevant microstructural details, e.g. morphology, constituent material properties. Spatially-varying random field based approaches are able to directly approximate the randomness through generation of spatial realizations of the properties associated to a given correlation structures, and the crack trajectory is modeled using finite element method within the context of Monte Carlo simulation.

This paper focuses on developing a computational modelling framework for simulation of crack propagation in brittle materials. We also report laboratory measurements on the mechanical properties of core samples of shale-gas reservoir rocks collected from the Dove's Nest site on the east coast of North Yorkshire, in England. We present data on the general mechanical behaviour of these rocks to delineate the basic parameters that control propagation of cracks in shale-gas rocks. We also discuss these data in the context of numerical models to better understand how anisotropy of the properties affect morphology and direction of cracks.

2. Fracture advancement methodology

The computational framework developed here, is on the basis of variational model for brittle fracture. Equilibrium of a body under conveniently set boundary conditions, is studied from the minimization of

$$E(f, K) = \int_{\Omega \setminus K} W(F(x)) dx + GH^{N-1}(K) \quad (1)$$

which is expressed as sum of a bulk energy and a surface energy. The Eq. (1) is solved using a regularization theory proposed by Del Piero et al. [2], which approximates it in the sense of gamma-convergence. The term H states the jump in the displacement field in correspondence of the fracture surface, and is approximated by a smooth scalar field which accounts for “damage” field. The regularized functional used for the resolution of the problem is given in the form

$$\mathfrak{S}_\varepsilon(f, s) = \int_{\Omega_0} (s^2(x) + \kappa_\varepsilon) W(\nabla_0 f(x)) dx_0 + G \int_{\Omega_0} \left(\frac{\varepsilon}{2} |\nabla_0 s(x_0)|^2 + \frac{1}{2\varepsilon} (1 - s(x_0))^2 \right) dx_0 \quad (2)$$

where s is damage parameter, κ_ε is a regularization parameter, G is Griffith’s Energy, ε is related to the material length scale. The resolution is obtained via alternate minimization of the Eq. 2. The formulation of bulk energy W is the one proposed by Amor et al. [3], as it is capable to account for both crack opening mode I and II.

3. Fracture toughness evaluation from experiments

A Brazilian test was conducted on a shale sample in order to indirectly measure its tensile strength and Griffith’s Energy. The sample was taken from the shale gas reservoirs in the Dove’s Nest site on the east coast of North Yorkshire, England, from a depth of 246 m. Measured values of Young’s modulus and Poisson ratio are 29.6 GPa, and 0.25 respectively. The local expression to calculate Griffith’s Energy G is given as [4]:

$$G = K^2 / E' \quad (3)$$

where $E' = E / (1 - \nu^2)$ is the Elastic modulus for plain strain condition, ν is Poisson’s ratio and K is the Stress Intensity Factor (SIF). Fracture occur in a solid when $K = K_{IC}$, where K_{IC} is the Fracture Toughness or Critical Stress Intensity Factor [5]. The general formula to express the stress field around the crack tip is given as a linear combination of the mode-I and mode-II SIFs, multiplied by opportune functions which are dependent on the crack initiation point location [6]:

$$\sigma_{ij}(r, \theta) = \frac{K_I}{\sqrt{2\pi r}} f_{ij}^I(\theta) + \frac{K_{II}}{\sqrt{2\pi r}} f_{ij}^{II}(\theta) \quad (4)$$

where $f_{ij}^I(\theta)$ and $f_{ij}^{II}(\theta)$ are the angular variation functions related to crack angle and r is the critical distance from the crack tip, K_I and K_{II} are respectively the mode I and II SIFs. In the shale sample, crack is considered to roughly initiate along the vertical diameter, making $\theta = 0^\circ$. So, the second term on the right hand side of Eq. 4 vanishes. For a given value of maximum stress, the value of critical K_I is determined by

$$K_I = \sigma_{ij} \sqrt{2\pi r} \quad (5)$$

SIF is a function of the applied force and the initial crack length [4]. Therefore, comprehending the location of the crack initiation point is crucial. Following conclusions from [7], we assume the crack initiation point located at $r_c/R \approx 0.83$, where R represents the radius of the specimen, and r_c represents the distance of the point from the disc center. Applying (5) and (3), one gets the value for Griffith’s Energy, which for our case is equal to 2.5×10^{-2} N/mm.

4. Results and discussion

Comparison of crack patterns generated from the experimental test and the numerical simulations is shown in Figure 1, where we can observe how the numerical model is capable to capture the crack path properly.

A statistical technique is employed to represent spatial variability of material properties in the computational framework. Weibull distribution function is used to generate random distributions of the properties, as it has a simple structure and its applicability for modeling failure of brittle materials has been proved in [6, 8]. In this study, fracture toughness has been considered as a random variable.

To investigate the influence of the rock bedding orientations on propagation of fractures, we considered four distinct models. The models differ by the angle between the direction of loading and the orientation of the bedding planes which is at 0, 30°, 60°, and 90° from the horizontal axis.

A fixed value of 0.025 N/mm for Griffith's Energy is assigned to all the bedding, while different values of Young's modulus and Poisson ratio are assigned to each layer. The evolution of the damage state of the body for all the models is shown in Figure 2. At the instant immediately prior to failure, damage parameter s reaches its lowest value in the local-damaged zone. Measured and predicted (using the stochastic and deterministic modelling approaches) stress-strain paths are presented in Figure 3(a). The Monte Carlo simulation with 100 random samples is conducted to predict average stress-strain response of the fracturing body. Both deterministic and stochastic models predict accurately the mechanical behaviour of the fracturing body at small strains. However, stochastic simulation provides a more realistic prediction beyond relatively small strains. It can be seen that deterministic simulation failure occurs at smaller strain. Therefore, neglecting heterogeneity of the body may result in underestimation of the failure strength.

We can observe in Figure 3(b) the effect of bedding angle on the tensile strength. Maximum values of tensile strength are obtained for angles of 0 and 90 degrees, and the minimum is associated to the 30 degree inclined bedding. Higher stiffness is found for horizontal and vertical layered materials.

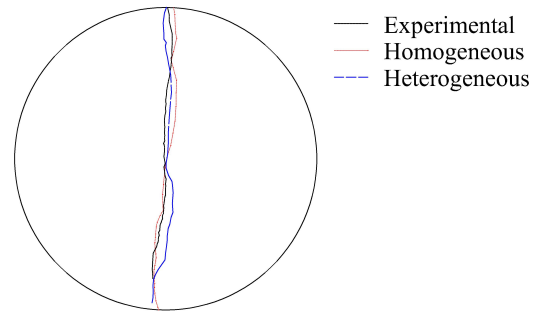


Figure 1: Comparison between experimental (black) and numerical modelled crack paths for homogeneous (red) and one of the heterogeneous (blue) models

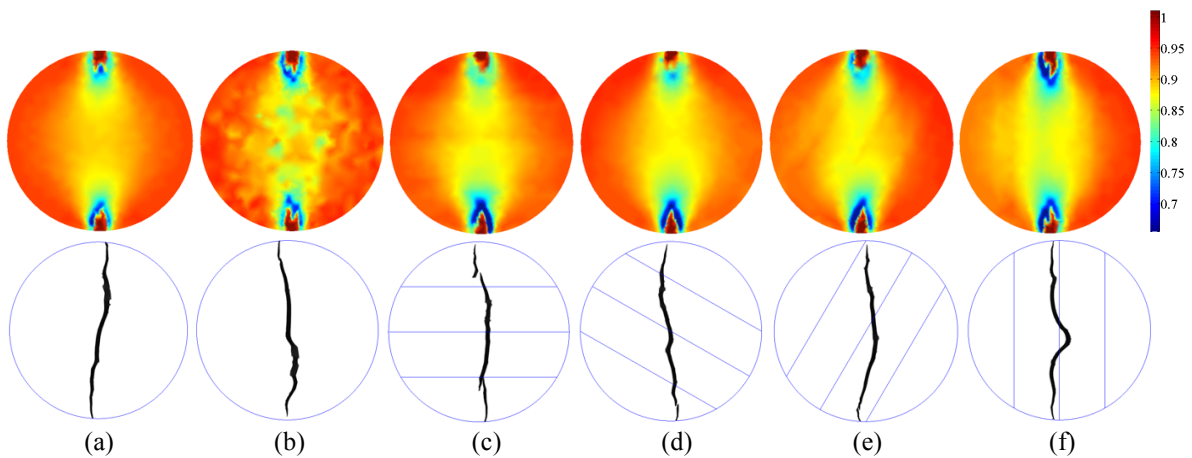


Figure 2: Damage state and crack paths from all the simulations: homogeneous (a); heterogeneous (b); bedding angle of 0° (c), 30° (d), 60° (e) and 90° (f).

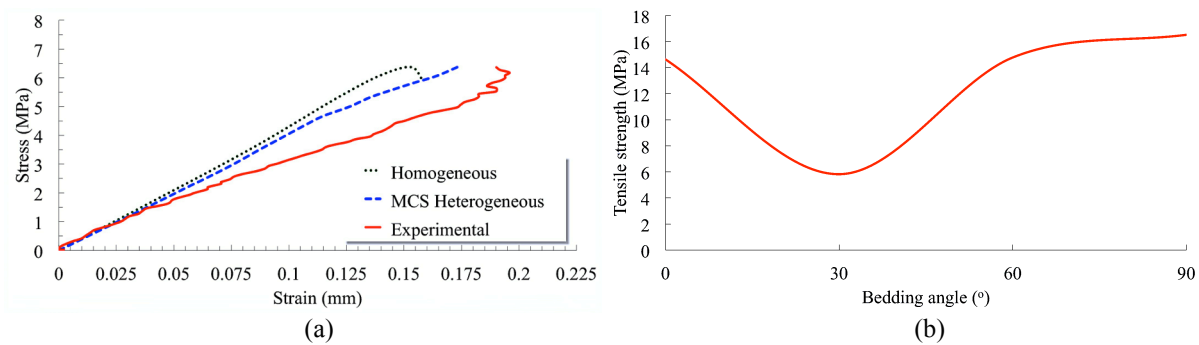


Figure 3: Stress-Strain plot comparing the experimental results and numerical data from homogeneous and heterogeneous models (a); tensile strength for layered materials (b)

5. Conclusions

Experimental data obtained from a Brazilian test conducted on a shale intact disc has been presented and employed for evaluating the material fracture toughness. The fracture toughness was calculated using the linear elastic fracture mechanics principles. A computational framework has been developed in this study that predicts the crack initiation and propagation based on a variational approach and the principle of energy minimization. The framework has been validated using the results of the Brazilian test. From the numerical analysis reported it may be concluded that inclusion of heterogeneity is likely to allow computational predictions to be more realistic of how rock masses actually fracture. Also, the simulation results show that the presence of bedding planes plays a major role in mechanical behavior of rocks.

Acknowledgements

This work was supported by Warwick Research Development Fund. We also acknowledge Prof. Toby Mottram for his helpful comments.

References

- [1] Warpinski N.R., Smith M.B., Rock Mechanics and Fracture Geometry. *Recent advances in Hydraulic Fracturing*, SPE Monographs, Vol.12, pp. 57-80, 1990.
- [2] Del Piero, G., Lancioni, G., & March, R., A variational model for fracture mechanics: numerical experiments. *Journal of the Mechanics and Physics of Solids*, 55(12), 2513-2537, 2007.
- [3] Amor, H., Marigo, J. J., & Maurini, C., Regularized formulation of the variational brittle fracture with unilateral contact: Numerical experiments. *Journal of the Mechanics and Physics of Solids*, 57(8), 1209-1229, 2009.
- [4] Knott, J.F., Elliott, D. (1979), Worked Examples in Fracture Mechanics. *The Institution of Metallurgists*. Monography No. 4, 1979.
- [5] Standard, A. S. T. M. E399-72, *Standard Method of Test for Plane-Strain Fracture Toughness of Metallic Materials*, 1972.
- [6] Bourdin, B., Francfort, G. A., & Marigo, J. J., Numerical experiments in revisited brittle fracture. *Journal of the Mechanics and Physics of Solids*, 48(4), 797-826, 2000.
- [7] Li, D., & Wong, L. N. Y., The Brazilian disc test for rock mechanics applications: review and new insights. *Rock mechanics and rock engineering*, 46(2), 269-287, 2013.
- [8] Lawn, B. R., *Fracture of brittle solids*. Cambridge University Press, 1993.

FEMME: A MULTI-SCALE FINITE ELEMENT MICROSTRUCTURE MESHFREE FRACTURE MODEL FOR QUASI-BRITTLE MATERIALS WITH COMPLEX MICROSTRUCTURES.

*Luis Saucedo-Mora¹ and Thomas James Marrow²

University of Oxford, ¹Department of Materials, ²Oxford Martin School,
Parks Road, Oxford OX1 3PH, United Kingdom

*luis.saucedomora@materials.ox.ac.uk

ABSTRACT

In this paper we develop a Finite Element Microstructure Meshfree (FEMME) method to account for the effect of microstructure on quasi-brittle properties within finite element simulations of damage. This method provides two sets or layers of elements representing the finite element model and the microstructure. The first is used to link the engineering scale problem with the microstructure, obtaining the stress and strain fields of the macro-mechanical problem; from these, we compute the micro-mechanical fields using the second set of elements, which describes explicitly the microstructure. We use the Meshfree approach to calculate damage development through the microstructure; the material properties of the finite elements are recomputed according to the microstructure damage and the fracture path is completely free with respect to the finite element mesh. Using this very efficient FEMME method, quasi-brittle fracture can develop freely throughout the microstructure, improving the accuracy and computational cost of calculations at engineering length-scales in materials with complex microstructures.

Keywords: *Quasi-brittle fracture, Meshfree, Multi-Scale*

1. Introduction

Quasi-brittle fracture is an emergent characteristic of heterogeneous brittle materials that cannot be treated satisfactorily with numerical methods that are based on macromechanics; because of their complex microstructure, the continuum approach can be too simple for these materials, requiring a finer discretization to obtain satisfactory results. In numerical terms, this means that the computational cost of advanced methods, such as cohesive elements or embedded cracks, is often too high for engineering scale problems. In order to reduce the computational cost, the numerical full-scale models of components and engineering structures are simplified to consider a continuum material with a coarse mesh, thus the modelling of complex multi-physic problems that involve the interaction between the large-scale component and the microstructure of the material becomes unachievable, despite of its great importance in structural integrity and its direct relationship with safety assessments. This makes progress in this field currently very limited.

The FEMME (Finite Element Microstructural Meshfree) [1] model is a multiscale model for quasi-brittle fracture capable of introducing the microstructure as a local enrichment in the damaged zones of the large-scale model of the full structure, releasing the spurious fracture energy of a coarse FE mesh. This novel approach is a variation of the Cellular Automata integrated with Finite Elements (CAFE) [2], which has been improved by the development of the Microstructural Adaptive Meshfree (MAM) model that uses the iso-geometry of the microstructural features to construct its local shape functions. This makes the multi-scale FEMME method fast and detailed compared with alternative approaches. The microstructure is simulated explicitly by the subdivision of a potentially damaged finite element into smaller cells, assigning to each one the fracture properties of the different phases, represented geometrically by the microstructural features, which are used also to compute the maximum entropy exponential shape functions [3] of the MAM model. With this, the influence of the finite element mesh is effectively removed during the development of the microstructure. Graded microstructures, textures, particle anisotropy and multiple phases can be readily simulated in the

damaged zones, such as those in composites and porous materials.

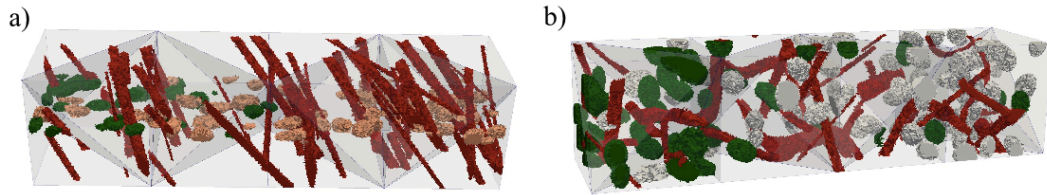


Figure 1: Creation of a mixed microstructure composed by different ellipsoidal particles with a) straight and b) curved fibres

The three layers used represent: (i) the macromechanical model (i.e. Finite Elements); (ii) the microstructural features (i.e. Microstructural Adaptive Meshfree); and (iii) the material of the different phases (i.e. Cellular Automata). In common with other damage models, such as Cohesive FE or X-FEM, these features are developed locally in the damaged zones of the macro-mechanical model. The damage information is shared between layers by the Hill-Mandell theorem of energy homogenization [4], changing the stiffness of every layer according to the damage in the microstructure. Hence, every finite element has an equivalent but variable cohesive behaviour, which avoids the effect of the artificial increment of the fracture energy by the FE coarse mesh. This allows the study of the damage development with discontinuous cracking and coalescence, and its sensitivity to microstructure.

2. The Microstructural Adaptive Meshfree model as a local enrichment of a coarse FE mesh

The FEMME methodology is a new basis for modelling multi-physic problems in graded or heterogeneous microstructures. Finite element (FE) models that deal with microstructures explicitly need a very fine discretization and consequently a high computational cost. This is because in heterogeneous materials the different phases and pores affect the distribution of the deformations that lead to the failure of the structural element. The computational cost is improved in the FEMME method by the use of a model that simplifies the microstructural features (i.e. ellipsoids with random orientation and size) and uses the minimum number of elements to characterize the displacements of the microstructure through the MAM layer (Microstructural Adaptive Meshfree model) [1]. The MAM discretization is composed of Inter Particle Domains (IPD), which represent the matrix of the material and link the microstructural features, and the Particle Domains (PD), which represent the interior of each microstructural feature; complex microstructures with pores and particles of different stiffness can be reproduced. The Boundary conditions in the MAM model are imposed through the imposition of the displacements of the IPD, which have nodes of the FE mesh inside.

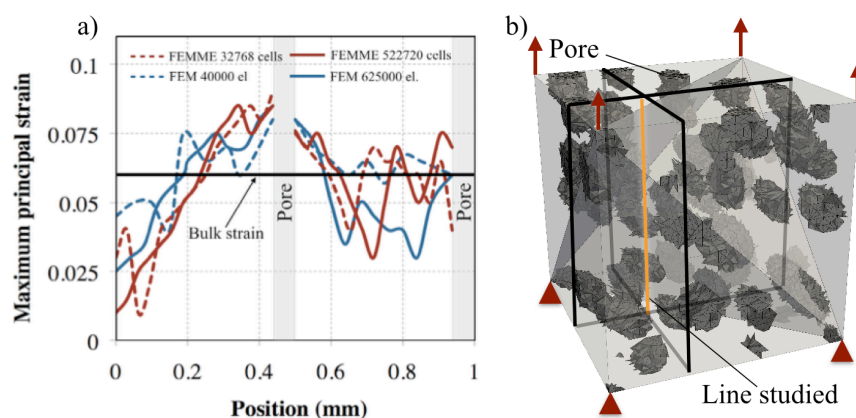


Figure 2: Strains predicted along different sections of a porous microstructure by the 3D FEMME and FEM simulations at equivalent levels of discretization.

Good agreement is demonstrated, consistent with the level of discretization, between the strains

computed by FE and the FEMME models, both with the same microstructure (Figure 2). The arbitrary material properties of the example are a Poisson's ratio of 0.2 and a Young moduli of 12 GPa for the matrix and 0 GPa for the pores. The FEMME model shown is composed in two cases by 5 Finite Elements (Figure 2b), 888 IPD and 70 PD, changing only the number of cells (i.e. 32768 and 522720), those are compared with 2 FE models with 40000 and 625000 elements and the same microstructure. This shows that the MAM model acts as a local enrichment of the FE model with the coarse mesh, achieving an equivalent solution. Due to the significant reduction of the number of operations (i.e. 2 orders of magnitude fewer for the coarse discretization and 4 orders for the fine discretization) in the FEMME model can significantly aid fracture modelling, as several iterations would be needed to reach convergence in every step.

3. Damage model

For large-scale numerical FE models, coarse meshes are needed to reach a feasible solution with a reasonable computational cost. In inelastic materials, such as quasi-brittle materials, the use of a coarse mesh over estimates the fracture energy released via damage of the component, and consequently a solution far from its real behaviour may be obtained. This is typically addressed by combination of a cohesive zone model and local refinement of the FE mesh, where the fracture path needs to be predefined, hence losing versatility; embedded cracks do not solve completely the over estimation of the fracture energy and considers a continuous material. Other methodologies, with a higher computational cost, use a large scale FE elastic model to compute the displacements of a certain region and implement these as the boundary conditions of a smaller-scale microstructural model in which the local damage is computed, obtaining the effect of the local damage on the full structure through energy homogenization. Both problems are solved by the MAM methodology, which releases the fracture energy of the damaged zone and the elastic energy of the surrounding area with the minimum discretization needed.

The MAM model is used to compute the displacements and strains of the microstructure from the displacements of the nodes of the coarse large-scale FE mesh. With this, the displacements are mapped into the cells to compute the strain of each cell and evaluate it against its critical strain, characteristic of the phase that is representing. After this, the energy is homogenized with the Hill-Mandell theorem and the mechanical properties of the MAM domain that contains the damaged cells is recomputed accordingly.

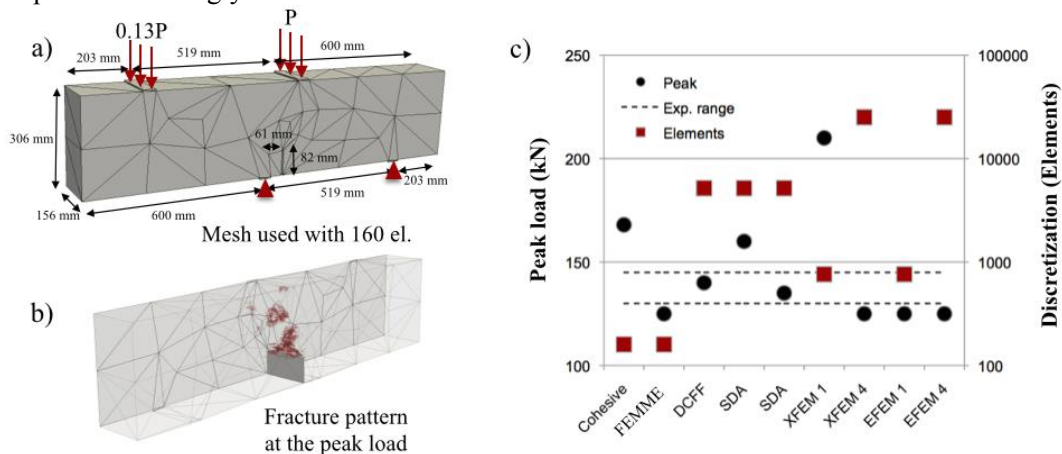


Figure 3: Comparison between different methodologies; a) mesh used in the FEMME model and its dimensions; b) fracture pattern at the peak load of the FEMME model; c) comparison of the peak load and discretization of the FEMME model and different numerical models based on FEM: Cohesive Elements, Cohesive Faces (DCFF) [5], Strong Discontinuities (SDA) [5], Nodal Enriched (XFEM 1, 4) [6] and Element Enrichment (EFEM 1, 4) [6].

In Figure 3 the FEMME method is compared with other methodologies that are typically used in computational fracture mechanics, of which E-FEM and X-FEM [6] are example enrichment

methodologies that can also reach a good solution with a coarse mesh; these require the assumption of a cohesive law. The release of the spurious fracture energy in the FEMME methodology is equivalent to that achieved by E-FEM. The four-point shear test carried out by Arrera and Ingraffea [7], which is a common benchmark test for numerical fracture models, is used for the comparison. We compare the FEMME simulation results, that takes in total 54 min to run in serial on a Intel Core i7-3930K 3.20 GHz machine, with the numerical models of Oliver et al [6] and Yu et al [5]; all were applied to this same problem, with the same geometry and material. The FE mesh used, with 160 tetrahedral elements with a single integration point, is shown in Figure 3a; fracture is defined at the peak load in Figure 3b. Comparison is made in Figure 3c, in terms of the predicted fracture load (data for the range of strength experimentally measured by Arrera and Ingraffea [7] are shown) and the number of elements, with other methodologies that either need to predefine a fine mesh along the fracture path, such as cohesive faces (DCFF), cohesive elements or strong discontinuities (SDA), and those that can deal with a mesh without a predefined fracture path, such as XFEM and EFEM. The FEMME model is shown to reach a good solution using a coarse mesh, demonstrating the potential for this methodology to simulate fracture using the coarse mesh in structural elements without requiring a predefined fracture path.

4. Conclusions

Through the multi-scale application of Meshfree and Cellular Automata models, we have demonstrated a novel Finite Element Microstructure Meshfree (FEMME) method of conducting a normalization of the energy release of a Finite Element Method calculation with a coarse mesh. This allows us to carry out, with significant efficiency, FE calculations of strain development with a coarse mesh without losing accuracy in the solution. This is achieved through a high fidelity reproduction of the microstructure and the adaptation of the Meshfree Model to its geometry. Importantly, the computational cost of the FEMME method is lower than a FEM with a similar discretization. This makes the FEMME model very promising for the fracture modeling of components at engineering scale, taking into account the effects of the microstructure of the material.

Acknowledgements

This work was carried out with the support of the UK EPSRC project “QUBE: Quasi-Brittle fracture: a 3D Experimentally-validated approach” (EP/J019992/1).

References

- [1] L. Saucedo-Mora and T.J. Marrow. FEMME: a multi-scale Finite Element Microstructure Meshfree fracture model for quasi-brittle materials with complex microstructures. Submitted to *Engineering fracture mechanics*.
- [2] A. Shterenlikht and I.C. Howard, The CAFE model of fracture-application to a TMCR steel. *Fatigue and Fracture of Engineering Materials and Structures*, 29 (9-10), 770-787, 2006
- [3] M. Arroyo and M. Ortiz. Local maximum-entropy approximation schemes: a seamless bridge between finite elements and meshfree methods. *International Journal for Numerical Methods*, 65, 2167-2202, 2006.
- [4] R. Hill. On the micro-macro transition in constitutive analysis of elastoplastic response at finite strain. *Math. Proc. Camb. Phil. Soc.*, 98, 579-585, 1985.
- [5] R.C. Yu, G. Ruiz and E.W.V. Chaves. A comparative study between discrete and continuum models to simulate concrete fracture. *Engineering Fracture Mechanics*, 75, 117-127, 2008.
- [6] J. Oliver, A.E. Huespe, P.J. Sánchez. A comparative study on finite elements for capturing strong discontinuities: E-FEM vs X-FEM. *Computational Methods in Applied Mechanics and Engineering*, 195, 4732-4752, 2006.
- [7] M. Arrea, A.R. Ingraffea. Mixed-mode crack propagation in mortar and concrete. *Report n°81-13: Department of Structural Engineering, Cornell University*, 1882.

3D CRACK ANALYSIS OF A CGRP CRUCIFORM UNDER BIAXIAL LOADING USING TWO NUMERICAL APPROACHES: XFEM AND A PROGRESSIVE DAMAGE MODEL

*J. Navarro-Zafra¹, J.L. Curiel-Sosa¹ and M.C. Serna Moreno²

¹ Department of Mechanical Engineering, University of Sheffield. Sir Fredrik Mappin Building, Mappin Street, Sheffield, S1 3JD, UK

² E.T.S. de Ingenieros Industriales de Ciudad Real, Universidad de Castilla La Mancha, Edificio Politécnico. Avda. Camilo José Cela s/n, Campus Universitario, 13071, Ciudad Real (Spain)

*jnavarrozafra1@sheffield.ac.uk

ABSTRACT

In order to simulate the 3D crack behaviour of a chopped glass-reinforced polyester (CGRP) subjected to biaxial in-plane loading, two different numerical techniques were considered. Firstly, the crack response of the CGRP cruciform structure was studied by means of eXtended Finite Element Method (XFEM). This approach allowed the discontinuity to be mesh-independent so no-conforming mesh was necessary contrary to the traditional Finite Element Method (FEM). In this case, crack initiation using XFEM was solution-dependent based on the maximum stress criterion defined, thus, as a natural output the crack initiates without any a priori crack definition. Secondly, a novel progressive damage model (PDM) for prediction of damage in fibre-reinforced composites was implemented to study the response of the CGRP specimen. For computing the dominant damage mode into the PDM, a new characterization of unitary damage directors was given. Finally, computational and experimental results were compared showing a reasonable agreement for the two numerical approaches.

Key Words: *Biaxial testing; Damage; XFEM; Chopped glass-reinforced polyester composite; Finite Element Analysis*

1. Introduction

Advanced composite materials (ACM) are well-known for being an essential part in, for example, aerospace structures. These materials are normally presented as a composite laminate i.e. a laminate is a layered material and composite in this case means that each ply is formed by two components: fibers e.g. glass and matrix such as epoxy. In the last decades its use has growth considerably principally motivated for its properties: high strength-weight ratio, excellent resistant to fatigue, elevate durability, etc. Predicting failure on these orthotropic materials its is not a trivial task because of the mixed damage modes appearing during loading. Therefore, many experimental tests are required in order to guarantee safety. Computational modelling of fracture has become an alternative for predicting the behaviour of ACM, and then, reduce the high experimental costs necessary for validating them.

In computational terms, stress analysis has been a powerful tool for understanding the distribution of loads throughout the ACM under consideration when its behaviour is linear-elastic. Once damage begins, the state of the art of computational modelling of ACM is in ongoing development and controversy exist in the way of representing crack initiation and propagation i.e. what parameters are relevant, different ways of representing crack, etc. Then, further research is required in that field.

In this work, we have used two numerical methods for modelling a 3D crack into a CGRP cruciform structure submitted to biaxial in-plane loading: a PDM for fibre reinforced composite materials and XFEM.

2. Progressive Damage Model (PDM)

In general terms, progressive damage modelling considers a gradual strength degradation before the macro-crack is appearing (failure). As Kachanov [1] first proposed, for making degradation possible in a one-dimensional case, a single damage variable d using the effective stress concept [2]. Thus, for example, the constitutive law in isotropic degradation is written as:

$$\boldsymbol{\sigma} = (1 - d) \cdot \mathbf{C}^e \cdot \boldsymbol{\epsilon} \quad (1)$$

Where \mathbf{C}^e is the constant elastic stiffness of the material, $\boldsymbol{\sigma}$ and $\boldsymbol{\epsilon}$ represent stress and strain respectively. Here and henceforth, bold characters denote tensors. The values of d ranges between 0 and 1, thus, the value 0 for this variable corresponds with the elastic behaviour in the constitutive model and the value 1 with the final state in the material.

The example showed in Equation 1 is used for a model with an isotropic material where a single damage variable is considered. In this work, a 3D PDM [3, 4, 5] for modelling the mixed damage on fibre reinforced composite laminates is implemented. Six different damage variables are defined associated with the six different damage modes considered: fibre rupture and buckling, matrix tensile and cracking in the first transverse direction and matrix tensile and cracking in the second transverse direction. Thus, for including damage into the constitutive relation, a diagonal second-order tensor \mathbf{D} (see Equation 2) is defined containing six damage variables, η_{ij} :

$$\mathbf{D} = \text{diag}\left[\frac{1}{1 - \eta_{11}}, \frac{1}{1 - \eta_{22}}, \frac{1}{1 - \eta_{33}}, \frac{1}{1 - \eta_{12}}, \frac{1}{1 - \eta_{23}}, \frac{1}{1 - \eta_{31}}\right] \quad (2)$$

Note that for each damage variable, the sub-index i, j represent the directions in a local coordinate system defined into the lamina. In this case, it is considered that direction 1 and 2 are the directions parallel and perpendicular to the fibre direction, respectively and 3 the out-of-plane perpendicular direction to the plane that form 1 and 2. Curiel-Sosa [7] defined for each damage mode a stress damage surface, f^ξ . Therefore, the undamaged domain is surrounded by the mentioned surfaces defining the elastic domain. For defining those surfaces, the so-called normalizes energy release rates (NERRs) are considered:

$$f^\xi(\boldsymbol{\sigma}, \boldsymbol{\eta}) = \boldsymbol{\sigma}^T \cdot \mathbf{F}^\xi \cdot (\boldsymbol{\eta}) \cdot \boldsymbol{\sigma} - 1 \quad (3)$$

$$g^\xi(\boldsymbol{\epsilon}, \boldsymbol{\eta}) = \boldsymbol{\epsilon}^T \cdot \mathbf{F}^\xi(\boldsymbol{\eta}) \cdot \boldsymbol{\epsilon} - 1 \quad (4)$$

Where ξ is the damage mode take into account. Once $f^\xi(\boldsymbol{\sigma}, \boldsymbol{\eta})$ is obtained, the strain damage surfaces, $g^\xi(\boldsymbol{\epsilon}, \boldsymbol{\eta})$, are calculated by mapping to in the strain space. In order to compute damage, damage variables are given a value of the damage occurring in the structure due to the different damage modes. The time variation of damage variables is obtained by the damage rule, Equation 5. In that equation, Φ^ξ are growth functions and \mathbf{v}^ξ the unitary damage directors. The mathematical definition of growth functions for each damage mode ξ are made according to Equation 6. In this equation the growth functions are defined as the non-negative inner product between the strain gradient of the damage surface in strain space, ∇_ϵ , and the strain gradient $\dot{\boldsymbol{\epsilon}}$. Note that if the strain increment vector is pointing to the interior of the damage surface, for a certain damage mode, then no progression of such damage mode occurs.

$$\dot{\boldsymbol{\eta}} = \sum_{\xi=1}^m \Phi^\xi \mathbf{v}^\xi \quad (5)$$

$$\Phi^\xi = \langle \nabla_\epsilon g^\xi, \dot{\boldsymbol{\epsilon}} \rangle_+ \quad (6)$$

3. eXtended Finite Element Method(XFEM)

XFEM [6] is based in the partition of unity property present in the Finite Element Method (FEM) i.e. sumatory of the shape function values in each degree of freedom has to be one. This method allows discontinuities to be mesh independently represented, so re-meshing is not necessary to model crack growth. Then, it become very attractive for modelling cracks since it is not necessary updating the mesh like the case of conventional FEM. The general idea of this method is including discontinuous enrichment functions to the approximation of displacements. For fracture analysis, the enrichment functions consist

of the near-tip asymptotic functions $\psi_\alpha(x)$ that capture the singularity on the crack tip and a function for representing the jump in the displacement field across the cracks faces, Heaviside function $H(x)$. The approximation for displacement vector \mathbf{u} is defined:

$$\mathbf{u} = \sum_{i=1}^{nnodes} \mathbf{N}_i(x)(\mathbf{u}_i + \mathbf{H}(x)\mathbf{a}_i + \sum_{\alpha=1}^4 \psi_\alpha(x)\mathbf{b}_i^\alpha) \quad (7)$$

Where $\mathbf{N}_i(x)$ are shape functions and $nnodes$ the number of nodes per element. The first term on the right-hand of displacement approximation equation is the displacement \mathbf{u}_i that corresponds with the nodal displacement vector; the second one is the product between the nodal enriched degree of freedom vector, \mathbf{a}_i and the Heaviside function $\mathbf{H}(x)$ and the third one is the product of nodal enriched degree of freedom \mathbf{b}_i^α and the corresponding elastic asymptotic crack-tip functions, $\psi_\alpha(x)$. The first term is applied for all nodes in the model, the second one is used whose shape functions are cut by the crack interior and the third one is used whose shape functions are cut by the crack tip. Interesting applications of this method are carried out since the model exists, for example, delamination in GLARE [7], analysis of a CFRP cruciform structure in a 2D context [8] [9], etc.

4. Numerical Framework and Results

A CGRP cruciform structure is analysed using a PDM and the XFEM implementation of *ABAQUSTM*. Both techniques are implemented into three difference cruciform specimens: A, B and C submitted to different biaxial loading cases. The dimensions and material properties of the cruciform structure are presented in [10]. The composite tested has a polymeric matrix with 20 % volume of glass reinforcement. Because of the random distribution of the fibres the composite under analysis has a quasi-isotropic. For the two models used, XFEM and PDM, a 3D cruciform has been modelled considering a 1/8 of the cross due to symmetry of it and in order to save computational resources.

For making the implementation of the PDM into the CGFP cruciform a VUMAT subroutine is written in FORTRAN. This subroutine is run into *ABAQUSTM* using explicit central-difference time integration. Six state variables are defined in the subroutine corresponding with the different damage modes appearing into the composite. Four different loading cases are studied into the three different cruciform structures [11], see Table 1. Thus, the original PDM proposed is modified for this specific application. In this case, it is considered that matrix cracking is caused by a loading in the directions of loading because of the random distribution of fibres. The results obtained by the PDM are satisfactory. The correct damage mode is computed (matrix tensile) and the location where the crack initiates its growth is well computed for the three different specimens under biaxial loading.

Table 1: Geometries and biaxial loading cases considered

Specimen	A	A	B	C
Biaxial loading case	1/2	1/1	1.5/1	0.5/1

In general terms, in progressive damage modelling the crack is viewed as a continuous band with a reduction of strength. However, using XFEM, the crack is represented in a more realistic way, as a discontinuity throughout material. Thus, XFEM is been used as well to model the crack response of the CGRP structure under analysis. The constitutive model used for this application is appropriate to represent the kind of fragile fracture processes here presented. Basically, in this approach are distinguished three characteristic parts:

- a) Linear elastic traction separation behaviour.
- b) Damage initiation based on the maximum stress criteria.
- c) Damage evolution.

5. Conclusions

A cruciform structure has been analysed using two different numerical techniques for modelling cracks under a biaxial loading. In first instance, a PDM is used. In this case, higher values of damage due to matrix tensile were localized in the zone where the macro-crack appears in experimental results. Thus, the PDM is validated for a biaxial loading in a CGRP composite. Secondly, XFEM is implemented into the cruciform obtaining crack initiation and evolution in the structure.

Acknowledgements

This work has been financially supported by EPSRC Doctoral Training Grant.

References

- [1] L. M. Kachanov, *On the time to failure under creep conditions*, Izv, AN SSSR, Otd. Tekhn. Nauk, vol. 8, pp. 26-31, 1958.
- [2] J.-L. Chaboche, *Continuous damage mechanics A tool to describe phenomena before crack initiation*, Nucl. Eng. Des., vol. 64, no. 2, pp. 233247, Apr. 1981.
- [3] J.L. Curiel Sosa, S. Phaneendra, and J. Munoz, *Modelling of mixed damage on fibre reinforced composite laminates subjected to low velocity impact* Int. J. Damage Mech., vol. 22, no. 3, pp. 356374, Apr. 2012.
- [4] J. L. Curiel-Sosa, N. Petrinic, and J. Wiegand, *A three-dimensional progressive damage model for fibre-composite materials* Mech. Res. Commun., vol. 35, no. 4, pp. 219221, 2008.
- [5] J. L. Curiel-Sosa, *Finite Element Analysis of Progressive Degradation versus Failure Stress Criteria on Composite Damage Mechanics*.
- [6] T. Belytschko and T. Black, *ELASTIC CRACK GROWTH IN FINITE ELEMENTS*, vol. 620, no. July 1998, pp. 601620, 1999.
- [7] J. L. Curiel-Sosa and N. Karapurath, *Delamination modelling of GLARE using the extended finite element method*, Compos. Sci. Technol., vol. 72, no. 7, pp. 788791, 2012.
- [8] M. C. Serna Moreno, J. L. Curiel-Sosa, J. Navarro-Zafra, J. L. Martínez Vicente, and J. J. López Cela, *Crack propagation in a chopped glass-reinforced composite under biaxial testing by means of XFEM*, Compos. Struct., Sep. 2014.
- [9] M.C. Moreno, J.L. Curiel-Sosa, J. Navarro-Zafra, *Initiation and evolution of cracks in a chopped glass reinforced composite under biaxial testing by means of XFEM*, 16th European Conference on Composite Materials. Seville, Spain, 22-26 June 2014.
- [10] M. C. Serna Moreno and J. J. López Cela, *Failure envelope under biaxial tensile loading for chopped glass-reinforced polyester composites*, Compos. Sci. Technol., vol. 72, no. 1, pp. 9196, Dec. 2011.
- [11] M.C Serna Moreno, J. L. Martínez Vicente, and J. J. López Cela, *Failure strain and stress fields of a chopped glass-reinforced polyester under biaxial loading*, Compos. Struct., vol. 103, pp. 2733, 2013.

Modelling of Dynamic Crack Propagation in 3D Elastic Continuum Using Configurational Mechanics

*Hassan Al-Budairi, Lukasz Kaczmarczyk and Chris J. Pearce

School of Engineering, Rankine Building, The University of Glasgow, Glasgow, UK, G12 8LT

*Hassan.Al-Budairi@glasgow.ac.uk

ABSTRACT

This paper presents the theoretical basis and numerical implementation for simulating dynamic crack propagation in 3D hyperelastic continua within the context of configurational mechanics. The approach taken is based on the principle of global maximum energy dissipation for elastic solids, with configurational forces determining the direction of crack propagation. The work builds on the developments made by the authors for static analysis [1], incorporating the influence of the kinetic energy. The nonlinear system of equations are solved in a monolithic manner using Newton-Raphson scheme. Initial numerical results are presented.

Keywords: *Dynamic fracture; 3D crack propagation; Configurational mechanics*

1. Introduction

Numerical simulation of dynamic crack propagation in three-dimensional hyperelastic materials is studied within the context of linear elastic fracture mechanics (LEFM) and configurational mechanics. Although dynamic fracture has been widely investigated in continuum mechanics, this is still a challenging topic. We require a physical and mathematical description to determine (a) when a crack will propagate, (b) the direction of propagation and (c) how far/fast the crack will propagate. Furthermore, we require a numerical setting to accurately resolve the evolving displacement discontinuity.

In this study, we present a mathematical derivation and numerical implementation that can achieve these goals, solving for conservation of momentum in both the spatial and material domains. The spatial (or physical) domain is what we observe and the material domain is the evolving reference domain due to crack evolution. The theory is an interpretation of linear elastic fracture mechanics and consistent with Griffith's fracture criterion. This paper represents a generalisation of the authors' previous work on static crack propagation [1]. The approach taken is based on the principle of global maximum energy dissipation for elastic solids, with configurational forces determining the direction of crack propagation. This approach has been successfully adopted by a number of other authors in the context of quasi-static analysis, e.g. [1,2]. At present we restrict ourselves to the consideration of elastic bodies with energy dissipation limited to the creation of new crack surfaces.

In the context of the numerical setting, we have adopted the Arbitrary Lagrangian-Eulerian (ALE) method, which is a kinematic framework to describe movement of the nodes of the finite element mesh independently of the material. Thus, we are able to resolve the propagating crack without influence from the original finite element mesh, and maintain mesh quality. We are primarily concerned with solving crack propagation in large 3D problems. The efficient solution of such problems, with a large numbers of degrees of freedom, requires the use of an iterative solver for solving the system of algebraic equations. In such cases, controlling element quality enables us to optimise matrix conditioning, thereby increasing the computational efficiency of the solver.

The resulting systems of equations are highly nonlinear and requires a solution strategy that enables us to trace the entire transient response.

2. Body with propagating crack

Differentiable mappings relate the reference material domain to both the current spatial and the current material domains. These mappings are utilized to independently observe the deformation of material in the physical space Ω_t and the evolution of the crack surface in the material space \mathcal{B}_t , see Figure 1.

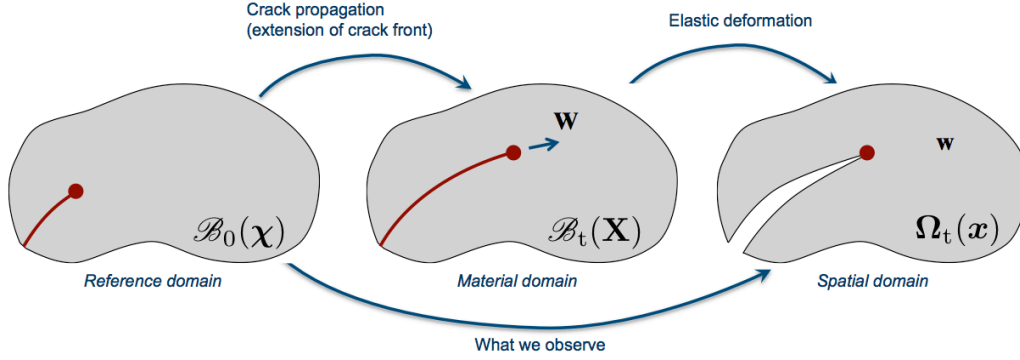


Figure 1: Deformation and structural change of a body with a propagating crack

The spatial domain defines a set of coordinates \mathbf{x} corresponding to the position of all mesh nodes in the body, while the material domain has set of coordinates \mathbf{X} corresponding to the position of all material points. These sets are used to calculate spatial \mathbf{w} and material \mathbf{W} displacement fields relative to the reference domain, χ :

$$\mathbf{w} = \mathbf{x} - \chi \quad (1)$$

$$\mathbf{W} = \mathbf{X} - \chi \quad (2)$$

The physical displacement \mathbf{u} is given by:

$$\mathbf{u} = \mathbf{w} - \mathbf{W} \quad (3)$$

3. Numerical implementation

The finite element approximation is applied for both the physical and material space. Three dimensional domains are discretised with tetrahedral elements with hierarchical basis functions of arbitrary polynomial order, following the work of Ainsworth and Coyle [3]. The higher-order approximations are only applied to displacements in the spatial configuration, whereas a linear approximation is used for displacements in the material space.

The resulting residuals in the spatial and material domain, that represent the two primary, nonlinear equations that need to be solved, are expressed as:

$$\mathbf{r}_s = \lambda(t) \mathbf{f}_{s,\text{ext}} - \mathbf{f}_{s,\text{int}} \quad (4)$$

$$\mathbf{r}_m = \mathbf{f}_{m,\text{res}} - \mathbf{f}_{m,\text{driv}} \quad (5)$$

where λ is the load factor that scales the external reference load, $\mathbf{f}_{s,\text{ext}}$, $\mathbf{f}_{s,\text{int}}$ is the internal force vector, $\mathbf{f}_{m,\text{res}}$ is the material resistance and $\mathbf{f}_{m,\text{driv}}$ is the driving force for crack propagation. These equations are linearised and solved using a Newton-Raphson procedure.

The spatial internal force vector is expressed as

$$\mathbf{f}_{s,\text{int}} = \int \mathbf{B}_X^T \mathbf{P} \, dV + \int \rho \mathbf{N}^T \mathbf{a} \, dV \quad (6)$$

and the material driving force is expressed as

$$\mathbf{f}_{m,driv} = \int \mathbf{B}_X^T \boldsymbol{\Sigma} dV - \int \rho_0 (\mathbf{F}^T \mathbf{a} + \dot{\mathbf{F}}^T \mathbf{v}) dV = \mathbf{G} - \int \rho_0 (\mathbf{F}^T \mathbf{a} + \dot{\mathbf{F}}^T \mathbf{v}) dV \quad (7)$$

where \mathbf{P} is the first Piola Kirchoff stress tensor, $\boldsymbol{\Sigma}$ is the Eshelby stress, \mathbf{a} is the spatial acceleration, $\mathbf{v} = \dot{\mathbf{u}} = \dot{\mathbf{w}} - \mathbf{F}\dot{\mathbf{W}}$ is the spatial velocity, \mathbf{F} is the deformation gradient and \mathbf{G} is the configurational force.

In the restricted case of quasi-static analysis, the inertia and velocity terms in (6) and (7) vanish and the formulation reverts to that presented in [1]. Thus, equations (6) and (7) represent an important development in the modelling of dynamic crack propagation, generalising the configurational mechanics formulation.

4. Mesh quality

The continuous adaptation of the finite element mesh to resolve the propagating crack will result in a degeneration of the mesh quality. For large problems, where it is necessary to use iterative solvers, we need to control the quality of the elements to ensure good matrix conditioning. The key challenge is to enforce constraints to preserve element quality for each Newton-Raphson iteration, without influencing the physical response. Thus, we introduce a measure of element quality for tetrahedral elements in terms of their shape and use this to drive mesh improvement. Here we include both node movement and changes in element topology (face flipping).

Thus, equations (4) and (5) are augmented by a third residual, \mathbf{f}_q , defined as

$$\mathbf{f}_q = \int \mathbf{B}_X^T \mathbf{Q} dV \quad (8)$$

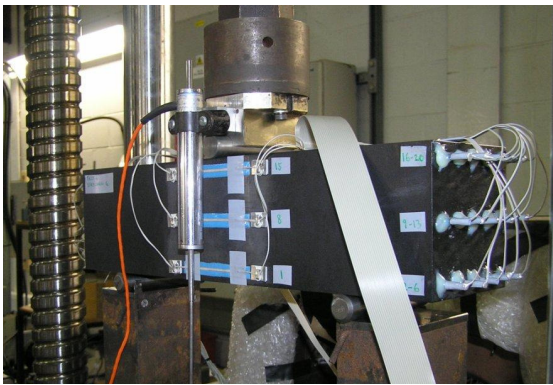
where \mathbf{Q} is a pseudo ‘‘stress’’ at the element level, as a counterpart to the first Piola Kirchoff stress. Since the conditioning of the finite element stiffness matrix is controlled by the quality of the worst elements, we advocate that \mathbf{Q} is a function of a log-barrier objective function as a means of evaluating the quality of an entire mesh (whilst punishing harshly the worst quality element), and the volume-length quality measure [4]. The latter does not directly measure dihedral angles, but it has been shown to be very effective at eliminating poor angles, thus improving stiffness matrix conditioning and interpolation errors. As the volume-length mesh quality measure is a smooth function of vertex positions, its gradient is straightforward and computationally cheap to calculate.

5. Time integration

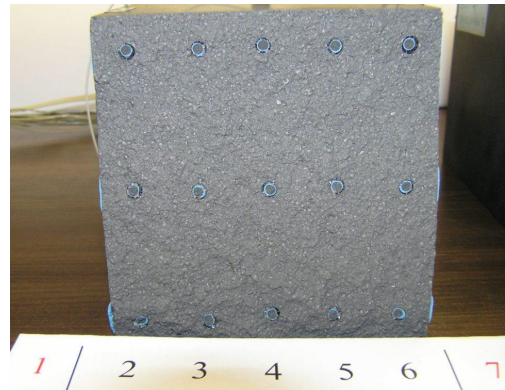
The dynamic problem is integrated in time using a Newmark scheme. The system of equations for conservation of the spatial (4) and material (5) momentum, and mesh quality (8) are solved using a Newton-Raphson iterative process within each time step. The challenge is to ensure that the time integration algorithm adapts the size of the time step. When the problem is behaving in a purely elastic manner, the time step can be relatively large. However, as we approach the time when a crack starts to propagate, potentially in an unstable manner, it is necessary to reduce the time step. Detecting this transition point in an effective manner is the current focus of this work.

6. Numerical example

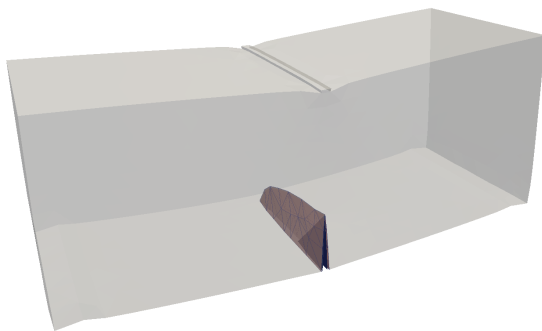
A three-point bend test with a corner notch is presented. The experiments include Figure 2(a) shows the crack development at an early stage. Figure 2(b) shows the nonlinear load-displacement path for two different meshes.



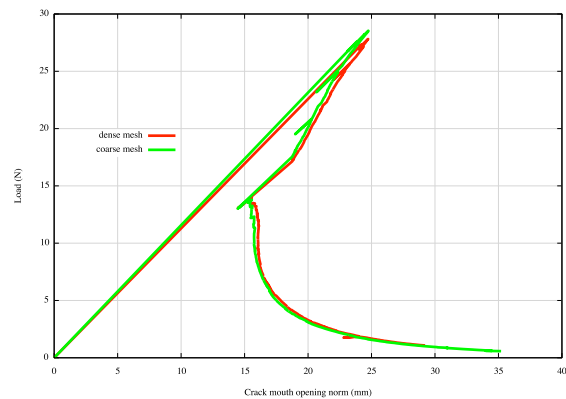
(a)



(b)



(c)



(d)

Figure 2: Three point bend test with corner notch. (a) Experimental set-up; (b) cracked beam, showing electrically isolated longitudinal rods for measuring crack front speed; (c) numerically predicted crack path, (d) load-displacement responses

7. Conclusions

In this study, the basis for dynamic crack propagation using configurational mechanics has been presented. The highly nonlinear system of equations are implemented in and solved using MoFEM, a finite element code for multi-physics problems which is developed at the University of Glasgow.

Acknowledgements

This work was supported by EDF Energy Nuclear Generation Ltd. The views expressed in this paper are those of the authors and not necessarily those of EDF Energy Nuclear Generation Ltd.

References

- [1] Ł. Kaczmarczyk, M. Mousavi and C. Pearce. Three-dimensional brittle fracture: configurational-force-driven crack propagation. *International Journal for Numerical Methods in Engineering*, 7, 531–550, 2014.
- [2] E. Gurses, C. Miehe. A computational framework of three-dimensional configurational-force-driven brittle crack propagation. *Computer Methods in Applied Mechanics and Engineering*, 198, 1413-1428, 2009.
- [3] M.A. Ainsworth, J. Coyle. Hierarchic finite element bases on unstructured tetrahedral meshes. *International Journal for Numerical Methods in Engineering*. 58, 2103–2130, 2003.
- [4] C.J. Pearce, R. MacKenzie, L. Kaczmarczyk. Numerical approaches for brittle crack propagation, in B.H.V. Topping, (Eds), *Computational Methods for Engineering Science*, Saxe-Coburg Publications, Stirlingshire, UK, Chapter 6, pp 135-155, 2014.

FRACTURE AND FAILURE 2

Failure Analysis of 3-D Graphite Bricks in an AGR Core

*Costy Kodsi, Lukasz Kaczmarczyk and Chris J. Pearce

School of Engineering, Rankine Building, The University of Glasgow, Glasgow, G12 8LT

*c.kodsi.1@research.gla.ac.uk

ABSTRACT

A methodology has been developed to study fracture in graphite bricks in an AGR core. This has required the combination of two modelling frameworks, namely multi-body contact mechanics and quasi-static crack propagation. A number of algorithms have been developed to achieve this coupling that address: (i) rigid body motion mitigation, (ii) automatic crack initiation and (iii) geometry modification.

Keywords: *Computational Modelling of Fracture, Crack Initiation, Rigid Body Motion, Boolean Intersection*

1. Introduction

The objective of this research is to computationally model fracture in three-dimensional graphite bricks in an Advanced Gas-Cooled Reactor (AGR) core subject to dynamic excitation. This involves developing tools to couple a dynamic multi-body contact finite element code, namely SOLFEC [1], with the quasi-static crack propagation capability available in the MoFEM library [2]. The motivation behind this work is life extension and safety-case modelling support.

The following assumptions provide the operating envelope for methodology development:

- (i) Graphite will be treated as an isotropic linear elastic material that is in a brittle state;
- (ii) Fracturing of a body will not influence contact force evolution with time, i.e. crack propagation will occur faster than the change in boundary conditions in a numerical time-step;
- (iii) Fracture in one body will not have a bearing on the fracture of other bodies.
- (iv) Cracks will not branch.

2. Background

The core in an AGR is a large assembly of graphite bricks that are stored in a multi-layer arrangement. Two types of bricks can be found in the core with differing geometry and dimensions as depicted in Figure 1(a): (i) fuels bricks with a circular hollow central channel, and (ii) interstitial bricks that contain control rod, coolant or secondary shutdown holes. The fuel bricks are loosely connected through graphite keys. While the interstitial brick geometry itself provides the connectivity to the fuel bricks. The fuel bricks stored on top of each other create a continuous channel that house the enriched uranium stored in fuel stringers.

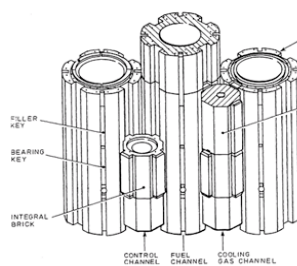


Figure 11: Diagram of the graphite keying structure

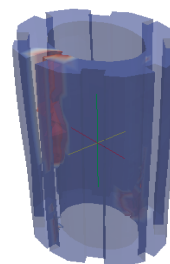


Figure 1. (a) Graphite blocks, and (b) example of MoFEM crack propagation.

SOLFEC implements an implicit formulation of contact dynamics [1]. This provides a physically

more accurate representation of reality and permits larger time-steps in simulations. SOLFEC has been developed with high performance computing in mind from the onset making it an ideal choice for modelling a large number of interacting bodies. Unfortunately, the parallelisation capability does not extend to the finite element analysis part of the code. Consequently, graphite bricks have been modelled with a very coarse mesh in past analyses.

MoFEM is a multi-physics finite element code that efficiently deals with an arbitrary level of approximation and supports mesh refinement. A global dissipation analysis in the form of the Clausius-Duhem inequality is exploited in MoFEM to provide a consistent thermodynamic framework for brittle fracture. The crack proceeds in the direction associated with the configurational force at the crack front subject to satisfaction of the Griffith energy condition as defined by the critical energy release rate G_c [2]. The local mesh topology near the crack is modified to accommodate crack propagation. This involves movement of the nodes on the crack front, while edge decimation/flipping and mesh refinement maintain the validity of the mesh. An example of crack propagation in a brick is shown in Figure 1(b). Currently, MoFEM cannot initiate cracks automatically and is restricted to crack propagation. Additionally, the mesh employed in the crack propagation simulation is significantly denser than that used in SOLFEC.

3. Computational Modelling of Fracture

The approach adopted to model the fracturing of bricks can be summarised in these steps:

- (i) SOLFEC analysis is set-up and run to completion;
- (ii) Bricks that will fracture are identified during the simulation and the contact forces as well as corresponding Lagrangian displacement (relative to the reference configuration) on the surface are recorded at the specific time-step;
- (iii) Rigid body motion is removed from the displacements of the identified bricks and a denser mesh is generated in preparation for crack propagation analysis;
- (iv) Location of crack initiation is determined in the identified bricks and propagation to failure is carried out in MoFEM, given the displacement boundary conditions as constraints;
- (v) The crack surfaces output from MoFEM are inserted into the original SOLFEC bricks and the mesh is re-generated with the minimum number of elements;
- (vi) SOLFEC is re-run with the fractured bodies to obtain the stress state in the bricks.

The bodies that will undergo fracture are identified in SOLFEC through an energetic criterion that monitors the strain energy of each element and has an empirically set threshold. Data communication between SOLFEC and MoFEM involves the VTK file format. The tools required to couple SOLFEC to MoFEM address the following areas: (i) rigid body motion mitigation in the Lagrangian displacements, (ii) automatic crack initiation in MoFEM, and (iii) new crack surface insertion into a SOLFEC brick mesh.

4. Rigid Motion Rotation Mitigation

The displacements have to be decomposed into a deformational \mathbf{u}^d and rotational part \mathbf{u}^r , and specifying

$$\mathbf{u}^r = (\mathbf{R} - \mathbf{I})\mathbf{X} \quad (1)$$

where \mathbf{R} is the rotation operator, \mathbf{I} the identity matrix and \mathbf{X} the reference configuration position vector. Taking advantage of the fact that the anti-symmetric part of the displacement gradient vanishes when there is no rotation and assuming that the rotation is constant over the body volume V , the anti-symmetric part of the displacement gradient averaged over all the elements in the surface mesh can be expressed as

$$\int \left(\left[\frac{\partial \mathbf{u}^d}{\partial \mathbf{X}} \right] - \left[\frac{\partial \mathbf{u}^d}{\partial \mathbf{X}} \right]^T \right) dV = 0. \quad (2)$$

Defining a pseudo-vector applied on the surface [3]:

$$\mathbf{h} = \int (\mathbf{n} \times \mathbf{u}^d) dS, \quad (3)$$

where n is the surface spatial normal. An objective function can then be defined and optimized to yield the rotation operator,

$$J(\mathbf{R}) = \mathbf{h}^T \mathbf{h}. \quad (4)$$

A number of algorithms were implemented and investigated for the optimization procedure: (i) finite difference method using the complex derivative, (ii) Cayley transform based method, (iii) Gauss-Newtonian approach, and a (iv) Newtonian approach based on local parameterization of the manifold $SO(3)$ [4]. The final method was selected as it proved to be the least computationally expensive and the most stable for large rotations.

5. Crack Initiation

A crack initiation criterion for materials in a brittle state has been proposed based on the notion that nucleation is a sudden and discrete rupture event, i.e. finite-length crack appearing abruptly, at the macroscopic level. At the heart of this criterion is the discrete setting of the energy release rate relation for stable crack propagation in a two-dimensional body with unit thickness,

$$G_c = - \frac{\Pi(l+a_c) - \Pi(l)}{a_c}, \quad (5)$$

where l is the existing crack length, a_c is the characteristic length representative of a small finite-length crack extension and Π is the total potential energy. The characteristic length is given by

$$a_c = \frac{2}{\pi} \left(\frac{K_{Ic}}{Y\sigma_c} \right)^2, \quad (6)$$

where K_{Ic} is the material toughness related to Mode-I deformation, σ_c is the material strength and Y is a non-dimensional constant accounting for crack location in a body; $Y = 1.122$ for an edge-crack. The generality of the criterion with respect to notch geometry is a result of the change in potential energy evaluation methodology. The concept of topological derivative is exploited to provide the sensitivity of the potential energy to crack extension. An expression for the change in energy can be subsequently formulated:

$$\Pi(l) - \Pi(l+a_c) = \frac{\pi \bar{\xi}^2}{2\bar{E}} \left[(\sigma_1 + \sigma_2)^2 + 2(\sigma_1 - \sigma_2)^2 \right], \quad (7)$$

where σ_1 and σ_2 are the principal stresses, \bar{E} is Young's modulus that is equal to $E/(1-\nu)^2$ for plane strain, ν is Poisson's ratio and $\bar{\xi}$ represents the radius of a circle that dissipates an equal amount of energy to the crack extension. The change in energy is evaluated at points in the unperturbed domain that are at a distance $\bar{\xi}$ from the boundary. The above calculation can be easily implemented as a post-processing procedure in a boundary or finite element framework.

Crack propagation at a V-notch tip is deemed to occur in the direction of the minimum change in potential energy, assume a polar coordinate system (r, θ) is centred at the tip, subject to

$$a_c G_c = \Pi - \Pi_{\xi}, \text{ where } \frac{\partial}{\partial \theta}(\Pi - \Pi_{\xi}) = 0 \text{ and } \frac{\partial^2}{\partial \theta^2}(\Pi - \Pi_{\xi}) > 0. \quad (8)$$

For a blunt notch, only the first condition in (8) need be satisfied. The circle radius ξ for a V-notch is

$$\xi = \frac{2}{\pi} \frac{G_c \bar{E}}{(Y \sigma_c)^2}, \text{ and for a blunt notch is } \xi = \sqrt{\frac{2a_c G_c \bar{E}}{3\pi \sigma_c^2}}.$$

6. Geometry Modification

The crack surface from a fractured brick is output from MoFEM and requires insertion into the relevant brick mesh in SOLFEC. This is achieved through a Boolean intersection operation and a geometry modification algorithm. The procedure for successful crack insertion is outlined below:

- (i) *Extraction of the surface boundary of a brick.* A robust and efficient algorithm has been developed to identify the non-shared faces of a tetrahedral volume mesh making use of the multimap facility in the C++ Standard Template Library.
- (ii) *Mesh simplification of the crack surface.* The edge collapse algorithm in CGAL [5] is employed to reduce the number of triangles whilst preserving the topology.
- (iii) *Boolean intersection.* The outer surface faces of the brick mesh are inserted into the AABB tree offered by CGAL. If a boundary edge of the crack surface mesh intersects the brick surface mesh, then a plane formed by the associated triangle is intersected with the tree. Exact calculations are therefore not required. Intersection points are recorded on relevant face data structures to ensure coincident vertices exist on the crack surface boundary and brick mesh.
- (iv) *Polyhedron generation.* The intersected triangles in the crack surface and brick mesh are re-generated without Delaunay triangulation. A CGAL functor has been written to generate the polyhedron formed by uniting crack surfaces with the brick geometry.
- (v) *Mesh cleaning.* The generated polyhedron may well contain small edges or triangles resulting from the geometry modification operation. The edge collapse algorithm is run once again but with an edge length threshold.
- (vi) *Volume Mesh generation using TetGen [6].*

Acknowledgements

This work was supported by EDF Energy Nuclear Generation Ltd. The views expressed in this paper are those of the authors and not necessarily those of EDF Energy Nuclear Generation Ltd.

References

- [1] T. Koziara and N. Bićanić. A distributed memory parallel multibody contact dynamics code. *International Journal for Numerical Methods in Engineering*, 87(1-5), 437-456, 2011.
- [2] Ł. Kaczmarczyk, M. M. Nezhad and C. J. Pearce. Three-dimensional brittle fracture: configurational-force-driven crack propagation. *International Journal for Numerical Methods in Engineering*, 97(7), 531-550, 2014.
- [3] Ł. Kaczmarczyk, T. Koziara and C. J. Pearce. Co-rotational formulation for 3d solids: An analysis of geometrically nonlinear foam deformation. *arXiv:1110.5321v2*, April 2013.
- [4] C. J. Taylor and D. J. Kriegman. Minimizations on the Lie group SO(3) and related manifolds. Yale Center for Systems Science, New Haven, CT, Tech. Rep. 9405, April 1994.
- [5] CGAL, Computational Geometry Algorithms Library, <http://www.cgal.org>.
- [6] H. Si. On Refinement of Constrained Delaunay Tetrahedralizations. *In Proceedings of the 15th International Meshing Roundtable*, September 2006.

A direct SIF approach for anisotropic materials using the Boundary Element Method

*Gabriel Hattori, Ibrahim A. Alatawi and Jon Trevelyan

School of Engineering and Computing Sciences, Durham University, DH1 3LE, Durham, UK

*gabriel.hattori@durham.ac.uk

ABSTRACT

Recently developments in numerical methods such as the Extended Finite Element Method (X-FEM) and the Extended Boundary Element Method (X-BEM) have significantly improved the accuracy in linear elastic fracture mechanics (LEFM) problems. Nevertheless, the postprocessing involved in the calculation of the Stress Intensity Factors still presents a computational burden. The most usual SIF evaluation techniques are the J-integral or the more general Interaction Integral (M-integral), which may require considerable computational resources of the order of those required to obtain the solution of the LEFM problem. A direct approach, where the SIFs are revealed in the solution vector, has been developed by [1] for isotropic materials and is further extended to anisotropic materials in this work.

Key Words: *Boundary element method; Anisotropic materials; Enrichment functions; Fracture mechanics*

1. Introduction

The boundary element method (BEM) is a well established discretisation method when dealing with fracture mechanics problems. It offers high accuracy and stability in providing results for the discontinuous, singular stress fields at crack tips than domain discretisation methods such as the Finite Element Method (FEM). However, in the last 15 years, the use of the partition of unity has improved the performance of the FEM, being further called Extended Finite Element Method (X-FEM) [1]. It was verified that the accuracy of the X-FEM could be similar to that found in BEM (see [2] for instance).

The partition of unity approach was first employed in [3] in a dual BEM formulation, in order to be more general than the quarter-point [4]. The quarter-point approach displaces the position of the central node to capture the proper \sqrt{r} behaviour at the crack tip (r being the distance from the crack tip). However, enrichment functions as specified in [2, 3] cause the linear system to suffer from ill-conditioning arising from the addition of new degrees of freedom to the problem. In a recent work, the authors [5] have developed an implicit enrichment, where only a couple of degrees of freedom are added to the problem for each crack tip, hence adding the enrichment to more elements and not increasing the total number of degrees of freedom of the fracture problem. This methodology was called direct approach, and was obtained using the displacement field around the crack tip with the Williams' expansion, valid for isotropic materials only.

In this work, we propose a more general form of enrichment functions for anisotropic materials, obtained from the Stroh formalism following the work of [2].

2. Governing equations

Consider an anisotropic elastic domain Ω , the static equilibrium equations in the presence of body forces \mathbf{b} are defined as

$$\sigma_{ij,j} + b_i = 0 \quad (1)$$

Symmetry holds for the stress and strain tensors, i.e.: $\sigma_{ij} = \sigma_{ji}$; $\varepsilon_{ij} = \varepsilon_{ji}$, where $\varepsilon_{ij} = \frac{1}{2}(u_{i,j} + u_{j,i})$

The linear constitutive equations are given by the generalized Hooke's law

$$\sigma_{ij} = C_{ijkl}\varepsilon_{kl} \quad (2)$$

where C_{ijkl} define the material constants tensor, satisfying the following symmetry relations

$$C_{ijkl} = C_{jikl} = C_{ijlk} = C_{klij} \quad (3)$$

3. Enrichment formulation

Adopting a polar coordinate system (r, θ) with origin at the crack tip, the asymptotic displacement field around a crack-tip in a plane anisotropic domain can be expressed by means of the Stroh formalism [6] as

$$u_i(r, \theta) = \sqrt{\frac{2}{\pi}} \Re \left(K_\alpha A_{im} B_{m\alpha}^{-1} \sqrt{r} (\cos \theta + \mu_m \sin \theta) \right) \quad (4)$$

where the summation convention over repeated indices holds; $i, m = 1, 2$; $\alpha = I, II$ is associated with the fracture modes; and $\Re(\cdot)$ is the real part of (\cdot) ; \mathbf{A} , \mathbf{B} and μ are obtained from the following eigenvalue problem

$$\left(\begin{array}{c|c} -\mathbf{C}_{22}^{-1} \mathbf{C}_{21} & -\mathbf{C}_{22}^{-1} \\ \hline \mathbf{C}_{11} - \mathbf{C}_{21}^T \mathbf{C}_{22}^{-1} \mathbf{C}_{21} & -\mathbf{C}_{21}^T \mathbf{C}_{22}^{-1} \end{array} \right) \begin{pmatrix} \mathbf{A}_m \\ \mathbf{B}_m \end{pmatrix} = \mu_m \begin{pmatrix} \mathbf{A}_m \\ \mathbf{B}_m \end{pmatrix} \quad (\text{no sum on } m) \quad (5)$$

with

$$\mathbf{C}_{11} := \mathbf{C}_{1ij1}; \quad \mathbf{C}_{21} := \mathbf{C}_{2ij1}; \quad \mathbf{C}_{22} := \mathbf{C}_{2ij2} \quad (6)$$

Expanding and rearranging the terms of Eq. (4) in the same way as in [2], the enrichment functions are calculated as

$$F_{Ij}(r, \theta) = \sqrt{\frac{2r}{\pi}} \begin{pmatrix} A_{11} B_{11}^{-1} \beta_1 + A_{12} B_{21}^{-1} \beta_2 & A_{11} B_{12}^{-1} \beta_1 + A_{12} B_{22}^{-1} \beta_2 \\ A_{21} B_{11}^{-1} \beta_1 + A_{22} B_{21}^{-1} \beta_2 & A_{21} B_{12}^{-1} \beta_1 + A_{22} B_{22}^{-1} \beta_2 \end{pmatrix} \quad (7)$$

where $\beta_i = \sqrt{\cos \theta + \mu_i \sin \theta}$, r is the distance between the crack tip and an arbitrary position, θ is the orientation measured from a coordinate system centred at the crack tip. Note that these enrichment functions are the equivalent of Williams' expansion for isotropic materials [5].

The anisotropic enrichment functions can also be used for isotropic materials, since this is a degenerated case from anisotropic materials (both eigenvalues are equal). For more details please refer to [2].

The displacement field can be defined in a similar fashion as [7]

$$u_j = \sum_{a=1}^M N^a u_j^a + \tilde{K}_I F_{Ij} + \tilde{K}_{II} F_{IIj} \quad (8)$$

where N^a represents the shape function for node a , u_j^a is a general coefficient rather than the nodal displacement, M is the number of nodes, \tilde{K}_I and \tilde{K}_{II} stand for the mode I and mode II Stress Intensity Factors (SIF), respectively, and they are now part of the solution vector instead of being calculated after the displacement solution is obtained. For the numerical discretisation of the fracture mechanics problem, the BEM is used.

4. Boundary Element Method (BEM)

The proposed enrichment is used with a Dual BEM formulation. The superposition of two boundaries (crack faces) can cause the degeneration of the linear system of equations if only the displacement boundary integral equation (DBIE) is employed. A traction boundary integral equation (TBIE) can be obtained from the differentiation of DBIE and further substitution into the constitutive laws equation (see [8] for details). The DBIE and the TBIE for the direct approach are given as [5].

$$c_{ij}(\xi) u_j(\xi) + \int_{\Gamma} p_{ij}^*(\mathbf{x}, \xi) u_j(\mathbf{x}) d\Gamma(\mathbf{x}) + \int_{\Gamma_c} p_{ij}^*(\mathbf{x}, \xi) \tilde{K}_{Ij} F_{Ij}(\xi) \mathbf{a}_k^\alpha d\Gamma = \int_{\Gamma} u_{ij}^*(\mathbf{x}, \xi) p_j(\mathbf{x}) d\Gamma(\mathbf{x}) \quad (9)$$

$$c_{ij}(\xi) p_j(\xi) + N_r \int_{\Gamma} s_{rij}^*(\mathbf{x}, \xi) u_j(\mathbf{x}) d\Gamma(\mathbf{x}) + N_r \int_{\Gamma_c} s_{rij}^*(\mathbf{x}, \xi) \tilde{K}_{Ij} F_{Ij}(\xi) \mathbf{a}_k^\alpha d\Gamma = N_r \int_{\Gamma} d_{rij}^*(\mathbf{x}, \xi) p_j(\mathbf{x}) d\Gamma(\mathbf{x}) \quad (10)$$

where $\Gamma_c = \Gamma_+ \cup \Gamma_-$ stands for the crack surfaces Γ_+ and Γ_- and N_r is the normal at the observation point. Let us recall that strongly singular and hypersingular terms arise from the integration of the p_{ij}^* , d_{rij}^* and s_{rij}^* kernels and they are regularised using the methodology proposed in [9], while the weakly singular terms are dealt using Telles transformation [10].

The addition of \tilde{K}_I and \tilde{K}_{II} requires two more equations so the linear system of equations can be solved. The additional equations come from a restriction in the crack faces, in order to remove the displacement discontinuity observed at the crack tip. The displacement continuity can be enforced as

$$\sum_{a=1}^L N^a u_j^{a, upper} = \sum_{a=1}^L N^a u_j^{a, lower} \quad (11)$$

where L is the number of nodes used for the crack tip extrapolation. Eq. (11) is applied for both x and y directions, resulting in two different equations.

5. Numerical results

To validate the proposed approach, an isotropic material model is used. As specified previously, the isotropic case is a special case of an anisotropic material, where both the eigenvalues are equal, and special measures must be taken [11]. A small disturbance can be imposed into the eigenvalues, so they will be no longer be equal and the enrichment functions can be used. In this example, $E = 10000$ is the Young's modulus and $\nu = 0.3$ is the Poisson ratio.

Figure 1 illustrates a rectangular plate ($h/w = 0.5$) with a single edge crack of length a under a uniform loading σ . The size of the crack is defined by $a/w = 0.5$. Results for the X-FEM are obtained using topological and geometrical enrichment, with a fixed area of $r_e/a = 0.2$. For more information about both adopted enrichment types please refer to [2] for instance. Results are illustrated in Figure 2, where the proposed direct approach for calculating the SIFs presents similar accuracy to other numerical approaches, such as the J-integral and an X-BEM formulation in [3].

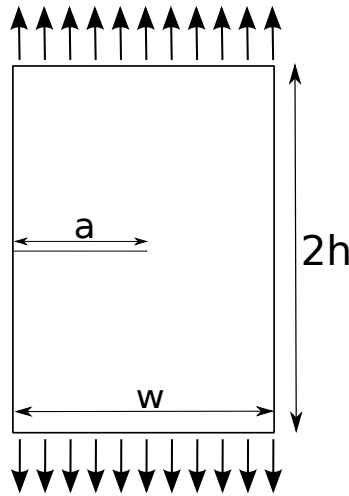


Figure 1: : Edge crack plate under a uniform load.

6. Conclusions

A direct approach for calculating the SIF in anisotropic materials has been presented in this work. The used enrichment functions have the advantage of depending only on the material properties, presented in a concise matrix form. Moreover, there are no further dependencies on the orientation of the material, which allow the enrichment functions to be as general as possible. The results are seen to match the reference solution, so we can conclude that the direct approach is an alternative method for obtaining the SIF, with similar precision to other evaluation methods for obtaining the SIF.

Acknowledgements

The first author acknowledges the Faculty of Science, Durham University, for his Postdoctoral Research Associate funding. The second author is supported by the Ministry of Education of Saudi Arabia under Ref. No. S11973.

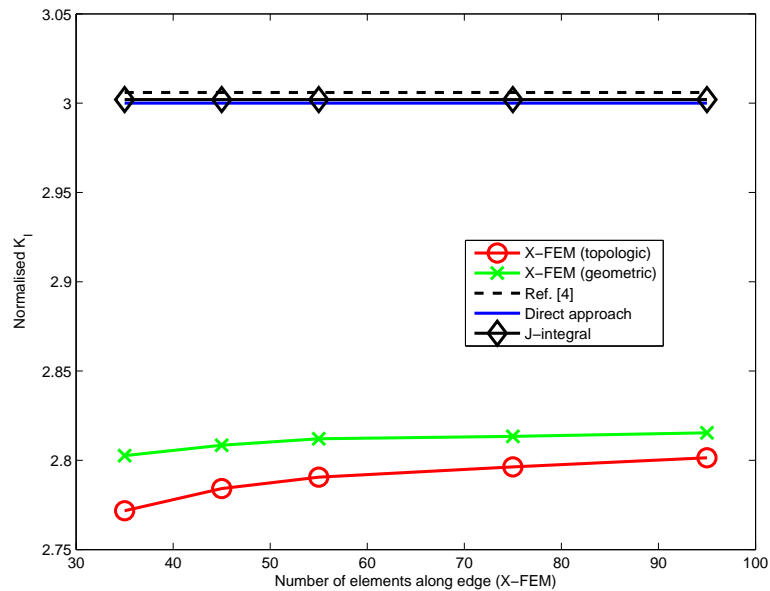


Figure 2: : Mode I SIFs for the edge crack problem.

References

- [1] N. Moes, J. Dolbow, and T. Belytschko, "A finite element method for crack growth without remeshing," *International Journal for Numerical Methods in Engineering*, vol. 46, pp. 131–150, 1999.
- [2] G. Hattori, R. Rojas-Díaz, A. Sáez, N. Sukumar, and F. García-Sánchez, "New anisotropic crack-tip enrichment functions for the extended finite element method," *Computational Mechanics*, vol. 50, no. 5, pp. 591–601, 2012.
- [3] R. Simpson and J. Trevelyan, "A partition of unity enriched dual boundary element method for accurate computations in fracture mechanics," *Computer Methods in Applied Mechanics and Engineering*, vol. 200, no. 1, pp. 1–10, 2011.
- [4] A. Sáez, R. Gallego, and J. Domínguez, "Hypersingular quarter-point boundary elements for crack problems," *International Journal for Numerical Methods in Engineering*, vol. 38, pp. 1681–1701, 1995.
- [5] I. Alatawi and J. Trevelyan, "A direct evaluation of stress intensity factors using the extended dual boundary element method," *Engineering Analysis with Boundary Elements*, vol. 52, pp. 56–63, 2015.
- [6] Z. Suo, "Singularities, interfaces and cracks in dissimilar anisotropic media," *Proceedings of the Royal Society of London. Series A, Mathematical and Physical Sciences*, vol. 427, no. 1873, pp. 331–358, 1990.
- [7] S. Benzley, "Representation of singularities with isoparametric finite elements," *International Journal for Numerical Methods in Engineering*, vol. 8, no. 3, pp. 537–545, 1974.
- [8] F. Garcia-Sanchez, R. Rojas-Diaz, A. Saez, and C. Zhang, "Fracture of magneto-electroelastic composite materials using boundary element method (BEM)," *Theoretical and Applied Fracture Mechanics*, vol. 47, no. 3, pp. 192–204, 2007.
- [9] M. Guiggiani, G. Krishnasamy, T. Rudolph, and F. Rizzo, "A general algorithm for the numerical solution of hypersingular boundary integral equations," *Journal of applied mechanics*, vol. 59, no. 3, pp. 604–614, 1992.
- [10] J. Telles, "A self-adaptive co-ordinate transformation for efficient numerical evaluation of general boundary element integrals," *International Journal for Numerical Methods in Engineering*, vol. 24, no. 5, pp. 959–973, 1987.
- [11] T. C. T. Ting, *Anisotropic Elasticity*. Oxford University Press, New York, 1996.

Nonlinear finite element analysis of quasi-brittle materials

W. F. Alnaas and A. D. Jefferson

School of Civil Engineering, Cardiff University, Queen's Buildings, Cardiff, CF24 3AA, UK

*AlnaasWF1@Cardiff.ac.uk

ABSTRACT

Much research has been conducted over the last four decades on the development of algorithms for a damage model when applied to the nonlinear finite element analysis of fracture problems in quasi-brittle materials. However, despite this large research effort there does not yet exist any one technique that overcomes all of the numerical instability and convergence difficulties which can arise when solving these problems with incremental-iterative Newton solution schemes. A new smooth unloading-reloading numerical approach which computes an approximate tangent matrix in an incremental iterative Newton type solution procedure is presented. A new method is also developed for calculating a predicted converged value of a damage evolution parameter. The performance of the new methods, named the smooth unloading-reloading (SUR) approach and the predictive-SUR approach, are assessed using analyses of a range of idealised quasi-brittle problems. The results show that the new SUR approach is robust and results in considerable savings, in terms of the number of iterations used in a complete solution, relative to solutions obtained with a reference model with secant unloading-reloading behaviour. Moreover, the numerical results show that the predictive-SUR algorithm is reliable and effective, and always resulted in overall iteration numbers equal or below those obtained with the standard SUR algorithm and in some cases, these savings were very significant.

Keywords: *Damage; Nonlinear finite element analysis; Quasi-brittle materials*

1. Introduction

The numerical modelling of the mechanical behaviour of quasi-brittle materials such as concrete can lead to some difficulties as a result of crack initiation which occurs due to the strain localization. The formation of cracks can produce convergence difficulties and numerical instabilities [1]. Therefore, the nonlinear finite element analysis of such materials is a truly numerical challenging undertaking.

The nonlinear equations resulting from the finite element simulation of quasi-brittle structures are frequently solved using incremental-iterative solution schemes based on Newton-Raphson algorithm [2]. The main reason of this is highly attributed to its potential quadratic convergence characteristics as well as its inherent simplicity and accuracy [3]. However, it is the poor convergence properties of these solution schemes, when solving problems involving quasi-brittle materials, which so frequently cause frustration to finite element analysts. It is this issue that provides the motivation for the work of this paper.

An important issue in relation to modelling the softening behaviour of quasi-brittle materials by iterative-incremental procedures is that the stiffness matrix can become non positive definite. In the initial time-steps of nonlinear analysis, before any cracking occurs, the tangent stiffness matrix is linear elastic and thus positive definite. However, in the subsequent steps, micro-cracks initiate and form; and the associated equilibrium solutions can become singular or non-unique, since the tangent stiffness matrix loses its positive definiteness. As a consequence, numerical instability and divergence can occur at certain time-steps of the incremental-iterative procedure [4]. Aforementioned difficulties have undoubtedly been behind the recent efforts to develop solution algorithms that either completely avoid iterations or minimise their use.

These methods include non-iterative Sequentially Linear Approach (SLA), which was proposed by Rots [5]. This method replaces the linear or nonlinear softening of negative slope by a series of saw-

teeth that ensure the tangent stiffness matrix is positive. The SLA is considered as secant stiffness based method. Rots et al [6] later improved SLA to achieve mesh independent behaviour. Another approach for solving nonlinear finite element equations is implicit/explicit approach of Oliver et al [4], in which a projected state variable (e.g. a damage parameter) is used to determine a predicted consistent tangent matrix that is exact for current increment but for which a correction is made in the subsequent stress-recovery phase. Although the robustness of SLA and implicit/explicit approaches is doubtless, and their capabilities for solving some type of problems has been manifested, they cannot deal well with all constitutive model that include non-linear crack closure in combined shear and normal modes, e.g solving soil-structure problems.

This paper is based on a recently completed journal paper [7] and presents a novel numerical technique called smooth unloading-reloading (SUR) that significantly improves the convergence properties of an isotropic damage model when applied to finite element analysis of a range of idealised quasi-brittle fracture examples. In addition, a new predictive-SUR algorithm is also proposed which accelerates the convergence of SUR approach.

2. Constitutive model

In the present study, the SUR approach is employed with an isotropic damage model. The constitutive equation for the isotropic damage model is expressed as [4]:

$$\boldsymbol{\sigma} = (1 - \omega) \mathbf{D}_0 : \boldsymbol{\varepsilon} \quad (1)$$

Where $\boldsymbol{\sigma}$ and $\boldsymbol{\varepsilon}$ are the stress and strain tensors respectively; \mathbf{D}_0 donates the elastic stiffness of the undamaged material and the damage variable ω is a function of a damage parameter r_p .

3. Smooth unloading-reloading and target damage evolution functions

The proposed SUR approach uses a target function $f_s(r_p)$ and a smooth unloading-reloading function $\sigma_p(r_p, r_{eff})$, as illustrated in figure 1. The SUR function depends on the damage evolution parameter (r_p), which is updated for every iteration within each load/displacement increment from the value obtained at the last converged increment.

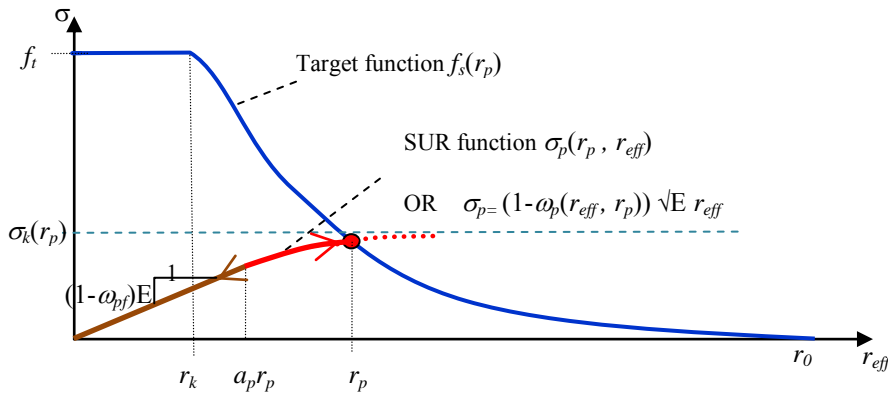


Figure 1: Target and unloading-reloading damage evolution functions.

$$f_s(r_p) = \begin{cases} f_t & \forall r_p < r_k \\ f_t \cdot e^{-c_r \left(\frac{r_p - r_k}{(r_0 - r_k)} \right)} & \forall r_p \geq r_k \end{cases} \quad (2)$$

$$\sigma_p(r_p, r_{eff}) = \sigma_k(r_p) \cdot \left(1 - \left(1 - \frac{a_p}{\nu} \right) \cdot e^{-\left(\frac{r_{eff} - a_p r_p}{(\nu - a_p) r_p} \right)} \right) \quad (3)$$

In which r_{eff} is effective damage parameter, E is Young's modulus, f_t is tensile strength, r_0 is final effective damage parameter, r_k is damage parameter at peak uniaxial tension, $c_I=5$, $a_p=0.70$, $\nu=0.75$.

4. Predictive-SUR function

The concept of the proposed predictive-SUR function relies on two main features which are the damage evolution parameter (r_p) and the number of iterations (it). The predictive function is mainly based on two principles; **1)** The relation between the number of iterations (it) within a time step and the differences between damage evolution parameters ($\Delta r_{pi} = r_{pi} - r_{pi-1}$) decays in semi-log space and approaches 0, once stable convergence has been achieved. **2)** When the slope of (it vs $\log(\Delta r_p)$) curve starts decreasing, a trail prediction of the damage evolution parameter (r_{ppi}) can be computed as in equations (4) but not used. Once the normalised difference between two consecutive prediction e.g (r_{ppi}) and (r_{ppi-1}) is less than 5%, then the damage evolution parameter (r_p) is set to the most recently computed trail value ($r_p = r_{ppi}$).

$$r_{pp} = r_{pit} + \frac{\Delta r_{pi}^2}{\Delta r_{pi-1} - \Delta r_{pi}} \quad (4)$$

5. Numerical results and conclusion

A 2D double notched specimen subjected to mixed mode loading by prescribed displacement, as shown in figure 2.a, is used to illustrate the performance of the proposed SUR and predictive-SUR approaches. The analysis was undertaken using 40 prescribed displacement increments, with the three approaches; Secant method, SUR approach and predictive-SUR approach. The material properties of the specimen are: Young's modulus ($E=20000$ MPa), Poisson's ratio ($\nu=0.2$), tensile strength ($f_t=2.5$ MPa), fracture energy ($G_f=0.1$ N/mm). The tolerance for convergence was 10^{-3} for both the out of balance force and iterative displacement norms. The savings gained by using the SUR approaches are considerable as illustrated in fig 4.

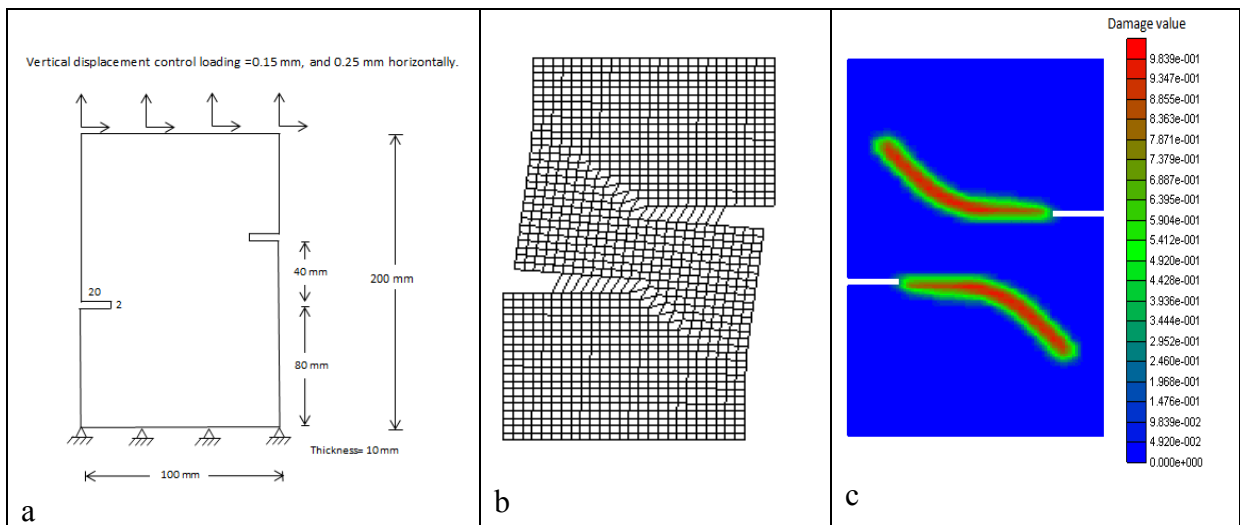


Figure 2: (a) specimen dimensions, (b) Exaggerated deformed mesh, (c) Damage indicator contour plot

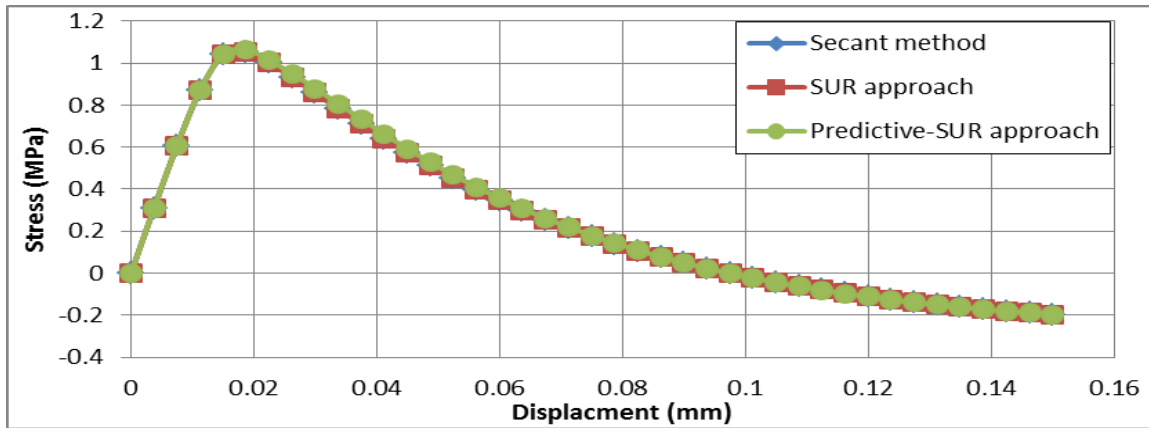


Figure 3: Displacement and vertical stress responses.

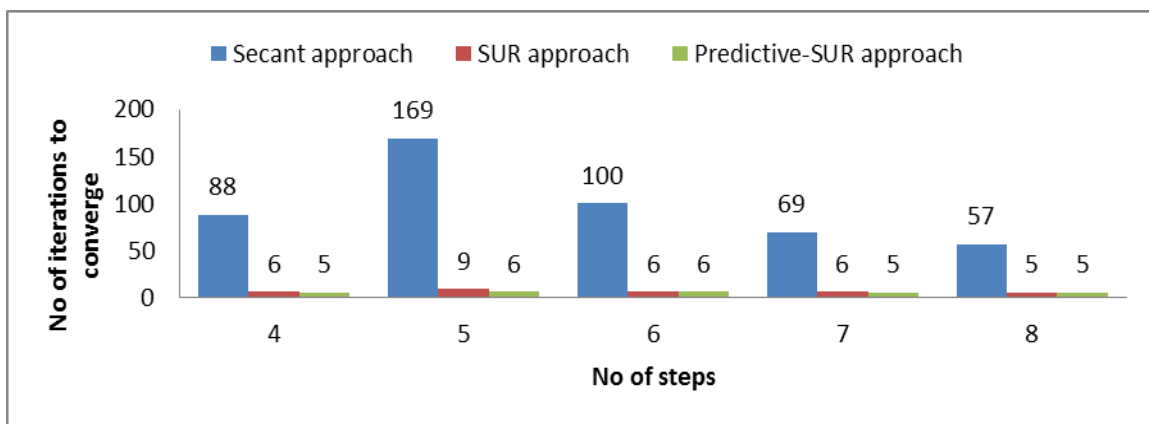


Figure 4: Number of iterations to achieve convergence for the most difficult increments.

Acknowledgements

The finite element company LUSAS (www.lusas.com) is gratefully acknowledged for their support.

References

- [1] Bažant, Z.P. and Planas, J., *Fracture and Size Effect in Concrete and Other Quasibrittle Materials*. 1997: Taylor & Francis.
- [2] Crisfield, M.A. *Non-linear Finite Element Analysis of Solids and Structures*. Vol. Vol.1. 1991, Chichester, UK.: John Wiley & Sons.
- [3] De Borst, R., Crisfield, M.A., Remmers, J.J.C. and Verhoosel, C.V., *Nonlinear Finite Element Analysis of Solids and Structures*. 2012: Wiley.
- [4] Oliver, J., Huespe, A.E. and Cante, J.C., An implicit/explicit integration scheme to increase computability of non-linear material and contact/friction problems. *Computer Methods in Applied Mechanics and Engineering*, 2008. 197(21–24): p. 1865-1889.
- [5] Rots, J.G., Sequentially linear continuum model for concrete fracture. In: de Borst R, Mazars J, Pijaudier-Cabot G, van Mier, JGM, Balkema AA, editors. *Fracture Mechanics of concrete Structures*. The Netherlands: Liss. 2001: p. 831-839.
- [6] Rots, J.G., Belletti, B. and Invernizzi, S., Robust modeling of RC structures with an “event-by-event” strategy. *Engineering Fracture Mechanics*, 2008. 75(3–4): p. 590-614.
- [7] Alnaas, W. and Jefferson, A., A smooth unloading-reloading approach for the nonlinear finite element analysis of quasi-brittle materials. *Submitted*.

Analysis of 3D Crack Problems by the Extended Boundary Element Method (XBEM)

*I.A. Alatawi, G. Hattori and J. Trevelyan

School of Engineering and Computing Sciences, Durham University, South Road, Durham, DH1 3LE

*i.a.alatawi@durham.ac.uk

ABSTRACT

We introduce an extension to 3D of the enriched boundary element formulation XBEM for linear elastic fracture mechanics. The enrichment approach makes use of the Williams expansions to enrich crack surface elements for accurate evaluation of Stress Intensity Factors (SIFs). Like other enrichment approaches, only a few degrees of freedom are added to the system. The number of these new degrees of freedom depends on the desired number of crack front points where SIFs need to be evaluated. The auxiliary equations required to yield a square system are derived by enforcing continuity of displacement at the crack front. SIFs are found from a J-integral evaluated over a disc perpendicular to the crack plane. The XBEM formulation has been shown to offer higher accuracy than the conventional BEM/J-integral, and can provide accurate results from a coarse mesh. A numerical example is included with preliminary results to demonstrate the enrichment effect.

Key Words: *Fracture Mechanics; Enriched BEM; J-Integral; Stress Intensity Factors; 3D*

1. Introduction

Mechanical properties in the vicinity of a crack tip need to be precisely obtained for better prediction of the crack behaviour. SIFs can provide accurate evaluation of stresses near the crack tip for linear elastic fracture mechanics problems. Many researchers have proposed different methods to estimate the correct SIFs for cracks in 3D. Hartranft and Sih [1] show that Williams expansions can be used for 3D problems directly on the local crack plane. However, they applied the Taylor series to the Williams expansions to allow for evaluation of the off crack local plane stresses and displacements.

Generally, crack problems in 3D can be classified as planar and nonplanar cracks. Cracks are considered to be planar if the crack exist on one plane; most crack growth methods focus on nonplanar cracks. Since, in LEFM all crack types experience physical singularity near the crack tip a certain care needs to be taken. The Extended Finite Element Method (XFEM) [2] was used to model cracks without the need for mesh refinement near the crack surface. On the other hand, the use of the Boundary Element Method (BEM) can yield direct evaluation of the SIFs [3]. Making use of Dual BEM [4], an enrichment approach coupled with forced crack tip displacement continuity has been implemented to evaluate SIFs directly. This locally enriched extended form of the BEM is known as XBEM.

The Griffith theory was extended by [5], to three dimensions by inclusion of the crack in a large sphere and imposing the condition of equilibrium across the spherical surface. The J-integral is another energy approach, where the integral is taken over the surface of a disc perpendicular to the crack plane and centred on the crack front. Decomposition of the J-integral in 3D reveals the value of SIF for each mode [6].

In the proposed approach a planar crack is considered and the Williams expansion for plane strain problems is used for enrichment. Elements on the crack surfaces have been arranged in a radial pattern to provide nodal information over radial lines for implementation of the displacement continuity constraints. A numerical example shows improved results of the J-integral when the XBEM is used.

2. Enrichment approach

The well known Dual Boundary Element Method (DBEM) [7] is used to overcome degeneration of the BEM matrix when collocating on crack surfaces. The Displacement BIE is used when collocating on the upper crack surface, and the Traction BIE is used on the lower crack surface. The DBIE used on the upper surface is given by;

$$C_{ij}(\hat{x})u_j(\hat{x}) + C_{ij}(\hat{x})u_j(\hat{x}) + \int_{\Gamma} T_{ij}(\hat{x}, x)u_j(x)d\Gamma = \int_{\Gamma} U_{ij}(\hat{x}, x)t_j(x)d\Gamma \quad (1)$$

where \hat{x} is the source point and \hat{x} is the projection of the source point to the opposite element. T_{ij} and U_{ij} are the 3D fundamental solutions. the traction Boundary Integral Equation (TBIE) is used when collocating on the opposite surface of the crack. TBIE can be written for a traction free surface as;

$$n_i(\hat{x}) \int_{\Gamma} S_{kij}(\hat{x}, x)u_k(x)d\Gamma = n_i(\hat{x}) \int_{\Gamma} D_{kij}(\hat{x}, x)t_k(x)d\Gamma \quad (2)$$

In a conventional discretized DBEM using a piecewise polynomial basis, the unknown u appearing in Eqs. (1) and (2) is approximated by

$$u_j = \sum_{a=1}^M N^a u_j^a \quad (3)$$

where M is the total number of nodes. In order to introduce the displacement contribution of Williams expansion to Eq. (3); we need to consider the variation of Stress Intensity factors (SIFs) along the crack front for 3D problems. The enriched form of the displacement local to a position on the crack front is;

$$u_j(r, \theta, \eta) = \{\tilde{K}_I(\eta) \tilde{K}_{II}(\eta) \tilde{K}_{III}(\eta)\}[R_{jc}(\eta)][\psi_c(r, \theta, \eta)] + \{N^a\}^T \{u_j^a\} \quad (4)$$

where r, θ are usual polar coordinates at the crack tip, η is the coordinate tracing the crack front 1 and $\tilde{K}_I, \tilde{K}_{II}, \tilde{K}_{III}$ express the continuous variation in SIFs with η . $[R]$ is a rotating matrix to transfer displacement from crack local coordinates (n, t, b) to global coordinates. ψ_c are our enrichment functions that come directly from the Williams displacement expansions, and defined as:

$$\psi_{In} = \frac{1}{2\mu} \sqrt{\frac{r}{2\pi}} \cos \frac{\theta}{2} \left[\kappa - 1 + 2 \sin^2 \frac{\theta}{2} \right] \quad (5a)$$

$$\psi_{IIn} = \frac{1}{2\mu} \sqrt{\frac{r}{2\pi}} \sin \frac{\theta}{2} \left[\kappa + 1 + 2 \cos^2 \frac{\theta}{2} \right] \quad (5b)$$

$$\psi_{Ib} = \frac{1}{2\mu} \sqrt{\frac{r}{2\pi}} \sin \frac{\theta}{2} \left[\kappa + 1 - 2 \cos^2 \frac{\theta}{2} \right] \quad (5c)$$

$$\psi_{IIb} = \frac{-1}{2\mu} \sqrt{\frac{r}{2\pi}} \cos \frac{\theta}{2} \left[\kappa - 1 - 2 \sin^2 \frac{\theta}{2} \right] \quad (5d)$$

$$\psi_{III} = \frac{1}{2\mu} \sqrt{\frac{r}{2\pi}} \sin \frac{\theta}{2} \quad (5e)$$

where μ is the shear modulus and $\kappa = 3 - 4\nu$ for plane strain. Enrichment of the crack surface elements is achieved by substituting the enrichment equation (4) into Eqs. (1) and (2), otherwise if the element is unenriched we use Eq. (3).

3. Implementation

When using the plane strain Williams expansions for 3D problems the expansions are valid only for points located on a plane perpendicular to the crack front. Nodes on the crack surface have been arranged in a radial lines, each of which is perpendicular to the crack front. We now discretise the variation in $\tilde{K}_I, \tilde{K}_{II}, \tilde{K}_{III}$ using Lagrangian interpolation between their values at points located at the intersection of the crack front with the radial lines on which the nodes lie, i.e.;

$$\tilde{K}_m = [\tilde{N}^a]^T \tilde{K}_m^a, \quad m = I, II, III \quad (6)$$

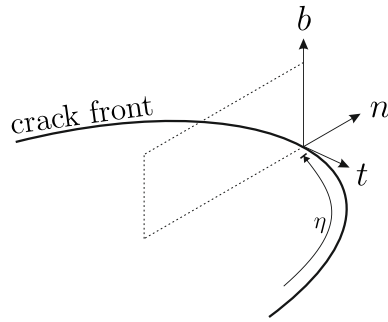


Figure 1: Crack coordinates system

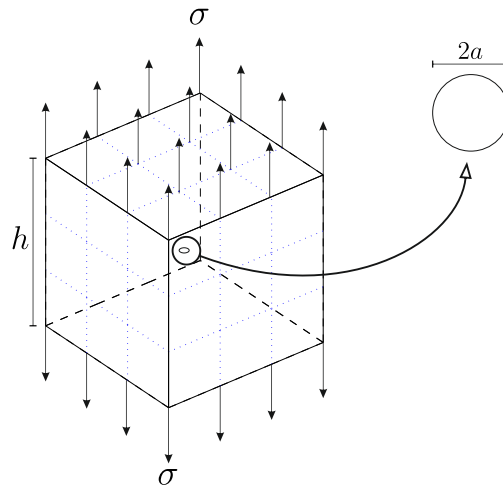


Figure 2: Penny shaped crack in a cube

The discrete variables \tilde{K}_m lie in the solution vector and are found as part of the XBEM solution. Enforcing Continuity of displacement at the crack tip for each radial line at the crack front yields enough equations for a square system, as illustrated in [4]. Then we solve the system to find the values of \tilde{K}_I , \tilde{K}_{II} and \tilde{K}_{III} along the crack front.

SIFs are found from a J-integral evaluated over a disc perpendicular to the crack plane and centred on the crack front. The decomposition of the J-integral in three dimensions provides the singular coefficients for Mode *I*, *II* and *III* as stated in [6]. Finally, the enrichment is applied to the J-integral by using the enrichment functions to evaluate the integrand in the J-integral at individual points on the J-integral contour. Singularity degrees of integrals that appear in the collocation method are not increased by the use of enrichment functions. Moreover, hypersingular and strongly singular integrals can be easily evaluated using the singularity subtraction technique [8].

4. Numerical Example

In this preliminary paper we consider only a mode *I* problem. A cube with a penny shaped crack in the middle is studied to show the effect of enrichment. Figure 2 shows applied stresses to the upper and lower surfaces; h is the cube side length and a is the radius of the crack where $h/a = 40$. Results represented in Fig. 3 show the convergence of the enriched DBEM and the J-integral. This example does not have an exact solution; however we have considered a small crack in comparison to the cube which allows for the use of the infinite domain solution. The exact solution for an infinite domain can be calculated as $K_{I0} = \frac{2}{\pi} \sigma \sqrt{\pi a}$.

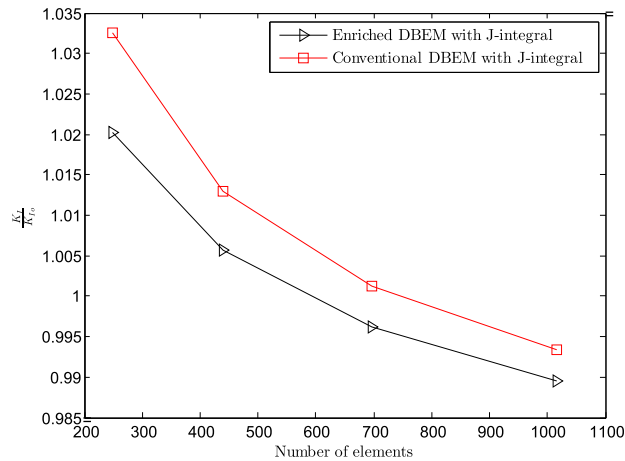


Figure 3: J-integral results with enriched and conventional DBEM

5. Conclusion

A new enrichment approach has been introduced to increase the accuracy of the DBEM. The enrichment affects only elements on the crack surfaces, while other elements are treated in conventional way. The enforcement of continuity in the crack tip displacement has generated enough equations to solve for the added degrees of freedom.

Acknowledgements

The first author acknowledges the financial support under Ref. No.S11973 by the Ministry of Education of Saudi Arabia.

References

- [1] R.J. Hartranft and G.C. Sih. Stress singularity for a crack with an arbitrarily curved front. *Engineering Fracture Mechanics*, 9(3), 705–718, 1977.
- [2] N Sukumar, N Moës, B Moran, and T Belytschko. Extended finite element method for three-dimensional crack modelling. *International Journal for Numerical Methods in Engineering*, 48(11), 1549–1570, 2000.
- [3] S Li, ME Mear, and L Xiao. Symmetric weak-form integral equation method for three-dimensional fracture analysis. *Computer Methods in Applied Mechanics and Engineering*, 151(3):435–459, 1998.
- [4] I.A. Alatawi and J. Trevelyan. A direct evaluation of stress intensity factors using the extended dual boundary element method. *Engineering Analysis with Boundary Elements*, 52, 56–63, 2015.
- [5] M.K. Kassir and G.C. Sih. Griffith’s theory of brittle fracture in three dimensions. *International Journal of Engineering Science*, 5(12):899–918, 1967.
- [6] R.H. Rigby and M.H. Aliabadi. Decomposition of the mixed-mode J-integral revisited. *International Journal of Solids and Structures*, 35(17), 2073–2099, 1998.
- [7] Y Mi and MH Aliabadi. Dual boundary element method for three-dimensional fracture mechanics analysis. *Engineering Analysis with Boundary Elements*, 10(2), 161–171, 1992.
- [8] M. Guiggiani, G. Krishnasamy, T. J. Rudolph, and F. J. Rizzo. A general algorithm for the numerical solution of hypersingular boundary integral equations. *Journal of Applied Mechanics*, 59(3), 604, 1992.

MESH GENERATION

A Low-Cost Elasticity Analogy Approach to Boundary Motion on Curved Finite Element Meshes

Lucas Franceschi¹ and Ruben Sevilla²

¹Universidade Federal de Santa Catarina, Florianopolis, 88040-900, Brasil.

²Zienkiewicz Centre for Computational Engineering, College of Engineering, Swansea University, Swansea, Wales SA2 8PP, UK

Franceschi.Lucas@grad.ufsc.br

R.Sevilla@swansea.ac.uk

ABSTRACT

A procedure that accounts for large boundary motion in curved meshes is presented. It benefits from a linear elasticity analogy, where the mesh is treated as an elastic continuum and boundary loads are applied in order to obtain the desired deformation or movement. The high-order meshes are generated from an initial linear mesh by applying loads to ensure that the curved boundary matches the real boundary. The motion of the boundary is accomplished using a similar strategy, with the addition of a locally defined set of material parameters that ensures a good quality of the elements near the boundary. The quality of the curved high-order finite elements is defined in terms of a measure of distortion, through the scaled Jacobian of the isoparametric mapping. An example of particular interest to the aeronautic industry is shown. The proposed technique is able to transform high-order meshes under extreme motions without re-meshing, what makes it a viable, cheap and simple to implement tool for boundary motion of curved meshes.

Key Words: *Boundary movement; Mesh generation; High-order meshes; Computational fluid dynamics; Elastic analogy*

1. Introduction

Much investment has been made in the last decade in the development of better methods of approximation for complex areas of engineering. Industries such as the aeronautic have been successfully using computational analysis as a central tool on design of aircrafts and structures. However, the current scenario shows that some complex simulations are still very expensive and time consuming; a problem that can be reduced by using methods with a higher degree of approximation, that give better accuracy with less degrees of freedom, which could in turn alleviate the cost of the simulations. Although high-order methods have been under development for more than 20 years, the automatic generation of high-order meshes that allow these methods to be applied is still an open problem [1]. This study presents a low-cost technique, built up from the studies in [2, 3], that allows to generate high-order meshes and, with a similar approach, transform them in order to account for large boundary displacements.

An elastic analogy is proposed, where the meshes are given theoretical elastic parameters that are controlled regionally to optimise its deformation. Linear meshes, that are easy to obtain, are used as a starting point for creating high-order meshes. In the faces of the initial linear mesh, new nodes are inserted that correspond to the desired order of the curved mesh. Then, material properties are assigned to the mesh, and a boundary load is prescribed that ensures that the high-order nodes match the true boundary. By solving the static elasticity problem, the deformed configuration gives the high-order curved mesh. It is important to emphasise that the elastic parameters are used as a theoretical tool only (hence the name of elastic analogy) so that they can be controlled in order to optimise the quality of the resulting curved mesh. The main advantage of generating meshes following this procedure is that fully automatic linear mesh generators are nowadays available and it is simple and inexpensive to solve the linear static elasticity problem through the finite element method.

Similarly to the proposed high-order mesh generation technique, incremental displacement steps can be imposed to account for boundary motion. A simple linear elasticity problem is then solved for each step in order to accommodate such displacements and obtain a deformed configuration of the rest of the mesh without the need of re-meshing. In this study this technique is presented and illustrated by examples of interest to the aeronautic industry. In particular, a 2D mesh around an aerofoil subject to drastic boundary movement is shown.

2. Finite element solution for the linear elasticity problem

The proposed approach is to treat the meshes as linear elastic continua, so that the finite element solution provides an inexpensive way of computing the deformation induced by curving or moving the boundary. Here, the equation used to describe the static deformation of a linear elastic medium Ω , with a closed boundary Γ , is considered to be

$$\nabla \cdot \boldsymbol{\sigma} = \mathbf{0} \quad \text{in } \Omega \quad (1)$$

The components of the stress tensor, $\boldsymbol{\sigma}$ are obtained in terms of the strain tensor $\boldsymbol{\varepsilon}$ by adopting the plane strain assumption:

$$\begin{Bmatrix} \sigma_{11} \\ \sigma_{22} \\ \sigma_{12} \end{Bmatrix} = \frac{E}{(1+\nu)(1-2\nu)} \begin{bmatrix} 1-\nu & \nu & 0 \\ \nu & 1-\nu & 0 \\ 0 & 0 & (1-2\nu) \end{bmatrix} \begin{Bmatrix} \varepsilon_{11} \\ \varepsilon_{22} \\ \varepsilon_{12} \end{Bmatrix} \quad (2)$$

where E and ν are respectively the Young's modulus (or modulus of elasticity) and Poisson's ratio.

In order to solve (1), appropriate boundary conditions are needed. Here, we consider an imposed displacement \mathbf{u}_D , on the Dirichlet boundary Γ^D , and an imposed traction \mathbf{f}_N on the Neumann boundary Γ^N . These boundaries must not overlap ($\Gamma^D \cap \Gamma^N = \emptyset$), and they must compose the whole boundary of the domain ($\Gamma = \Gamma^D \cup \Gamma^N$).

The solution for the displacement \mathbf{u} of the nodes is then approximated by \mathbf{u}^h , that is a linear combination of basis functions \mathbf{N}_j and coefficients \mathbf{u}_j .

$$\mathbf{u}^h(\boldsymbol{\xi}) = \sum_{j=1}^{N_{en}} \mathbf{u}_j \mathbf{N}_j(\boldsymbol{\xi}) \quad (3)$$

The shape functions \mathbf{N}_j are Lagrange polynomials of order p defined on a reference element \mathbf{R} and the classical isoparametric formulation is considered.

3. Generation of high-order meshes

In order to obtain a high-order mesh around a curved boundary, say for example an aerofoil, this procedure starts by using an unstructured linear mesh generator to discretise the domain around the object, as seen in Figure 1(a). The characteristic mesh size h of the linear mesh is chosen to be such that the characteristic mesh size of the final high-order mesh, h/p , provides a mesh suitable for the problem under consideration. High-order nodes, appropriate to the degree of approximation p , are added in the boundary faces. In Figure 1(b) the new nodes are equally spaced on the element face, although other distributions can be considered. The displacements required to move the internal edge nodes to the boundary curve are then calculated as the difference between their original position and a distribution of nodes defined on the true boundary, as shown in Figure 1(c). Knowing the displacement needed in order to make the high-order boundary nodes match the exact boundary, these are imposed as Dirichlet boundary conditions to the elastic problem, and the static solution to the problem gives the displacement field. Figure 1(d) shows how the elements in the leading edge of the aerofoil deform.

In an attempt to optimize the result of this technique and also having in mind the problem of moving boundaries, variable material parameters are introduced. The motivation is that if the elements nearest to the boundary are made of a nearly incompressible material, their distortion will be minimum (i.e., their quality maximum), and the elements in the far-field of the mesh will in turn account for the imposed deformation. The section of numerical examples shows the benefits of locally defining the material parameters.

To achieve this, the strategy is to introduce an interpolation, where the elastic properties of every element are calculated as a function of the distances (d) from the vertices of the element to the closer node on

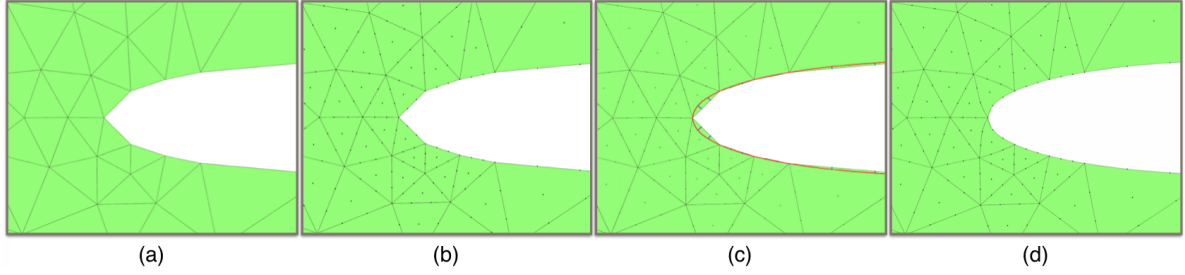


Figure 1: Illustration of the presented procedure: (a) Generated unstructured linear mesh in the surrounding domain of a NACA aerofoil; (b) Distribution of nodes according to the desired degree of polynomial approximation $p = 3$; (c) Close detail of the straight sided mesh and the displacement needed to move the new nodes to the boundary curve; (d) Detail of the resulting high-order mesh obtained from the elastic accommodation of the required conditions.

the boundary. This interpolation can be of various natures, depending on the mesh and the problem at hand. It is possible to manipulate the degree of the interpolatory curve, defined in an interval d_0 to d_1 , outside of which two constant values can be imposed. To simplify the implementation and without loss of generality, we consider the material parameters constant within each element. The constant value is computed as the average between the nodal values that are defined by the desired interpolation.

The quality of the produced high-order curved meshes is assessed based on [4], by means of the scaled jacobian $\hat{\mathbf{I}}$, here defined by:

$$\hat{\mathbf{I}} = \frac{\min_{\xi \in \mathbf{R}} |\mathbf{J}(\xi)|}{\max_{\xi \in \mathbf{R}} |\mathbf{J}(\xi)|} \quad (4)$$

where J is the Jacobian of the isoparametric mapping between the reference element, \mathbf{R} , and the physical element.

4. Boundary movement

The next objective of this work is to be able to account for boundary movement of high-order meshes. This is accomplished with the same technique proposed before, the elastic analogy with variable material parameters. If we consider the boundary motion as known, it is possible to split this movement into multiple steps, and impose the desired movement for each step as a Dirichlet boundary condition in order to obtain the deformed configuration. This approach is also applicable in fluid-structure interaction problems, where the displacement wouldn't be prescribed but determined by the solution of the solid problem at each step.

As an example, consider the two-dimensional mesh obtained in the previous section. Suppose that the aerofoil is subject to two movements: a translation with amplitude of two times its chord length and a rotation of 180 degrees. Using the proposed algorithm, a region is created around the boundary where ν and E make the material nearly incompressible ($\nu_0 = 0.49999$ and $E_0 = 10$), and this parameters are reduced in the far-field of the mesh ($\nu_1 = 0.15$ and $E_1 = 0.2$). Both movements are performed incrementally with 40 steps. Figure 2 shows some snapshots of the mesh as it deforms to accommodate the imposed boundary displacement.

Monitoring the quality of the elements at all steps during the imposed translation we observe that when the displacement is maximum, 82% of the elements have a quality greater than 0.9, and the minimum quality is $\hat{\mathbf{I}} = 0.78$. Similarly, monitoring the quality of the elements at all steps during the imposed rotation we observe that after a rotation of 180 degrees, 79% of the elements have a quality greater than 0.9, with the worse element quality being $\hat{\mathbf{I}} = 0.59$.

To illustrate the advantages of using variable material parameters, we implement the same translation, now with constant material parameters ($E = 10$, $\nu = 0.485$). First, it is worth noting that in order to perform the translation, three times more steps are required, compared to the proposed technique of using locally defined material parameters. Furthermore, the minimum quality is almost zero (i.e., $\hat{\mathbf{I}} = 0.04$). The deformed configuration with constant material parameters is shown in Figure 3, where a zoom near the airfoil is also included to illustrate that the element with the lower quality are found in the vicinity

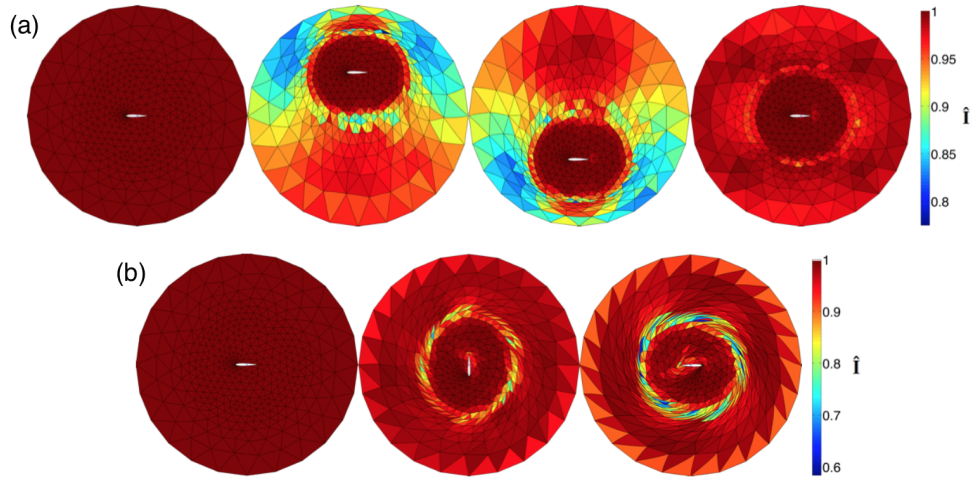


Figure 2: Progress of the mesh under movement using the technique proposed. (a) Translation with amplitude equal to twice the wing length. (b) Rotation of 180 degrees. The colour indicate the Scaled Jacobian (\hat{I}) of the elements

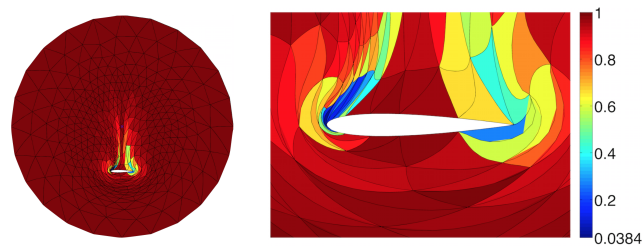


Figure 3: Mesh and detail of one of the extremes of the sinusoidal translation. Obtained with constant material parameters $E = 10$ and $\nu = 0.485$.

of the boundary. This is in contrast with the approach where the material parameters are locally defined, where the elements near the airfoil have a very good quality (see Figure 2).

5. Conclusion

This paper proposes a linear elastic analogy for the generation and motion of high-order curved finite element meshes without re-meshing. The unique characteristic of the proposed approach is that the material parameters are defined locally. Numerical examples show that this new approach enables to account for extremely large boundary motion maintaining a very good quality of the resulting mesh. Numerical examples demonstrate that this is not feasible if the parameters are defined constant in the whole domain.

Acknowledgements

The authors gratefully acknowledge the financial support provided by Conselho Nacional de Desenvolvimento Científico e Tecnológico - Brasil (CNPq).

References

- [1] Sherwin SJ, Peiró J (2002) *Mesh generation in curvilinear domains using high-order elements*. International Journal for Numerical Methods in Engineering 53(1):207-223
- [2] Z. Xie, R. Sevilla, O. Hassan, and K. Morgan, *The generation of arbitrary order curved meshes for 3d finite element analysis*, Computational Mechanics, vol. 51, no. 3, pp. 361-374, 2013.
- [3] Persson PO, Peraire J (2009) *Curved mesh generation and mesh refinement using Lagrangian solid mechanics*. In: Proceedings of the 47th AIAA aerospace sciences meeting and exhibit. AIAA
- [4] Roca X, Gargallo-Peiró A, Sarrate J (2011) *Defining quality measures for high-order planar triangles and curved mesh generation*. In: 20th International Meshing Roundtable. Sandia National Laboratories, USA, pp 365-383

Generating dual orthogonal meshes suitable for Co-Volume techniques.

*S. Walton, O. Hassan, K. Morgan

College of Engineering, Swansea University, Swansea, SA2 8PP

*s.p.walton@swansea.ac.uk

Key Words: *Co-volume, mesh generation, mesh optimisation, dual orthogonal meshes, marker and cell, Yee scheme*

ABSTRACT

This paper outlines recent advances in generating dual orthogonal meshes suitable for co-volume techniques around general industrial geometries. The two key advancements presented are an enhanced advancing front technique and an adaptive mesh cosmetics algorithm. The effectiveness of these methods is shown first by meshing an F16 geometry. Using traditional techniques 66% of the elements are suitable and using the presented techniques 98% are suitable. Finally the techniques are used to generate a mesh to solve an electromagnetic wave scattering problem. It was found that the cosmetics procedure increased the minimum time step by an order of magnitude, which reduced the total CPU time to calculate a solution from 37 hours to 4.3 hours. The cosmetics algorithm could be easily adapted to any quality measure of interest.

1. Introduction

The marker and cell (MAC) algorithm [1] and the Yee scheme [11] are examples of co-volume methods for the solution of the Navier Stokes and Maxwell's equations respectively. These algorithms exhibit a high degree of computational efficiency, both in terms of low operation count and storage requirements. One outstanding problem limiting the use of co-volume algorithms is that of mesh generation.

Co-volume schemes require mutually bisecting orthogonal meshes [4] which immediately brings the Delaunay-Voronoi dual to mind. These two mutually orthogonal meshes are termed the primal and dual mesh. For integrations to remain valid each primal element needs to contain its dual node. In two dimensions this can be achieved by eliminating obtuse triangles, however there is no such geometric simplification in three dimensions [5].

It has been shown that sufficient element quality can be achieved on near uniform three dimensional meshes [10]. Meshes targeted at three dimensional MAC solvers introduce the requirement to change the element size throughout the mesh which increases the difficulty of the problem. Advances in generating *non uniform* three dimensional meshes suitable for co-volume schemes around industrial geometries are presented here.

The full mesh requirements for co-volume schemes have been presented previously [7]. For the purposes of this paper the focus is on the most crucial, which is that dual mesh nodes lie inside their corresponding primal mesh element. If this condition is not met solvers will diverge if high gradients appear in non satisfying elements. The remaining conditions are relaxed at the cost of a loss of local accuracy in order to avoid divergence. The percentages presented in this paper represent the number of elements which do not contain their dual node.

2. Methodology

2.1. Enhanced Advancing Front Technique

Boundary elements are the most crucial when considering the eventual solution quality obtained. In the following section a strategy adopted for creating the first few layers of elements close to the surface is outlined. Advancing front techniques are characterised by marching the volume mesh into empty space from the surface mesh by sequentially generating elements [2]. In the case of tetrahedral elements this traditionally consists of placing a single new node above each face on the surface. However, in an ideal dual orthogonal mesh nodes lie above the edges of the slab of elements below them. This is illustrated for a few edges in Figure 1. For this reason, the technique adopted here is to advance nodes from edges rather than faces. To identify this set of edges on a general unstructured mesh a blossom algorithm is used to pair triangles on the surface [3]. The common edge to each pair of triangles is then advanced from.

The positioning of the advancing node is determined by considering the set of rules presented by VanderZee et al. [5] for constructing well centred tetrahedra. These nodes are inserted using standard Delaunay insertion, and the remaining nodes are inserted using the automatic Delaunay refinement method [9].

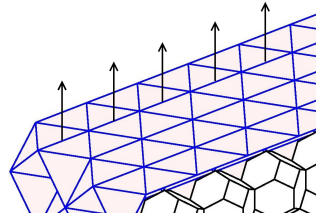
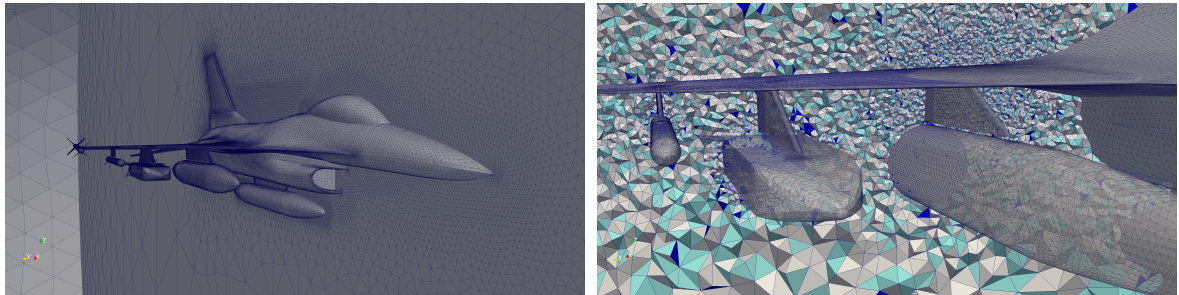


Figure 1: Detail of a mesh of ideal tetrahedral elements, showing the surface Delaunay faces and the internal Voronoi cells. The arrows indicate where the next layer of nodes would be placed.



(a) Surface mesh

(b) Cut through the final mesh generated and optimised using the new techniques, the solid dark blue elements do not contain their dual node

Figure 2: The F16 surface and volume mesh

2.2. Adaptive Mesh Optimisation

It has previously been shown that the best strategy for improving dual orthogonal meshes is using direct optimisation [7]. This is achieved in two dimensional meshes using the gradient-free optimisation technique Modified Cuckoo Search (MCS) [8, 6], which was developed with this application in mind. The objective function to be optimised was simply a summation, over elements considered, of the distances between their dual node and centroid. This objective function can be replaced with any mesh quality measure of interest, depending on solver requirements.

Since the number of degrees of freedom in a three dimensional mesh is much higher than in two dimensions, a number of modifications were made to the scheme presented previously [7]. Firstly, the problem was separated by first grouping elements into bins based on their quality. The bins were considered in order from the worst quality to the best. Within each bin the elements were optimised in a random order. This both gave priority to the worst elements and avoided premature convergence by introducing randomness. Then swap diagonal and element collapse cosmetics are applied. Finally, each iteration the effectiveness of the optimisation is measured. If the effectiveness of the process decreases, new parameters for the various processes, such as MCS tuning parameters or number of bins to split the elements up into, are tested. This is continuously monitored and a simple optimisation algorithm adapts the parameters as the optimisation progresses. The optimisation process is repeated until either no further improvement is made or 24 hours has passed.

3. Results

3.1. F16

Figure 2(a) shows the surface mesh of the F16 geometry. This is a complex full aircraft with missiles and fuel tanks unconnected but close to the wing. This leads to very small gaps between separate surfaces. The surfaces are made up of 170104 triangular elements. Table 1 shows the percentage of elements which do not contain their dual nodes in the resulting meshes. A comparison is made between using the enhanced advancing front technique and not. The new technique reduces the number of boundary elements with dual nodes outside from 42% to 12%. The adaptive cosmetics scheme reduces the total number of elements with dual nodes outside from 33% to 1.7%.

3.2. Electromagnetic Wave Scattering Simulation

To illustrate the effectiveness of the proposed strategies a three-dimensional electromagnetic wave scattering simulation is considered. An unstructured co-volume solver for the Maxwell's equations was used [10]. Interaction between a plane single frequency incident wave and a perfect electrical conductor (PEC) body with two pairs of rear fins is considered. A plot of the surface mesh is shown in Figure 3. The wave frequency is specified such that the length of the

Table 1: Percentage of elements whose dual node are outside in the F16 mesh generated using automatic delaunay refinement with and without the enhanced advancing front technique, before and after cosmetics.

Before Cosmetics			
Generation method	Total Outside	Boundary Outside	N_e
Automatic Delaunay Refinement	34%	42%	5518276
... with Enhanced Advancing Front	33%	12%	5612485
After Cosmetics			
Generation method	Total Outside	Boundary Outside	N_e
Automatic Delaunay Refinement	2.3%	6.2%	5216038
... with Enhanced Advancing Front	1.7%	3.9%	5245402

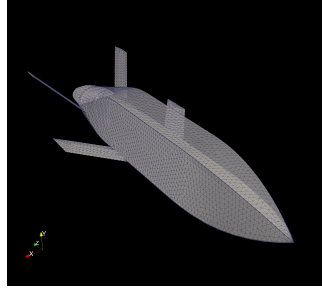


Figure 3: The surface mesh of the PEC body in the electromagnetic wave scattering problem

body is 6λ , where λ is the wavelength. The incident wave propagates in the $x - y$ plane and the main axis of the body is aligned with the z axis of a standard Cartesian coordinate system. In all cases the simulation was run for 15 cycles of the plane wave, which was enough to provide a converged solution. The number of time steps required per cycle was determined by the time step size, which in turn is calculated using the minimum dual edge length in the mesh [10]. Previous techniques only have the capability to generate uniform meshes so this was all that was considered. The findings are summarised in Table 2. Globally the mesh generated using the Xie et al. [10] technique has less elements with their dual node outside. However the prioritisation of boundary elements in the new technique is shown as the percentage of boundary elements with their dual node outside is 0.04% compared with 0.4% using the old technique. Mesh generation using the new technique takes significantly longer, 24 hours compared with 5 minutes. However the reduction in time step, from 3.47×10^{-5} to 2.93×10^{-4} has led to reduction in total CPU cost from 37 hours to 4.3 hours.

A study was carried out whereby the time allowed for the adaptive mesh optimisation was reduced. It was found that 3 hours of the adaptive mesh optimisation was needed to generate a suitable mesh for the problem. Using the 3 hour case the total CPU time from surface geometry to a converged solution using the newly proposed techniques was 7.8 hours, using the technique previously proposed in Xie et al. [10] the total time is 37 hours. Clearly this is a significant time saving, and illustrates the point that more time spent on optimising a mesh can lead to big savings in time later in the pipeline.

Table 2: Comparing the meshes generated for the PEC body with a uniform target spacing function

Mesh			
Generation method	Total Outside	Boundary Outside	CPU Cost
Xie et al. [10]	0.18%	0.40%	5 minutes
New techniques	0.75%	0.04%	24 hours
Solution			
Generation method	Time Step	CPU Cost per cycle	Total CPU Cost
Xie et al. [10]	3.47×10^{-5}	148 minutes	37 hours
New Techniques	2.93×10^{-4}	17 minutes	4.3 hours

4. Conclusions and Future Work

Examples were presented which show the effectiveness of the new mesh generation and optimisation algorithms. The enhanced advancing front technique is able to produce boundary elements which contain their dual node. The adaptive mesh optimisation algorithm is effective in significantly reducing the number of elements which do not contain their dual node. This does not only result in an improvement of accuracy but it was shown that the increase in minimum time step makes up for the extra CPU effort applied to the mesh optimisation. In the future it might be beneficial to apply this optimisation scheme to different mesh quality measures. In addition this research might open the door to fully unstructured compressible MAC solvers.

Acknowledgements

Sean Walton acknowledges the financial support for this work provided by the UK Engineering and Physical Sciences Research Council (EPSRC) under Research Grant EP/K000705.

References

- [1] F. H. Harlow, J. E. Welch, Numerical calculation of time-dependent viscous incompressible flow of fluid with free surface, *The Physics of Fluids* 8 (1965) 2182–2189.
- [2] J. Peraire, M. Vahdati, K. Morgan, O. C. Zienkiewicz, Adaptive remeshing for compressible flow computations, *Journal of Computational Physics* 72 (1987) 449–466.
- [3] J.-F. Remacle, J. Lambrechts, B. Seny, E. Marchandise, A. Johnen, C. Geuzainet, Blossom-quad: A non-uniform quadrilateral mesh generator using a minimum-cost perfect-matching algorithm, *International Journal for Numerical Methods in Engineering* 89 (9) (2012) 1102–1119. doi:10.1002/nme.3279.
URL <http://dx.doi.org/10.1002/nme.3279>
- [4] I. Sazonov, O. Hassan, K. Morgan, N. P. Weatherill, Smooth Delaunay–Voronoi dual meshes for co-volume integration schemes, in: P. P. Rebay (Ed.), *Proceedings of the 15th International Meshing Roundtable*, Springer, Berlin, 2006, pp. 529–541.
- [5] E. Vanderzee, A. N. Hirani, D. Guoy, V. Zharnitsky, E. A. Ramos, Geometric and combinatorial properties of well-centered triangulations in three and higher dimensions, *Comput. Geom. Theory Appl.* 46 (6) (2013) 700–724. doi:10.1016/j.comgeo.2012.11.003.
URL <http://dx.doi.org/10.1016/j.comgeo.2012.11.003>
- [6] S. Walton, Open source project; <http://code.google.com/p/modified-cs/> (2011) [cited 2012].
URL <http://code.google.com/p/modified-cs/>
- [7] S. Walton, O. Hassan, K. Morgan, Reduced order mesh optimisation using proper orthogonal decomposition and a modified cuckoo search, *International Journal for Numerical Methods in Engineering* 93 (5) (2013) 527–550. doi:10.1002/nme.4400.
URL <http://dx.doi.org/10.1002/nme.4400>
- [8] S. Walton, O. Hassan, K. Morgan, M. R. Brown, Modified cuckoo search: a new gradient free optimisation algorithm, *Chaos, Solitons & Fractals* 44 (9) (2011) 710–718.
- [9] N. P. Weatherill, O. Hassan, Efficient three-dimensional Delaunay triangulation with automatic point creation and imposed boundary constraints, *International Journal for Numerical Methods in Engineering* 37 (1994) 2005–2040.
- [10] Z. Q. Xie, O. Hassan, K. Morgan, Tailoring unstructured meshes for use with a 3d time domain co-volume algorithm for computational electromagnetics, *International Journal for Numerical Methods in Engineering* 87 (1-5) (2011) 48–65. doi:10.1002/nme.2970.
URL <http://dx.doi.org/10.1002/nme.2970>
- [11] K. Yee, Numerical solution of initial boundary value problems involving Maxwell’s equations in isotropic media, *IEEE Transactions on Antennas and Propagation* 14 (1966) 302–307.

MESHES APPROPRIATE FOR USE WITH NURBS-ENHANCED FINITE ELEMENT METHOD

Luke Rees, Ruben Sevilla and Oubay Hassan

Zienkiewicz Centre for Computational Engineering, College of Engineering,
Swansea University, Singleton Park, Swansea, SA2 8PP

{635876, R.Sevilla, O.Hassan}@swansea.ac.uk

ABSTRACT

This paper presents an automatic unstructured mesh generation technique using a variant of the advancing front method whereby mesh fronts coincident with the NURBS boundary match the exact geometric definition from CAD independently on the element size. The method allows the possibility to have elements much larger than small geometric features, reducing the overall number of elements required. Special attention has been paid to ensure the capability to produce boundary elements which may be formed of multiple curves, while still maintaining the exact geometric representation. Meshes of proven quality and increasing complexity in 2D are presented.

Key Words: *Mesh generation; NURBS-enhanced FEM; Exact geometry representation; CAD; Curved Finite Elements*

1. Introduction

With recent developments in the finite element method, the need for an accurate geometric description has been well noted. At present, curved boundaries are typically represented by isoparametric elements, see [1]. However, this representation is far from providing optimal results for a given discretisation as shown by Sevilla et al. [2].

Nowadays, the standard geometric representation used in computer-aided design (CAD) is that of non-uniform rational B-splines (NURBS) [3]. The inability of isoparametric elements to reproduce some curve representations available using NURBS, and the known geometric errors induced by isoparametric elements have encouraged the development of methodologies such as the NURBS-enhanced finite element method (NEFEM), see [4, 5]. NEFEM guarantees that the exact (CAD) boundary representation of the domain is an integral part of the finite element solution. However, to represent this geometry in a mesh is an outstanding issue.

This paper will focus on the steps required to produce meshes capable of providing the geometrically exact discretisation required for computation with NEFEM. Section 2 will recall the fundamental steps followed in producing such meshes. Section 3 will present a range of examples of varied complexity followed by a brief conclusion in Section 4.

2. Methodology

The use of an accurate boundary description is of utmost importance in finite element analysis. With the widespread implementation of a NURBS representation of geometry in CAD, it is of significant interest to develop a technique suitable for the discretisation of domains described by NURBS into geometrically exact elements.

The proposed mesh generation technique employs a variant of the advancing front method with modifications to allow for the generation of elements with curved edges only on the boundary. The advancing front method was initially developed to generate triangulations from an existing set of points. In later variations, topological edges were discretised separately and joined to form a piecewise linear approximation of the boundary, see Figure 1a. When coupled with automated point creation, this method was capable of discretising a domain into triangular elements to form a mesh, see [6].

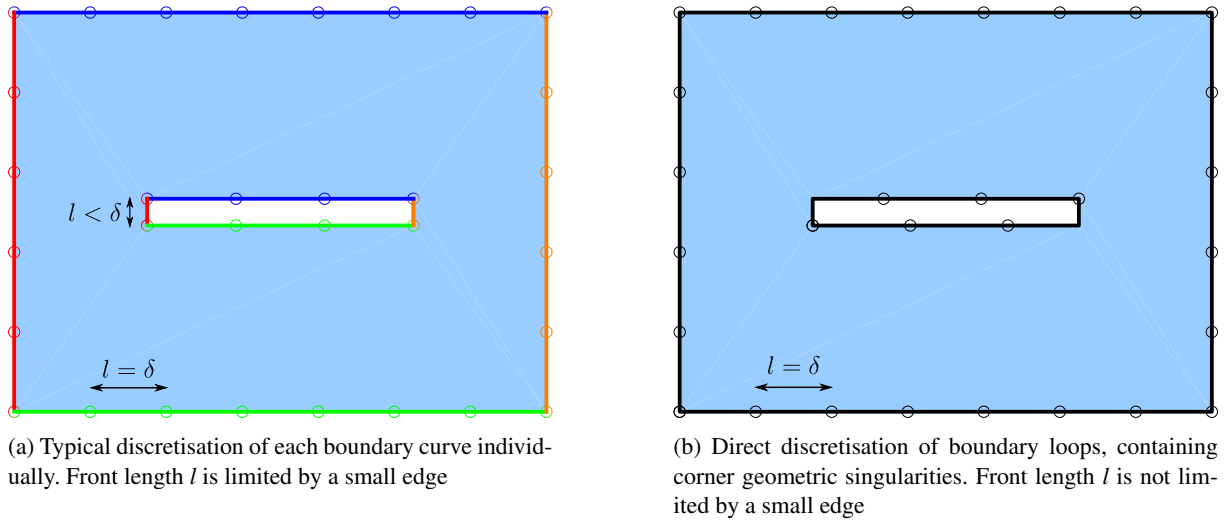


Figure 1: Discretised geometry where lines represent the boundary, circles show the discretised points, l is the distance between discretised points and δ is the prescribed spacing

The technique considered in this paper first assembles boundary curves into loops to allow a discretisation directly on the closed boundary. This eliminates the need for mesh nodes at the topological vertices which often restricts the maximum size of mesh elements, see Figures 1a for an illustration of a standard discretisation limited by a small edge and Figure 1b for a discretisation directly on the closed boundary independently of any small geometric features.

In standard advancing front techniques, the geometric description is redundant beyond the discretisation of the boundary. However, the proposed technique will tie the exact geometric description to the boundary elements of the mesh. Figure 2a shows an example of how these boundary elements are formed. In order to determine the position of the internal node, angles α are increased in equal measure until the average internal edge length is equal to the prescribed spacing. For each boundary node, α is measured from the NURBS boundary horizon (red) to the internal edge common to that node.

The NURBS-enhanced finite element method uses a convex linear combination to parametrise the elements in contact with a NURBS boundary in order to perform the numerical integration. However, by definition, this parametrisation requires a line of sight from the interior point to any part of the curved edge without self-intersection as illustrated in Figure 2b. To satisfy this visibility constraint, elements need to be subdivided into sub-elements.

To subdivide elements which violate the visibility constraint, a recursive algorithm is proposed. Figure 3a shows how the algorithm sweeps through pre-existing sampling points on the boundary until an intersection is found (red arrow). Figure 3b shows how a sub-element is formed with the last non-intersecting sampling point. The algorithm continues to sweep until a point without an intersecting line of sight is detected, a second sub-element joins this point to the interior edge of the first sub-element. The unfilled region of sampling points is flagged for a second pass of the algorithm and the sweep continues until

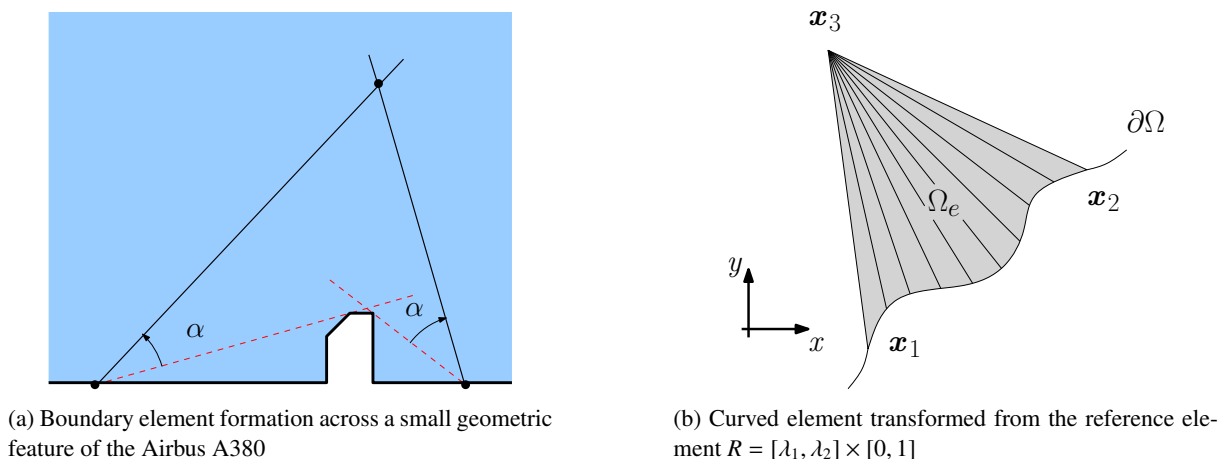


Figure 2: Boundary element generation (a); Curved element parametrisation (b)

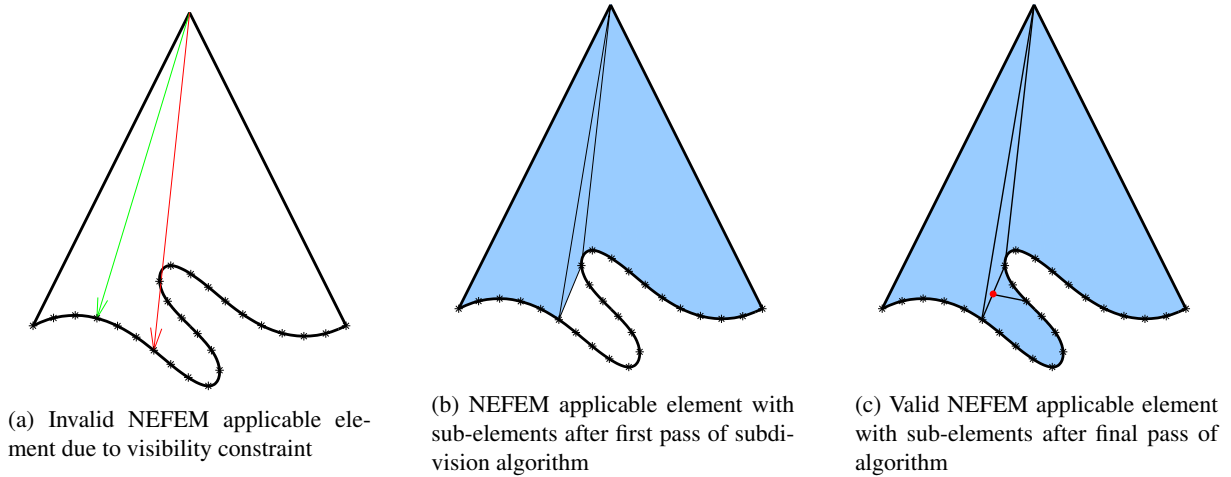


Figure 3: Showing the progression of sub-element generation for boundary elements violating the visibility constraint

it reaches another intersection or the end of the sampling points where a final sub-element is placed. Finally, the algorithm is repeated along any unfilled sections, where the midpoint of the straight line bounding the unfilled region is taken as the interior vertex. Figure 3c shows the completed sub-division of the element into a set of sub-elements which do not violate the visibility constraint.

A second case requiring the subdivision of such elements into sub-elements is that of an element bounded by multiple NURBS. This subdivision is trivial once the visibility constraint has been validated in each element.

3. Examples

A good geometric representation of the boundary is key for accurate finite element analysis. Figure 4a shows a planar mesh for a domain containing a thin plate. It has 1882 elements, a minimum edge length 0.4805 and a maximum edge length 1.7932. Clearly, the minimum element edge length is dictated by the small edge of the plate. Figure 4b shows a mesh for the same thin plate geometry generated using the proposed technique. It has 1353 elements, a minimum edge length 1.4240 and a maximum edge length 1.7826. Clearly the minimum edge length for a mesh generated using the proposed technique is not dictated by small geometric features such as the small edge of the plate. It is well known that transient simulations utilising explicit time marching are subject to a minimum time step which is proportional to the minimum edge length of the mesh. Since the proposed method universally increases the minimum edge length, the restriction on the time step size is more lenient. Greater time step sizes lead to reduced simulation times, an advantage that is augmented by a reduced number of elements.

The proposed method is able to produce meshes which capture exactly the geometry of the domain (Figure 5a). Such representations are not restricted to smooth geometries, but are also capable of capturing small geometric features (Figure 5b). For geometries encompassing features with vastly differing characteristic sizes (Figure 5c), element savings are clearly significant, a benefit which will be more profoundly felt in 3D.

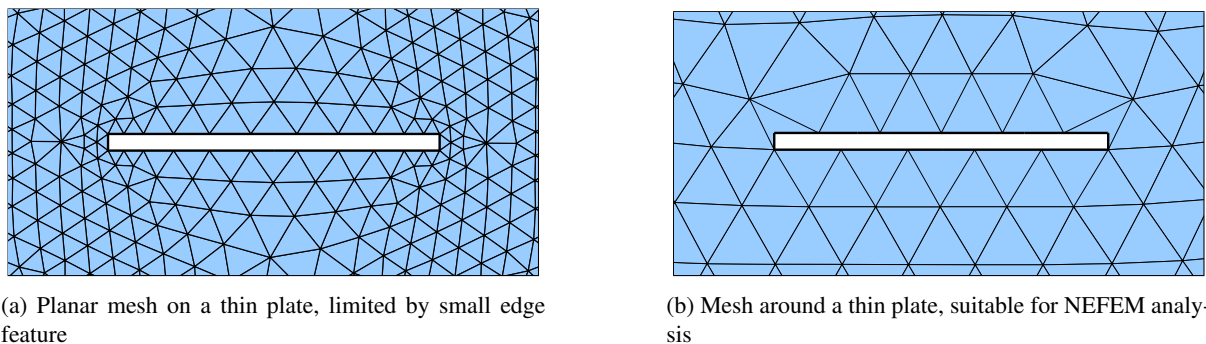
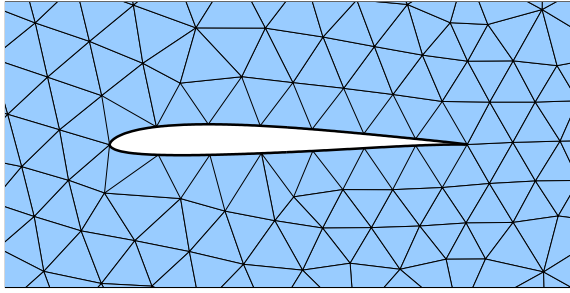
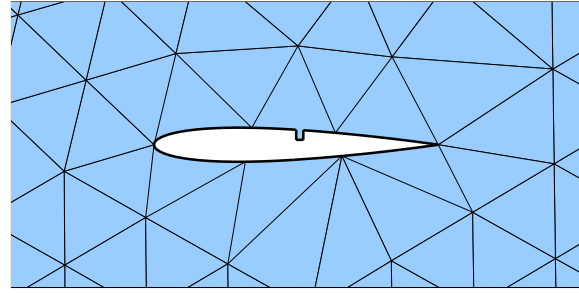


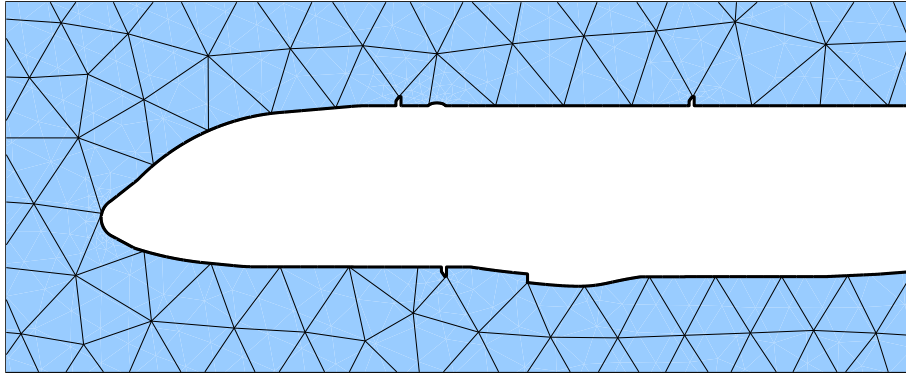
Figure 4: Planar mesh (a) and mesh suitable for NEFEM analysis (b) around a thin plate



(a) Mesh around an SD7003 aerofoil, suitable for NEFEM analysis



(b) Mesh around a NACA0012 aerofoil with a small geometric feature, suitable for NEFEM analysis



(c) Mesh around an Airbus A380 fuselage with small geometric features, suitable for NEFEM analysis

Figure 5: A selection of meshes suitable for NEFEM analysis

4. Conclusions

A fully automatic technique for generating geometrically exact meshes suitable for NEFEM analysis has been outlined. The method shows a clear advantage for small geometric feature and complex geometry representation. Fewer elements can be used to *exactly* represent geometries that would otherwise require large numbers of planar elements to adequately *approximate* the geometry. In addition to accuracy benefits, computational efficiency is increased and memory requirements are reduced.

References

- [1] O. C. Zienkiewicz, R. L. Taylor, J. Z. Zhu, *The Finite Element Method: Its Basis and Fundamentals*, 6th Edition, Elsevier/Butterworth-Heinemann, 2005.
- [2] R. Sevilla, S. Fernández Méndez, A. Huerta, Comparison of high-order curved finite elements, *International Journal for Numerical Methods in Engineering* 87 (2011) 719–734.
- [3] L. Piegl, W. Tiller, *The NURBS Book*, 2nd Edition, Springer-Verlag, Berlin, New York, 1997.
- [4] R. Sevilla, S. Fernández Méndez, A. Huerta, NURBS-enhanced finite element method (NEFEM), *International Journal for Numerical Methods in Engineering* 76 (2008) 56–83.
- [5] R. Sevilla, S. Fernández Méndez, A. Huerta, NURBS-enhanced finite element method (NEFEM) - A seamless bridge between CAD and FEM, *Archives of Computational Methods in Engineering* 18 (2011) 441–484.
- [6] J. Peraire, J. Peiró, K. Morgan, Advancing Front Grid Generation, *Handbook Of Grid Generation*, CRC Press LLC, 1999, Ch. 17.

Boundary aligned PEBI-Grid Generation and CVD-MPFA Discretization

*S. Manzoor¹, M.G. Edwards¹, A.H. Dogru² and T.M. Shaalan²

¹ZCCE College of Engineering, Swansea University, Singleton park, Swansea, SA2 8PP

²EXPEC Advanced Research Center, Saudi Aramco, Saudi Arabia

*642969@swansea.ac.uk

ABSTRACT

Grid generation for reservoir simulation, must honor classical key constraints and be boundary aligned such that control-volume boundaries are aligned with geological features such as layers, shale barriers, fractures, faults, pinchouts and multilateral wells. A grid generation procedure is proposed that automates control-volume and/or control point boundary alignment and yields an essentially PEBI-mesh. The grids generated are employed to study comparative performance of cell-vertex versus cell-centred CVD-MPFA finite-volume formulations using equivalent degrees of freedom. The relative benefits of both types of approximation are made clear in terms of flow resolution and degrees of freedom required.

Key Words: PEBI-Grid; BAG; Delaunay triangulation; CVD-MPFA; Cell-centred vs vertex-centred CVD-MPFA

1. Introduction

Grid generation for large scale porous media poses the challenge of complex geometries and random distribution of spatial heterogeneities in the domain e.g. [1]. In addition to robust numerical methods for solving the flow equations, grid generation methods are required which can honour geometric complexity and permit local grid cell density control. Standard reservoir simulators were originally based on simple grid blocks i.e. squares and cubes primarily using structured grids. Although it is relatively easy to implement simulation techniques on such simple grids, they inherently lack the ability to adapt to complex geologies e.g. [2]. Unstructured grid generation offers the desired flexibility by employing triangles and tetrahedra as grid elements. Unstructured grids allow grid cells to adapt to various flow and geometric constraints and also local refinement with smooth transition[1, 2, 5, 6]. However, unstructured grids require special data structures, and are computationally more involved.

Unstructured grids used in reservoir modelling, commonly employ Delaunay-*voronoi*(PEBI) grids for spatial discretization of domain[3]. Delaunay triangulation(DT) is the dual of the *voronoi* diagram, given a DT or a *voronoi* grid, the dual can be constructed. *Voronoi* grids can be made to conform to geological features by special treatment such that their cells become aligned to these features. In contrast, flow based grids concentrate local grid refinement in high flow regions and apply to heterogeneous media[4], vorticity based grids have a similar objective. Here we focus on constructing feature based *voronoi* meshes, some of the most commonly employed PEBI gridding techniques can be found in [1, 2, 3]. In this work an unstructured PEBI-grid generation technique is presented, which generates quality meshes for reservoir geometries, honouring geological features both in primal and dual(*voronoi*) configuration. Grids generated are employed to simulate pressure fields, and a comparative study of cell-centred versus cell-vertex control volume distributed(CVD) multipoint flux approximation(MPFA) schemes is presented.

2. Geological Feature Based Grid Generation Technique:

In the meshing technique presented, feature preserving grids are generated through the use of advancing front point placement, used in conjunction with the Delaunay criteria[5, 6]. An initial protection area is constructed around key geological features. The advancing front is initiated from discretized interior boundaries embedded inside a domain and as each front propagates, a set of cells are created on either side of it, providing protection as shown in figure 1. In order to construct dual-cell feature based grids, it is a prerequisite to build a (protection) layer of quadrilaterals, with a geological feature defining the median line inside the quadrilateral layer, we call this additional protection layer a *halo*. In what follows a brief description of *halo* construction is outlined.

Methods for halo construction: In order to honour features in the dual setting, curves characterizing geological features require special treatment, thereby enclosing them with *halos*. To elucidate construction of a *halo*, consider a feature *ab* as shown in figure 2a, embedded in the empty mesh in discrete form. To start with *halo* construction, a spear comprised of two triangles is first built as shown in figure 2b, which is then propagated until the last point (*b*) of the feature is encountered. The *halo* propagated via the use of spear triangles enables quadrilateral cell construction (one by one). Construction of the *halo* is demonstrated in figures 2b–2c, and requires points defining the feature, that are split by the spear, to be enclosed. This is achieved by in effect, treating feature points as double

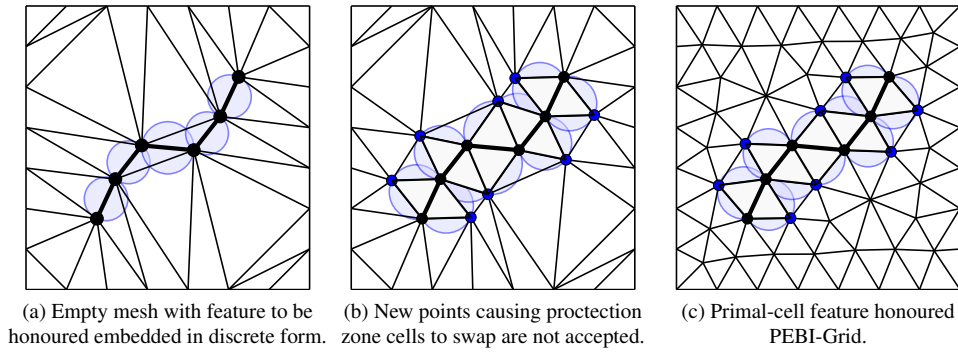


Figure 1: A protection layer constructed by advancing front point placement around feature to be honoured.

points, then pushing the underlying feature points in directions normal (upward and downward) to the feature edges in an average sense, a distance assumed to be a fraction ($\alpha = 0.10$) of average length of the feature edges attached to the point to be split. Finally, the spear head is opened to fully enclose the feature by the quadrilateral *halo*, as shown in figure 2c. Note that the feature is recovered as a medial line of the *halo*, and is thus honoured in the dual configuration. The *halo* construction around intersecting features can be easily dealt with by using spear

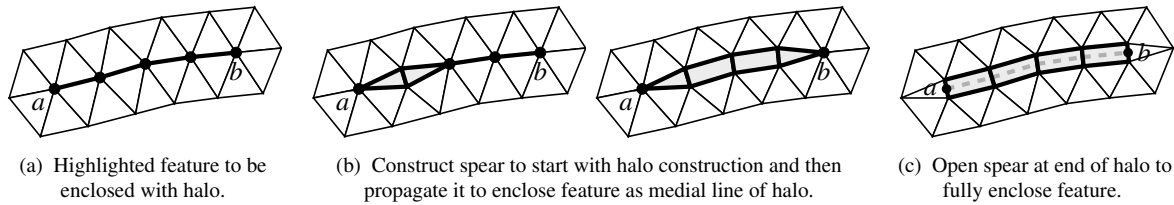


Figure 2: Constructing halo around feature which is retrieved as median line of halo.

simplices. We propose to start the *halo* from the point of intersection of features, also called a junction point. Once the *halo* construction has taken place, the junction point is merged thereby introducing a polygon with number of edges equal to number of curves emanating from the junction point, e.g. see figure 3a. In three dimensions the construction of protection zone involves tetrahedra, whereas construction of a *halo* is accomplished through the use of prisms. Figures 4 and 5 show some test case geological feature based grids generated by the proposed mesh techniques. Note that embedded features have been honoured both in primal and dual configurations.

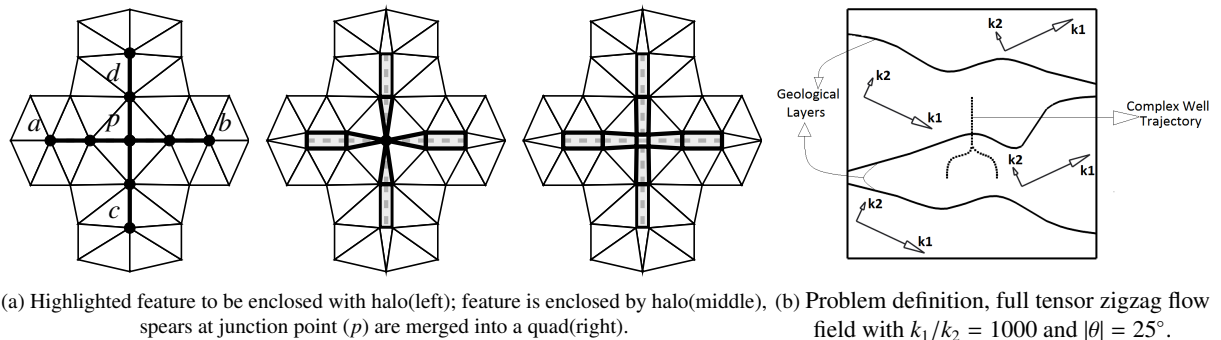


Figure 3: Construction of halo around intersecting features; also shown is the problem definition of test case selected to study comparative performance of cell-centred vs cell-vertex CVD-MPFA schemes.

3. Flux Approximation Schemes:

Continuous flux approximation schemes employed in reservoir simulation are generally control-volume distributed (CVD) [4], where a piecewise constant representation of rock properties is assigned to control-volumes, and flow variables are computed at their control points [3]. In selecting control-volumes normally there are two choices i.e. either primal or dual cells. The resulting schemes are called cell-centred or vertex-centred approximations respectively. Formulation of CVD schemes in cell-centre and cell-vertex modes is analogous, and requires switching control volume from primal to dual or vice versa together with appropriate boundary conditions. A comparison between cell-centred and cell-vertex CVD schemes is presented, using flow fields resulting from the

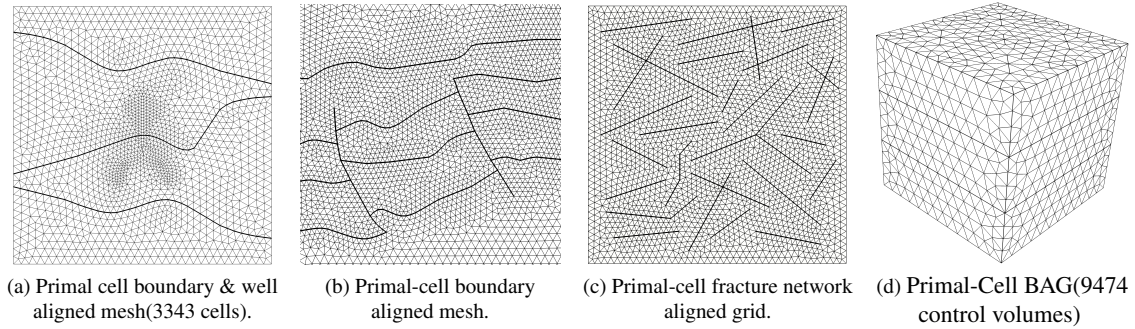


Figure 4: Primal-cell boundary aligned meshes generated with the proposed meshing technique.

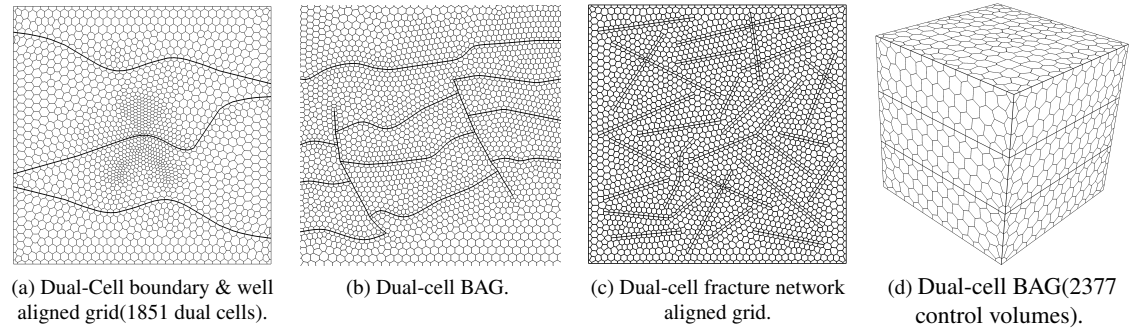


Figure 5: Dual-cell boundary aligned meshes generated by employing the proposed meshing technique, are constructed from underlying primal-grids where features have been honoured with the use of quadrilateral *halos*.

respective approximations of the pressure equation. The pressure equation arises from mass conservation together with Darcy's law after application of Gauss divergence theorem is written in integral form as:

$$-\oint (K\nabla\phi) \cdot \vec{n} d\Gamma = -\sum_{i=1}^{n_f} \int_{\Delta\Omega_i} (K\nabla\phi \cdot \vec{n}_i) d\Gamma = q \quad (1)$$

where ϕ represents field pressure; ∇ is the gradient operator, K is the elliptic symmetric permeability tensor; q is the source term. Furthermore Γ corresponds to the boundary of control-volume Ω , $\Delta\Omega_i$ is the i^{th} face of the control-volume and n_f is the number of faces; \vec{n}_i is the outward unit normal to face i . The resolution of Darcy velocity $-K\nabla\phi$ along the unit normal n_i is called the Darcy-flux through face i . Approximation of Darcy-flux is a key step in a finite-volume formulation and in the following, we compare standard two point flux approximation (TPFA) and CVD-MPFA schemes for computing fluxes. Details of CVD-MPFA schemes can be found in e.g. [4, 7, 8], and basically divide into two types, namely triangular pressure support (TPS) and full pressure support (FPS) schemes.

Numerical results: Full tensor zigzag field embedded with a complex well trajectory and a layered system:

A unit square heterogeneous domain contains an embedded layered system, which partitions the computational domain into four distinct regions as shown in figure 3b, is selected to study comparative performance of cell-centred versus vertex-centred CVD-MPFA schemes. A piecewise constant permeability tensor is assumed in each sub-domain with principle anisotropic ratio of 1000 : 1, and its orientation is varied so as to define a zigzag flow field. A vertical well trajectory is located in the middle of domain, that intersects a layer and bifurcates into another region, e.g. see figure 3b. The well trajectory is considered as a geometrical object, and has prescribed pressure $\phi = 1$. We impose homogeneous Dirichlet boundary conditions ($\phi = 0$) at the walls of the computational domain.

This problem presents significant challenges to both the grid generation methods and the numerical schemes. We employ non-uniform triangulation and generate boundary and well-aligned grids, with refinement in the near well regions, using the new meshing technique. The resulting primal and dual-cell boundary and well-aligned meshes thus obtained are shown in figures 4a and 5a respectively. Note that number of control volumes required in cell-centred (3343) approximations are roughly twice that of vertex-centred (1851) simulations.

Figure 6 shows the numerical pressure fields obtained by employing TPFA, and the CVD-MPFA schemes, both in cell-centred (top row) and vertex-centred (bottom row) frameworks. The TPFA schemes are inconsistent and cannot resolve the anisotropy of the problem. The cell-centred CVD-MPFA TPS formulation has been found to violate M-matrix conditions and introduces non-physical oscillations due to decoupling [8], e.g. see figure 6b, whereas other formulations i.e. vertex-centred TPS (on dual mesh) and both cell and vertex-centred FPS yield solutions that are essentially free of spurious solutions. We conclude that cell-vertex formulations are more robust when compared to cell-centred formulations, and FPS formulations are more robust than corresponding TPS formulations.

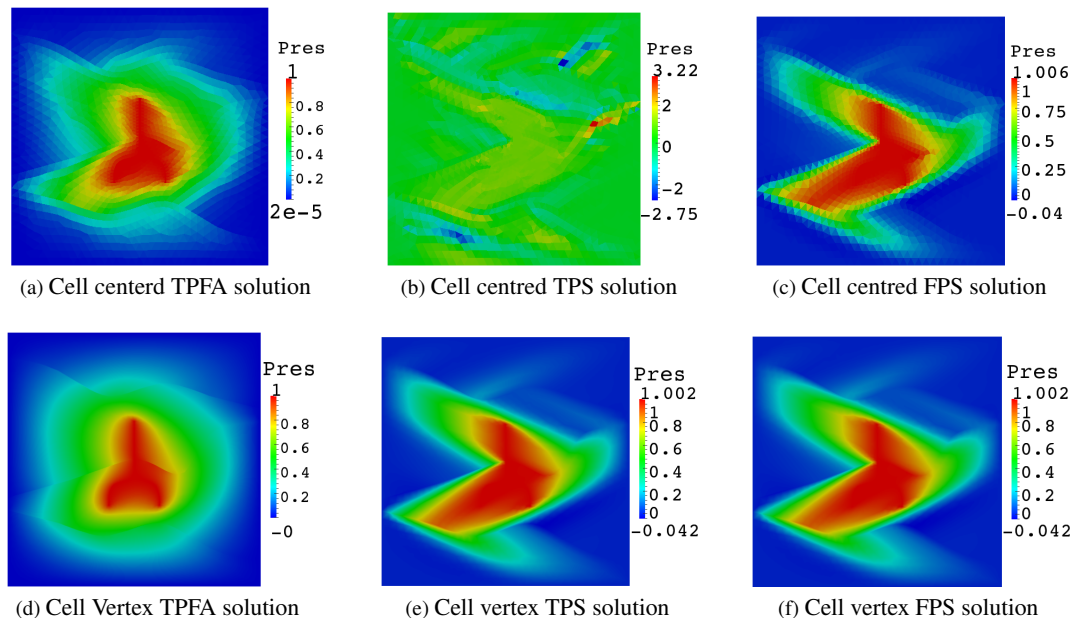


Figure 6: Contour plot of pressure field simulated by employing TPFA, TPS and FPS schemes in cell centred(top row) vs cell vertex(bottom row) formulations respectively(read from left to right).

4. Conclusions:

Boundary aligned grid(BAG) generation requires control-volume face alignment to geological features, whereas well aligned grids(WAG) demands control-point alignment to predefined well trajectories. A triangulation technique has been presented which enjoys the salient features of both advancing front and Delaunay triangulation methods and results in quality feature based triangulations. A comparative study of cell-centred versus vertex-centred formulations has been carried out on essentially the same primal mesh, and key observations are noted:

TPFA is inconsistent on non K-orthogonal grids. Cell-vertex simulation requires much less computational time compared to the cell-centred formulation. This is because the cell-vertex formulation involves approximately half the number of degrees of freedom compared to cell-centred formulation when using the same primal grid in two-dimensions. Cell-vertex CVD-MPFA formulations are computationally more robust than their cell-centred counterpart formulations, even with approximately half number of degrees of freedom, the cell-vertex formulation yields consistent well resolved solutions, such resolution is not achieved by the cell-centred formulation even though the cell-centred method uses twice the number of degrees of freedom.

Acknowledgements

We gratefully acknowledge Saudi Aramco for supporting this work.

References

- [1] R. Merland, B. Lévy, and G. Caumon. Building PEBI Grids Conforming to 3D Geological Features Using Centroidal Voronoi Tessellations. In: Marschallinger, R. and Zolb, R. (Eds.) *Mathematical Geosciences at the Crossroads of Theory and Practice – Proceedings of IAMG conference*. Slazburg, 254-265, 2011.
- [2] L.S.K. Fung, X.Y. Ding, and A.H. Dogru. An Unstructured Gridding Method for Densely-Spaced Complex Wells in Full-Field Reservoir Simulation. *SPE Reservoir Simulation Symposium (The Woodlands, Texas, USA)*, 995-1007, 2013.
- [3] C.L. Palagi and K. Aziz. Use of Voronoi Grid in Reservoir Simulation. *Society of Petroleum Engineers*, 2(2), 69-77, 2007.
- [4] M.G. Edwards. Unstructured, Control-Volume Distributed, Full-Tensor Finite Volume Schemes With Flow Based Grids. *Computational Geosciences*, 6, 433-452, 2002.
- [5] D.L. Marcum and N.P. Weatherill. Unstructured grid generation using iterative point insertion and local re-connection. *AIAA Journal*, 33, 1619-1625, 1995.
- [6] I. Sazonov, D. Wang, O. Hassan, K. Morgan and N. Weatherill. A stitching method for the generation of unstructured meshes for use with co-volume solution techniques. *Computer Methods in Applied Mechanics and Engineering*, 195, 1826-1845, 2006.
- [7] I. Aavatsmark. An Introduction to Multipoint Flux Approximations for Quadrilateral Grids. *Computational Geosciences* 6(3),405-432, 2002.
- [8] M.G. Edwards and H. Zheng. Double-families of quasi-positive Darcy-flux approximations with highly anisotropic tensors on structured and unstructured grids. *Journal of Computational Physics*, 229, 594-625, 2010.

OPTIMISATION

THE USE OF COMPUTATIONAL TECHNIQUES FOR THE OPTIMISATION OF METAL POWDER PARTICLE SIZE DISTRIBUTION (PSD) FROM THE GAS ATOMISATION (GA) PROCESS

*Jennifer S Thompson[†], Oubay Hassan[†], Sam Rolland[†] and Johann Sienz[†]

[†]College of Engineering, University of Swansea, Singleton Park, Swansea, SA2 8PP

*Jennifer.Thompson@swansea.ac.uk

ABSTRACT

Gas Atomisation (GA) is an efficient processing route for the production of fine powders, directly from a molten metal melt. Typically, the melt is atomised in two stages, termed Primary break-up and Secondary break-up. Utilising Computational Fluid Dynamics (CFD) a 2D-axisymmetric simulation has been developed of an actual GA system; this has allowed the study of nozzle geometry on the fluid dynamic structures. Additionally, to understand the effect of process parameter changes on particle size distribution (PSD) of the metal powders produced, a discrete particle model (DPM) has been implemented. In an attempt to capture the Secondary break-up phenomenon, different models, including the Kelvin-Helmholtz (KH), Taylor Analogy Break-up (TAB) and Kelvin-Helmholtz Rayleigh-Transport (KHRT), have been incorporated, and the subsequent results compared to actual process data. It is the intention that further development and validation of this model will allow for the better control or optimisation of produced powder's PSD with respect to operational process parameters.

Key Words: *Gas Atomisation, closed-wake, break-up, aspiration pressure, DPM and PSD.*

1. Introduction

Gas Atomisation (GA) is a complex, multi-physics process, extensively used as an efficient manufacturing method for the production of fine powders. Described as the breaking-up of a molten metal to fine droplets, due to high energy impact from jets of inert gas. Issues can arise however, with controlling deviation in the sizes of powders produced using this method. Subsequently, optimisation of the GA process with respect to particle size distribution (PSD) would be highly beneficial to the powder metallurgy industry.

Extensive research has been ongoing into modelling GA, in an attempt to find a robust technique which adequately simulates the full process. The modelling can be considered in two halves: the computational fluid dynamic (CFD) simulation of the high speed gas; and, the incorporation of the melt and its subsequent break-up into the gas flow. The most common approach implemented for the simulation of the melt is a two-way coupled Euler-Lagrangian Discrete Particle Model (DPM) [1] [3], with additional models for approximating the break-up of the melt from large to small droplets. It is this method that has been utilised for a project undertaken with a local metal powder production company, LSN Diffusion, to produce a simulation of their GA process that will allow for an assessment to be made on the effect of altering process parameters on PSD.

2. The Gas Atomisation Process

Close-coupled GA involves the molten stream being delivered into the atomising gas via a ceramic melt delivery tube and is the most commonly utilised configuration. From utilising CFD to study the gas-only flow, predictions can be made of aspiration pressure - the sucking pressure just under the melt exit; and, the formation of flow structures, such as shock waves. Particularly, identification of a phenomenon known as "closed wake", which occurs when a Mach Disc forms downstream of the melt exit [2]. Generally, a

strong sub-ambient pressure at the melt exit is required for stable atomisation. If this pressure rises to near or above ambient, then melt “freeze-off” can occur; where, the melt solidifies, halting the process.

The GA break-up process occurs in two stages: a Primary stage, during which the melt is shredded to form large droplets; and a Secondary stage, where the droplet size is further reduced prior to solidification. Focussing on the Secondary break-up, the process is a balance between the aerodynamic forces acting on the droplet and the droplet’s resistance to break-up due to surface tension (σ). This balance of forces is represented by the dimensionless Gas Weber number (We) [1]:

$$We_g = \frac{\rho_g \Delta U D}{\sigma} \quad (1)$$

where ρ_g is the gas density, ΔU is the relative gas to droplet velocity, D is the droplet diameter and σ is the molten metal’s surface tension.

Whether We is low or high, dictates the mechanism of break-up. A low value results in the *bag break-up* process; best represented by the Taylor Analogy Breakup (TAB) model, which is based upon comparing an oscillating-distorting droplet to a spring-mass system [1]. Whilst, at a high We , *ligament break-up* occurs; for this, the Kelvin-Helmholtz (KH) model considers the break-up to be induced by the relative velocity between gas and liquid phases and is derived from Jet Stability Analysis [5]. Alternatively, the Kelvin-Helmholtz Rayleigh-Taylor (KHRT) model, combines the effects of the KH model with Rayleigh-Taylor instabilities due to acceleration of shed droplets ejected into the free-stream [5]. The transition value of We between break-up processes is discussed in Section 3.

3. The computational model

For this study, using the commercially available Fluent v15.0 software [5], a steady-state, 2D-axisymmetric CFD simulation was undertaken, of an axisymmetrically idealised GA nozzle configuration, where discrete atomising jets are represented as an annulus. Fluent utilises a cell-centred finite volume method with the governing equations discretised by a second order upwind scheme, using the SIMPLE algorithm to couple the momentum and pressure equations [5]. Both the Standard $k - \epsilon$ and the $k - \omega$ Shear Stress Transport (SST) turbulence models were considered; with the latter identified as producing a sharper approximation of the shock waves [4] and adopted for this study. A full convergence and mesh sensitivity study was undertaken. Several meshes were constructed, each with elements focussed in the region of the issuing jet and at the walls. Considering an arbitrary element dimension of δ , mesh independence was achieved with a mesh of element dimension 2δ (130,380 elements); with meshes having been considered in the range δ to $\frac{5}{2}\delta$. The domain extended 20 gas nozzle diameters (ND) downstream from the melt delivery tube exit and was 10 ND wide. Using Fluent’s material database, Nitrogen was selected for the simulated gas; with the “Ideal Gas” formulation used in place of a density value, as the flow was anticipated to be compressible. The boundary conditions are labelled in Figure 1, which is not drawn to scale. The gas to the inlet was supplied in keeping with the Company’s operational pressure; and the pressure outlet maintained at atmospheric. To aid with validation, several different protrusion lengths of the melt delivery tube were considered, ranging from 0 to 5 units, with increments of 1 unit considered (actual values omitted to protect the Company’s design). The results from these could be compared to observations supplied by the Company regarding the effect of this parameter on operation; particularly, that as protrusion length was decreased past a certain value, “freeze-off” occurred.

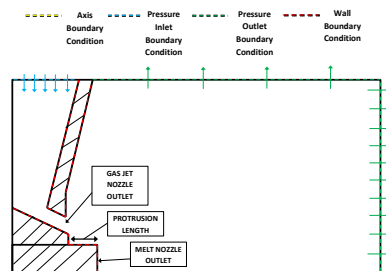


Figure 1: Boundary conditions and features of the 2D-axisymmetric geometry of the GA system

In an attempt to approximate the PSD of the powder produced, a simulation of the Secondary break-up phase only, was considered; and, as presented in work by [1] and [3], a transient, two-way coupled

Euler-Lagrangian DPM model was utilised. The DPM model available within Fluent was used, with particles of diameter 1 mm injected at the melt nozzle outlet's top corner. Suitable break-up models were implemented to capture these injected droplets' further disintegration. The flow-rate of particles was set to achieve a Gas to Melt Ratio (GMR) of 28. Two different approaches for simulation of the break-up mechanisms were considered and subsequently compared: first, a code developed by Zeoli [1] and integrated into Fluent's DPM model by User Defined Function (UDF), which uses both the KH model and the TAB model, with a transition between the two at a We of 80; second, utilised the KHRT model within Fluent's DPM. An alloy was simulated with: density 7700 kg/m^3 ; specific heat capacity 723 J/kg K ; viscosity 0.0056 kg/m s ; and surface tension of 1.2 N/m . The transient simulation was started from the converged steady-state gas-only simulation and run with a time-step of 10^{-6} .

4. Results and Discussion

4.1. CFD simulation results and discussion

Data was extracted from the simulation along the axis of symmetry and just downstream but parallel with the melt nozzle outlet, to ascertain aspiration pressure. In addition to these, velocity contours were generated to help distinguish any fluid structures formed. Figure 2 shows velocity contours generated for a protrusion length of 0 and 5 units; and, a plot of the effect of protrusion length on aspiration pressure. Generally, the velocity contours illustrate a series of shocks as would be expected from an under-expanded compressible jet [2]. Additionally, a Mach Disc is present, indicating that a “closed-wake” phenomenon has been observed. The graph illustrates that as the protrusion length is decreased the aspiration pressure approaches ambient and higher. These findings are in keeping with information provided from the Company, which stated that a decrease in protrusion length resulted in “freeze-off”.

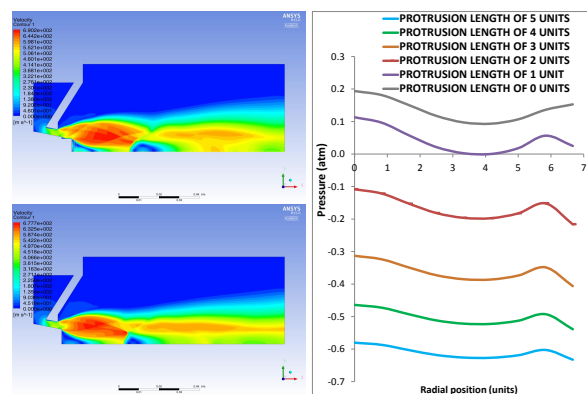


Figure 2: Vel. contours at protrusion lengths (p.l.): a.) 5 units & b.) 0; c.) effect of varying p.l. on aspiration pressure

4.2. Discrete Particle Model (DPM) with break-up simulation results and discussion

Figure 3 provides a comparison of the trajectories and particle sizes of the melt droplets as they undergo break-up when using Zeoli's KH-TAB model and Fluent's KHRT, at a GMR of 28. It can be seen that the latter produces a “comet-like” cloud of droplets, constrained within the atomising gas jet, particularly for the first 10 NDs downstream. Whereas, Zeoli's results in a line of droplets of decreasing size that initially follows the outside of the atomising jet, before tailing onto the axis as the jet becomes weaker.

Figure 4 compares the cumulative mass size distributions of droplets, achieved when using Zeoli's model and the KHRT, at a GMR of 28, along with data provided from the Company. For each set of data, a measure of the width of the PSD in the form of d_{84}/d_{50} has been calculated. It is evident that both simulation techniques produced a narrower PSD width than the Company's process data; with the KHRT 29 % narrower and Zeoli's 40 % narrower. When considering the average particle size, the Company's data resulted in a value of $81.7 \mu\text{m}$; the KHRT, $31.4 \mu\text{m}$; whilst, Zeoli's greatly over-predicted the size at $372 \mu\text{m}$.

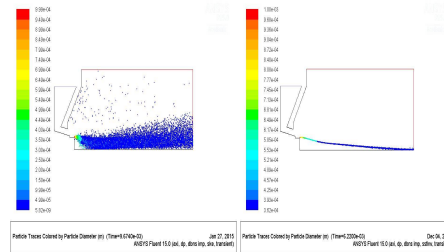


Figure 3: The droplet trajectories produced by Fluent’s KHRT and Zeoli’s KH-TAB break-up models

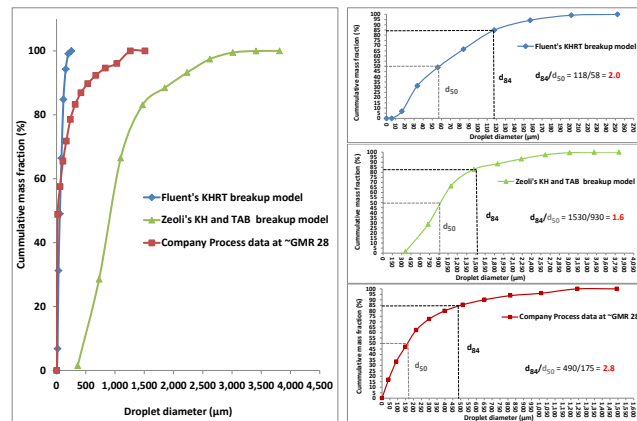


Figure 4: Cumulative mass size of droplets achieved from the break-up models compared to LSN’s process data

5. Conclusions and Further work

The CFD, gas only, simulation of the atomising jet produced a realistic set of contours and pressure data, that could be used to help explain phenomenon such as “freeze-off” experienced in the Company’s actual process. Considering the introduction of a DPM model with two different mechanisms to simulate Secondary break-up; the Fluent KHRT break-up model appeared to capture the process more accurately than Zeoli’s. However, to aid with further validation and improvement of the Secondary break-up model, simulations at a range of different GMR values, operating pressures and protrusion lengths are required. By comparison of these results with trends observed in the Company’s process data, a conclusion can be drawn as to whether either approach will result in a tool that can be used to assess (at least qualitatively) the effect of such parameters on the PSD of powders produced, allowing optimisation.

Acknowledgements

Thanks is given for the assistance provided by LSN Diffusion in the form of data and feedback; integral to the development and refinement of work undertaken for this research. Additional thanks is given for the ERDF funding received through WEFO as part of the ASTUTE project.

References

- [1] N. Zeoli. Multiphase modelling of the characteristics of close coupled gas atomization (Phd). Aston University, Birmingham, June 2011.
- [2] J. Ting and I. E. Anderson. A computational fluid dynamics (CFD) investigation of the wake closure phenomenon. *Materials Science and Engineering: A*, Vol 379, pp264-276, 2004.
- [3] D. A. Firmansyah et al. Numerical simulations of supersonic gas atomization of liquid metal droplets. *Japanese Journal of Applied Physics*, Vol 53, 2014.
- [4] V. Zapryagaev et al. Experimental Investigation of Base Pressure with Hot Supersonic Jet for External Supersonic Flow. *4th Symposium on Aerothermodynamics for Space Vehicles*, pp579-584, 2002.
- [5] Ansys Inc. Ansys Fluent Theory Guide v14.0, New Hampshire, 2011.

Topology Optimisation of Additively Manufactured Impact Resistant Structures

*H. Alicia Kim¹, Joao Duro¹, Graham J. McShane² and Peter S. Theobald³

¹Department of Mechanical Engineering, University of Bath, Bath, BA2 7AY

²Department of Engineering, University of Cambridge, Cambridge, CB3 9ET

³School of Engineering, Cardiff University, Cardiff, CF24 3AA

*H.A.Kim@bath.ac.uk

ABSTRACT

Topology optimisation is a design optimisation approach that can provide the most creative solutions. A new scheme that has emerged in recent years is the level set topology optimisation method, which produces smooth structural boundaries with a homogenous material throughout the structure. This means no further post-processing is necessary, making it ideally suited to the latest additive manufacturing processes. This enables optimum design and manufacture of highly complex geometries that would not have been possible with traditional manufacturing technology. This paper develops topology optimisation for nonlinear dynamic impact problems. The behaviour of a structure under impact is first computed using nonlinear transient finite element analysis. The nonlinear dynamics over time are then approximated by a series of equivalent static load cases and subjected to topology optimisation at multiple load cases. Optimisation then minimises the mass of the structure such that the displacement and acceleration at critical locations are below the requirements. Numerical examples are presented to demonstrate the methodology.

Keywords: *impact resistant material; topology optimisation; additive manufacturing*

1. Introduction

Topology optimisation is able to produce the most creative design solutions to an engineering problem as it is not dependent upon an initial material configuration, and is thus able to explore the largest design space. Topology optimisation has, however, been criticised for producing designs with highly complex geometries that are not easy to manufacture. There have been to date limited efforts to incorporate traditional manufacturing constraints [1,2], though additive manufacturing (AM) now provides a convenient means to realise such complex geometries [3,4]. The synergy between topology optimisation and AM has been widely recognised and their potentially disruptive nature has been identified [5] and demonstrated through case studies where a mass reduction of 50% is common [6].

The first successful application of topology optimisation was to minimise strain energy (or minimise compliance) subject to a volume constraint [7]. Whilst this remains the most popular problem type for developing and benchmarking topology optimisation methods, they have subsequently been applied to a wide variety of structural and multidisciplinary design problems. They include stress [8], buckling [9], natural frequency [10], compliance mechanism [11], antenna [12], aerodynamic flutter [13] and photonic metamaterial [14]. Examining the type of problems to which topology optimisation has been applied, the majority have been under static load cases. Topology optimisation for dynamic problems, such as impact energy absorption, has seen comparatively limited progress.

One reason for this arises from the common formulation of topology optimisation. Solid Isotropic Materials with Penalisation (SIMP) has emerged to be the most popular method in topology optimisation over the last two decades. This approach discretises the design domain using finite elements and the existence of each element becomes the design variable. This turns topology optimisation into a material distribution problem with a large number of binary design variables. Typical mathematical programming requires the problem to be differentiable. Therefore the binary design variables are relaxed to continuous design variables in the range 0 to 1, but the solutions with

intermediate values (i.e. neither 0 or 1) are penalised using a power law. Whilst these fictitious intermediate design variables are penalised, they are not completely eliminated from the design solution and they create spurious dynamic behaviour which can affect optimisation.

In contrast to the traditional approach, we propose to apply a level set topology optimisation method. The level set topology optimisation method employs the level set function which is an implicit signed distance function to represent the boundaries and optimisation moves these boundaries to determine an optimum solution. This means there are no elements with intermediate design variable values eliminating the fictitious dynamics behaviour and this has been demonstrated in natural frequency and aerodynamic flutter problems [10,13].

This presentation will develop a preliminary study of optimisation for impact resistant structures. We develop topology optimisation for dynamic loading by creating a set of multiple static load cases from the equivalent static loading method [15]. We employ nonlinear transient finite element (FE) analysis via the commercial code Abaqus to create a set of static loads which are then used in level set topology optimisation to produce an optimum structure.

2. Topology Optimisation Methodology for Impact Resistant Structures

2.1 Sequentially linear programming level set topology optimisation

This section briefly outlines the sequentially linear programming (SLP) level set topology optimisation. Further details can be found in Dunning and Kim [10]. The level set method typically employs a discrete form of the Hamilton-Jacobi equation, (3) to move the boundaries.

$$\phi_i^{k+1} = \phi_i^k - \Delta t |\nabla \phi_i^k| V_{n,i} \quad (3)$$

where ϕ is the level set function, i is a discrete point within the domain, k is the current iteration number. The key quantity here for optimisation is the boundary update velocity $V_{n,i}$ defined at a discrete set of boundary points. These points are located where the structural boundary intersects the finite element mesh. The change in a function f with respect to the domain Ω changes is given by,

$$\frac{\partial f(\Omega)}{\partial \Omega} = \int_{\Gamma} (s_f \cdot V) d\Gamma \quad (4)$$

where s_f is the shape sensitivity function for f . We discretise the shape derivative boundary integrals to determine the function changes with respect to a velocity function. Thus, (4) can be written as,

$$\Delta t \cdot \frac{\partial f(\Omega)}{\partial \Omega} \approx \Delta t \cdot \sum_{j=1}^n (s_{f,j} \cdot V_j \cdot l_j) = \mathbf{c} \cdot \mathbf{V}, \quad c_j = \Delta t \cdot s_{f,j} \cdot l_j \quad (5)$$

where l_j is a discrete length of the boundary (or surface area in 3D) around a discrete boundary point j , $s_{f,j}$ is a discrete value of the shape sensitivity function, n is the number of discrete points, \mathbf{c} is a vector of integral coefficients and \mathbf{V} is a vector of discrete velocity function values,

$$\mathbf{V}(\boldsymbol{\lambda}) = \lambda_j \cdot \mathbf{s}_j + \sum_{i=1}^p \lambda_i \cdot \mathbf{s}_i, \quad \mathbf{V}_{\min} \leq \mathbf{V} \leq \mathbf{V}_{\max} \quad (6)$$

where λ are weights for each shape sensitivity function and p is the total number of constraints. The linear sub-problem is then to find the optimal weight values and this is solved using SLP.

$$\begin{aligned}
& \text{Minimise: } \mathbf{c} \cdot \mathbf{V}(\boldsymbol{\lambda}) \\
& \text{Subject to: } \mathbf{a}_i \cdot \mathbf{V}(\boldsymbol{\lambda}) = h_i, \quad i = 1 \cdots m \\
& \quad \mathbf{b}_i \cdot \mathbf{V}(\boldsymbol{\lambda}) \leq g_i, \quad i = 1 + m \cdots p \\
& \quad \boldsymbol{\lambda}_{\min} \leq \boldsymbol{\lambda} \leq \boldsymbol{\lambda}_{\max}
\end{aligned} \tag{7}$$

where \mathbf{a}_i and \mathbf{b}_i are the integral coefficients for the equality and inequality constraints, respectively, h_i and g_i are constraint change targets in the sub-problem for constraint i , m is the number of equality constraints and p is the total number of constraints.

2.2 Equivalent Static Load Method

This section briefly outlines the method for calculating the equivalent static loads from the dynamic loading. The details can be found in Kang et al [15]. The general equation of motion is represented by,

$$\mathbf{M}\ddot{\mathbf{d}} + \mathbf{K}\mathbf{d} = \mathbf{l}_{\text{dyn}} \tag{8}$$

where \mathbf{M} is a mass matrix, \mathbf{d} is a displacement vector, \mathbf{K} is a stiffness matrix and \mathbf{l}_{dyn} is a dynamic load vector. The standard finite element equation for a static analysis is,

$$\mathbf{K}\mathbf{x} = \mathbf{l}_{\text{stat}} \tag{9}$$

where \mathbf{x} is a static displacement vector and \mathbf{l}_{stat} is a static load vector. Combining (8) and (9) lead to (10) which computes a static load vector that generates identical displacement fields as those of the dynamics load vector. So at a given time t_a , the equivalent static load is given by,

$$\mathbf{l}_{\text{stat}} = \mathbf{K}\mathbf{d}(t_a) \tag{10}$$

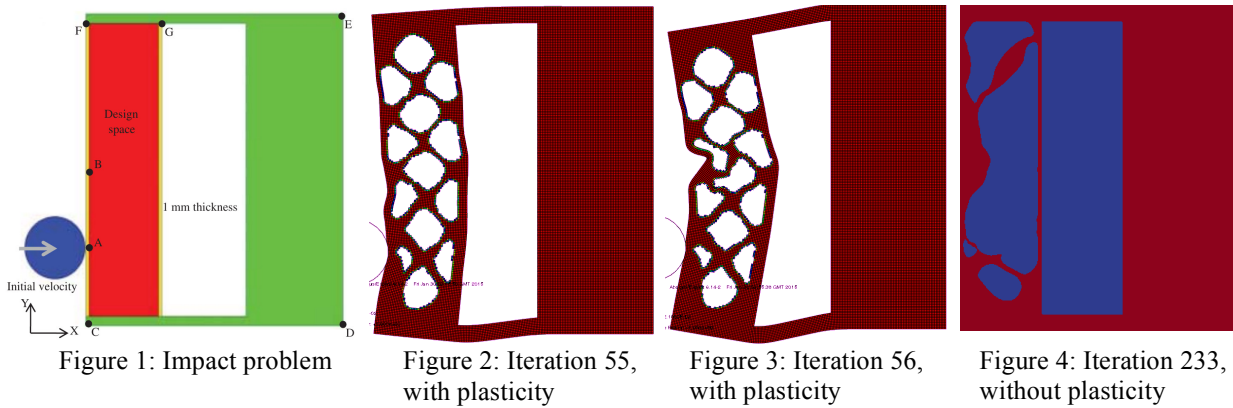
The question is how to select the time steps at which the displacements should be considered for the equivalent static load. The literatures agree that critical time steps are where the maximum displacements are observed. They also suggest that including as many time steps as possible would produce the best result. This however, is to be balanced with the computational cost and how the time steps would be selected to compute the necessary equivalent static load cases is unclear.

2.3 Topology optimisation for impact

The topology optimisation methodology for impact combines the methods outlined above. For a given impact scenario, a nonlinear transient FE analysis is conducted using Abaqus. Based on the dynamic displacements, the time steps are selected based on the maximum displacements and they are used to compute a set of equivalent static loads, (Section 2.2). These static loads are considered as multiple loading conditions which are applied to modify the structural design using the level set topology optimisation (Section 2.1). If not converged, it returns to conduct another nonlinear transient analysis using Abaqus and the iteration continues.

3. Numerical Examples

We apply the optimisation methodology to the impact problem introduced in [16]. The equivalent static loads are selected at the maximum displacement load step based on full nonlinear transient FE analysis at every iteration. As optimisation continues from iteration 55 (figure 2) to iteration 56 (figure 3), we find that the large plastic deformation of material results in the equivalent static loads to change their patterns significantly and this destabilises optimisation. By removing material plasticity and assuming linear elasticity, optimisation continues. Figure 4 shows the topology at iteration 233 where 16% of volume has been removed and displacement is at 19.6mm, where the constraint is specified at 20mm. The iterations are currently on-going and the complete results will be presented.



4. Conclusion

This paper presented a SLP level set topology optimisation method for impact materials integrating nonlinear transient FE analysis and computing the equivalent static load cases. The presentation will show the outcome of the numerical studies and the realisation and validation of the resulting optimum solutions using additive manufacturing.

Acknowledgements

The authors are grateful to the EPSRC Centre for Innovative Manufacturing in Additive Manufacturing, University of Nottingham, for financial support through grant RGS:113874.

References

- [1] M. Zhou, Y.K. Shyy, Topology optimization with manufacturing constraints. *4th WCSMO*, 2001.
- [2] Q. Xia, T. Shi, M. Y. Wang and S. Liu. A level set based method for the optimization of cast part, *Structural and Multidisciplinary Optimisation*, 41, 735-747, 2010.
- [3] D. Brackett, I. Ashcroft and R. Hague. Topology optimization for additive manufacturing. *24th Solid Freeform Fabrication Symposium (SFF 11)*, 2011.
- [4] Z. Doubrovski, J. C. Verlinden and J. M. Geraedts. Optimal design for additive manufacturing: opportunities and challenges. *ASME 2011 International Design Engineering Technical Conferences*, 635-646, 2011.
- [5] N. Hopkinson, R. Hague and P. Dickens *Rapid manufacturing: an industrial revolution for the digital age*. John Wiley & Sons. 2006.
- [6] T. Wohlers. *Additive Manufacturing State of the Industry Annual Worldwide Progress Report*, Wohlers Associates, 2010.
- [7] M. P. Bendsoe, N. Kikuchi, Generating optimal topologies in structural design using a homogenization method. *Comp Methods In Applied Mechanics and Engineering*, 71, 197-224, 1988.
- [8] C. Le, J. Norato, T. Bruns, C. Ha, D. Tortorelli. Stress-based topology optimization for continua. *Structural and Multidisciplinary Optimization* 41, 605-620, 2010.
- [9] A. Ben-Tal, F. Jarre, M. Kocvara, A. Nemirovski, J. Zowe. Optimal design of trusses under a nonconvex global buckling constraint. *Optimization and Engineering* 1, 189-213, 2000
- [10] P.D. Dunning, H.A. Kim. Introducing the sequential linear programming level-set method for topology optimization. *Structural and Multidisciplinary Optimization*, 2014
- [11] O. Sigmund. On the design of compliant mechanisms using topology optimization. *Mechanics of Structures and Machines*. 25, 493-524, 1997.
- [12] K. Fuchi, A.R. Diaz, E. Rothwell, R. Duedraogo, A. Temme, Topology optimization of periodic layouts of dielectric materials. *Structural and Multidisciplinary Optimization*. 42, 483-493, 2010.
- [13] P.D. Dunning, B.K. Stanford, H.A. Kim HA. Level-set topology optimisation with aeroelastic constraints. *AIAA SciTech Conference*, 2015.
- [14] C.Y.Kao, S. Osher, E. Yablonovitch. Maximizing band gaps in two-dimensional photonic crystals by using level set methods. *Applied Physics B: Lasers and Optics*. 81, 235-244, 2005.
- [15] B.S. Kang, W.S. Choi, G.J. Park. Structural optimization under equivalent static loads transformed from dynamics loads based on displacement, *Computers & Structures* 79, 145-154, 2001.
- [16] A. Kaushik, A. Ramani. Topology optimization for nonlinear dynamic problems." *Engineering Optimization* 46, 487-502, 2014

A NOVEL IMPLEMENTATION OF AERODYNAMIC SHAPE OPTIMISATION USING MODIFIED CUCKOO SEARCH

*D. S. Naumann, B. Evans and O. Hassan

College of Engineering, Swansea University, Swansea SA2 8PP, UK

*717761@swansea.ac.uk

ABSTRACT

This paper presents the development and application of an automated aerodynamic design optimisation algorithm using a novel method of parameterising a computational mesh using ‘control nodes’. The shape boundary movement as well as the mesh movement is coupled to the movement of pre-defined control nodes via an extended Delaunay Graph Mapping technique that contains a second order smoothing step to act on the boundary during the mesh movement. A Modified Cuckoo Search (MCS) algorithm is employed for optimisation within the prescribed design space defined by the allowed range of control node displacement. A finite volume compressible Navier–Stokes solver is used for aerodynamic modelling to predict aerodynamic design ‘fitness’. The resulting coupled algorithm is applied to a range of test cases in two dimensions including the design of a race car front wing and subsonic, transonic and supersonic intake duct optimisation.

Key Words: *mesh movement, Cuckoo search, computational fluid dynamics, aerodynamic shape optimization, shape parametrization*

1. Motivation

During the last 30 years, the aerodynamic design problems faced by the aerospace industry have been revolutionised by computational fluid dynamics (CFD). At the same time, the development of Computer Aided Design (CAD) has had a strong impact on the design cycle of aerodynamic problems [1]. In light of this, CFD and CAD have become integral parts of a typical aerodynamic design cycle apparent in current aerodynamic design projects.

Despite these advancements, significant challenges remain for the computational modelling community in order to efficiently transfer geometry between CAD and CFD systems and improve the computationally expensive mesh re-generation process during optimisation [2, 3].

This paper presents a novel implementation of computational aerodynamic shape optimisation in which the parameterisation approach makes use of ‘control nodes’ in the mesh as the method for both defining the geometry movements and as the design parameters for the optimisation process. Additionally, an extended version of the Delaunay Graph (DG) mapping technique called ‘Fast Dynamic Grid Deformation’ (FDGD) [4] applied to both move the boundary and the mesh. This results in a self-contained algorithm formulated to propagate the effect of the ‘control nodes’ displacement given by the optimiser throughout the boundary and mesh making a mesh regeneration step redundant. Also, there is no requirement to convert the geometry definition ‘stored’ in the mesh into any other format during the optimisation process.

2. Methodology

2.1. Geometry Shape Parameterisation

The developed approach is of the category mesh-based parameterisation thus utilizing the mesh itself. Once the initial computational mesh has been created (which could have originated as a CAD geometry), the geometry is then parameterised by choosing ‘control nodes’ at critical positions defined by the user on the geometry. The number and position of these control nodes is important in determining how the geometry will evolve. A definition of the boundary transformation is

$$\mathbf{B}_{i+1} = \mathbf{B}_i + \Delta\mathbf{B}(\Delta C_1, \dots, \Delta C_{n_{cn}}) \quad (1)$$

where \mathbf{B}_i is the initial boundary definition, \mathbf{B}_{i+1} is the new boundary shape and C is a control node. Note, that a change of the boundary $\Delta\mathbf{B}$ is controlled by the displacement of the control nodes ΔC given an initial geometry rather than the control node positions itself.

2.2. Modified Cuckoo Search

Modified Cuckoo Search [5] is an evolutionary algorithm applying the ‘survival of the fittest’ strategy to a given population. Each agent within the population exhibits a fitness value which is defined the objective function as for example Lift to Drag ratio. The population is separated into good and bad agents dictated by the fitness. All good agents are ‘cross-bread’ and the bad agents perform a random walk called Lévy flight in search of an improved agent. The process of replacing and creating eggs continues until a stopping criteria is met.

2.3. Mesh Movement

The entire mesh alteration is a three step process to propagate the initial movement of the ‘control nodes’ throughout the entire computational mesh. Initially, the optimisation algorithm dictates new locations of the control nodes by analysing the fitness of each geometry. In a second step, the boundary of the geometry is deformed given the displacement of the ‘control nodes’. Finally, the domain nodes are moved. The latter two steps were merged to obtain one integrated methodology based on the FDGD method as detailed in [4]. However, an extension was required to embed the deformation of the boundary.

The FDGD method generates a coarse background Delaunay triangular mesh using all boundary nodes. Then, each domain node is located within a triangle of the background mesh. Afterwards, the area coefficients $e_i = S_i/S, i = 1, 2, 3$ of each domain mesh node can be calculated with S_i being the areas of the triangles spanned by the points of the coarse triangle with area S and the domain node. In order to include the deformation of the boundary itself, a ‘hyper-coarse’ background mesh had to be introduced only considering the ‘control nodes’ for the Delaunay triangulation rather than all boundary nodes. Also, the resulting shapes depend heavily on the original shape of the geometry. To maintain smoothness of the geometry as required for aerodynamic optimisation, a second order smoothing was implemented acting on the entire boundary before propagating the movement through the domain.

$$\mathbf{B}_{i+1} = \mathbf{B}_{i+1} + \alpha(\nabla\mathbf{B}_{i+1} - \nabla\mathbf{B}_i) \quad (2)$$

α is a constant dependent on the desired level of smoothing.

The enhanced FDGD methodology can be summarized as visualised in Figure 1 and following the steps:

1. Generate coarse and hyper-coarse background DG
2. Locate the boundary nodes in the hyper-coarse DG and the domain nodes in coarse DG
3. Calculate Area Coefficients of boundary nodes in hyper-coarse DG and domain nodes in coarse DG
4. Move the hyper-coarse DG according to the 'control nodes' displacement
5. Relocate boundary nodes by maintaining Area Coefficients
6. Apply 2nd order smoothing
7. Move the coarse DG according to the boundary node movement
8. Relocate domain nodes by maintaining Area Coefficients

The mesh M is now solely influenced by the 'control node' displacements ΔC and can be described by the equation

$$M_{i+1} = M_i + \Delta M(\Delta C_1, \dots, \Delta C_{n_{cn}}) \quad (3)$$

where M_i is the initial mesh, M_{i+1} is the new mesh.

Figure 1: Delaunay Graphs visualising each Step of the mesh movement

3. Case Studies

3.1. Intake Duct Optimisation

An engine intake duct of a land-based supersonic vehicle was optimised for distortion. Distortion provides a measure of standard deviation of the total pressure P_t related to the mean total pressure \bar{P}_t across a plane of interest. The mesh utilized exhibits 82868 mesh nodes and 163419 mesh elements including 7 boundary layers. Solutions to the problem were sought at a range of Mach numbers $Ma = [0.5, 0.8, 1.1, 1.4]$ using four control nodes with a specified explorable design space of $x_C \in [-0.3, 0.3]$ and $y_C \in [-0.3, 0.3]$ for each control node C . The mesh as well as the initial and final pressure field are visualized in Figure 2.

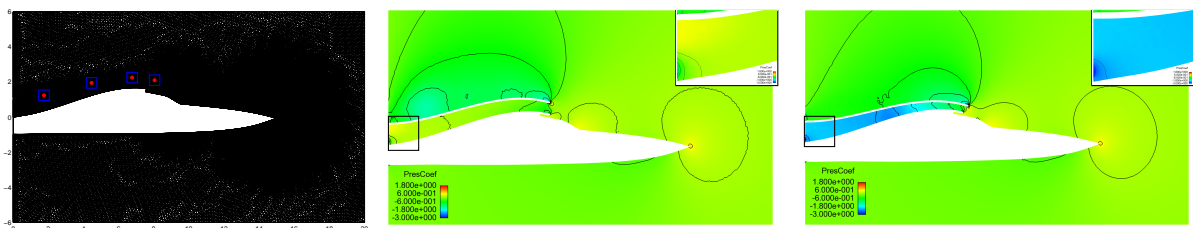


Figure 2: A supersonic vehicle with engine intake duct showing (a) detailed mesh including the control node locations and their range of motion (b) the pressure field of the initial geometry (c) the pressure field of the optimised geometry for Ma 0.5

3.2. Multicomponent Optimisation

A three aerofoil front wing of a race car was optimised for down-force to drag ratio. Downforce was measured as the negative lift according to $F = -\oint p(\mathbf{n} \bullet \mathbf{j}) dB$ and drag has been determined by $D = \oint p(\mathbf{n} \bullet \mathbf{i}) dB$ with p is the non-dimensionalized static pressure, \mathbf{n} is the normal unit vector directing into the surface and \mathbf{i} and \mathbf{j} are the parallel and vertical unit vectors in relation to the freestream velocity direction. The mesh utilized exhibits 65451 mesh nodes and 145432 mesh elements including 12 boundary layers. Six control nodes were defined to find a solution at a Mach number of $Ma = 0.05$.

4. Conclusions

An automated aerodynamic shape optimisation algorithm has been developed making use of ‘control nodes’ in the mesh. The approach has been coupled to an extended version of the FDGD mesh movement technique allowing to cut the mesh regeneration step and reduce the problem inherent in translating geometries from CAD-based geometry definitions to CFD meshes. Modified Cuckoo Search (MCS), an evolutionary optimisation approach, has been implemented to find the global optimum. The resulting algorithm is self-sufficient during the entire optimisation cycle and has been successfully applied to various different aerodynamic problems including multicomponent optimisation and subsonic, transonic and supersonic engine intake duct optimisation. It demonstrated to be robust in terms of the diverse applicability as well as its ease of implementation for all test cases and improvements in the fitness were achieved with a fast convergence in terms of number of generations. Additionally it showed very good shape preservation characteristics making it suitable for applications requiring only translation of shapes such as optimising the engine mounting location.

For future work, ‘dynamic’ control nodes will be tested with the position being an optimisation by itself in order to increase the explorable design space whilst maintaining the rapid convergence. Also, enhancing the optimisation methodology may be exploited by implementing hybrid schemes combining this evolutionary approach with local gradient-based searching. Ultimately, the code will be extended to 3D.

Acknowledgements

The authors would like to acknowledge the support provided by Fujitsu and the HPC Wales PhD scholarship scheme as well as the computational power provided to pursue such computationally expensive simulations.

References

- [1] A. J. Keane and P. B. Nair, *Computational Approaches for Aerospace Design*. Wiley, June 2005.
- [2] S. Shahpar, “Challenges to overcome for routine usage of automatic optimisation in the propulsion industry,” *The Aeronautical Journal*, vol. 115, no. 1172, 2011.
- [3] A. Jameson and J. C. Vassberg, “Computational fluid dynamics: Its current and future impact,” *AIAA Paper 2001-0538*, 2001.
- [4] X. Liu, N. Qin, and H. Xia, “Fast dynamic grid deformation based on delaunay graph mapping,” *Journal of Computational Physics*, vol. 211, pp. 405–423, 2006.
- [5] S. Walton et al., “Modified cuckoo search: A new gradient free optimisation algorithm,” *Chaos, Solitons and Fractals*, 2011.

RELIABILITY BASED OPTIMIZATION OF COMPOSITE SPHERICAL SHELLS

*S. Dey, T. Mukhopadhyay, H. Haddad Khodaparast and S. Adhikari

College of Engineering, Swansea University, Swansea, SA2 8PP, United Kingdom

*infosudip@gmail.com; S.Dey@swansea.ac.uk

ABSTRACT

The composite materials are extensively used in the structures of aerospace, marine, civil and automobile engineering due to their tailorable capability. This article aims to develop a novel approach for minimizing the weight of composite shells considering probability of failure due to resonance. The stochasticity in material properties and geometric parameters are taken into account to optimise the volume employing design variables as width and thickness. The present study utilizes genetic algorithm to apply the reliability based design optimization (RBDO) in composite spherical shell.

Keywords: Reliability based optimization; genetic algorithm; natural frequency; uncertainty; spherical shells

1. Introduction

The development of reliable composite structures in production process is always subjected to large variability due to manufacturing imperfection and uncertain operational factors. In practice, an additional factor of safety is assumed by designers due to difficulty in assessing reliability to avoid resonance in conjunction to uncertainties of stochastic natural frequencies. This existing practice of designer results in either an ultraconservative (overestimation of material cost) or an unsafe design. Hence, this is urgently needed to overcome the current limitation wherein the design of composites are restricted to a deterministic regime despite of rapidly increasing demands of technological, economical and safety needs. Moreover, the reliability in conjunction to cost component involved in weight optimization of such composite structures are always a challenge for the designers. In the present study, genetic algorithm is employed for weight optimization of composite spherical shells.

As per Charles Darwin's natural selection and evaluation and his philosophy of survival of the fittest facilitates to solve numerical optimization problems, the natural evaluation and adaptation to environmental uncertain variation can be simulated mathematically by using genetic algorithm (GA). This algorithm works based on an iterative procedure consisting of a constant-sized population of individuals, usually encoded as binary strings (chromosomes), representing candidate solutions in a given search space comprising of all the possible solutions to the optimization problem [1-3]. It is then encouraged to evolve over generations to produce new better or fitter generations using genetic operators until the problem is satisfactorily solved. The three fundamental genetic operators are selection (fitness of individual solutions so that the number of times an individual is dependent on its relative performance in the population.) crossover (to form new individuals by exchanging chromosome between two selected individuals segments) and mutation (to prevents premature convergence by randomly changing part of one selected individual's chromosome). However, most of the previous related studies are limited to deterministic conditions, without considering the effects of uncertainties in the natural frequency of composite shell structures. The present study utilized single objective GA approach for reduction of material cost complying with resonance-free composite structures. A composite cantilever shallow spherical shells with length 'L', width 'b', thickness 't', principal radii of curvature R_x and R_y , along x- and y-direction, respectively and radius of curvature in xy-plane ' R_{xy} ' is considered as furnished in Figure 1.

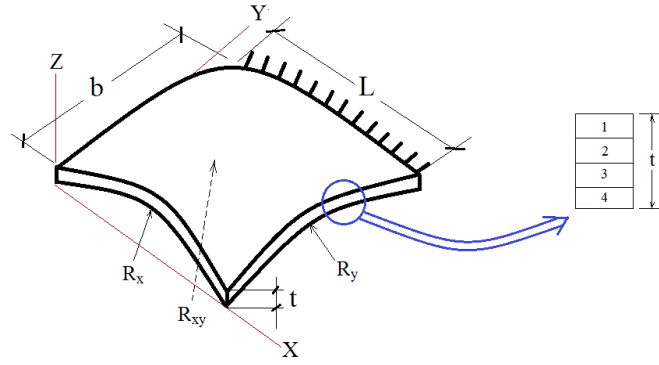


Figure 1: Composite shallow cantilever shell

2. Theoretical formulation

The energy functional for Hamilton's principle using Lagrange's equation, the dynamic equilibrium equation for free vibration of graphite-epoxy spherical composite shell can be expressed as [4]

$$[M(\tilde{\omega})]\{\ddot{\Delta}\} + [K(\tilde{\omega})]\{\Delta\} = 0 \quad (1)$$

In the above equation, $[M(\tilde{\omega})]$ is the mass matrix, $[K(\tilde{\omega})]$ is the stiffness matrix while $\{\Delta\}$ is the vector of generalized coordinates. The governing equations are derived based on Mindlin's theory [5] incorporating rotary inertia, transverse shear deformation. For free vibration, the stochastic natural frequencies $[\omega_n(\tilde{\omega})]$ are determined from the standard eigenvalue problem and is solved by the QR iteration algorithm.

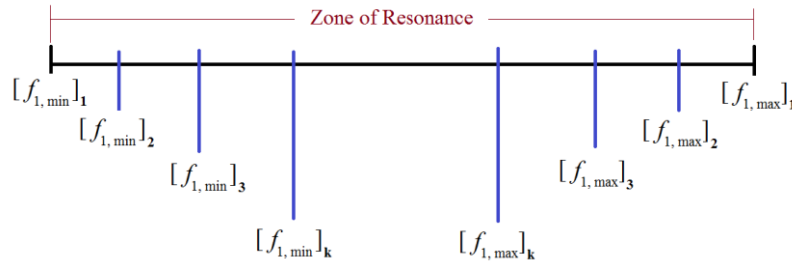


Figure 2: Reliability based weight optimization scheme

There are two types of variables considered in the present analysis, namely stochastic variables (material properties, fibre parameters, laminate dimensional parameters) and design variables (width and thickness) of the composite spherical shells. The upper and lower bounds of design variables and stochastic variables are furnished in Table 1. The reliability based optimization problem is studied with an objective of weight minimization subjected to different level of probability of failure due to resonance. Monte Carlo simulation is employed to obtain the lower and upper bound of stochastic fundamental natural frequency for combined variation of stochastic variables. The optimization problem can be described as follows:

Minimize Volume (V) (for weight optimization, $\text{weight} = V \times \rho$)

Subjected to

$$f_1 < (f_{1,\min})_i, \quad f_1 > (f_{1,\max})_i, \quad b_{lcl} \leq b \leq b_{ucl} \quad \text{and} \quad t_{lcl} \leq t \leq t_{ucl} \quad (2)$$

where $i=1,2,\dots,k$ denotes different levels of confidence to avoid resonance in the design. The levels of confidences are quantified by evaluating probability of failure within corresponding zone of resonance as shown in Figure 2.

$$\text{Here the fitness function is } F(x) = \{V\} = \pi t \left[\frac{b^2}{4} + R^2 \left\{ 1 - \frac{b^2}{4R^2} \right\} \right] \quad (3)$$

where for spherical shell $R_x = R_y = R$

The probability of failure (P_F) can be estimated by performing Monte Carlo simulation on the first- or second-order approximation $\tilde{g}(x^i)$ of the original implicit limit performance function $\tilde{g}(x^i)$ and is given by

$$P_F = \frac{1}{N_{\text{samp}}} \sum_{i=1}^{N_{\text{samp}}} \Pi [\tilde{g}(x^i) < 0] \quad (4)$$

where x^i is i -th realization of X , N_{samp} is the sampling size, Π is a deciding function of the fail or the safe state such that $\Pi = 1$, if $\tilde{g}(x^i) < 0$ otherwise zero. The reliability index corresponding to the failure probability (P_F) can be obtained by

$$\beta = -\phi^{-1}(P_F) \quad (5)$$

where $\phi(\cdot)$ is the cumulative distribution function of a standard Gaussian random variable. In the present analysis, genetic algorithm with hybridization function is employed for weight optimization in compliance with avoiding the resonance. The hybridization function, *fmincon* in Matlab is utilised for determining the constrained minimum of a scalar function of several variables starting at an initial estimate. In general, it can be referred to as constrained nonlinear optimization.

Table 1: Upper and lower control limits of stochastic and design variables

Parameters	Symbol	Stochastic Variables		Design Variables	
		Upper control limit (UCL)	Lower control limit (LCL)	Upper control limit (UCL)	Lower control limit (LCL)
Width	b	1.1 m	0.9 m	1.5 m	0.5 m
Thickness	t	0.0055 m	0.0045 m	0.007 m	0.003 m
Ply angle	θ	50°/-40°/50°/-40°	40°/-50°/40°/-50°	-	-
Elastic modulus (longitudinal)	E_1	151.8 GPa	124.2 GPa	-	-
Elastic modulus (transverse)	E_2	9.79 GPa	8.01 GPa	-	-
Shear modulus (longitudinal)	G_{12}	7.81 GPa	6.39 GPa	-	-
Shear modulus (transverse)	G_{23}	3.1249 GPa	2.556 GPa	-	-
Poisson ratio	ν	0.33	0.27	-	-
Mass density	ρ	3522.2 kg/m ³	2881.8 kg/m ³	-	-

Table 2: Non-dimensional fundamental frequencies $[\omega = \omega_n L^2 [12\rho(1-\mu^2)/E_1 t^2]^{1/2}]$ of isotropic, corner point-supported spherical shells considering $a/b=1$, $a'/a=1$, $a/t = 100$, $a/R = 0.5$, $\mu = 0.3$.

R_x/R_y	Present FEM	Leissa and Narita [6]	Chakravorty et al. [7]
1	50.74	50.68	50.76

3. Results and Discussion

In the present study, four layered graphite-epoxy angle-ply laminated composite cantilever shallow spherical shells are considered. Finite element formulation of the composite spherical shell structure is

based on Mindlin's theory considering an eight noded isoparametric quadratic element. Table 2 represents the non-dimensional fundamental frequencies of isotropic, corner point-supported spherical shells [6,7]. The volume of shell is optimised to reduce the weight which is an essential requirement for aircraft structures. Due to paucity of space, only a few important representative results are furnished. The probability of failure with respect to width, thickness and volume of the spherical composite shell is furnished in Figure 3. Clearly the objective is to minimise the weight while keeping the probability of failure as low as possible. The most reliable design points are shown as blue solid circles in Figure 3 where the minimum weight is obtained with zero probability of failure. It is observed that as the probability of failure increases, the volume decreases making the overall design more economic. Depending on the constraints of probability of failure (e.g., $P_F < 0.05$) the optimal solutions for width, thickness and volume can be found from Figure 3.

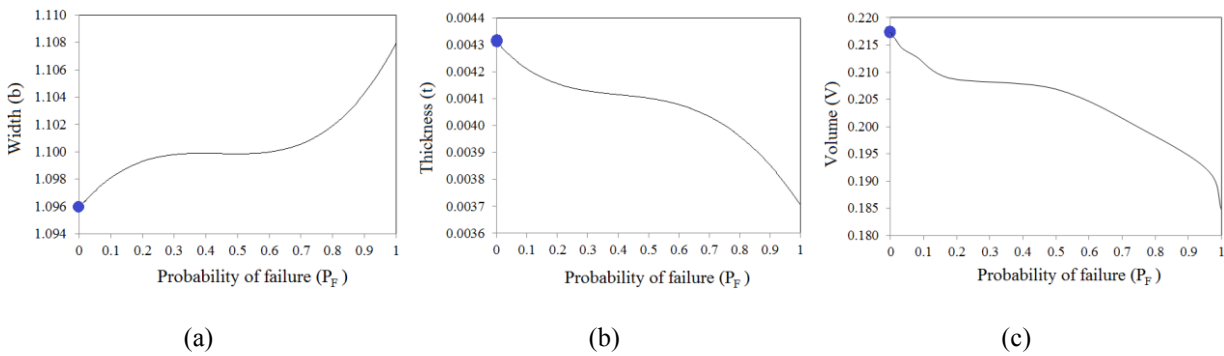


Figure 3: Probability of failure with respect to width (m), thickness (m) and volume (m^3) for spherical shells

4. Conclusions

The present approach includes the reliability based optimization for spherical composite cantilever shells with the constraint of resonance. Single objective genetic algorithm is employed to minimise the weight by optimising the width and thickness of the spherical shell corresponding to different levels of probability of failure. The notion of a trade off between reliability and design economy is needed to be addressed on the basis of design criteria. The optimised data obtained are the first known results of the type of analyses carried out here and the results could serve as reference solutions for future investigators. More complex system of laminated composite structures can be explored by the present approach.

References

- [1] K. Deb. *Multi-objective optimization using evolutionary algorithms*, John Wiley & Sons, 2001.
- [2] S. Sandesh and K. Shankar. Application of a hybrid of particle swarm and genetic algorithm for structural damage detection. *Inverse Problems in Science and Engineering*, 18(7) 997-1021, 2010.
- [3] M.K. Apalak, M. Yildirim and R. Ekici. Layer optimisation for maximum fundamental frequency of laminated composite plates for different edge conditions. *Comp. Sci. and Tech.*, 68(2), 537-550, 2008.
- [4] K.J. Bathe. *Finite Element Procedures in Engineering Analysis*, PHI, New Delhi, 1990.
- [5] R.D. Cook, D.S. Malkus and M.E. Plesha. *Concepts and applications of finite element analysis*, New York, John Wiley and Sons, 1989.
- [6] A.W. Leissa and Y. Narita. Vibrations of corner point supported shallow shells of rectangular planform. *Earthquake Engng Struct. Dynam.*, 12, 651-661, 1984.
- [7] D. Chakravorty, J.N. Bandyopadhyay and P.K. Sinha. Free vibration analysis of point supported laminated composite doubly curved shells – A finite element approach. *Computers & Structures*, 54(2), 191-198, 1995.

SOLIDS AND STRUCTURES 1

XCT Image-based Homogenisation of Elastic Properties of Ultra High Performance Fibre Reinforced Concrete (UHPFRC)

A. Qsymah*¹, R. Sharma¹, Z.J. Yang^{1,2} and L. Margetts^{3,4}

¹ School of Mechanical, Aerospace and Civil Engineering, University of Manchester, UK, M13 9PL

² College of Civil Engineering and Architecture, Zhejiang University, China

³ School of Earth, Atmospheric and Environmental Sciences, University of Manchester, UK, M13 9PL

⁴ Oxford eResearch Centre, University of Oxford, UK, OX1 3QG

* ansam.qsymah@postgrad.manchester.ac.uk

ABSTRACT

Micro-scale X-ray computed tomography images of UHPFRC are used to construct finite element models for prediction of elastic properties using a two-step homogenization approach. In the first step, the mortar matrix with a large number of small voids is homogenized, and in the second the fewer large voids and steel fibres are modelled with the homogenised matrix. This leads to significant reduction in computational costs over one-step approaches. The results are compared favourably with experimental data. The effects of RVE size are also studied.

Keywords: UHPFRC ;Computed Tomography; Homogenization; image-based modelling.

1. Introduction

The ultra-high performance fibre reinforced concrete (UHPFRC) is a relatively new material with superior properties over conventional fibre reinforced concrete (FRC). Its tensile and compressive strength can be higher than 10MPa and 150MPa respectively. It also has high ductility, durability and energy absorption capacity [1, 2]. To make full use of these excellent properties of the material, accurate mechanical properties must be obtained. This is particularly important for designing slimmer sections and slender structures [3].

Numerical homogenisation is nowadays applied widely to evaluate elastic properties of composites. Most studies use one-step approaches which consider all multi-phases in a single finite element (FE) model. However, the FE models may become very complicated with high computational cost, if the phases span a wide range of length scales. This has led to development of two-step homogenisation approaches. For example, Gal and Kryvork [4] presented a two-step homogenisation approach for conventional FRC. The aggregates and the aggregate-mortar interfaces were modelled first, and the homogenised aggregates were then integrated with mortar and fibres to obtain elastic properties of the whole. Zhang et al. [5] extended this approach by adding interfaces between fibres and the surrounding matrix. However, most existing homogenisation studies of fibre composites use assumed internal structures with little attention to the effects of voids.

This study uses 3D images acquired from X-ray computed tomography (XCT) scans to build FE models so that the realistic microstructures of the UHPFRC are modelled. A two-step homogenisation approach is developed, considering the statistical characteristics of void size and distribution, to compute elastic properties of UHPFRC.

2. Methodology

A cube of 20x20x20 mm³ of UHPFRC was scanned using a micro-XCT scanner at the University of Manchester. The voxel resolution is 24.8µm. The steel fibres are straight, 2000 MPa in strength, 13mm in length and 0.2mm in diameter [1-2]. Fig.1 shows a 2D XCT image slice with the mortar in grey, the fibres in white and the voids in black. The 3D image was segmented, using grayscale thresholding, into different phases using the software Avizo standard 8 [VSG,USA]. The volume fraction of the voids and the fibres is 2.99% and 3.75% respectively. The sizes, shapes and distribution of the voids were then analysed using a Matlab code. It was found that most voids were spherical with equivalent diameters from 25-1400 µm, and 98% have an equivalent diameter less than 600 µm (small voids). Including all the voids and fibres in one FE model could result in a very large

number of elements in the mesh, which would be prohibitively expensive computationally. Therefore, the mortar and all the small voids are modelled first, and the homogenised mortar is then modelled with fibres and large voids. The elastic properties predicted in the first step are used as inputs in the second. Fig.2 illustrates the two-step homogenisation approach.

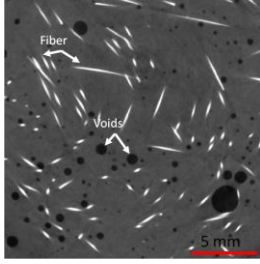


Fig.1 A 2D slice of UHPFRC

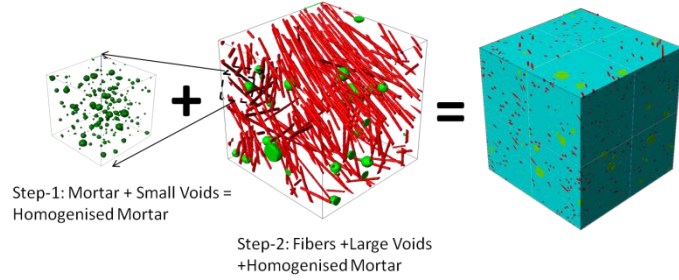


Fig.2: The two step homogenisation

To determine the size of the representative volume elements (RVEs) of the homogenised mortar to be used in the second step, the distances between large voids were analysed. It was found that the mean distance was about 5mm. So five 5mm cubical RVEs at different locations of the 20mm cube were constructed and modelled in the first step. The elastic modulus of the virgin mortar (mortar without voids) was assumed equal to 45GPa and its Poisson's ratio is 0.2. In the second step, models with four sizes (see Fig. 3), 5, 6.5, 9 and 13mm, were analysed to investigate the size effect and to determine the size of RVE of the whole composite. For each size, three models were built using scan data from three randomly chosen locations in the dataset and the results were averaged. The 3D images were converted to FE meshes using ScanIP (Simpleware, Ltd, UK). Both mortar and fibres were meshed using four-noded tetrahedron elements (C3D4). The fibres were embedded into mortar, assuming a perfect bond. The elastic modulus of the steel fiber is 200GPa and its Poisson's ratio is 0.3. ABAQUS v6.13 [Simulia, Providence, RI] was used for all FE analyses.

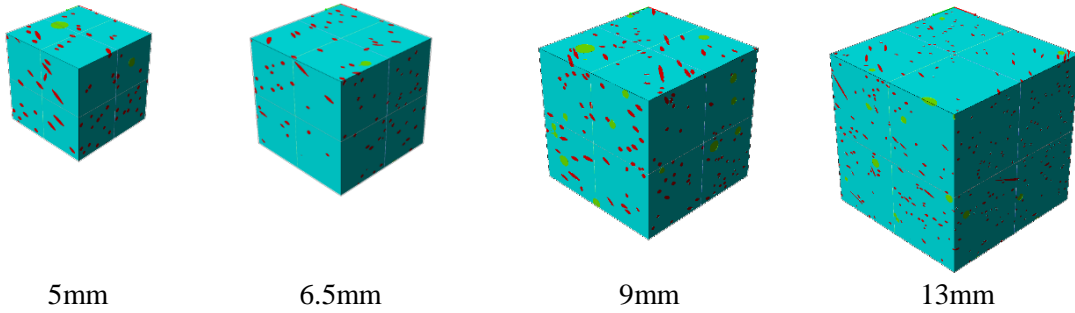


Fig.3. The models for UHPFRC: large voids in green, fibres in red and homogenised mortar in blue

To predict the effective elastic constants, six separate unit strain with periodic boundary conditions, were applied on each RVE under tensile loading [6]. The homogenised stiffness matrix C_{ijkl}^H of the equivalent homogenous material can be obtained from the following constitutive relation:

$$\langle \sigma_{ij} \rangle = C_{ijkl}^H \langle \varepsilon_{kl} \rangle \quad (1)$$

where $\langle \varepsilon_{kl} \rangle$ and $\langle \sigma_{ij} \rangle$ are the respective macro stress and strain tensors.

3. Results and discussion

The anisotropy ratio A for the RVEs is defined as:

$$A = \frac{2C_{44}}{C_{11} - C_{12}} \quad (2)$$

where C_{11} , C_{12} and C_{44} are coefficients of the homogenised stiffness matrix defined in Eq.1. The anisotropy ratio of the planes in the mortar with the small voids from the first step is about 0.994. So the homogenised mortar can be regarded as an isotropic material. The average homogenised E is

41.8±0.57GPa, which is very close to the experimental value 42 GPa in [1]. The Poisson's ratio is 0.199±0.0001. Fig.4 shows stress distributions in the mortar model with small voids for each deformation mode. It can be seen that stress concentrates around voids.

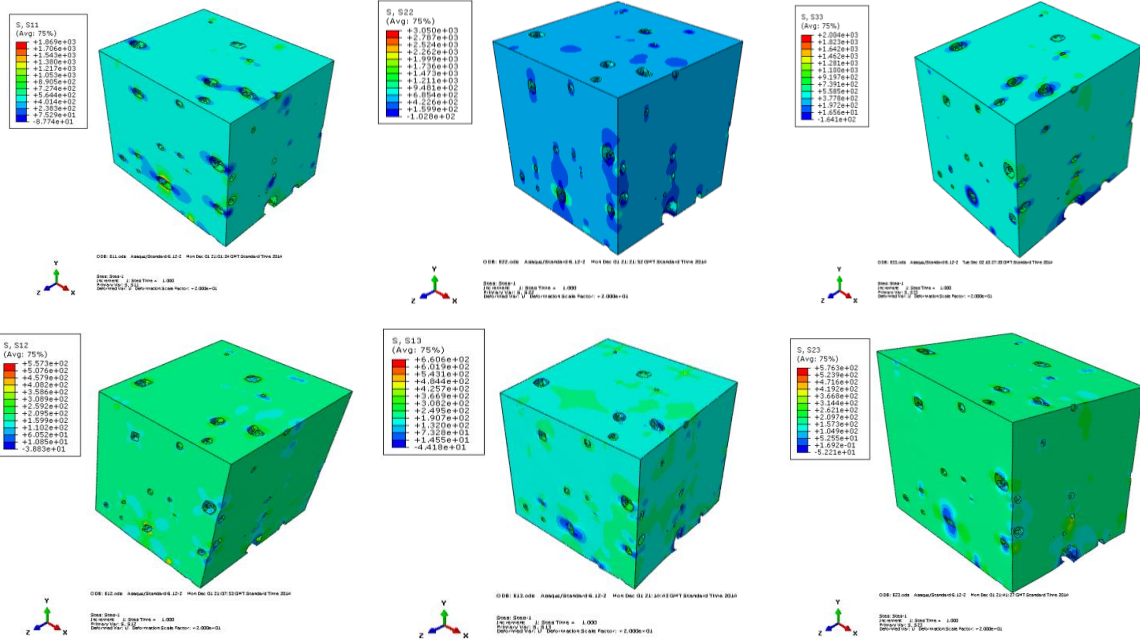


Fig.4: Deformed meshes and stress distributions in mortar RVE under six independent loading conditions.

Fig.5 and Fig. 6 show the stress distributions in the mortar and the fibres respectively, obtained from the second step of homogenisation for 9mm RVE. It can be seen that stress concentration occurs around the big voids and also in the mortar around the fibres. The stresses in the fibres depend greatly on their orientations with respect to the loading direction.

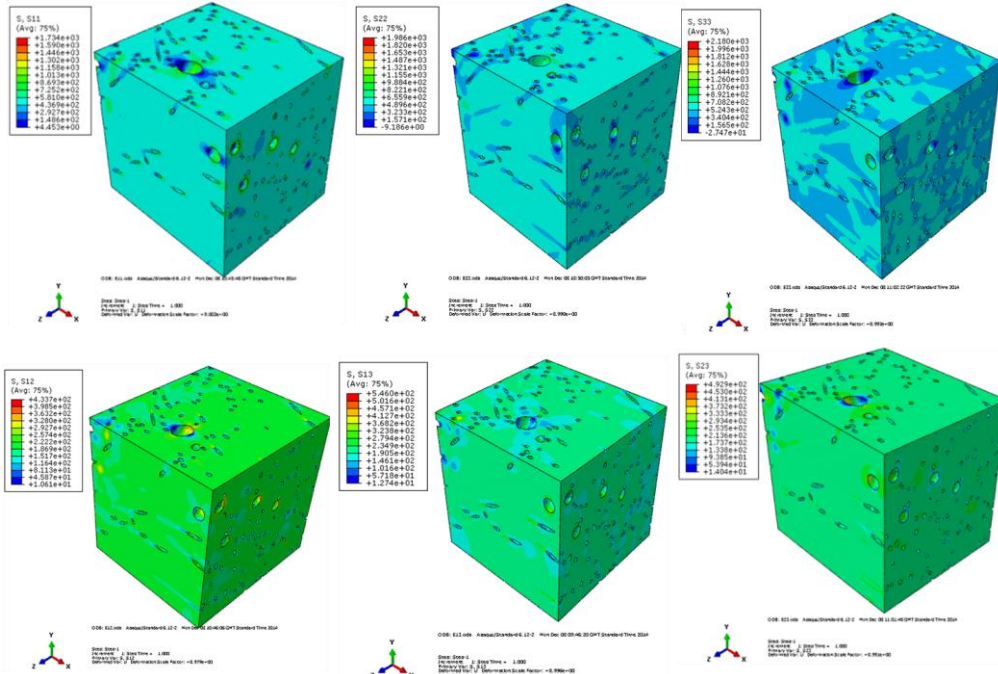


Fig. 5 Deformed meshes and stress distributions in the matrix under six loading conditions (9mm RVE).

The anisotropy ratio of the planes for different sizes ranges from 0.970 to 1.008, showing that the UHPFRC can be considered as an isotropic material. The effects of model size on effective E are shown in Fig.7. The average effective E for UHPFRC ranges from 42.2GPa for a 13mm cube to 43.6 GPa for a 5mm cube. The standard deviation decreases with the size increase. The suitable RVE size

with respect to E is about 9mm, over which it remains at $43\pm 0.51\text{GPa}$, very close to the experimental value 45GPa [1]. The predicted Poisson's ratio is about 0.203.

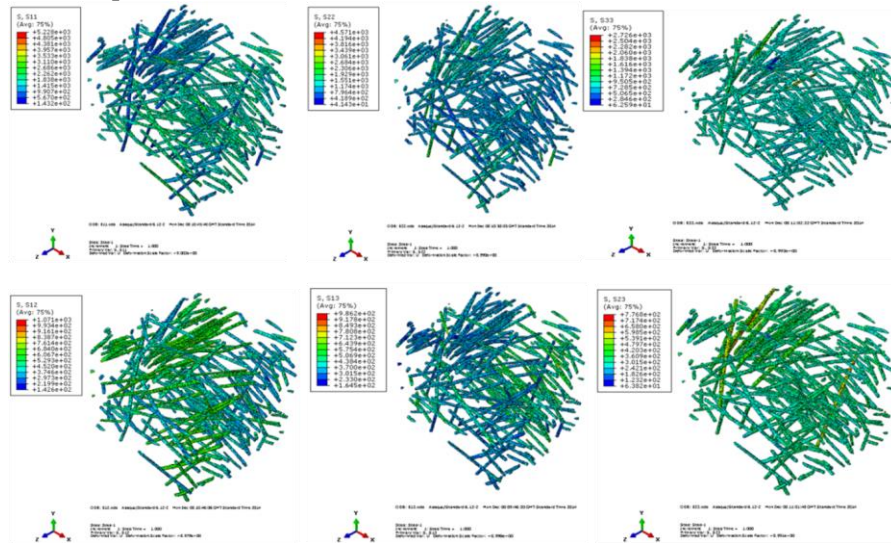


Fig. 6 Deformations and stress distribution in fibres under six loading conditions (9mm RVE).

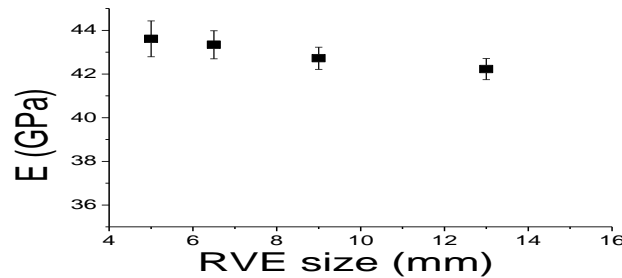


Fig.7: The average homogenized elastic modulus of UHPFRC with the standard deviation for different sizes

4. Conclusions

In this paper, the XCT scanned images have been used to construct finite element models to compute elastic properties of UHPFRC using a two-step homogenisation approach. In the first step the mortar with small voids are modelled, showing that the homogenised mortar is isotropic with $E=41.8\pm 0.57\text{GPa}$ and $\nu=0.199$. In the second step, models of different sizes consisting of homogenized mortar, fibres and larger voids were built and analysed. It was found that the UHPFRC is nearly isotropic with $E=43\pm 0.51\text{GPa}$ and $\nu=0.203$.

Acknowledgement

The research is funded by UK EPSRC (EP/J019763/1) and a PhD studentship from the Jordanian government.

References

- [1] A . Hassan, S. Jones and G. Mahmud, Experimental test methods to determine the uniaxial tensile and compressive behaviour of ultra high performance fibre reinforced concrete (UHPFRC). *Construction and Building Materials*, 37, 874-882, 2012.
- [2] G. Mahmud, Z.J. Yang and A. Hassan, Experimental and numerical studies of size effects of Ultra High Performance Steel Fibre Reinforced Concrete (UHPFRC) beams, *Construction and Building Materials*, 48, 1027-1034, 2013.
- [3] M. Gul, A. Bashir and J.A. Naqash, Study of modulus of elasticity of steel fibre reinforced concrete. *International Journal of Engineering and Advanced Technology*, 3(4), 304-309, 2014.
- [4] E. Gal and R. Kryvoruk, Meso-scale analysis of FRC using a two-step homogenization approach. *Computers & Structures*, 89(11), 921-929, 2011.
- [5] J. Zhang, X. Liu, Y. Yuan and H. Mang, Multiscale modeling of the effect of the interfacial transition zone on the modulus of elasticity of fibre-reinforced fine concrete. *Computational Mechanics*, 55(1), 37-55, 2015.
- [6] R. Sharma, W. Ren and Z.J. Yang, Homogeneous response of random structured material concrete with realistic microstructure. *22nd UK Conference on Computational Mechanics(ACME-UK)*, 206-209, 2014.

Finite Element Analysis and optimal design of joints for Concrete Filled Tubes in Steel Structure

*Zheng Cui, Y.T. Feng and Chengyuan Wang

Zienkiewicz Centre for Computational Engineering, College of Engineering, Swansea University, SA2 8PP

*639600@swansea.ac.uk

ABSTRACT

In this project, the mechanical behaviour of a single CFT as a column subjected to axial compression will be analysed by finite element method. Both linear and nonlinear material properties of steel and concrete will be considered and the numerical results will be compared with a set of test results conducted by Harbin Institute of Technology, China. Then some interface defects between the steel and the filled concrete will be introduced to investigate their effects on the overall behaviour of the CFT and also the possible local buckling of the steel tube which has been observed in tests and in real structures. At the next stage, a few commonly used CFT joint sections will be modelled under both static and dynamic loading conditions, and their performance will be compared in terms of the maximum stresses and their locations identified. Finally, based on these simulations, some optimised designs of CFT joints will be proposed.

Keywords: Concrete Filled Tubes; Finite Element Analysis; Composite structure; optimal design

1. Introduction

Concrete Filled steel Tubes (CFT) are composite members consisting of steel tubes filled with concrete. CFTs have been widely used in many areas as the structural foundation, especially in high-rise structures and bridge piers, because of their preferred and unique features. Furthermore, CFTs may be utilized for improving stability of structures in an earthquake zone [1]. Compared with ordinary steel or reinforced concrete systems, CFT has many advantages. The main one is that, local buckling of the steel tube is delayed due to the restraining effect of the concrete. On the other hand, the strength of concrete is increased by the confining effect provided by the steel tubes [2]. Many research works have been done to understand its mechanical behaviour of a single beam or column, in both of experimental and numerical. However, joints, either between two or several CFTs or between a CFT and other structural member, can cause major problems, as the foundation will carry a higher load. Therefore, the joints have become the critical part to be analysed. There are different designs and methods that have been used in practice, but detailed investigations are still lacking.

2. Global buckling analysis

At this stage, the main aim is to simulate the buckling behaviour of columns under a unit axial load. The computational results will be compared with analytical solutions. In this stage, 4 models will be simulated, one is 1D-steel column by using wire element, one is 3D reinforced concrete column by using solid element, and the rest two 3D steel tube finite element models, one uses 8-noded solid elements and the other uses 4-noded shell elements, are constructed. For the two models, all of the boundary conditions are fully fixed at the centre point and roller connected to the edge at the base. A unit axial load is placed at the top of the column. Furthermore, the material properties are 210E9 for Young's modulus of steel and 30E9 for Young's Modulus of concrete. Then a linear buckling analysis is performed by using the buckle solver.

After simulating from ABAQUS, global buckling behaviours are generated as shown in Figure 1. The axial load has been set up as a unit load, so the eigenvalue is equal to the value of critical load for buckling.

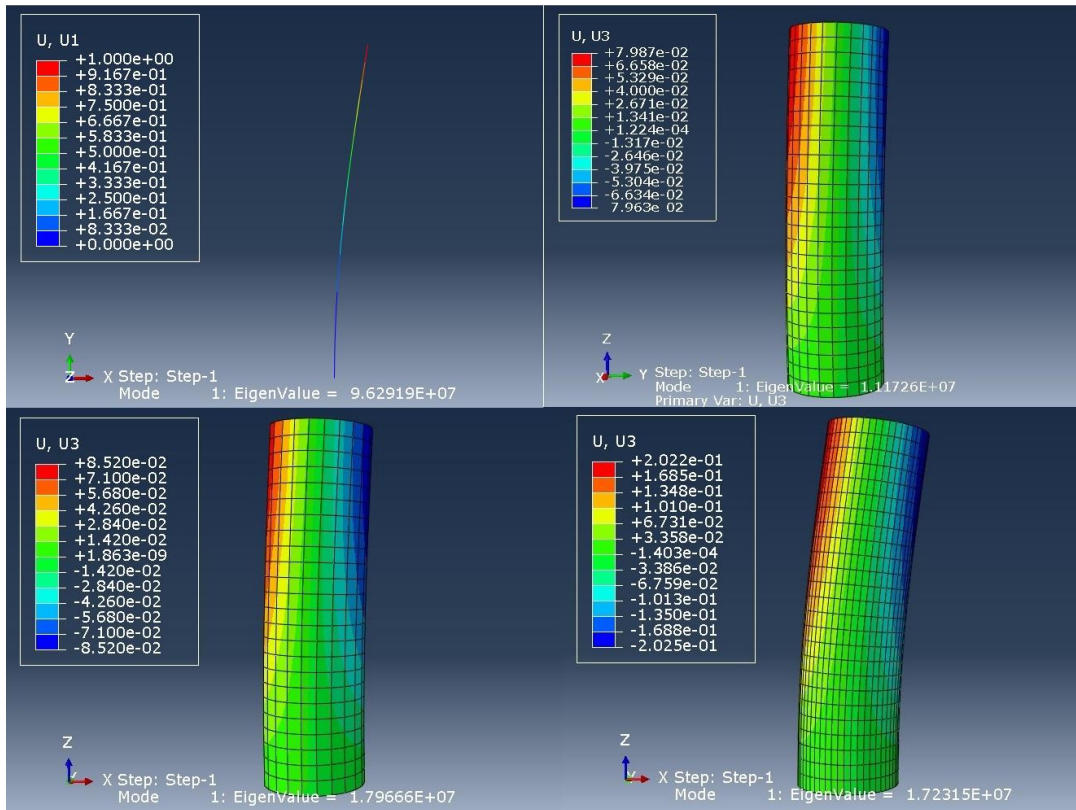


Figure 1: Global buckling generated for 1D-steel column, 3D-concrete column, 3D-steel shell tube and 3D-steel solid tube.

Table 1: Comparison of computational and analytical buckling loads

	Abaqus (N)	Analytical solution (N)
1D beam	9.63E+07	9.96E+07
3D RC column	1.12E+07	1.16E+07
3D Shell steel tube	1.80E+07	1.85E+07
3D solid steel tube	1.72E+07	1.85E+07

All of the computational results are compared with analytical solutions which are calculated using Euler's buckling formula.

$$F = \frac{\pi^2 EI}{(KL)^2} \quad (1)$$

Where E is the Young's modulus, I is the moment of inertia and L is the length of the column. K is the column effective length factor, whose value depends on the conditions of end support of the column. The models have been used is one end fully fixed and the other end free to move laterally. Therefore, the value of K is equal to 2.0.

Table 1 shows that, for 1D beam and 3D reinforced concrete, the computational and analytical results are relatively similar, with about 3.3% differences. However, by comparing the 3D shell steel tube and 3D solid steel tube models, they have the similar behaviour. But the critical load for buckling has

a slightly different computational results from the ABAQUS software. After increasing the density of the mesh at the thickness of the tube, the results are approaching closely.

3. Local buckling for 3D models

Analysing the buckling effects in ABAQUS normally involves two steps. In the first step, the eigenvalue can be calculated by using buckling simulations, which is the global buckling analysis. This step is linear and for small deformations. The aim of this step is to calculate the critical value. After the buckling has been found, the local buckling is a concern, as the axial load is placed, this is happening in the local buckling simulation which is a nonlinear analysis because large deformation needs to be considered. This simulation is employed by displacement control with arc-length corrections.

In order to work out the limited value, the local buckling will be simulated in ABAQUS by using IMPERFECTION Command. All of the procedures are the same with the global buckling in the last step, apart from the step and load modules. In step module, “Static, Riks” will be selected. The critical load, which has worked out from global buckling, will be placed at the top of the tube or column. This performance will only be simulated for 3D models. While the keyword is edited, the imperfection command is inputted with a geometric imperfection. This geometric imperfection is a scale factor which is normally equal to 1% of the thickness of the Shell.

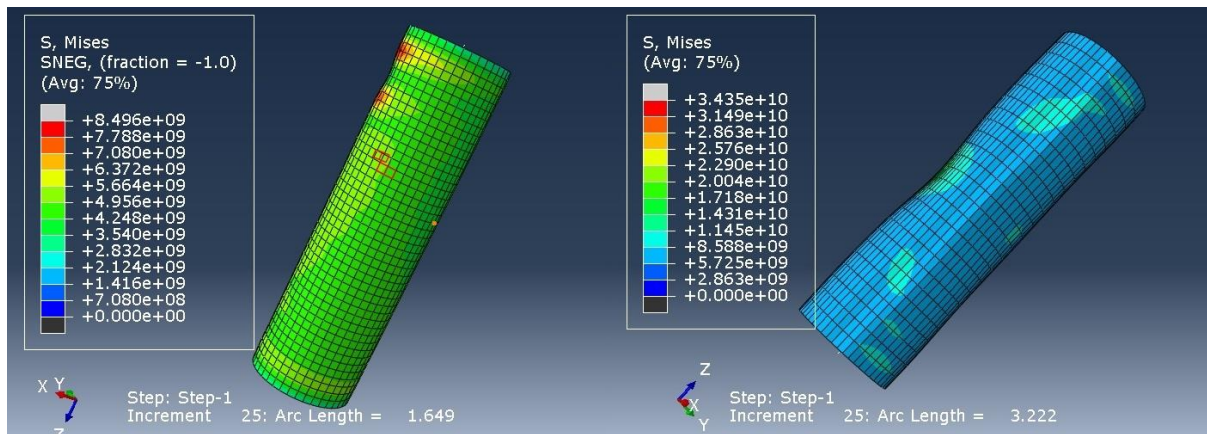


Figure 2: local buckling for 3D Shell Steel tube and Solid Steel tube

ABAQUS has produced deformed configurations for both tubes. The time steps are replaced by the arc length in Riks analysis. These configurations show how the tube deforms under an axial load with imperfection analysis. Figure 2 shows a local buckling occurring at the top of the tube.

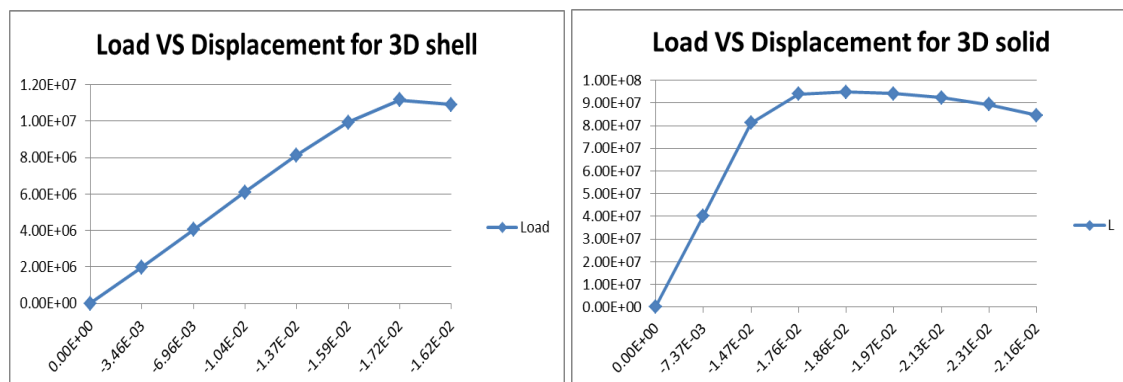


Figure 3: Critical load for 3D Shell Steel tube and Solid Steel tube

Table 2: result comparison between perfect buckling and buckling with imperfection

3D shell critical load (N)		3D solid critical load (N)	
Global buckling	Buckling with imperfection	Global buckling	Buckling with imperfection
1.80E+07	1.12E+07	1.87E+07	9.49E+06

Figure 3 is shown that the load verse displacement behaviours after placing the axial load on the top. The critical load could be found in this figure. Table 2 shows the comparative results of buckling and local buckling simulations, both are produced from ABAQUS software. It clearly indicates that the critical load for local buckling is smaller than that for global buckling. Therefore, the geometric imperfection is decreased the load capability dramatically.

4. Interface defect consideration

The interface defects happen internally between concrete and steel tube, which can weaken the behaviour of the CFT and cause great problems in structural constructions. Within the linear range, the theory is now reasonably well known. However, there are still many relative questions that remain to be answered. The bonding condition between the reinforce concrete and steel tube remains a significant concern, because the debonding due to the possibility of shrinkage of mass concrete can reduce the confinement effect of steel tube on the concrete core and may decrease the load-carrying capacity and the ductility of the CFT structures. In a long term effect, temperature, creep and improper concrete casting will lead to the debonding separation at the interface between reinforced concrete and steel tube. Also, in practice, many defects have been found at the steel-concrete interface, which is like concrete inanity. It is also caused by reinforced concrete shrinkage [3].

Another interface defect is caused by diametric growth while there is an axial load happened at the top of the CFT. For steels, the problem of diametric growth increases with an increase in percentage thickness reduction. Diametric growth is a function of the ratio of the circumferential contact length A to the axial contact length L . The higher the $A:L$ ratio, the better the diametric control. As the axial load placed at the top, the steel tube will be increased in the cross-sectional area. So there will be more space that has been generated between the concrete and the steel tube. That will cause major problems in the structural frames. These interface defects will decrease the structural performance and stability of the composite columns.

5. Conclusion

To sum up, the steel tubes have been simulated separately by applying ABAQUS software. The results showed that the critical loads with and without imperfection effects of steel tube. The imperfection factor will affect the stability and carry capability of the structure frames. In practical situations, many factors will cause imperfections. For example, if the load position is offset from the actual middle point. This will cause the CFT itself bending easily to one side. Also, if the steel tube has internal porosities inside the tube wall, which will be similar to the local buckling models. The data showed that the critical load has decreased dramatically. Moreover, this kind of imperfection is hard to predict in real life. Therefore, it will cause major problems.

References

- [1] Brian Beck, Gregory S. Lauer, Quinton Champer, C. Douglas Goode. (10/10/2012) Concrete-Filled Steel Tubes. Available at:http://www.northeastern.edu/compositesystems/wiki/Concrete-Filled_Steel_Tubes. Last accessed 16/12/2014.
- [2] Dawn E. Lehman, Charles W. Roeder. Foundation connections for circular concrete-filled tubes. Journal of Constructional Steel Research, 4 (1), 2 July 2012.
- [3] Creep and shrinkage of concrete - Wikipedia, the free encyclopedia. 2015. Creep and shrinkage of concrete - Wikipedia, the free encyclopedia. [ONLINE] Available at:http://en.wikipedia.org/wiki/Creep_and_shrinkage_of_concrete. [Accessed 08 February 2015].

A COMPARISON BETWEEN PERIODIC AND FIXED BC FOR STRUCTURAL ANALYSIS OF FLEXIBLE RISERS

*M.T. Rahmati, H. Bahai. and G. Alfano

Department of Mechanical, Aerospace and Civil Engineering

Brunel University

Uxbridge

UB8 3PH, UK

*mt.rahmati@gmail.com

ABSTRACT

The accurate structural modelling of flexible risers which are used for transporting oil and gas between the seabed and surface in ultra-deep waters is a great challenge for the oil and gas industry. This is because they have a very complex internal structure consist of several polymer and steel layers. Constitutive laws based on beam models which allow the large-scale dynamics of pipes to be related to the behaviour of its internal components can be used for multi-scale analysis of flexible risers. An integral part of these models is the small-scale FE model chosen and the detailed implementation of the boundary conditions. The emphasis of the present work is on the implementation of the periodic boundary condition for small-scale modelling of flexible risers. By applying periodic boundary conditions, only a small fraction of a flexible pipe can be used for detailed analysis. The computational model is firstly described. Then, the capability of the method in capturing the detailed nonlinear effects and the great advantage in terms of significant CPU time saving entailed by this method are demonstrated. The approach is applied on a simplified 3-layer pipe made of inner and outer polymer layers and an intermediate armour layer made of 40 steel tendons.

Keywords: *Periodic Boundaries, Fixed Boundaries, Flexible risers*

1. Introduction

Unbonded flexible consist of several polymer and steel layers that are, to a certain extent, free to move internally relative to each other. This gives low bending stiffness and makes them highly valuable tools for subsea oil and gas companies. Their ability of withstanding both horizontal and vertical large displacements makes them ideal for floating platforms. Due to the complex geometry of flexible risers, the conventional stress prediction and fatigue analysis tools based on analytical formulations and linear methods are not adequate. Instead, detailed non-linear computational methods are required to take into account contact and friction between layers.

One of the first FE methods for analysing flexible risers was presented by Felippa and Chung [1]. They described the formulation and algorithmic implementation of a geometrically nonlinear beam model. Tan et al. [2] demonstrated a three-dimensional time domain analysis of the bending hysteresis phenomenon of flexible risers. Sævik [3,4] presented a finite element model to predict stresses under axisymmetric and bending loading. The axisymmetric model was used to analyze the boundary conditions with regards to initial contact pressure in both formulations. Leroy et al. [5] used a FE model to predict stresses in flexible pipe layers. In this model periodic solutions are assumed (given constant curvature in the pipe) and an analytical solution of equilibrium of wires on a torus (the bend pipe) was used.

Although FE models can account for the complex internal structure of flexible risers, their computational requirements limit their applicability to just a few meters in length at most. So, a more efficient methodology with lower computational cost is required to bridge the gap between large-scale nonlinear dynamic simulations and detailed finite element models at the small scale. One approach is computational homogenisation procedures currently in widespread use for the modelling of composite materials. These methods allow the large-scale dynamics of large installed pipes to be related to the behaviour of the small scale through a nested approach. More precisely, at each integration point (i.e. cross section) of the large-scale beam model, the stress resultants corresponding to assigned

generalised strains are determined through the solution of the small-scale FE problem. This requires recasting the computational homogenisation problem in a more general theory which can link different structural models at different scales [6, 7].

This paper describes an efficient modelling approach for the small-scale analysis, which exploits the cyclic symmetry of the riser detailed structure, and its implementation based on the introduction of periodic boundary conditions for detailed finite element models in small scale simulations. The capability of the boundary condition treatment method in capturing the non-linear effects and the great advantage of significant CPU time saving by this method over using a larger model is shown.

2. Small scale model

Two models, see figure 1, are created using the finite element package ABAQUS 6.13.1. All components are modelled with fully-integrated 8-noded 3D solid elements with incompatible strains, with surface-to-surface frictional contact between all components. The number of nodes in model a and model b are 7901 and 225852 respectively. Details of the material, dimensions and arrangement of constituent layers are given in Tables 1.

A fully implicit nonlinear static analysis is used to solve the model. The analyses were carried out in parallel on a computer cluster with two dual-core 1.8 GHz processors (32 processors in total) using 8MB of RAM. Whilst the run time for the small scale model is only few minutes, it takes over 11 hours to complete the analysis of a model with one pitch.

Each tendon of the armour layer forms a helix with a pitch length of 320 mm. One key idea used here is to consider an element of pipe of length equal to 1/40 of the pitch length of the tendons. For this small slice of pipe the position of each tendon on one end cross section is the same as the position of the adjacent tendon on the other end cross section. This makes this slice of 1/40 of length the smallest repeating unit of the pipe. Furthermore, the assumption is made that the variation of the internal stress resultant is small enough that, for the element of pipe under consideration, it can be neglected. Therefore, to within a rigid motion, the assumption of period kinematics is made, resulting in the enforcement of periodic boundary conditions.

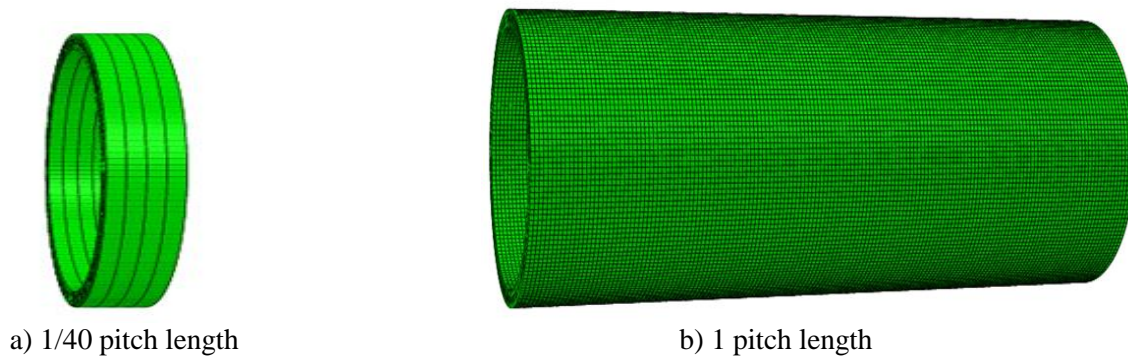


Figure 1: FE Models with different length

Table 1: Dimensions and materials of components in the model.

Layer	r_0, r_1 (mm)	Material	E(MPa)	ν
1	48, 50	Polyethylene	0.35	0.4
2	50, 52	Carbon Steel	210	0.3
3	52, 54	Polyethylene	0.35	0.4

3. Boundary conditions

A set of linear constraint equations was generated relating the degrees of freedom of each pair of nodes on the boundaries having the same position on the cross-section. The equations link the nodes N_R and N_L to the projected nodes, N_P , in a plane parallel to the cross section (as shown in Figure 2). The link is enforced for all displacement and rotation degrees of freedom. The degrees of freedom of the projected nodes are rigidly constrained to those of a reference point at their center, R_P , using the rigid body constraint. This forces the projected nodes to remain in the plane and follow the displacement and rotations of the reference point. In this way, displacements and rotations of the reference point correspond to generalized strains in the model. For example, prescribing a rotation ϕ_{R_P} of the reference point about one axis in the cross section is equivalent to prescribing periodic boundary conditions corresponding to a bending curvature equal to ϕ_{R_P}/L , L being the length of the model.

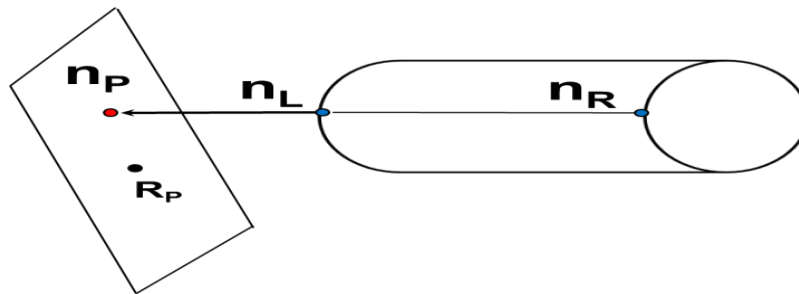


Figure 2: Periodic boundary condition

4. Numerical results

The analyses were conducted by applying internal and external pressure in a first step, after which one symmetric cyclic history of bending curvature was prescribed, the maximum and minimum curvatures being 0.125 and -0.125 m^{-1} . The internal and external pressures were equal to 2 and 2.25 MPa , respectively. The curves in Figures 3 show the bending moment against the (prescribed) bending curvature for all models. It can be appreciated that the difference in the results of the models with different lengths is practically negligible for the smaller pressure values considered and still very small for the larger pressure value when periodic BC is used. These results confirm that use of the smallest repeating unit as the model to be used at the small scale of a multi-scale analysis is a valid choice. The huge saving in CPU time, from 11 hours for the longest model of one pitch length (considered in the past in [6, 7]) to only few minutes, allows the smallest model to be effectively used in a nested multi-scale strategy. It is important to note that there a large difference in the bending moment vs bending curvatures for the longest model with fixed and periodic beaneries. Although not reported here, this difference is even higher for the shorter models, as expected.

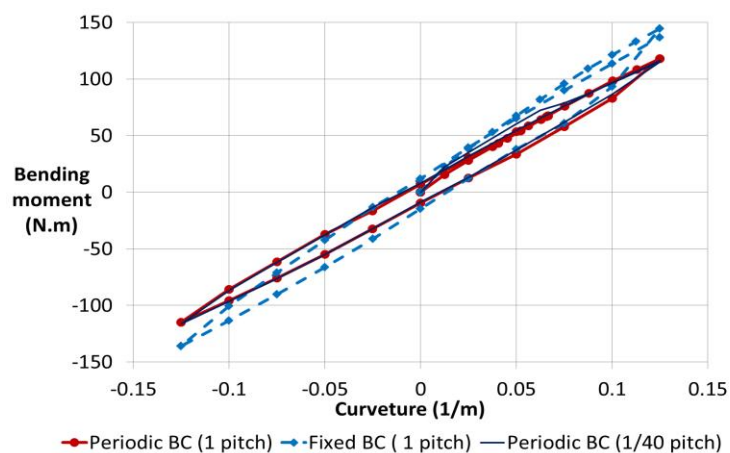


Figure 3: Bending moment hysteresis using periodic and fixed in-plane boundary conditions

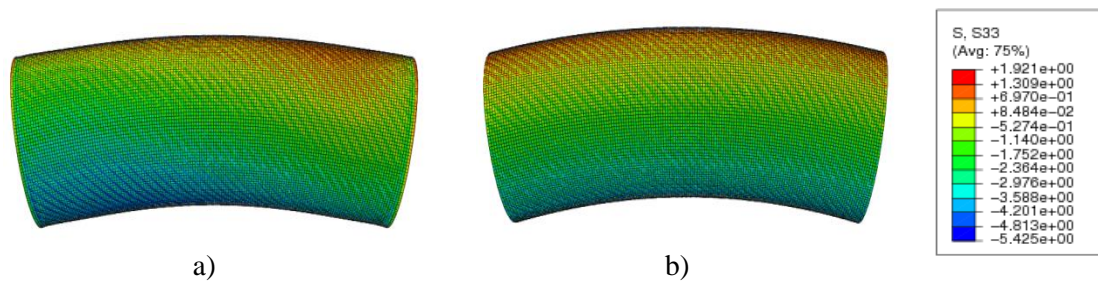


Figure 4: Axial stress on the outer layer using a) fixed in-plane boundary conditions and b) periodic boundary conditions

As shown in Figure 4 by using a periodic BC in a more uniform and realistic stress distribution on the outer layer can be predicted.

5. Conclusions

An effective approach to the development of detailed FE models of unbonded flexible risers has been presented and the approach has been applied to a simple 3-layer pipe made of inner and outer polymer layers and an intermediate 40-tendons armour layer. Exploiting the cyclic symmetry of the riser the smallest repeating unit is considered together with the largest corresponding to one entire pitch length of the helix formed by each tendons of the armour layer. Periodic boundary conditions are enforced, which is essential when only a fraction of the length of flexible risers is used for detailed FE analysis, because the shorter the pipe element is the more pronounced the effects of fixed boundary conditions would be. The accuracy of the proposed approach is demonstrated by comparing the results of the models with different lengths. It is shown that the difference in results is negligible, while using a fraction of the riser for detailed structural analysis reduced the computational cost by 2 or 3 orders of magnitude. This makes the smallest repeating unit with periodic boundary conditions the ideal candidate for being used as small-scale model in a nested (i.e. FE2 type) computational homogenization approach of the type

Acknowledgements

The authors would like to acknowledge the financial support by EPSRC (grant EP/K034243/1).

References

- [1] Felippa, C.A., Chung, J.S., 1981. Nonlinear static analysis of deep ocean mining pipe. *Transactions of the ASME: Journal of Energy Resources Technology* 103, 11{25.
- [2] Tan, Z., Quiggin, P., Sheldrake, T., 2007. Time domain simulation of the 3D bending hysteresis behaviour of an unbonded flexible riser, in: *Proceedings of the 26th International Conference on O shore Mechanics and Arctic Engineering*. OMAE2007-29315.
- [3] Sævik, S., 2010, Comparison between theoretical and experimental flexible pipe bending stresses, in: *Proceedings of the ASME 2010 29th International Conference on Offshore, Ocean and Arctic Engineering*, OMAE2010-20352
- [4] Sævik, S., 2011, Theoretical and experimental studies of stresses in flexible pipes, *Computers and Structures*, 89, pp. 2273-2291
- [5] Leroy, J.M., Estrier, P., et al, T.P., 2010, Stress assessment in armour layers of flexible risers, in: *Proceedings of the ASME 2010 29th International Conference on Offshore, Ocean and Arctic Engineering*. OMAE2010-20932
- [6] Edmans, B., 2012. *Non-linear Finite Element Analysis of Flexible Pipes for Deep-water Applications*. Ph.D. thesis, Department of mechanical engineering, Brunel University, London, UK
- [7] B. Edmans, G. Alfano, H. Bahai. Nonlinear multi-scale homogenization with different structural models at different scales. *International Journal for Numerical Methods in Engineering* 2013, 94(4): 355-373.

VIBRATING BEHAVIOURS OF COATED CARBON NANOTUBES

*Y. Xiao, C.Y. Wang and Y.T. Feng

Zienkiewicz Centre for Computational Engineering, College of Engineering, Swansea University, Singleton
 Park, Swansea, SA2 8PP

*599275@swansea.ac.uk

ABSTRACT

This paper aims to study the vibration of hybrid nanotubes comprising multiwall carbon nanotubes (MWCNTs) wrapped by different coating materials. Based on Timoshenko beam theory, dynamics equations have been developed for these hybrid nanotubes to calculate their possible vibration modes and associated frequency. In doing these, attention has been paid to the effect of coating materials, coating thickness and the van der Waals (vdW) interaction existing between the adjacent layers of MWCNTs.

Keywords: coating CNTs; vibrating behaviours; Timoshenko beam theory; vdW interaction

1. Introduction

Techniques have been developed to coat Carbon nanotubes (CNTs) by a variety of functional materials, e.g., transition metals, oxidized materials [2], superconductive alloy [1] and conductive polymers [3]. These hybrid nanotubes (HNTs) are promising for applications in biological nanoprobe [2,3], the pressure/stress sensors and nanoresonators, whose performance depends crucially on their mechanical properties. It is thus imperative to gain an in-depth understanding of the mechanical responses of the novel nanomaterials. This provides impetus for us to study the mechanics of the HNTs. In particular we are interested in the vibration of the HNT as it plays a crucial role in a range of HNT applications. In what follows, the Titanium-CNT HNTs will be selected as a typical example and investigated by using equivalent continuum mechanics theory. Effort will also be made to extend the study to more general cases for other HNTs.

2. Analysis method

Fig. 1 shows an illustration of the HNT, i.e., a double wall carbon nanotube with Titanium (Ti) coating layer. Here, the red tube represents the inner single wall carbon nanotube (SWCNT) (5, 5) (as beam 1); the blue one represents the outer SWCNT (10, 10) and the Ti coating layer is denoted by green colour. Specifically the outer SWCNT (10, 10) and Ti layer are considered as a single composite beam (beam 2) with a perfect bond at the interface. It should be pointed out that Fig. 1 shows the equilibrium position of the HNT prior to vibration.

In this study, beams 1 and 2 are treated as two Timoshenko beams which have circular cross sections and coupled via the interlayer vdW interaction between the inner SWCNT and outer SWCNT. Based on the model, the governing equations considering the effect of the van der Waals (vdW) interaction can be derived as follows for the HNT shown in Fig.1.

$$\begin{cases} -(GA)_i k \left(\frac{\partial \varphi_i}{\partial x} - \frac{\partial^2 w_i}{\partial x^2} \right) + p_i(x) = (\rho A)_i \frac{\partial^2 w_i}{\partial t^2} \\ (EI)_i \frac{\partial^2 \varphi_i}{\partial x^2} - (GA)_i k \left(\varphi_i - \frac{\partial w_i}{\partial x} \right) = (\rho I)_i \frac{\partial^2 \varphi_i}{\partial t^2} \end{cases} \quad (1)$$

where i represents the quantities of beam i in the system, w_i and φ_i are transverse deflection and rotation angle; $k = 0.8$ is the shear coefficient; $(EA)_i$, $(EI)_i$ and $(GA)_i$ are extensional rigidity, bending

rigidity and shear rigidity respectively; $(\rho A)_i$ is mass density per unit length and mass moment of inertia is denoted as $(\rho I)_i$. The vdW force in the transverse direction $p_i(x)$ is given by [4]

$$\begin{cases} p_1(x) = c(w_2 - w_1) \\ p_2(x) = -c(w_2 - w_1) \end{cases} \quad (2)$$

where c is the interlayer vdW interaction coefficient:

$$c = \frac{320(2R_1) \text{erg} / \text{cm}^2}{0.16d^2}, \quad d = 0.142 \text{ nm} \quad (3)$$

R_1 is the radius of beam 1. In addition, the simply supported boundary conditions are imposed on the two ends of the HNT. The functions of w_i and φ_i satisfying the boundary conditions are [2]:

$$\begin{cases} w_i = A_i \cdot \sin\left(\frac{m\pi}{L}x\right) \cdot e^{i\omega t} \\ \varphi_i = \Phi_i \cdot \cos\left(\frac{m\pi}{L}x\right) \cdot e^{i\omega t} \end{cases} \quad (4)$$

Substituting Eq. (4) into Eq. (1) leads to the algebraic equations $\mathbf{M}(\omega)_{4 \times 4} \cdot [A_1 \ A_2 \ \Phi_1 \ \Phi_2]^T = 0$, it can be rearranged as follows:

$$[\mathbf{K}_1 - \lambda \mathbf{K}_2] \cdot \mathbf{V} = 0 \quad (5)$$

where ω is the angular frequency, $\mathbf{K}_1 - \lambda \mathbf{K}_2 = \mathbf{M}(\omega)_{4 \times 4}$, $\lambda = \omega^2$ and $\mathbf{V} = [A_1 \ A_2 \ \Phi_1 \ \Phi_2]^T$.

Eq. (5) defines a generated eigenvalue problem. Solving the eigenvalue problem one can obtain ω as the eigenvalue and the vibration frequency $f = \omega / 2\pi$. The vibration mode associated with ω is given by the eigenvectors corresponding to ω , i.e., the amplitude ratio A_1 / A_2 .

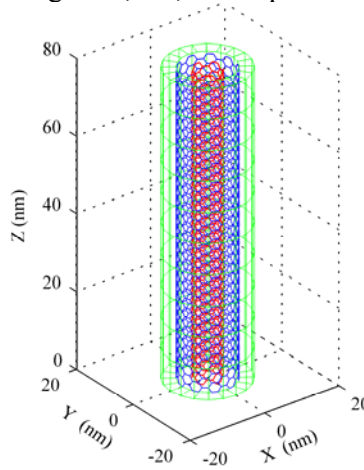


Fig. 1: The layout of the Ti-DWCNT structure.

The values of parameters used here are obtained from [2]. For SWCNT (5, 5) considered as a hollow beam, the mean radius $R_1 = 0.34$ nm. Value for SWCNT (10, 10) is $R_2 = 0.68$ nm. The effective thickness of SWCNTs is $h = 0.1$ nm, the equivalent Young's modulus is $E_{cnt} = 3.5$ TPa, the Poisson ratio $\nu_{cnt} = 0.2$, and the mass density per unit lateral area $\rho_{cnt} = 2.27 \text{ g/cm}^3 \times 0.34$ nm. For the Ti coating layer, the Young's modulus and Poisson ratio are $E_{Ti} = 110.3$ GPa and $\nu_{Ti} = 0.34$, respectively. The density of Ti is 4.43 g/cm^3 . The shear modulus of these two materials can be calculated by $G = E / 2(1 + \nu)$. In addition, the thickness H of Ti coating layer vary from 0 to 30 nm and the length of the HNT is fixed at 80 nm.

3. Results and discussion

Using the method demonstrated above we have calculated the frequency of the HNTs and the associated amplitude ratios A_1 / A_2 . It is found that the lowest and the second lowest frequencies are associated with $A_1 / A_2 = 1$ and $A_1 / A_2 < 0$ giving the in-phase (Fig. 2a) and out-of-phase (Fig.2b)

transverse vibrations, respectively, where beams 1 and 2 vibrate in the same and opposite directions. In Fig. 2 we showed the in-phase and out-of-phase vibrations of the first three modes.

Subsequently, the fundamental frequencies associated with the in-phase modes are present in Fig. 3 for the THNs with different thickness of the Ti layer. Those of the out-of-phase modes are given in the inset of the figure. As shown in Fig. 3, similar trend of in-phase mode frequency f_1 is found for the first five vibration modes, where f_1 first decreases with H to reach the lowest value at a critical thickness $H \approx 0.816$ nm. Afterword it grows up for thicker coating layer. When H is great enough f_1 is even higher than that of carbon nanotubes with $H = 0$. On the other hand, it is noted in the inset that f_2 decreases with rising H first. Then it approaches to a constant independent of H . Thus, it is expected that the out-phase mode is mainly the vibration of the SWCNT (5, 5) while the beam 2 is not significantly involved. This later has been confirmed by $A_1 / A_2 \ll -10$ computed for the out phase modes of the HNT with $H > 0.816$ nm.

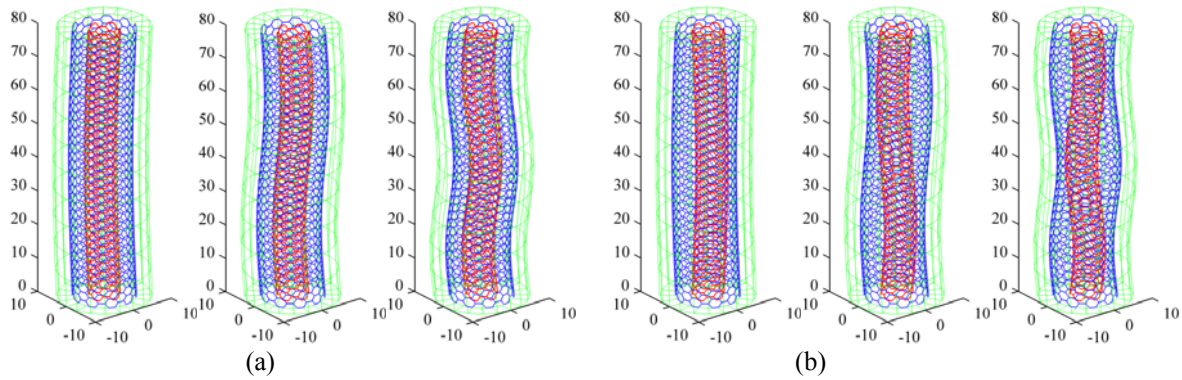


Fig. 2: First three vibrations of the HNTs: (a) in-phase mode shapes and (b) the out-of-phase vibration modes.

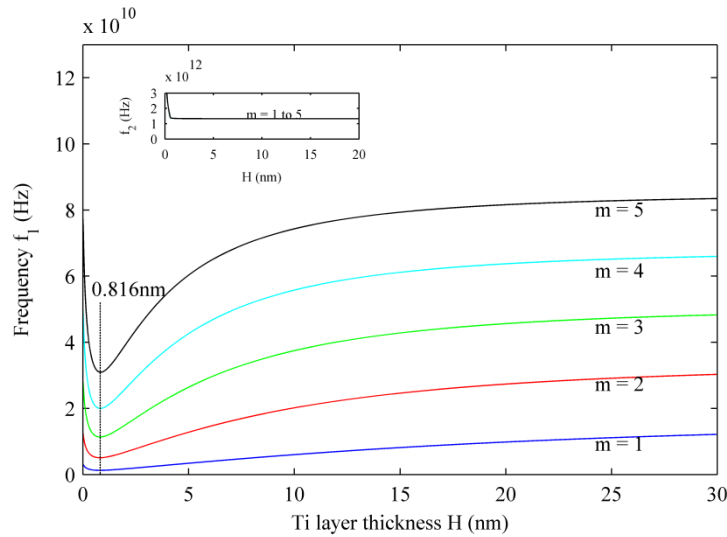


Fig. 3: First five transvers vibrations f_1 of the HNTs associated with the in-phase modes. Those of the out-of-phase mode f_2 are shown in the inset.

In this study, the focus is on the Ti coated carbon nanotubes, while, as mentioned before there are HNTs with different coating materials e.g. Ferrum (Fe), Aluminium (Al), silicon dioxide (SiO_2), Aluminium oxide (Al_2O_3) and so on. Using the above method we can expect the results qualitatively similar to Fig. 3. However, the lowest fundamental frequency (i.e., the lowest f_1 with $m = 1$) associated with the critical H could be different due to the different coating materials. In particular, the lowest frequency is of major interest in vibration analysis. Thus, in this work, we examined the

dependency of the lowest f_1 at the critical thickness H on the Young's modulus (E) and the mass density (ρ).

The results are shown in Fig. 4, the lowest frequency of the HTNs increases with decreasing ρ of the coating materials. Specifically, when ρ falls in the range of $[0, 5\text{g/cm}^3]$, the frequency upshifts rapidly with the decreasing ρ . This trend remains unchanged for coating materials with different E . It is also noted that the lowest frequency increases gradually with increasing E for coating materials with relatively large ρ . This E -dependence of the lowest frequency becomes even more pronounced for the materials with lower ρ .

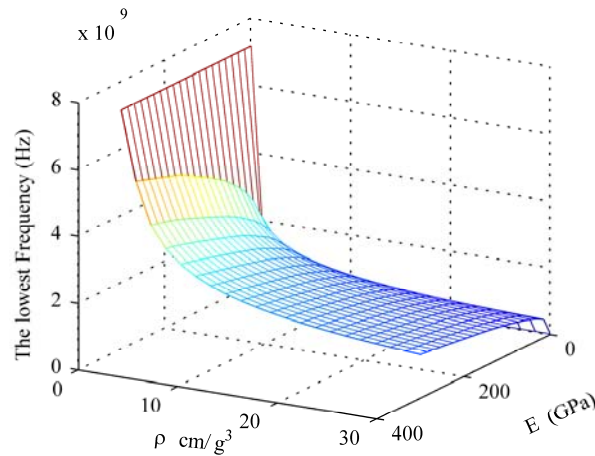


Fig. 4: The lowest frequency against the Young's modulus and mass density.

4. Conclusions

We have investigated the hybrid nanotubes (HNTs) fabricated by coating a double-wall carbon nanotube (5, 5) @ (10, 10) with a uniform Titanium layer. The analyses were carried out based on Timoshenko beam theory modified by considering the interlayer vdW interaction. The in-phase and out-of-phase transverse vibrations have been achieved for the HNTs, corresponding to the lowest frequency and the second lowest frequency, respectively. The frequency of the in-phase mode reaches its lowest value at a critical coating thickness $H \approx 0.816$ nm and can be even higher than the frequency of inner carbon nanotubes at a large thickness. The frequency of the out-of-phase mode however remains a constant for any thickness larger than 0.816 nm. After this, the HNTs with different coating materials have also been considered. The lowest frequency associated with $m=1$ and the critical coating thickness are computed and found to increase with the rising Young's modulus and decreasing mass density. In particular, the latter has more important role in determining the lowest frequency of the HNTs.

References

- [1] A. Bezryadin, C. Lau, and M. Tinkham, Quantum suppression of superconductivity in ultrathin nanowires. *Nature*, 404(6781), 971-974, 2000.
- [2] C.Y. Wang, and S. Adhikari, ZnO-CNT composite nanotubes as nanoresonators. *Physics Letters A*, 375(22), 2171-2175, 2011.
- [3] G.Z. Chen, et al., Carbon nanotube and polypyrrole composites: coating and doping. *Advanced Materials*, 12(7), 522-526, 2000.
- [4] J. Yoon, C. Ru, and A. Mioduchowski, Noncoaxial resonance of an isolated multiwall carbon nanotube. *Physical Review B*, 66(23), 233402, 2002.
- [5] R.H. Baughman, A.A. Zakhidov, and W.A. de Heer, Carbon nanotubes--the route toward applications. *Science*, 297(5582), 787-792, 2002.

SOLIDS AND STRUCTURES 2

“The doctor will see you now!” Diagnosing models with ill conditioning problems and curing them.

*Ramaseshan Kannan, Stephen Hendry

Arup, Technical Software Group, 3 Piccadilly Place, Manchester M1 3BN, UK.

*ramaseshan.kannan@arup.com

SHORT ABSTRACT

Ill conditioning can manifest itself in finite element models due to a wide variety of causes, including user errors, i.e. errors in the definition of the FE model. In floating point finite precision arithmetic, an ill-conditioned stiffness matrix can lead to inaccurate results. Therefore it is important to ensure the stiffness matrix is well-conditioned.

In this talk we first present a procedure for detecting ill conditioning in stiffness matrices arising in structural analysis. This method has been implemented in the commercial FE software Oasys GSA [4]. We then present a new method that we have developed and implemented in the software that enables engineers to detect sources of ill conditioning in their models and rectify them. We give the theoretical background and illustrate our discussion with examples of real-world structural models to which this tool has been applied and found useful. Typically, condition numbers of stiffness matrices reduce from $O(10^{16})$ for erroneous models to $O(10^8)$ or less for the corrected model.

Key Words: *ill conditioning; floating point errors; condition number; stiffness matrix;*

1. Errors

Modelling structural response using the FE method introduces errors in the solution. While quantifying the nature and extent of these errors is a well explored area in the literature, user errors have received much less attention. User errors, i.e., errors in the definition of the model within the software from say, erroneous input, arise arbitrarily which makes it challenging to analyse them rigorously. Irrespective of whether the error arose from approximation or from erroneous input data, it can lead to an ill-conditioned problem during its analysis, that is, one for which the stiffness matrix of the model has a large condition number with respect to inversion. We present a novel method, called model stability analysis, to detect the sources of errors that lead to ill-conditioned stiffness matrices.

As computers are becoming increasingly powerful, the size and complexity of FE models has increased too. Newer workflows adopted by practitioners involve automatic generation of such models from CAD and BIM packages. The implication of these developments is that the presence of errors could go undetected, which necessitates rigorous checking techniques so that practitioners have confidence in analysis results. Model stability analysis uses numerical properties of an ill-conditioned stiffness matrix to track parts of the model that cause the ill conditioning. In [3] we present the method, the theoretical basis of its derivation and demonstrate its use on real-life FE models created by practitioners.

2. Condition number estimation

Given a symmetric, positive-definite stiffness matrix $K \in \mathbb{R}^{n \times n}$, linear static analysis for calculating the displacement $u \in \mathbb{R}^n$ under the action of loads $f \in \mathbb{R}^n$ yields the system $Ku = f$. If ΔK and Δu represent the errors in K and u respectively, then perturbation analysis gives us the relationship

$$\frac{\|\Delta u\|}{\|u\|} \leq \kappa(K) \frac{\|\Delta K\|}{\|K\|}, \quad (1)$$

where $\kappa(K) = \|K\| \|K^{-1}\|$ is the condition number (with respect to inversion). Inequality (1) tells us that the relative error in u depends on relative errors in K amplified by its condition number. In double precision floating point arithmetic we have as little as $16 - \log_{10} \kappa(K)$ digits of accuracy in the computed solution. When a matrix has a condition number greater than 10^{16} , the solution algorithm can return results with no accuracy at all—such a matrix is numerically singular and linear systems with this matrix should not be solved. Therefore it is essential to compute or estimate the condition number of the stiffness matrix K to ensure it is well conditioned.

Computing the 2-norm condition number is an expensive operation since it involves computing the extremal eigenvalues of K . In practice we need just an estimate of the condition number that is of the correct order of magnitude, and we can choose any convenient norm to work with [1, chap. 15]. If such an estimate could be computed cheaply, it could provide a basis for further investigation into the conditioning.

In Oasys GSA, therefore, the presence of ill conditioning is detected using a method that estimates the 1-norm condition number $\kappa_1(K)$. The estimation procedure is triggered every time a linear static analysis is performed on the model. The method first computes $\|K\|_1$ and then uses the algorithm of Higham and Tisseur [2, Algorithm 2.4] to estimate $\|K^{-1}\|_1$, which costs only a few matrix-vector multiplications. The algorithm can be used to estimate the norm of the inverse of a matrix K as long as one can form the product $K^{-1}v =: g$, which is equivalent to solving the linear system $Kg = v$. Since the analysis already requires the Cholesky factorization of K to be computed, the condition estimate comes at a nominal cost of a few triangular system solves.

The implementation of this algorithm generates a user warning that prompts the engineer to investigate the cause of ill conditioning.

3. Detecting the causes of ill conditioning

We now describe our method Model Stability Analysis for debugging the causes of ill conditioning. To establish the notation, our stiffness matrix K is constructed using element stiffness matrices $K^{(e)} \in \mathbb{R}^{n_e \times n_e}$ for each element $e \in \Omega$, where Ω is the domain. The matrix $K^{(e)}$ is symmetric and it is defined in a coordinate system local to the element. The transformation matrix $T^{(e)}$ maps $K^{(e)}$ to the global coordinate system and we use a set m_e of n_e variables to map the locally numbered dofs to the global dof numbering. Therefore the stiffness matrix K is the sum of contributions from all elements in Ω transformed to global:

$$K = \sum_{e \in \Omega} G^{(e)}, \quad (2)$$

where

$$G^{(e)}(m_e, m_e) = T^{(e)T} K^{(e)} T^{(e)}.$$

The matrix K becomes ill conditioned when its columns are nearly linearly dependent. This can happen when

- (a) the structure has one or more pairs or tuples of dofs that do not have sufficient connectivity with the rest of the model or
- (b) certain dofs have stiffnesses disproportionate with the rest of the model.

We say a pair (i, j) of dofs connected to each other has insufficient connectivity when the stiffness contributions of terms k_{is} and k_{rj} for $r, s \in (1, n)$ with $r, s \notin (i, j)$ are either very small or at roundoff level compared with k_{ii} , k_{jj} , and k_{ij} . (The definition can be easily expanded for higher tuples of dofs.)

Possibility (a) occurs when elements do not have sufficient connectivity, for example a beam element that is connected to nodes at which there is no torsional restraint. Typically the resultant matrix would be singular since the structure is a mechanism, but it is possible that due to rounding during coordinate transformations, entries in columns k_i or k_j acquire small nonzero values. More generally, a tuple $\mathcal{S} \subseteq \{1, \dots, n\}$ of dofs can arise such that for $i \in \mathcal{S}$, k_{ij} is nonzero only for $j \in \mathcal{S}$.

The situation that would result in (b) is when certain elements that are disproportionately stiff in particular directions connect with more flexible elements in the neighbourhood. This results in a badly scaled matrix, and can be seen, for example, when beam or column members are split in numerous line elements—usually the result of importing a CAD drawing as an FE assembly.

Model stability analysis [3, sec. 4] makes use of the numerical properties of the eigenvectors of K to detect elements that cause the above scenarios. The key insight of our method is that eigenvectors corresponding to the largest and smallest eigenvalues, which we call the largest and smallest eigenvectors respectively, of K are numerically sparse. When the ill conditioning is caused by insufficient connectivity the eigenvectors corresponding to the one or more smallest eigenvalues are numerically sparse, whereas when the ill conditioning is from the presence of elements with disproportionately large stiffnesses the largest eigenvectors exhibit numerical sparsity. If we define the inner product terms

$$v^{(e)} = \frac{1}{2} u_i(m_e)^T u_i(m_e), \quad e \in \Omega \quad (3)$$

and

$$s^{(e)} = \frac{1}{2} u_i(m_e)^T T^{(e)T} K^{(e)} T^{(e)} u_i(m_e), \quad e \in \Omega \quad (4)$$

for a normalized eigenvector u_i and element e , then the elements that cause ill conditioning are those that have large relative values of either $v^{(e)}$ for the smallest eigenvectors or $s^{(e)}$ for the largest eigenvectors. The element-wise scalars $v^{(e)}$ and $s^{(e)}$, respectively, can be thought of as virtual kinetic and virtual strain energies associated with the modes of displacements defined by the eigenvectors; therefore we refer to them as virtual energies. The derivation of (3) makes use of perturbation theory for invariant subspaces. For (4) we employ a combination of sub-structuring and norm identities to prove the relationship. These are presented in [3] in detail.

Based on these relationships, model stability analysis computes the smallest and largest eigenpairs of K and then computes the virtual energies for each eigenvector. It is triggered when the condition number estimate is larger than a certain threshold τ in Algorithm 1. These virtual energies are then either printed as numerical output or graphically visualized as ‘contours’ on elements. Once the elements with large relative virtual energies are identified, the user must examine their definition (e.g., support conditions, nodal connectivity or section properties) for anomalies and fix discrepancies.

Algorithm 1 Algorithm for model stability analysis.

This algorithm has the following user-defined parameters: $n_s \geq 0$: the number of smallest eigenpairs; $n_\ell \geq 0$: the number of largest eigenpairs; $\tau > 1$: the condition number threshold for triggering analysis; $\text{gf} \geq 1$: the order of the gap between a cluster of smallest eigenvalues and the next largest eigenvalue.

1. Compute a condition number estimate $\text{est} \approx \kappa_1(K)$.
2. If $\text{est} < \tau$, exit.
3. Issue ill conditioning warning.
4. Compute the n_s smallest eigenvalues $\lambda_1, \lambda_2, \dots, \lambda_{n_s}$ and n_ℓ largest eigenvalues $\lambda_{n-n_\ell+1}, \dots, \lambda_n$ of K and normalize the associated eigenvectors.
5. With the smallest eigenpairs: determine if a gap exists, i.e., if there is a $k < n_s$ such that

$$\frac{\lambda_{k-1}}{\lambda_k} > \text{gf} \times \frac{\lambda_k}{\lambda_{k+1}}$$

If no such k is found go to step 7.

6. For each eigenvector u_i , $i = 1$ to k , calculate $v^{(e)}$ for all elements.
 7. With the largest eigenpairs: for each eigenvector u_i , $i = n - n_\ell + 1$ to n , compute $s^{(e)}$.
-

4. Examples

Model stability analysis has been applied on several real-world industrial models analysed in Oasis GSA. We present one example here, leaving the others to be presented in our talk.

Figure 1a shows a small portion of a larger model of façade cladding of a structure that consists of about 32000 elements and 21000 nodes resting on pinned supports. The glass façade panels are modelled using four noded plane-stress elements, supported on a grid of beam elements. Each panel rests on the grid of beams through springs at each of its four corners, as shown in the zoomed in view in Figure 1b. The model had a large condition estimate of $O(10^{12})$. Model stability analysis was run and it identified elements

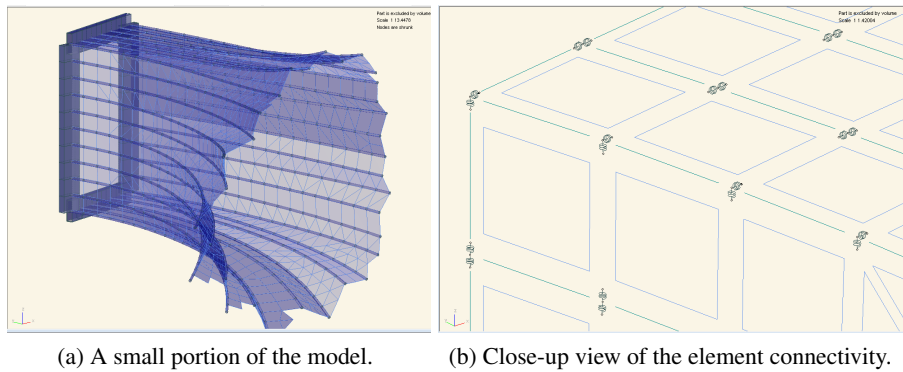


Figure 1: Façade model

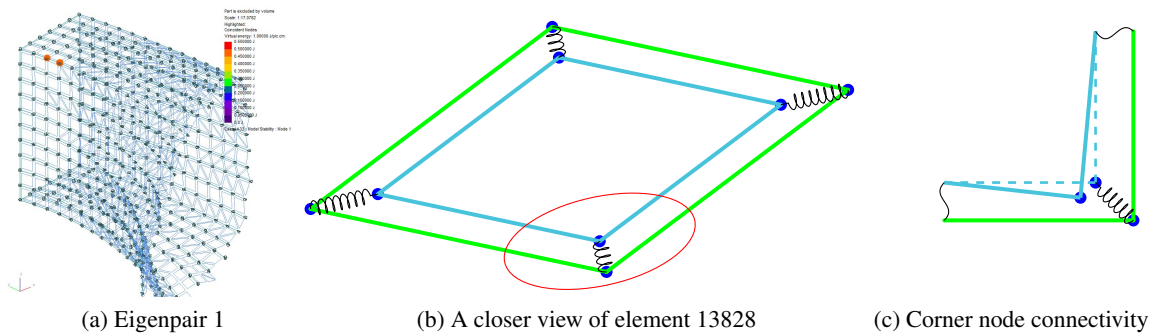


Figure 2: Element virtual energy visualization and nodal connectivity errors.

with large virtual strain energies (Fig. 2a). On investigation, we found an error in nodal connectivity: the element was connected to a nearby node instead of the node that is connected to the spring (see Fig. 2b and 2c). Fixing the nodal connection to the correct node brought the condition number down to $O(10^8)$.

5. Conclusion

Our work identifies a combination of two techniques to improve numerical accuracy of the solution from FE structural models: detecting the presence of ill conditioning using an condition number estimation and debugging the cause of ill conditioning using the novel method Model Stability Analysis. Often there might only be a handful poorly-defined elements (that cause ill conditioning) in a model with several hundreds of thousands of elements and nodes and, as such, it is time consuming and tedious to manually examine the definition of each entity in a FE model. Model stability analysis allows the practitioner to converge on these handful of elements relatively quickly and robustly.

Numerical ill conditioning and its affect on floating point arithmetic is under-discussed within the community of FE practitioners, so it is hoped that these techniques help understand its relevance and allow users to gain confidence in their results.

References

- [1] Nicholas J. Higham. *Accuracy and Stability of Numerical Algorithms*. Society for Industrial and Applied Mathematics, Philadelphia, PA, USA, second edition, 2002.
- [2] Nicholas J. Higham and Françoise Tisseur. A block algorithm for matrix 1-norm estimation, with an application to 1-norm pseudospectra. *SIAM J. Matrix Anal. Appl.*, 21(4):1185–1201, 2000.
- [3] Ramaseshan Kannan, Stephen Hendry, Nicholas J. Higham, and Françoise Tisseur. Detecting the causes of ill-conditioning in structural finite element models. *Computers and Structures*, 133(0):79 – 89, 2014.
- [4] Oasys Limited. Oasys GSA, available from <http://www.oasys-software.com/gsa>. Retrieved on January 20, 2015.

AN ALTERNATIVE METHOD FOR BEVERAGE CAN PARAMETER SCREENING

Andrew D. Evans, T.Nick Croft and Amit. Das
College of Engineering, Swansea University, Singleton Park, Swansea, SA2 8PP

487056@swansea.ac.uk

ABSTRACT

In the “Die Necking” process, a defect called wrinkling has huge cost and efficiency implications. To identify the cause of the defect, ten parameters including starting can height, percentage reduction, internal pressure, tool concentricity, thickness frequency, thickness amplitude, relative knockout speed, starting can radius and friction have been identified. Due to large number of parameters, a screening process must be adopted to narrow the parameters to four or less. A screening method combing the Plackett Burman and Taguchi method has been successfully developed to reduce computational time, while identifying possible trends. The study identified tool clearance, percentage reduction and friction as key parameters.

Keywords: Parameter Study; Die Necking; Finite Element Analysis; Beverage Can; Wrinkling

1. Introduction

The beverage can industry is continually improving manufacturing processes to reduce the overall consumption and wastage of aluminium, process energy consumption and defects in the product. Even though there has been huge investment into improving these factors, research has stagnated in recent years. This is mainly caused by omitting some (possibly important) parameters from investigation, and the continued increase in defects. Much of the research conducted in recent years has been focussed on structural requirements that the can must meet, rather than the formability of the can [2].

The “Die Necking” process (Figure 1) is one of the final metal forming operations in the beverage can production line. It is responsible for reducing the diameter of the can body in preparation for the attachment of the lid. Currently, there are increasing concerns over the appearance of “Wrinkles”, which are caused by the inherent compressive instability of thin sheet metal. There is very little data that can definitely isolate a parameter that is responsible for initiating the failure, or affecting the magnitude of the wrinkle.

The parameters that are linked to this case are, starting can height, percentage reduction, internal pressure, tool concentricity, thickness frequency, tool clearance, friction, thickness amplitude and thickness frequency. With this quantity of parameters, it becomes very computationally expensive to conduct a comprehensive Design of Experiments; therefore, an adequate screening process must be introduced to reduce the parameter selection to four or less.

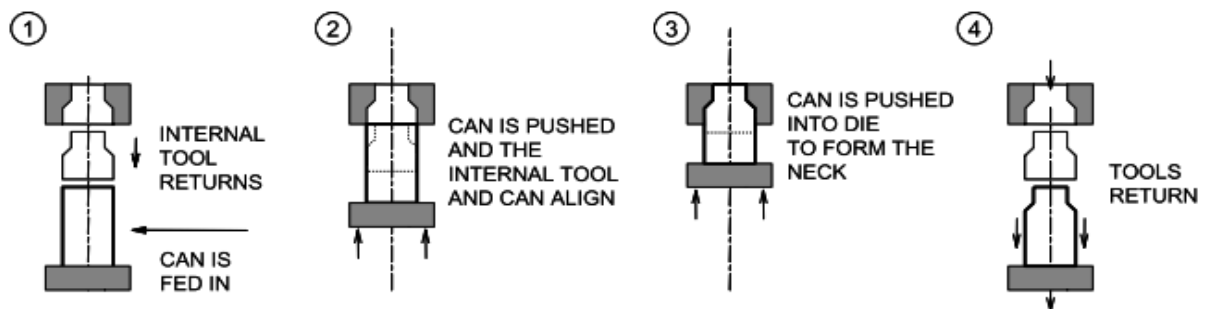


Figure 1: Operation of the Necking Process [1].

2. The “Die Necking” Process

In Figure 1, it is shown that each stage of the process operation is split into four steps. Step one simply feeds the can into the process, where the knockout (internal tool) is returned to the starting state. Step two pushes the can into the die, where the knockout and can have a synchronised movement. In step three, the can is pressurised once a seal is formed and the can is pushed and formed round the die, while the knockout provides internal support and deflects the can onto the die. Step four releases the can using a combination of air pressure and the knockout.

Thin metals are generally known to be unstable during compressive forces. This compressive instability can result in failure defects such as wrinkles, pleats and buckles. Due to the compressive nature of this process, the susceptibility of the can to defects is increased.

3. Wrinkle Definition

Wrinkles are increasingly the most common defect in the “Die Necking” process due to the inherent compressive instability of the material. In Figure 2 (Left), the appearance of the wrinkle profile appears to be a linear indentation in the can wall. They can appear one or more times round the circumference of the can.

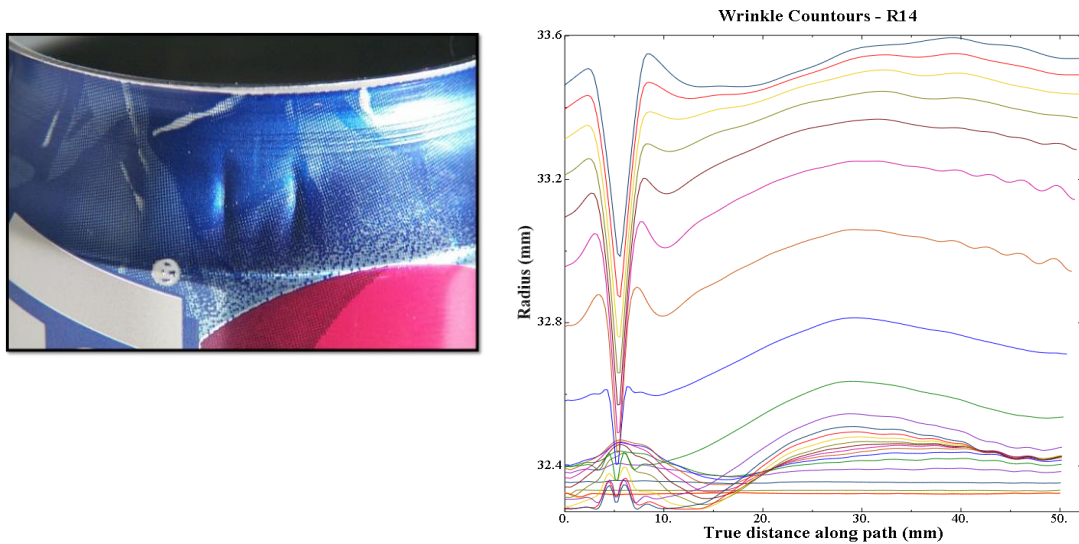


Figure 2: Showing a Double Wrinkle (Left) and a graph showing the radius vs path length (Right).

Numerically, it can be difficult to identify and quantify a wrinkle using stress alone. Therefore, the use of a “wrinkle factor” is used. The wrinkle factor is calculated by creating multiple node paths following the circumference of the can, and outputting the local coordinates position to generate the radius R at each node point, and the path length L_w as shown in Figure 2 (Right). The wrinkle factor f_w is represented as [1]:

$$f_w = \frac{L_w - L_{nom}}{L_{nom}} * 100 \quad (1)$$

From this the nominal arc length L_{nom} for each path is calculated,

$$L_{nom} = \frac{R_{avg} \pi \theta}{180} \quad (2)$$

Where R_{avg} is the average radius along path, and θ is the angle of the section i.e. if a quarter model is used $\theta=90^{\circ}$.

4. Parameter Study

For the parameter study, it was important to have a system that could run the minimum number of simulations, and supply enough data to eliminate some of the parameters. It is also beneficial to visually identify trends for future more in-depth studies. For this to occur, experiments where the parameter is assigned a high and low setting – such as Plackett Burman Designs – become obsolete; To get better resolution in the result, multiple parameter settings are more desirable, and in this case five settings desired. The Taguchi method allows for five settings per parameter to be applied; however, this would require one hundred simulations for ten parameters. Therefore, a method combining the minimal number of simulations in the Plackett Burman method is combined with the number of parameters in Taguchi method [3].

Table 1: showing the construction of the experiment where i is the parameter, j is the response number, k is the run number, x_{k+n} is the “high runs”, H_{ij} is the high response, z_{k+n} is the “low runs” and L_{ij} is the low response.

(i)	x_k	x_{k+1}	x_{k+n}	H_{ij}	z_k	z_{k+1}	z_{k+n}	L_{ij}
A	2	1	0	-1	-2	$H_{A,j}$	-2	1	0	-1	-2	$L_{A,j}$
B	-2	2	1	0	-1	$H_{B,j}$	-2	-2	1	0	-1	$L_{B,j}$
C	-1	-2	2	1	0	$H_{C,j}$	-1	-2	-2	1	0	$L_{C,j}$
D	0	-1	-2	2	1	$H_{D,j}$	0	-1	-2	-2	1	$L_{D,j}$
E	1	0	-1	-2	2	$H_{E,j}$	1	0	-1	-2	-2	$L_{E,j}$

As shown in Table 1, the settings for the parameters range from -2 to 2, where the value of a parameter increases with the setting value. The value should not be repeated in the corresponding row or column for the high set of runs x_{k+n} . The low set of runs z_{k+n} should have the same values as the high set, with an acceptance made for the highlighted (Blue) values, where the sign is inversed when compared to the highlighted (Red) values. The red and blue highlighted settings effectively become the high and low (respectively) settings similar to Plackett Burman.

Once the runs are completed, the response for the high values H_{ij} and the low values L_{ij} can be evaluated:

$$|H_{ij} - L_{ij}| = R_{ij} \quad (3)$$

Table 2: showing the construction of the Weighted Average table.

(i)	$R_{i,j}$	Rank (A_j)	$R_{i,j+1}$	Rank (A_{j+1})	$R_{i,j+n}$	Rank (A_{j+n})	Weighted Average (Wa_i)
A	...	1	...	1	...	1	...
B	...	2	...	2	...	2	...
C	...	3	...	3	...	3	...
D	...	4	...	4	...	4	...
E	...	5	...	5	...	5	...

The response is ranked from one to the total number of parameters, where one represents the largest effect. The weighted average is calculated as follows, where the smaller the number the larger the effect:

$$\sum_{j=1}^n \left(\frac{A_{j+1}}{R_{i,j+1}} \right) = Wa_i \quad (4)$$

The use of a weighted average reduces the risk of multiple parameters having the same rank average, and therefore ensures multiple parameters cannot be given the same overall rank position.

5. Results

To generate the results, the responses consisted of the wrinkle factor, change in average von Mises stress and change in von Mises stress variance, where the parameter study method described in section 4, was applied.

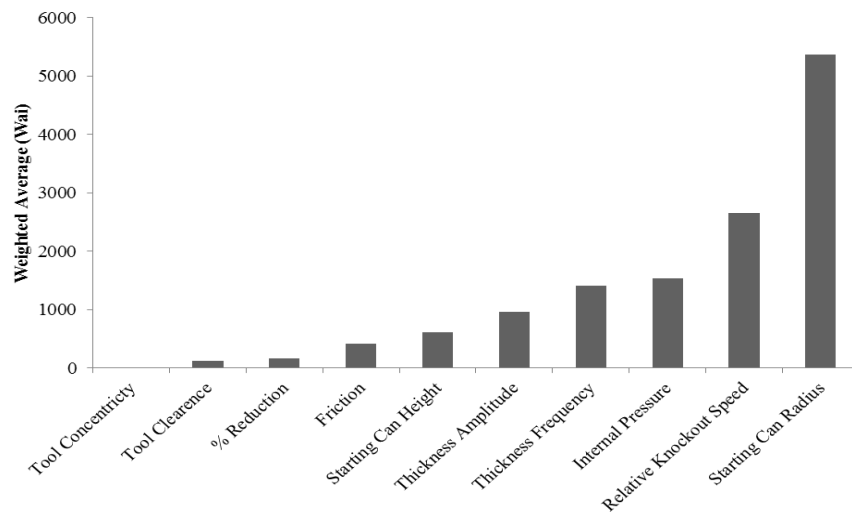


Figure 3: Showing the weighted average of each parameter.

As shown in Figure 3, the weighted average ranks tool concentricity, tool clearance, percentage reduction and friction as the most influential parameters. It is clear from these results, that tooling related effects have the biggest effect on the defect. In-fact, it was also shown that when the tooling become more in-concentric, the wrinkle factor increased by 0.5 each time, thus showing a potential trend; however it seems concentricity causes a buckle rather than a wrinkle. Friction had the largest effect on the wrinkle factor, where the difference was recorded at 3.63. Moreover, it was found that a change in the can radius and height affected the difference in von Mises stress by 12.55 MPa and 9.45MPa relatively. Can height and tool clearance have the biggest effect on the von Mises stress variance measured at 127 MPa and 88 MPa (relative).

6. Conclusions

As shown from the results, combining Plackett Burman and Taguchi methods provides a new and useful method for screening parameters. Some possible trends have been identified by using the multiple parameter settings, while keeping computational time at a minimum. This method has narrowed the parameters to tool clearance, percentage reduction and friction for the Taguchi Method parameter study.

References

- [1] A. Jordan-Cordera, J.C. Miranda-Valenzuela, Simulation and Analysis of the Beverage Can Necking Process Using LS-DYNA, in: *8th International LS-DYNA Users Conference*, 2004.
- [2] J.W. Yoon, R.P.R. Cardoso and R.E. Dick. Puncture Fracture in an Aluminium Beverage Can. *International Journal of Impact Engineering*, 37, 150-160, 2010.
- [3] R.L. Mason, R.F. Gunst and J.L. Hess, *Statistical Design and Analysis of Experiments*, 2nd Edition, Wiley – Interscience, 2003.

A Powell-Sabin B-spline method for Kirchhoff-Love plates

*Stefan May, Julien Vignollet and René de Borst

School of Engineering, University of Glasgow, Oakfield Avenue, Rankine Building, Glasgow G12 8LT

*s.may.2@research.gla.ac.uk

ABSTRACT

Since quadratic Powell-Sabin B-splines result in C^1 -continuous shape functions, they are of sufficiently high continuity to capture Kirchhoff-Love plate theory when cast in a weak form. Unlike Non-Uniform Rational B-Splines (NURBS) and T-splines which are commonly used in isogeometric analysis, Powell-Sabin B-splines do not necessarily capture the geometry exactly. However, the fact that they are defined on triangles instead of on quadrilaterals increases their flexibility in meshing, and can make them competitive with respect to NURBS or T-splines, as no bending strip method for joined NURBS-patches is needed, and no extraordinary points exist, which may deteriorate convergence upon mesh refinement. This is illustrated in a study of a circular plate, comparing the performance of quadratic Powell-Sabin B-splines, NURBS and T-splines.

Key Words: *Powell-Sabin B-splines; isogeometric analysis; higher continuity; NURBS; T-splines*

1. Introduction

The idea of applying basis functions like NURBS or T-splines, which are routinely used in Computer Aided Design (CAD), to analysis as well, was introduced in [1] and is now commonly termed IsoGeometric Analysis (IGA). Since, in practice, it can happen that different NURBS-patches have to be joined, the bending strip method was proposed in order to preserve C^1 -continuity at the boundaries between the patches [2]. Nevertheless, when three or more than four NURBS-patches are joined, extraordinary points can be introduced, which may influence convergence upon mesh refinement. In fact, the convergence behaviour of the bending strip method has not been tested for the latter case. T-splines make it possible to remove some lines that are C^0 -continuous between NURBS-patches. However, T-spline meshes still exhibit C^0 -lines around extraordinary points, which may impair convergence upon mesh refinement.

Quadratic Powell-Sabin (PS) B-splines also provide shape functions that give a higher continuity [3]. They are based on a linear triangulation and have quadratic shape functions that are C^1 -continuous across elements. It is noted that Powell-Sabin B-splines are not based on the isogeometric concept as they can only approximate the exact geometry.

In this work, we compare two isogeometric analysis methods (NURBS and T-splines) with Powell-Sabin B-splines. As a test problem we take a circular Kirchhoff-Love plate. Particular attention is given to the cases when extraordinary points are introduced into the mesh, as the effect of extraordinary points on the convergence behaviour of fourth-order partial differential equations has so far not been studied.

2. The representation of a disc with NURBS, T-splines and Powell-Sabin B-splines

In this section, a number of representations for a disc using NURBS, T-splines and Powell-Sabin B-splines is created. The first two methods can represent a circular boundary exactly, but the triangulation for Powell-Sabin B-splines is based on a finite element triangulation and therefore approximates a circle.

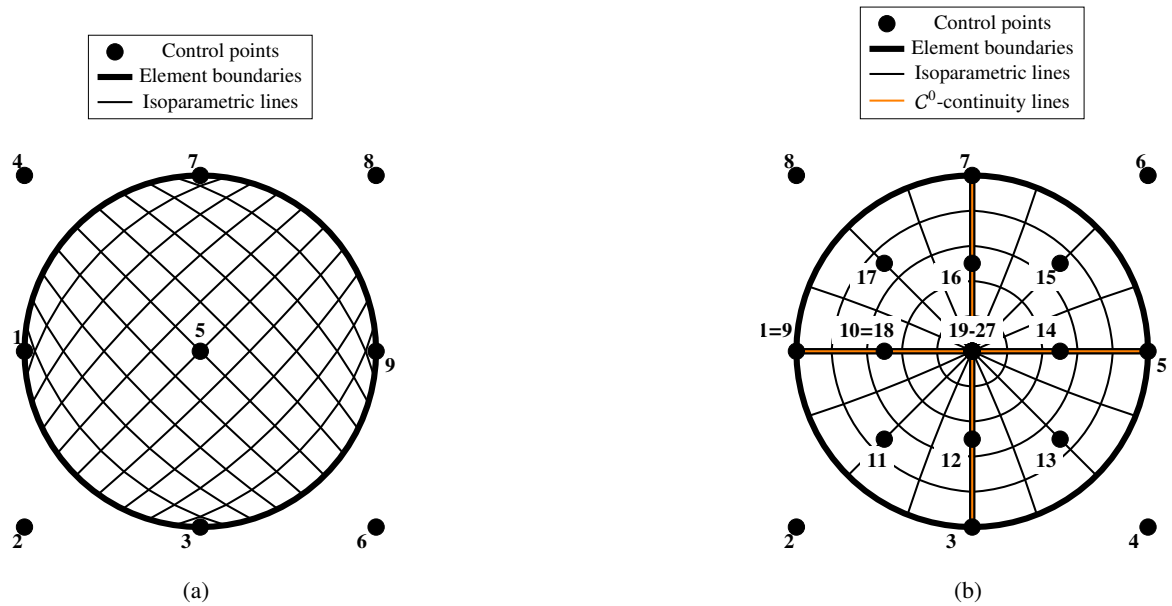


Figure 1: Representation of a disc using NURBS with (a) one single quadratic element / patch and (b) a polar parameterisation using four patches.

2.1. Representing a disc with NURBS

An area with a circular boundary can be created with a single NURBS-patch (one element), see Figure 1(a) or by a polar parameterisation that uses four NURBS-patches, Figure 1(b). The polar parameterisation results in a singular / degenerated point in the centre. Also, four C^0 -continuity lines (orange) are introduced. The bending strip method proposed in [2] will be employed in Section 3 at these C^0 -continuity lines.

In real world applications, CAD geometries contain NURBS-patches which meet at extraordinary points (vertices, which are touched by less or more than four edges). The convergence behaviour of the bending strip method in [2] has not been investigated for meshes with extraordinary points, and a study will therefore now be carried out. The disc will be modelled using five patches as shown in Figure 2(a).

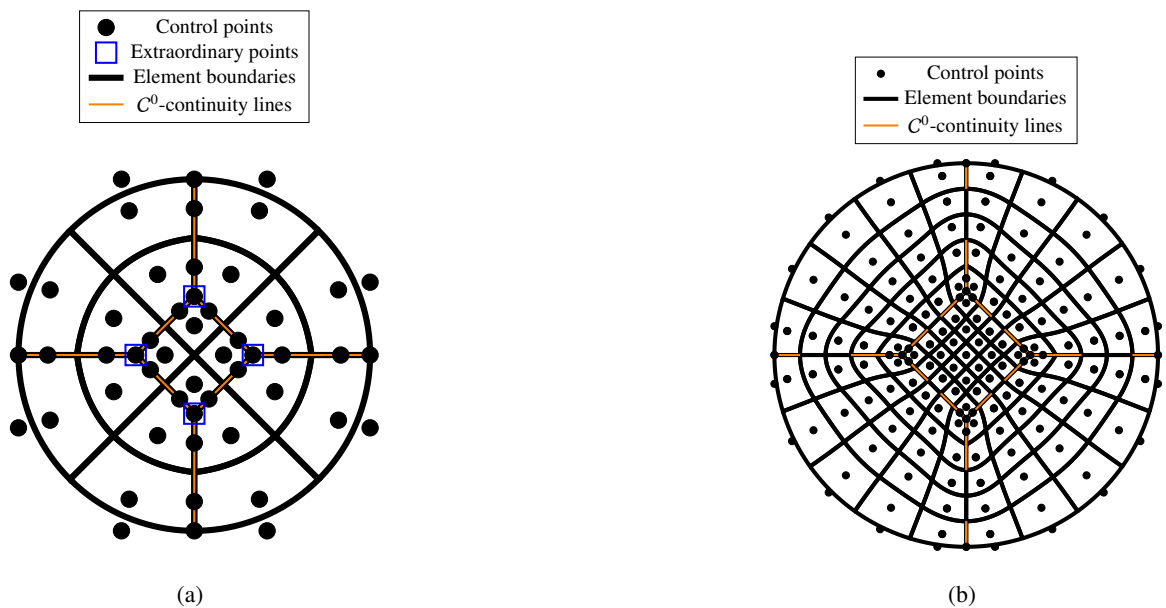


Figure 2: Representation of a disc using (a) five NURBS-patches and (b) T-splines

The mesh in Figure 2(a) contains four extraordinary points (marked with blue squares) and eight C^0 -continuity lines (orange). Similar to the polar parameterisation, the bending strip method will be applied in Section 3 along the C^0 -continuity lines.

2.2. Representation of a disc using T-splines

Using T-spline technology, some of the C^0 -continuity lines in Figure 2(a) can be removed. The T-spline mesh in the physical domain for the whole disc is shown in Figure 2(b). It can be observed that for the T-spline mesh C^0 -continuity lines emerge from the extraordinary points which span over two elements. Furthermore, there are C^0 -continuity lines on the boundary spanning over one element.

2.3. Representing a disc with PS B-splines

A linear C^0 finite element triangulation \mathcal{T} can be transformed into a C^1 Powell-Sabin B-spline mesh \mathcal{T}^* , cf. Figure 3. For this case, the circular boundary of the disc is only approximated.

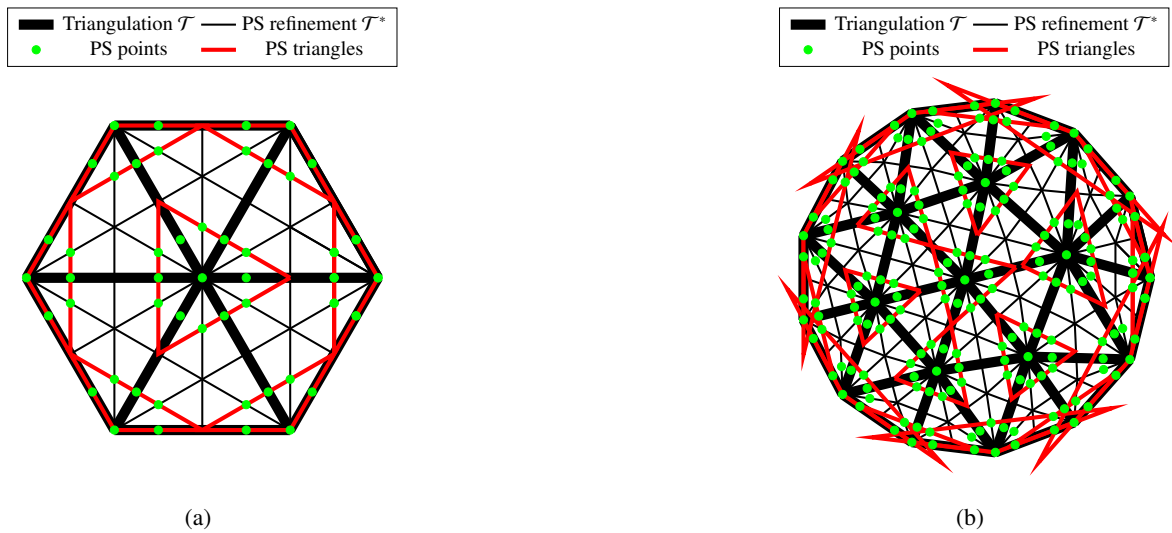


Figure 3: Approximation of a circle using Powell-Sabin B-splines for two different levels of refinement.

3. Numerical results

In this section the circular Kirchhoff-Love plate is considered for the simply supported case. In the following, the results for the single NURBS-patch will be plotted in all convergence plots for comparison.

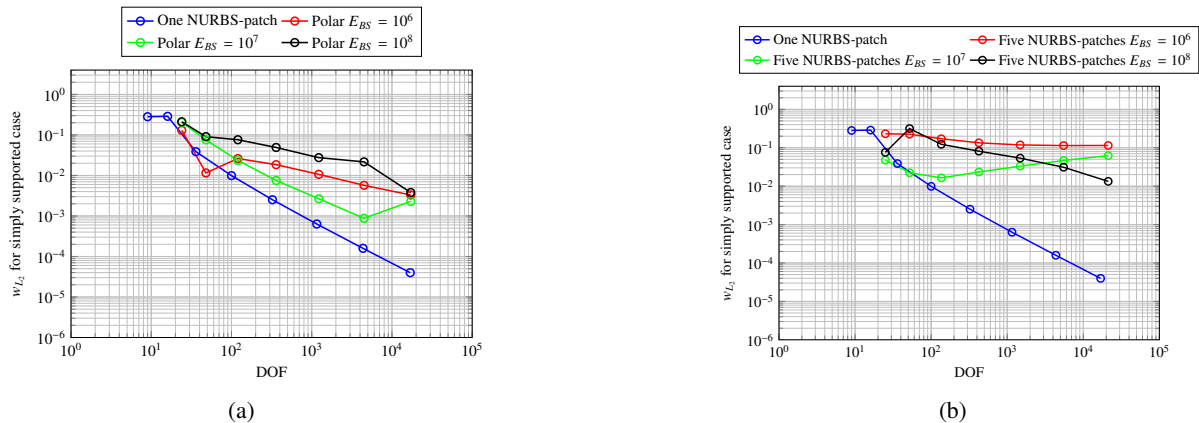


Figure 4: Convergence plots for the single NURBS-patch and (a) for the polar NURBS parameterisation using four NURBS-patches and (b) for the representation using five NURBS-patches with extraordinary points.

Figure 5(a) shows the error in the L^2 -norm when the circle is represented with four NURBS-patches and a polar parameterisation. The bending strip method has been applied at the C^0 -lines for different values of the penalty stiffness. The results do not converge well for the polar parameterisation with a singular point in the centre, in particular for the finer meshes.

In Figure 4(b) a convergence study is presented for the configuration that consists of five NURBS-patches with extraordinary points. Again, the bending strip method has been applied at C^0 -lines with different

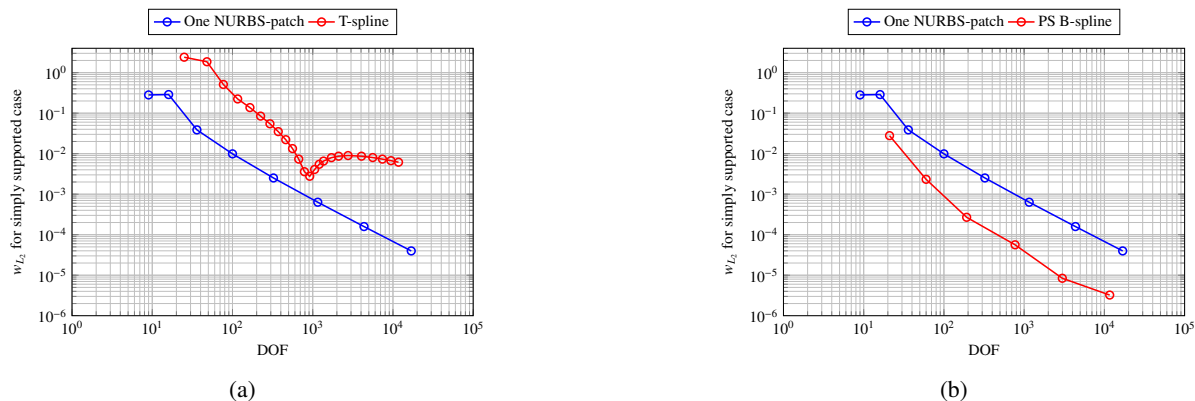


Figure 5: Convergence plots for the single NURBS-patch and (a) the T-spline mesh and for (b) the Powell-Sabin B-splines.

values of the penalty stiffness. Also in this case, convergence is poor, and for some values of the penalty parameter no convergence is observed at all.

Figure 5(a) gives the results upon mesh refinement for the T-spline representation of Section 2.2, again together with the results that stem from the single NURBS-patch for comparison. The graph for the error w_{L_2} exhibits a clear kink. This convergence behaviour is surprising since one could have assumed that due to the decrease in size of the C^0 -continuity lines upon mesh refinement, the convergence rates for the T-spline meshes would have improved.

Finally, the results for the standard Powell-Sabin B-spline computations are given in Figure 5(b). Unexpectedly, the Powell-Sabin B-spline mesh, which only *approximates* the geometry, gives a lower error w_{L_2} than the single NURBS-patch.

4. Concluding remarks

In this work a method has been developed to solve boundary value problems that stem from Kirchhoff-Love plate theory using quadratic Powell-Sabin B-splines. By virtue of the fact that these interpolation functions are C^1 -continuous, the resulting fourth-order partial differential equation can be solved properly.

Quadratic Powell-Sabin B-splines have a disadvantage compared to NURBS and T-splines as the geometry is generally not captured exactly. Conversely, the fact that they are based on a triangular discretisation facilitates meshing and avoids using the bending strip method [2] for joined NURBS-patches, or the emergence of extraordinary points in T-spline meshes, which can deteriorate convergence upon mesh refinement.

To give a first assessment of the advantages and drawbacks of quadratic Powell-Sabin B-splines compared to NURBS and T-splines a circular Kirchhoff-Love plate has been considered. Different representations of the disc have been examined, including a single NURBS-patch, a polar parameterisation consisting of four NURBS-patches, five NURBS-patches with extraordinary points, T-spline meshes (also with extraordinary points), and Powell-Sabin B-splines. The numerical results show that the use of the bending strip method and the existence of extraordinary points (with the attendant C^0 -continuity lines in their vicinity) can impair convergence significantly when the discretisation is refined.

References

- [1] Hughes TJR, Cottrell JA, Bazilevs Y. Isogeometric analysis: CAD, finite elements, NURBS, exact geometry and mesh refinement. *Computer Methods in Applied Mechanics and Engineering* 2005; 194(39-41):4135–4195.
- [2] Kiendl J, Bazilevs Y, Hsu MC, Wüchner R, Bletzinger KU. The bending strip method for isogeometric analysis of Kirchhoff-Love shell structures comprised of multiple patches. *Computer Methods in Applied Mechanics and Engineering* 2010; 199(37–40):2403–2416.
- [3] Powell MJD, Sabin MA. Piecewise Quadratic Approximations on Triangles. *ACM Transactions on Mathematical Software* 1977; 3(4):316–325.

NUMERICAL STUDY OF EFFECTIVE BOND LENGTH FOR EXTERNALLY BONDED CFRP PLATE UNDER CYCLIC LOADING

*Raid Daud ^{1,2}, Lee Cunningham ¹ and Yong Wang ¹

¹ School of Mechanical, Aerospace and Civil Engineering, The University of Manchester, Pariser Building,
Manchester, UK, M13 9PL

² Department of Civil Engineering, Al-Nahrain University, Baghdad, Iraq

*raid.daud@postgrad.manchester.ac.uk

ABSTRACT

The reliability of bond is crucial to the performance of concrete structures strengthened with externally mounted CFRP plate. This paper presents a detailed description of a finite element model constructed using ABAQUS 6.10-1, to simulate the behaviour of CFRP-to-concrete bonded joints in single shear pull out tests. Nonlinear finite element analysis with the cohesive surface approach for single shear pull out tests was investigated and validated against existing test results (monotonic and post-fatigue) in order to demonstrate the accuracy of the model. The influence of bond length for different carbon fibre plate stiffness on the ultimate load as well as the de-bonding strain for the post-fatigue analysis was investigated and then compared with existing analytical models. The numerical results suggest that existing analytical models can be non-conservative in estimating the FRP effective bond length in the post-fatigue load regime.

Keywords: *Post-fatigue; Effective bond length; CFRP*

1. Introduction

Recent research has shown that repetitive loading may lead to degradation of bond behaviour between carbon fibre reinforced plate (CFRP) and concrete, Harries and Aidoo [1]. Thus, catastrophic failure may occur at a much smaller load than that adopted for static design. The main focus of this study is to understand the effect of the CFRP plate bond length on the ultimate load capacity and de-bonding strain in a post-fatigue loading regime through detailed finite element (FE) simulation. The effective bond length (L_e) may be defined as the active bond zone required to transfer the tension in CFRP plate to the concrete via interfacial shear stresses, Khalifa et al. [2]. Using the commercially available software ABAQUS [3], a 3D FE model of single shear pull-out tests was developed and then validated against the author's experimental results. The experimental work consisted of a series of six specimens subjected to monotonic loading and other six specimens subjected to fatigue loading. The fatigue load specimens were loaded until an interfacial slip of 0.4 mm was reached then monotonic loading was applied until failure. The specimens consisted of 50 x 500 mm CFRP plate and a concrete substrate with dimensions 150x200x500 mm. A 300 mm length of CFRP was bonded to the concrete substrate, whereas a 40 mm (notch) was left unbonded near the loaded end to avoid sudden localised failure, adopting a similar set-up to previous researchers, Yao et al. [4]. This paper describes the FE model and compares the numerical load-slip curves with existing experimental data. Additionally the strain profile for both monotonic and post-fatigue tests with the current analysis is investigated. Further to this post-fatigue analysis is conducted to estimate the effective bond length for different CFRP plate stiffnesses and a comparison made with existing analytical models.

2. Finite Element Model

The simulation model is constructed using the general finite element software ABAQUS. Figure 1 shows the structure to be modelled. Two different element types (soild, shell) have been used to model the different materials. For the concrete substrate, the three dimensional eight-node linear brick elements with reduced integration and hourglass control (C3D8R) were adopted. For the CFRP plate,

linear three dimensional four-node doubly curved general purpose shell elements with reduced integration and hourglass control were used, these account for the finite membrane strains with five degrees of freedom per node (S4R5).

The adhesive joint was modelled using the cohesive surface approach. This technique represents the surface interaction properties by selecting the concrete surface as a master surface and the CFRP surface as a slave surface to assign a contact pair. Figure 1 shows the support conditions in the single shear pull out test, the concrete substrate facing was restricted in the X, Y, Z directions to prevent movement in the direction of loading to simulate the real case. Further details of the modelling procedure can be found in Daud et. al. [5].

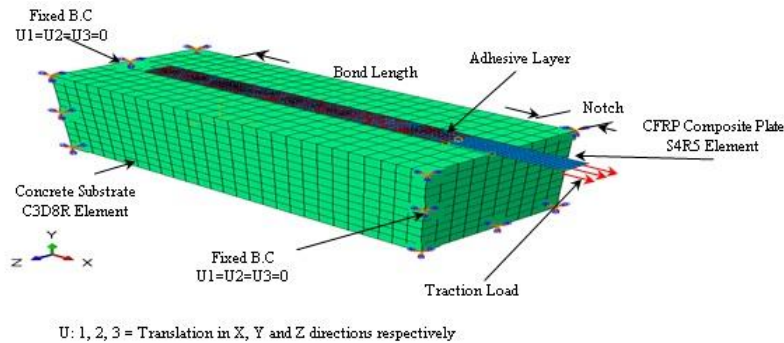


Figure 1: Specimen Characteristics and The Test Configuration for The Single Shear Pull-out Test

3. Interfacial Bond Stress and Fracture Energy

In the experimental series conducted by the author, the post-fatigue interfacial bond stress-slip relationship showed that both the ultimate bond strength and fracture energy reduces with increase in CFRP plate stiffness for the range of the concrete compressive strengths tested (22.6 MPa - 52.8 MPa). These results indicated that the post- fatigue bond stress-slip relationship is more sensitive to plate stiffness compared to the concrete compressive strength. These reductions are due to cyclic loading history, whereby each single shear pull-out test was subjected to load cycles until 0.4 mm slip between the CFRP and concrete substrate was reached. From the experimental series, the relationship between the CFRP plate stiffness with the ultimate bond strength reduction and the fracture energy degradation are deduced and shown in Figure 2 (a) and (b), respectively. The fracture energy degradation is calculated as a difference between the monotonic and post-fatigue fracture energy. Also, the fracture energy was estimated by measuring the area under the bond-slip curve. Numerical simulations were then implemented to validate the current interfacial bond stress- slip model, as will be discussed in the next section. This experimental data is needed in the cohesive surface approach to define the interaction properties between the CFRP plate and concrete.

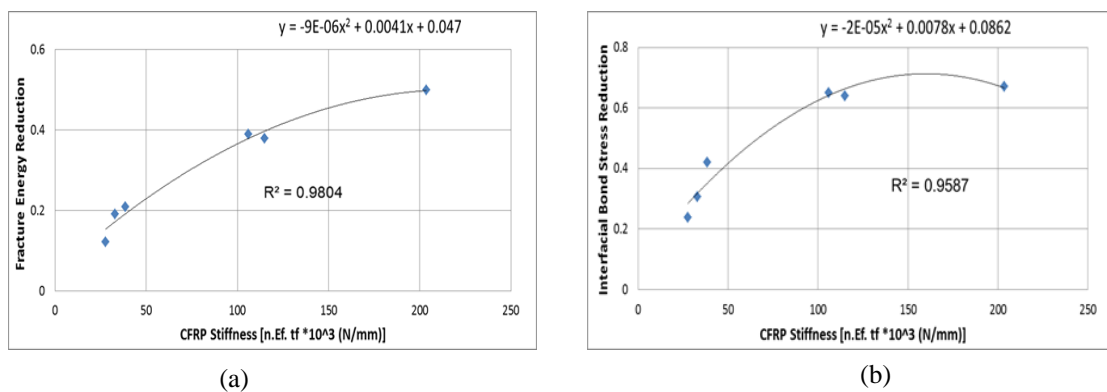


Figure 2: (a) Experimental Interfacial Bond Stress Reduction CFRP Stiffness Relationship (b) Experimental Fracture Energy Reduction CFRP Stiffness Relationship

4. Validation of The Finite Element Results

Figure 3 shows the comparison between the numerical results and their corresponding experimental results for representative specimens (0.4 mm M46J), respectively. These results are given in the form of strain distribution along the middle of the bonded CFRP and load slip curves. The favourable comparison indicates the validity of the numerical models in capturing the test results for both the monotonic and post-fatigue cases through the entire behaviour of the single shear pull out test.

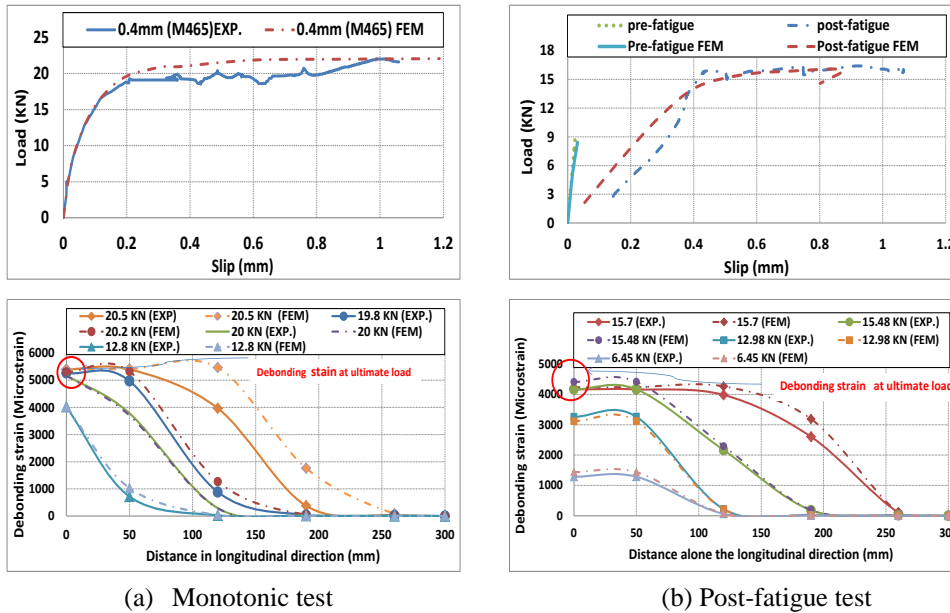


Figure 3: Representative Comparisons between Numerical and Experimental Load-Slip Relationships and Stain Distribution along CFRP Plate (0.4 mm M46J)

5. Effect of Bond Length Based on FE Post-fatigue Analysis

The effects of bond length on the de-bonding strain and ultimate load are studied for the six post-fatigue single shear pull-out test specimens (i.e. different CFRP plate type and different thicknesses) and then compared with Chen and Teng's [6] analytical model. Figure 4 demonstrates the effect of bond length on the ultimate load and de-bonding strain for six different CFRP plate stiffnesses (E_{tf}).

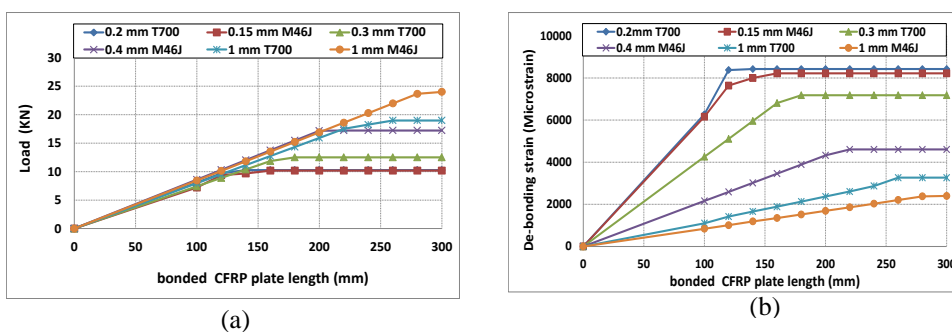


Figure 4: Effect of Bonded CFRP Plate Length. (a) Ultimate Load; (b) De-bonding Strain

A comprehensive study of the effect of variations in length on the bonded CFRP plate was conducted. During this study, separate analyses were performed at 100 mm to 300 mm lengths, at intervals of 20 mm. It can be seen that the ultimate load and de-bonding strain increases with increasing bond length until an effective bond length (L_e) is reached, beyond which an extension of the bond length cannot increase the ultimate load and de-bonding strain. The effective length ranges from 140 mm for specimen (0.2 mm T700) to 280 mm for specimen (1 mm M46J). Figure 5 shows a plot of effective length against CFRP stiffness. It is clear that the effective length increases linearly with $\sqrt{E_f \cdot t_f}$ in a

similar way to the behaviour predicted by the analytical model proposed by Chen and Teng [6]. However, the values predicted by the analytical model show a significant difference and potential non-conservatism with the current post-fatigue FE effective length results. This is largely because the Chen and Teng's [6] analytical model was based on experimental data obtained from monotonic tests. Hence, the anchorage designs of an externally bonded plate have to consider the effective bond length limit in the fatigue and post-fatigue regime in practice in order to mobilise full tensile strength of the CFRP plate.

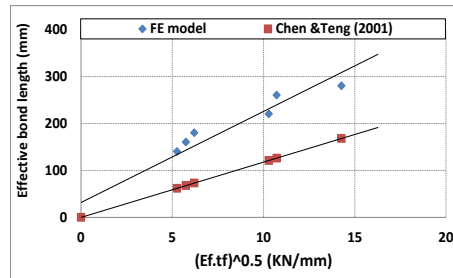


Figure 5: Effect of Bonded CFRP Plate Stiffness on Effective Bond Length

6. Conclusions

- The surface cohesive based model can adequately describe the bond between the CFRP plate and the concrete.
- The experimentally obtained reductions of interfacial bond stress and fracture energy due to previous cyclic loading have been input as interaction properties in the post-fatigue numerical model.
- The post-fatigue numerical study has highlighted the CFRP plate stiffness influence on the effective bonded length, the specimen with CFRP plate stiffness = 27.67 kN/mm the effective length = 140 mm while the specimen with CFRP plate stiffness = 203.5 kN/mm the effective length = 280 mm.
- Chen and Teng's [6] analytical model shows non-conservatism in estimating the post-fatigue FE effective length results for the range of specimens investigated.
- In practice, the anchorage design of externally bonded CFRP plates needs to consider the effective bond length limit for the fatigue and post-fatigue loading regimes.

Acknowledgments

Our thanks to “*The Higher Committee for Education Development in Iraq*” for funding this research. Sincere thanks are expressed to *School of Mechanical, Aerospace and Civil Engineering* of the University of Manchester for providing the facilities to undertake this research.

References

- [1] Harries KA, Aidoo J. Debonding- and fatigue-related strain limits for externally bonded FRP. *Journal of Composites for Construction*; 2006, 10 (1):87–90.
- [2] Khalifa, A., Gold, W. J., Nanni, A., & MI, A. A. Contribution of externally bonded FRP to shear capacity of RC flexural members. *Journal of Composites for Construction*, 1998, 2(4), 195-202.
- [3] ABAQUS Theory Manual, User Manual and Example Manual, Version 6.10, Providence, RI. 2011.
- [4] Yao, J Teng, J. G.; Chen, J. F. Experimental study on FRP-to-concrete bonded joints. *Composites Part B: Engineering*, 2005, 36.2: 99-113
- [5] Daud R, Cunningham L, Wang Y. Non-linear FE Modelling of CFRP-Strengthened RC Slabs under Cyclic Loading. Atiner's Conference Paper Series. 2014, CIV2014-0971.
- [6] Chen, J. F., Teng, J. G. Anchorage strength models for FRP and steel plates bonded to concrete. *Journal of Structural Engineering*. 2001, 127(7), 784-791.

SOLIDS AND STRUCTURES 3

A Comparison of Response Surface Methodologies to Represent Crushing Behaviour of Thin-Walled Tubes

*Charles G. T. Mortished^{1,2}, Johann Sienz¹ and Peter Benzie²

¹College of Engineering, Swansea University, Singleton Park, Swansea, SA2 8PP

²Altair Product Design, Imperial House, Holly Walk, Leamington Spa, CV32 4JG

*charles.mortished@uk.altair.com

ABSTRACT

Thin-walled tubes are used in automotive crash structures to absorb energy. Traditional methods of automotive crash analysis are time consuming; reduced fidelity modelling techniques can decrease this requirement. Crushable frame springs can be employed to replace the shell element representations of these thin-walled tubes. One of the main drawbacks of the crushable frame spring method is that a full shell finite element analysis of the cross-section must first be carried out. A cross section library would alleviate this by providing pre-calculated sections. The results of this study show that response surface methodologies can be utilised in lieu of a finite element analysis for each possible cross-section when populating this library. It was found that of the examined response surface methodologies the moving least squares method was the most suitable for this purpose.

Keywords: *Concept Crash Analysis; Crushable Frame Spring; Moving Least Squares; Kriging; Neural Network*

1. Introduction

Traditional methods of automotive vehicle crash analysis are expensive in terms of human and computational resource. Reduced fidelity models, such as the crushable frame spring (CFS) method, decrease the demand on both these resources; thus providing information earlier in the concept design phase of a vehicle development programme than would otherwise be possible. The concept design phase is where there is most design freedom and the highest rate of design change. In order to provide meaningful design direction creation and analysis of models must be rapid. The CFS method allows the user to map the crush response of a thin-walled cross section from a detailed shell analysis to a specially formulated spring element for later use. The CFS element, available in RADIOSS 13.0 [1], is similar to a traditional 6 degrees of freedom non-linear spring, however may also communicate its collapse status to neighbouring elements and has response curves for collapsed and un-collapsed crush phases allowing it to better capture crush response. A section library would give the user to access a selection of properties relating to different cross sections; however a discrete library containing every possible variation of a cross-section would require a prohibitively large number of data points to fill. In the field of optimisation, response surface technologies such as the moving least squares (MLS) method, Kriging (KR) and back propagating neural networks (NN) are used to approximate non-linear responses such as the crush properties of thin-walled tubes [2]. The MLS method was first described by Lancaster and Salkauskas for “smoothing and interpolating scattered data”[3]. The KR method, originally developed for mining applications, takes into account the statistical importance of the points as described in [4]. NN are constructed from a network of nodes, which output a function of the summation of inputs, connected by weights which may be optimised such that a desired output can be obtained for a given input.

Using these methods a parameterised cross section library could be created using fewer evaluation points than would be required for a discrete library. This would allow the user or optimisation algorithm access to any combination of variations of a cross section within given bounds.

In this case study the geometry and material thickness of a simple cross section, typical of an automotive front rail, are varied and three main responses relating to the crush properties of the sections are captured. Three different response surfaces are created using three different

methodologies, the results from finite element and these response surfaces are then compared to assess accuracy.

2. Methodology

To assess the suitability of the response surface methodologies under evaluation for creation of a parameterised section library, the test section shown in Figure 1 was evaluated with varying dimensions. These variations were achieved through perturbations of the points labelled A to D for variation in overall height and width of the section and, the points E and F allowing for movement of the cross plate in the Y-axis. In this study the cross plate was kept parallel to the Z-axis. The material thickness can also be varied. Three test cases of varying complexity were evaluated, (i) overall height & width, (ii) overall height & width and position of cross plate and, (iii) overall height & width, position of cross plate and, material thickness. A baseline height and width of 40mm and a material thickness of 1.5mm was used. From this, a variation in the height and width of 20mm, a variation in the position of the cross-plate of 10mm and, a variation of 1mm of material thickness is permitted.

The design of experiments (DoE) used to populate the response surfaces are created using an Optimal Latin Hypercube [5] to ensure that the evaluation points are evenly spread about the design space. To assess the effect of the resolution of populating the DoE, six levels are considered; 20, 50, 100, 200, 300 and, 400. The DoEs are imported into the optimisation, statistics and run managing environment HyperStudy, from here the points in the DoE are converted to geometry and finite element decks through the use of a custom TCL script and HyperMesh. The automatically created sections are then analysed using the explicit finite element solver RADIOSS.

Of three different response surface methodologies under investigation the MLS, and KR methods are assessed using the inbuilt functionality within HyperStudy and the NN is assessed using the FANN library [6]. The MLS method was a first order method using a Gaussian weighting function and a fit parameter of 5, the NN used two hidden layers with 13 nodes each.

To assess the accuracy of the response surface methods, a validation DoE is used to compare the results obtained from finite element and the response surface methodologies. The error is calculated as shown in equation (1). The validation DoE is a combination of two Optimal Latin Hypercubes of 55 & 25 points respectively and 20 random points; to ensure that the validation set differs from the populating sets.

$$Absolute\ Error = 100 * \sqrt{\left(\frac{Finite\ Element\ Result - Response\ Surface\ Result}{Finite\ Element\ Result}\right)^2} \quad (1)$$

Three responses are considered, as show in Figure 2; the initial peak force, the crush length or crushable length and, the mean crush force over the crushable length.

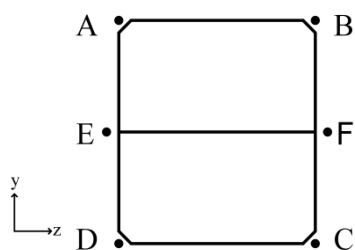


Figure 1: Cross Section Diagram

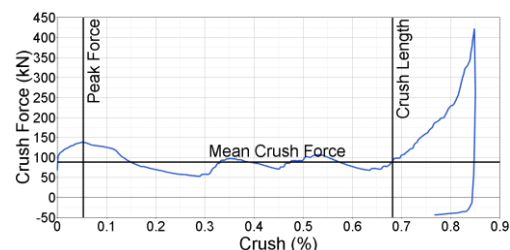


Figure 2: Baseline Load - Crush Profile

3. Results

The average error for the two degree of freedom test case shown in Figure 3 decreases as the number of populating DoE points increase until 100 points, after which the error plateaus. This suggests that the minimum error possible has been reached. The three degree of freedom test case shown in Figure 4 shows a similar decline up to 100 DoE points after which the decline in error is reduced reaching a similar level to the two degree of freedom test case at 400 DoE points with an error of around 1.5%.

The four degree of freedom test case starts with a higher error and does not plateau after 100 DoE points as shown in Figure 5, this is due to the higher relative complexity of the design space in comparison with the two and three degree of freedom test cases.

The maximum error exhibited by the MLS method is shown in Figure 6. The four degree of freedom test case shows a far higher dependence on the number of populating DoE points than the other two test cases.

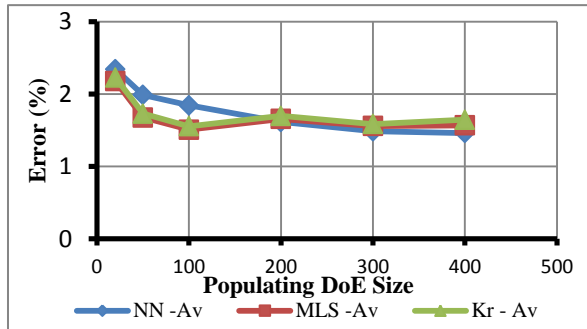


Figure 3: Two Degrees of Freedom Average Error

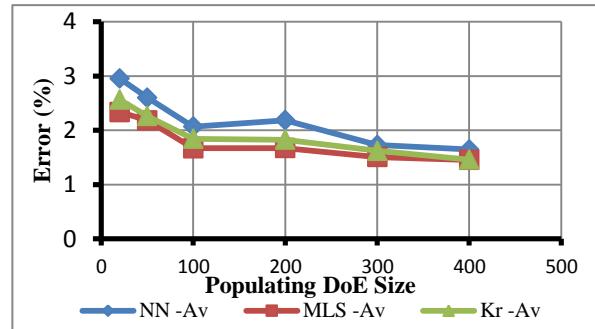


Figure 4: Three Degrees of Freedom Average Error

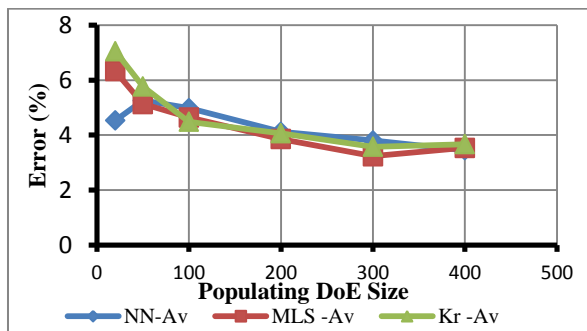


Figure 5: Four Degrees of Freedom Average Error

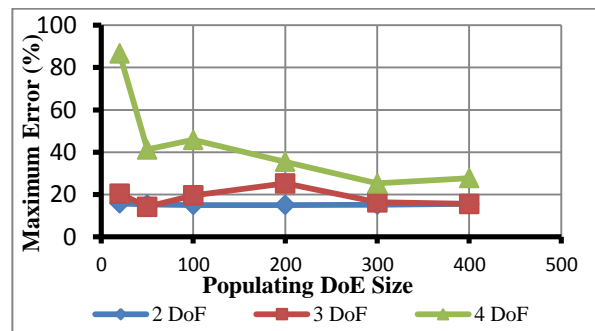


Figure 6: MLS Maximum Error

Table 1 shows that the peak force is captured most accurately, followed by the mean force, then crushable length. This is also observed in the other test cases and number of populating DoE points. As the mean force is evaluated at the maximum crush length improving the identification of the crush length could improve both results.

Table 1: Results from Four Degrees of Freedom and 300 Populating DoE Points

	NN Error (%)		MLS Error (%)		KR Error (%)	
	Average	Max	Average	Max	Average	Max
Peak Force	1.628756	16.876	0.705225	3.903254	0.640054	4.246445
Crush Length	6.731962	23.52859	5.90077	25.25833	6.834888	33.65096
Mean Force	3.40903	33.64207	3.097757	17.38501	3.252548	19.92343

4. Discussion

The results show that it is possible to obtain low average errors for the crush properties of the cross section shown in Figure 1. Errors around this level would be acceptable for the creation of a parameterised section library. The maximum errors for the two and three degree of freedom test cases make these approximations useable, however, for the four degree of freedom test case the error is higher than would be acceptable. In the four degree of freedom test case roughly 20% evaluated cross sections exhibit over 10% error in the crushable length. For mean crushing force this is true for only 8% with no errors over 10% for the peak crushable force. Of the points with over 10% error, 70% are not in the same position when evaluated with each of the different response surfaces methodologies. This means that if responses from all three response surfaces are compared, discrepancies could alert the user to a possible high error at that evaluation point.

As the complexity of the test cases increased, the number of DoE points required to capture the response is higher. The maximum error is more sensitive to the increase in complexity than the average error.

The MLS method consistently shows the lowest average error, this is followed by the KR method. The NN method shows lower maximum error for the two and three degrees of freedom test cases, closely followed by the MLS method which shows better performance in the four degrees of freedom test case.

Creation of the MLS and KR response surfaces can be performed quickly and are repeatable; however the NN surface requires training. Training can require far more time to perform than creation of the other response surfaces, and in this case takes the form of a gradient based optimisation. This means that the optimisation is dependent on starting weights, and as such may converge to a local minimum and therefore is not repeatable if the weights are initialised with random points.

A coarse cross-section library with sections at a geometry incremented at 1mm and thickness at .5mm would require 441, 4851 & 24255 finite element analysis for the two, three & four degree of freedom test cases respectively to fill the design space explored in this study, this would not be practical.

5. Conclusion

The CFS method has the potential to provide engineers with vehicle crash performance information earlier within the automotive design phase than would be possible with traditional crash analysis methods. One of the major drawbacks of the CFS method is the need to first obtain cross-section crush properties. A cross-section library can be used; however, the number of points required to coarsely fill the design space for even a single cross-section type would be prohibitive.

A parameterised cross-section library for axial crush response could be created using any of the discussed response surfaces methodologies. For the most complex test case, a parameterised library with less than 4% average error could be created with 1.7% of the computation required for a discrete library. The MLS method has been shown to be the most suited as it provides the lowest average error and the response surface created is repeatable with the same parameters and inputs.

The maximum errors observed in the four degree of freedom test case are higher than would be suitable for a cross-section library. 70% of the high errors observed in this test case are not present in all three response surface methodologies at the same evaluation point, for these cases it is possible to alert the user when there is an elevated likelihood of a large error for a given cross-section.

Acknowledgements

The author would like to thank Altair and the MATTER scheme for providing research funding and expertise and, HPC Wales providing for the computer resources to train the neural networks.

References

- [1] Altair, *HyperWorks Online Help*, 2014. Available at: http://www.altairhyperworks.com/hwhelp/Altair/hw13.0/help/hwsolvers/hwsolvers.htm?prop_type44.htm
- [2] X. Song, G. Sun, G. Li, W. Gao, Q. Li, Crashworthiness optimization of foam-filled tapered thin-walled structure using multiple surrogate models, *Structural and Multidisciplinary optimisation*, 47, 221-231, 2012.
- [3] P. Lancaster, K. Salkauskas, Surfaces Generated by Moving Least Squares Methods, *Mathematics of Computation*, 37, 141-158, 1981.
- [4] D. Krige, *Lognormal-de Wijsian Geostatistics for Ore Evaluation*, South African Institute of Mining and Metallurgy, 1981.
- [5] S. Bates, J. Siem, V. Topopov, Formulation of the optimal Latin Hypercube design of experiments using a permutation genetic algorithm. *45th AIAA/ASME/ASCE/AHS/ASC Structures, Structural Dynamics, and Materials Conference*, 2004.
- [6] S. Nissen, *Implementation of a Fast Artificial Neural Network (FANN)*, Department of Computer Science University of Copenhagen, 2003.

ISOGEOMETRIC BASED PSEUDO-ELASTIC ANALYSIS OF INELASTIC STRUCTURES

*M. Dinachandra and Raju Sethuraman

Department of Mechanical Engineering, Indian Institute of Technology, Madras, India, 600036

*dina63bms@gmail.com

ABSTRACT

The increasing demand in robust and ergonomic design of engineering components has led to more complexity in shapes, hence a method with more accurate representation of geometry for analysis is required. Isogeometric Analysis (IGA) based on Non-Uniform Rational B-Splines (NURBS) basis represents the geometry exactly and is demonstrated to be more efficient for analysis of complex shapes. Moreover an inelastic analysis is always needed for reliable design of the components. This paper presents the implementation of pseudo-elastic method based on IGA for small deformation analysis of inelastic structures. A pseudo-elastic analysis is an iterative method which takes care of the inelasticity using linear analysis by updating the material parameters for each iteration based on Hencky's total deformation theory. The robustness and simplicity in applying the method based on IGA is presented for two material models viz., bilinear and Ramberg-Osgood model. The performance of the method is demonstrated using two case studies. The results obtained have shown to be in good agreement with the existing Non-Linear Finite Element (NFEM) results. The method can be applied easily with the existing linear IGA codes for inelastic analysis without changing the complete structure of the code.

Key Words: *Isogeometric analysis; NURBS; Pseudo-elastic method; Small inelastic deformation*

1. Introduction

With the advancement of technology, complexity in shapes of engineering components have also increased. Analysis of the components require more accurate methods for robust and ergonomic design. Hence, a method is needed which can represent the geometry efficiently. Hughes et al[1] proposed Isogeometric Analysis (IGA) which uses NURBS basis for defining the geometry as well as the trial solution and showed better performance for complex shapes. IGA has been implemented in many areas of engineering like structural mechanics, fluid mechanics etc [2]. Hassani[3] presented stress recovery in IGA based on Superconvergent patch recovery (SPR) proposed by Zienkiewicz[4] in which stress is also considered as a field variable using the same bases for displacement. Since engineering components may undergo plastic deformation due to the uncertainty in the nature of loadings in real life applications, an inelastic analysis of the components is beneficial to know the reliability. Elguedj et al[5] showed the implementation of inelastic analysis in IGA using F bar and B bar approach. Adam et al[6] have proposed an approach for selective and reduced numerical integrations in IGA and showed to alleviate numerical lockings. Rypl [7] presented the object oriented approach for programming IGA. The structure of nonlinear IGA is different from linear IGA code requiring a complex code structure and makes it complicated due to the mapping of the physical domain to parametric domain and the recursive nature of the NURBS basis. Another approach to analyse small plastic deformation is proposed by Desikan[8] as pseudo-elastic analysis and implemented based on Hencky's total deformation theory in FEM. The results obtained showed good agreement with NFEM results. It uses linear analysis and updates the material properties iteratively taking care of the nonlinearity. The method can be applied to update any existing linear FEM code for inelastic analysis. In this paper, isogeometric based pseudo elastic analysis is presented. In section 2, the methodology and its implementation is explained. In section 3, two case studies considering bilinear and Ramberg-Osgood material models viz. internally pressurized cylinder and plate with circular hole are presented.

2. Methodology

In pseudo-elastic analysis, a linear analysis is done in each iteration by updating the material parameter based on Hencky's total deformation theory. Based on linearized theory, the elastic strain is given by

$$\epsilon_{ij}^e = \frac{1+\nu}{E} \sigma_{ij} - \frac{\nu}{E} \sigma_{kk} \delta_{ij} \quad (1)$$

And the plastic strain is given as

$$\epsilon_{ij}^p = \phi S_{ij} \quad (2)$$

where

$$S_{ij} = \sigma_{ij} - \frac{1}{3} \sigma_{kk} \delta_{ij} \quad (3)$$

is the deviatoric part of the stress tensor and ϕ is a scalar valued function given by

$$\phi = \frac{3 \epsilon_{ep}^p}{2 \sigma_{eq}} \quad (4)$$

The total strain using additive decomposition is given as

$$\epsilon_{ij} = \left(\frac{1+\nu}{E} + \phi \right) \sigma_{ij} - \left(\frac{\nu}{E} + \frac{\phi}{3} \right) \sigma_{kk} \delta_{ij} \quad (5)$$

The above equation is considered as

$$\epsilon_{ij} = \frac{1+\nu_{eff}}{E_{eff}} \sigma_{ij} - \frac{\nu_{eff}}{E_{eff}} \sigma_{kk} \delta_{ij} \quad (6)$$

where ν_{eff} and E_{eff} are the effective Poisson's ratio and Young's modulus respectively. These two variables are considered as material parameters and the parameters are expressed as

$$\frac{1}{E_{eff}} = \frac{1}{E} + \frac{2}{3} \phi \quad (7)$$

$$\nu_{eff} = E_{eff} \left(\frac{\nu}{E} + \frac{\phi}{3} \right) \quad (8)$$

E_{eff} is found using strain control iteratively as [8]

$$E_{eff}^{i+1} = E_{eff}^i \frac{\sigma_y^i}{\sigma_{eq}^i} \quad (9)$$

where $i = 0, 1, 2, 3, \dots$; $E_{eff}^0 = E$; $\nu_{eff}^0 = \nu$; $\sigma_y^0 = \sigma_y$ (material initial yield stress); σ_{eq}^i is the equivalent stress at i^{th} iteration. E_{eff}^{i+1} used in equation (7) and (8) to find ν_{eff}^{i+1} . In Isogeometric based pseudo elastic analysis, the basis used for describing the geometry is also used to approximate the solution. NURBS basis is used to represent the geometry efficiently. The B-spline bases are obtained from Cox-de Boor formula [2]. The NURBS basis with weights w_i at each control points is given by

$$R_{i,p}(t) = \frac{N_{i,p}(t) w_i}{\sum_{i=1}^n N_{i,p}(t) w_i} \quad (10)$$

where p is the degree of polynomial and t is the parameter for mapping to the physical domain. The solution is approximated as $\hat{u} = R_{i,p}(t) u_i$ and applied to the weak form of the governing equation of 2D elastostatics problem which gives

$$[K] \{U\} = \{F\} \quad (11)$$

where

$$[K] = \int_{\Omega} (J_1^{-1} B)^T D_{eff} (J_1^{-1} B) d\Omega \quad (12)$$

$$\{F\} = \int_{\Gamma} \bar{t} R_{i,p} d\Gamma \quad (13)$$

with J_1 as the Jacobian mapping from the physical domain to the parametric domain and \bar{t} is the applied traction. B represents the shape function derivative matrix and D_{eff} represents the elasticity matrix using the updated material parameters for each iteration. The algorithm for implementing pseudo elastic analysis is presented in the box given below.

1. Read geometry and material properties.
2. Compute B matrix and Jacobian matrix at each Gauss points.
3. Obtain F vector using equation (13).
4. Loop using an error estimator.
 - Obtain K^e and form Global stiffness matrix $[GK]$ using equation (12) and step 2.
 - Solve $\{U\} = [GK]^{-1} \{F\}$ and obtain the stresses at each Gauss points.
 - For $\sigma_{eq}^i > \sigma_y^i$, update E_{eff}^i and ν_{eff}^i using equation (7), (8) and (9).
 - Error = $\frac{\max |E_{eff}^i - E_{eff}^{i-1}|}{E_{eff}^i}$ (over each Gauss points)
5. After convergence, using SPR, evaluate the stress coefficients at the control points.

3. Numerical examples

Two case studies are presented to illustrate the isogeometric based pseudo-elastic analysis. An internally pressurized cylinder and a plate with circular hole are considered. In both the cases, NFEM results obtained using PLANE183 - Q8 Structural Solid elements in ANSYS 12.0, are compared with the solution of the present method.

3.1. Internally pressurized cylinder

A quarter model of a cylinder with $R_i=10$ mm and $R_o=20$ mm is considered with 400 control points and a polynomial degree of $p = 2$. An internal pressure of 250 MPa is applied. Bilinear model is considered with $E=210$ GPa, $E_T = 0.1E$, $\nu = 0.3$ and $\sigma_y = 400$ MPa. For NFEM, the geometry is represented with 661 nodes. The radial, hoop and von-Mises stress variations along the radius is shown in figure 1. The results are found to be in good agreement with NFEM results.

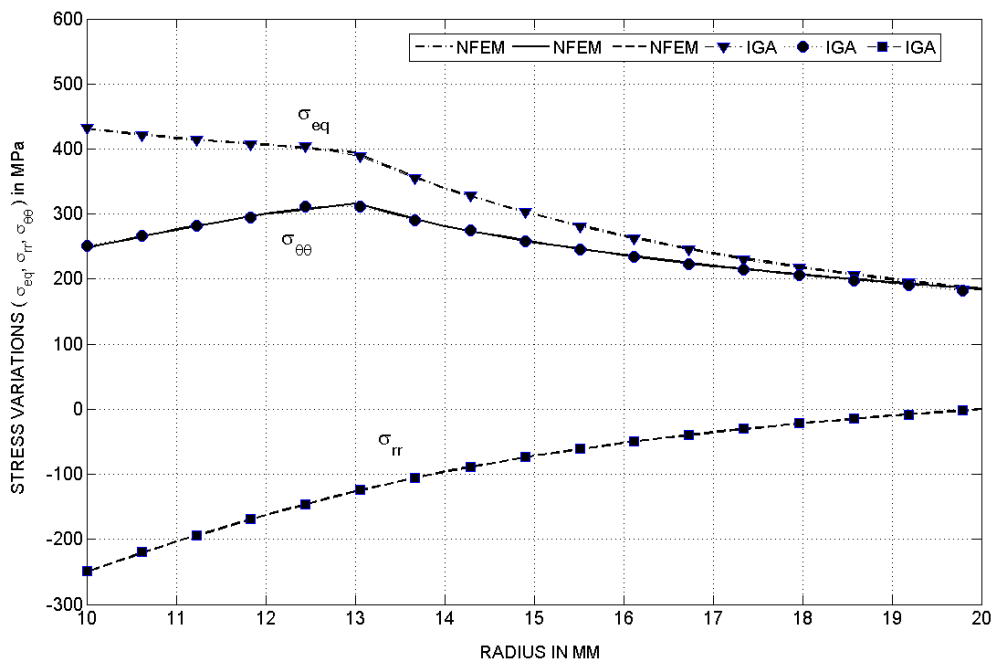


Figure 1: σ_{eq} , σ_{rr} and $\sigma_{\theta\theta}$ variations along the radius

3.2. Plate with circular hole

A quarter model of a square plate with $L=100$ mm and hole radius (r)=5 mm is considered. A traction force of 200 MPa is applied (tensile). Ramberg-Osgood model is considered with material parameters

$E=210$ GPa, $\nu=0.3$, $\alpha=3/7$ and $n=5$. 1800 control points and a polynomial degree of $p=2$ is used to represent the geometry in IGA while 2361 nodes are used in NFEM. The stress variation along $x=0$ and $y=0$ are shown in figure 2 and noticed that the results are in good agreement with NFEM results.

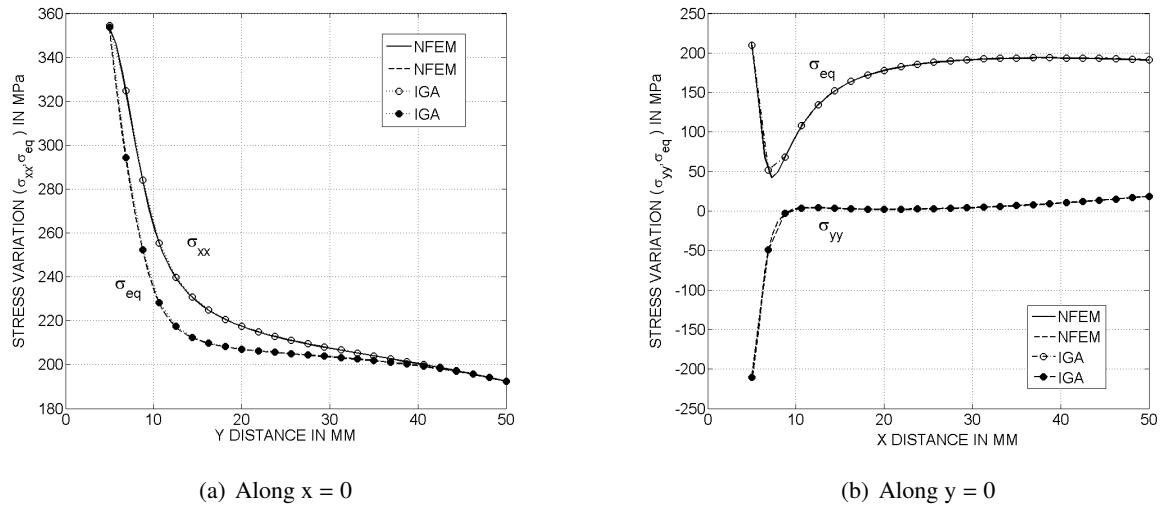


Figure 2: Stress variations

4. Conclusion

In this paper, the algorithm of isogeometric based pseudo elastic analysis is presented. The comparison of stress variations for the considered case studies demonstrate a good agreement of the results obtained using IGA based pseudo elastic analysis with NFEM. Furthermore the use of linear analysis at each iteration makes the analysis more simpler and can be used to easily modify any linear IGA code for inelastic analysis.

References

- [1] T.J.R. Hughes, J.A. Cottrell, Y. Bazilevs. Isogeometric analysis: CAD, finite elements NURBS, exact geometry and mesh refinement, *Computer Methods in Applied Mechanics and Engineering*, 194, 4135–4195, 2005.
- [2] J.A. Cottrell, T.J.R. Hughes, Y. Bazilevs. *Isogeometric Analysis: Toward Integration of CAD and FEA*, 1st. Edition, Wiley, 2009.
- [3] Behrooz Hassani, Ahmad Ganjali, Mehdi Tavakkoli. An isogeometrical approach to error estimation and stress recovery. *European Journal of Mechanics A/Solids*, 31, 101–109, 2012.
- [4] O.C. Zienkiewicz, J.Z. Zhu. The superconvergent patch recovery (SPR) and adaptive finite element refinement. *Computer Methods in Applied Mechanics and Engineering*, 101, 207–224, 1992.
- [5] T. Elguedj, Y. Bazilevs, V.M. Calo, T.J.R. Hughes. \bar{B} and \bar{F} projection methods for nearly incompressible linear and non-linear elasticity and plasticity using high-order NURBS elements. *Computer Methods in Applied Mechanics and Engineering*, 197, 2732–2762, 2008.
- [6] C. Adama, T.J.R. Hughes, S. Bouabdallah, M. Zarroug, H. Maitournam. Selective and reduced numerical integrations for NURBS-based isogeometric analysis. *Computer Methods in Applied Mechanics and Engineering*, 284, 732–761, 2015.
- [7] D. Rypl and B. Patzák. From the finite element analysis to the isogeometric analysis in an object oriented computing environment. *Advances in Engineering Software*, 44(1), 116–125, 2012.
- [8] V. Desikan and R. Sethuraman. Analysis of material nonlinear problems using pseudo elastic finite element method. *ASME Journal of Pressure Vessel Technology*, 122(4), 457–461, 2000.

ON THE CONTACT FORCE AND BOUNDARY TREATMENT IN SMOOTHED PARTICLE HYDRODYNAMICS WITH APPLICATIONS IN GLASS FORMING

*W. Tan¹, M. Profit² and Y. T. Feng¹

¹Zienkiewicz Centre for Computational Engineering, Swansea University, Swansea SA2 8PP, UK

²Rockfield Software Ltd., Swansea SA1 8AS, UK

*682845@swansea.ac.uk

ABSTRACT

The forming process of glass results in a mechanical-thermal coupling problem. Although the finite element method (FEM) has been developed for its 2-D symmetric modelling of commercial containers [1], it is thorny to deal with some glass models with irregular shapes due to its grid-based nature that an inappropriate re-mesh may lead to a computational failure [2]. Solving the governing equations by kernel interpolations, the smoothed particle hydrodynamics (SPH) initially used for the modelling of astronomical phenomena takes the advantage that re-meshing technique and grids are not required for this nonlinear large strain problem. However, the major difficulty of this formulation is found in computing the contact force as the boundary treatment with ambiguous boundary conditions is historically regarded as a weakness of the particle methods [3]. This paper briefly introduces the process of glass forming, presents a total Lagrangian methodology of SPH to obtain the internal force, describe some possible solid boundary treatments (SBT) to compute the contact force between the viscous glass gob and the fixed mould and discusses the applicability of these implementations.

Keywords: smoothed particle hydrodynamics; solid boundary treatment; meshless method; glass forming

1. Introduction

The manufacture of a glass product can be subdivided into several processes consisting of melting, forming, annealing and surface treatment [4]. The process of glass forming is considered as the trickiest part where the thickness of a glass product is sensitively influenced by many actual factors, which is difficult to be controlled in the mould.

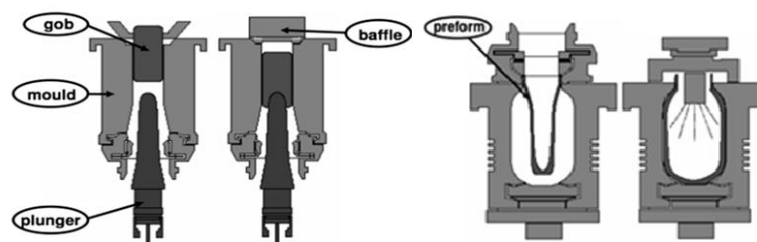


Figure 1: A standard press-and-blow process of glass forming

Figure 1 illustrates that how a glass gob with the temperature around 1200 °C drops down into a so-called blank mould, is pressed by a plunger to become a preform and is blown to its final shape in the final mould. Consequently, the modelling of this process using SPH method can be classified as a problem of: (1) mechanical-thermal coupling; (2) large deformation; (3) free surface and contact with solid boundaries. The following sections only discuss the SPH solution to its high nonlinearity and treatments for the contact force, where the thermal issue is not considered.

2. SPH Methodology

A standard SPH formulation follows that

$$f(\mathbf{x}_a)|_h = \sum_{b=1}^{N_a} V_b f(\mathbf{x}_b) W_{ab} \quad \text{and} \quad \nabla f(\mathbf{x}_a)|_h = \sum_{b=1}^{N_a} V_b f(\mathbf{x}_b) \nabla W_{ab} \quad (1)$$

with a particular bell function for glass modelling, i.e.

$$W_{ab}(R, h_a) = \alpha_{nD} \begin{cases} (2-R)^5 - 16(1-R)^5 & 0 \leq R \leq 1 \\ (2-R)^5 & 1 < R \leq 2 \\ 0 & 2 < R \end{cases} \quad (2)$$

where $R = |\mathbf{x}_a - \mathbf{x}_b|/h_a$ (h is the smoothing length) and a dimension-related parameter is defined as

$$\alpha_{1D} = \frac{1}{16h_a} \quad \alpha_{2D} = \frac{3}{16h_a^2\pi} \quad \alpha_{3D} = \frac{7}{40h_a^3\pi} \quad (3)$$

To ensure its linear completeness, a linear correction to the kernel gradient is given (see reference [5] for more details), i.e.

$$\nabla f(\mathbf{x}_a)|_h = \sum_{b=1}^{N_a} V_b f(\mathbf{x}_b) \mathbf{L}_a (\nabla W_{ab} + \delta_{ab} \mathbf{k}_a) \quad (4)$$

where two correction terms can be obtained from

$$\mathbf{k}_a = -\frac{1}{V_a} \sum_{b=1}^{N_a} V_b \nabla W_{ab} \quad \text{and} \quad \mathbf{L}_a = \left\{ \sum_{b=1}^{N_a} V_b [\nabla W_{ab} \otimes (\mathbf{x}_b - \mathbf{x}_a)] \right\}^{-1} \quad (5)$$

Due to its nonlinearity of strain, the deformation gradient tensor \mathbf{F} [6] is introduced and interpolated by the corrected SPH kernel,

$$\mathbf{F}_a = \frac{\partial \mathbf{x}_a}{\partial \mathbf{x}_a^0} = \nabla^0 \mathbf{x}_a = \sum_{b=1}^{N_a} V_b \mathbf{x}_b \otimes [\mathbf{L}_a^0 (\nabla^0 W_{ab} + \delta_{ab} \mathbf{k}_a^0)] \quad (6)$$

Once each \mathbf{F} of SPH particles is obtained at a time step, the first Piola-Kirchhoff tensor is computable from the relationship given below,

$$\mathbf{P}_a = J_a \sigma_a \mathbf{F}_a^{-T} \quad (7)$$

where the Jacobian is defined as $J_a = \det \mathbf{F}_a = \rho_a^0 / \rho_a$ and the constitutive law used in glass modelling is the compressible Neo-Hookean model

$$\boldsymbol{\sigma} = \frac{\mu}{J} (\mathbf{b} - \mathbf{I}) + \frac{\lambda}{J} (\ln J) \mathbf{I} \quad (8)$$

The equation for computing internal force can be derived from virtual work theorem [7],

$$\mathbf{T}_a = \sum_{b=1}^{N_a} V_b V_a^0 \mathbf{P}_a [\mathbf{L}_a^0 (\nabla^0 W_{ab} + \delta_{ab} \mathbf{k}_a^0)] \quad (9)$$

3. Solid Boundary Treatments

The computation of contact force between the glass gob and the mould is important but seems not straightforward to be implemented. The reason behind this is that it lacks a continuously well-defined solid boundary and the supporting domain of a SPH particle in the vicinity of the boundary is always partly truncated.

The simplest approach for this issue is the bounce back method. However, this method only satisfies the conservation of linear momentum if the interactive boundary is perfectly elastic [5]. In addition, the difficulty is found when modelling is conducted at the sharp corner.

Another popular approach is called mirror (or image) particle method, where a series of so-called ‘‘ghost’’ particles are generated in the vicinity of the solid boundary according to a particular symmetric rule. However, it is not suitable for glass forming as it can be computationally expensive on computing those correction terms [5].

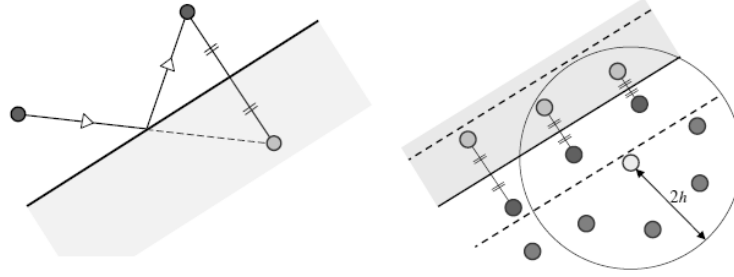


Figure 2: Bounce back method (left) and mirror particle method (right)

Based on the mirror particle method, Liu [3] proposes an improved scheme called “coupled dynamic SBT algorithm” in 2012. This method combines repulsive and dynamic particle features and enhanced the accuracy of calculations for ghost particles in the vicinity of boundaries with complex geometries. It is proven that this method runs favourable for fluid cases.

The last possible approach for glass forming discussed here is the variational formulation of boundary contact force. The governing equation for SPH particles near the boundary in this method is modified and extended to

$$m_a \mathbf{a}_a = m_a \mathbf{g} + \mathbf{F}_{\text{ext},a}(t) - \mathbf{T}_a - \mathbf{T}_a^B \quad (10)$$

where \mathbf{T}_a^B is the boundary contact force that is given by

$$\mathbf{T}_a^B = -\frac{m_a P_a}{\rho_a \gamma_a} \nabla \gamma_a \quad (11)$$

γ is defined by

$$\gamma_a(\mathbf{x}_a, h_a) = \int W_{ab} d\mathbf{x} \quad (12)$$

and indicates the effective area (or volume) of the truncated supporting domain of a SPH particle in the vicinity of the boundary.

The core idea of this method is that it converts the difficulty because of the SPH nature into a geometric issue and it has been proven that the boundary force evaluation can be exact in 2-D cases, which means it performs well for commercial glass containers with 2-D symmetric shapes (see [5] for detailed derivations of obtaining γ and $\nabla \gamma$).

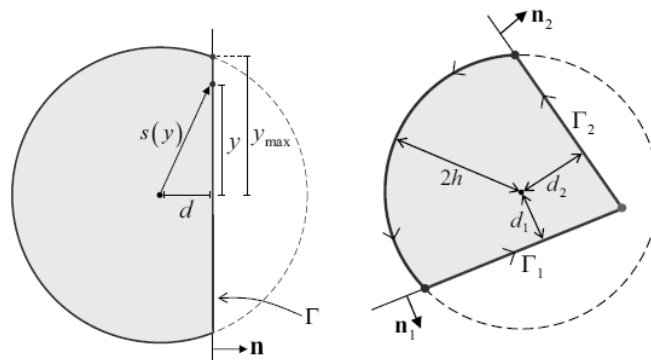


Figure 3: Evaluation of γ and $\nabla \gamma$ in cases of straight (left) and corner (right) boundaries

4. Discussion & Conclusion

Unlike many fluid cases using SPH are well developed, the practice of SPH for solid problems is relatively rare as the mesh-based method, for instance, the finite element method, overshadows its potential. The other reason is that the solid boundary plays an important role in the modelling of solid problems whilst SPH method is weak at this issue.

This paper reveals that the modelling of glass forming using SPH method is feasible. With the use of corrected SPH formulation, it saves the computational cost in a total Lagrangian framework [8]. Furthermore, the variational formulation of boundary contact force presents an exact evaluation for the boundary treatment [5].

Compared with the FEM that has been employed in commercial software, SPH method without mesh generation can perform better for those glass products with complex and irregular shapes and has a better future prospect in 3-D modelling of glass forming.

References

- [1] J. M. A. César de Sá. Numerical modelling of glass forming processes. *Eng. Comput.*, 3, 266–275, 1986.
- [2] P. W. Cleary and et al.. Modelling of metal forging using SPH. *Appl. Math. Modell.*, 36(8), 3836-3855, 2012.
- [3] M. B. Liu, J. R. Shao and J. Z. Chang. On the treatment of solid boundary in smoothed particle hydrodynamics, *Sci. China Tech. Sci.*, 55, 244-254, 2012.
- [4] C. L. Babcock. *Silicate Glass Technology Methods*. John Wiley & Sons, Inc., U.S.A., 1977.
- [5] J. Feldman and J. Bonet. Dynamic refinement and boundary contact forces in SPH with applications in fluid flow problems. *Int. J. Numer. Meth. Engng.*, 72, 295-324, 2007.
- [6] J. Bonet and R.D. Wood, *Nonlinear Continuum Mechanics for Finite Element Analysis*. 2nd ed., Cambridge University Press, New York, 2008
- [7] J. Bonet and et al.. Variational formulation for the smooth particle hydrodynamics (SPH) simulation of fluid and solid problems. *Comput. Methods. Appl. Mech. Engrg.*, 193, 1245-1256, 2004
- [8] J. Bonet and S. Kulasegaram. Alternative total Lagrangian formulations for corrected smooth particle hydrodynamics (CSPH) methods in large strain dynamic problems. *Revue Européenne des Éléments Finis*, 11, 893-912, 2012
- [9] L. B. Lucy. A numerical approach to testing the fission hypothesis. *Astron. Journal*, 82, 1013-1024, 1977
- [10] R. A. Gingold and J. J. Monaghan. Smoothed particle hydrodynamics: theory and application to non-spherical stars. *Mon. Not. R. Astron. Soc.*, 181, 375-389, 1977.
- [11] G. R. Liu and M. B. Liu. *Smoothed Particle Hydrodynamics: A Meshfree Particle Method*, 1st Edition, World Scientific, 2003.
- [12] J. Bonet and S. Kulasegaram. Correction and stabilization of smooth particle hydrodynamics methods with applications in metal forming simulations. *Int. J. Numer. Meth. Engng.*, 47, 1189-1214, 2000.
- [13] M. B. Liu and G. R. Liu. Smoothed particle hydrodynamics (SPH): An overview and recent developments. *Arch. Comput. Method Eng.*, 17(1), 25-76, 2010

Preliminary Outcomes on Isogeometric Trefftz Method

M. Horák¹, B. Patzák¹, *J. Novák^{2,1}

¹Department of Mechanics, Faculty of Civil Engineering, Czech Technical University in Prague, Thákurova 7, Prague, 166 29

²Department of Structural Mechanics, Faculty of Civil Engineering, Brno University of Technology, Veverří 95, Brno, 602 00

*novakj@cml.fsv.cvut.cz

ABSTRACT

In this contribution we present a coupling formalism between the hybrid Trefftz stress finite element method and isogeometric analysis. The structure of the isogeometric extension of the Trefftz method is formally the same as for its standard counterpart, except the separate approximation of the boundary displacements that is carried out using the Non-Uniform Rational B-spline (NURBS) basis. Our theoretical outcomes are accompanied by a simple two-dimensional numerical example.

Keywords: *Isogeometric analysis; Hybrid-Trefftz method; hybrid approach*

1. Problem setup

For a simpler exposition we focus on the planar elasticity problem. Within a domain Ω , free of body forces, the problem is governed by equilibrium $\nabla \cdot \boldsymbol{\sigma} = \mathbf{0}$, compatibility $\boldsymbol{\varepsilon} = \nabla^s \mathbf{u}$, and constitutive $\boldsymbol{\sigma} = \mathbf{D} : \boldsymbol{\varepsilon}$ equations. The problem is completed by the kinematic and static conditions prescribed on the kinematic and traction portions of the boundary $\partial\Omega$, respectively, as $\mathbf{u} = \bar{\mathbf{u}}$ and $\mathbf{n} \cdot \boldsymbol{\sigma} = \bar{\mathbf{t}}$. Here $\boldsymbol{\sigma}$ is the stress tensor, ∇ is the nabla operator, $\boldsymbol{\varepsilon}$ stands for the small strain tensor, \mathbf{u} represents the displacement vector, \mathbf{D} is the fourth-order elasticity tensor, \mathbf{n} denotes the outward unit normal vector, and $\bar{\mathbf{t}}$ and $\bar{\mathbf{u}}$ are prescribed tractions and displacements, respectively.

2. HTSE: Hybrid Trefftz stress element formulation

In the Hybrid-Trefftz method [1, 2], the domain Ω is divided into separate elements inside of which we sought for displacement and stress fields approximations. In other words, the method approximates the solution to the problem from **Section 1** using a linear combination of functions which satisfy a-priori the equations defined in Ω , however they do not satisfy in general the boundary conditions on $\partial\Omega$. Thus, the so called intra-element fields \mathbf{u} and $\boldsymbol{\sigma}$, this time written in Voigt-Mandell vector-matrix notation for tensors of the second and fourth orders, are approximated as

$$\mathbf{u} = \sum_{I=1}^n \mathbf{N}_I \mathbf{d}_I = \mathbf{N} \mathbf{d}, \quad \boldsymbol{\sigma} = \sum_{I=1}^n \mathbf{T}_I \mathbf{d}_I = \mathbf{T} \mathbf{d} \quad (1)$$

where \mathbf{d}_I stands for the generalized degrees of freedom associated with the element interior, \mathbf{N} is the matrix of displacement interpolation functions while \mathbf{T} stand for its stress related counterpart. Taking the constitutive relation to Eq. (1)², it gives

$$\mathbf{T}_I = \mathbf{D} \mathbf{L}^T \mathbf{N}_I \quad (2)$$

such that it yields, after applying the divergence operator \mathbf{L} , to Navier's equation in the form

$$\mathbf{L} \mathbf{D} \mathbf{L}^T \mathbf{N} \mathbf{d} = \mathbf{0} \quad (3)$$

In other words, enforcing the equilibrium equation in Eq. (2), yields approximation functions satisfying Navier's homogeneous equation Eq. (3). Such a basis can be generated e.g. by making use Muskhelishvili's solution, see [6], or [7] for further details.

The intra-element continuity is given unambiguously by compatibility equation applied to displacement approximation \mathbf{u} . Nonetheless, there exist many approaches to enforce the inter-element continuity and the boundary conditions. Keeping up with the title of this section, we use the so-called hybrid approach which proceeds from the introduction of an independent boundary field \mathbf{u}_Γ [3, 5]. It enforces the boundary conditions and the continuity across the elements through the modified functional

$$\Phi^e = \frac{1}{2} \int_{\Omega^e} \boldsymbol{\sigma}^\top \boldsymbol{\varepsilon} \, d\Omega - \int_{\Gamma_i^e} (\mathbf{t} - \bar{\mathbf{t}})^\top \mathbf{u}_\Gamma \, d\Gamma - \int_{\Gamma_u^e} \mathbf{t}^\top \bar{\mathbf{u}} \, d\Gamma - \int_{\Gamma_t^e} \mathbf{t}^\top \mathbf{u}_\Gamma \, d\Gamma \quad (4)$$

Integrating the first term in Eq. (4) by parts, we obtain

$$\int_{\Omega^e} \boldsymbol{\sigma}^\top \boldsymbol{\varepsilon} \, d\Omega = \int_{\Gamma^e} \mathbf{t}^\top \mathbf{u} \, d\Gamma \quad (5)$$

Substituting this equation back into Eq. (4) and using the fact that $\Gamma^e = \Gamma_u^e + \Gamma_i^e + \Gamma_t^e$, where Γ_i^e is the interelement boundary of an element I , and that $\mathbf{u}_\Gamma = \bar{\mathbf{u}}$ on Γ_u^e , we arrive at

$$\Phi^e = \frac{1}{2} \int_{\Gamma^e} \mathbf{t}^\top \mathbf{u} \, d\Gamma + \int_{\Gamma_i^e} \bar{\mathbf{t}}^\top \mathbf{u}_\Gamma \, d\Gamma - \int_{\Gamma_t^e} \mathbf{t}^\top \mathbf{u}_\Gamma \, d\Gamma \quad (6)$$

According to **Section 1**, namely the Neumann boundary conditions at the static boundary Γ_t^e and Eq. (1)², the approximation of the traction field can be expressed as

$$\mathbf{t} = \mathbf{A}\mathbf{T}\mathbf{d} \quad (7)$$

where \mathbf{A} consist of the components of the unit outward normal to $\partial\Omega$. In addition, the approximation of the independent boundary displacement field is introduced as

$$\mathbf{u}_\Gamma = \mathbf{N}_\Gamma \mathbf{d}_\Gamma \quad (8)$$

where \mathbf{N}_Γ is the matrix containing approximation functions of the inter-element boundary field \mathbf{u}_Γ and \mathbf{d}_Γ are the appropriate nodal degrees of freedom as in conventional FEM. The discretization of Eq. (6), by making use of Eq. (7) and Eq. (8), yields

$$\Phi_d^e = \frac{1}{2} \mathbf{d}^\top \int_{\Gamma^e} (\mathbf{A}\mathbf{T})^\top \mathbf{N} \, d\Gamma \, \mathbf{d} + \mathbf{d}_\Gamma^\top \int_{\Gamma_i^e} \mathbf{N}_\Gamma^\top \bar{\mathbf{t}} \, d\Gamma - \mathbf{d}^\top \int_{\Gamma_t^e} (\mathbf{A}\mathbf{T})^\top \mathbf{N}_\Gamma \, d\Gamma \, \mathbf{d}_\Gamma \quad (9)$$

The stationary condition leads to

$$\frac{\partial \Phi_d^e}{\partial \mathbf{d}^\top} = \int_{\Gamma^e} (\mathbf{A}\mathbf{T})^\top \mathbf{N} \, d\Gamma \, \mathbf{d} - \int_{\Gamma_t^e} (\mathbf{A}\mathbf{T})^\top \mathbf{N}_\Gamma \, d\Gamma \, \mathbf{d}_\Gamma = 0, \quad \frac{\partial \Phi_d^e}{\partial \mathbf{d}_\Gamma^\top} = \int_{\Gamma_i^e} \mathbf{N}_\Gamma^\top \bar{\mathbf{t}} \, d\Gamma - \int_{\Gamma_t^e} \mathbf{N}_\Gamma^\top \mathbf{A}\mathbf{T} \, d\Gamma \, \mathbf{d} = 0 \quad (10)$$

Finally, recasting the above system of equations in the compact reads as

$$\begin{bmatrix} \mathbf{F} & -\mathbf{Q}^\top \\ -\mathbf{Q} & \mathbf{0} \end{bmatrix} \begin{bmatrix} \mathbf{d} \\ \mathbf{d}_\Gamma \end{bmatrix} = \begin{bmatrix} \mathbf{p}_u \\ \mathbf{p}_t \end{bmatrix} \quad (11)$$

where $\mathbf{F} = \int_{\Gamma^e} (\mathbf{A}\mathbf{T})^\top \mathbf{N} \, d\Gamma$, $\mathbf{Q} = \int_{\Gamma^e} \mathbf{N}_\Gamma^\top \mathbf{A}\mathbf{T} \, d\Gamma$, $\mathbf{p}_u = \int_{\Gamma_u^e} (\mathbf{A}\mathbf{T})^\top \bar{\mathbf{u}} \, d\Gamma$, and $\mathbf{p}_t = \int_{\Gamma_t^e} \mathbf{N}_\Gamma^\top \bar{\mathbf{t}} \, d\Gamma$. Note, that the symmetry of matrix \mathbf{F} can be simply shown, since it is obtained as a discretization of the strain energy as

$$\int_{\Omega^e} \boldsymbol{\sigma}^\top \boldsymbol{\varepsilon} \, d\Omega = \int_{\Gamma^e} \mathbf{t}^\top \mathbf{u} \, d\Gamma \approx \mathbf{d}^\top \int_{\Gamma^e} (\mathbf{A}\mathbf{T})^\top \mathbf{N} \, d\Gamma \, \mathbf{d} \quad (12)$$

Besides, individual components in Eq. (11) can be evaluated by integrating over the element boundaries only. Using static condensation, the intra-element degrees of freedom can be eliminated and the classical system of equations at the element level is obtained. This enables to couple the HTSE with standard Lagrangian elements. In particular, the global system reads as

$$\mathbf{K} \mathbf{d}_\Gamma = \mathbf{f} \quad (13)$$

where $\mathbf{K} = \mathbf{Q}\mathbf{F}^{-1}\mathbf{Q}^\top$ stands for the stiffness matrix of the boundary valued problem under consideration and $\mathbf{f} = \mathbf{p}_t - \mathbf{Q}\mathbf{F}^{-1}\mathbf{p}_u$ is the right-hand side vector.

3. IGA: Isogeometric analysis

Isogeometric analysis (IGA) has been introduced recently by Hughes et al. [4]. Basically, it is an alternative to the standard polynomial-based (p-adaptivity) finite element method. The main motivation for IGA was to bridge the gap between the engineering design and a structural analysis. Roughly speaking, in the isogeometric analysis, geometry is approximated exactly using rational Bezier functions of a high degree and these functions are used as the basis for the approximation of unknown mechanical fields, which is a concept rather opposite to the standard isoparametric finite element method in which the basis functions for mechanical fields are chosen a-priori and the geometry is then approximated using these functions. Recently, Scott and co-workers [8] have introduced an isogeometric version of the Boundary Element Method - IGABEM in which NURBS are used to represent the geometry along with the unknown fields at the boundary. Following this work we introduce an extension of the Hybrid-Trefftz method based on the Isogeometric analysis.

4. IGAT: HTSE-IGA coupling formalism

The extension of the standard Hybrid-Trefftz method lies in the isogeometric approximation of the boundary field \mathbf{u}_Γ . Using this approach, NURBS approximation functions, Fig. (1), are introduced on $\partial\Omega_e$, and the boundary integration is performed in order to calculate submatrices in Eq. (11).

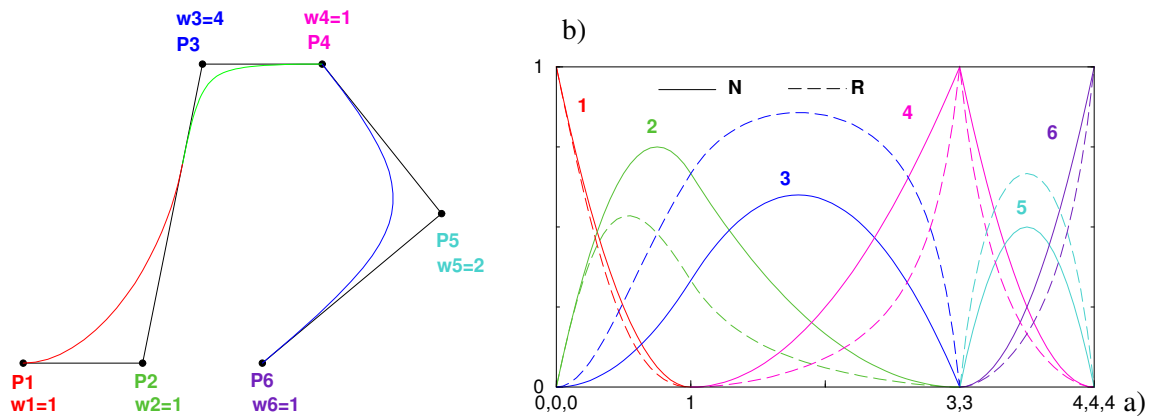


Figure 1: Quadratic NURBS curve: (a) control polygon in black; labels and weights of individual control points in color corresponding to the associated basis and shape function; segments of the curve in red/green/blue corresponding to non-zero knot spans 0-1/1-3/3-4, (b) B-spline basis functions and curve shape functions corresponding to individual control points are plotted over the entire span of the knot vector $\{0, 0, 0, 1, 3, 3, 4, 4, 4\}$, see [9].

5. Numerical example

The infinite plate with a circular hole is a standard benchmark example for IGA analysis. Owing to the symmetry, only a quarter of the plate was modeled using a single IGAT element. The comparison of the IGAT contour plots of the normal stress σ_x with the detailed solution by conventional finite elements with linear basis is shown in Fig. (5). A detailed examination reveals that the quality of the response obtained by the IGAT is very accurate despite only the single element discretization.

6. Conclusions

In this contribution, Isogeometric formulation of the Hybrid-Trefftz method has been introduced. Using this approach, domains of arbitrary shapes can be exactly described and effectively simulated. This approach has a computational advantage over the classical IGA method, since only boundary integration is performed. Moreover, quite complex shapes can be described using low number of elements due to the hierarchical bases of the Trefftz method. In the future work we will focus on comparison of computational costs of the IGAT method and the classical IGA formulation.

Acknowledgement

This outcome has been achieved with the financial support of the Czech Science Foundation under the project No. 13-22230S and the European Social Fund, grant No. CZ.1.07/2.3.00/30.0005.

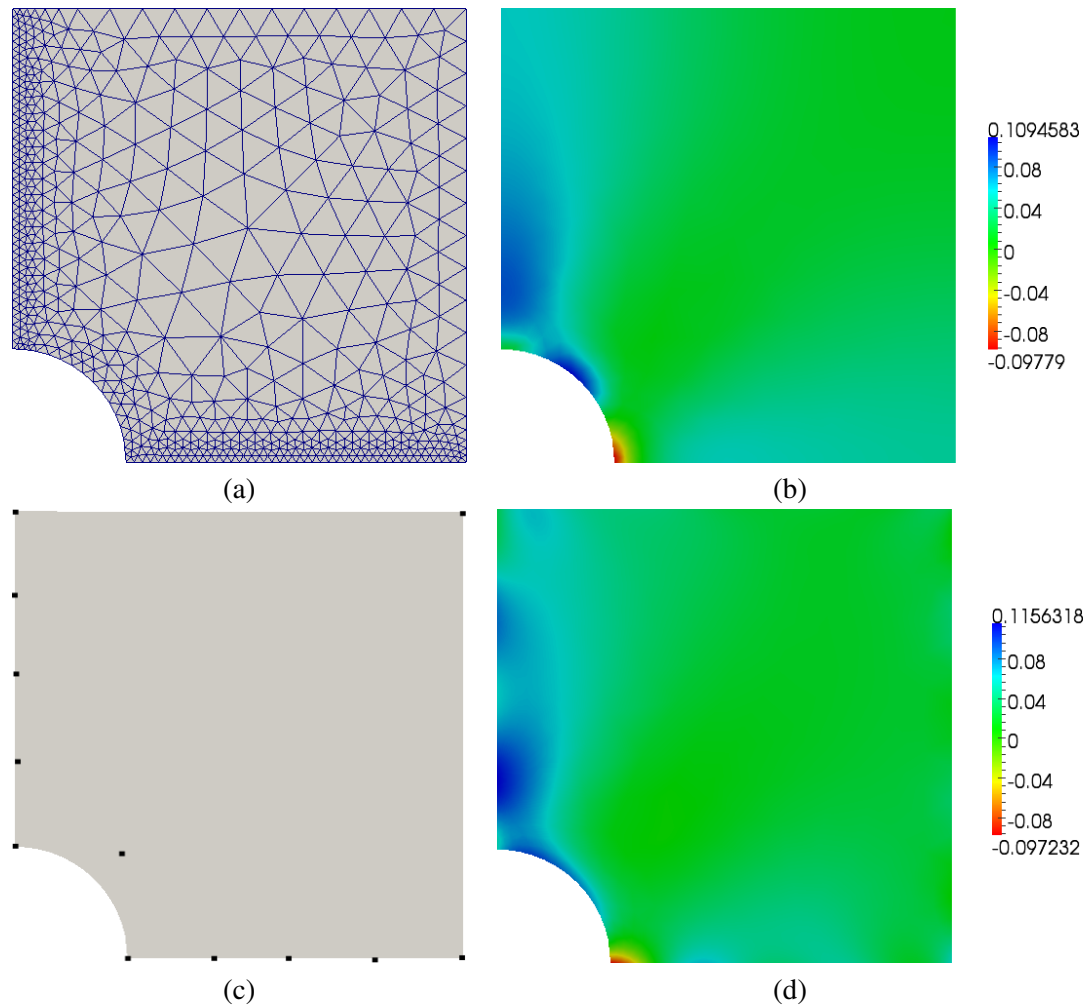


Figure 2: Comparison of IGAT solution with conventional FEM; (a) FE mesh with 2560 linear elements, (b) contours of σ_x by FEM, (c) geometry with IGAT control points, (d) contours of σ_x by IGAT.

References

- [1] E. Trefftz. Ein gegenstück zum ritzschen verfahren. *Proc. 2nd Int. Cong. Appl. Mech. Zurich*, edited by G. Massing (Orell Füssly Verlag), pp.131–137, 1926.
- [2] I. Herrera. General variational principles applicable to the hybrid element method. *Proceedings of the National Academy of Sciences*, 74, 2595–2597, 1977.
- [3] J. Jiroušek. Basis for development of large finite elements locally satisfying all field equations. *Computer Methods in Applied Mechanics and Engineering*, 14, 65–92, 1978.
- [4] T.J.R. Hughes, J.A. Cottrell, Y. Bazilevs. Isogeometric analysis: CAD, finite elements, NURBS, exact geometry and mesh refinement. *Computer Methods in Applied Mechanics and Engineering*, 194, 4135–4195, 2005.
- [5] J. Teixeira de Freitas, Formulation of elastostatic hybrid-trefftz stress elements. *Computer Methods in Applied Mechanics and Engineering*, 153, 127–151, 1998.
- [6] Muskhelishvili, N. I. *Some basic problems of the mathematical theory of elasticity*. No. 1. Springer, (1977).
- [7] Qin, Qing-Hua, and Hui Wang *Matlab and C programming for Trefftz finite element methods*. CRC Press, (2010).
- [8] Scott, M. A., et al. *Isogeometric boundary element analysis using unstructured T-splines*. *Computer Methods in Applied Mechanics and Engineering* 254 (2013): 197-221.
- [9] Piegl, Les, and Wayne Tiller. *The NURBS book*. 1997. Monographs in Visual Communication (1997).

SOLIDS AND STRUCTURES 4

Evaluation of Elasto-Plastic Stress and Strain Fields using Pseudo-Elastic Finite Element Method for Non Proportional Loading

*K. Adi Navaneetha Kumari and Raju Sethuraman

Department of Mechanical Engineering, Indian Institute of Technology Madras, Chennai -600036,

*aditya1457@gmail.com

ABSTRACT

This paper presents a methodology for the evaluation of elasto-plastic stress and strain fields using Pseudo-Elastic Finite Element Method based on the deformation theory of plasticity for non proportional loading. Sequential non proportional load steps are of much importance especially in the case of pressure vessels. In the proposed method, an iterative linear analysis is carried out to determine the stress field at the end of each load step using effective material parameters as field variables. The effective material parameters are obtained from the experimental uniaxial tensile test curve in an iterative manner using strain controlled projection method. Incremental plastic strain in subsequent load steps is determined using numerical integration incorporating the stress at the end of each load step since deformation theory is path independent. Application of the present methodology is illustrated by considering 2D case studies with Ramberg-Osgood material model subjected to non proportional sequential loading. Obtained results are found to be in good agreement with the incremental solutions from ANSYS when the subsequent load angle is less than the optimum angle proposed by Budiansky(1959).

Keywords: Pseudo Elastic Finite Element Method; Elasto-plastic; Non proportional loading

1. Introduction

Most of the structural components undergo inelastic deformation due to the unexpected presence of voids, notches, microcracks, overloads etc. in practice. It necessitates the elasto-plastic analysis of material behaviour. Pseudo Elastic Finite Element Method was originally developed by Raju Sethuraman et al. [4] for the analysis of material non linear problems in the elasto-plastic range. Though deformation plasticity is used for proportional loading, [2] discussed the applicability of deformation theory for non proportional loading with no unloading. He proposed an optimum angle as the maximum allowable non proportionality of subsequent loading and proved that deformation theory could predict accurate results when the angle(α), between deviatoric stress tensor and incremental deviatoric stress tensor at a point is less than the optimum angle(β) at the yield surface in deviatoric plane. This paper proposes a methodology based on the deformation theory of plasticity for the elasto-plastic analysis of material non linear problems subjected to non proportional sequential loading with no unloading.

2. Formulation

2.1 Effective Material Parameters Determination

Pseudo-elastic constitutive law for the elasto-plastic analysis of strain hardening materials is given by

$$\varepsilon_{ij} = \left(\frac{1+\nu}{E} + \Phi \right) \sigma_{ij} - \left(\frac{\nu}{E} + \frac{1}{3} \Phi \right) \sigma_{kk} \delta_{ij} \quad (1)$$

$$\text{Where } \Phi = \frac{3}{2} \frac{\varepsilon_{eq}^p}{\sigma_{eq}} \quad (2)$$

Where ε_{eq}^p and σ_{eq} are equivalent plastic strain and equivalent stress respectively.

The above equation can be rewritten as an equivalent linear elastic constitutive law as

$$\varepsilon_{ij} = \left(\frac{1 + \nu_{eff}}{E_{eff}} \right) \sigma_{ij} - \left(\frac{\nu_{eff}}{E_{eff}} \right) \sigma_{kk} \delta_{ij} \quad (3)$$

Where E_{eff} and ν_{eff} are the effective material parameters and are defined as

$$\frac{1}{E_{eff}} = \frac{1}{E} + \frac{2}{3} \Phi \quad ; \quad \nu_{eff} = E_{eff} \left(\frac{\nu}{E} + \frac{\Phi}{3} \right) \quad (4)$$

2.2 Plastic Strain Recovery

Prandtl –Reuss flow theory suggests that the incremental plastic strain is proportional to current deviatoric stress is given by

$$d\varepsilon_{ij}^p = \Phi S_{ij} \quad (5)$$

Multiplying LHS and RHS by $d\Phi$, we get

$$d\varepsilon_{ij}^p d\varepsilon_{ij}^p = d\Phi^2 S_{ij} S_{ij} \quad (6)$$

$$d\varepsilon_{eq}^p = \sqrt{\frac{2}{3} d\varepsilon_{ij}^p d\varepsilon_{ij}^p} \quad , \quad \sigma_{eq} = \sqrt{\frac{3}{2} S_{ij} S_{ij}} \quad \text{and} \quad d\sigma_{eq} = E_p d\varepsilon_{eq}^p \quad (7)$$

Substituting (7) in (6)

$$d\Phi = \frac{3}{2} \frac{1}{E_p} \frac{d\sigma_{eq}}{\sigma_{eq}} \quad (8)$$

Substituting (8) in (5)

$$d\varepsilon_{ij}^p = \frac{3}{2} \frac{1}{E_p} \frac{d\sigma_{eq}}{\sigma_{eq}} S_{ij} \quad (9)$$

Plastic equivalent strain part of Ramberg-Osgood material model is given by

$$\varepsilon_{eq}^p = \alpha \left(\frac{\varepsilon_0}{\sigma_0^m} \right) \sigma_{eq}^m \quad (10)$$

Where α -yield offset, m-strain hardening exponent and σ_0 -yield stress

Differentiating (10) with respect to σ_{eq} , we get

$$\frac{d\varepsilon_{eq}^p}{d\sigma_{eq}} = \alpha m \left(\frac{\varepsilon_0}{\sigma_0^m} \right) \sigma_{eq}^{m-1} \quad (11)$$

From [3], stress at any point in the second load step can be written as

$$S_{ij} = S_{ij}^A + K (S_{ij}^B - S_{ij}^A) \quad (12)$$

Where K varies from 0 to 1. A and B denote the end states of load step 1 and load step 2 respectively.

Substituting (12) in σ_{eq} in (7), we get

$$\sigma_{eq}^2 = K^2 [\Delta\sigma_{eq}]^2 - K \left([\Delta\sigma_{eq}]^2 + [\sigma_{eq}^A]^2 - [\sigma_{eq}^B]^2 \right) + [\sigma_{eq}^A]^2 \quad (13)$$

Differentiating (13) with respect to K and substituting in (9) yields the expression for the incremental plastic strain between A and B for Ramberg-Osgood material model

$$\Delta\varepsilon_{ij|A}^p = \frac{3}{4} m \alpha \left(\frac{\varepsilon_0}{\sigma_0^m} \right) \int_0^1 \left[(2K-1) [\Delta\sigma_{eq}]^2 - [\sigma_{eq}^A]^2 + [\sigma_{eq}^B]^2 \right] * \left[K^2 [\Delta\sigma_{eq}]^2 - K \left([\Delta\sigma_{eq}]^2 + [\sigma_{eq}^A]^2 - [\sigma_{eq}^B]^2 \right) + [\sigma_{eq}^A]^2 \right]^{\frac{m-3}{2}} * [S_{ij}^A + K(S_{ij}^B - S_{ij}^A)] dK \quad (14)$$

3. Numerical Implementation

2-D case studies of thick walled cylinder subjected to sequential loading are considered. The material is assumed to follow Ramberg-Osgood behaviour with strain hardening index, $m=5$. Finite element code is generated in Matlab and results are compared with those from [1].

3.1 Thick walled cylinder under Internal pressure-Shear traction

Five load cases of sequential non proportional loadings as per Table 1 are considered for the analysis. Thick cylinder with outer(R_o) to inner radius(R_i) ratio equal to five is considered for the analysis. Domain is discretized using 2820 nodes and 900 elements. The following material property values are used for the analysis: Young's modulus $E=200$ GPa, yield offset (α) = 3/7, strain hardening exponent (m) =5, and Poisson's ratio=0.3. Identical mesh is generated in [1] and is used for both pseudo Elastic (PEA) and incremental elastic-plastic analysis (FEA). One of the load cases (load case IV) is discussed below.

3.1.1 Load case IV: In load case IV, only shear traction is applied in the second load step keeping the pressure same as in the first load step. Though load angle (109°) as per [2] is higher than the maximum allowable load angle (65.9°), the results are found to match well with incremental solution and are shown in Figures 1 and 2.

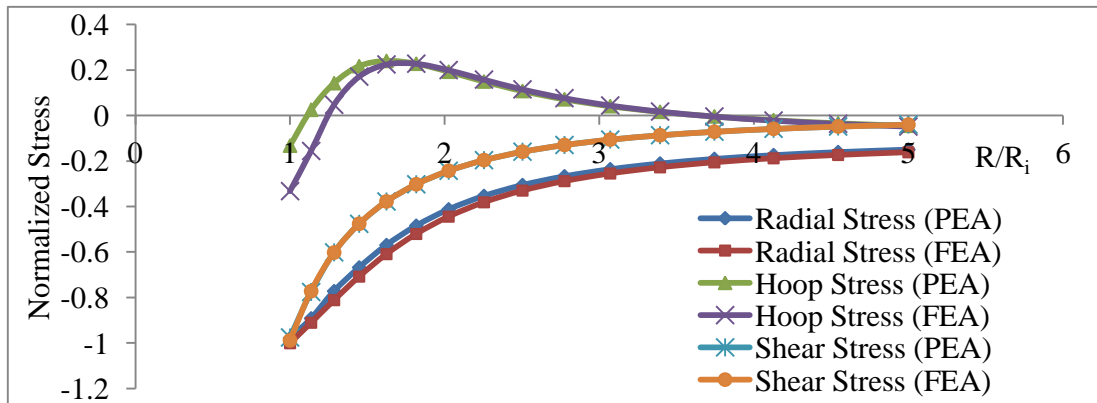


Figure 1: Variation of normalized stresses along the radial direction at the end of load step II

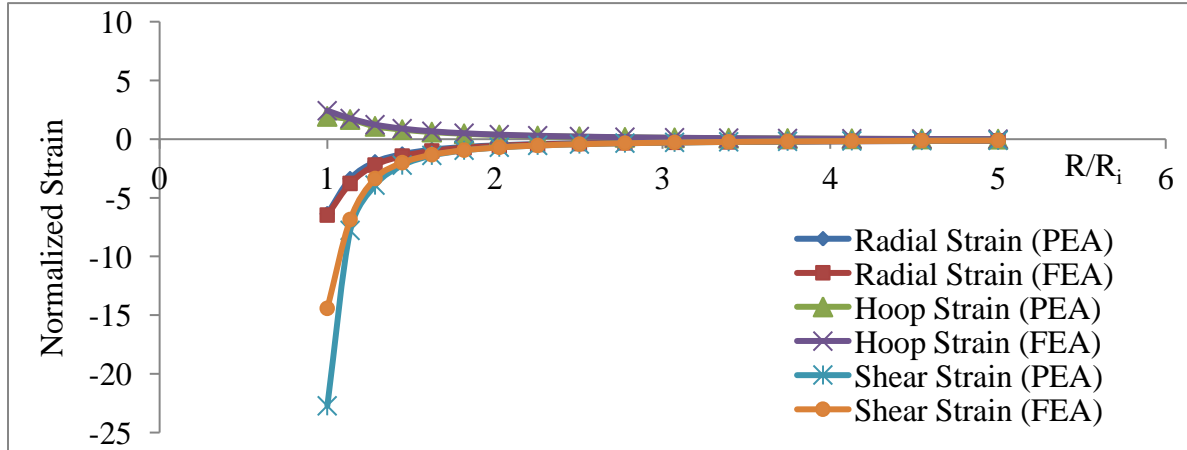


Figure 2: Variation of normalized strains along the radial direction at the end of load step II

Table 1: Load Cases

Case	Type of loading	Load step I	Load step II	Max load angle α ($^{\circ}$)	Allowable load angle β ($^{\circ}$)
I	Int.Pr. (MPa)	0-200	200-300	26.09	65.9
	Shear traction (MN/m/m)	0-200	200-250		
II	Int.Pr. (MPa)	0-200	200-300	66.88	65.9
	Shear traction (MN/m/m)	0-200	200		
III	Int.Pr. (MPa)	0-200	200	62.72	65.9
	Shear traction (MN/m/m)	0-200	200-250		
IV	Int.Pr. (MPa)	0-200	200	109.2	65.9
	Shear traction (MN/m/m)	0	0-200		
V	Int.Pr. (MPa)	0	0-200	91.44	65.9
	Shear traction (MN/m/m)	0-200	200		

4. Conclusions

Pseudo elastic methodology based on the deformation theory of plasticity is proposed for the elasto-plastic analysis of material non linear problems subjected to non proportional sequential loading with no unloading. It involves only iterative linear analysis and as a result significantly reduces computational time compared to incremental analysis.

References

- [1] ANSYS, v 12.0, *Structural Analysis Guide*. ANSYS Inc. Canonsburg, PA-15317, USA, 2009.
- [2] Budiansky B. A reassessment of deformation theory of plasticity. *ASME Journal of Applied Mechanics*, 26, 259-264, 1959.
- [3] Jahed H, S. B. Lambert and R. N. Dubey. Total deformation theory for non-proportional loading. *International Journal of Pressure Vessel and Piping*, 75, 633-642, 1998.
- [4] Raju Sethuraman and Desikan V.. Analysis of material nonlinear problems using pseudo elastic finite element method. *ASME Transaction, Journal of Pressure Vessel Technology*, 122, 457-461, 2000.

PREDICTION OF EQUIVALENT ELASTIC PROPERTIES OF IRREGULAR CELLULAR SOLIDS

T. Mukhopadhyay¹, *S. Adhikari¹

¹College of Engineering, Swansea University, Swansea, UK

*S.Adhikari@swansea.ac.uk

ABSTRACT

An analytical formulation has been developed in this article for predicting the equivalent elastic properties of irregular cellular solids. There is huge amount of literature available concerning the study of equivalent elastic properties of regular cellular solids. Unit cell approach is commonly used to obtain equivalent elastic properties of such regular cellular solids. For predicting equivalent elastic properties of irregular cellular structures, computational expensive finite element analysis has been found to be followed in available literature. This paper aims to develop an analytical approach for predicting equivalent in-plane elastic properties of irregular cellular solids. For the purpose of demonstration of the proposed approach, irregular auxetic honeycombs have been studied in this article. The results have been obtained for different degree of irregularity and validated with finite element results.

Key Words: *cellular solids; random cell angle; irregularity; auxetic honeycomb*

1. Introduction

The materials, which exhibit negative Poisson's ratio are called "auxetic". In the last decade auxetic honeycombs have gained considerable attention of the research community due to its interesting mechanical properties. Generally honeycombs are modelled as a continuous solid having an equivalent elastic moduli throughout to eliminate the need of detail finite element modelling of honeycombs in complex structural systems like sandwich structures. To date, extensive amount of research has been carried out to predict the equivalent elastic properties of regular honeycombs including regular auxetic honeycombs [1, 2, 3, 4]. Analysis of two dimensional honeycombs presented in these studies are commonly based on unit cell approach, which is applicable only for perfectly periodic cellular structures.

A significant limitation of the aforementioned unit cell approach is that it can not account for the spatial irregularity, which is practically inevitable. Spatial irregularity in honeycomb may occur due to manufacturing uncertainty, structural defects, variation in temperature, pre-stressing and micro-structural variability in naturally occurring honeycombs. To include the effect of irregularity, voronoi honeycombs have been considered in several studies including the effect of structural defect [5, 6, 7, 8]. Of late the effect of manufacturing irregularity on auxetic honeycomb are found to be studied [9]. All the published researches that explore the effect of different form of irregularity on elastic properties and structural responses of honeycombs are based on expensive finite element (FE) simulation. The present research aims to develop an analytical approach for predicting equivalent in-plane elastic properties of irregular auxetic honeycombs having spatially random variations in cell angle. Closed form formulae developed in this article can be a computationally efficient and less-tedious alternative to the expensive FE modelling and simulation approach for many applications. In the preceding section fundamental idea to obtain in-plane elastic moduli of auxetic honeycombs including the closed form formulae are discussed briefly. Subsequently representative results are presented to validate the proposed analytical approach with finite element simulation.

2. Elastic properties of irregular honeycombs

The basic idea to obtain the effective in-plane elastic moduli of the entire irregular auxetic honeycomb structure is that it is considered to be consisted of several representative unit cell elements (RUCE) having different individual elastic moduli. Elastic properties of each RUCE depends on its structural geometry and material properties. Thus the irregularity is accounted implicitly by means of RUCES. The RUCE considered in this study for deriving the expressions of different in-plane elastic moduli for an irregular honeycomb structure is shown in figure 1(b). The expressions for elastic moduli of a RUCE is derived first and subsequently the expressions for effective in-plane elastic moduli of the entire irregular honeycomb are derived by assembling the individual elastic moduli of these RUCES using basic principles of mechanics. These formulae are applicable for both tensile as well as compressive stresses.

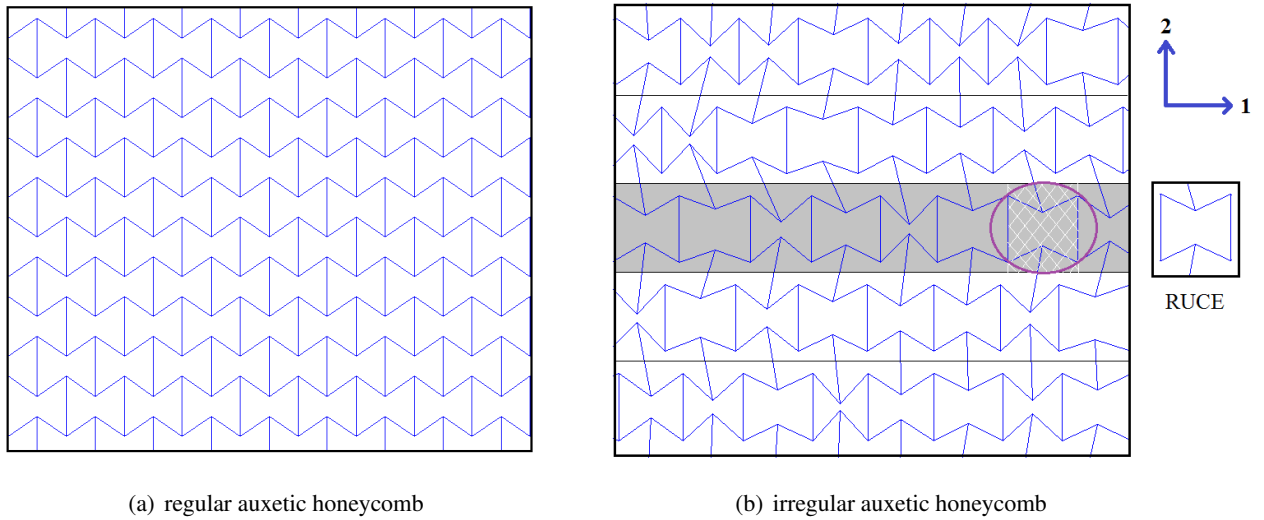


Figure 1: Typical representation of regular and irregular auxetic honeycombs

Expressions for elastic moduli of a single RUCE (figure 2) is derived first. Due to paucity of space, detail derivations can not be presented here, but the final expressions of two Young's moduli are given below for illustration:

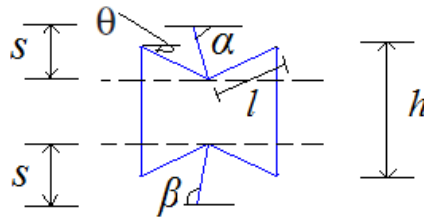


Figure 2: RUCE considered for the analysis of irregular auxetic honeycomb

$$E_{1U} = E_s \left(\frac{t}{l}\right)^3 \frac{\cos\theta}{\left(\frac{h}{l} + \sin\theta\right) \sin^2\theta} \quad (1)$$

$$E_{2U} = E_s \left(\frac{t}{l}\right)^3 \frac{\left(\frac{h}{l} + 2\frac{s}{l} + 2\sin\theta\right)}{\cos\theta \left(2\cos^2\theta + 8\left(\frac{s}{l}\right)^3 \left(\frac{\cos^2\alpha}{\sin^3\alpha} + \frac{\cos^2\beta}{\sin^3\beta}\right) + 2\left(\frac{s}{l}\right)^2 (\cot^2\alpha + \cot^2\beta)\right)} \quad (2)$$

In the next step elastic moduli of the RUCES are assembled using principles of mechanics to get the final closed form formulae of the entire irregular auxetic honeycomb. In the present analysis, the entire irregular honeycomb structure (figure 1(b)) is assumed to have m and n number of RUCES in direction-1

and direction-2 respectively. A particular cell having position at i^{th} column and j^{th} row is represented as (i, j) , where $i = 1, 2, \dots, m$ and $j = 1, 2, \dots, n$.

$$E_{1eq} = \frac{1}{\sum_{j=1}^n B_j} \sum_{j=1}^n \left(\frac{\sum_{i=1}^m l_{ij} \cos \theta_{ij}}{\sum_{i=1}^m \frac{l_{ij} \cos \theta_{ij}}{E_{1Uij}}} \right) B_j \quad (3)$$

$$E_{2eq} = \frac{1}{\left(\frac{\sum_{j=1}^n B_j \frac{\sum_{i=1}^m l_{ij} \cos \theta_{ij}}{\sum_{i=1}^m E_{2Uij} l_{ij} \cos \theta_{ij}} \right)} \sum_{j=1}^n B_j \quad (4)$$

Here B_j represents the height of a RUCE. Z_U and Z_{eq} represent the elastic moduli of a single RUCE and elastic moduli of the entire irregular auxetic honeycomb respectively, where ‘Z’ denotes a particular in-plane elastic modulus. Following similar approach, two Poisson’s ratios (ν_{12} and ν_{21}) and shear modulus (G_{12}) can be obtained for irregular auxetic honeycomb. It is worthy to note that all these formulae for irregular honeycombs can be reduced to the formulae provided by Gibson and Ashby [1] in case of regular uniform honeycombs (i.e. $B_1 = B_2 = \dots = B_n$; $s = h/2$; $\alpha = \beta = 90^\circ$; $l_{ij} = l$ and $\theta_{ij} = \theta = -30^\circ$, for all i and j).

3. Results and discussions

A FE code has been developed using Matlab [10] to obtain the in-plane elastic moduli numerically for auxetic honeycombs having spatially random structural variation. The purpose of the FE model in the present study is to validate the proposed analytical approach for obtaining in-plane elastic moduli of irregular auxetic honeycombs. The FE code has been validated using the formulae provided by Gibson and Ashby [1].

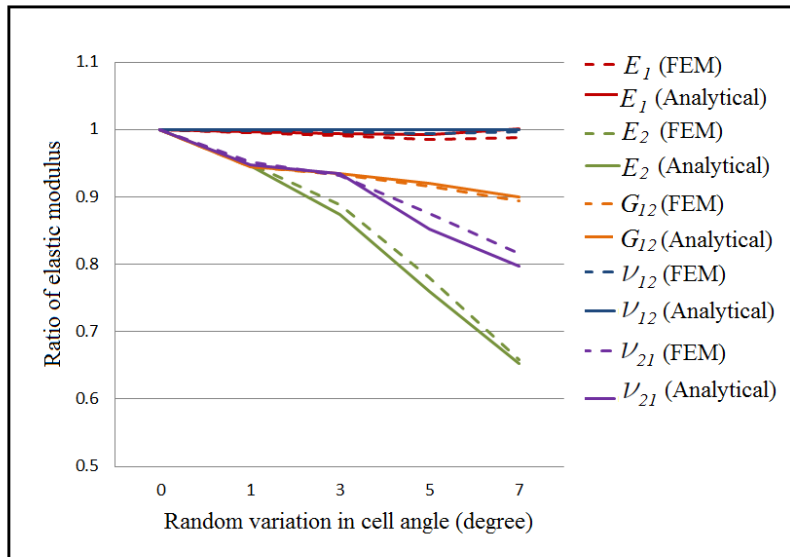


Figure 3: Variation of elastic moduli with different degree of spatial irregularity (Ratio of the elastic moduli for irregular auxetic honeycomb and elastic moduli for perfectly periodic uniform auxetic honeycombs have been plotted)

In figure 3, ratio of the mean elastic moduli for irregular auxetic honeycombs and elastic moduli for perfectly periodic uniform auxetic honeycombs (obtained using the formulae presented by Gibson and Ashby [1]) have been plotted with different degree of random spatial variation in cell angles. The figure shows that, though the effect of variations in cell angle to E_1 and ν_{12} is negligible, E_2 , ν_{21} and G_{12} reduce significantly with increasing degree of random variations in cell angle. The elastic moduli of irregular auxetic honeycombs obtained using the proposed analytical method are in good agreement with that of FE solutions.

4. Conclusions

This article presents a computationally efficient analytical approach to predict the in-plane elastic properties of irregular auxetic honeycombs. The proposed analytical method has been validated with the results of finite element simulation approach. The study shows that, random variations in cell angle has considerable influence on the values of E_2 , ν_{21} and G_{12} . It is essential to take into account such effect of irregularity in subsequent analysis and design. The idea presented in this article to efficiently deal with spatial irregularities in honeycombs can be extended further to other cellular structures considering appropriate representative unit cell element.

Acknowledgements

SA acknowledges the financial support from The Royal Society of London through the Wolfson Research Merit award. TM acknowledges the financial support through Zienkiewicz scholarship during the course of this research.

References

- [1] L. Gibson, M. F. Ashby, Cellular Solids Structure and Properties, Cambridge University Press, Cambridge, UK, 1999.
- [2] I. G. Masters, K. E. Evans, Models for the elastic deformation of honeycombs, *Composite Structures* 35 (4) (1996) 403–422.
- [3] F. Scarpa, P. Panayiotou, G. Tomlinson, Numerical and experimental uniaxial loading on in-plane auxetic honeycombs, *The Journal of Strain Analysis for Engineering Design* 35 (5) (2000) 383–388.
- [4] R. Critchley, I. Corni, J. A. Wharton, F. C. Walsh, R. J. K. Wood, K. R. Stokes, A review of the manufacture, mechanical properties and potential applications of auxetic foams, *Physica Status Solidi B* 250 (10) (2013) 1963–1982.
- [5] M. J. Silva, W. C. Hayes, L. J. Gibson, The effects of non-periodic microstructure on the elastic properties of two-dimensional cellular solids, *International Journal of Mechanical Sciences* 37 (11) (1995) 1161–1177.
- [6] H. X. Zhu, J. R. Hobdell, W. Miller, A. H. Windle, Effects of cell irregularity on the elastic properties of 2d voronoi honeycombs, *Journal of the Mechanics and Physics of Solids* 49 (4) (2001) 857–870.
- [7] K. Li, X. L. Gao, G. Subhash, Effects of cell shape and cell wall thickness variations on the elastic properties of two-dimensional cellular solids, *International Journal of Solids and Structures* 42 (5-6) (2005) 1777–1795.
- [8] A. Ajdari, H. Nayeb-Hashemi, P. Canavan, G. Warner, Effect of defects on elastic-plastic behavior of cellular materials, *Materials Science and Engineering: A* 487 (1-2) (2008) 558 – 567.
- [9] W. Liu, N. Wang, J. Huang, H. Zhong, The effect of irregularity, residual convex units and stresses on the effective mechanical properties of 2d auxetic cellular structure, *Materials Science and Engineering: A* 609 (2014) 26–33.
- [10] MATLAB, version 8.2.0.701 (R2013b), The MathWorks Inc., 2013.

NURBS based Differential Quadrature Method (N-DQM) for Free Vibration Analysis of Linearly Tapered Circular Plate Resting on Pasternak Foundation

*S. Srivastava, Raju Sethuraman

Department of Mechanical Engineering, IIT Madras, India

*srivastavass@yahoo.co.in

ABSTRACT

Non Uniform Rational B-Spline(NURBS) based Differential Quadrature Method (N-DQM), a numerical collocation technique, has been presented for vibration analysis of linearly tapered circular plates resting on an elastic foundation. The governing differential equations of motion have been derived by using Hamilton's energy principle based on classical (Kirchhoff) plate theory. Here, we obtained the first three natural frequencies of circular plate resting on Pasternak foundation for clamped and simply-supported boundary conditions. Further, we show the applicability of N-DQM for a curved geometry by solving the two dimensional Laplace equation in the sector of an annular plate. Using NURBS as a basis functions, one can extend the applicability of DQM for complex geometries. The method has been useful for complex engineering problems like machine design etc.

Key Words: DQM; NURBS; Kirchhoff plate; Pasternak foundation; Laplace equation.

1. Introduction

The study of vibration of plates are often encountered in engineering applications and their use in machine design, nuclear reactor technology, naval and aerospace structures are quite common. The plates of appropriate variation in thickness has significantly greater efficiency for vibration as compared to the plates with uniform thickness. The problem of plates resting on elastic foundation is very important in structural foundation engineering such as pavement slab of roads, foundation of tall buildings etc. From the various available foundation model viz. Winkler's, Hetenyi, Reissner, Vlasov, Pasternak etc., Pasternak model provides a better approximation, as it takes into account not only its transverse reaction but also the shear interaction between the spring elements. Here, we have study the axisymmetric vibrations of circular plates of linear thickness variation resting on a Pasternak foundation on the basis of classical (Kirchhoff) plate theory. The closed form analytical solutions for such complex problems are extremely hard to find therefore, numerical approximation techniques have been used for solution, such as Finite element method, Finite difference method, Frobenius method, Ritz method, Differential quadrature method etc. Of the various available numerical techniques, differential quadrature (DQ) methods[1-2] have distinguished themselves because of their high accuracy and straightforward implementation. The choice of shape function also effects the accuracy and convergence of the method for a problem. The concept of isogeometric analysis has been introduced by Hughes et al.[3] in 2005. A detailed study of NURBS has been given by Pigel and Tiller[4]. Shojaee et al.[5] studied the free vibration of thin plates using Isogeometric approach. In this work, the proposed method has been used for obtaining the natural frequencies for clamped and simply supported boundary for the first three modes of vibration. The effect of foundation parameters together with taper parameter on natural frequencies has been investigated for first three modes of vibration. Also, the method has been employed for solving Laplace equation in complex domain. The consideration of NURBS as basis function makes N-DQM applicable for a variety of problems.

2. NURBS Basis Function

NURBS basis function of order p for a given knot vector $T = [t_1, t_2, \dots, t_{n+p+1}]$, control point $B = [b_1, b_2, \dots, b_n]$ and weight $w = [w_1, w_2, \dots, w_n]$ associated with n^{th} control point, is given by

$$R_{i,p}(t) = \frac{N_{i,p}(t)w_i}{\sum_{i=1}^n N_{i,p}(t)w_i}. \quad (1)$$

Derivative of NURBS basis function is given by,

$$\frac{d^k}{dt^k} R_{i,p}(t) = \frac{C_i^k(t) - \sum_{j=1}^k (kj) F^j(t) \frac{d^{(k-j)}}{dt^{(k-j)}} R_{i,p}(t)}{F(t)} \quad (2)$$

where,

$$F(t) = \sum_{i=1}^n N_{i,p}(t)w_i, C_i^k(t) = w_i \frac{d^k N_{i,p}(t)}{dt^k}, F^k = \frac{d^k F(t)}{dt^k}.$$

and Basis spline function $N_{i,p}(t)$ and their derivatives are given by[4].

In this paper, the NURBS basis function is employed for parameterization of the geometry and trial solution as follows

$$\mathbf{x}(\mathbf{t}) = \sum_{I=1}^{n \times m} (R_I(\mathbf{t}) B_I) \quad (3)$$

$$\mathbf{U}^h(\mathbf{t}) = \sum_{I=1}^{n \times m} (R_I(\mathbf{t}) U_I) \quad (4)$$

where, $\mathbf{t} = (u, v)$ is the parametric coordinates, $\mathbf{x} = (x, y)$ is the physical coordinates, B_I represents the control points of a $n \times m$ control mesh, $R_I(\mathbf{t})$ are the bivariate NURBS basis functions of order p and q in u and v directions, respectively, and U_I represent the deflection field at each control point. Figure(1).

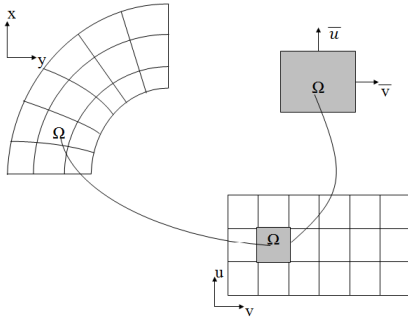


Figure 1: Transformation of physical space to parametric space

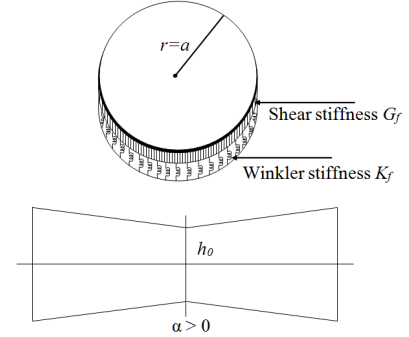


Figure 2: Geometry of circular plate resting on Pasternak foundation with linear variation in thickness

3. Vibration of circular plate

Consider a homogeneous isotropic circular plate of radius a and density ρ with varying thickness $h(r)$ and resting on a Pasternak foundation with spring and shear stiffness K_f and G_f , respectively, referred to a system of cylindrical polar coordinates (r, θ, z) . The axis of the plate is taken as the line $r = 0$ and its middle surface as the plane $z = 0$, (Figure(2)).

The governing differential equation of motion of such plates has been given by:

$$P_0 \frac{d^4 W}{dx^4} + P_1 \frac{d^3 W}{dx^3} + P_2 \frac{d^2 W}{dx^2} + P_3 \frac{dW}{dx} + P_4 W = 0. \quad (5)$$

where,

$$P_0 = 1, \quad P_1 = \frac{2}{x}(1 + 3A), \quad P_2 = \frac{1}{x^2}[-1 + 3(2 + \nu)A + 6A^2 - \frac{Gx^2}{(1 + \alpha x)^3}],$$

$$P_3 = \frac{1}{x^3}[1 - 3A + 6A^2\nu - \frac{Gx^2}{(1 + \alpha x)^3}], \quad P_4 = \frac{K}{(1 + \alpha x)^3} - \frac{\Omega^2}{(1 + \alpha x)^2},$$

$$A = \frac{\alpha x}{(1 + \alpha x)}, \quad K = \frac{ak_f}{D_0}, \quad G = \frac{ag_f}{D_0}, \quad D_0 = \frac{Eh_0^3}{12(1 + \nu^2)}, \quad \Omega^2 = \frac{12\rho a^2 \omega^2 (1 - \nu^2)}{Eh_0^3}.$$

An approximate solution of equation(5) together with the boundary conditions at the edge $x = 1$ and regularity condition at the center of the plate, constitutes a boundary value problem in the range $(0, 1)$, which can be solved by N-DQM.

Solution Technique: N-DQM

The differential equation(5) is solved by using NURBS based differential quadrature method. Here, we consider the degree of polynomial as p , number of control point n , and size of open knot vector $m = n + p + 1$. Let t_1, t_2, \dots, t_n be the collocation point in the parametric space in the applicability range $[0,1]$. According to differential quadrature rule, the k^{th} order derivative of $W(t)$ with respect to t can be expressed discretely at the point t_i as

$$W^k(t_i) = \sum_{j=1}^n R_{i,j}^k W_j(t), \quad k = 1, 2, 3, 4, i = 1, 2, \dots, n. \quad (6)$$

where, $R_{i,j}^k$ are weighting coefficients associated with n^{th} order coefficients of $W(t)$ with respect to t at discrete point t_i . The following boundary conditions are used to solve the problem

Clamped boundary: $W = 0, \frac{dW}{dx} = 0$; Simply-supported boundary: $W = 0, \frac{d^2W}{dx^2} + \frac{\nu}{x} \frac{dW}{dx} = 0$.

Results

Here, we have obtained the first three natural frequencies of circular plate resting on Pasternak foundation for clamped and simply supported boundary conditions. Figure 3(a) and 3(b) shows the relative % error in the frequency parameter with increasing number of control points for clamped and simply supported plate respectively.

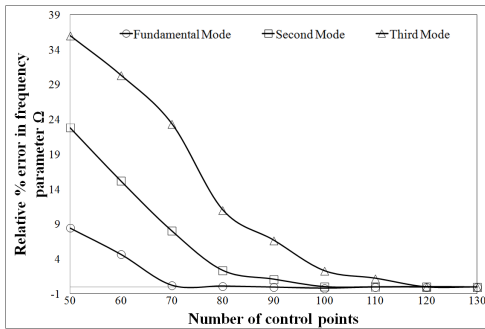


Figure 3(a): Relative % error in Ω of clamped plate for $K=500, G=25, \alpha = 0.5$.

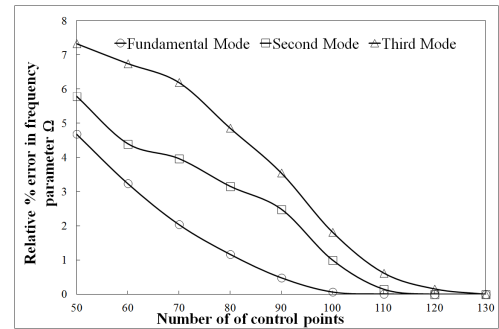


Figure 3(b): Relative % error in Ω of S-S plate for $K=500, G=0.25, \alpha = 0.5$.

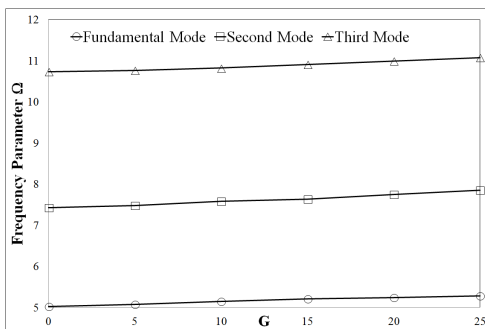


Figure 4: Variation of Ω with shear stiffness parameter G for clamped plate; $\alpha = 0.5, K=500$.

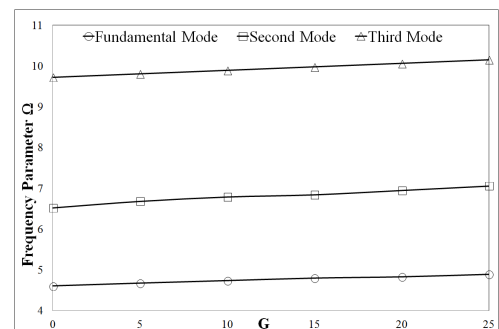


Figure 5: Variation of Ω with shear stiffness parameter G for S-S plate; $\alpha = 0.5, K=500$.

The number of control points is fixed at 130 since further increase in the number of control points doesn't have significant influence on the results, order of polynomial is taken as 5 throughout the study. Results are reported in figures 4-5. It has been observed that the values of frequency parameter for clamped

plate is higher than that of simply supported plate. Also the rate of increase of frequency parameter get pronounced as we moved towards the higher mode.

4. 2D case study

The proposed method can be extended for multi-dimensional problems. Here, we show the solution of Laplace equation given by(7) in the domain of a sector of an annular plate. The results are shown in figures 6-7.

$$\nabla^2 U = 0; \quad (7)$$

Boundary conditions:

$U=0$ at $x = 0$, $U=0$ at $y = 0$, $U=0$ at $x^2 + y^2 = R_1^2$, $U=\sin(x\pi/2)$ at $x^2 + y^2 = R_2^2$, where, $R_1(= 10)$; and $R_2(= 20)$ are the inner and outer radius of the plate respectively. Order of spline in u-direction=3, order of spline in v-direction=3.

Equation(7) is first transformed into parametric form and then solved by using N-DQM. The solution is approximated by using(4).

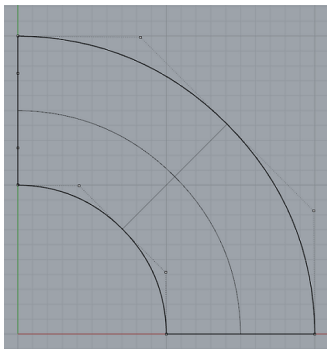


Figure 6: Control Mesh for the sector of an annular disk

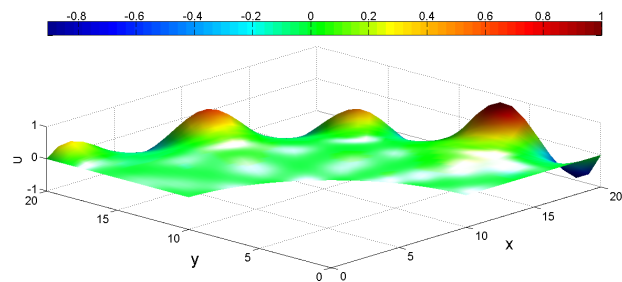


Figure 7: Surface plot for the solution of Laplace equation in the sector of an annular disk

5. Conclusion

The proposed method named N-DQM gives optimized results. By using NURBS as a basis function one can extend the applicability of usual DQM (which is based on Lagrange's polynomial) for complex geometry. This method is applicable for all types of linear problems. Also N-DQM will be very beneficial for the conditions where we have to deal with nonlinearity, discontinuity, irregularity etc. specially in the field of computational science and engineering. The accuracy of the method can be enhanced by choosing the higher order polynomial and by increasing the number of control points. The proposed method has been very useful in various practical engineering problems as fluid mechanics, structural shape optimization, fracture mechanics, structural vibration etc.

References

- [1] C. Shu. *Differential Quadrature and Its Application in Engineering*, Springer, London, 2000.
- [2] S. Sharma, S. Srivastava, R. Lal. Free vibration analysis of Circular Plate of Variable Thickness Resting on Pasternak Foundation, *Journal of International Academy of Physical Sciences*, Vol. 15, 1-13, 2011.
- [3] T. J. R. Hughes, J. A. Cottrell, Y. Bazilevs. Isogeometric Analysis: CAD, Finite Elements, NURBS, Exact Geometry and Mesh Refinement, *Computer Methods in Applied Mechanics and Engineering*, Vol. 194, 4135-4195, 2005.
- [4] L. Pigel, W. Tiller. *The NURBS Book (Monograph in Visual Communication)*, Second Edition, Springer-Verlag, Berlin, Heibelberg GmbH 1997.
- [5] S. Shojaee, E. Izadpanah, N. Valizadeh, J. Kiendl. Free Vibration Analysis of Thin Plates by Using a NURBS-based Isogeometric Approach, *Finite Elements in Analysis and Design*, Vol. 61, 23-34, 2012.

A first order mixed formulation for fast solid dynamics using Smooth Particle Hydrodynamics

*G. Greto¹, S. Kulasegaram¹, C. H. Lee², A. J. Gil², and J. Bonet²

¹College of Physical Sciences & Engineering, Cardiff University, The Parade, Cardiff, CF24 3AA

²Zienkiewicz Centre for Computational Engineering, Swansea University, Singleton Park, SA2 8PP

*GretoG@cardiff.ac.uk

ABSTRACT

An explicit Total Lagrangian mixed momentum/strains formulation [1–5], in the form of a system of first order conservation laws, has been recently proposed to overcome the shortcomings posed by the traditional second order displacement-based formulation, namely: (1) bending and volumetric locking difficulties; (2) hydrostatic pressure fluctuations; and (3) reduced order of convergence for derived variables. Following the work of Bonet and Kulasegaram [6, 7], one of the key novelties in this paper is to adapt a Smoothed Particle Hydrodynamics meshless method, in conjunction with a total variation diminishing two-stage Runge-Kutta time integrator, in the context of first order conservation laws for fast solid dynamics experiencing large deformation. The two-field version of this mixed methodology performs extremely well in bending dominated scenarios [8] and, more importantly, alleviates spurious pressure oscillations. As both linear momentum and deformation gradient are used as primary variables of the system, equal order of approximation is achieved in both fields. A series of numerical examples are carried out drawing key comparisons between the proposed formulation and some other recently published numerical techniques.

Key Words: Conservation laws; SPH; Locking; Incompressibility; Fast dynamics

1. Introduction

Dynamic explicit displacement-based finite element codes, based on low order finite element technology, are commonly used for the simulation of large strain impact problems by aerospace, automotive, biomedical, defence and manufacturing industries. In these codes, the 8-noded underintegrated hexahedral element is the preferred option to model solid components. Many practical applications (i.e. crashworthiness and drop-impact modelling), however, involve geometries that are far too complex to be meshed using hexahedra in three dimensions. The presence of large solid deformations accompanied by severe mesh distortion may lead to poorly shaped elements, unless some form of adaptive remeshing is applied.

From the viewpoint of spatial discretisation, the standard displacement-based formulation for low order elements is known to experience locking difficulties in nearly-incompressible, bending dominated scenarios. It is also known that the use of linear interpolation within a finite element leads to second order convergence for the primary variables, but one order less for derived variables. From the time discretisation point of view, the Newmark method has a tendency to introduce high frequency noise in the solution field, especially in the vicinity of sharp spatial gradients.

To overcome the shortcomings mentioned above, a mixed methodology is presented in the form of a system of first order conservation laws, where the linear momentum and the deformation gradient tensor are regarded as the two main conservation variables. This approach enables the stresses to converge at the same rate as the velocities (or displacements).

The main goal of this paper is to develop a new Smooth Particle Hydrodynamics (SPH) formulation, tailor-made for this mixed formulation, which borrows concepts from a Jameson-Schmidt-Turkel (JST) finite volume methodology [1]. JST will be used to provide artificial dissipation and shock-capturing capabilities. In SPH, the second order (harmonic) and fourth order (biharmonic) operators employed in the JST scheme can be readily obtained by closed-form differentiation of the interpolating kernel functions. Crucially, SPH derivatives are smooth even in the presence of very large deformations.

2. Reversible elastodynamics

The motion of a deformable continuum body from an initial (or undeformed) configuration $\mathbf{X} \in V \subset \mathbb{R}^3$ to a current (or deformed) configuration $\mathbf{x} \in v(t) \subset \mathbb{R}^3$ can be described by the relation $\mathbf{x} = \boldsymbol{\phi}(\mathbf{X}, t)$, where $\boldsymbol{\phi}$ links each material particle in \mathbf{X} to its current position \mathbf{x} at time t during the motion. Under the assumption that thermal effects and plastic dissipative mechanisms might be neglected, a mixed formulation in the form of a system of first order conservation laws for elastodynamics can be cast as [1, 2]:

$$\frac{\partial \mathbf{p}}{\partial t} - \nabla_0 \cdot \mathbf{P}(\mathbf{F}) = \rho_0 \mathbf{b}; \quad \frac{\partial \mathbf{F}}{\partial t} - \nabla_0 \cdot \left(\frac{1}{\rho_0} \mathbf{p} \otimes \mathbf{I} \right) = \mathbf{0}.$$

Here, $\mathbf{p} = \rho_0 \mathbf{v}$ is the linear momentum per unit of undeformed volume, ρ_0 is the material density, \mathbf{v} represents the velocity field, \mathbf{P} is the first Piola-Kirchhoff stress tensor, \mathbf{b} is the body force per unit mass, \mathbf{F} is the deformation gradient and \mathbf{I} is the identity matrix. The notation ∇_0 denotes the material gradient operator in undeformed space, where $[\nabla_0]_I \equiv \frac{\partial}{\partial X_I}$. The above laws can be cast in a more compact form:

$$\frac{\partial \mathcal{U}}{\partial t} + \frac{\partial \mathcal{F}_I}{\partial X_I} = \mathcal{S}; \quad \forall I = 1, 2, 3; \quad (1)$$

where \mathcal{U} is the vector of conservation variables, \mathcal{F}_I is the flux vector in the material direction I and \mathcal{S} is the source term described by:

$$\mathcal{U} = \begin{bmatrix} \mathbf{p} \\ \mathbf{F} \end{bmatrix}; \quad \mathcal{F}_N = \mathcal{F}_I N_I = \begin{bmatrix} -PN \\ -\frac{1}{\rho_0} \mathbf{p} \otimes N \end{bmatrix}; \quad \mathcal{S} = \begin{bmatrix} \rho_0 \mathbf{b} \\ \mathbf{0} \end{bmatrix}. \quad (2)$$

For the closure of system (1), it is necessary to introduce an appropriate constitutive law by relating \mathbf{P} with \mathbf{F} . In this paper, a standard hyperelastic Neo-Hookean model is used, whereby the first Piola \mathbf{P} can be additively decomposed into the summation of deviatoric, \mathbf{P}_{dev} , and volumetric, \mathbf{P}_{vol} , contributions:

$$\mathbf{P} = \mathbf{P}_{dev} + \mathbf{P}_{vol}; \quad \mathbf{P}_{dev} = \mu J_F^{-2/3} \left(\mathbf{F} - \frac{1}{3} (\mathbf{F} : \mathbf{F}) \mathbf{F}^{-T} \right); \quad \mathbf{P}_{vol} = p \mathbf{H}_F; \quad p = \kappa (J_F - 1). \quad (3)$$

Note that both the Jacobian J_F and the cofactor of deformation \mathbf{H}_F appearing in expression (3) are computed based on \mathbf{F} , which can be expressed as $J_F = \det \mathbf{F}$ and $\mathbf{H}_F = J_F \mathbf{F}^{-T}$.

3. Numerical methodology

3.1. Spatial discretisation

In the present work, system (1) is spatially discretised using the SPH method. Being a mesh-free technique, SPH can be employed effectively in the simulation of high-velocity impacts and high strain-rate deformations. Another advantage of SPH is the locality of the spatial discretisation, with consequent savings in computational power [9]. In a discretised domain, the SPH interpolation at the position \mathbf{x} of a quantity $\phi(\mathbf{x})$, denoted here as $\langle \phi(\mathbf{x}) \rangle$, can be approximated by a summation over all neighbouring particles \mathbf{x}_b :

$$\langle \phi(\mathbf{x}) \rangle = \sum_b V_b \phi(\mathbf{x}_b) W(\mathbf{x}_b - \mathbf{x}, h), \quad (4)$$

where h is the smoothing length, and $W(\mathbf{x} - \mathbf{x}', h)$ is usually a polynomial function with compact support (W vanishes for $\|\mathbf{x} - \mathbf{x}'\|_{L^2} \geq 2h$) for which the following properties are valid:

$$\int W(\mathbf{r}, h) d\mathbf{r} = 1; \quad \lim_{h \rightarrow 0} W(\mathbf{r}, h) \rightarrow \delta(\mathbf{r}).$$

Calculation of the first derivative of a function ϕ in SPH involves the derivation of the kernel function W :

$$\nabla \phi(\mathbf{x}) = \sum_b V_b \phi(\mathbf{x}_b) \nabla W(\mathbf{x}_b - \mathbf{x}, h). \quad (5)$$

To improve the accuracy of the SPH interpolation and to exactly preserve momentum, corrections must be introduced on both the kernel, and the kernel gradient [6, 7, 10]. These corrections lead to the Corrected SPH (CSPH) formulation. CSPH greatly enhances the accuracy and the consistency of the discretisation.

3.2. Temporal discretisation

The spatial discretisation discussed above yields a system of ordinary differential equations of the form:

$$\frac{d\mathbf{U}_a}{dt} = \mathcal{R}_a(\mathbf{U}_a, t), \quad (6)$$

where $\mathcal{R}_a(\mathbf{U}_a, t)$ represents the right-hand-side of SPH spatial discretisation associated with particle a . To advance (6) in time from t_n to t_{n+1} , an explicit, two-stage Total Variation Diminishing Runge-Kutta time integrator is used:

$$\mathbf{U}_a^* = \mathbf{U}_a^n + \Delta t \mathcal{R}_a(\mathbf{U}_a^n, t^n); \quad \mathbf{U}_a^{**} = \mathbf{U}_a^* + \Delta t \mathcal{R}_a(\mathbf{U}_a^*, t^{n+1}); \quad \mathbf{U}_a^{n+1} = \frac{1}{2}(\mathbf{U}_a^n + \mathbf{U}_a^{**}). \quad (7)$$

The time step $\Delta t = t^{n+1} - t^n$ is calculated based upon Courant-Friedrichs-Lewy number α_{CFL} , by means of $\Delta t = \alpha_{CFL} (h / c_{p,max})$ where $c_{p,max}$ is the maximum p -wave speed and h the smoothing length.

4. Applications

In this section, two numerical examples, namely a 1D elastic bar and a 3D twisting column, are assessed to show clear advantages in the use of the mixed momentum/strains formulation over the use of a classical, displacement-based methodology. Figure 1 illustrates that an equal second order of convergence for velocity and stress can be obtained using a library of stabilised finite element and finite volume mixed methodologies.

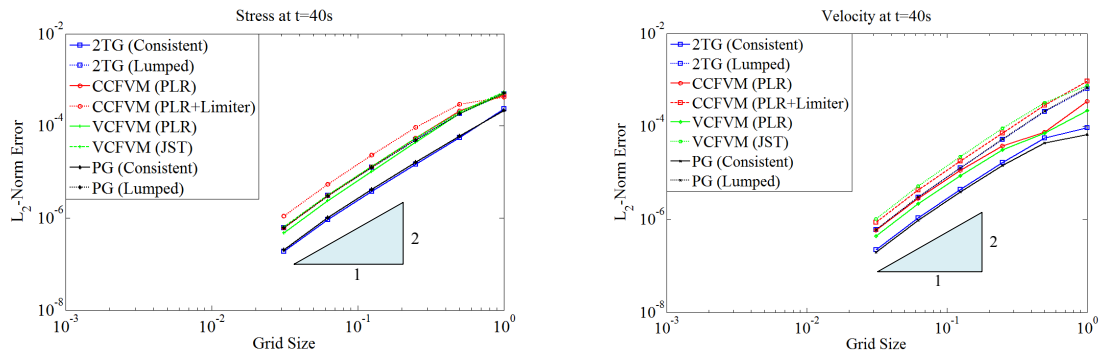


Figure 1: Convergence analysis of a 1D bar using various in-house numerical methodologies; for instance, 2TG represents two step Taylor-Galerkin method, CCFVM represents cell centred finite volume algorithm, VCFVM represents vertex centred finite volume algorithm and PG represents stabilised Petrov-Galerkin methodology.

To show the applicability and robustness of the proposed mixed formulation, a twisting column experiencing highly nonlinear deformations is examined. Figure 2 shows a sequence of deformed states spatially discretised using CSPH on traditional total Lagrangian displacement-based formulation without any artificial stabilisation. Numerical instabilities, in the form of locking effects and hydrostatic pressure fluctuations, can be clearly observed. The deficiencies of the displacement-based formulation are in clear contrast with the accuracy displayed by the mixed formulation, as shown in Figure 3 (in this case solved using a Petrov-Galerkin finite element based approach).

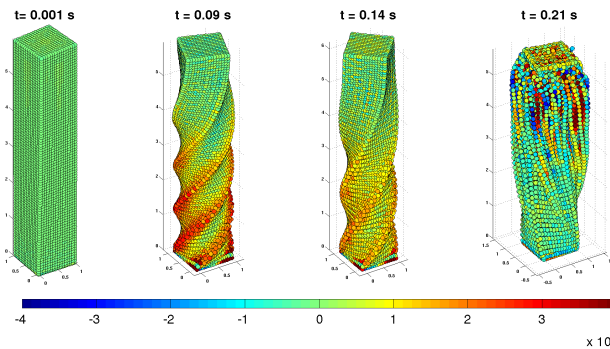


Figure 2: Twisting column, sequence of deformed shapes simulated using displacement-based CSPH methodology.

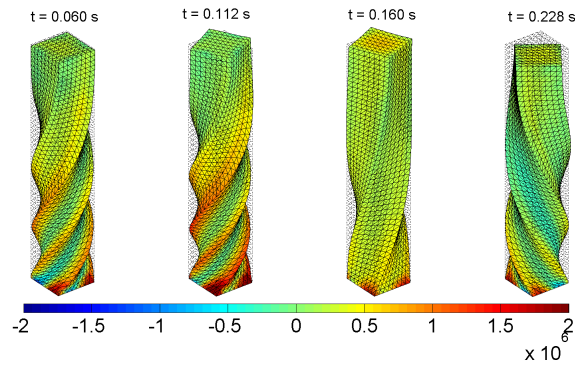


Figure 3: Twisting column, sequence of deformed shapes simulated using stabilised PG mixed methodology.

5. Conclusions

In this paper, a new computational methodology has been presented for the numerical analysis of nearly incompressible, bending dominated large deformations in fast solid dynamics. The methodology is based upon a system of first order conservation laws, where the linear momentum \mathbf{p} and the deformation gradient \mathbf{F} are treated as primary variables. A CSPH spatial discretisation, together with the use of nodal-based JST techniques, has been employed for stabilisation of the governing equations. Numerical examples have then been shown in order to demonstrate the applicability of the methodology.

6. Acknowledgements

The authors gratefully acknowledge the financial support provided by the Sêr Cymru National Research Network for Advanced Engineering and Materials, United Kingdom.

References

- [1] M. Aguirre, A. J. Gil, J. Bonet, A. A. Carreño. A vertex centred Finite Volume Jameson-Schmidt-Turkel (JST) algorithm for a mixed conservation formulation in solid dynamics. *JCP*, 259, pp.672–699, 2014.
- [2] C. H. Lee, A. J. Gil, J. Bonet. Development of a stabilised Petrov-Galerkin formulation for conservation laws formulation in Lagrangian fast solid dynamics. *CMAME*, 268, pp.40–64, 2014.
- [3] C. H. Lee, A. J. Gil and J. Bonet. Development of a cell centred upwind finite volume algorithm for a new conservation law formulation in structural dynamics. *Computers and Structures*, 118, 13–38, 2013.
- [4] I. A. Karim, C. H. Lee, A. J. Gil and J. Bonet. A Two-Step Taylor Galerkin formulation for fast dynamics. *Engineering Computations*, 31, 366–387, 2014.
- [5] J. Bonet, A. J. Gil, C. H. Lee, M. Aguirre, R. Ortigosa. A first order hyperbolic framework for large strain computational solid dynamics. Part I: Total Lagrangian isothermal elasticity. *CMAME*, 283, pp. 689–732, 2015.
- [6] J. Bonet, S. Kulasegaram. Correction and stabilization of smooth particle hydrodynamics methods with applications in metal forming simulations. *IJNME*, 47, pp.1189–1214, 2000.
- [7] J. Bonet, S. Kulasegaram. Remarks on tension instability of Eulerian and Lagrangian corrected smooth particle hydrodynamics (CSPH) methods. *IJNME*, 52, pp.1203–1220, 2001.
- [8] A. J. Gil, C. H. Lee, J. Bonet and M. Aguirre. A stabilised Petrov-Galerkin formulation for linear tetrahedral elements in compressible, nearly incompressible and truly incompressible fast dynamics. *CMAME*, 276, 659–690, 2014.
- [9] R. A. Gingold, J. J. Monaghan. Smoothed particle hydrodynamics: Theory and application to non-spherical stars. *Monthly Notices of the Royal Astronomical Society*, 181, pp.375–389, 1977.
- [10] J. Bonet, T.-S.L. Lok. Variational and momentum preservation aspects of Smooth Particle Hydrodynamic formulations. *CMAME*, 180, pp.97–115, 1999.

SIMULATION OF SMALL PUNCH TEST FOR RAPID PROTOTYPING OF ALLOYS

***S. Mehraban, E. Enticknap, J. Cullen, C. Pleydell-Pearce, D. Bould, S.G.R. Brown, N.P. Lavery**

Materials Research Centre, Swansea University Singleton Park, Swansea SA2 8PP

*S.Mehraban@swansea.ac.uk

ABSTRACT

High throughput, rapid prototyping of alloys requires a quick way to determine the mechanical properties of alloy compositions. Due to the nature of this manufacturing method only small samples are fabricated. To test mechanical properties of small samples the disk punch indenter approach was developed [1]. The disc-shaped specimens used in the disk punch indenter are representative for characterizing the macroscopic material behaviour of the alloy [2]. The deformation information measured from the disk punch is fed into a computer model. Using implicit large-deformation finite element solver in ANSYS with non-linear modelling for the plasticity models, total strain is determined and from this the Upper Tensile Strength (UTS) and anisotropic information is calculated. This gives a comparison to tensile testing (uniaxial testing) to verify empirical relationships for yield stress and ultimate tensile stresses and to predict tensile properties.

Keywords: *Small Disk Punch; ANSYS; Rapid Prototype; Alloy; High Throughput.*

1. Introduction

The small disk punch was originally developed in the 1980's and is used to measure the ductility of metals in critical environments when mechanical properties of operating components is needed and is a key element for enhanced component reliability [2]. The advantage of this test is that a small sample size can be used to determine the mechanical properties of a material.

The limitation of the method is that output is a simple force displacement curve and the UTS is not directly determined as with a tensile specimen. Using the computer simulation developed by MACH1[3] these properties can be determined. A Comparison with tensile testing (uniaxial testing) to verify empirical relationships (e.g. for yield stress and ultimate tensile stresses) is used for verification of the computer simulation. This paper will focus on the computer simulation of the disk punch indenter and validation of the model.

2. Background

The proprietary method used by MACH1 for the rapid prototyping of alloys allows many samples of varying compositions to be fabricated quickly. To enable the rapid fabrication of these samples a small specimen is produced. To mechanically test samples with these dimensions the small punch disk is used. The small disk punch works by pushing a rod with a pre-determined radius through a disk shaped sample see figure 1. From this the force required and the position are measured and a Force – Displacement curve is generated, see figure 2.

This work combines rapid alloy fabrication, mechanical testing and computer simulation of the mechanical test to predict the properties of the alloy. Using this method a route to rapid, specific alloy design is possible. Using regression analysis the data from the disk punch can be fed into the computer simulation to improve the accuracy of the model.

3. Modelling Methodology

- Small punch model uses implicit large-deformation finite element solver in ANSYS with non-linear modelling for the plasticity models (Total strain = elastic strain + plastic strain)
- **Elastic criterion** – Model assumes linear isotropic elastic behaviour. In which case E , ν gives shear and bulk moduli.
- **Yield criterion** defines the material state at the transition from elastic to elastic-plastic behaviour. (Von Mises or Hill)
- **Flow rule** determines the increment in plastic strain from the increment in load. Associated flow rule (metals) and non-associated (soils/granular).
- **Hardening rule** that gives the evolution in the yield criterion during plastic deformation.
 - Isotropic hardening (expansion of the yield surface)
 - Kinematic hardening (translation of the yield surface due to e.g. cyclical loading)

The Modelling geometry used is shown in figure 3.

4. Validation of Computer Model.

The computer simulation generates a force displacement curve, see figure 4. The output from simulation is the characteristic shape the force displacement curve from the small disk punch. There is some limitation to this model in the cracking region and so the simulation limits are set to end before this point.

The material used to validate the computer model is a dual phase steel produced by TATA steel with a UTS (R_m) of 640Mpa (DP600®) as tensile specimen data is readily available. Initially the model has been validated through geometrical comparison of the graphical output from the computer simulation and images of mechanically deformed disk samples that were sectioned and analysed (see figure 5).

5. Figures

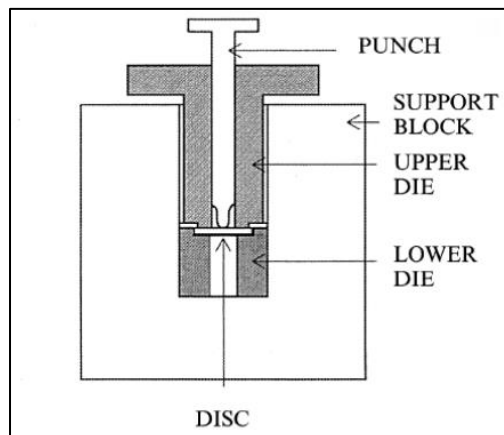


Figure 1. Theoretical Schematic of small disk punch (Norris Parker 1995)

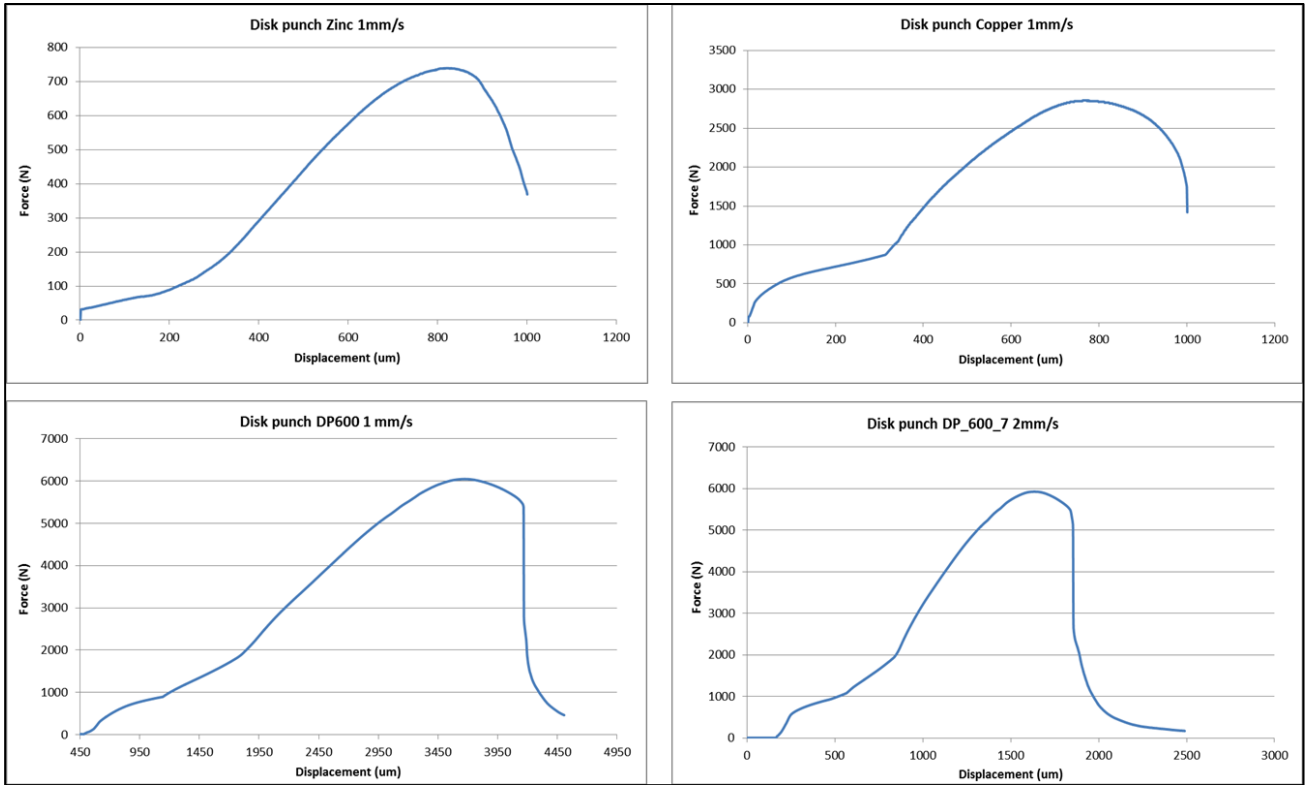


Figure 2. Typical Force displacement curve for the small disk punch for Zinc, Copper and DP600 Steel, these curves are characteristic of the output of the small punch disk.

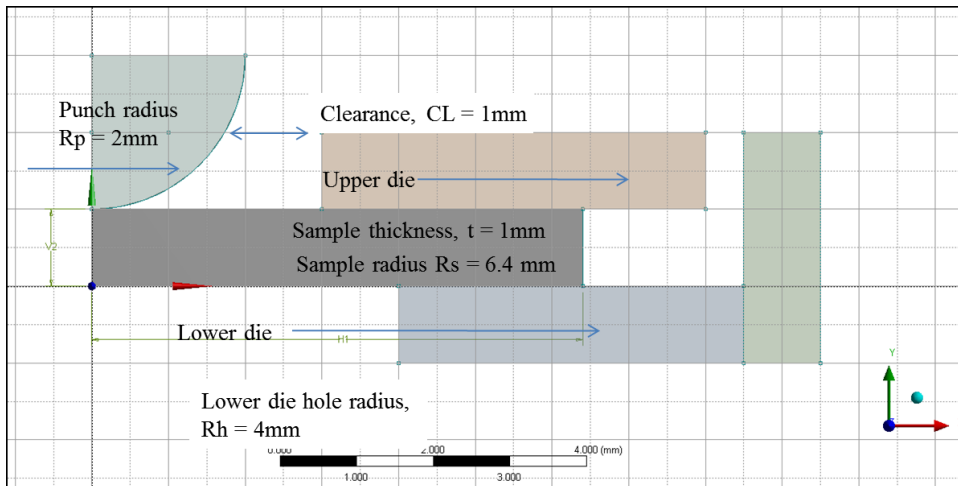


Figure 3. Modelling geometry used in computer simulation.

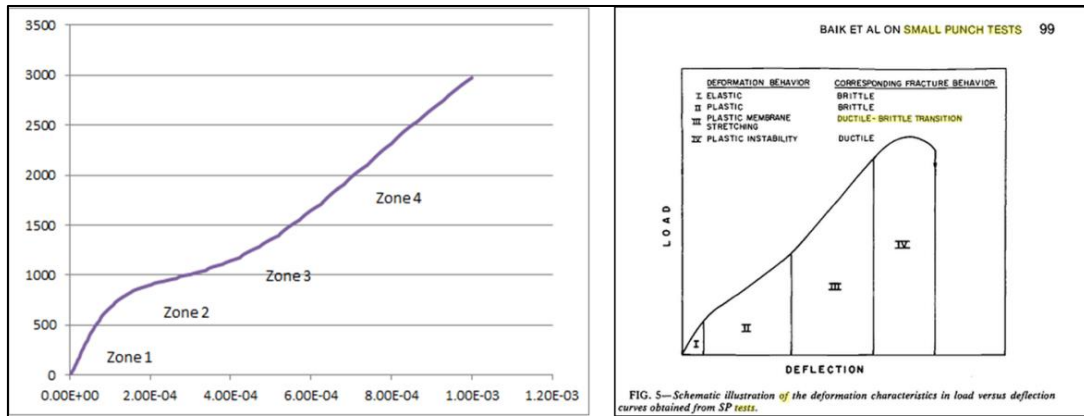


Figure 4. Comparison of simulation output with typical Force Displacement curve obtained from small disk punch test.

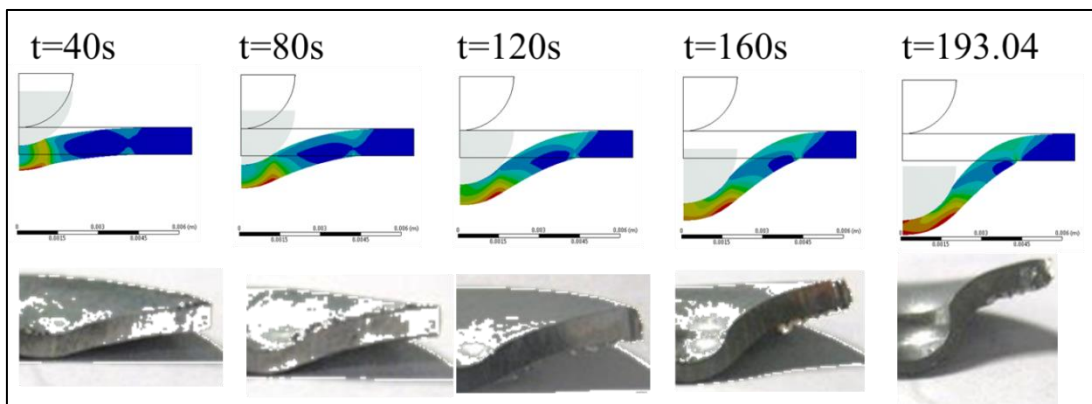


Figure 5. Comparison of simulation with deformed disks showing coherent profile.

Acknowledgements

The authors would like to thank Academia 4 Business (A4B) of the Welsh Government and the Advanced Sustainable Manufacturing Technologies (ASTUTE) project, which is part funded from the EU's European Regional Development Fund through the Welsh European Funding Office for their continued support.

References

- [1] S. D. Norris and J. D. Parker, "Deformation processes during disc bend loading," *Mater. Sci. Technol.*, vol. 12, no. 2, pp. 163–170, 1996.
- [2] S. Rasche and M. Kuna, "Improved small punch testing and parameter identification of ductile to brittle materials," *Int. J. Press. Vessel. Pip.*, Sep. 2014.
- [3] "MACH 1 Webpage." [Online]. Available: <http://www.swansea.ac.uk/engineering/mach1/>.

SOLIDS AND STRUCTURES 5

Finite element modelling of braided fibres subject to large deformations

*M. Cortis¹, L. Kaczmarczyk² and C.J. Pearce³

¹School of Engineering and Computing Science, Durham University, Durham, DH1 3LE

^{2,3}School of Engineering, University of Glasgow, Rankine Building, Glasgow, G12 8LT

*michael.cortis@durham.ac.uk

ABSTRACT

This paper presents a numerical methodology to model elastic braided fibres. Elastic transversely isotropic material was used due to the anisotropy of the strands. Large deformation finite analysis based on large rotations / small strains total Lagrangian formulation was used to account for geometrical non-linearities. Pre-processing was necessary to insert interface elements where strands are in self contact and with other materials, followed by a potential flow analysis that was undertaken to evaluate the fibre directions for every individual strand. An FE model of a knot demonstrates the importance of defining interface elements, while a three plait braided model shows the importance of using a transversely isotropic model compared to an isotropic model. A twelve strand sinnet rope (T12) was also modelled using the proposed methodology and highlights new challenges when using different types of braiding.

Key Words: *fibre reinforced concrete; braided ropes; knots; large deformation; transversely isotropic; interface elements*

1. Introduction

Braided sinnet ropes made from synthetic materials such as carbon and Technora fibre can be used as flexural strengthening of concrete structures but it is essential that their mechanical behaviour and interaction with other materials is well understood. A system was developed, using technora T12 rope braided over a series of glass beads, creating ribbing which increases the adhesion and pull-out strength when embedded in concrete [1]. This continuous braided fibre reinforcement system could eventually replace FRPs reinforcement and producing fire resistant concrete structures. The resin matrix of FRPs have a low glass transition temperature (GTT) of around 200°C, losing its composition and bond strength by 80-90% [3, 4]; in comparison, continuous braided fibre reinforcement systems make use of braiding to bind fibres and mitigate problems related to polymeric resins.

In this paper we propose a finite element modelling approach to simulate the mechanical behaviour of elastic braided fibres subject to large deformations. The importance of such technique is demonstrated by modelling a knot and a three braided plait under tension.

2. Large Deformation for transverse isotropic material

Braided geometries can experience two types of geometric non-linearities, large material rotations due to inter-winding geometries, and large strains when they are made for soft materials. In this paper we use elastically stiff materials such as carbon and Technora fibres and hence the finite deformation formulation is restricted to large rotations and small strains. The strain energy density function is based on the simplest potential energy function $\Psi = \frac{1}{2} \mathbf{E} : \mathbf{D} : \mathbf{E}$ for elastic materials, where \mathbf{E} is the Green strain tensor and \mathbf{D} is the elastic transversely isotropic stiffness matrix. A total Lagrangian formulation was used, although updated Lagrangian formulation is recommended for better convergence of geometric non-linearities.

For curved strands it is necessary to automate the process of calculating the fibre orientations in order to correctly define the transversely isotropic stiffness. To achieve this a steady-state laminar incompressible potential flow analysis is undertaken and the gradient of the resulting potential field computed for every

strand [2] to give the fibre orientation. One of the numerical examples below (three plait model under tension) demonstrates the importance of using transverse isotropy and large deformation for such cases.

Where strands are in contact, zero thickness interface elements are inserted before the potential field is computed, as demonstrated in the knot's example below, Figure 1. Furthermore, the mechanical interaction between materials can be simulated using cohesive models providing resistance due to tangential and shear gap opening. Normal penetration was avoided by using a high penalty stiffness in the normal direction [2]. Computation of the fibre orientation and construction of the interface elements was implemented as a pre-processing stage in MoFEM (FE code developed at the University of Glasgow) before mechanical analysis was undertaken.

3. Knot Model

To illustrate the importance of interface elements, and finite deformations, a knot made from a 1 mm diameter strand was modelled and subjected to stretching. The elastic transversely isotropic material parameters were $E_z = 135GPa$ and $E_p = 50GPa$ as the principal and transverse stiffness of strands, $\nu_p = 0.4$ as the Poisson's ratio in the transverse plane, and $\nu_{pz} = 0.1$ and $G_{zp} = \frac{E_z}{2(1+\nu_{pz})}$ as the Poisson's ratio and shear modulus between the principal axis and transverse plane respectively. Elastic interface elements were considered with penalty stiffness of $D_n = 1350GPa$ and $D_{t1} = D_{t2} = 1GPa$ for the normal and two tangential components. Interface elements were inserted where the knot self touches as shown in Figure 1-left. The approach undertaken was to physically detach any surface in contact and determine fibre orientations (Figure 1-right) from the gradient of the computed potential field having all the zero flux boundary walls defined. This avoids 'leakages' through contact areas (Figure 1-middle).

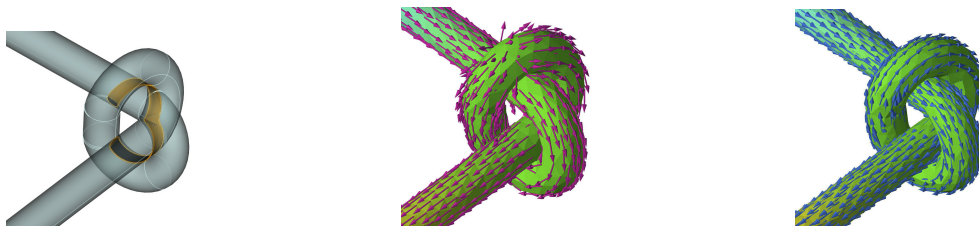


Figure 1: Left: Interface within the knot; Middle: Wrong fibre orientation; Right: Correct fibre orientation

The model was fixed on one end and pulled at an angle of 45° from the other end. Exponential stiffening was observed in the first phase due to straightening, followed by changes in stiffness during tightening and repetitive slipping/re-tightening process of the knot. This is a common mechanism of knots, mainly dependent on the coefficient of friction and the type of knot in use. Large deformation modelling was essential due to the large rotations experienced - see Figure 2.

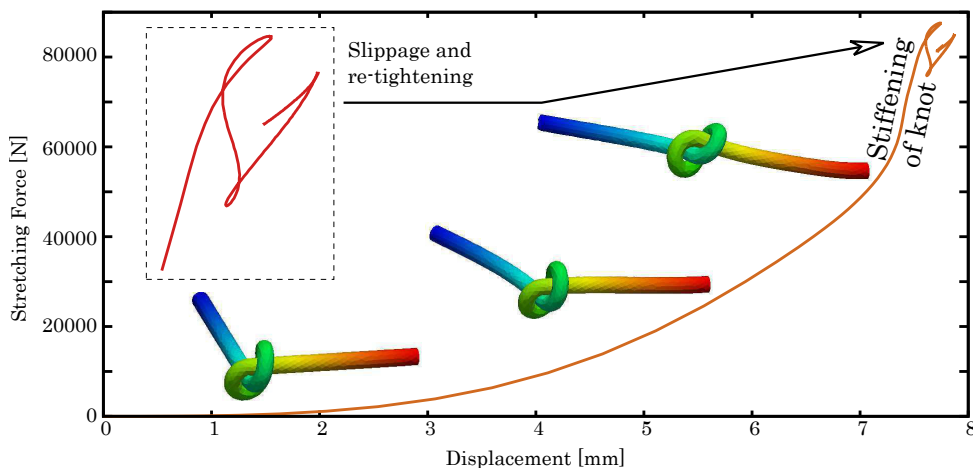


Figure 2: Axial load-displacement graph for stretching behaviour of knot

4. Modelling of Braided Geometries

Two different models of braided geometries were investigated in this section. The first model consisted of a three plait geometry (dimensions shown in Figure 5). The second model represented a twelve strands

sinnet (T12) rope clamped between two steel plates (Figure 6). The same material parameters as for the knot example were used, except $\nu_p = 0.3$ in the T12 model.

The three plait model was subject to tension and modelled assuming both small and large deformation theorem. Small deformation modelling exhibited spurious bending (Figure 3) compared to the large deformation model (Figure 5) assuming small strains/large rotations. This bending was due to material swelling and emphasises that geometric non-linearity cannot be ignored.

Another test was defined to illustrate the importance of using transverse isotropy when modelling braided fibrous strands. The same three plait model was analysed using both elastic isotropic ($E = 135GPa$ and $\nu = 0.1$) and transversely isotropic material, taking into consideration geometric non-linearities. Artificial torsion was observed with the maximum twist taking place towards the centre in the isotropic model, as shown by the overlap image in Figure 4.

The overall stiffening mechanism can be observed in Figure 5, while p-refinement using hierarchical higher-order approximations indicate that the solution is converging. A Newton iterative solver with arc-length procedure and secant line search was used to improve the convergence of the geometrically non-linear problems.

The modelling of the T12 sinnet rope was more challenging due to the geometric formation of a rigid lattice structure arrangement with a nearly constant stiffness, as shown in Figure 6. It is suggested that further investigation is required as to how different geometry configurations and material parameters affect the overall mechanism of sinnet braids. Similar to the three plait model, p-refinement showed convergence but required significant increase in computational resources.

A major problem when using transversely isotropic materials is the possibility of stiffness matrix ill-conditioning if E_z and E_p are very different in magnitude. The same problem occurs at the interface when D_n is significantly larger or smaller than $D_{t1,t2}$.

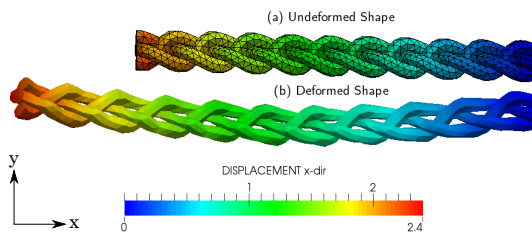


Figure 3: Un/defomed shape using small deformation

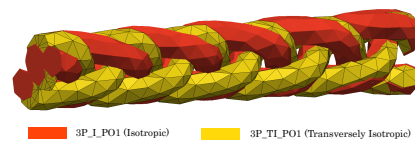


Figure 4: Deformed shape (half model) of Isotropic and Transversely Isotropic using large deformation

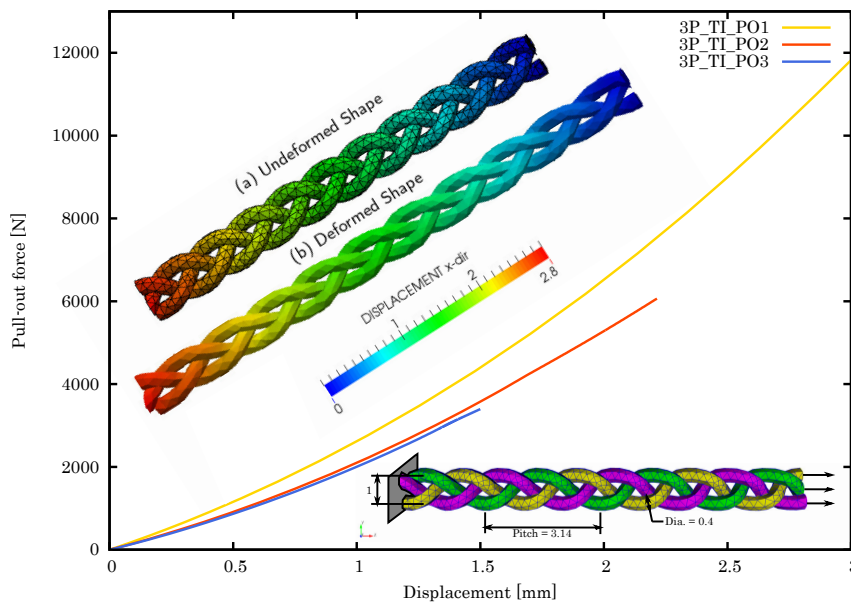


Figure 5: Load-displacement graph for 3-plaited model using finite deformation theorem

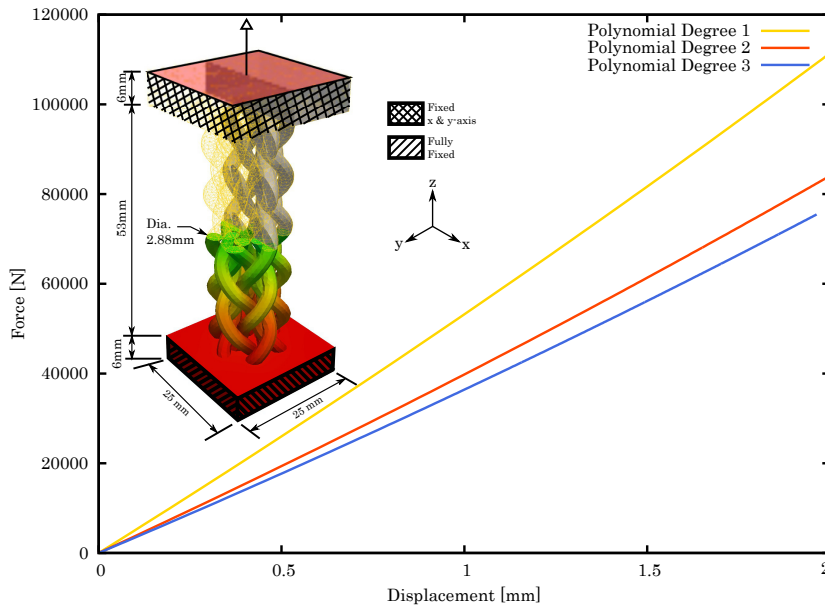


Figure 6: Load-displacement graph for T12 sinnet rope (including p-refinement)

5. Conclusions

This paper presented a numerical methodology to model braided fibres leading to better understanding of their overall mechanical behaviour. An elastic transversely isotropic material model was used to represent strands made from materials such as carbon, glass, kevlar or technora. It was essential to consider stiffness in the transverse plane of the strands, in particular when modelling braided fibres. Geometric non-linear analysis was vital due to large rotations during deformation. It was also found that large variations in the anisotropic stiffness properties and differences between the stiffness in the normal and tangential directions of the interface elements leads to numerical instabilities during pre-conditioning of the global stiffness matrix. The examples have shown the importance of the adopted approach while further studies are required to demonstrate its applicability on different types of braiding/weaving and the influence of different material parameters.

Acknowledgements

The research work undertaken in this publication is funded by the Strategic Educational Pathways Scholarship (Malta). The scholarship is part-financed by the European Union European Social Fund (ESF) under Operational Programme II Cohesion Policy 2007-2013, Empowering People for More Jobs and a Better Quality of Life.

References

- [1] M.Cortis, L.Kaczmarczyk, C.J. Pearce. Computational modelling and experimental investigation of the bond behaviour between concrete and braided fibre ropes, *International Conference on Computational Mechanics (CM13)*, Durham, March 2013
- [2] M. Cortis, L. Kaczmarczyk, C.J. Pearce. Computational modelling of braided fibre for reinforced concrete, *22nd UK Conference of the Association for Computational Mechanics in Engineering (CM14)*, Exeter, April 2014
- [3] A. Katz, N. Berman, and L.C. Bank. Effect of high temperature on bond strength of FRP rebars. *Journal of Composites for Construction*, 3(2): 73 81, May 1999.
- [4] A. Katz and N. Berman. Modelling the effect of high temperature on the bond of FRP reinforcing bars to concrete. *Cement and Concrete Composites*, 22(6):433 443, December 2000.

A first order conservation law formulation for Lagrangian fast solid dynamics in OpenFOAM

Jibran Haider, Antonio J. Gil, Javier Bonet and Chun Hean Lee

Zienkiewicz Centre for Computational Engineering, College of Engineering, Swansea University,
Singleton Park, SA2 8PP, United Kingdom

{m.j.haider; a.j.gil; j.bonet; c.h.lee}@swansea.ac.uk

ABSTRACT

An explicit Lagrangian two-field Mixed Formulation (MF) [1–4], in the form of a system of first order conservation laws, has recently been published to overcome the shortcomings posed by the traditional second order displacement formulation. The formulation, where the linear momentum and the deformation gradient are treated as unknown variables, has performed extremely well in bending dominated nearly incompressible scenarios [5, 6]. One of the main objectives in this paper is to implement a second order upwind cell centre based finite volume algorithm, in conjunction with a total variation diminishing Runge-Kutta time integrator, in OpenFOAM. The presence of jump in properties at the cell interfaces motivates the use of a Riemann solver by introducing an upwind bias into the evaluation of the numerical contact flux. A series of benchmark cases are tested to examine the robustness of the proposed methodology. The numerical solutions are found to be in good agreement with the available results without any spurious oscillations, yielding an equal order of convergence for velocities and stresses.

Key Words: *First order conservation laws; Finite Volume Method; OpenFOAM; Riemann solver; Locking*

1. Introduction

Over the past few decades, computational fast solid dynamics has become an increasing share of interest in major engineering industries, namely aerospace, automotive, biomedical, defense and software industries. Traditionally, the displacement based formulation [7], typically discretised using Finite Element Method, has been employed to carry out the computational simulations for relevant applications. However, several drawbacks associated with this classical formulation need to be addressed: (1) Reduced order of convergence for derived variables (i.e. strains and stresses); (2) High frequency noise in the vicinity of shocks; (3) Numerical instabilities in terms of volumetric locking, shear locking and hydrostatic pressure fluctuations.

Within the OpenFOAM environment, it is essential to point out that the existing cell centred solid mechanics solver [7] is only capable of solving linear elastic infinitesimal deformation. Extension to a large deformation framework via traditional formulation still remains unclear due to the shortcomings mentioned above.

One of the main novelties in this paper is to develop a robust mixed solid solver, borrowed from the CFD community, for geometric and material nonlinear solid dynamics. Following [1, 2], a two field momentum/strains formulation written in a form of first order conservation laws will be employed. This formulation alleviates numerical instabilities associated with locking, noise and pressure oscillations, and more importantly, yields equal order of convergence for velocity and stresses.

2. Governing Equations for Reversible Elastodynamics

Let us consider the motion of a continuum which in its initial or material configuration is defined by a domain $V \subset R^3$ of boundary ∂V with outward unit normal \mathbf{N} . After the motion, the continuum occupies a spatial configuration defined by a domain $v \subset R^3$ of boundary ∂v with outward unit normal \mathbf{n} . The

motion is defined by a time t dependent mapping field ϕ which links a material particle from material configuration $\mathbf{X} \in V$ to spatial configuration $\mathbf{x} \in v$ according to $\mathbf{x} = \phi(\mathbf{X}, t)$. It is possible to define the motion through a system of first order conservation laws expressed in a Total Lagrangian setting as follows:

$$\frac{\partial \mathbf{p}}{\partial t} - \nabla_0 \cdot \mathbf{P} = \rho_0 \mathbf{b}, \quad (1a)$$

$$\frac{\partial \mathbf{F}}{\partial t} - \nabla_0 \cdot \left(\frac{1}{\rho_0} \mathbf{p} \otimes \mathbf{I} \right) = \mathbf{0}. \quad (1b)$$

Expressions (1a) and (1b) represent the conservation of linear momentum \mathbf{p} and the conservation of deformation gradient \mathbf{F} , respectively. Note here that ρ_0 is the material density of the continuum, \mathbf{b} is a body force per unit of mass, \mathbf{P} is the first Piola Kirchhoff stress tensor and \mathbf{I} is an identity matrix. The above laws can be combined into a system of first order conservation equations as

$$\frac{\partial \mathcal{U}}{\partial t} + \frac{\partial \mathcal{F}_I}{\partial X_I} = \mathcal{S}, \quad \forall I = 1, 2, 3; \quad (2)$$

where \mathcal{U} is the vector of conservation variables, \mathcal{F}_I denotes the flux vector in the material direction I and \mathcal{S} the source term:

$$\mathcal{U} = \begin{bmatrix} \mathbf{p} \\ \mathbf{F} \end{bmatrix}, \quad \mathcal{F}_N = \mathcal{F}_I N_I = \begin{bmatrix} -\mathbf{P}N \\ -\frac{1}{\rho_0} \mathbf{p} \otimes N \end{bmatrix}, \quad \mathcal{S} = \begin{bmatrix} \rho_0 \mathbf{b} \\ \mathbf{0} \end{bmatrix}. \quad (3)$$

For closure of the system (1a-1b), it is necessary to introduce an appropriate constitutive model obeying both the laws of thermodynamics and the principle of objectivity [1, 5]. One of the simplest models satisfying the above conditions is the standard hyperelastic Neo Hookean model where its first Piola Kirchhoff stress tensor \mathbf{P} can be additively decomposed into a deviatoric contribution \mathbf{P}_{dev} and a volumetric contribution \mathbf{P}_{vol} defined by:

$$\mathbf{P} = \mathbf{P}_{dev} + \mathbf{P}_{vol}; \quad \mathbf{P}_{dev} = \mu J_F^{-2/3} \left(\mathbf{F} - \frac{1}{3} (\mathbf{F} : \mathbf{F}) \mathbf{F}^{-T} \right); \quad \mathbf{P}_{vol} = p \mathbf{H}_F; \quad p = \kappa (J_F - 1). \quad (4)$$

Notice that the Jacobian and the co-factor of deformation are computed based on \mathbf{F} , namely, $J_F = \det(\mathbf{F})$ and $\mathbf{H}_F = J_F \mathbf{F}^{-T}$.

3. Numerical Methodology

3.1. Spatial discretisation

The above system (3) can now be spatially-discretised using the standard cell centred finite volume algorithm together with the use of linear reconstruction procedure, which is typically used in OpenFOAM for fluid flows. To achieve this, it is essential to employ an acoustic Riemann solver [1] for discontinuities by introducing an upwind bias into the evaluation of the numerical contact flux \mathcal{F}_N^C :

$$\frac{d\mathcal{U}_e}{dt} = -\frac{1}{V_e} \left[\sum_{\substack{f \\ f \ni e}} [\mathcal{F}_N^C]_f A_f \right] \quad (5)$$

Here, subscript e refers to the cell e under consideration, f represent the faces belong to cell e , V_e is the local volume of cell e , and A_f the area of surface f .

3.2. Temporal discretisation

Insofar the resulting set of semi-discrete equations (5) is rather large, it will only be suitable for explicit type of time integrator. For simplicity, an explicit two step Total Variation Diminishing Runge-Kutta (TVD-RK) scheme has been used. This is described by the following time update equations from time step t_n to t_{n+1} :

$$\begin{aligned} \mathcal{U}_{n+1}^* &= \mathcal{U}_n + \Delta t \dot{\mathcal{U}}_n \\ \mathcal{U}_{n+2}^* &= \mathcal{U}_{n+1} + \Delta t \dot{\mathcal{U}}_{n+1}^* \\ \mathcal{U}_{n+1} &= \frac{1}{2} (\mathcal{U}_n + \mathcal{U}_{n+2}^*) \end{aligned} \quad (6)$$

The time step $\Delta t = t_{n+1} - t_n$ is calculated based upon Courant-Friedrichs-Lewy condition α_{CFL} , to give:

$$\Delta t = \frac{\alpha_{CFL} h}{U_{p,max}} \quad (7)$$

where $U_{p,max}$ is the maximum p -wave speed and h the characteristic length.

4. Numerical Examples

4.1. One dimensional case

The wave propagation in a one-dimensional linear elastic pile is assessed using the proposed numerical methodology. The length L of 10 m long pile has its left end ($x = 0$) fixed and a forcing function $P(L, t)$ is applied to the free right end ($x = L$). Two different types of external loading would be enforced: (1) A shock dominated case with a step loading function; (2) A smooth sinusoidal function. In the first case, the computational domain is discretised using 100 cells. A compressive stress is applied at the free end which leads to the propagation of a shock wave down the pile.

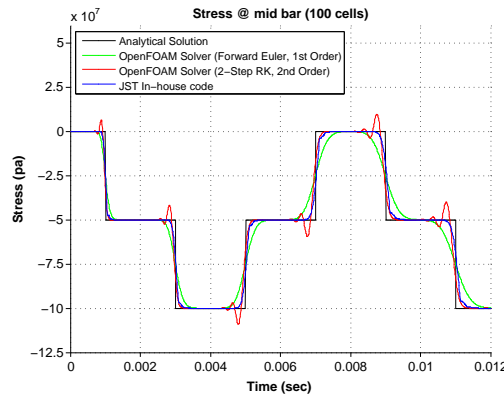


Figure 1: Stress evolution at mid-bar for the step loading case with $P(L, t) = -5 \times 10^7$ pa. The linear elastic model is used with density = 8000 kg/m^3 , Young's Modulus = 200 GPa , Poisson's Ratio = 0 , $\alpha_{CFL} = 0.5$ and $\Delta t = 1 \times 10^{-5}$ s.

In the second scenario, a smooth sinusoidal function is applied at the free end which allows the calculation of norm convergence errors.

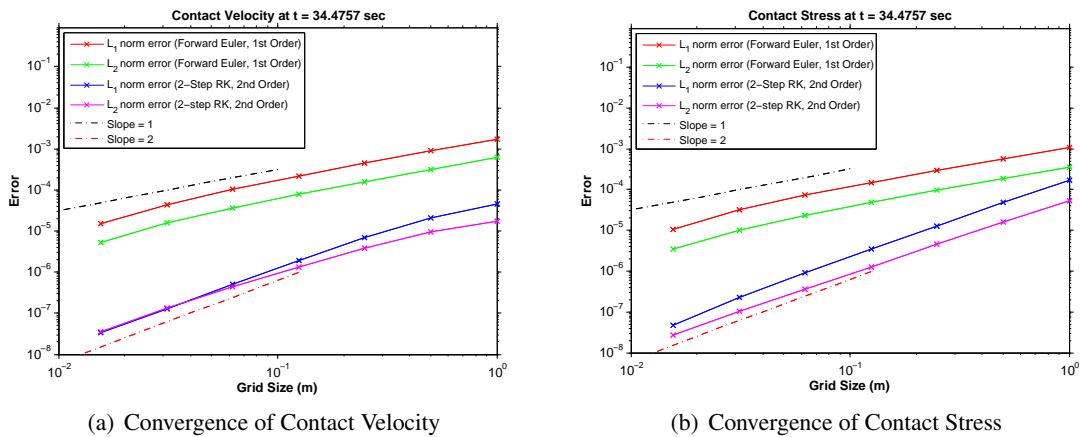


Figure 2: L_1 and L_2 convergence norms for the sinusoidal loading case with $P(L, t) = 0.001 [\sin(\pi t/20 - \pi/2) + 1]$. The linear elastic model is used with density = 1 kg/m^3 , Young's Modulus = 1 Pa , Poisson's Ratio = 0.3 and $\alpha_{CFL} = 0.5$.

4.2. Two dimensional case

In this example a square plate of unit length with unit thickness is discretised using 20×20 quadrilateral cells. The plate is released without any constraints with an initial angular velocity of $\Omega = 105 \text{ rad/sec}$.

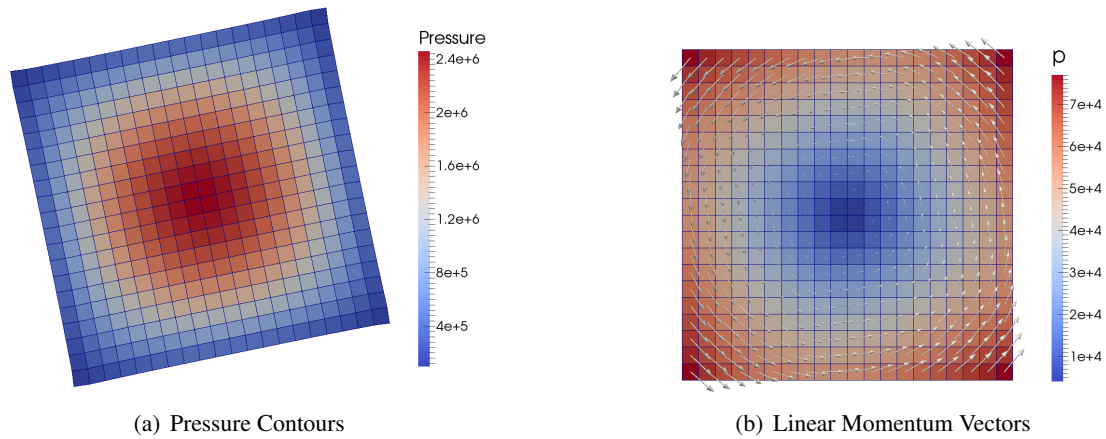


Figure 3: Contour plots for the spinning plate case at a particular time $t = 0.001976$ s. The nearly incompressible Neo-Hookean constitutive model is used with density = 1100 kg/m^3 , Young's Modulus = $1.7 \times 10^7 \text{ Pa}$, Poisson's Ratio = 0.45 , $\alpha_{CFL} = 0.4$ and $\Delta t \approx 8 \times 10^{-5} \text{ s}$.

5. Conclusions

An explicit total Lagrangian mixed velocity/strains formulation has been successfully implemented in the open source OpenFOAM code for the numerical analysis of fast solid dynamics experiencing large deformation. A total variation diminishing two-stage Runge-Kutta time integration scheme along with a piecewise linear reconstruction for spatial discretisation has been introduced. The discontinuity of the conservation variables across the control volume interfaces leads to a Riemann problem where the contact flux is evaluated by introducing an upwind bias. The algorithm has been successfully tested in both linear and non-linear scenarios, alleviating locking difficulties and pressure instabilities, as well as yielding equal second order of convergence for velocities and stresses.

6. Acknowledgements

The first author would like to thank the European Union for providing the financial support under the Erasmus Mundus Joint Doctorate Programme (SEED). The second, third and fourth authors gratefully acknowledge the financial support provided by the Sêr Cymru National Research Network for Advanced Engineering and Materials, United Kingdom.

References

- [1] C. H. Lee, A. J. Gil and J. Bonet. Development of a cell centred upwind finite volume algorithm for a new conservation law formulation in structural dynamics. *Computers and Structures*, 118, 13–38, 2014.
- [2] M. Aguirre, A. J. Gil, J. Bonet and A. A. Carreño. A vertex centred finite volume Jameson-Schmidt-Turkel (JST) algorithm for a mixed conservation formulation in solid dynamics. *JCP*, 259, 672–699, 2014.
- [3] C. H. Lee, A. J. Gil and J. Bonet. Development of a stabilised Petrov-Galerkin formulation for conservation laws in Lagrangian fast solid dynamics. *CMAME*, 268, 40–64, 2014.
- [4] I. A. Karim, C. H. Lee, A. J. Gil and J. Bonet. A Two-Step Taylor Galerkin formulation for fast dynamics. *Engineering Computations*, 31, 366–387, 2014.
- [5] A. J. Gil, C. H. Lee, J. Bonet and M. Aguirre. A stabilised Petrov-Galerkin formulation for linear tetrahedral elements in compressible, nearly incompressible and truly incompressible fast dynamics. *CMAME*, 276, 659–690, 2014.
- [6] J. Bonet, A. J. Gil, C. H. Lee, M. Aguirre and R. Ortigosa. A first order hyperbolic framework for large strain computational solid dynamics. Part I: Total Lagrangian isothermal elasticity. *CMAME*, 283, 689–732, 2015.
- [7] H. Jasak and H. G. Weller. Application of the finite volume method and unstructured meshes to linear elasticity. *IJNME*, 48, 267–287, 2000.

On the implicit implementation of the Generalised Interpolation Material Point method

*T.J.Charlton, W.M.Coombs and C.E.Augarde

Mechanics Research Group, School of Engineering and Computing Sciences,
Durham University, South Road, Durham, DH1 3LE

*t.j.charlton@durham.ac.uk

ABSTRACT

The modelling of solid mechanics problems often requires a method which allows large deformations and can account for non-linear behaviour. The Material Point Method (MPM) allows this by modelling a problem domain using particles (or Material Points, MPs) at which state variables are stored and tracked. Calculations are then carried out on a regular background mesh to which state variables are mapped from the particles. This background mesh is reset after each load (or time) step whereas the positions of the MPs are updated by the transfer of mesh displacements to the MP locations. In the standard MPM a problem can arise when a particle crosses the boundary between one background element and another. This is due to the fact that the shape functions are not continuous between elements. A significant advance in the MPM was made in [1] where this cell crossing instability was addressed using the Generalised Interpolation Material Point (GIMP) method. The GIMP method attempts to alleviate the problem associated with particles crossing between elements by modifying the particle characteristic functions so that particles influence nodes other than those associated with the element they are inside. In the current literature the GIMP method has been implemented using an explicit time stepping scheme. In this paper the GIMP method is recast in an implicit form. In particular, the formulation presented in this paper provides a method to determine the element stiffness matrix, giving a truly implicit approach. The method is demonstrated first on 1D stress analysis problems for clarity and then extended to 2D.

Key Words: Material Point Method; Implicit; Generalised Interpolation Material Point Method

1. Introduction

The Material Point Method (MPM) is a solid mechanics computational method developed in [2] by adapting the FLuid Implicit Particle (FLIP) method [3], itself an extension of the Particle In Cell (PIC) method [4] used in fluid mechanics. The problem domain is modelled using particles (or Material Points, MPs) that move through a fixed background mesh on which calculations take place. Variables are stored on the particles and are mapped to and from nodes belonging to this background mesh each loadstep, after which the mesh is reset. The advantage to this approach over the Finite Element Method (FEM) is that the level of deformation is not limited by distortion of finite elements. The MPM was implemented using an implicit integration approach in [5] and was reported to allow a larger loadstep (or timestep) as well as giving more accurate results.

In the MPM a problem can arise when particles cross the boundary between background elements causing unrealistic particle displacements or oscillations. To alleviate this, the Generalised Interpolation Material Point (GIMP) method was proposed by Bardenhagen [1] as an extension to the MPM. Here, each particle rather than acting only as a point, carries around an influence zone allowing it to overlap multiple elements, and influence grid nodes other than those belonging to the element in which it is located. These influence zones are created based on particle characteristic functions which are then used to calculate a weighting function that is used instead of the standard shape functions. In this paper, the GIMP method is recast in an implicit form (implicit Generalised Interpolation Material Point (iGIMP)) to allow the determination of element stiffness matrices by splitting the weighting functions at nodes to be the sum of contributions from elements instead. In [6] the GIMP method is discussed in an implicit form however it was implemented in a matrix free fashion, very different to the approach taken in this work.

2. Weighting Functions

When mapping between nodes and particles in the MPM standard finite element shape functions (N) are used. For example

$$\{u\} = [N]\{u_g\} \quad (1)$$

where $\{u\}$ are displacements at a point and $\{u_g\}$ are nodal displacements. In 1D

$$N_i = \frac{1 \pm \xi}{2}, \quad [N] = \begin{bmatrix} N_1 & 0 \\ 0 & N_2 \end{bmatrix} \quad (2)$$

where ξ is the local coordinate (in a domain $-1,+1$).

The key difference in the GIMP method when compared to the MPM is that these MPM shape functions are replaced by weighting functions (S_{vp}). These functions can be calculated in a local coordinate system in one dimension (ξ) from the standard shape functions and a particle characteristic function $\chi_p(\xi)$ as presented in [1] and shown in Equations (3) and (4). The particle characteristic function specifies an influence domain rather than a MP acting only as a point as in the MPM. The weighting function (S_{vp}), and gradient thereof (∇S_{vp}), are given by

$$S_{vp} = \frac{1}{V_p} \int_{\Omega_p \cap \Omega} \chi_p(\xi) N(\xi) d\xi \quad \text{and} \quad (3)$$

$$\nabla S_{vp} = \frac{1}{V_p} \int_{\Omega_p \cap \Omega} \chi_p(\xi) \nabla N(\xi) d\xi, \quad (4)$$

where V_p is the volume the particle represents (in 1D this is equal to the length of its influence domain, l_ξ), $\Omega_p \cap \Omega$ is the area of the particle influence domain overlapping the current element and $\chi_p(\xi)$ is the characteristic function, in this situation defined as the hat function

$$\chi_p(\xi) = \begin{cases} 1, & \text{if } \xi \in \Omega_p \\ 0, & \text{otherwise.} \end{cases} \quad (5)$$

Figure 1(a) shows graphically how the calculation can be thought of as a convolution between the standard shape functions and the characteristic functions.

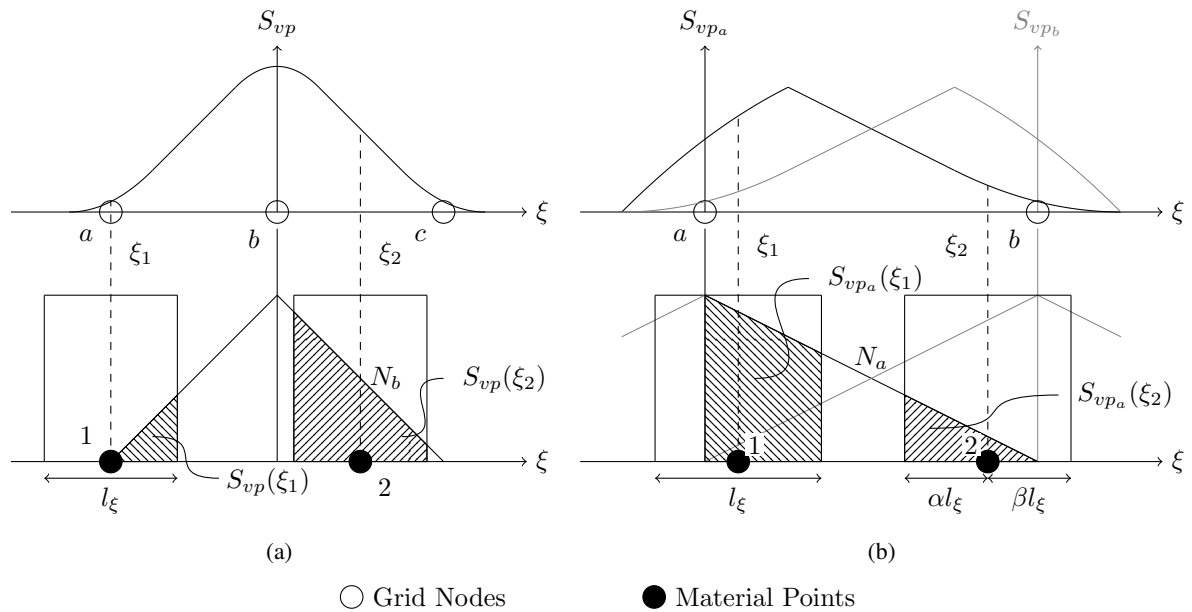


Figure 1: (a) GIMP weighting functions for a node, (b) iGIMP weighting functions for nodes in an element.

To be able to calculate stiffness within an element using the iGIMP the convolution is carried out as the overlap of shape functions with χ_p within an element, rather than at a node. This can be seen in Figure 1(b). When considering the weight functions at a node from elements either side, these weighting functions add up to the GIMP shape functions (Figure 1(a)) and thus still have partition of unity. The

weighting functions allow a particle to affect not only the nodes of the element within which it is located but also those elements overlapped by the particle's influence domain, smoothing any transition between elements. It is possible to extend this to more than one dimension using the tensor product of these one dimensional functions Eqn (3) and Eqn (4).

3. Implementation for Linear Static Stress Analysis

To be able to find displacements and stresses for a solid under load, the linear system needed to be solved is

$$[K_g]\{d\} = \{f^{ext}\} \quad (6)$$

Where $\{d\}$ are nodal displacements, $[K_g]$ is the global stiffness matrix and $\{f^{ext}\}$ are the external forces at nodes. To arrive at this, initially the shape functions in Eqn (1) are replaced with the weighting function Eqn (3) to give

$$\{u\} = [S_{vp}]\{u_g\}. \quad (7)$$

Through substitution into the weak form of equilibrium and some manipulation, a non-symmetric element stiffness matrix $[K_e]$ is obtained as

$$[K_e] = \sum_{i=1}^{n_{mp}} [B]^T [D] [B_R] \det(J_i) w_i \quad (8)$$

where $[B]$ and $[B_R]$ are strain displacement matrices, $[D]$ relates to the material properties, J_i is the Jacobian, w_i is the particle weight calculated from its original domain width and n_{mp} is the number of material points in the element. The difference in the iGIMP method is that $[B_R]$ is constructed from the gradient weighting functions in Eqn (4), whereas $[B]$ is still calculated using the derivatives of the standard shape functions. The global stiffness matrix can then be assembled and displacements calculated as in the FEM. Once the displacements of the background grid nodes have been calculated these are then mapped back to the particles, whose positions are updated, strains and stresses calculated and then the background grid reset.

When implementing the iGIMP method it is necessary, at the beginning of each loadstep, to calculate not only which element particles are located in but also any elements that a particle's influence domain overlaps. It is possible for this to be achieved simply by selecting a uniform background grid so that coordinates of particles can be compared with those of the nodes. Any elements that do not contain particles are identified and degrees of freedom not required for the computation are determined. It is then necessary to calculate the local positions of each particle within an element. With this information it is possible to calculate the weighting functions shown above in Eqn (3). Boundary conditions are set in the same manner as in the FEM by prescribing displacements to nodes in the background grid. Forces are applied to material points and then mapped using the standard shape functions to the grid on each step.

4. Numerical Example

To demonstrate the method, the response of a uniform linear elastic solid column to the application of a body force due to increasing gravity is modelled (as also modelled in [1]). The problem is modelled in one dimension using iGIMP and then compared with FEM and MPM solutions.

A problem domain of 50 units was discretised into 50 elements with $u(x=0)=0$. Each element initially contains two particles positioned so that the influence domain of each particle consists of half the element. A Young's modulus of $E = 1 \times 10^6$ and a density of $\rho = 81.549$ in compatible units is assigned to the domain to give an total force once gravity is applied of 40,000. The stresses at the end of the simulation are then calculated to allow comparison against stresses using the standard MPM, the FEM using the same discretisation using linear elements and the analytical solution given in Eqn (9). The MPM and GIMP simulations were run using 20 loadsteps and the FEM, using a single step.

The analytical solution for vertical stress is

$$\sigma(x) = E \left\{ \sqrt{\frac{2\rho_0 b}{E}(L-x) + 1} - 1 \right\} \quad (9)$$

where

$$L = L_0 + \frac{\rho_0 b}{2E} L_0^2 \quad (10)$$

where L is the current length of the column, ρ_0 is density of the column, b is body force and L_0 is the original column length.

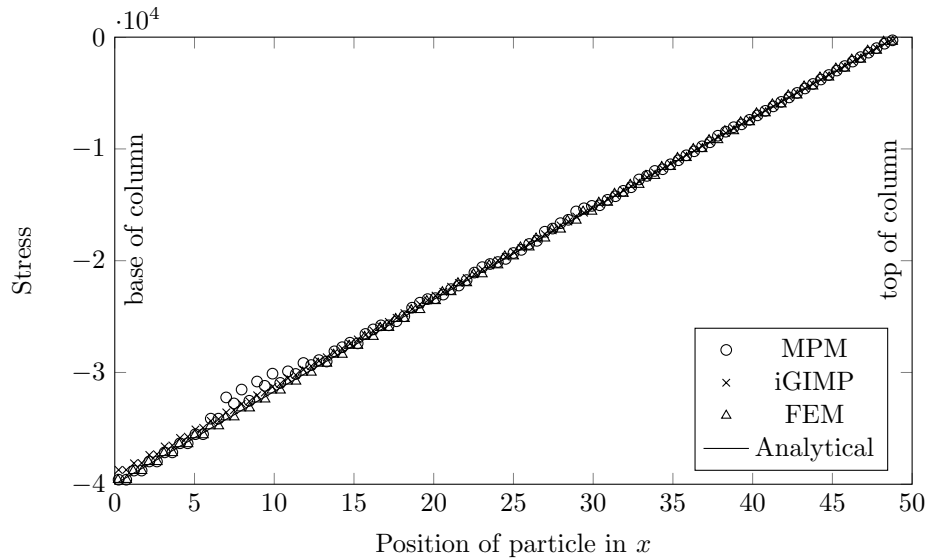


Figure 2: Computational and analytical stress throughout 1D column after final load has been applied.

It can be seen in Figure 2 that the standard MPM method experiences an oscillation in its response around $x = 10$, this can be attributed to the crossing of element boundaries by particles. The smoother transitions in iGIMP because of the particle influence domains mean that this does not occur in the iGIMP simulation and it closely follows both the analytical and FEM solutions.

5. Conclusions and Future Work

It has been shown how an implicit version of the GIMP method can successfully be implemented by modifying how weighting functions are calculated thus allowing element stiffness to be calculated. It has shown to have good agreement with the FEM and MPM solutions, showing an improvement over the MPM for a simple one-dimensional problem. In this paper a linear elastic constitutive model has been used, this results in a method that, although linear within a single step, still exhibits some non linear behaviour. To achieve greater accuracy in large deformation problems in the future this may need to be replaced with a non-linear model. Other future work will involve extending to two dimensions and after being demonstrated on a selection of test problems.

References

- [1] S. Bardenhagen, E. Kober, The generalized interpolation material point method, *Computer Modeling in Engineering and Sciences* 5 (6) (2004) 477–496.
- [2] D. Sulsky, Z. Chen, H. Schreyer, A particle method for history-dependent materials, *Computer Methods in Applied Mechanics and Engineering* 118 (1994) 179 – 196.
- [3] J. Brackbill, H. Ruppel, Flip: A method for adaptively zoned, particle-in-cell calculations of fluid flows in two dimensions, *Journal of Computational Physics* 65 (2) (1986) 314 – 343.
- [4] M. W. Evans, F. H. Harlow, E. Bromberg, The particle-in-cell method for hydrodynamic calculations, Tech. rep., DTIC Document (1957).
- [5] J. E. Guilkey, J. A. Weiss, Implicit time integration for the material point method: Quantitative and algorithmic comparisons with the finite element method, *International Journal for Numerical Methods in Engineering* 57 (9) (2003) 1323–1338.
- [6] A. Nair, S. Roy, Implicit time integration in the generalized interpolation material point method for finite deformation hyperelasticity, *Mechanics of Advanced Materials and Structures* 19 (6) (2012) 465–473.

Geometrically exact beams under impact: Nonsmooth formulation and energy conserving scheme.

*Tien Long Nguyen¹, Carlo Sansour² and Mohammed Hjiaj¹

¹Civil Engineering department, Institut National des Sciences Appliquées de Rennes, 20 Avenue des
Buttes de Coesmes, 35708, Rennes, France

²Faculty of engineering, University of Nottingham NG7, Nottingham, United Kingdom

*tien-long.nguyen@insa-rennes.fr

ABSTRACT

Non-linear geometrically exact rod dynamics is of great interest in many areas of engineering. However, when the excitation of the dynamical system is due not to a classical force but rather to a non-standard force such as those generated through collisions or impact, the solutions require special techniques. Over decades, divers approaches have been proposed. Some people have used the so-called force integration method (penalty method) which are proven to be very efficient for deformable projectiles, where the force is proportional to the deformation of projectiles. The extension to the case of rigid projectile by increasing its stiffness is numerically problematic. However, the most rigorous mathematical models are the ones taking the non-smooth properties of velocities and forces into account. Non-smooth formulations with set-value force laws of normal cone are very suitable to tackle these problems. The force is defined following the solution of the normal cone inclusion as proximal point in unilateral constraint problems, thus, the set-value force laws is applied together with Newtons' impact laws. This approach has been used to study the impact of discrete bodies. So far, applications in continuous systems such as beams or shells remain very limited, especially in nonlinear cases. In this paper, we will deliver a new non-smooth impact formulation for in-plane geometrically exact Euler Bernoulli beams in combination with an energy-momentum method, the total energy and momentum are perfectly conserved.

Key Words: *Geometrically exact beams, computational method, impact, nonsmooth method, coefficient of restitution*

1. Summary of kinematics of beams and strain measure

In this section we briefly introduce the beam's strain measures. We consider a general Cartesian coordinate basis $e_i, i = 1, 2, 3$ and a curve $X_0(s)$, with s being the arc-length. We understand $X_0(s)$ as describing the centre line of the rod cross section. However, we restrict the deformations to planar ones in the $e_1 - e_2$ plane and introduce the tangent vector $G_0 = \frac{dX_0(s)}{ds}$. Perpendicular to this vector, we define N to be the normal vector with z as the corresponding coordinate in the direction of N .

In addition to the Cartesian system, we define a suitable convected curvilinear coordinate system given by the triple s, z, x_3 . We define the vector $X(s, z) = X_0(s) + zN(s)$ as the position vector of points in the direction of N at the reference configuration. In a general cross section the boundary is defined by z being a function of x_3 . Note that the third direction is not explicitly included in this equation, though it is implicitly understood that it is in the direction of e_3 and that the deformation is independent of that direction. Consequently, a local basis in the reference configuration is defined by the triple (G, N, e_3) , with $G = \frac{\partial X}{\partial s}$, $N = \frac{\partial X}{\partial z} = \frac{\partial X}{\partial z}|_{z=0}$ and $G_0 = G|_{z=0}$. We have also the following relations $G \cdot N = G_0 \cdot N = 0$, $|N| = 1$, $N = e_3 \times \frac{G}{|G|} = e_3 \times G_0$, where $|\bullet|$ denotes the absolute value of a vector, \times and (\cdot) denotes the cross and scalar product of vectors, respectively. The corresponding contra-variant basis vectors are then given by (G^*, N, e_3) , with $G^* = \frac{G}{|G|^2}$.

A deformation is given as $x = \varphi(X)$ which defines the actual configuration. For our geometrically exact beam theory we make use of the Bernoulli model where the cross sections are assumed to be rigid

and remain perpendicular to the centre line. Thus, the corresponding tangent vectors at the deformed configuration are defined as $(\mathbf{g}, \mathbf{n}, \mathbf{e}_3)$ with $\mathbf{g}_0 = \mathbf{g}|_{z=0}$, and the relations hold $\mathbf{g} = \frac{\partial \mathbf{x}}{\partial s}$, $\mathbf{n} = \mathbf{e}_3 \times \frac{\mathbf{g}}{|\mathbf{g}|} = \mathbf{e}_3 \times \frac{\mathbf{g}_0}{|\mathbf{g}_0|}$. The deformation of points in the direction of \mathbf{n} can be characterized by the following relation

$$\mathbf{x} = \mathbf{X}(s) - z\mathbf{N}(s) + \mathbf{u}(s) + z\mathbf{n}(s) = \mathbf{X}_0(s) + \mathbf{u}(s) + z\mathbf{n}(s), \quad (1)$$

where $\mathbf{u}(s)$ is the displacement vector of the centre line. From this we obtain immediately $\mathbf{g} = \mathbf{X}_{0,s} + \mathbf{u}_{,s} + z\mathbf{n}_{,s}$. The deformation gradient is written down in the curvilinear basis system as $\mathbf{F} = \mathbf{g} \otimes \mathbf{G}^* + \mathbf{n} \otimes \mathbf{N} + \mathbf{e}_3 \otimes \mathbf{e}_3$. The Green strain tensor is defined as $\mathbf{E} = \frac{1}{2}(\mathbf{C} - \mathbf{1})$, where $\mathbf{C} = \mathbf{F}^T \mathbf{F}$. It has only one non-trivial component $E_{11} = \mathbf{u}_{,s} \cdot \mathbf{X}_{0,s} + \frac{1}{2}\mathbf{u}_{,s} \cdot \mathbf{u}_{,s} + z(\mathbf{n}_{,s} \cdot (\mathbf{X}_{0,s} + \mathbf{u}_{,s}) - \mathbf{N}_{,s} \cdot \mathbf{X}_{0,s})$, where the term in z^2 has been neglected. E_{11} is split into two components as $E_{11} = \varepsilon_{11} + z\kappa$, the definition of which are given by $\varepsilon_{11} = \mathbf{u}_{,s} \cdot \mathbf{X}_{0,s} + \frac{1}{2}\mathbf{u}_{,s} \cdot \mathbf{u}_{,s}$, $\kappa = \mathbf{n}_{,s} \cdot (\mathbf{X}_{0,s} + \mathbf{u}_{,s}) - \mathbf{N}_{,s} \cdot \mathbf{X}_{0,s}$. The first is the axial strain and the second is the classical change of curvature.

2. Impact equations

2.1. Equations of motion

Hamilton's principle in nonsmooth mechanics has been studied by many authors [2, 5]. For our conservative system, the classical form still holds:

$$\delta \int_{t_1}^{t_2} \mathcal{L} dt = 0, \quad (2)$$

where t refers to time and t_1 and t_2 are boundaries of the time interval, \mathcal{L} is defined as the Lagrangian given by

$$\mathcal{L} = T - \Psi_{int} - \Psi_{ext}, \quad (3)$$

where T is the kinetic energy of the system and Ψ_{int} , Ψ_{ext} are respectively the internal and the external potential energies. Our body is non-conducting linear elastic solid and thermodynamic effects are not included in the system. The quantities in (3) are defined as

$$\delta T = \int_V \rho \dot{\mathbf{x}} \cdot \delta \dot{\mathbf{x}} dV, \quad \delta \Psi_{int} = \int_V (E E_{11} \delta E_{11}) dV, \quad \delta \Psi_{ext} = \lambda_N \delta \mathbf{u}, \quad (4)$$

where E is Young's modulus of the material, V is the volume of the system, L is the length of the beam, λ_N is the contact force during the impact time and equal to zero elsewhere. Let t_k be the moment of impact. t_k^- and t_k^+ are the starting and the closing time of the impact event, as a result, $\Delta t = t_k^+ - t_k^- = \frac{1}{n}$, with $n \rightarrow +\infty$. The impact event is assumed to happen in an infinitesimal time. The displacement is continuous but the velocity is discontinuous[2, 3, 4, 5], which read $\mathbf{x}(t_k^-) = \mathbf{x}(t_k^+)$, $\dot{\mathbf{x}}(t_k^-) \neq \dot{\mathbf{x}}(t_k^+)$. For $t < t_k^-$ and $t > t_k^+$ the equation of motion has its regular form, from (2), (3), together with an integration over the cross section, and due to the fact that the variations vanish at the boundaries, standard arguments of the calculus of variation deliver

$$\int_L \rho A \ddot{\mathbf{u}} \cdot \delta \mathbf{u} ds + \int_L \rho I \ddot{\mathbf{n}} \cdot \delta \mathbf{n} ds + \int_L (E A \varepsilon_{11} \delta \varepsilon_{11} + E I \kappa \delta \kappa) ds = 0, \quad (5)$$

where A and I is the area and the moment of inertia of the cross section. The equation of motion for projectile holds

$$M_1 \ddot{\mathbf{y}} = 0, \quad (6)$$

where M_1 and \mathbf{y} are the mass and the position vector of the projectile, respectively. For $t_k^- < t < t_k^+$, from (2), (3), the relation holds

$$\int_{t_k^-}^{t_k^+} \int_V \dot{\mathbf{x}} \delta \dot{\mathbf{x}} dV dt - \int_{t_k^-}^{t_k^+} \int_V E E_{11} \delta E_{11} dV dt + \int_{t_k^-}^{t_k^+} \lambda_N \delta \mathbf{u} dt = 0. \quad (7)$$

Let's define the acceleration $\{\ddot{\mathbf{x}}\}$ as follows $\{\ddot{\mathbf{x}}\} \xrightarrow{n \rightarrow +\infty} \frac{\dot{\mathbf{x}}(t_k^+) - \dot{\mathbf{x}}(t_k^-)}{t_k^+ - t_k^-}$. From (7), the fact that the variations vanish at the boundary and the calculation of the integral over Δt and then the integral over the cross section, we obtain

$$\int_L A (\dot{\mathbf{u}}(t_k^+) - \dot{\mathbf{u}}(t_k^-)) \delta \mathbf{u} ds + \int_L I (\dot{\mathbf{n}}(t_k^+) - \dot{\mathbf{n}}(t_k^-)) \delta \mathbf{n} ds + \int_L (E A \varepsilon_{11} \delta \varepsilon_{11} + E I \kappa \delta \kappa) \Delta t ds - \lambda_N \delta \mathbf{u} = 0, \quad (8)$$

where $\Lambda_N = \lambda_N \Delta t$ is the impulsive force during impact. The equation of motion for projectile during impact holds

$$M_1 (\dot{\mathbf{y}}^+ - \dot{\mathbf{y}}^-) = -\lambda_N. \quad (9)$$

(5), (6), (8) and (9) are fundamental equations of motion for our system before, after and within the impact event.

2.2. Unilateral constraints

Let's define \mathbf{D}_N as the generalised distance between the projectile and the contact point on the beam. On displacement level we have the following constraint between contact forces and \mathbf{D}_N holds $\mathbf{D}_N \geq 0$, $\lambda_N \geq 0$ and $\mathbf{D}_N \lambda_N = 0$. Due to the equivalence between Signorini's force laws and normal con inclusion of force laws[2, 3, 4], one can be written as $\mathbf{D}_N \in \mathcal{N}_{\mathcal{B}}(-\lambda_N)$, where \mathcal{B} is the convex set containing all available values of $-\lambda_N$. Equivalently, on velocity level, the constraint is written as $\zeta_N \in \mathcal{N}_{\mathbb{R}^-}(-\Lambda_N)$, where ζ_N is the relative velocity between the projectile and the beam contact point. Please refer to [2, 3, 4] to have more details on the solution of normal cone inclusion as proximal point.

2.3. Newton's impact laws

Newton's impact laws states: $\zeta_N^+ = -\alpha \zeta_N^-$, where ζ_N^- and ζ_N^+ are the relative velocities just before and after impact, $\alpha = [0, 1]$ is the coefficient of restitution. Therefore, the constraint on velocity level can be generalized to have the form:

$$\zeta_N^+ + \alpha \zeta_N^- \in \mathcal{N}_{\mathbb{R}^-}(-\Lambda_N). \quad (10)$$

(10) can be solved using proximal point equation [2, 3, 4] as follows

$$-\Lambda_N = \text{prox}_{\mathcal{B}}^{\mathbb{R}^-} \left(-\Lambda_N + R^{-1} (\zeta_N^+ + \alpha \zeta_N^-) \right), \quad (11)$$

where R is a chosen parameter to speed up the convergence.

3. Space and time discretisation and local iteration

Before and after impact ($t < t_k^-$, $t > t_k^+$, $\mathbf{D}_N > 0$), beams deform as in regular cases which result from (5). After the spatial discretisation which is standard as presented in[1], the numerical approach is completed by using our newly developed energy-momentum method for geometrically exact Euler-bernoulli beams has been proven to have long-term stability and perfect conservation of energy and momentum [1]. The summary of the energy-momentum method is given as follows:

$$\varepsilon_{n+\frac{1}{2}} = \varepsilon_n + \frac{1}{2} \Delta T \dot{\varepsilon}_{n+\frac{1}{2}}, \quad \kappa_{n+\frac{1}{2}} = \kappa_n + \frac{1}{2} \Delta T \dot{\kappa}_{n+\frac{1}{2}}, \quad \dot{\mathbf{n}}_{n+\frac{1}{2}} = \dot{\mathbf{n}}_n + \frac{1}{2} \Delta T \ddot{\mathbf{n}}_{n+\frac{1}{2}}, \quad (12)$$

The mathematical proof of conservations are presented in [1]. The same time integration scheme is applied for the equation of motion of projectiles.

During impact ($t_k^- < t < t_k^+$, $\mathbf{D}_N = 0$), the value of the impulsive force is determined via a internal iteration to have the solution of proximal point [2, 3, 4]:

$$\Lambda_N^{j+1} = \max \left(\Lambda_N^j - R^{-1} (\zeta_{N_{n+1}}^+ + \alpha \zeta_{N_n}^-) \right), \quad |\Lambda_N^{j+1} - \Lambda_N^j| \leq \text{error}, \quad (13)$$

4. Examples

To verify the validity of the formulation, we first examine an example of impact between a rigid projectile and a clamped Euler-Bernoulli beam at two ends, Fig 1. The mass and initial velocity of the projectile and beams parameters are given below.

Projectile's mass: $M_1 = 100 \text{ Kg}$
 Projectile's initial velocity: $V_1 = -40 \text{ m/s}$
 Projectile's initial position: $d = 2 \text{ cm}$
 Beam length $L = 3 \text{ m}$
 Cross section area $A = 1E3 \text{ cm}^2$
 Cross section inertia $I = 8330 \text{ cm}^4$
 Young's Modulus $E = 0.2E12 \text{ Pa}$
 Density $\rho = 3000 \text{ Kg/m}^3$
 Number of elements = 6
 Time increment $\Delta T = 1E - 5 \text{ s}$
 Coefficient of restitution = 1

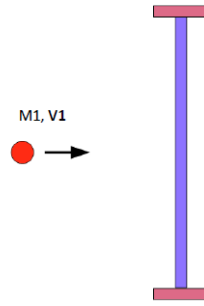


Figure 1: Initial configuration

From Fig. 2a, we see the motion of the projectile and the beam contact point. Jumps in velocities are illustrated in Fig. 2c. Impulsive force are plotted in Fig. 2b which have value only at the moments of impact. At the same time, Fig. 2d shows clearly the conservation of the total energy, however the conserved energy is proportional to the coefficient of restitution, which in this example is set to be 1. To verify the conservation of momentum, the same example has been studied but the beam doesn't have any support. The momentum is perfectly conserved, total momentum is independent of the coefficient of restitution and always equal to the initial momentum of the projectile, Fig. 2e.

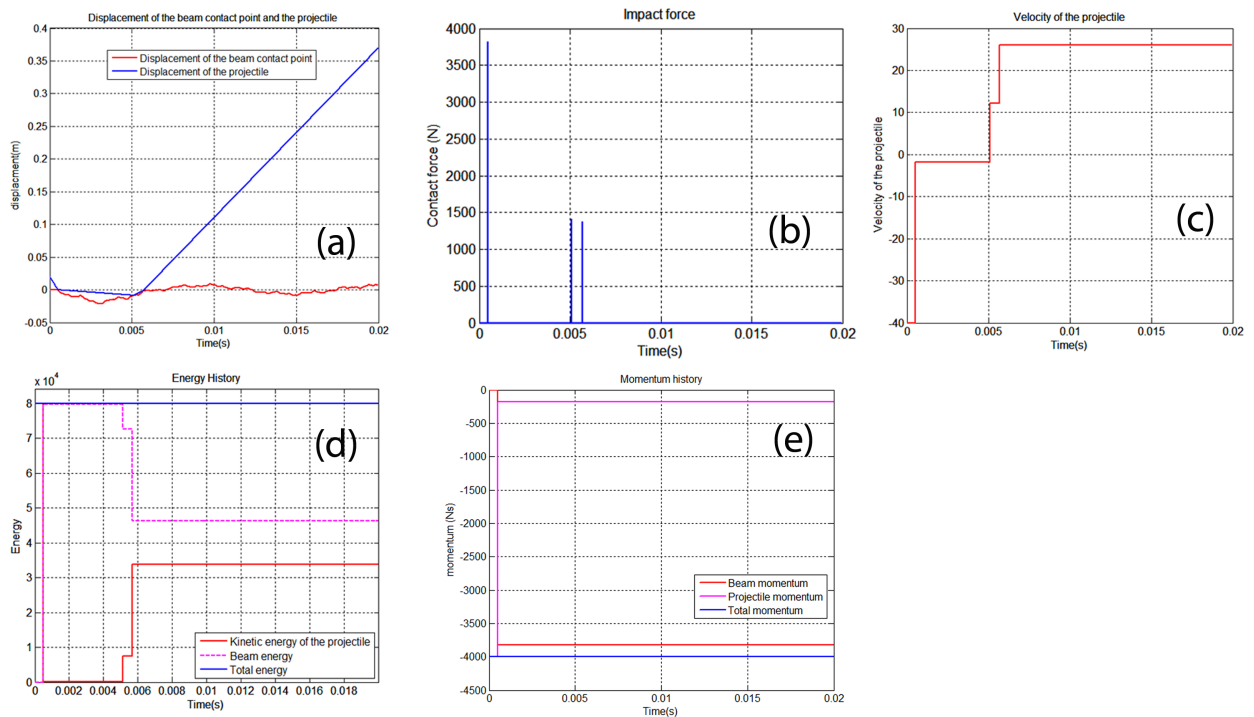


Figure 2: (a)displacement history, (b)contact force, (c)velocity of projectile, (d)energy history, (e)momentum history

References

- [1] C. Sansour, T.L. Nguyen, M.Hjiaj. An energy-momentum method for in-plane geometrically exact Euler-Bernoulli beam dynamics. *International Journal for Numerical Methods in Engineering*, 2015.
- [2] B.Brogliato. *Nonsmooth Mechanics: Models, Dynamics and Control*, 2th. Edition, 1999.
- [3] C.Glocker. *Set-Valued Force Laws: Dynamics of Non-Smooth Systems*, Lecture Notes in Applied Mechanics. 2001, Springer.
- [4] M.H.Moller. *Consistent Integrators for Non-Smooth Dynamical Systems*, Department of Mechanical and Process Engineering 2011, ETH Zurich.
- [5] R. C. Fetecau, J. E. Marsden, M. Ortiz and M. West. *Nonsmooth Lagrangian Mechanics and Variational Collision Integrators*, SIAM J. Appl. Dyn. Syst., Vol. 2, No. 3, 381–416,2003.

STOCHASTICS

A COMPARISON STUDY OF STATISTICAL RECONSTRUCTION OF HETEROGENEOUS MATERIALS

*S. Q. Cui and C. F. Li

Zienkiewicz Centre for Computational Engineering, College of Engineering, Swansea University, Swansea
SA2 8PP, United Kingdom

* E-MAIL: 714627@swansea.ac.uk

ABSTRACT

Predicting macroscopic properties of the materials with random microstructures is an important problem in many scientific and engineering fields, such as material science and geology etc. A critical part for property prediction is to reconstruct the material's 3D microstructure, especially for heterogeneous media with random morphology. This research performs a comprehensive comparison study to test a number of popular approaches for microstructure reconstruction, including the energy-minimization approach, the descriptors-based approach, the direct reconstruction approach using correlation function and the data classification approach. Two cases were chosen to compare the accuracy and efficiency of these methods. The first case is porous materials, for which the reconstruction concerns the effective permeability, and the second one is composite materials, for which the target is predicting effective mechanical properties.

Keywords: *statistical reconstruction; heterogeneous materials; energy-minimization approach; descriptors-based approach; direct reconstruction approach*

1. Introduction

Predicting macroscopic properties of materials with random microstructures is required in such fields as material science and geology etc. In materials science, the prediction capability contributes to the materials design by inverse design that is reversing the information flow from the interest properties to morphological structure and components. In geology, the prediction capability of the mechanical properties of the oil reservoir is critical for oil exploitation, as well as for the analysis of the seismic effect on geologic structures.

The most challenging problem about microstructure reconstruction is how to efficiently achieve a realistic three-dimensional computational model with a highly accurate representation of the random heterogeneous material [4]. The three-dimensional microstructure of media can be directly reconstructed by using a large number of sectioning and imaging, but these 3D imaging techniques are often costing and have restrictions in sample size and shape. Therefore, based on the statistical information obtained from several two-dimensional slices (thin sections) of a random medium or experimental images, it is desirable to reconstruct the full three-dimensional medium that matches the statistical information of the original microstructure, enabling computational and theoretical prediction of the macroscale properties (e.g., permeability, conductivity and elastic moduli).

There are two obvious advantages by employing the statistical reconstruction. The first one is reducing the experimental cost. Secondly, the statistical reconstruction is extremely suitable for the reconstruction of large-scale media. By extracting the statistical information from the real microstructure, the statistical properties of the reconstruction samples can be matched to those of a real target microstructure. Up to now, there are many existing methodologies for microstructure reconstruction. These methods can be roughly divided into four categories: the energy-minimization approach, the descriptors-based approach, the direct reconstruction approach using correlation function, the data classification approach respectively.

2. Energy-Minimization Approach

In the energy-minimization approach, an error E is defined to measure in the statistical context the difference between the reconstructed sample and the section scan of the real material, which is then minimized through an optimization procedure, e.g. simulated annealing, ant colony and genetic algorithms etc. This can be explained by considering reconstruction of a two-phase isotropic medium whose statistic information (e.g., two-point correlation function $f_0^i(\mathbf{r})$) is known [3]. Here, r is the displacement between two points in the medium. Initially, a reconstructed sample can be guessed with a two-point correlation function $f_s^i(\mathbf{r})$. Then, the following step is performed to evolve $f_s^i(\mathbf{r})$ towards $f_0^i(\mathbf{r})$ of the target via an optimization procedure. The error E can be set as

$$E = \sum_i [f_s^i(\mathbf{r}) - f_0^i(\mathbf{r})]^2 \quad (1)$$

After the optimization procedure, the correlation functions of the samples can match those of the target image. Many different energy functions can be employed in this approach (e.g., the two-point probability function, lineal-path function, pore-size distribution function, two-point cluster function and chord-length distribution function). Normally, the energy-minimization approach is always combined with the Fast Fourier transform algorithms. According to Fast Fourier transform algorithms, the number of operations can be reduced from N^2 operations in discrete Fourier transform to the order of $N \log N$. However, the efficiency of this kind of methods still leaves much to be desired.

3. Descriptors-based Approach

In the systemic approach using first-order descriptors, the samples can be reconstructed based on the integrated information that includes volume fraction of components, grain size, texture, and misorientation distribution etc. Out of these, a popular descriptor is the integral geometry, which provides a suitable family of morphological descriptors [1]. A well-known descriptor for the integral geometry characteristic is the Minkowski function [2], which contains information like the volume fraction of components, surface area (or called the particle size), mean curvature integral and Euler characteristic. Moreover, in the basic assumption, the grains can be approximated as ellipsoids. Each ellipsoid can be completely described by its semi-axes.

$$\left(\frac{x}{a}\right)^2 + \left(\frac{y}{b}\right)^2 + \left(\frac{z}{c}\right)^2 \leq 1 \quad (2)$$

The full formulation can be approximated by

$$f(a, b, c) = f(a, b) \cdot f(c | b) \quad (3)$$

After the representation of grains, the packing step processes, the samples are assembled closer and closer to the target microstructure through the optimized Monte Carlo movement. The simulation domain is a $1 \otimes 1 \otimes 1$ cubical box. The series of ellipsoids is drawn in this box based on the distribution $f(a, b, c)$. In the packing step, the system energy is minimized via a simulated annealing algorithm [5]. The total energy of the system is evaluated where the energy is calculated in terms of overlap and gaps between the ellipsoids contained in the simulation domain. This energy is then minimized by a series of adding, subtracting, swapping and jogging transactions. After the packing step, the interest properties of the samples can be predicted.

4. Direct Reconstruction Approach

In the direct reconstruction approach using correlation functions [6, 7], the random field can be represented directly from its first-order moment function (the porosity ε) and autocorrelation function (the autocorrelation function $C(\mathbf{u})$, the normalized auto-covariance function $Rz(\mathbf{u})$). The pore space of a porous media can be described via the phase function $Z(\mathbf{x})$:

$$Z(\mathbf{x}) = \begin{cases} 1, & \text{when } x \text{ belongs to the pore space} \\ 0, & \text{otherwise} \end{cases} \quad (4)$$

Taking the statistical averages, the statistics are shown as follows

$$\varepsilon = \overline{Z(\mathbf{x})} \quad (5)$$

$$C(\mathbf{u}) = \overline{Z(\mathbf{x})Z(\mathbf{x} + \mathbf{u})} \quad (6)$$

$$R_z(\mathbf{u}) = \frac{([\overline{Z(\mathbf{x})} - \varepsilon] \cdot [\overline{Z(\mathbf{x} + \mathbf{u})} - \varepsilon])}{(\varepsilon - \varepsilon^2)} \quad (7)$$

The reconstructed samples have the same porosity and autocorrelation function as the target. The basic procedures to generate a $N_x \otimes N_y \otimes N_z$ realization from known porosity and autocorrelation function using the Fourier transform method [7] are

- Measurement of porosity ε and normalized autocovariance function $Rz(\mathbf{u})$
- Calculation of $Ry(\mathbf{u})$ from the measured $Rz(\mathbf{u})$ [6].
- Power spectrum: by definition, the power spectrum is the Fourier transform of the autocorrelation function.
- Fourier spectrum: the Fourier spectrum can be obtained from square root of the power spectrum.
- Phase angle: the generation of phase angle is taken randomly from a uniform distribution between 0 and 2π .
- Inverse Fourier transform: by calculating the inverse Fourier transform, the discrete Gaussian field $Y(\mathbf{x})$ is obtained.
- Nonlinear filter: to takes a value 1 for the pore phase and 0 for the solid phase [6].

5. Results

Based on the aforementioned approaches for statistical reconstruction, some results are listed below.

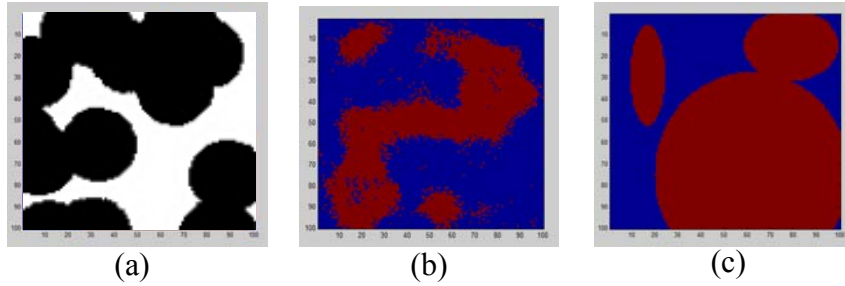


Figure 1: Case 1 (porous materials); (a) target image; (b) the reconstruction sample via the energy-minimization approach; (c) the reconstruction sample via the descriptor-based approach.

Case 1 is a 100×100 image of cross section of porous material. As shown in Figure 1, the reconstruction sample via the energy-minimization approach achieves a better result than the reconstruction sample via the descriptor-based approach. The latter is not good when particles overlap. However, the computation time for the energy-minimization approach is 1hr, while the computation time for the descriptor-based approach is only 10s. There is a huge difference in the efficiency between these two approaches. Case 2 is a 50×50 image, which is a local image of Case 1. It can be seen in Figure 2 that the reconstruction sample via direct reconstruction approach achieved the similar result as the sample via the energy-minimization approach. For the computation time, the former, even combined with the FFT algorithm, is 20min, while the latter is only 5s. Case 3 is a 240×240 image of the cross section of composite materials. In this case, the descriptor-based shows a better performance than the direct reconstruction. The computation time of these two approaches are 8s and 10s respectively. However, the particles of the sample for the descriptor-based approach can only be in the shape of ellipse.

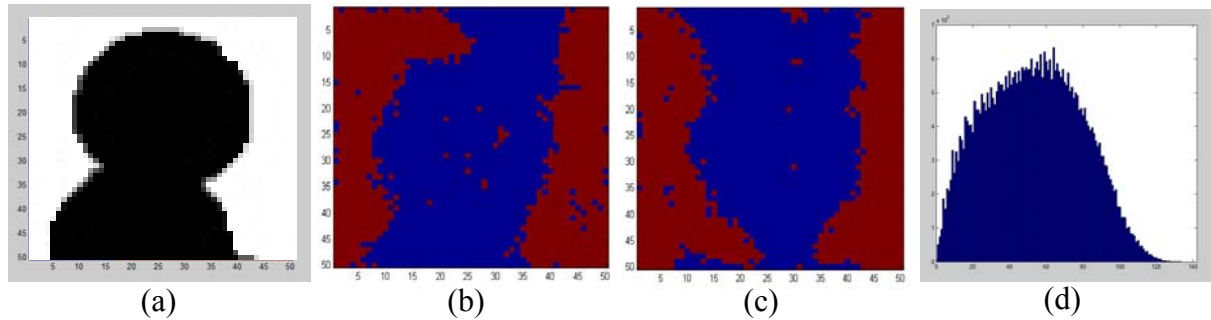


Figure 2: Case2 (microstructure of porous materials); (a) target image; (b) the reconstruction sample via the direct reconstruction approach; (c) the reconstruction sample via the energy-minimization approach; (d) the two-point correlation function of the target image.

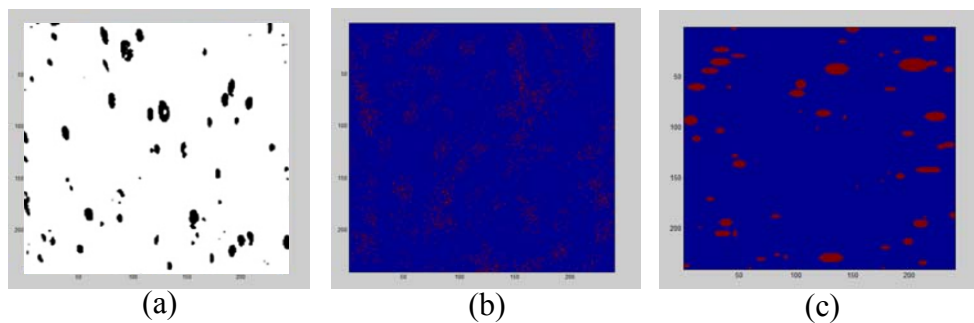


Figure 3: Case3 (composite materials); (a) target image; (b) the reconstruction sample via the direct reconstruction approach; (c) the reconstruction sample via the descriptor-based approach.

6. Conclusions and Future Work

Statistic reconstruction of heterogeneous media is important for material property prediction. Several tests have shown that the statistic reconstruction approaches discussed in this work all have their own advantages and disadvantages. Three main testing points are considered for their performance, i.e. computation time, shape of particles and similarity. The energy-minimization approach is suitable for almost all kinds of images, but its computational cost is high. The direct reconstruction approach is the most efficient reconstruction approach. But for the periodic images and the images consisting of small particles, it still leaves much to be desired. The descriptor-based approach is efficient, but the shape of the particles of the sample is restricted. Generally, for different heterogeneous media, based on the different situation, different approaches should be chosen for the best performance. Due to the restriction in abstract length, more results will be presented in the ACME conference.

References

- [1] B. S. Fromm, B. L. Adams, S. Ahmadi, Grain size and orientation distributions: Application to yielding of α -titanium, *Acta Materialia*, 57, 2339–2348, 2009.
- [2] C.H.Arns, Mark A. Knackstedt, W.V. Pinczewski, Euler-Poincare' characteristics of classes of disordered media, *PHYSICAL REVIEW E*, vol 63, 031112, 2001.
- [3] C. L. Y. Yeong and S. Torquato. Reconstructing random media. *PHYSICAL REVIEW E*, vol 57, no.1, 1998.
- [4] D.S. Li, Review of Structure Representation and Reconstruction on Mesoscale and Microscale, *The Minerals, Metals & Materials Society*, 16, No. 3, 2014.
- [5] H. Y. Xu, Y. Li, C. Brinson, A Descriptor-Based Design Methodology for Developing Heterogeneous Microstructural Heterogeneous Microstructural, *Journal of Mechanical Design*, Vol. 136, 051007, 2014
- [6] P.M. Adler, C.G. Jacquin, J.A. Quiblier, Flow in simulated porous media, *International Journal of Multiphase Flow*, vol 16, Issue 4, 691–712, 1990.
- [7] Z.R. Liang, C.P. Fernandes, F.S. Magnani, A reconstruction technique for three-dimensional porous media using image analysis and Fourier transforms, *Journal of Petroleum Science and Engineering*, 21, 273–283, 1998.

HIGH PERFORMANCE COMPUTING STRATEGIES FOR NONLINEAR FINITE ELEMENT ANALYSIS OF LONG HETEROGENEOUS SOIL SLOPES

*Yajun Li, Michael A. Hicks and Philip J. Vardon

Department of Geoscience and Engineering, Delft University of Technology, Stevinweg 1, 2628 CN, Delft

*y.li-4@tudelft.nl

ABSTRACT

In the field of dyke engineering, soil strength heterogeneity and the so-called length effect have drawn much attention in recent years. Reliability and risk analysis of dykes, taking account of the length effect, poses a great challenge for engineers and researchers. This paper presents one possible way to investigate the length effect using the random finite element method; that is, by analysing the reliability of longer and longer slopes using a 3D nonlinear finite element code within a Monte Carlo framework. However, this is computationally prohibitive for a standard desktop computer, as both the memory and running time requirements can be very high. Moreover, thousands of realisations of soil spatial variability are sometimes required to get a meaningful reliability result, although, usefully, each realisation is a largely independent calculation. To this end, Cloud and Grid computing technologies are naturally the most suitable for running multiple independent jobs. In this paper, a case study using the Dutch national Grid e-infrastructure is presented and performances for different computing strategies discussed. Especially, the use of a pilot framework using a Python client based on a central server is presented in detail. Various issues involved in selecting the best strategy for the example problem are discussed. The strategy presented in this paper can be easily applied in computational geo-engineering involving many independent tasks.

Keywords: *Cloud computing; finite elements; Grid computing; heterogeneity; Monte Carlo simulation*

1. Introduction

Soil properties vary spatially in the ground as a result of the combined action of physical, chemical and/or biological processes that act at different spatial and/or temporal scales, i.e. they fluctuate over various distances. The characterisation and modelling of the spatial variability is essential to achieve a better understanding of the relationships between soil properties and geotechnical soil structure performance. For example, in the Netherlands, it is particularly important to realistically assess the reliability of existing dykes and the risk posed by their failure. As these dykes are characterised by three dimensional heterogeneous soils and a large length to cross-section ratio, both locally and regionally, the length effect must be considered, e.g. by a full 3D analysis [4-5]. The benefits are cost-effective maintenance of existing dykes and new construction of dykes with lower risk.

The Authors are looking at one possible way of investigating dyke safety using the random finite element method [6]. Thousands of realisations of soil properties that satisfy the point and spatial statistics of the soil are here generated using a random field generator based on local average subdivision [2], so that the designed dyke reliability and risk can be assessed. However, the subsequent nonlinear finite element analysis for each realisation requires hundreds of plastic iterations before reaching an equilibrium state [3], which is a time consuming process. In order to make the calculations feasible, the Authors need to develop a suitable framework for carrying out this kind of computational task, which, in this case, is based on high performance computing (HPC) Cloud and Grid computing. This paper presents a primary development of the computing framework for geotechnical computations involving multiple realisations of physically large nonlinear problems.

Bash scripts and Python scripts can be provided upon request for whoever is interested. The modification is only limited to organising the input and output files according to the user's specific project.

2. Computing Strategies

There are basically two computing strategies for these largely independent calculations; i.e. Cloud computing and Grid computing. In its basic form, Cloud computing can be seen as a virtualising environment where the users can build their own cluster comprised of multiple virtual machines. To deploy their applications, Cloud users install operating system images and their application software on the Cloud infrastructure. Users are free to build their computing nodes (virtual machines) themselves by arranging CPU, memory, network and storage together. The Cloud infrastructure has 960 HPC cores (Intel Xeon(R) CPU E7/E5 @ 2.13/2.70GHz, 8GB RAM/core), 80 ‘light’ cores (AMD Opteron™ 6212 CPU, 8GB RAM/core) and one high memory node (Intel Xeon(R) CPU E7-4850 @ 2.00 GHz, 40 cores, 2TB RAM). The following resources were allocated for our project on the Cloud: 40,000 core hours, 100GB of disk storage and 1TB of VirDir storage (i.e. virtual directory storage). A master/worker design is implemented and adopted here. The procedure is shown in Fig. 1-left.

The computing capacity on the Cloud is not as large as on the Grid, so it was decided to also investigate using the Grid. Grid computing is a collection of geographically distributed computers, data storage capabilities and services, that can dynamically join to reach a common goal involving non-interactive workloads with a large number of files. For assessing the reliability of longer and longer dykes, typically 500-1,000 realisations are needed to ensure a converged solution. As each realisation or job can be run independently on a single serial computer, Grid computing is ideally suited for such computational tasks. The Authors were granted access to the national computing and data storage environment with the following resources: 500,000 core hours of Grid, 500 GB of disk storage, 500 GB of tape storage and 3 computing clusters (4,400 cores for gina cluster, 900 cores for rug cluster and 3800 cores for nikhef cluster). All of the clusters are heterogeneous, and for example, the gina cluster has nodes with Intel Xeon(R) CPU E5-2650 @ 2.60GHz, RAM memory 3-8 GB/core.

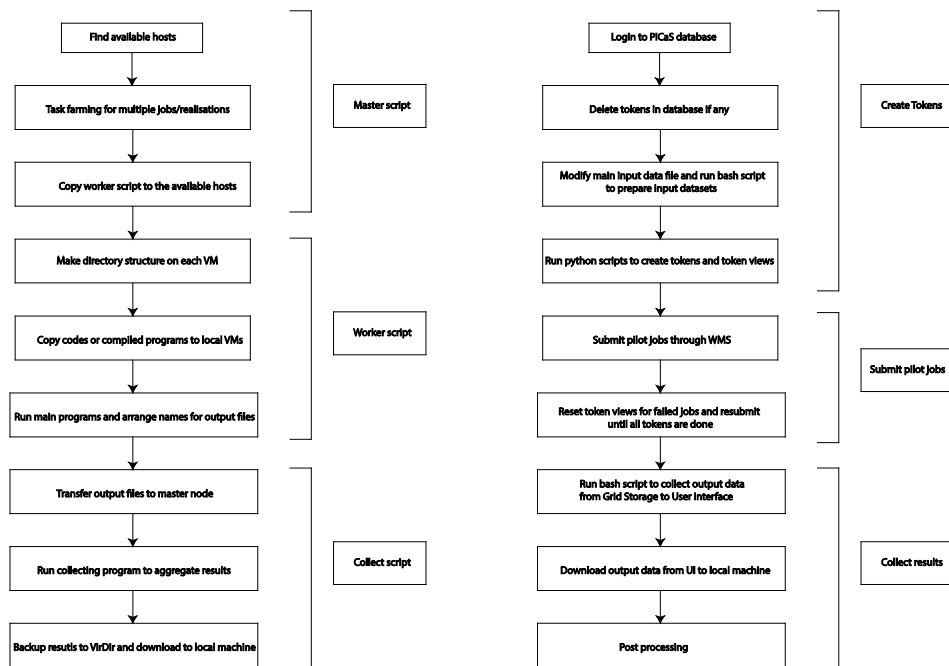


Fig. 1. Flow chart for Cloud computing (left) and Grid pilot computing (right)

Two approaches were tested, on the Grid, for the Monte Carlo simulation involved in assessing the reliability and risk of long 3D slopes: (1) using parametric jobs through WMS; (2) using the pilot framework (i.e. PiCaS token pool server, Fig. 1-right).

The computational jobs are submitted by a jdl (job description language) file. Each job in the form of a jdl file is then submitted to the Workload Management System (WMS) [1]. This system schedules submitted jobs to clusters each consisting of several machines (Worker Nodes). While, for Cloud computing, it is necessary for the user to write their own master scripts for polling tasks (Fig. 1-left), this is handled by the WMS in the Grid computing environment.

One job type worth mentioning is the parametric job. A parametric job causes a set of jobs to be generated from one jdl file. This is invaluable in cases where many similar (but not identical) jobs must be run, as is the case for a Monte Carlo simulation where many realisations need to be initiated from a different seed.

The first approach follows the procedures below, for the example of a Monte Carlo simulation comprising 500 realisations: 1. Define a parametric job consisting of $N_p = 50$ realisations; 2. Submit 10 parametric jobs using a single bash script; 3. Check status of submitted jobs and retrieve the output results; 4. Download output files to local computer for post-processing. Note that in practice one shouldn't send more than $N_p = 50$ to 100 jobs in the first step.

While the above approach works quite well, there are sometimes inevitable failing jobs (due to time limit, system problems, etc). It is a cumbersome task to track down these failed jobs and resubmit them, with the potential risk of ending up with some other job failures for the resubmitted jobs. The second approach (Fig. 1-right), the Pilot framework (PiCaS, a Python module using CouchDB as token pool server) was used to handle failed jobs automatically. The user should not look at the pilot jobs submitted, but to the number of tokens being processed. There is no need to keep track of submitted jobs and the user needs to resubmit only those that failed. The working philosophy of the pilot framework is shown in Fig. 2-left.

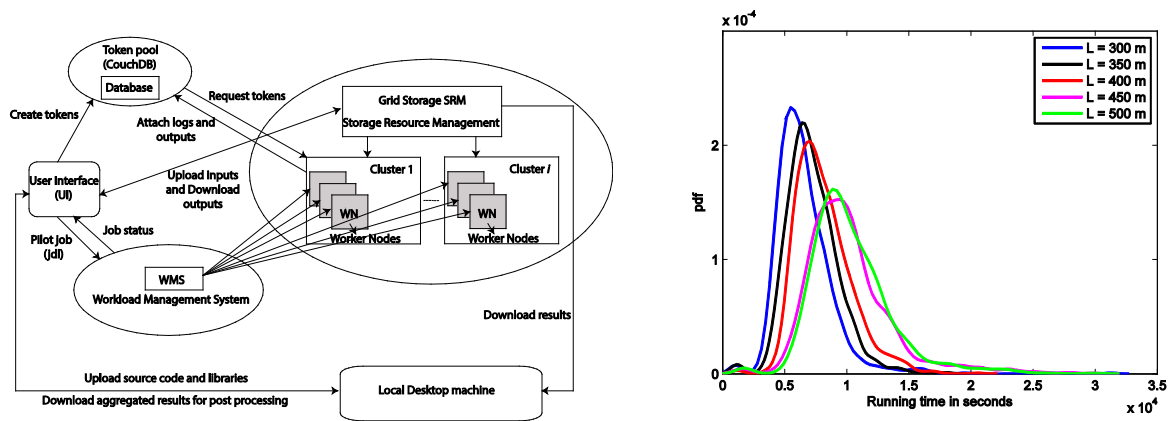


Fig. 2. A global overview of the pilot job framework (left) and timings for slope stability calculations with various slope length L (right)

3. Performance

In order to investigate the length effect, various slope lengths with the same soil property statistics need to be analysed. Here, an example of slope length $L = 50$ -500 m with an interval of 50 m is presented (all cases comprised 1,000 realisations). The timings for the ten cases are shown in Fig. 2-right in terms of probability density functions. Also, the average time and maximum time for a single realisation is tabulated in Table 1 in seconds, minutes and hours.

Table 1: Average and maximum time (t_a and t_m) for different slope lengths L on 2 cores on the Grid

L (m)	50	100	150	200	250	300	350	400	450	500
t_a (s)	977	1958	2768	3850	5182	6546	7217	8096	10134	10349
(min)	(16.3)	(32.6)	(46.1)	(64.2)	(86.4)	(109.1)	(120.3)	(134.9)	(168.9)	(172.5)
(hour)	(0.3)	(0.5)	(0.8)	(1.1)	(1.4)	(1.8)	(2.0)	(2.2)	(2.8)	(2.9)
t_m (s)	3456	6382	8506	11067	17476	31313	18204	20528	29886	29850
(min)	(57.6)	(106.4)	(141.8)	(184.5)	(291.3)	(521.9)	(303.4)	(342.1)	(498.1)	(497.5)
(hour)	(1.0)	(1.8)	(2.4)	(3.1)	(4.9)	(8.7)	(5.1)	(5.7)	(8.3)	(8.3)

The average time for different cases is in the range of 15 minutes to 3 hours, and the maximum time is in the range of 1 to 9 hours. The wall clock time should be considered carefully, as, in the Grid system, short queues are limited to 4 hours and medium queues to 36 hours. The decision on the

requirement for jobs to be submitted to the Grid is based upon the maximum time. For example, for the first 4 cases (i.e. L ranges from 50 m to 200 m), the short queues suffice. However, for the other cases, the medium queues must be specified in the jdl file. There is no point submitting short jobs to medium queues, as the waiting time is usually longer in the medium queues. On the other hand, if a long job is submitted to a short queue, it could result in a large proportion of job failures. So a general idea of how long one realisation takes for each case helps to improve the calculation efficiency.

With all the available resources, it is possible to carry out a detailed investigation for a 500 m long slope. Usually it takes 15-18 hours to finish 2,000 jobs for the 500 m case, including the waiting time in the queue. In comparison, running the analysis serially would be unfeasible, taking 250 days ($3 \text{ hours} \times 2000 \text{ realisations} / 24 = 250$), which clearly demonstrates the power of Grid computing. Even the 50 m case could take as long as 25 days ($0.3 \times 2000 / 24 = 25$) on a standard desktop computer, which is still unacceptable in most cases. For scientific purposes, it is always necessary to carry out a sensitivity analysis for several sets of statistics. For example, when investigating the influence of anisotropy of the heterogeneity on the reliability of a long 3D slope, about 10 cases are needed. In such cases, the benefits are clearly more apparent. It is worth mentioning that, for the 50 m case, it takes about 30 minutes per realisation on the Cloud virtual machines, which is 2 times slower than on the Grid. This is the penalty of using virtual machines to ensure the portability of Cloud applications across all the different types of real hardware.

One may choose to run 10 realisations for 1 job instead of 1 realisation per job to reduce the job submitting overhead (i.e. mainly the waiting time in the queue, which could take 0-5 hours depending how busy the clusters are at that moment). However, the latter has the advantage of downloading and post-processing the output results for one set of input data, while, at the same time, submitting a second job and waiting for the results for a second set of input data.

4. Conclusions

Two computing strategies have been developed to cope with a traditionally challenging computational task using desktop computers; one based on HPC Cloud and the other based on Grid computing. They are particularly suitable for many largely independent calculations for physically large and time consuming problems. These HPC strategies are readily applicable for researchers demanding a great deal of computing power in various scientific fields and they provide a way for researchers to work 'out of the box' to achieve their scientific goals.

Acknowledgements

This work was carried out on the Dutch National e-infrastructure with the support of SURF Foundation. Special thanks are given to SURFsara advisor Anatoli Danezi for her kind support on developing the computing strategy.

References

- [1] EGEE. Job description language attributes specification for the Glite workload management system https://grid.surfsara.nl/wiki/index.php/Job_Description_Language; last accessed 16/01/15.
- [2] G.A. Fenton and E.H. Vanmarcke. Simulation of random fields via local average subdivision. *Journal of Engineering Mechanics*, 116(8), 1733–1749, 1990.
- [3] I.M. Smith, D.V. Griffiths, L. Margetts, *Programming the finite element method*, 5th Edition, John Wiley & Sons, 2013.
- [4] M.A. Hicks, J.D. Nuttall, J. Chen. Influence of heterogeneity on 3D slope reliability and failure consequence. *Computers and Geotechnics*, 61, 198–208, 2014.
- [5] M.A. Hicks and W.A. Spencer. Influence of heterogeneity on the reliability and failure of a long 3D slope. *Computers and Geotechnics*, 37, No. 7-8, 948–955, 2010.
- [6] Y. Li and M.A. Hicks, Comparative study of embankment reliability in three dimensions, in: *8th European Conference on Numerical Methods in Geotechnical Engineering (NUMGE)*, Delft, Netherlands, pp.467–472, 2014.

A COMPARISON STUDY ON STOCHASTIC FINITE ELEMENT METHODS FOR STRUCTURAL RELIABILITY ANALYSIS

*M. H. Aldosary¹, C. F. Li² and M. Benamer³

^{1,2,3} Zienkiewicz Centre for Computational Engineering, College of Engineering, Swansea University, Swansea SA2 8PP, United Kingdom

* 716663@swansea.ac.uk

ABSTRACT

Stochastic finite element methods (SFEM) for structural reliability analysis have potential to become a major numerical technique for uncertainty quantification in many scientific and engineering fields, e.g. seismic analysis of structures and material science etc. The task of SFEM is to evaluate the uncertainty in responses caused by the uncertainty from the input data, i.e. uncertainty quantification. A common problem in computational statistics and stochastic analysis entails calculating a multi-dimensional integral to determine the probabilistic characteristics of random output when input uncertainties are characterized either partially by moments or fully by probability density functions. This research performs a comprehensive comparison study on a series of popular SFEM schemes. Existing stochastic finite element methods can be roughly classified into two major categories: approximation-based methods and sampling-based methods. The approximation-based SFEM schemes include the perturbation method, the Neumann expansion method, the decomposition method, the polynomial chaos expansion method and the joint-diagonalization method etc. These methods simplify or reorganize the underlying stochastic partial differential equations using analytical or numerical approximation techniques, such that the response statistics can be obtained without time-consuming computation of individual sample solutions. The sampling-based SFEM schemes, including direct Monte Carlo simulation, quasi-Monte Carlo simulation, importance sampling and directional simulation etc., compute solutions for a set of selected samples and obtain the response statistics through the sample solutions.

All aforementioned methods are tested for seismic reliability analysis of a frame building subject to uncertainties in materials, seismic loading and geometry. In particular, the study focuses on chooses of the best schemes which reduce the numerical effort required for analysis when there are a large numbers of a random variables or random fields. In a probability-based approach, the seismic action and the structural capacity are functions of random variables. In particular, the ground motion includes uncertain variables like its peak intensity, the form of the record itself and the duration of the strong segment. The dynamic response of interest also depends on the structural geometry and the uncertain characteristics of the material properties, including nonlinear effects leading to hysteretic damping, stiffness or strength degradation. Problems in earthquake engineering are characterized by nonlinear dynamic behavior, and it is not possible to establish an explicit relationship between the input variables and the structural responses. Thus, it is not feasible to write explicit forms for the different performance limit states, and the calculation of failure probabilities must rely on simulation. Finally, after a comprehensive comparison study, the advantages and disadvantages of each methodology are discussed and the improvements are provided whenever applicable.

Keywords: *stochastic finite element, seismic load, reliability analysis, perturbation method, the Neumann expansion method, polynomial chaos expansion method, Monte Carlo simulation.*

1. Introduction

Structural reliability analysis and the associated risk assessment are becoming increasingly important in engineering, e.g. for aging buildings and critical infrastructures, and have attracted considerable attention from both academia and industry (Figure 1). The main challenge here is how to cope with the various uncertainties arising from material properties, geometry and loading conditions, predicting the uncertainty propagation in the structure and estimating the associated risk.

The finite element method, which has become a basic numerical tool in many scientific and engineering fields, is built on deterministic mathematical models. In other words, to use FEM, all system parameters such as loads, geometric configurations and material properties, have to be

uniquely specified in order to perform a successful analysis. In reality, however, the practical situation is different because there are many factors cannot be predicted and measured up to a unique value. In a large number of scientific and engineering problems where the scale of the random fluctuation is relatively small, the deterministic model provides a good approximation. However, it is often extremely difficult, if not impossible, to obtain valid estimation from deterministic FEM if the underlying problem is subjected to significant uncertainties. Such problems include soil and rock formation, groundwater flow, structural response with large uncertainties and microstructure of materials; and the deterministic model may cease to be useful in the presence of these cases. Hence, stochastic finite element methods (SFEM), which take into consideration various uncertainties in the finite element formulation, are required for modelling random phenomena [1]. The research into SFEMs has been increasing steadily for over two decades (Shinozuka, 1972; Yamazaki et al., 1988; Papadrakakis and Kotsopoulos, 1999; Charmpis and Papadrakakis, 2005; Pradlwarter et al., 2005; Liu et al., 1986a, b; Kami ski and Kleiber, 1996; Hien and Kleiber, 1997; Ghanem and Spanos, 1991; Babuska and Chatzipantelidis, 2002; Frauenfelder et al., 2005; Vanmarcke and Grigoriu, 1983; Li and Derkiureghian, 1993; Harada and Shinozuka, 1986; Li et al.).

Following Fig. 1 shows the histogram of the papers published in the last 30 years, on the topic of structural reliability analysis methods. It can be observed from Fig.1 that the Monte Carlo Method was the most widely used simulation method for reliability analysis. This method generally requires a large number of simulations to calculate low probability or higher-order moments. As a result, researchers have developed or examined faster methods, such as the Perturbation Method, the Neumann Expansion and polynomial chaos expansion method.

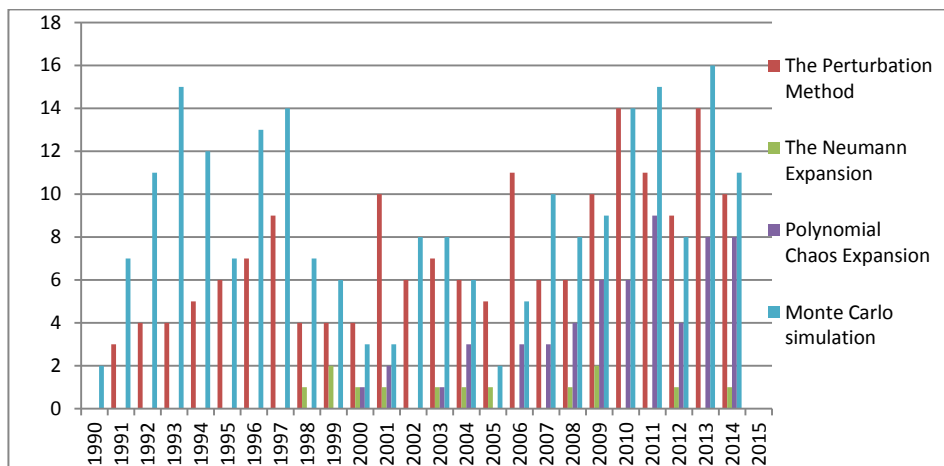


Figure 1: Histogram of Publications on Structure Reliability Analysis.

2. Approaches in formulating SFEMs

Generally, for many engineering applications, the final linear SFEM equations take the following form:

$$(\alpha_1 A_1 + \alpha_2 A_2 + \dots + \alpha_m A_m)x = b \quad (1)$$

where the deterministic $n \times n$ real symmetric matrices A_i ($i=1, \dots, m$), unknown real random vector x and deterministic real vector b have essentially the same physical meanings as their deterministic counterparts in FEM; real scalars α_i ($i=1, \dots, m$) denote a series of dimensionless random factors that capture various intrinsic uncertainties in the system.

In this study, we investigated the performance of the most popular SFEM approaches in structural reliability analysis. In particular, we tested the Taylor expansion or perturbation methods [5], the Neumann expansion method [10], the decomposition method [11], the polynomial chaos expansion method [5], the statistically equivalent solution [11] and the point estimate method.

2.1 The Perturbation Method

In a perturbation scheme, all random variables α_i ($i=1\dots m$) are first decomposed into a deterministic part and a random part, i.e.

$$\alpha_i = E(\alpha_i) + \alpha_i^s \quad (i = 1, \dots, m) \quad (2)$$

where $E(\alpha_i)$ and α_i^s denote respectively the mean value and the centred deviation random variable. As a result, Eq. (1) is then transformed into

$$(A_0 + \alpha_1^s A_1 + \alpha_2^s A_2 + \dots + \alpha_m^s A_m)x = b \quad (3)$$

where $A_0 = \sum_{i=1}^m E(\alpha_i) A_i$ is the deterministic mean of sum $\sum_{i=1}^m \alpha_i A_i$. Meanwhile, the random solution x is approximated by Taylor's series

$$x \approx x|_{\alpha_i^s=0 (i=1,\dots,m)} + \sum_{i=1}^m \frac{\partial x}{\partial \alpha_i^s} \alpha_i^s = x_0 + \sum_{i=1}^m c_i \alpha_i^s \quad (4)$$

In the literature, the aforementioned procedure is called the first-order perturbation method and similarly, the second-order perturbation method follows immediately from expanding the first-order Taylor series (4) to the second order. Applications of higher-order perturbations are, however, rare due to the increasingly high complexity of analytic derivations as well as computational costs. Very recently, the convergence criterion and *a priori* error estimation are established for the stochastic perturbation method [13].

2.2 The Neumann Expansion Method

The Neumann expansion method consists of Neumann series expansion of the inverse of random matrices (or other mathematical operators).

The Neumann expansion method starts with the following equation

$$(A_0 + \Delta A)x = b \quad (5)$$

The solution of Eq. (5) yields

$$x = (I + A_0^{-1} \Delta A)^{-1} A_0^{-1} b \quad (6)$$

The term $(I + A_0^{-1} \Delta A)^{-1}$ can be expressed in a Neumann series expansion giving

$$x = (I - B + B^2 - B^3 + \dots) A_0^{-1} b \quad (7)$$

The most significant feature of this approach is that the inverse of matrix A_0 is required only once for all samples and, at least in principle, the statistical moments of the solution in (7) can be obtained analytically by recognising that there is no inverse operation in Eq. (5). However, the algebra and numerical effort required for a relatively low-order Neumann expansion can be enormous when there are a large number of random variables or random fields [12].

2.3 The Polynomial Chaos Expansion Method

The polynomial chaos expansion involves alternative series expansions that can be exploited for stochastic analysis. The polynomial chaos expansion method is mean-square convergent and can approximate a square integrable random variable by Hermite or chaos polynomials of Gaussian variables [3]. However, depending on the order of polynomial expansion, this method may provide inaccurate estimates of higher-order moments (e.g. skewness, kurtosis, etc.), as recently demonstrated by Grigoriu [1]. For problems involving large number of input variables, the number of polynomial coefficients grows exponentially and the resultant calculations become prohibitively large. Statistically equivalent solutions are based on a selection of model parameters, which can be determined from the condition that the difference between exact and approximate responses is in some sense minimized. However, this difference cannot be calculated directly since the exact probability law of output is unknown.

2.4 Direct Monte Carlo simulation

The Monte Carlo method (Shinozuka, 1972; Yamazaki et al., 1988; Papadrakakis and Kotsopoulos, 1999; Charmpis and Papadrakakis, 2005; Pradlwarter et al., 2005). This method first generates a set of sample paths for the given random medium, then, for each sample path, a standard deterministic simulation is performed to obtain the corresponding solution sample. From the solution samples the empirical probability distribution and empirical statistical quantities of the random solution can be calculated. Until recently, it appears that only the Monte Carlo method, inclusive of improvements, has been widely accepted as a versatile and practical approach in many engineering situations, such as dynamic reliability assessment of general systems (Pradlwarter et al., 2005). However, the Monte Carlo method is generally attributed as being computationally expensive.

As a result, researchers have developed or examined faster sampling-based methods, such as quasi-Monte Carlo simulation [11], importance sampling [2], directional simulation [3], and others [4]. Nevertheless, all sampling-based methods today require considerably more extensive calculations than analytical methods. Consequently, sampling-based methods have found their utility when alternative methods are inapplicable or inaccurate, and/or analytical methods require validation.

3. Summary and Conclusions

The problem of structural reliability under parameter uncertainties is considered. This research performs a comprehensive comparison study on a series of popular SFEM schemes. Finally, after a comprehensive comparison study, the advantages and disadvantages of each methodology are discussed and the improvements are provided whenever applicable.

References

- [1] C.F. Li, Y.T. Feng and D.R.J. Owen, Explicit solution to stochastic system of linear algebraic equations $(\alpha_1 A_1 + \alpha_2 A_2 + \dots + \alpha_m A_m)x = b$, *Computer Methods in Applied Mechanics and Engineering*, 195 (44-47) (2006) 6560-6576.
- [2] Grigoriu M. *Stochastic calculus: applications in science and engineering*. Basel/New York, NY: Birkhäuser/Springer; 2002.
- [3] Genz AC, Monahan J. A stochastic algorithm for high-dimensional integrals over unbounded regions with Gaussian weight. *J Comput Appl Math* 1999;112:71–81.
- [4] Kleiber M, Hien TD. *The stochastic finite element method*. New York, NY: Wiley; 1992.
- [5] Rahman S, Rao BN. A perturbation method for stochastic meshless analysis in elastostatics. *Int J Numer Meth Engng* 2001;50:1969–91.
- [6] Kleiber M, Hien TD. *The stochastic finite element method*. New York, NY: Wiley; 1992.
- [7] Liu WK, Belytschko T, Mani A. Random field finite elements. *Int J Numer Meth Engng* 1986;23:1831–45.
- [8] Shinozuka M, Astill J. Random eigenvalue problems in structural mechanics. *AIAA J* 1972;10:456–62.
- [9] Adomian G, Malakian K. Inversion of stochastic partial differential operators: the linear case. *J Math Anal Appl* 1980;77:505–12.
- [10] Yamazaki F, Shinozuka M. Neumann expansion for stochastic finite element analysis. *ASCE J Engng Mech* 1988;114:1335–54.
- [11] Spanos PD, Ghanem RG. Stochastic finite element expansion for random media. *ASCE J Engng Mech* 1989;115:1035–53.
- [12] Ghanem RG, Spanos PD. *Stochastic finite elements: a spectral approach*. NY: Springer; 1991.
- [13] Wang XY, Cen S, Li CF and Owen DRJ, A priori error estimation for the stochastic perturbation method, *Computer Methods in Applied Mechanics and Engineering*, 2015; 286: 1-21.

Modelling of crack propagation on brittle heterogeneous materials

*E. Gironacci¹, M. Mousavi Nezhad¹ and M. Rezaia²

¹Computational Mechanic, Civil Research Group, School of Engineering, University of Warwick, Coventry,
CV4 7AL, UK

²Nottingham Centre for Geomechanics, Department of Civil Engineering, Faculty of Engineering, University of
Nottingham, Nottingham, NG7 2 RD, UK

*E.Gironacci@warwick.ac.uk

ABSTRACT

Fractures tend to propagate along the least resistance paths, and homogeneous-based models may not be able to reliably predict true crack paths. This paper presents a stochastic numerical modelling approach for simulating fracturing in natural heterogeneous materials. Through this approach, at a specified point of localized damage, the probability density function of the total energy of the system is defined, the direction of crack propagation is probabilistically determined and the reliability of the system is estimated. The Monte Carlo Simulation technique is adopted to obtain satisfactory convergence when comparing with experimental results. Reliability and performance of the methodology are examined through simulation of numerical examples.

Key Words: *stochastic modelling; non-local mechanics; crack propagation*

1. Introduction

In the recent years, many researchers have focused on the problem of modelling heterogeneous material systems that contain discontinuities. Although, multi-scale modelling approaches have been proved to be a powerful method for incorporation of the heterogeneity, an increasing interest is now spreading to stochastic approaches. The stochastic approaches allow probabilistically estimating the degree of material heterogeneity, through quantifying fluctuations of mechanical properties, such as elastic modulus or fracture toughness.

In the context of stochastic modelling, we define energy release rate as a function of the randomly variable bulk modulus, introducing randomness in the stiffness matrix. We consider the non-local nature of the method to probabilistically define fracture toughness, which is function of initial crack angle, loading condition and specimen geometry, by assigning a random value to the initial crack angle at the crack initiation point. The value of the angle is correlated to damage state of a body which is evaluated using a variational approach [2]. The non-local evaluation of the damage state is conducted using an Inverse Multiquadratic (IMQ) Radial Basis Function (RBF) method, in which a weighted value is assigned to each node. A probabilistic distribution for crack direction is defined and then used for sampling the angle and calculating fracture toughness for the heterogeneous materials.

2. Fracture advancement methodology and damage state of the body

A computational framework based on the variational method was used to model crack propagation. Equilibria of a body under a specified boundary condition is studied from minimization of the total energy, which is expressed as sum of a bulk energy and a surface energy,

$$\mathfrak{F}_\varepsilon(f, s) = \int_{\Omega_0} (s^2(x) + \kappa_\varepsilon) W(\nabla_0 f(x)) dx_0 + \frac{\gamma}{2} \int_{\Omega'_0} (\varepsilon |\nabla_0 s(x_0)|^2 + \frac{1}{\varepsilon} (1 - s(x_0))^2) dx_0 \quad (1)$$

where, s is damage parameter, κ_ε is a regularization parameter, γ is fracture toughness, ε is a parameter related to the material length scale.

3. Nonlocal spatial discretization

A local zone is selected around the crack tip where the evolution of damage is expected. A series of nodes is distributed in the domain forming a grid of points. The values for damage state parameter s over the grid are calculated through an iterative finite element method. These values are then employed to probabilistically estimate the crack initiation angle. A lower value of s denotes a more damaged material. The direction of the crack propagation is influenced by the damage state of the local zone. The damage state of the points closer to the tip has higher influence on the crack propagation direction. To take into account this influence, we calibrate the values of s associated to each point according to their position. To do this, we use an Inverse MultiQuadratic Radial Basis Function formulation proposed by Evangelastos and Spanos [1]

$$g_t = \frac{1}{\sqrt{(x-x_t)^2 + (y-y_t)^2 + s^2}} \quad (2)$$

where x_t and y_t are the coordinates of the crack tip, and x , y are the coordinates of the points within the selected zone, and we calibrate the s through multiplying it by g_t . According to this theory, nodes with a sufficiently low value of calibrated s significantly contribute in the propagation process. Then, for a specified angle of the propagation path, the probabilistic contribution of each node in the crack propagation process is evaluated. Probability Density Function (PDF) and Cumulative Density Function (CDF) of the calibrated s is identified and used to randomly generate samples for both mode I and mode II Stress Intensity Factors, and consequently, for the material fracture toughness.

4. Fracture Toughness as function of a random θ_0

The fracture toughness is a function of the stress distribution inside the specimen, the initial crack length and the initial crack direction that for mixed-mode propagation condition is defined as [3]:

$$K_{IC} = \cos \frac{\theta_0}{2} \left[K_I \frac{1}{2} (1 + \cos \frac{\theta_0}{2}) - K_{II} \frac{3}{2} \sin \theta_0 \right] \quad (3)$$

where θ_0 is the angle between orientation of the initial crack and direction of crack propagation, K_I and K_{II} are Stress Intensity Factors for mode I and mode II , respectively.

For this specific example, K_I and K_{II} can be expressed as [3]:

$$K_I = \sigma \sqrt{\pi a} \sin^2 \beta \quad K_{II} = \sigma \sqrt{\pi a} \sin \beta \cos \beta \quad (4)$$

where, σ is applied stress to the body, a is half length of the initial notch, and β is inclination angle of the notch with respect to the horizontal axis. Random samples are generated for θ_0 using the inverse cumulative distribution function method discussed above.

5. Discussion of results

A benchmark example was simulated to verify the methodology. Figure 1 shows the geometry of the example. In this example $\sigma = 6.25$ MPa, $a = 0.02$ m and $\beta = 45^\circ$ [3]. Figure 2 shows the distribution of calibrated values of s . The probability distribution of s is presented in Figure 3, which has a mean value of 6.33° and standard deviation of 0.23.

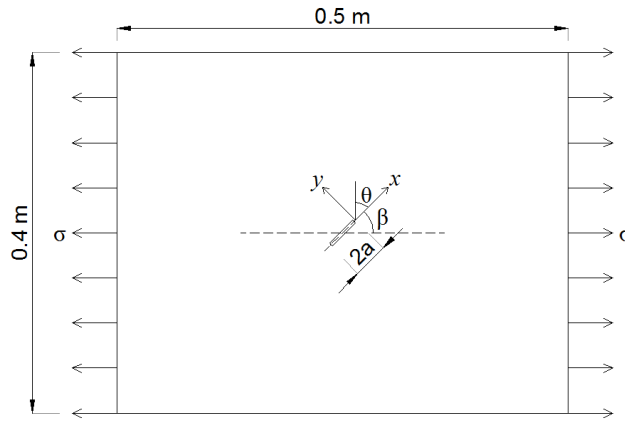


Figure 1: Geometry and load of the considered example.

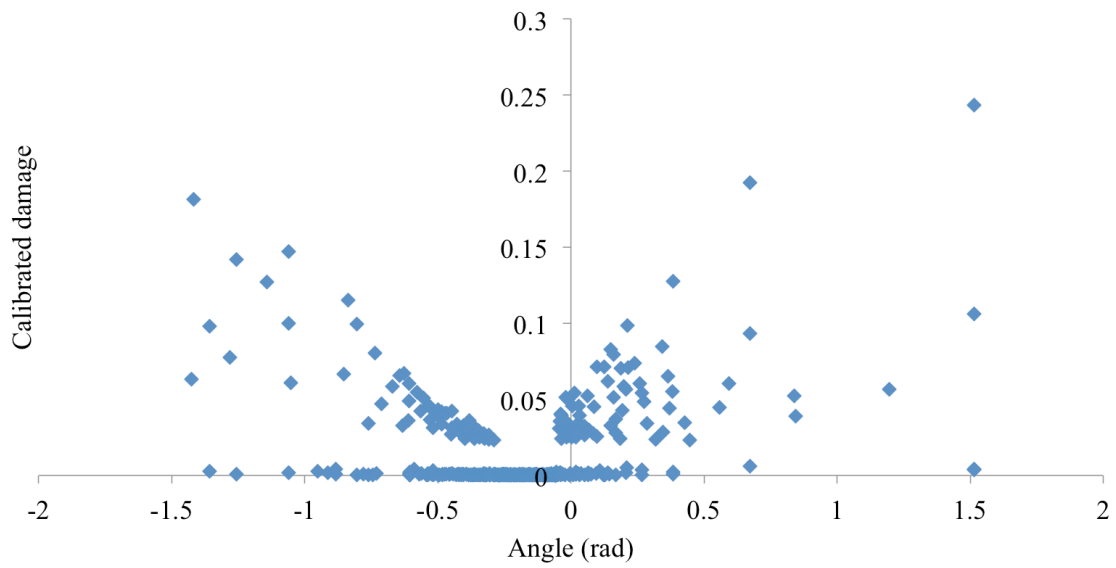


Figure 2: Values for s calibrated according the IMQ RBFs method.

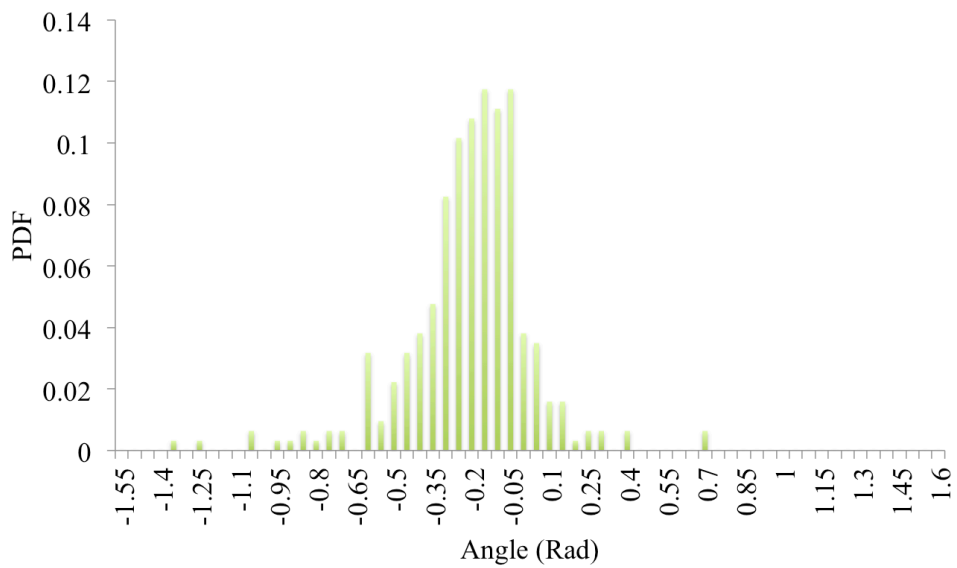


Figure 3: Probability of damage as function of crack initiation angle.

Figure 4 compares the crack patterns obtained through homogeneous and heterogeneous simulations. Using the same finite element mesh, a symmetrical crack path is predicted via the deterministic model. However, including the heterogeneity leads to prediction of an unsymmetrical crack path.

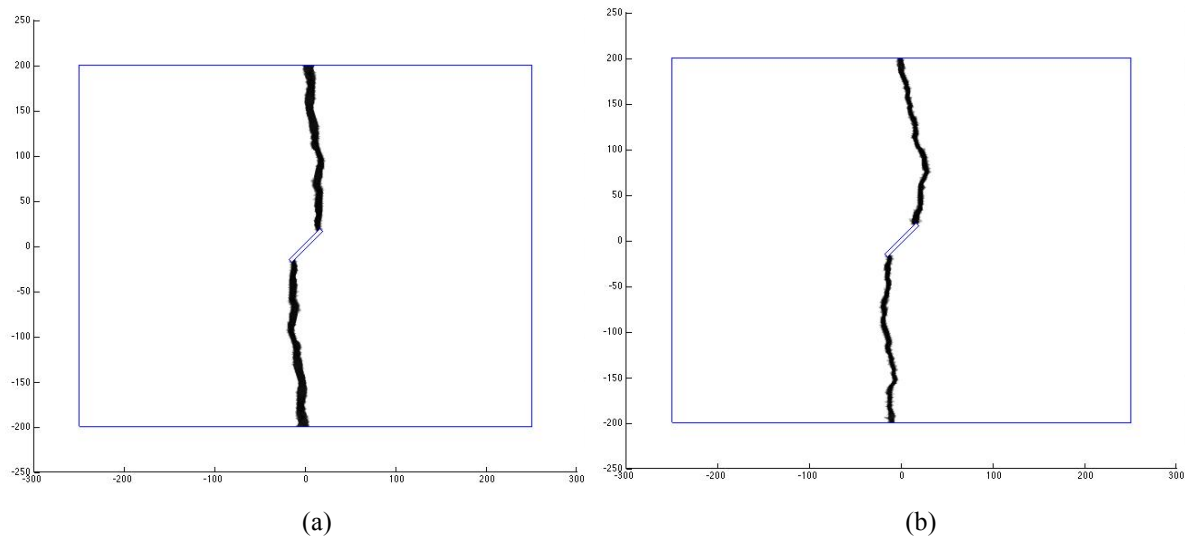


Figure 4: Comparison between homogeneous (a); and heterogeneous (b) crack patterns.

6. Conclusions

A non-local approach for the definition of a Probability Density Function capable to give an estimate of crack propagation angle has been proposed. Pseudo-random values are sampled from the given distribution and employed to calculate fracture toughness for mixed-mode crack propagation condition. Preliminary simulations show the effect of the heterogeneity on the crack paths in the computational simulations. Monte Carlo method is used to get an adequate convergence of the results.

References

- [1] Evangelatos, G. I., Spanos P. D. A collocation approach for spatial discretization of stochastic peridynamic modeling of fracture. *Journal of Mechanics of Materials and Structures* 6.7: 1171-1195, 2011.
- [2] Del Piero, G., Lancioni, G., & March, R., A variational model for fracture mechanics: numerical experiments. *Journal of the Mechanics and Physics of Solids*, 55(12), 2513-2537, 2007.
- [3] Dan Huang, Guangda Lu, and Yiming Liu, Nonlocal Peridynamic Modeling and Simulation on Crack Propagation in Concrete Structures, *Mathematical Problems in Engineering*, Article ID 858723, in press.

THERMODYNAMICS

MATHEMATICAL FRAMEWORK FOR PREDICTING THE THERMAL BEHAVIOUR OF SPECTRALLY SELECTIVE COATINGS WITHIN INDUSTRIAL NEAR INFRARED FURNACES

*D.A. Brennan¹, I. Mabbett¹, J. Elvins², N.P Lavery³ and D.A Worsley¹

¹SPECIFIC, College of Engineering, Swansea University, BBIC, Port Talbot, SA12 7AX, United Kingdom

²Tata Steel, SPECIFIC, Baglan Bay Innovation Centre, Port Talbot, SA12 7AX, United Kingdom

³Materials Research Centre, Swansea University, Singleton Park, Swansea, SA2 8PP, United Kingdom

*brennanda@physics.org

ABSTRACT

A transient finite difference thermal model is formulated, valid for spectrally selective surface coatings on any substrate material within an ultra-fast near infrared (NIR) furnace and based on the heat equations. The irradiation from the NIR emitters provides the heat source and the model accounts for both radiative and convective cooling. A novel Monte Carlo ray tracing algorithm has been developed and is capable of determining the radiation view factor across a surface as well as for each node. The radiative flux is split into absorbed and reflected bands using UV-Vis-IR reflectance spectra measured within the 250-2500nm wavelength range, enabling the model to predict the thermal build-up of coatings with very different absorption properties. Results show that the transient temperature distribution of spectrally selective organic coatings can be modelled within an NIR oven and used to demonstrate how different spectrally selective coatings behave during NIR curing. The model shows the expected relationship between colour and absorption, with darker coatings displaying greater absorption and heating rates than lighter coatings. Surprisingly, colours which appear similar to one another can display wildly different heating rates; a result of their varied infrared absorption properties.

Keywords: *Material modelling; heat transfer; applied mathematics; Monte Carlo methods.*

1. Introduction

Widely used in the construction industry as an effective material for roofing and cladding applications; organically-coated steel (OCS) products are galvanised, hot rolled or cold rolled strip steels that have been coated with a functional organic coating system prior to use¹. A diverse range of coatings are available, with modern paint formulations being able to perform a variety of functions that includes energy generation, CO₂ capture and corrosion resistance². Spectrally selective coatings have been specifically formulated to provide particular thermal characteristics which often contradict intuitive associations of colour and temperature i.e. dark and light coatings no longer necessarily have to have the greatest and lowest thermal build-up respectively³. OCS products are produced in continuous roll-to-roll processes, vital to the sustainability of which is the development of fast and efficient heating methods⁴.

Near infrared (NIR) heating technology is a rapid radiative heating technique capable of dramatically reducing a number of heating, drying and curing process times throughout OCS production⁵. Infrared (IR) emitters are characterised by the type of IR radiation they emit, their operating temperature and by their peak wavelength of emission⁶. Typical NIR emitters utilise tungsten-halogen filaments, operate at colour temperatures of between 2000-3140K and emit a broad spectrum of electromagnetic radiation, predominantly focused within the high energy density, near-wave IR sub-division of between 750-1400nm. At maximum operating temperature, the peak wavelength of emission, λ_{\max} , is approximately 900nm. Heating is achieved by irradiating the coating with this broad spectrum of electromagnetic energy. NIR technology has become a realistic option for the OCS market due to the ability to reduce the cure time of a typical polyester coating from 20-30s achieved via conventional heating methods down to < 10s, depending on the coating thickness, enabling production at elevated line speeds⁷.

The thermal build-up of coatings within an NIR furnace is a result of the absorption of the NIR irradiation received from the emitters. As various coatings, particularly spectrally selective coatings, display wildly differing absorption characteristics, wildly different heating rates are often observed between different coatings when exposed to NIR radiation. This can become problematic to the manufacturing process; strongly absorbing coatings can over-cure, whilst weakly absorbing coatings can under-cure, both of which result in unwanted surface defects that can lead to product failure within its agreed lifespan⁸. The variation in heating rates observed for each coating results in different coatings reaching the cure temperature, roughly 503K for organic polyesters, within different exposure times, offering the potential to optimise production speed for each coating.

The aim of this work was to develop a mathematical framework that can determine the heating rate of a variety of spectrally selective organic coatings within a NIR furnace that utilises tungsten-halogen emitters. The desired inputs are their UV-Vis-IR reflectance spectrums and their basic material properties such as thermal diffusivity, heat capacity and density etc. The model is of particular interest to coating developers as a tool to simulate the behaviour of a coating within a NIR furnace without the need to conduct expensive and time consuming trials, with the model being utilised to assess a coatings suitability to NIR curing and to gain an insight into the optimal line speed and how this differs between coatings.

2. Model description

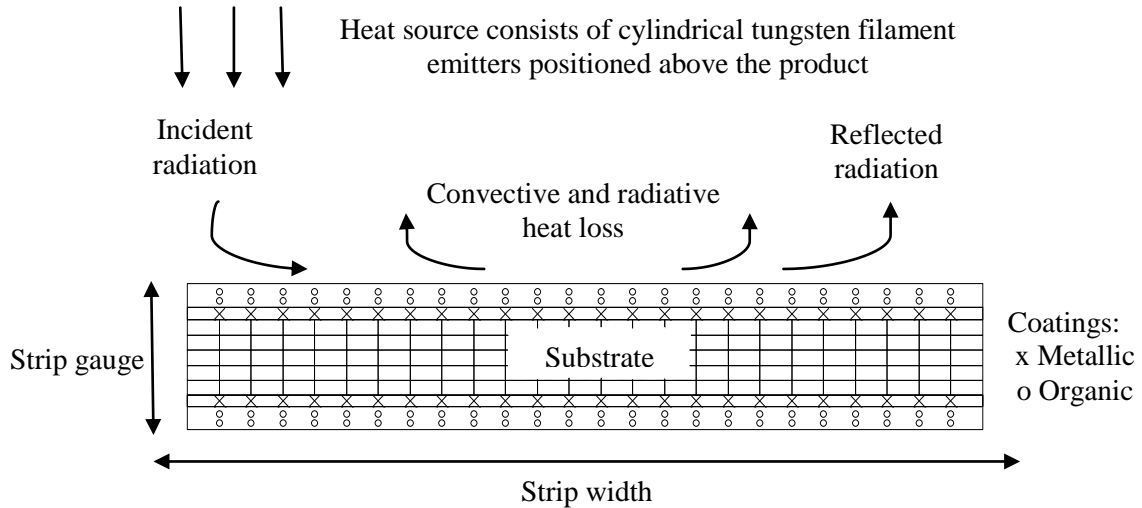


Figure 1: Geometry of the problem, showing the modelled heat transfer mechanisms

Fig.1 shows the heat transfer mechanisms accounted for by the model. Radiative heat transfer occurs between the NIR emitters and the product surface, and radiative and convective heat transfer occurs between the environment and the product surface. The model assumes that the tungsten-halogen NIR lamps are diffuse, grey emitters, all surfaces are opaque and that the medium within the furnace is non-participating.

$$q_{irrad} = \epsilon_e \sigma F_{ij} A (T_c^4 - T_s^4), \quad (1)$$

The irradiative flux from the emitters, q_{irrad} , is determined by using Eqn.1, the Stefan-Boltzmann equation, where ϵ_e is the emissivity of the emitters, σ is the Stefan-Boltzmann constant, F_{ij} is the radiation view factor between the emitters and the product surface, A is the products surface area and T_c and T_s are the temperatures of the emitters and product surface respectively. The radiation view factor is calculated using a Monte Carlo ray tracing algorithm that is capable of yielding the average view factor across the surface and the infinitesimal view factor at each node. The incident flux is separated into absorbed and reflected bands through the calculation of the total absorptance coefficient, α , from UV-Vis-IR total reflectance spectra, within the 250-2500nm wavelength bands. The absorptance coefficient is obtained numerically by solving Eqn.2, where $E_{\lambda b}(\lambda, T_c)$, is Planck's

law for the emissive power of a blackbody and $\alpha_\lambda(\lambda)$, is the spectral absorptance obtained from the spectral reflectance, $\rho_\lambda(\lambda)$, through the expression: $\alpha_\lambda(\lambda) = 1 - \rho_\lambda(\lambda)$, as the surface is opaque. Radiative heat losses are also described using the Stefan-Boltzmann equation. The model can account for natural and forced convective heat losses by calculating the convective coefficient, h (W/m²K), of the system empirically, in a process described in detail in [3].

$$\alpha = \frac{\int_0^\infty \alpha_\lambda(\lambda) E_{\lambda b}(\lambda, T_c) d\lambda}{\int_0^\infty E_{\lambda b}(\lambda, T_c) d\lambda}, \quad (2)$$

The two-dimensional, time-dependent conduction heat transfer equation with radiative flux and convective boundary conditions can be written as:

$$\rho C_p \frac{\partial T}{\partial t} - k \left(\frac{\partial^2 T}{\partial x^2} + \frac{\partial^2 T}{\partial y^2} \right) = Q, \quad (3)$$

Where T is the temperature, t is time, ρ is the density, C_p is the specific heat capacity and k is the thermal conductivity. Q is the net radiative and convective heat flux into the surface. The initial condition that governs the heat equation is:

$$T(x, y, t) = T_\infty \text{ at } t = 0, \quad (4)$$

In Eqn.4, T_∞ , is the ambient temperature. An explicit forward-time, centred-space (FTCS) finite difference solution is used. The time derivative is replaced with a forward difference expression and the spatial derivative is replaced with a centred-difference expression as seen in Eqn.5. The FTCS scheme is conditionally stable and it was necessary to linearize the Stefan-Boltzmann equation through the radiative heat transfer coefficient, h_r .

$$\begin{aligned} \text{(a)} \quad \frac{\partial T}{\partial t} &= \frac{T_i^{n+1} - T_i^n}{\Delta t}, & \text{(b)} \quad \frac{\partial^2 T}{\partial x^2} &= \frac{T_{i+1}^n - 2T_i^n + T_{i-1}^n}{\Delta x^2}, \\ \text{(c)} \quad \frac{\partial^2 T}{\partial y^2} &= \frac{T_{i+1}^n - 2T_i^n + T_{i-1}^n}{\Delta y^2}, \end{aligned} \quad (5)$$

3. Results

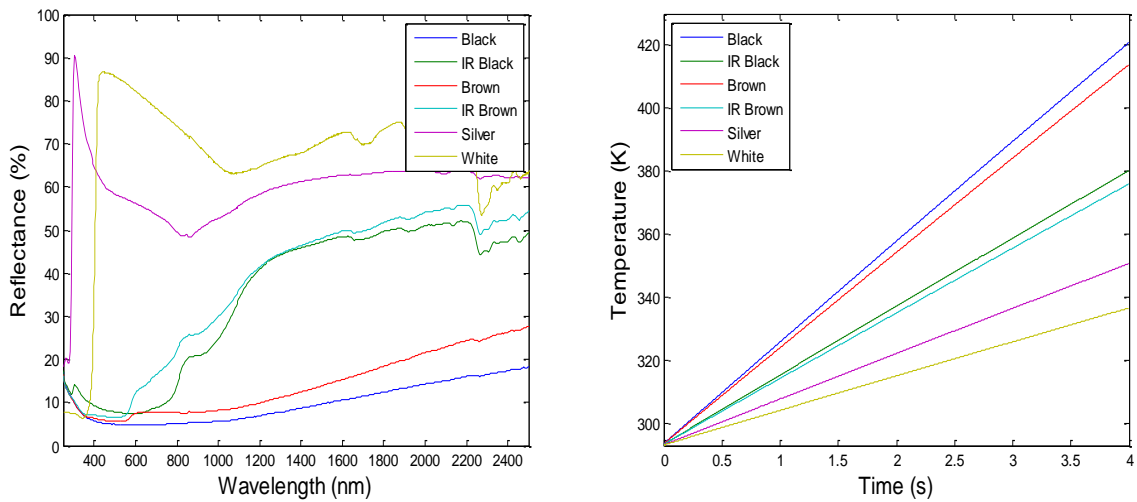


Figure 2: Reflectance spectra and simulated temperature profiles for a 4 second exposure of a number of coloured polyester coatings, with $T_c = 2600\text{K}$ and $\epsilon_e = 0.12$

Table 1: The total reflectance, ρ , total absorptance, α , and predicted, T_s , and measured, T_m , temperatures after an exposure of 4 seconds, with $T_c = 2600\text{K}$ and $\epsilon_e = 0.12$

	ρ	α	T_s (K)	T_m (K)
Black	0.09	0.91	420.79	435.56
IR Black	0.38	0.62	380.52	378.37
Brown	0.14	0.86	413.80	419.37
IR Brown	0.41	0.59	375.97	392.13
Silver	0.59	0.41	350.70	358.78
White	0.69	0.31	336.64	345.10

The reflectance spectra of a number of organic polyester coatings are measured using a Perkin Elmer Lambda 750s spectrophotometer and used to calculate the total reflectance and total absorptance following the method described in Section 2; their simulated temperature profiles for an exposure of 4 seconds have been plotted, with $T_c = 2600\text{K}$ and $\epsilon_e = 0.12$. Results can be seen in Fig.2. IR Black and IR Brown contain IR reflective pigments. The total reflectance, total absorptance and simulated and measured temperatures after a 4 second exposure have been recorded in Tab.1.

4. Conclusions

A transient, finite difference thermal model has been presented valid for spectrally selective coatings on any substrate during heating within a near infrared furnace. Temperature profiles exhibit the classic relationship between colour and absorption with darker coatings displaying the greatest thermal build-up. The model demonstrates how coatings that appear similar can have wildly differing temperature build-ups, such as the black/brown and IR black/IR brown coatings; a result of their differing IR reflectivity's. The ultra-fast heating potential of NIR technology is demonstrated effectively, with coatings heating at a much faster rate than with conventional curing technology. Interestingly, the thermal build-up of the black coating is almost double than that of the white coating; giving rise to the possibility of accelerated line speeds in the production of the darker coated products.

Acknowledgements

The first author would like to thank all co-authors for their support, and Swansea University, Tata Steel Colors and EPSRC for the financial assistance to make this work possible.

References

- [1] C. Gowenlock, *Near infrared curing of high performance coil coatings*, EngD Thesis, College of Engineering, Materials Research Centre, Swansea University, 2014.
- [2] I. Mabbett, *Applications of near infrared heating of interest to the coil coating industry*, EngD Thesis, College of Engineering, Materials Research Centre, Swansea University, 2011.
- [3] N.P. Lavery, *Mathematical framework for predicting the solar thermal build-up of spectrally selective coatings at the Earth's surface*, Applied Mathematical Modelling, 2006.
- [4] S.F. Cassidy, *Mathematical modelling of infrared heating of thermoplastic composites in diaphragm forming*, PhD Thesis, University College Galway, 1994.
- [5] T. Watson, I. Mabbett, H. Wang, L. Peter and D. Worsley, *Ultrafast near infrared sintering of TiO_2 layers on metal substrate for dye-sensitized solar cell*, Prog. Photovolt: Res Appl; 2010.
- [6] M.T. Brogan and P.F. Monaghan, *Thermal simulation of quartz tube infra-red heaters used in the processing of thermoplastic composites*, Composites: Part A 301-306, 1996.
- [7] I. Mabbett, J. Elvins, C. Gowenlock, C. Glover, P. Jones, G. Williams and D.Worsley, *Addition of carbon black NIR absorber to galvanised steel primer systems: Influence on NIR cure polyester melamine topcoats and corrosion protection characteristics*, Prog. In Organic Coatings, 2013.
- [8] D.A. Brennan, *NIR curing of high performance coatings*, MRes Thesis, College of Engineering, Materials Research Centre, Swansea University, 2014

***a-Posteriori* Error Estimate for the Partition of Unity Method for Transient Heat Diffusion Problems**

*M. Iqbal¹, H. Gimperlein², M.S. Mohamed¹, O. Laghrouche¹

¹Institute for Infrastructure and Environment, Heriot Watt University, Edinburgh EH14 4AS

²Maxwell Institute for Mathematical Sciences and Department of Mathematics, Heriot Watt University, Edinburgh EH14 4AS

*mi130@hw.ac.uk

ABSTRACT

This paper investigates an error estimate for the partition of unity method (PUM) for the solution of time dependent diffusion problems. The PUM is used to enrich the finite element space to solve a transient diffusion problem. We consider a problem for which we know the exact solution. We compute actual error in the solution and its derivatives and compare this error to a mathematically rigorous, computable error estimate. Results are computed using different values of time steps and enrichment functions. It is confirmed that at each time step the error estimate decrease similar to the actual error as the number of enrichment functions is increased.

Key Words: *Partition of Unity Method; Transient Heat Diffusion; a-Posteriori; Error Estimate*

1. Introduction

In recent decades various generalized and meshless numerical methods have been introduced to solve complex engineering problems with ease and sufficient accuracy. One of the important subclass of these methods is the Partition of Unity Method (PUM). This method was introduced by Melenk and Babuska [1], who developed the mathematical background of this method. The Partition of Unity Method has gained increasing importance for solution of complex engineering and scientific problems. The fact that PUM uses coarse meshes to approximate the finite element solution of complex problems, it is necessary to address the accuracy and reliability of this method.

This paper deals with the accuracy of PUM for transient heat diffusion problems. Shadi *et al* [2] used PUM to solve two dimension transient heat diffusion problem having an exact solution. The authors showed the effectiveness of PUM compared to FEM. A full description of previous work related to heat transfer problems can be found in their work. In our present work we used the PUM to solve a transient diffusion problem and calculate the actual errors in the solution. We define mathematically rigorous computable error indicators and compare the actual errors in the solution with these error indicators. For an acceptable numerical solution, the actual errors in the solution should be less than these error indicators. We define the governing PDE for transient diffusion problem in the next section with appropriate initial and boundary conditions and its transformation to weak form. In Section 3, we define the error estimates followed by results of numerical analysis in Section 4. Section 5 includes some concluding remarks.

2. Boundary value problem and weak form

Given an open bounded domain $\Omega \subset \mathbb{R}^2$ with boundary Γ and a given time interval $]0, T]$, we are interested to solve the following transient diffusion equation

$$\frac{\partial u}{\partial t} - \lambda \nabla^2 u = f(t, \mathbf{x}), \quad (t, \mathbf{x}) \in]0, T] \times \Omega \quad (1)$$

where $\mathbf{x} = (x, y)^T$ are the spatial coordinated, t is the time variable, λ is the diffusion coefficient and $f(t, \mathbf{x})$ represents the effects of internal sources/sinks. We consider an initial condition and Robin type boundary condition

$$u(t = 0, \mathbf{x}) = u_0(\mathbf{x}), \quad (\mathbf{x}) \in \Omega, \quad \frac{\partial u}{\partial n} + hu = g(t, \mathbf{x}), \quad (t, \mathbf{x}) \in]0, T] \times \Gamma \quad (2)$$

where $u_0(\mathbf{x})$ is a prescribed initial field, \mathbf{n} is the outward unit normal on the boundary Γ and g is a given boundary function. To solve equation (1)-(2) numerically, the time interval is divided into N_t subintervals $[t_n, t_{n+1}]$ with duration $\Delta t = t_{n+1} - t_n$ for $n = 0, 1, \dots, N_t$ and then discretized it using an implicit scheme

$$\frac{u^{n+1} - u^n}{\delta t} - \lambda \nabla^2 u^{n+1} = f(t_{n+1}, \mathbf{x}) \quad (3)$$

This can be rearranged as

$$-\nabla^2 u^{n+1} + ku^{n+1} = F \quad (4)$$

where F and k are defined as

$$F = k(\delta t f(t_{n+1}, \mathbf{x}) + u^n), \quad k = \frac{1}{\lambda \delta t}$$

To solve equation (4) with the finite element method we first multiply the equation with a weighting function, W , and then integrate over Ω

$$-\int_{\Omega} W \nabla^2 u^{n+1} d\Omega + \int_{\Omega} W k u^{n+1} d\Omega = \int_{\Omega} W F d\Omega \quad (5)$$

The final weak form of our problem which will be solved using the PUM is given by

$$\int_{\Omega} (\nabla W \cdot \nabla u^{n+1} + W k^2 u^{n+1}) d\Omega + \int_{\Gamma} W h u^{n+1} d\Gamma = \int_{\Omega} W F d\Omega + \int_{\Gamma} W g(t, \mathbf{x}) d\Gamma \quad (6)$$

To solve the weak form (6) with PUFEM, the nodal values u_i are written as a combination of enrichment functions. We considered the following sum of global exponential functions to enrich the solution space

$$F_{enr} = G_1, G_2, G_3, \dots, G_Q \quad (7)$$

where

$$G_q = \frac{e^{-\left(\frac{R_0}{C}\right)^q} - e^{-\left(\frac{R_c}{C}\right)^q}}{1 - e^{-\left(\frac{R_c}{C}\right)^q}}, \quad q = 1, 2, \dots, Q \quad (8)$$

with $R_0 := |\mathbf{x} - \mathbf{x}_c|$ being the distance from the function control point \mathbf{x}_c to \mathbf{x} . The constants $R_c = \sqrt{\frac{14}{1.195}}$ and $C = \sqrt{\frac{1}{1.195}}$ control the shape of enrichment function G_q .

3. Definition of Error Estimates

In this section we define the actual errors in the solution and the error estimates. We use the PUM to find the actual errors in the solution and will compare these to the error estimates.

Let define

$$u(\mathbf{x}, t) = \frac{t - t_n}{t_{n+1} - t_n} u^{n+1}(\mathbf{x}) + \frac{t_{n+1} - t}{t_{n+1} - t_n} u^n(\mathbf{x})$$

and

$$\hat{u}(\mathbf{x}, t) = u(\mathbf{x}, t_{n+1}), \quad \hat{f}(\mathbf{x}, t) = f(\mathbf{x}, t_{n+1}), \quad t \in [t_n, t_{n+1}]$$

Let U and u be the exact and numerical solution of the equations (1) - (2) then

$$\int_{\Omega} |U - u|^2 + \lambda \int_{t_n}^{t_{n+1}} \int_{\Omega} |\Delta(U - u)|^2 \leq \eta_1^2 + \eta_2^2 + \eta_3^2 + \eta_4^2 + \eta_5^2 \quad (9)$$

The LHS of expression (9) indicates the actual errors in the method and RHS indicates the error estimates comprising of five error indicators η_1^2 to η_5^2 , where

$$\eta_1^2 = \|U_o - u_o\|_{(0,\Omega)}^2, \quad \eta_2^2 = \int_{t_n}^{t_{n+1}} \|(f - \partial_t u + \lambda \Delta u)\|_{H^{-1}(\Omega)}^2 \quad (10)$$

$$\eta_3^2 = \int_{t_n}^{t_{n+1}} \|(f - \hat{f})\|_{H^{-1}(\Omega)}^2, \quad \eta_4^2 = \lambda \int_{t_n}^{t_{n+1}} \|\nabla(u - \hat{u})\|_{L^2(\Omega)}^2, \quad \eta_5^2 = \lambda \sum_{edges} \int_{t_n}^{t_{n+1}} \left\| \left[\frac{\partial \hat{u}}{\partial n} \right] \right\|_{L^2(E)}^2$$

For our case we calculate the values of η_2^2 , η_4^2 and η_5^2 only. η_1^2 and η_3^2 are zero in our case as η_1^2 is based on the initial condition and the function f in η_3^2 is computed using the exact solution.

4. Numerical Results

The PUM approach is used to solve a transient heat diffusion problem given by equations (1) - (2). We consider a square domain Ω defined by $(\mathbf{x} \in \Omega ; 0 \leq \mathbf{x} \leq 2)$ with reaction term $f(t, \mathbf{x})$, the boundary function g and the initial condition $u_0(\mathbf{x})$ are chosen such that the exact solution is given by

$$U(\mathbf{x}, t) = x^{20} y^{20} (2-x)^{20} (2-y)^{20} (1 - e^{-\lambda t}) \quad (11)$$

where $\mathbf{x} = (x, y)^T$ are the spatial coordinated and t is the time variable. We use a course mesh of only 25 elements using different number of enrichment functions $Q = 2, 3, \dots, 6$. For all the analyses the heat diffusion coefficient is assumed to be $\lambda = 0.1 \text{ kg m/K s}^2$, and the convection heat transfer coefficient $h = 1 \text{ kg/K s}^2$. Figure (1) shows comparison of temperature distribution using exact analytical solution and numerical solution using PUFEM.

To quantify the error in the solution, we compute the actual errors in the solution and the error indicators and compare these values as defined by expression (9). When compared to the exact solution, the LHS of expression (9) calculates the actual error in the numerical solution and its derivatives. For an acceptable numerical solution, these errors should be less than the summation of error indicators $\eta_1^2 + \eta_2^2 + \dots \eta_5^2$. Figures (2)-(4) show the comparison of these quantities for different values of time steps. In graphs the term 'Error' represents the actual error in the method whereas 'ET' is the summation of η_2^2 , η_4^2 and η_5^2 . The enrichment functions 'Q' are plotted on abscissa while the errors on the ordinate; both in logarithmic scale. Figure (2) shows the results for $\Delta t = 0.0001$, Figure (3) for $\Delta t = 0.001$ while Figure (4) for $\Delta t = 0.01$. All the figures show that the actual errors in the solution are well below the summation of η_2^2 , η_4^2 and η_5^2 . The actual error in the solution decreases with increasing number of enrichment functions. The error estimate also follows similar decreasing pattern as we increase the number of enrichment functions.

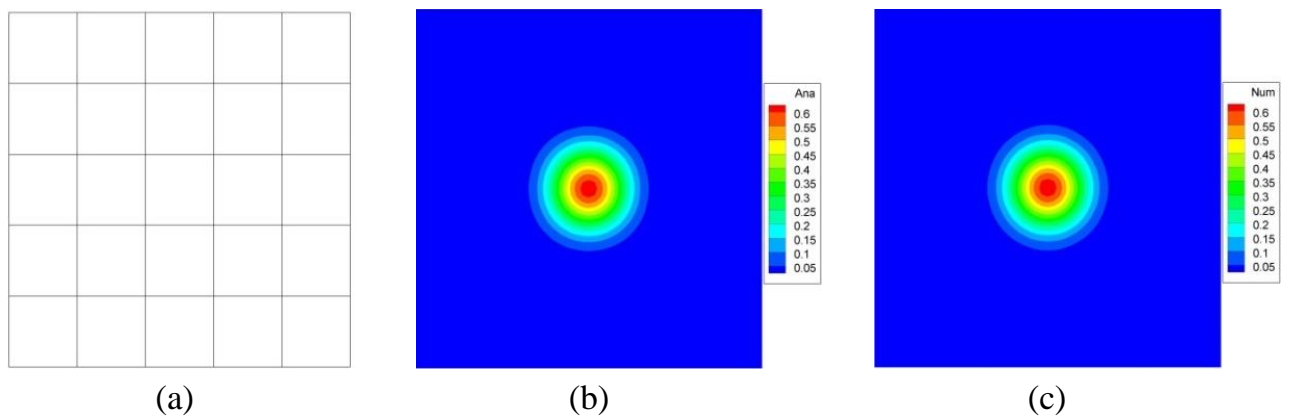


Figure 1: Temperature distribution for $\Delta t = 0.01$ and $t = 10 \text{ s}$. (a) Finite element mesh (b) Analytical result (c) Numerical result obtained using PUFEM with $Q = 6$

5. Conclusions

We used the PUFEM to solve the time dependent diffusion equation. We calculated the errors in the solution and its derivatives and compared these errors with the error estimate. Based on the analysis, we can draw the following conclusions:

- Results of the actual error are well below the defined error estimate.
- With increasing number of enrichment functions, the actual error and the error estimate show a similar decrease.
- Results are obtained with three different values of time step Δt , and for each value of Δt , the results are within the range of error estimate, which shows the effectiveness of the method for time dependent diffusion problem.

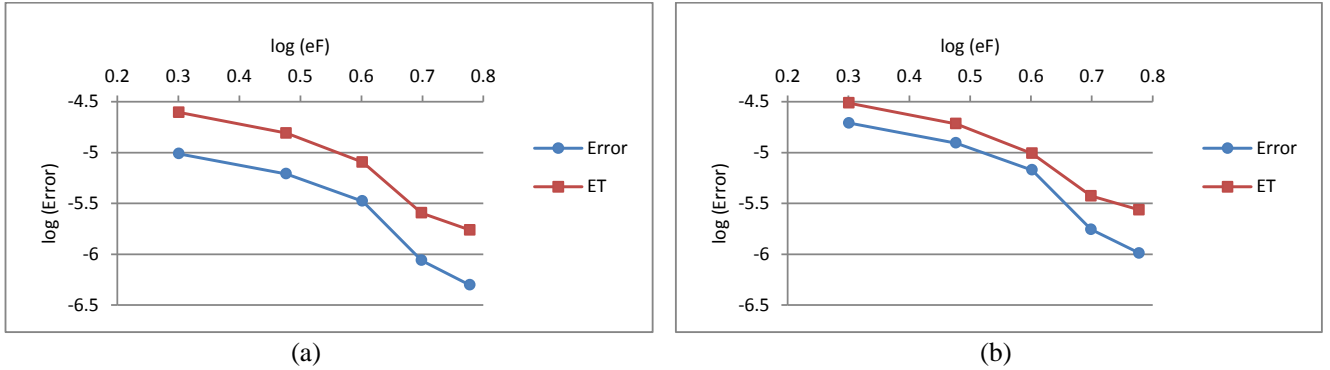


Figure 2: Comparison of actual error and error estimate for $\Delta t = 0.0001$ (a) at 50^{th} time step, (b) at 100^{th} time step

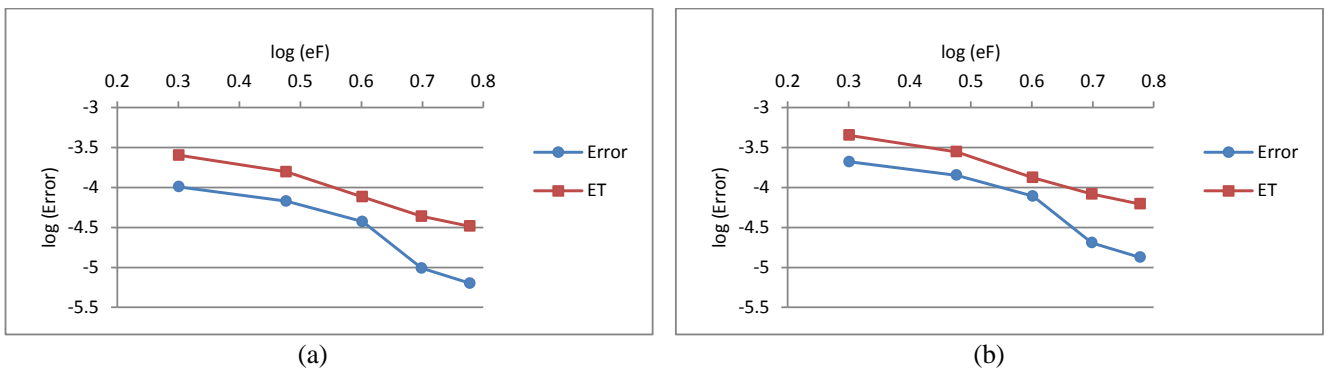


Figure 3: Comparison of actual error and error estimate for $\Delta t = 0.001$ (a) at 50^{th} time step, (b) at 100^{th} time step

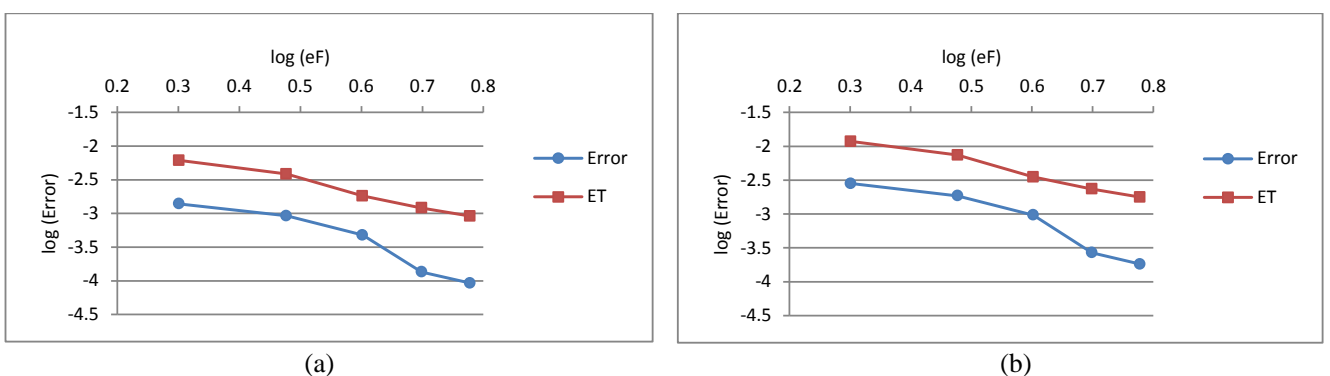


Figure 4: Comparison of actual error and error estimate for $\Delta t = 0.01$ (a) at 50^{th} time step, (b) at 100^{th} time step

References

- [1] J.M. Melenk and I. Babuska. The partition of unity finite element method: basic theory and applications. *Computer methods in applied mechanics and engineering*, 139(1): 289-314, 1996.
- [2] M.S. Mohamed, M. Seaid, J. Travekyan and O. Laghrouche. A partition of unity FEM for time-dependent diffusion problems using multiple enrichment functions. *International Journal for Numerical Methods in Engineering*, 93(3): 245-265, 2013.

A Temperature-based thermodynamically consistent time integration for discrete thermoelastodynamics

*Sergio Conde Martín¹, Juan Carlos García Orden¹, Peter Betsch²

¹ETSI Caminos, Canales y Puertos, Technical University of Madrid, c/ Profesor Aranguren s/n, 28040 Madrid, Spain

²Institut für Mechanik, Karlsruher Institut für Technologie, Gebäude 10.30, Otto-Ammann-Platz 9, D-76131 Karlsruhe, Germany

*sergio.conde@upm.es

ABSTRACT

This work proposes a novel GENERIC-based thermodynamically consistent (TC) time integration scheme for discrete thermoelastodynamics. Its main contribution relies on the fact that the formulation proposed makes use of the temperature to describe the thermodynamic state which has so far been believed unreachable within the GENERIC approach. As expected, this election makes the new TC scheme overcome the reported drawbacks found in the already developed entropy formulation. Proof for these claims as well as numerical examples that illustrate the performance of the novel scheme are provided and will be exposed in the oral presentation.

Key Words: Time integration; structure preservation; geometric integration; thermodynamics; GENERIC formalism

1. Introduction

The concept of thermodynamically consistent (TC) time integration schemes encompasses any numerical integration method intended to solve thermodynamical systems in such a way that the laws of thermodynamics are discretely satisfied by design. In the particular case of reversibility, i.e. Hamiltonian systems, a well-known example is the energy-momentum method due to Simó and Tarnow [1]. Recently, Romero [2] has introduced a general framework to attain TC time integration methods for evolution systems with irreversible processes such as those involving thermo-coupling and/or internal dissipation mechanisms: (thermo)viscoelasticity, (thermo)plasticity, damage, etc. This generalization was made possible by the use of the GENERIC form [3] of the evolution equations of the thermodynamical system at hand.

The election of the thermodynamical variable was reported to become crucial in the formulation. Thus, TC methods have been successfully formulated using the entropy, since it was reported to best fit in the GENERIC formalism. However, this choice obliged to assume important restrictions to the formulation and the applicability of the resulting TC method, such as the necessity for material models to enable the analytical provision of its potentials in terms of the entropy and, more importantly, the incapability to impose Dirichlet's boundary conditions.

2. GENERIC formalism for finite dimensional systems

Given a state vector $\mathbf{z} \in \mathcal{S}$, the total energy function $E(\mathbf{z}): \mathcal{S} \rightarrow \mathbb{R}$ and the total entropy function $S(\mathbf{z}): \mathcal{S} \rightarrow \mathbb{R}$, the GENERIC formalism [3] for finite dimensional systems reads

$$\dot{\mathbf{z}} = \mathbf{L}(\mathbf{z})\nabla E(\mathbf{z}) + \mathbf{M}(\mathbf{z})\nabla S(\mathbf{z}), \quad \mathbf{z}(0) = \mathbf{z}_0, \quad \text{with } \nabla S(\mathbf{z})^T \mathbf{L}(\mathbf{z}) = \mathbf{0}, \quad \nabla E(\mathbf{z})^T \mathbf{M}(\mathbf{z}) = \mathbf{0} \quad (1)$$

$\nabla(\bullet)$ being the gradient operator with respect to the state space vector, \mathbf{z}_0 containing the prescribed initial conditions and $\mathbf{L}, \mathbf{M} : \mathcal{S} \rightarrow \mathbb{R}^{\dim(\mathbf{z}) \times \dim(\mathbf{z})}$ being the skew-symmetric Poisson matrix and the symmetric and positive semi-definite Dissipative matrix, respectively. The above definitions ensure the fulfillment

of laws of thermodynamics since the rate of the total energy and total entropy of the system can be shown to be

$$\dot{E} = \nabla E \cdot \dot{\mathbf{z}} = \nabla E^T \mathbf{L} \nabla E + \nabla E^T \mathbf{M} \nabla S = 0, \quad \dot{S} = \nabla S \cdot \dot{\mathbf{z}} = \nabla S^T \mathbf{L} \nabla E + \nabla S^T \mathbf{M} \nabla S \geq 0 \quad (2)$$

According to [2], the GENERIC form (1) can be approximated by the following one-step implicit second order accurate scheme

$$\frac{\mathbf{z}_{n+1} - \mathbf{z}_n}{\Delta t} = \mathbf{L}(\mathbf{z}_{n+1}, \mathbf{z}_n) \mathbf{D}E(\mathbf{z}_{n+1}, \mathbf{z}_n) + \mathbf{M}(\mathbf{z}_{n+1}, \mathbf{z}_n) \mathbf{D}S(\mathbf{z}_{n+1}, \mathbf{z}_n), \quad (3)$$

where the operator $\mathbf{D}(\bullet)(\mathbf{z}_{n+1}, \mathbf{z}_n)$ is the discrete gradient in the sense of [4] and $\mathbf{L}(\mathbf{z}_{n+1}, \mathbf{z}_n)$ and $\mathbf{M}(\mathbf{z}_{n+1}, \mathbf{z}_n)$ are second order approximations of the continuous Poisson and Dissipative matrices evaluated at mid-point which satisfy

$$\mathbf{D}S(\mathbf{z}_{n+1}, \mathbf{z}_n)^T \mathbf{L}(\mathbf{z}_{n+1}, \mathbf{z}_n) = \mathbf{0}, \quad \mathbf{D}E(\mathbf{z}_{n+1}, \mathbf{z}_n)^T \mathbf{M}(\mathbf{z}_{n+1}, \mathbf{z}_n) = \mathbf{0} \quad (4)$$

The use of the discrete gradient operator is justified due to its directionality property that is responsible for the laws of thermodynamics to be discretely fulfilled. Such property thus enables the total energy and entropy balances in any time step to be expressed by

$$E_{n+1} - E_n = \mathbf{D}E(\mathbf{z}_{n+1}, \mathbf{z}_n) \cdot (\mathbf{z}_{n+1} - \mathbf{z}_n) = \Delta t \mathbf{D}E(\mathbf{z}_{n+1}, \mathbf{z}_n)^T \mathbf{L}(\mathbf{z}_{n+1}, \mathbf{z}_n) \mathbf{D}E(\mathbf{z}_{n+1}, \mathbf{z}_n) + \Delta t \mathbf{D}E(\mathbf{z}_{n+1}, \mathbf{z}_n)^T \mathbf{M}(\mathbf{z}_{n+1}, \mathbf{z}_n) \mathbf{D}S(\mathbf{z}_{n+1}, \mathbf{z}_n) = 0 \quad (5)$$

$$S_{n+1} - S_n = \mathbf{D}S(\mathbf{z}_{n+1}, \mathbf{z}_n) \cdot (\mathbf{z}_{n+1} - \mathbf{z}_n) = \Delta t \mathbf{D}S(\mathbf{z}_{n+1}, \mathbf{z}_n)^T \mathbf{L}(\mathbf{z}_{n+1}, \mathbf{z}_n) \mathbf{D}E(\mathbf{z}_{n+1}, \mathbf{z}_n) + \Delta t \mathbf{D}S(\mathbf{z}_{n+1}, \mathbf{z}_n)^T \mathbf{M}(\mathbf{z}_{n+1}, \mathbf{z}_n) \mathbf{D}S(\mathbf{z}_{n+1}, \mathbf{z}_n) \geq 0 \quad (6)$$

3. Discrete thermoelastodynamics: Thermo-spring system

We consider the simple but meaningful model problem of a thermoelastic double pendulum which was first proposed by Romero [2]. Such system is insulated and consists of two point masses m_1 and m_2 connected with thermo-springs. The position and linear momentum of the particles are given by the vectors $\mathbf{q}_1, \mathbf{p}_1$ and $\mathbf{q}_2, \mathbf{p}_2$ relative to the inertial reference frame $\{\mathbf{e}_1, \mathbf{e}_2, \mathbf{e}_3\}$. The two thermo-springs have a natural length of λ_1^0 and λ_2^0 , respectively, and exchange heat according to a unidimensional Fourier's law of the form $h = k(\theta_2 - \theta_1)$, θ_α being the absolute temperature of the spring α and $k \geq 0$ being the coefficient of thermal conductivity. Each spring behaves according to the Helmholtz free-energy function given by

$$\Psi_\alpha(\lambda_\alpha, \theta_\alpha) = \frac{C_\alpha(\theta_\alpha)}{2} \log^2 \frac{\lambda_\alpha}{\lambda_\alpha^0} - \beta_\alpha(\theta_\alpha - \theta_{\text{ref}}) \log \frac{\lambda_\alpha}{\lambda_\alpha^0} + c_{0,\alpha} \left(\theta_\alpha - \theta_{\text{ref}} - \theta_\alpha \log \frac{\theta_\alpha}{\theta_{\text{ref}}} \right), \quad (7)$$

$\lambda_\alpha = f_\alpha(\mathbf{q}_\beta)$ being the elongations. Then, the internal energy of each spring follows from the application of the Legendre transform to the above free-energy function yielding

$$e_\alpha(\lambda_\alpha, s_\alpha(\lambda_\alpha, \theta_\alpha)) = \Psi_\alpha(\lambda_\alpha, \theta_\alpha) - \theta_\alpha \frac{\partial \Psi_\alpha(\lambda_\alpha, \theta_\alpha)}{\partial \theta_\alpha}, \quad \text{with } s_\alpha(\lambda_\alpha, \theta_\alpha) = -\frac{\partial \Psi_\alpha(\lambda_\alpha, \theta_\alpha)}{\partial \theta_\alpha}. \quad (8)$$

4. Temperature-based thermodynamically consistent integration scheme

Let us consider a state vector which includes the temperatures of the springs as the thermodynamical variables

$$\mathbf{z} = [\mathbf{q}_1, \mathbf{q}_2, \mathbf{p}_1, \mathbf{p}_2, \theta_1, \theta_2]^T, \quad (9)$$

Then, the total energy and total entropy of the two thermo-spring system may be expressed in terms of the above state vector (9) as

$$E(\mathbf{z}) = \sum_{\alpha=1}^2 \left[\frac{\mathbf{p}_\alpha \cdot \mathbf{p}_\alpha}{2m_\alpha} + e_\alpha(\lambda_\alpha, \theta_\alpha) - \mathbf{f}_\alpha \cdot \mathbf{q}_\alpha \right], \quad S(\mathbf{z}) = \sum_{\alpha=1}^2 s_\alpha(\lambda_\alpha, \theta_\alpha) = \sum_{\alpha=1}^2 -\frac{\partial \Psi_\alpha(\lambda_\alpha, \theta_\alpha)}{\partial \theta_\alpha} \quad (10)$$

If the spring entropies are used in the state vector instead of the spring temperatures, the obtention of the function $e_\alpha(\lambda_\alpha, s_\alpha)$ is required, see [2, 5]. This requirement has to be viewed as severe restriction to the applicability of specific thermoelastic models.

The discrete gradient applied to the total energy and total entropy (10) can be elaborated by using the partitioned definition of the discrete gradient operator to give

$$DE(\mathbf{z}_{n+1}, \mathbf{z}_n) = \begin{bmatrix} D_{\mathbf{q}_1} e_1 + D_{\mathbf{q}_1} e_2 - \tilde{\mathbf{f}}_1 \\ D_{\mathbf{q}_2} e_2 - \tilde{\mathbf{f}}_2 \\ D_{\mathbf{p}_1} (\mathbf{p}_1 \cdot \mathbf{p}_1 / 2m_1) \\ D_{\mathbf{p}_2} (\mathbf{p}_2 \cdot \mathbf{p}_2 / 2m_2) \\ D_{\theta_1} e_1 \\ D_{\theta_2} e_2 \end{bmatrix}, \quad DS(\mathbf{z}_{n+1}, \mathbf{z}_n) = \begin{bmatrix} D_{\mathbf{q}_1} s_1 + D_{\mathbf{q}_1} s_2 \\ D_{\mathbf{q}_2} s_2 \\ \mathbf{0} \\ \mathbf{0} \\ D_{\theta_1} s_1 \\ D_{\theta_2} s_2 \end{bmatrix} \quad (11)$$

where $D_k f$ might be interpreted as the second order accurate discrete counterpart to the respective partial derivative of the function f at midpoint. Furthermore, the terms $\tilde{\mathbf{f}}_\alpha$ are second order accurate approximations to the external forces \mathbf{f}_α . Accordingly, the discrete Poisson and Dissipative matrices take the form of

$$\mathbf{L} = \begin{bmatrix} \mathbf{0} & \mathbf{0} & \mathbf{1} & \mathbf{0} & \mathbf{0} & \mathbf{0} \\ \mathbf{0} & \mathbf{0} & \mathbf{0} & \mathbf{1} & \mathbf{0} & \mathbf{0} \\ -\mathbf{1} & \mathbf{0} & \mathbf{0} & \mathbf{0} & \frac{D_{\mathbf{q}_1} s_1}{D_{\theta_1} s_1} & \frac{D_{\mathbf{q}_1} s_2}{D_{\theta_1} s_1} \\ \mathbf{0} & -\mathbf{1} & \mathbf{0} & \mathbf{0} & \mathbf{0} & \frac{D_{\mathbf{q}_2} s_2}{D_{\theta_2} s_2} \\ \mathbf{0} & \mathbf{0} & -\frac{D_{\mathbf{q}_1} s_1^T}{D_{\theta_1} s_1} & \mathbf{0} & \mathbf{0} & \mathbf{0} \\ \mathbf{0} & \mathbf{0} & -\frac{D_{\mathbf{q}_1} s_2^T}{D_{\theta_1} s_1} & -\frac{D_{\mathbf{q}_2} s_2^T}{D_{\theta_2} s_2} & \mathbf{0} & \mathbf{0} \end{bmatrix}, \quad \mathbf{M} = \begin{bmatrix} \mathbf{0} & \mathbf{0} & \mathbf{0} & \mathbf{0} & \mathbf{0} & \mathbf{0} \\ \mathbf{0} & \mathbf{0} & \mathbf{0} & \mathbf{0} & \mathbf{0} & \mathbf{0} \\ \mathbf{0} & \mathbf{0} & \mathbf{0} & \mathbf{0} & \mathbf{0} & \mathbf{0} \\ \mathbf{0} & \mathbf{0} & \mathbf{0} & \mathbf{0} & \mathbf{0} & \mathbf{0} \\ \mathbf{0} & \mathbf{0} & \mathbf{0} & \mathbf{0} & \frac{k\theta_1^* \theta_2^*}{D_{\theta_1} e_1^2} & -\frac{k\theta_1^* \theta_2^*}{D_{\theta_1} e_1 D_{\theta_2} e_2} \\ \mathbf{0} & \mathbf{0} & \mathbf{0} & \mathbf{0} & -\frac{k\theta_1^* \theta_2^*}{D_{\theta_2} e_2 D_{\theta_1} e_1} & \frac{k\theta_1^* \theta_2^*}{D_{\theta_2} e_2^2} \end{bmatrix} \quad (12)$$

where, for the sake of simplicity and interpretability, the algorithmic temperatures θ_1^* and θ_2^* have been chosen to be

$$\theta_\alpha^* = \frac{D_{\theta_\alpha} e_\alpha}{D_{\theta_\alpha} s_\alpha} \quad (13)$$

Finally, inserting relationships (11) through (13) into (3), the following TC scheme is obtained

$$\begin{aligned} \frac{\mathbf{q}_{\alpha, n+1} - \mathbf{q}_{\alpha, n}}{\Delta t} &= D_{\mathbf{p}_\alpha} (\mathbf{p}_\alpha \cdot \mathbf{p}_\alpha / 2m_\alpha) = \frac{\mathbf{p}_{\alpha, n+\frac{1}{2}}}{m_\alpha} \\ \frac{\mathbf{p}_{\alpha, n+1} - \mathbf{p}_{\alpha, n}}{\Delta t} &= -\sum_{\beta=1}^2 (D_{\mathbf{q}_\alpha} e_\beta - \theta_\beta^* D_{\mathbf{q}_\alpha} s_\beta) + \tilde{\mathbf{f}}_\alpha \\ \frac{\theta_{1, n+1} - \theta_{1, n}}{\Delta t} &= \frac{1}{D_{\theta_1} e_1} \left[-\theta_1^* D_{\mathbf{q}_1} s_1^T \frac{\mathbf{p}_{1, n+\frac{1}{2}}}{m_1} + k(\theta_2^* - \theta_1^*) \right] \\ \frac{\theta_{2, n+1} - \theta_{2, n}}{\Delta t} &= \frac{1}{D_{\theta_2} e_2} \left[-\theta_2^* \sum_{\beta=1}^2 D_{\mathbf{q}_\beta} s_2^T \frac{\mathbf{p}_{\beta, n+\frac{1}{2}}}{m_\beta} + k(\theta_1^* - \theta_2^*) \right] \end{aligned} \quad (14)$$

5. Numerical simulation

We illustrate next the performance of the new scheme by integrating a case impossible to be solved by current existing TC schemes based on the entropy [2]. To this end, considering a non-linear temperature-dependent function for the spring stiffness expressed by

$$C_\alpha(\theta_\alpha) = C_\alpha^0 - C_\alpha^1 \theta_{\text{ref}} \log \left(\frac{\theta_\alpha}{\theta_{\text{ref}}} \right) \quad (15)$$

Then, the data employed in this example is: $m_1 = 10$, $m_2 = 20$, $C_1^0 = 5000$, $C_2^0 = 10^4$, $C_1^1 = 50$, $C_2^1 = 60$, $\lambda_1^0 = 2$, $\lambda_2^0 = 1$, $k = 300$, $\beta_1 = \beta_2 = 20$, $c_{0,1} = 5000$, $c_{0,2} = 2000$ and $\theta_{\text{ref}} = 300$. The motion of the two thermo-spring system is integrated in the time interval $[0, 25]$ with initial conditions:

$$\mathbf{q}_{1,0} = 3\mathbf{e}_1 + 0.5\mathbf{e}_3, \quad \mathbf{q}_{2,0} = 3\mathbf{e}_1 + \mathbf{e}_2 + \mathbf{e}_3, \quad \mathbf{p}_{1,0} = 10\mathbf{e}_2, \quad \mathbf{p}_{2,0} = -20\mathbf{e}_3, \quad \theta_{1,0} = 380, \quad \theta_{2,0} = 298$$

The solution of this example is obtained with three methods: the standard midpoint rule, the trapezoidal rule and the temperature-based TC method using the same time step of $\Delta t = 0.1$. Moreover, a reference solution is computed with the midpoint rule with time step $\Delta t_{\text{ref}} = 0.005$. Their results are summarized in Figure 1 where can be seen that, in contrast to the failure of the standard schemes, the Temperature-based TC scheme provides solutions which strictly comply with both laws of thermodynamics and symmetries: angular momentum conservation.

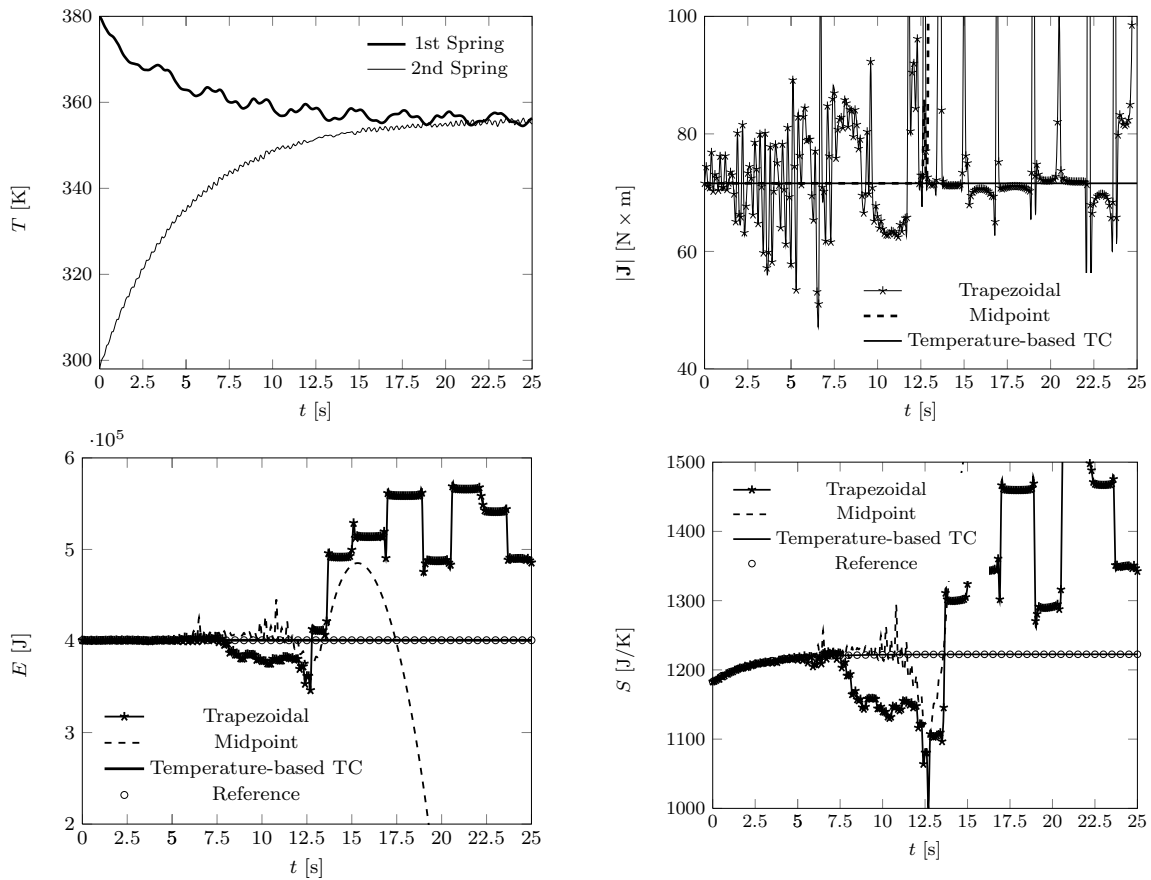


Figure 1: Temperatures, angular momentum, total energy and total entropy evolution for different schemes.

6. Concluding remarks

The newly proposed TC scheme relies on the notion of discrete gradient applied to the internal energy and entropy functions. It is worth noting, however, that the present approach requires about twice as much implementation effort and computational cost compared to the entropy-based approach that only needs the elaboration of the discrete gradient for the internal energy expressed in terms of entropy. Despite of this, the present approach resolves the drawbacks resulting from the use of the entropy as state variable. Thus, common constitutive formulations in terms of the temperature can directly be applied. Moreover, the extension to the continuous case will make possible to directly impose Dirichlet boundary conditions for the temperature.

References

- [1] J.C. Simó, N. Tarnow. *Zeitschrift für Angewandte Mathematik und Physik (ZAMP)*, 43(5), 757–792, 1992.
- [2] I. Romero. *International Journal for Numerical Methods in Engineering*, 79(March):706–732, 2009.
- [3] Öttinger. John Wiley & Sons, New Jersey, 2005.
- [4] O. González. PhD thesis, Stanford, 1996.
- [5] J. C. García Orden and I. Romero. *European Journal of Mechanics - A/Solids*, 32:76–87, October 2011.

Effects of Hatch Pattern and Laser Parameters on the Multi-Scale Thermal Modelling of Selective Laser Melting

*Adam M. Philo, S.G.R. Brown, J. Cherry, J. Sienz, N.P. Lavery

College of Engineering, Swansea University, Singleton Park, Swansea, SA2 8PP

* 716062@Swansea.ac.uk

ABSTRACT

In the work presented a 3D explicit transient finite difference solution has been developed to predict the thermal distribution and evolution during the build of a single layer of 316L steel powder. The aim of the model is to capture the general overall thermal distribution within a build which could potentially be used in a multiple-layer prediction of residual stresses; which is an ongoing area of research within Selective Laser Melting (SLM). Such complex phenomena such as surface tension, fluid flow and capillary forces are not considered yet due to their complex and computationally intensive nature. The model provides a good indication of the overall thermal distribution and allows for the meso-scale effects within the thermal distribution to be understood and visualised. This work provides a foundation model which will be extended to predict areas of high residual stress in a build, and to provide a method for analysing various hatch patterns as opposed to undertaking many time-consuming and expensive experimental tests.

Keywords: *Selective Laser Melting; Numerical Modelling; Heat Transfer*

1. Introduction

Power-bed Selective Laser Melting (SLM) is a subsection of Additive Layer Manufacturing (ALM). Within SLM a laser or electron beam energy is absorbed within a metal powder, the powder melts, re-solidifies and the volume of the material is reduced. Within SLM there is a very wide range of physical phenomena which can make understanding and modelling of the process particularly challenging. These include, but are not limited to: melting, solidification, vapourisation, fluid flow, surface tension and capillary forces, and also thermo-capillary convection (Marangoni-convection). In addition the selection of machine parameters has a large effect on the finished product, which is also very material dependent. The main operating input parameters are: laser power, the exposure time of a laser pulse, thickness of the powder layer, the hatch spacing (the distance between laser tracks) and the point distance (the distance between each consecutive laser pulse).

In such small time and space frames the temperature distribution and evolution is an important aspect of SLM which needs to be understood so that optimum components can be constructed. Residual stresses are an inherent problem within the SLM process due to large temperature gradients between the melt pool, substrate and the powder material. This work calculates the temperature distribution and time evolution within a powder-bed SLM process for 316L steel and predicts the overall temperature distribution for a range of input parameters.

2. Modelling Approach

In the modelling presented we consider the SLM thermal evolution as a heat transfer process. The 3D Fourier heat conduction equation is solved by using an explicit and transient finite difference solution. The 3D Fourier heat conduction equation can be written as;

$$\rho c_p \frac{\partial T}{\partial t} = \kappa \left(\frac{\partial^2 T}{\partial x^2} + \frac{\partial^2 T}{\partial y^2} + \frac{\partial^2 T}{\partial z^2} \right) \quad (2.1)$$

Where κ is the thermal conductivity $\left(\frac{W}{m K}\right)$, ρ is the density $\left(\frac{kg}{m^3}\right)$, c_p is the specific heat capacity $\left(\frac{J}{K}\right)$,

and T is the temperature (K) in a Cartesian coordinate system. When discretised using an explicit finite difference solution Eq. 2.1 can be written;

$$\begin{aligned}
T^{T+1} = & \alpha \frac{\Delta t}{\Delta x^2} [T_{i+1,j,k} + T_{i-1,j,k} + T_{i,j+1,k} + T_{i,j-1,k}] \\
& + \alpha \frac{\Delta t}{\Delta z^2} [T_{i,j,k+1} + T_{i,j,k-1}] - \alpha \frac{\Delta t}{\Delta z^2} [2T_{i,j,k}] \\
& + T_{i,j,k} \left[1 - \alpha \frac{\Delta t}{\Delta x^2} \right]
\end{aligned} \tag{2.2}$$

Where, α is the thermal diffusivity ($\frac{m^2}{s}$), Δt is the time step size, Δx is the spatial step size in the x-direction (here $\Delta x = \Delta y$), Δz is the spatial step size in the z-direction and $T_{i,j,k}$ indicates a temperature at a location in a Cartesian coordinate system. To solve the equation two boundary conditions are specified for each principal axis. For the bottom z-surface, and all boundary conditions in the x and y direction are set to be insulators. The additional boundary conditions are;

$$\text{Input heat flux: } -\kappa \frac{\partial T}{\partial z} \hat{n} = (1 - r_f)q(r) \tag{2.3}$$

$$\text{Surface convection: } -\kappa \frac{\partial T}{\partial z} \hat{n} = h (T - T_o)$$

Where \hat{n} is the unit normal to the top surface, r_f is the surface reflectivity, $q(r)$ is the thermal heat flux from the laser, h is the heat transfer coefficient of the surface and T_o is the ambient temperature in the chamber. The laser energy is modelled using a Gaussian distribution where the maximum flux is at the centre of the laser beam which can be written as;

$$q(r) = \frac{P}{\pi r_0^2} e^{-\frac{2(r^2)}{2r_0^2}} \tag{2.4}$$

Where r is a radial distance from the centre of the laser beam, P is the laser power (W) and r_0 is the radius of the laser.

3. Results and Discussion

Simulations were run for 316L powder steel on a solid 316L baseplate. Temperature dependent properties for thermal conductivity κ , specific heat capacity c_p and the density ρ were used from experimental data for solid and powder properties, generated in the MACH1 laboratories at Swansea. To ensure stability of the simulation the Courant-Friedrichs-Lewy (CFL) number was calculated based on simulation input parameters which calculated the necessary time step size for each simulation based on a worst case scenario. A mesh independence study was performed so that values which were being produced were not mesh-dependent. The main factor of influence was the discretisation of the heat flux, $q(r)$ in all three principal axes. It was found that under the laser area, πr_0^2 that a minimum of three spatial steps dx would be needed to ensure that the solution would not be influenced by the mesh. In addition, the layer thickness, L_t needed to be discretised by ten spatial steps, dz . It was found that a mesh of 600,000 elements was sufficient.

The Table 1 outlines the input parameters for the simulations. Parameters which are changed in proceeding simulations will be explicitly outlined.

Table 1: Simulation parameters

Exposure time (μs)	Laser Power (W)	Laser Focal Diameter (μm)	Point Distance (μm)	Hatch Spacing (μm)	Layer Thickness (μm)
70	100	70	50	100	50

Simulations were run to investigate the effect input parameters had on the thermal distribution on the top layer of the powder bed. Different exposure times, power, point distances and hatch distances were simulated. The effects of laser power and exposure time are presented in Figure 1 which were simulated for one line moving forward in the positive y-direction.

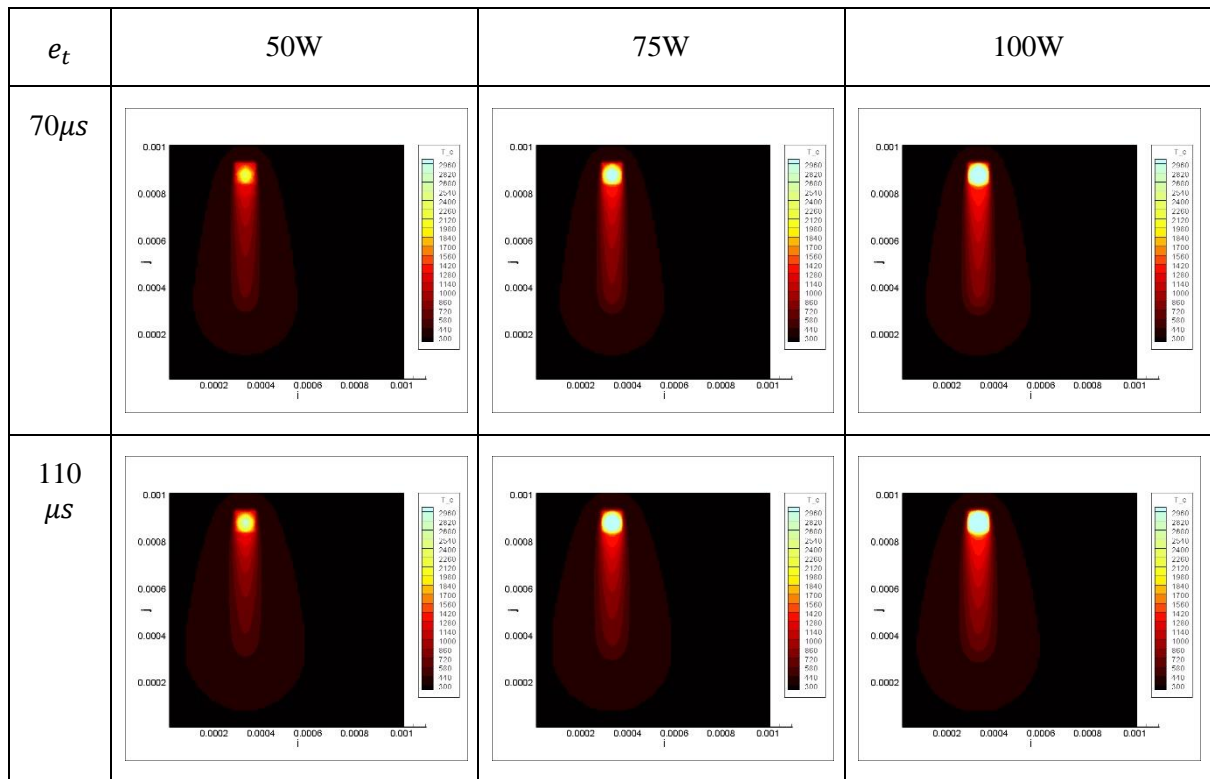


Figure 1: Effects of Exposure Time and Laser Power. T(K)

As expected as the laser power and/or exposure time is increased the maximum temperature increases while causing a slightly wider spread of the temperature distribution. The effects of the point distance p_d are shown in Figure 2 where, as the point distance increases the distribution of temperature becomes disjointed and individual laser exposures can be visibly seen. In a real-life scenario this may not be desired as this may cause un-bonded melted regions potentially causing porosity in the part.

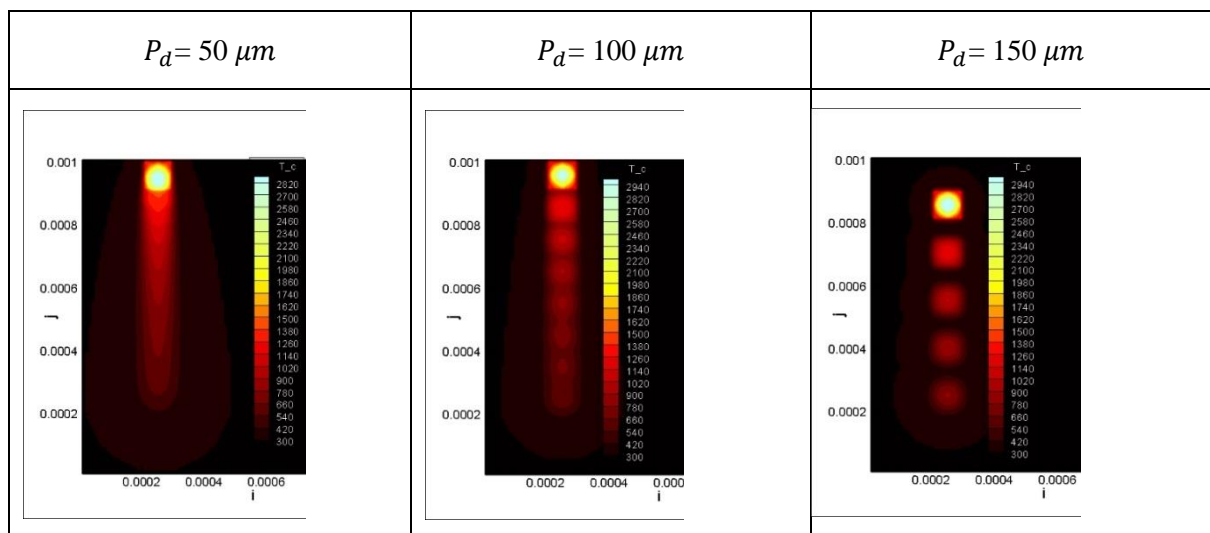


Figure 2: Effect of Point Distance. T(K)

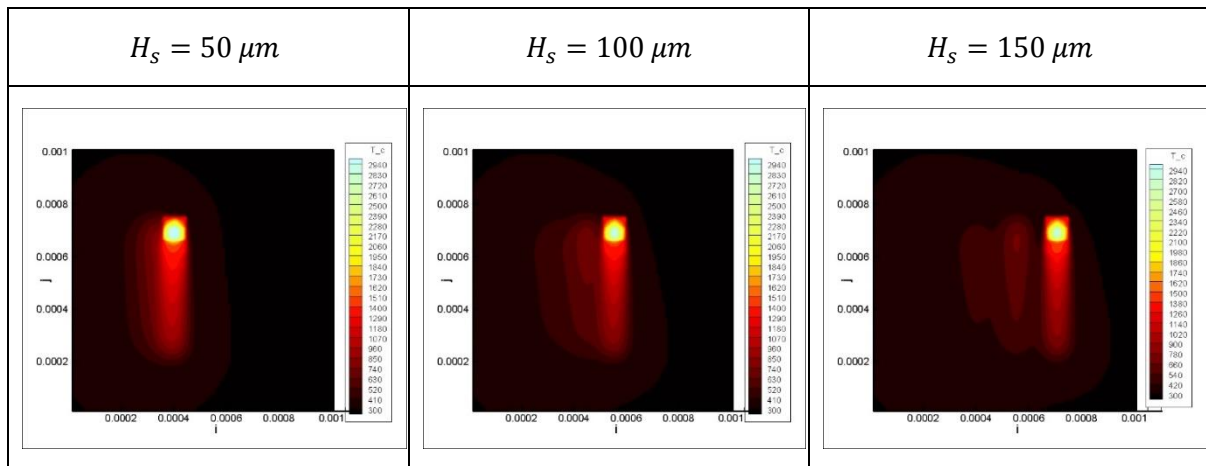


Figure 3: Effects of Varying Hatch Spacing. T(K)

This model is the precursor to a variable grid approach for coupling to micro-scale models. Figure 3 shows the effect of increasing the hatch spacing, H_s in a simulation. As expected, results illustrate a similar effect to that of the point distance. The results clearly show that the choice of input parameters has an effect on the overall distribution of heat within a build. If large temperature gradients are experienced then this can lead to residual stresses which need to be avoided. In addition it is important that the melted powder is consolidated to build optimum parts.

4. Conclusions

A 3D finite difference solution to the 3D Fourier heat conduction equation is presented to simulate the effects of varying input parameters for the simulation of the SLM process for a stainless steel 316L powder material. It is found that varying such input parameters can have a large effect on the thermal distribution within a build. These thermal distributions are important to understand as to avoid the inherent problem of residual stresses with SLM. Further work will analyse the effect of more complex laser paths, and analyse the potential effect on predicting residual stresses in multiple layer builds.

5. Acknowledgements

The authors would like to thank the Additive Manufacturing Products Division at Renishaw Plc. and the Engineering and Physical Sciences Research Council (EPSRC) for funding this work and the Welsh Government A4B funded Centre for Advanced Materials Characterisation (MACH1).

References

- [1] D.Q. Zhang, Q.Z. Cai, J.H. Liu, L Zhang, R.D.Li. Select laser melting of w-ni-fe powders: simulation and experimental study. *International Journal of Advanced Manufacturing Technology* 51, 649-658 (2010).
- [2] I. A. Roberts, C. J. Wang, R. Esterlein, M. Stanford and D. J. Mynors. A three-dimensional finite element analysis of the temperature field during laser melting of metal powders in additive layer manufacturing. *International Journal of Machine Tools & Manufacture* 49, 916-923 (2009).
- [3] Michael F. Zaeh and Gregor Branner. Investigations on residual stresses and deformations in selective laser melting. *Production Engineering Research and Development* 4, 35-45 (2010).
- [4] N. Contuzzi, S.L. Campanelli, A.D. Ludovico. 3D finite element analysis in the selective laser melting process. *International Journal of Simulation Modelling* 10 (2011) 3, 113-121.
- [5] L. Dong, A. Makradi, S. Ahzi, Y. Remond. Three-dimensional transient finite element analysis of the selective laser sintering process. *Journal of Materials Processing Technology* 209 (2009) 700-706

NUMERICAL COMPUTATION OF HEAT AND MASS TRANSFER BY NATURAL CONVECTION THROUGH A FLUID-SATURATED POROUS MEDIUM IN HORIZONTAL ELLIPTICAL ANNULUS

Hichem Boulechfar, *Mahfoud Djeddar

Physics and Energy Laboratory, Faculty of Exact Sciences, University of Constantine 1,
Aïn El Bey Street, 25000 Constantine, Algeria

*mdjeddar@umc.edu.dz

ABSTRACT

Bidimensional heat and mass transfer of natural convection in an annular elliptical space filled with fluid-saturated porous medium, is analyzed by solving numerically the mass balance, momentum, energy and concentration equations, using Darcy's law and Boussinesq approximation. Both walls delimiting the annular space are maintained at two uniform different temperatures and concentrations. The external parameter considered is Rayleigh-Darcy number. The heat and mass transfer for natural convection is studied for the case of aiding buoyancies, where the flow is generated in a cooperative mode by both temperature and solutal gradients. The local Nusselt and Sherwood numbers are presented in term of the external parameter.

Keywords: heat and mass transfer; natural convection; porous media; elliptical annulus

1. Introduction

Natural convection of heat and mass transfer confined into different vertical and horizontal annular enclosures was a subject of many theoretical, numerical and experimental studies. These annular spaces have different geometries and can be partly or completely filled with porous material. Interest in the phenomena of heat and mass transfer by natural convection is due to many potential applications in the engineering processes which involve the chemical and oil and gas industries, thermal recovery process...etc.

Khanafer and al. [1] studied a numerical investigation of natural convection heat transfer within a two-dimensional, horizontal annulus that is partially filled with a fluid-saturated porous medium. [2] Studied the unsteady natural convection flow from a horizontal cylindrical annulus filled with a non-Darcy porous medium. [3] Presented experimental and numerical studies for natural convection in two dimensional region formed by constant flux heat horizontal elliptic tube concentrically located in a larger, isothermally cooled horizontal cylinder were investigated. [4] Studied numerically a double-diffusive natural convection in a rectangular cavity filled with a saturated anisotropic porous medium. [5] Solved two-dimensional Darcy-Boussinesq equations, governing natural convection heat transfer in a saturated porous medium, in generalized orthogonal coordinates, using high-order compact finites differences on a very fine grid. [6] Carried a numerical investigation of two-dimensional and three-dimensional free convection flows in a saturated porous horizontal annulus heated from the inner surface, using a Fourier-Galerkin approximation for the periodic azimuthal and axial directions.

2. Problem Formulation and Basic Equations

Figure 1 (a) represents a cross section of the system. Both elliptic internal and external walls are isothermal and impermeable, kept at constant temperatures and concentrations T_1 , C_1 and T_2 , C_2 respectively with $T_1 > T_2$ and $C_1 > C_2$. The physical properties of the fluid are constant, apart from the density ρ whose variations are at the origin of the natural convection. Viscous dissipation and the radiation are neglected, Soret and Dufour effects are also neglected and we admit that the problem is bidimensional, permanent and laminar. The porous medium is considered isotropic and homogeneous; the natural convection heat and mass transfer is represented by the following dimensionless equations

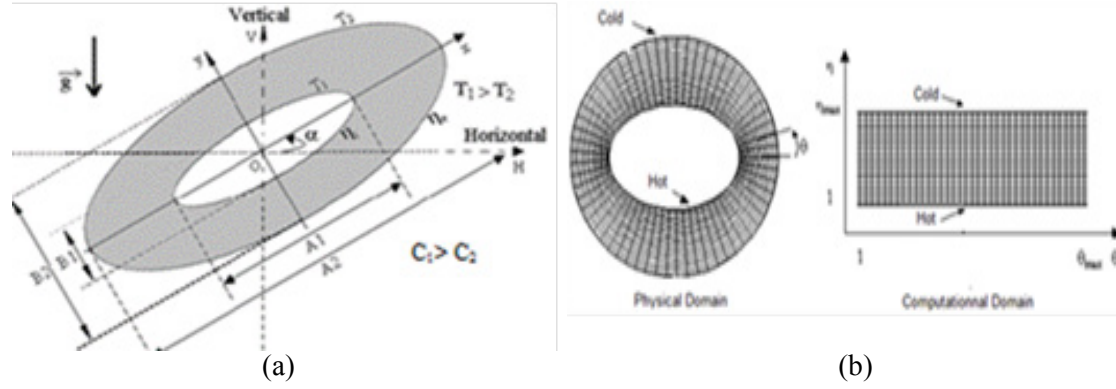


Figure 1: (a) The cross section of the system, (b) Physical and computational domain

within the framework of the Boussinesq approximation after the transformation from the Cartesian to the elliptic coordinates:

Continuity Equation:

$$\frac{\partial}{\partial \eta}(HV_{\eta}^+) + \frac{\partial}{\partial \theta}(HV_{\theta}^+) = 0 \quad (1)$$

Momentum Equation:

$$\frac{1}{h} \left[\frac{\partial^2 \psi^+}{\partial \eta^2} + \frac{\partial^2 \psi^+}{\partial \theta^2} \right] = -Ra_m H \left([\cos(\alpha)F(\eta, \theta) - \sin(\alpha)G(\eta, \theta)] \left(\frac{\partial T^+}{\partial \eta} + N \frac{\partial C^+}{\partial \eta} \right) - [\sin(\alpha)F(\eta, \theta) + \cos(\alpha)G(\eta, \theta)] \left(\frac{\partial T^+}{\partial \theta} + N \frac{\partial C^+}{\partial \theta} \right) \right) \quad (2)$$

Heat Equation:

$$HV_{\eta}^+ \frac{\partial T^+}{\partial \eta} + HV_{\theta}^+ \frac{\partial T^+}{\partial \theta} = \left[\frac{\partial^2 T^+}{\partial \eta^2} + \frac{\partial^2 T^+}{\partial \theta^2} \right] \quad (3)$$

Concentration Equation:

$$HV_{\eta}^+ \frac{\partial C^+}{\partial \eta} + HV_{\theta}^+ \frac{\partial C^+}{\partial \theta} = \frac{1}{Le} \left[\frac{\partial^2 C^+}{\partial \eta^2} + \frac{\partial^2 C^+}{\partial \theta^2} \right] \quad (4)$$

V_{η} and V_{θ} are the velocity components in the directions η and θ , $F(\eta, \theta)$, $G(\eta, \theta)$ used in (2) are the coefficients resulting from the transformation and H represent the metric coefficients in the elliptic coordinates.

Ra_m represents Rayleigh-Darcy number which is defined as: $Ra_m = Ra \cdot Da$

The boundary conditions are expressed as following:

Hot inner wall with high concentration ($\eta = \eta_i = \text{cst}$):

$$V_{\eta}^+ = V_{\theta}^+ = \frac{\partial \psi^+}{\partial \eta} = \frac{\partial \psi^+}{\partial \theta} = 0, T_1^+ = 1, C_1^+ = 1$$

Cold outer wall with low concentration ($\eta = \eta_e = \text{cst}$):

$$V_{\eta}^+ = V_{\theta}^+ = \frac{\partial \psi^+}{\partial \eta} = \frac{\partial \psi^+}{\partial \theta} = 0, T_2^+ = 0, C_2^+ = 0$$

3. Numerical method

Figure 1 (b) shows the physical and computational domain, to solve (1), (3) and (4) with the associated boundary conditions; we consider a numerical solution by the finite volumes method, exposed by [7]. The power law scheme was used for the discretization. To solve (2), we consider a numerical solution by the centred differences method. The iterative method used for the numerical solution of algebraic system of equations is the Gauss-Seidel with an under-relaxation process. Once the temperature and concentration distributions are available, the local Nusselt and Sherwood numbers in the physical domain are defined as:

$$Nu = -\frac{1}{h} \frac{\partial T^+}{\partial \eta} \Big|_{\eta=cst}, \quad Sh = -\frac{1}{h} \frac{\partial C^+}{\partial \eta} \Big|_{\eta=cst}$$

4. Results and discussion

Our objective is to analyze the effect of Rayleigh-Darcy number for the case of a cooperative mode of the heat and mass transfer. For this reason, we presented streamlines, isotherms and concentration contours for different values of Rayleigh-Darcy number (Ra_m) for the case when the buoyancy ratio $N=1$ and for a determined value of Lewis number $Le=10$. The Nusselt and Sherwood numbers are presented for different values of Ra_m . The study was carried out using the air as fluid. The eccentricities of the internal and the external ellipses are respectively given by $e_1=0.9$ and $e_2=0.5$ and $\alpha=0^\circ$ is the inclination of the system.

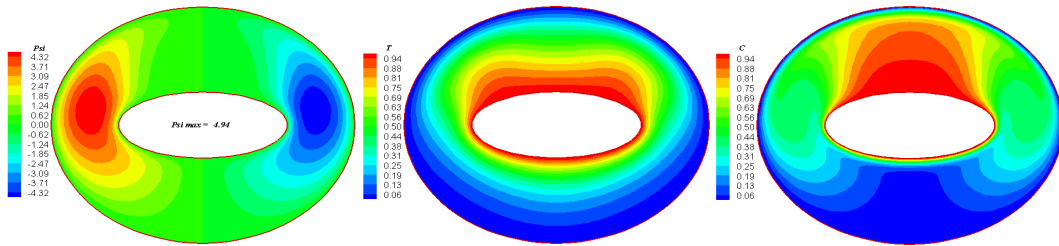


Figure 2: Streamlines, isotherms and concentration contours for $Ra_m=50$, $N=1$ and $Le=10$

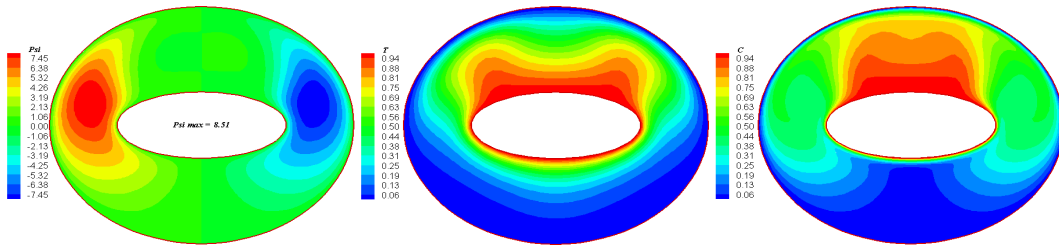


Figure 3: Streamlines, isotherms and concentration contours for $Ra_m=100$, $N=1$ and $Le=10$

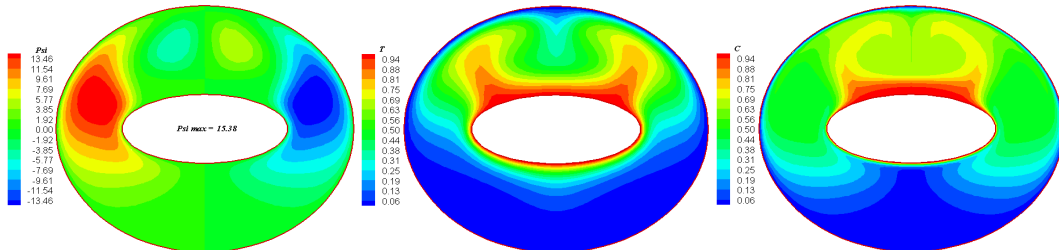


Figure 4: Streamlines, isotherms and concentration contours for $Ra_m=250$, $N=1$ and $Le=10$

Figures 2 to 4 represent the streamlines, isotherms and concentration contours; we note that these contours are symmetrical about the median fictitious vertical plane. The streamlines of the figure 2 show that the flow is organized in two main cells that rotate in opposite directions. This is due to upward movement of the fluid particles under the aiding buoyancy effect related to temperature and solutal gradients, the fluid heat up along the hot wall and the downward movements of the fluid particles which cool along the cold wall under the gravity. Isotherms in figure 3 show that the heat transfer is mainly by conduction in the bottom of the annular space, in the other hand; isotherms deform in the upper space where there is presence of two counter-rotating vortices.

Figure 3 illustrates with the increase in Rayleigh-Darcy number, the convection mode become predominant for both heat and mass transfers with an increase in the thermal and solutal gradients which generate a bifurcation in the upper annular space in figure 4.

Figure 5 illustrate the variation of local Nusselt and Sherwood numbers, for the local Nusselt number this variation allows us to note that with the increase of Rayleigh-Darcy number, the value of local Nusselt number increase significantly due to the increase in the thermal gradient which is obvious. The local Sherwood number which interprets the mass transfer allows us to note that the Sherwood number increases with increasing of Rayleigh-Darcy number due to the aiding effect of thermal and solutal buoyancies. The mass transfer is enhanced due the convection mode that take place in the upper annular space, with the contribution of the solutal diffusivity which is ten times less compared to the thermal diffusivity when $Le=10$.

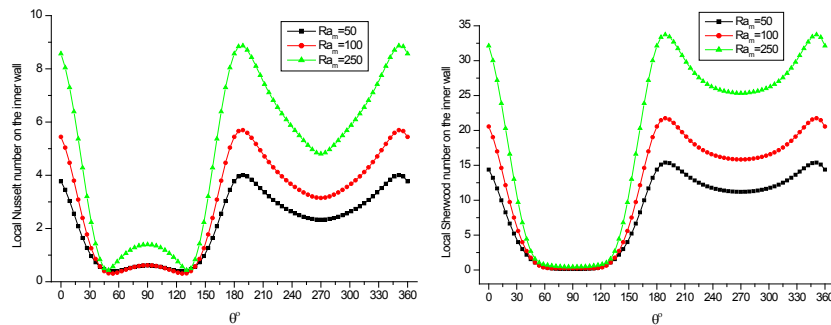


Figure 5: Local Nusselt and Sherwood numbers for different values of Ra_m

5. Conclusions

Heat and mass transfer of natural convection in a porous elliptical annulus saturated by a Newtonian fluid was studied by a numerical method using the method of finite volumes and the vorticity-streamline formulation. We examined, in particular, the influence of Rayleigh-Darcy number when the thermal and the solutal buoyancies are equal and cooperating in the generation of the flow structure. The structures of bicellular convection take place according to the value of the Rayleigh-Darcy number. Both heat and mass transfer distributions are very sensitive to the variation of Rayleigh-Darcy number. When increasing Rayleigh-Darcy number, the heat transfer is dominated by the convective mode in the upper annular space. The mass transfer is dominated by a convective mode due to the low solutal diffusivity in the entire annular space.

References

- [1] Khalil Khanafar, Abdalla Al-Amiri, Ioan Pop "Numerical analysis of natural convection heat transfer in a horizontal annulus partially filled with a fluid-saturated porous substrate," *Int. J. Heat and Mass Transfer* (2008), 51, pp.1613-1627.
- [2] Kumari, M. and Nath, G. "Unsteady natural convection from a horizontal annulus filled with a porous medium, *Int. J. Heat and Mass Transfer* (2008)," 51, pp. 5001-5007.
- [3] Ramadan Y. Sakr, Nabil S. Berbish, Ali A. Abd-Aziz, Abdalla Said Hanafi "Experimental and Numerical Investigation of Natural Convection Heat Transfer in Horizontal Elliptic Annuli" *Int. J. of Chemical Reactor Engineering* (2008), Volume 6, Article A45.
- [4] Rachid Bennacer, Abdelwahab Tobbal, Hassen Beji, Patrick Vasseur "Double diffusive convection in a vertical enclosure filled with anisotropic porous media" *Int. J. Therm. Sci.* (2001) 40, pp.30-41.
- [5] J.P.B. Mota, I.A.A.C. Esteves, C.A.M. Portugal, J.M.S.S. Esperanca, E. Saadjan "Natural convection heat transfer in horizontal eccentric elliptic annuli containing saturated porous media," *Int. J. Heat and Mass Transfer* (2000), 43, pp. 4367-4379.
- [6] Charrier-Mojtabi, M. C. "Numerical simulation of two- and three-dimensional free convection flows in a horizontal porous annulus using a pressure and temperature formulation," *Int. J. Heat and Mass Transfer* (1997), 40, pp. 1521-1533.
- [7] Patankar, S.V. (1980) "Numerical heat transfer and fluid flow," Hemisphere, Washington D.C.

WAVE PROPAGATION 1

Characterization of the magnetic field in magnetic flux leakage type nondestructive testing at high specimen speed

Fawzi Belblidia, Ian Cameron, Johann Sienz and *Lintao Zhang

Advanced Sustainable Manufacturing Technologies (ASTUTE) project, College of Engineering,
Swansea University, Singleton Park, Swansea SA2 8PP, UK

*L.Zhang@Swansea.ac.uk

ABSTRACT

We investigate the influence of the specimen velocity on the magnetic flux leakage and the sensing sensitivity with the aim of selecting the optimum sensor locations. Parametric numerical simulations where the specimen velocity was in the range $[0.1-20] \text{ m}\cdot\text{s}^{-1}$ were carried out. As the specimen velocity is increased, the magnetic field varies from being symmetrical to being asymmetric. For the radial magnetic induction B_z , the position at which the maximum difference between the minimum and maximum signal moves from the centre of the bridge towards the direction of the specimen movement. Furthermore, the sensing sensitivity to detect the defect follows the same rule, compared with the radial magnetic induction.

Key Words: *Nondestructive testing; magnetic flux leakage; specimen velocity; sensing sensitivity*

1. Introduction

Magnetic flux leakage (MFL) method, which originates from the magnetic particle technique, is widely used in the nondestructive evaluation process. The principle of the MFL method can be understood as follows: when a magnetic field is applied to a ferromagnetic material, the leakage of the magnetic field which is caused by the discontinuity of the geometry can be captured by the sensors, such as Hall probe *etc.*. The main reason for the leakage is due to the difference, $\sim O(10)$, of the magnetic permeability of the mediums at the interface [1]. The defect characteristics can be determined by the leakage signals and a large amount of relevant numerical and experimental research has been carried out from this point of view. Practically, the nature of such NDT problems is transient rather than static and simply using the results obtained from static simulations to predict transient problems may cause errors, especially under the condition of high velocity. A velocity induced current can be generated by a conducting material moving in a magnetic field [2] and this phenomenon can alter the distribution of the magnetic field [3, 4, 5, 6]. The distortion of the magnetic field points in the specimen movement direction and is independent to the orientation of the magnetizing source. Therefore, the optimum location of the sensor may be altered, especially for high velocities. This is not well defined in the previous research. In order to cover an extensive range of parameter in term of specimen velocity, we shall combine a detailed analysis of a pure two-dimensional (2D) geometry with targeted numerical simulations of the full three-dimensional (3D) problem. Clearly, this is the task which shall be undertaken in this paper.

2. Configuration and numerical setup

We consider a ferromagnetic specimen (conductivity $\sigma = 6.993 \times 10^6 \text{ S}\cdot\text{m}^{-1}$, having B-H curve) moving with velocity \mathbf{V}_s (in $\text{m}\cdot\text{s}^{-1}$ in this paper) under a magnetic flux leakage evaluation system which uses permanent magnets as the magnetising source as shown in Fig.1. The direction of specimen movement is taken as the y -axis. A near-side rectangular defect is located on the specimen and the reason for the selection of a rectangular shaped defect is because 2D finite element methods (FEM) can provide sufficient information for the sharp-shaped defect characterisation. The dimensions (in mm) of the bridge, magnet, brush and the defect are shown in the figure as well. S_i^j denotes the potential sensor locations

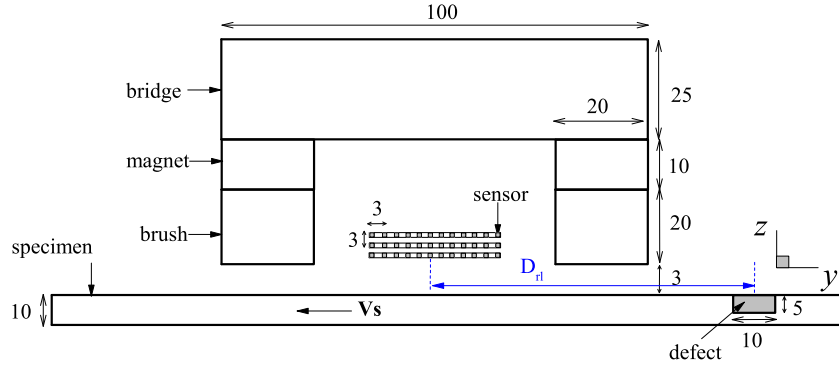


Figure 1: Schematic representation of numerical simulation model for MFL evaluation system.

where $i \in [1,11]$ (along $+y$ axis) and $j \in [1,3]$ (along $+z$ axis), where i and j are the column and row numbers. These potential sensor locations S_i^j are equally spaced 3 mm apart. Furthermore, the relative distance between S_i^j and the centre of the defect is defined as D_{rl} . $D_{rl} > 0$ (*resp.* $D_{rl} < 0$) denotes the centre of the defect is approaching (*resp.* is departing away from) the sensor.

We study the 2D magnetic flux leakage problem using Ansoft Maxwell (version 14.0) FEM software. The governing equations for the 2D transient MFL problem can be expressed as:

$$\nabla \times \frac{1}{\mu} \nabla \times \mathbf{A} = \mathbf{J}_s - \sigma \frac{\partial \mathbf{A}}{\partial t} - \sigma \nabla V + \nabla \times \mathbf{H}_c + \sigma \mathbf{V}_s \times \nabla \times \mathbf{A}, \quad (1)$$

$$\mathbf{B} = \nabla \times \mathbf{A}, \quad (2)$$

where μ , \mathbf{A} , \mathbf{J}_s , σ , V , \mathbf{V}_s and \mathbf{H}_c are the permeability, magnetic vector potential, source current density, electric conductivity, electric potential, velocity and the coercivity of the permanent magnets, respectively. For the MFL evaluation system investigated in this paper, Equation 1 becomes:

$$\nabla \times \frac{1}{\mu} \nabla \times \mathbf{A} = -\sigma \frac{\partial \mathbf{A}}{\partial t} + \nabla \times \mathbf{H}_c + \sigma \mathbf{V}_s \times \nabla \times \mathbf{A}, \quad (3)$$

which is solved using FEM with infinite boundary conditions, together with Equation 2. The whole computing domain is discretised into 2D triangular elements. and the first-order implicit Euler method is adopted as the time discretization method. A computational domain percentage, 200%, is selected. A mesh sensitivity analysis to determine the mesh density required for the simulations to give a mesh independent solution is also carried out.

3. Characterization of the radial magnetic field B_z

3.1. General feature and defect width detection

The distribution of B_z with D_{rl} at S_6^1 for different specimen velocity is shown in Fig.2. The result shows that the minimum value of B_z (respectively maximum values of B_z) B_z^{min} (respectively B_z^{max}) occurs near the front (respectively back) edge of the defect for all values of specimen velocity. This is because that in the vicinity of $D_{rl}=0.005$, sensor S_6^1 meets the front edge of the defect. The leakage has a trend to return into the specimen due to the high permeability of the specimen. Under this condition, an angle between the y -axis and \mathbf{B} is presented, which has the effect of enlarging the negative component of B_z . When $D_{rl}=-0.005$, S_6^1 meets the back edge of the defect. The leakage occurs due to the existence of the forthcoming defect and this results in B_z reaching B_z^{max} . Therefore, the locations where the maximum and minimum values of B_z occur can be adopted to predict the edges of the defect and the distance of these two locations can be used to detect the width of the rectangular defect, as we studied in this paper. As the specimen velocity is increased, the locations where the B_z^{max} and B_z^{min} may vary due to the distortion of the magnetic field. Furthermore, distribution of B_z on S_i^j , where $i \in [1-11]$ and $j \in [1-3]$, follows the same trend. The distribution of B_z shifts downwards, as specimen velocity is increased. As we discussed before, the distortion of the magnetic field occurs at high value of the specimen velocity. This distortion causes the anticlockwise rotation of the magnetic induction between the two brushes of the MFL evaluation system.

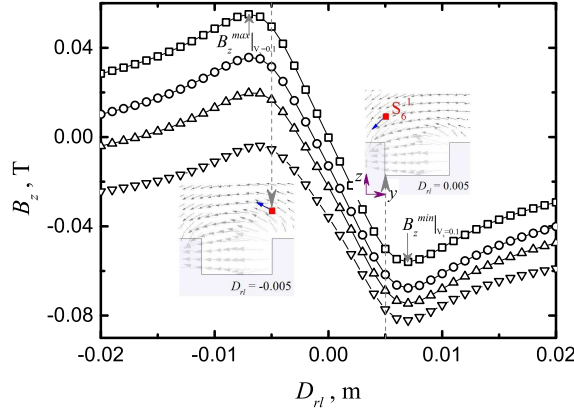


Figure 2: Distribution of B_y v.s. D_{rl} at S_6^1 for different \mathbf{V}_s : 0.1 (\square), 5 (\circ), 10 (\triangle), 20 (∇). The maximum and minimum values are presented when the sensor meets the defect edges. B_z moves downwards as \mathbf{V}_s is increased.

3.2. Peak to peak value B_z^p and sensing sensitivity

In this paper, B_z^p is defined as the peak to peak value of the radial magnetic induction [3]. It is defined as follows:

$$B_z^p = B_z^{max} - B_z^{min}, \quad (4)$$

where B_z^{max} and B_z^{min} are the maximum and the minimum value of B_z (as shown in Fig.2). The distribution of B_z^p at different S_i^j for different \mathbf{V}_s is shown in Fig.3. Firstly, the maximum B_z^p occurs at S_6^j when the

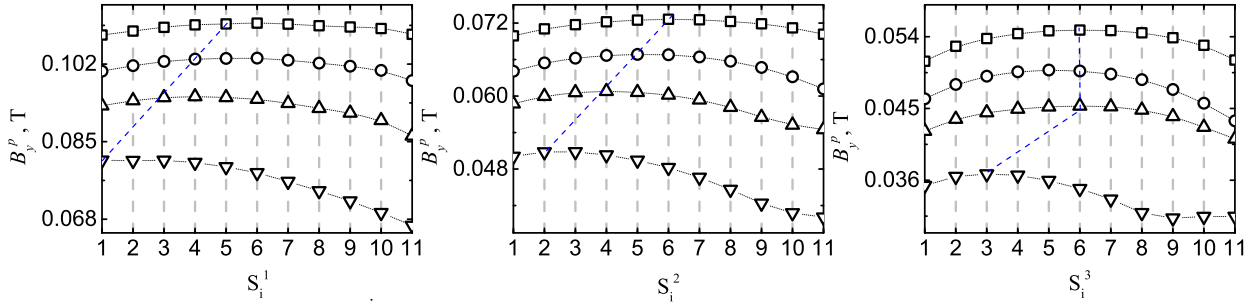


Figure 3: Variations B_z^p with S_i^j for different \mathbf{V}_s . Left: $j=1$; middle: $j=2$; right: $j=3$ for $\mathbf{V}_s=0.1$ (\square), 5 (\circ), 10 (\triangle), 20 (∇). B_z^p moves towards the specimen movement direction as \mathbf{V}_s is increased.

specimen velocity is low, e.g. $\mathbf{V}_s = 0.1$ (\square in the figure), which is located centrally between the two permanent magnets, for all values of j . For low specimen velocities, the magnetic field is symmetric about the centre of the defect at $D_{rl} = 0$ and B_z^{max} and B_z^{min} are mainly caused by the edges of the defect. B_z^p varies a little at S_i^j and the curve remains relative flat. Secondly, as specimen velocity is increased, the maximum value of B_z^p occurs further towards the direction of the specimen movement. This phenomenon is mentioned by Shin [3], whose findings are based on an MFL system which uses direct current electromagnets as the magnetising, however, the underlying reason for the phenomenon was not well discussed. The phenomenon is mainly due to the distortion of the magnetic field caused by specimen movement. This can be understood as follows. As we mentioned before, B_z^{min} and B_z^{max} occur at the moment when the sensor meets the front edge and back edge, respectively. However, the optimum sensor location is not only depends on the B_z^p , but also depends on the sensing sensitivity at different locations. Due to this reason, an simulation with a perfect (without defect) specimen passing by the MFL system for a give velocity is carried. ΔB_z is selected to represent the sensing sensitivity to the leakage signal which is purely caused by the defect of the plate. It is defined as follows:

$$\Delta B_z = B_z^1 - B_z^2, \quad (5)$$

where, B_z^1 and B_z^2 denote the B_z results obtained from the specimen with defect and without the defect. The result shows that the peak to peak value for ΔB_z at S_1^1 is larger than that at S_{11}^1 . This indicates us that for the geometry investigated, the sensing sensitivity has the same trend with the movement of the B_y^p .

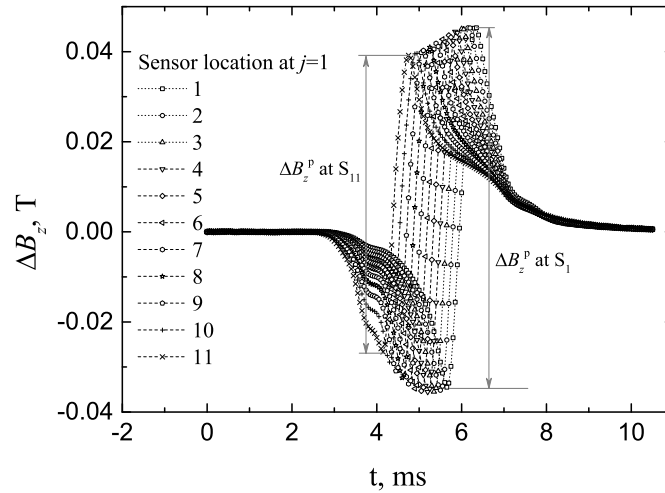


Figure 4: ΔB_z v.s. simulation time t at $V_s=20$ m/s.

4. Conclusions

A detailed analysis of the influence of specimen velocity on the magnetic flux leakage signal using finite element analysis are carried out in this paper. The main results can be summarised as follows:

- distortion of the magnetic field occurs as the specimen velocity is increased,
- for the radial magnetic induction B_z , the maximum variation of the leakage signal moves towards the specimen movement direction. The reason for this is that the leakage that escapes from the specimen increases much faster than the leakage which returns back to the specimen as the specimen velocity is increased,
- the sensing sensitivity to detect the defect is also moves towards the specimen movement direction,
- this indicates that the optimal sensor location, from B_z point of view, is not in the middle of the bridge, but at a location some distance from this point in the direction of the specimen movement, especially for higher speed MFL evaluations.

Acknowledgements

The authors would like to acknowledge Advanced Sustainable Manufacturing Technologies (ASTUTE) part-funded by the European Regional Development Fund (ERDF) through the Welsh Government.

References

- [1] Y. Sun and Y. Kang. Magnetic mechanisms of the magnetic flux leakage nondestructive testing. *Appl. Phys. Lett.* 2013; 103184104.
- [2] S. Niikura and A. Kameari. Analysis of eddy current and force in conductors with motion. *IEEE Transactions on Magnetics* 1992; 28(2): p 1450-3.
- [3] Y. Shin. Numerical prediction of operating conditions for magnetic flux leakage inspection of moving steel sheets. *IEEE Transactions on Magnetics* 1997; 33(2): p 2127-30.
- [4] G. Katragadda, Y. S. Sun, W. Load and L. Udipa. Velocity effect and their minimization in MFL inspection of pipelines: a numerical study. New York: Plenum Press Div Plenum Publishing Corp; 1995.
- [5] P. Wang, Y. Gao, G. Tian and H. Wang. Velocity effect analysis of dynamic magnetization in high speed magnetic flux leakage inspection. *NDT&E International* 2014; 64: p 7-12.
- [6] Y. Li, G. Y. Tian and S. Ward. Numerical simulation on magnetic flux leakage evaluation at high speed. *NDT&E International* 2006; 39: p 367-73.

Numerical simulation of a geometrically parametrised electromagnetic problem

Mar Giralt, Ruben Sevilla and Oubay Hassan

Zienkiewicz Centre for Computational Engineering, College of Engineering
 Swansea University, Singleton Park, SA2 8PP, United Kingdom

{750768, r.sevilla, o.hassan}@swansea.ac.uk

ABSTRACT

In this work, we propose the use of the PGD method to solve an electromagnetic problem where the geometry is parametrised with an extra coordinate. The space and time discretisations are performed using a high-order accurate DG method in space and an explicit time marching algorithm. The discretisation of the geometrical coordinate is performed using a standard continuous Galerkin method.

Key Words: *electromagnetics, geometry, Proper Generalized Decomposition method, Discontinuous Galerkin.*

1. Introduction

One of the crucial points in the simulation of electromagnetic devices is that small changes in the geometry can lead to important changes in the device performance [3]. In the design stage, many geometric configuration have to be assessed in order to guarantee the desired properties of a manufactured device, sometimes resulting in a prohibitive computational cost. We propose a more efficient alternative, where a generalised solution with a parametrised geometry is computed.

We will consider, besides the typical space-time coordinates, geometric parameters as extra coordinates on the solution. This will result in a higher dimensional problem and to reduce its cost, the Proper Generalized Decomposition (PGD) method will be employed [1]. This technique assumes a separated representation of the solution which splits our high-dimensional problem in two or more lower-dimensional problems. In this way, we can efficiently obtain a solution for any geometric configuration.

To implement this procedure we will approximate the solution of the transient Maxwell's equations using a high-order discontinuous Galerkin (DG) method in space and an explicit time marching algorithm. This choice will guarantee a high-fidelity solution of the electromagnetic equations [2].

2. DG formulation for Maxwell's equation

Maxwell's curl equations, governing the propagation of electromagnetic waves, can be written in dimensionless conservation form as

$$\frac{\partial \mathbf{U}}{\partial t} + \sum_{k=1}^{n_{sd}} \frac{\partial \mathbf{F}_k(\mathbf{U})}{\partial x_k} = \mathbf{0}, \quad (1)$$

where n_{sd} denotes the number of spatial dimensions. The conservative variable \mathbf{U} is given by $\mathbf{U} = (\varepsilon \mathbf{E}, \mu \mathbf{H})^T$ where $\mathbf{E} = (E_1, E_2, E_3)^T$ and $\mathbf{H} = (H_1, H_2, H_3)^T$ are the dimensionless electric and magnetic field intensity vectors respectively, ε is the electric permittivity and μ is the magnetic permeability.

In two spatial dimensions, the system of equations (1) decouples into the transverse electric (TE) mode and the transverse magnetic (TM) mode. The TE mode is described using (1) with

$$\mathbf{U} = \begin{pmatrix} \varepsilon E_1 \\ \varepsilon E_2 \\ \mu H_3 \end{pmatrix}, \quad \mathbf{F}_1(\mathbf{U}) = \begin{pmatrix} 0 \\ H_3 \\ E_2 \end{pmatrix}, \quad \mathbf{F}_2(\mathbf{U}) = \begin{pmatrix} -H_3 \\ 0 \\ -E_1 \end{pmatrix}.$$

The domain Ω is represented by an unstructured assembly of elements and a DG weak formulation for equation (1) may be expressed over each element, Ω_e , as

$$\int_{\Omega_e} \mathbf{W} \cdot \frac{\partial \mathbf{U}_e}{\partial t} d\Omega - \sum_{k=1}^{\text{nsd}} \int_{\Omega_e} \frac{\partial \mathbf{W}}{\partial x_k} \cdot \mathbf{F}_k(\mathbf{U}_e) d\Omega + \int_{\Gamma_e} \mathbf{W} \cdot \mathbf{F}_n(\mathbf{U}_e) d\Gamma = 0. \quad (2)$$

Here, \mathbf{U}_e denotes the restriction of \mathbf{U} to the element Ω_e , $\mathbf{F}_n = \sum_{k=1}^{\text{nsd}} \mathbf{F}_k n_k$ is the normal flux on the boundary Γ_e of Ω_e , n_k is the k th component of the outward unit normal vector \mathbf{n} to the boundary and \mathbf{W} is a vector of test functions.

In DG methods, the discontinuous nature of the approximation is accounted for by replacing the physical normal flux at the boundary by a consistent numerical flux, $\widetilde{\mathbf{F}}_n(\mathbf{U}_e, \mathbf{U}^{\text{out}})$. This numerical flux is evaluated in terms of the trace of the solution on the element Ω_e and the trace of the solution, \mathbf{U}^{out} , on the other element adjacent to Γ_e . A natural choice, for the linear hyperbolic system of interest here, is to employ a flux splitting technique which corresponds to an upwind approximation.

The normal flux \mathbf{F}_n is decomposed into incoming flux (superscript $-$) and outgoing flux (superscript $+$)

$$\mathbf{F}_n(\mathbf{U}) = \mathbf{F}_n^-(\mathbf{U}) + \mathbf{F}_n^+(\mathbf{U}),$$

where the incoming and outgoing fluxes are associated with the negative and positive eigenvalues of the jacobian matrix $\mathbf{A}_n = \frac{\partial \mathbf{F}_n}{\partial \mathbf{U}}$ respectively. The numerical flux is then computed as

$$\widetilde{\mathbf{F}}_n(\mathbf{U}, \mathbf{U}^{\text{out}}) = \mathbf{F}_n^+(\mathbf{U}) + \mathbf{F}_n^-(\mathbf{U}^{\text{out}}).$$

Introducing the resulting numerical normal flux into equation (2) and performing a second integration by parts, the DG weak formulation for an element Ω_e can be re-written as

$$\int_{\Omega_e} \mathbf{W} \cdot \frac{\partial \mathbf{U}_e}{\partial t} d\Omega + \sum_{k=1}^{\text{nsd}} \int_{\Omega_e} \mathbf{W} \cdot \frac{\partial \mathbf{F}_k(\mathbf{U}_e)}{\partial x_k} d\Omega + \int_{\Gamma_e} \mathbf{W} \cdot \mathbf{A}_n^- \llbracket \mathbf{U}_e \rrbracket d\Gamma = 0,$$

where $\llbracket \mathbf{U}_e \rrbracket = \mathbf{U}_e - \mathbf{U}^{\text{out}}$ denotes the jump of the solution across Γ_e and $\mathbf{A}_n^- \llbracket \mathbf{U}_e \rrbracket = \mathbf{F}_n^-(\mathbf{U}_e) - \mathbf{F}_n^-(\mathbf{U}^{\text{out}})$.

3. Parametrization of the geometry

In order to illustrate the methodology proposed in this work, we consider a rectangular domain Ω with dimensions $L_1 \times L_2$ of a material with parameters (ε_2, μ_2) with a circular inclusion of a material with parameters (ε_1, μ_1) .

The objective is to compute the solution of an electromagnetic problem for any radius R of the circular inclusion, within a given range $I^R = [R_1, R_2]$. Therefore the solution is now dependent on space, time and the new *coordinate* R , this is $\mathbf{U} = \mathbf{U}(\mathbf{x}, t, R)$.

To achieve this goal, we consider a reference domain, $\widehat{\Omega}$, equal to Ω with the sole difference that the radius is fixed at $R = 1$, as we can see in Figure 1 and we define the following mapping from $\widehat{\Omega}$ to Ω :

$$\mathbf{\Lambda}^R(\hat{x}, \hat{y}) := \left(a(R)\hat{x} + b(R)\frac{\hat{x}}{\hat{r}}, a(R)\hat{y} + b(R)\frac{\hat{y}}{\hat{r}} \right),$$

with $\hat{r} = \sqrt{\hat{x}^2 + \hat{y}^2}$ and,

$$a(R) := \begin{cases} R & \text{if } 0 \leq \hat{r} \leq 1 \\ \frac{l-R}{l-1} & \text{if } 1 \leq \hat{r} \leq l \\ 1 & \text{otherwise} \end{cases}, \quad b(R) := \begin{cases} \frac{l(R-1)}{l-1} & \text{if } 1 \leq \hat{r} \leq l \\ 0 & \text{otherwise} \end{cases},$$

where $l := \min\{L_1, L_2\}$, with $l > 1$.

The weak formulation for the problem in the higher dimensional space including the new coordinate R is then

$$\int_{I^R} \int_{\Omega_e} \mathbf{W} \cdot \frac{\partial \mathbf{U}_e}{\partial t} d\Omega dR + \sum_{k=1}^{\text{nsd}} \int_{I^R} \int_{\Omega_e} \mathbf{W} \cdot \mathbf{A}_k \frac{\partial \mathbf{U}_e}{\partial x_k} d\Omega dR + \int_{I^R} \int_{\Gamma_e} \mathbf{W} \cdot \mathbf{A}_n^- \llbracket \mathbf{U}_e \rrbracket d\Gamma dR = 0. \quad (3)$$

where $\mathbf{A}_k = \frac{\partial \mathbf{F}_k}{\partial \mathbf{U}}$. Introducing the mapping Λ^R into the weak form in equation (3), we transform our problem from the physical domain, Ω , to the reference domain, $\widehat{\Omega}$, resulting in

$$\sum_{i=1}^2 \alpha_i + \sum_{j=1}^3 \beta_j + \sum_{k=1}^3 \gamma_k + \sum_{d=1}^2 \delta_d = 0, \quad (4)$$

where

$$\begin{aligned} \alpha_1 &:= \int_{I^R} \int_{\widehat{\Omega}_e} a^2(R) \mathbf{W} \cdot \frac{\partial \mathbf{U}_e}{\partial t} d\widehat{\Omega} dR, & \alpha_2 &:= \int_{I^R} \int_{\widehat{\Omega}_e} a(R) b(R) \frac{1}{\hat{r}} \mathbf{W} \cdot \frac{\partial \mathbf{U}_e}{\partial t} d\widehat{\Omega} dR, \\ \beta_1 &:= \int_{I^R} \int_{\widehat{\Omega}_e} a(R) \mathbf{W} \cdot \mathbf{A}_1 \frac{\partial \mathbf{U}_e}{\partial \hat{x}} d\widehat{\Omega} dR, & \gamma_1 &:= \int_{I^R} \int_{\widehat{\Omega}_e} b(R) \frac{\hat{x}\hat{y}}{\hat{r}^3} \mathbf{W} \cdot \mathbf{A}_2 \frac{\partial \mathbf{U}_e}{\partial \hat{x}} d\widehat{\Omega} dR, \\ \beta_2 &:= \int_{I^R} \int_{\widehat{\Omega}_e} b(R) \frac{\hat{x}^2}{\hat{r}^3} \mathbf{W} \cdot \mathbf{A}_1 \frac{\partial \mathbf{U}_e}{\partial \hat{x}} d\widehat{\Omega} dR, & \gamma_2 &:= \int_{I^R} \int_{\widehat{\Omega}_e} a(R) \mathbf{W} \cdot \mathbf{A}_2 \frac{\partial \mathbf{U}_e}{\partial \hat{y}} d\widehat{\Omega} dR, \\ \beta_3 &:= \int_{I^R} \int_{\widehat{\Omega}_e} b(R) \frac{\hat{x}\hat{y}}{\hat{r}^3} \mathbf{W} \cdot \mathbf{A}_1 \frac{\partial \mathbf{U}_e}{\partial \hat{y}} d\widehat{\Omega} dR, & \gamma_3 &:= \int_{I^R} \int_{\widehat{\Omega}_e} b(R) \frac{\hat{y}^2}{\hat{r}^3} \mathbf{W} \cdot \mathbf{A}_2 \frac{\partial \mathbf{U}_e}{\partial \hat{y}} d\widehat{\Omega} dR, \\ \delta_1 &:= \int_{I^R} \int_{\widehat{\Gamma}_e} a^2(R) \mathbf{W} \cdot \mathbf{A}_n^- [\mathbf{U}_e] d\widehat{\Gamma} dR, & \delta_2 &:= \int_{I^R} \int_{\widehat{\Gamma}_e} a(R) b(R) \frac{1}{\hat{r}} \mathbf{W} \cdot \mathbf{A}_n^- [\mathbf{U}_e] d\widehat{\Gamma} dR. \end{aligned}$$

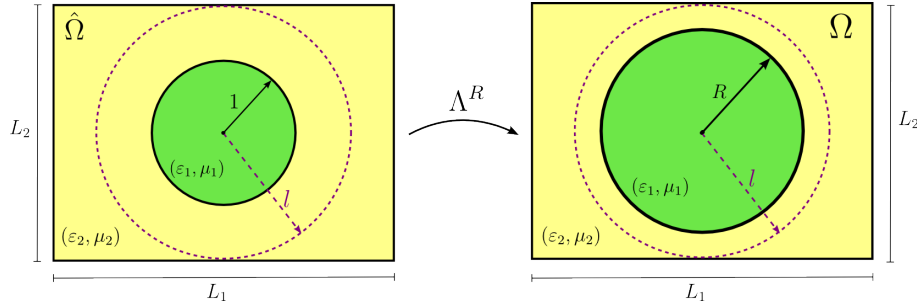


Figure 1: Mapping between the reference and the original domain

4. Proper Generalised Decomposition (PGD) formulation

It is worth noting that solving the problem for the generalised solution $\mathbf{U}(\hat{\mathbf{x}}, t, R)$ is intractable with traditional methods if a three dimensional structure is considered and specially if other geometric parameters are introduced, not just the radius of the circle.

Therefore, we propose the use of the PGD method in order to transform this high-dimensional problem in lower-dimensional problems resulting in an affordable computation of the generalised solution.

Firstly, the PGD method assumes that the solution can be approximated by a rank- M separable approximation

$$\mathbf{U}(\hat{\mathbf{x}}, t, R) \approx \mathbf{U}^M(\hat{\mathbf{x}}, t, R) = \sum_{i=1}^M \mathbf{F}_i(\hat{\mathbf{x}}, t) \circ \mathbf{G}_i(R).$$

Consequently, the functions \mathbf{F}_i and \mathbf{G}_i are computed in sequence using the weak formulation (4). This means that, assuming \mathbf{F}_i and \mathbf{G}_i known for $i = 1, \dots, m-1$, a so-called enrichment step consists on computing \mathbf{F}_m and \mathbf{G}_m . The solution at the enrichment step m is:

$$\mathbf{U}^m(\hat{\mathbf{x}}, t, R) = \mathbf{U}^{m-1}(\hat{\mathbf{x}}, t, R) + \mathbf{T}(\hat{\mathbf{x}}, t) \circ \mathbf{S}(R) = \sum_{i=1}^{m-1} \mathbf{F}_i(\hat{\mathbf{x}}, t) \circ \mathbf{G}_i(R) + \mathbf{T}(\hat{\mathbf{x}}, t) \circ \mathbf{S}(R), \quad (5)$$

and the test functions are also separated as $\mathbf{W} = \mathbf{T}^*(\hat{\mathbf{x}}, t) \circ \mathbf{S}(R) + \mathbf{T}(\hat{\mathbf{x}}, t) \circ \mathbf{S}^*(R)$.

Introducing these expressions of \mathbf{U} and \mathbf{W} into the weak formulation, a nonlinear system of equations is obtained. Although several options to solve the nonlinear system can be considered, a simple fixed point iteration is employed here.

In the first step of the iteration method we compute $\mathbf{T}(\hat{\mathbf{x}}, t)$ assuming $\mathbf{S}(R)$ is known. To do so, we introduce the expression of \mathbf{U} given in equation (5) and $\mathbf{W} = \mathbf{T}^*(\hat{\mathbf{x}}, t) \circ \mathbf{S}(R)$ into (4). This will leave us with a

PDE in space-time, similar to original's Maxwell's equations, that is solved with the previously detailed DG formulation.

The second step consists on computing $\mathbf{S}(R)$, assuming $\mathbf{T}(\hat{\mathbf{x}}, t)$ known, and introducing the expression of \mathbf{U} given in equation (5) and $\mathbf{W} = \mathbf{T}(\hat{\mathbf{x}}, t) \circ \mathbf{S}^*(R)$ into (4). This procedure will result in a one-dimensional problem computationally inexpensive.

It is worth noting that other alternatives for the separated representation are feasible. For instance, we could separate the solution \mathbf{U} as

$$\bar{\mathbf{U}}(\hat{\mathbf{x}}, t, R) \approx \sum_{j=1}^K \bar{\mathbf{F}}_j(\hat{\mathbf{x}}) \circ \bar{\mathbf{G}}_j(t) \circ \bar{\mathbf{H}}_j(R),$$

but due to the hyperbolic character of the equation, we anticipate that this will lead to a large number of modes to be able to appropriately represent the solution of the problem.

As stated before, the PGD method allows us to transform a high dimensional problem into a sequence of two lower-dimensional problems. The underlying algorithm of this method is illustrated in Figure 2.

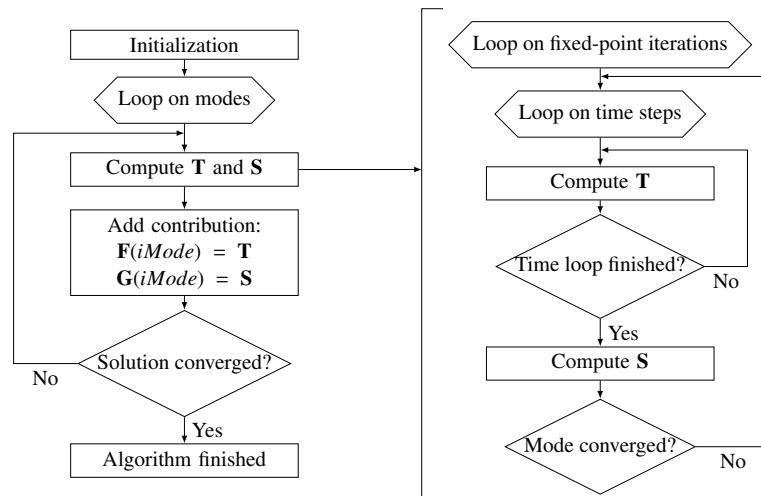


Figure 2: Flowchart of the PGD algorithm applied to the Maxwell's problem

5. Conclusions

In this work, we propose the use of the PGD method to solve an electromagnetic problem where the geometry is parametrised with an extra coordinate. This approach allows us to transform a high dimensional problem into a sequence of lower dimensional problems. The space and time discretisations are performed using a high-order accurate DG method in space and an explicit time marching algorithm. The discretisation of the geometrical coordinate is performed using a standard continuous Galerkin method. Numerical examples will be presented to demonstrate the applicability and performance of the proposed methodology. In addition, we will study the accuracy of the separated representation of the solution and the efficiency of the proposed approach by means of the number of modes required to represent the solution in a separated form.

Acknowledgements

The authors gratefully acknowledge the financial support provided by the Sêr Cymru National Research Network in Advanced Engineering and Materials.

References

- [1] Francisco Chinesta, Roland Keunings and Adrien Leygue. *The Proper Generalized Decomposition for Advanced Numerical Simulations A Primer*, Springer, 2014.
- [2] Jan S. Hesthaven and Tim Warburton. *Nodal Discontinuous Galerkin Method. Algorithms, Analysis, and Applications*, Springer, 2008.
- [3] Xia Ji, Tiao Lu, Wei Cai and Pingwen Zhang. Discontinuous Galerkin Time Domain (DGTD) methods for the study of 2-D waveguide-coupled microring resonators. *Journal of Lightwave Technology*, 23(11), 3864-3874, 2005.

Unstructured 3D leapfrog Solver for Electromagnetic Modelling and Simulation of Arbitrary Shaped Anisotropic Objects

*A. Gansen^{1,2}, M. El Hachemi², O. Hassan¹, K. Morgan¹

¹Civil and Computational Engineering Centre, Swansea University, Singleton Park,
Swansea SA2 8PP, U.K

²Transparent & Optically Tuneable Electronics Unit, Research and Technology Department (MRT),
5 Avenue des Hauts-Fourmeaux L-4362 Esch-sur-Alzette, Luxembourg

*alex.gansen@list.ac.uk

ABSTRACT

In computational electromagnetics, the standard Yee algorithm [1] is commonly used because of its simplicity and divergence free nature. A generalization of the classical Yee Scheme to unstructured meshes, which allows us to circumvent the accuracy losses of the standard Yee-scheme resulting from stair-cased representation of curved interfaces for perfect electric conducting [2] and isotropic conducting dielectric [3] materials, has been successfully implemented. In this work, we present a 3D leapfrog-scheme for unstructured meshes, which is able to model the electric and magnetic anisotropic materials which are becoming of increasing importance in our society, due to the use of composite and metamaterials.

Keywords: *Unstructured; FDTD; Anisotropic; Conducting Dielectric*

1. Introduction

The standard Yee algorithm is a low order method which is commonly applied in industrial electromagnetic simulations because of its simplicity, its low operation count and its low storage requirements. The orthogonal Cartesian grid that is usually employed results in an important loss of accuracy when the scheme is used for objects of arbitrary shape. To circumvent this problem, an unstructured mesh process is implemented. Maxwell's equations require the electric and magnetic fields to be orthogonal to each other. This is achieved by employing a primal Delaunay mesh, where we store the projections of the electric field vector, and its orthogonal dual graph the Voronoi mesh where we store the projections of the magnetic field vectors [2]. In previous work, we demonstrated the capability of this method to accurately model the radar cross section (RCS) of an arbitrarily shaped lossy dielectric object [3]. Now we want to extend the method to anisotropic materials, such as composite or metamaterials, because they offer new interesting perspectives in engineering. A thin anisotropic coating may, for example, significantly change the radar cross section of an aircraft. Furthermore anisotropy is the basis of metamaterials, a new kind of materials with electromagnetic properties which cannot be found in nature. For example, these materials may have a negative index of refraction, which could lead to invisible cloaking devices. To deal with such materials, we present a 3D leapfrog-scheme for unstructured meshes, which is able to model anisotropic materials.

2. Problem Formulation

The formulation employs the integral form of Maxwell's equations [2]. For a three dimensional lossy dielectric medium, of permittivity ϵ , permeability μ , electric conductivity σ and magnetic conductivity σ_m . Ampère's and Faraday's law in the scattered field equations are expressed as

$$\frac{\partial}{\partial t} \int_A \mathbf{D}_{scat} dA = \oint_{\partial A} \mathbf{H}_{scat} d\mathbf{l} - \frac{\partial}{\partial t} \int_A (\bar{\epsilon} - \bar{\epsilon}_0) \mathbf{E}_{inc} dA - \int_A \bar{\sigma}_{av} \mathbf{E}_{scat} dA - \int_A \bar{\sigma}_{av} \mathbf{E}_{inc} dA \quad (1)$$

and

$$\frac{\partial}{\partial t} \int_A \mathbf{B}_{scat} dA = - \oint_{\partial A} \mathbf{E}_{scat} d\mathbf{l} - \frac{\partial}{\partial t} \int_A (\bar{\mu} - \bar{\mu}_0) \mathbf{H}_{inc} dA - \int_A \bar{\sigma}_m \mathbf{H}_{scat} dA - \int_A \bar{\sigma}_m \mathbf{H}_{inc} dA \quad (2)$$

Here, ∂A denotes the closed curve bounding a surface A , dA is an element of surface area directed normal to the surface and $d\mathbf{l}$ is an element of curve length in the direction of the tangent to the curve. In addition, $\mathbf{E}_{inc}, \mathbf{H}_{inc}$ and $\mathbf{E}_{scat}, \mathbf{H}_{scat}$ represent the incident electric and magnetic fields and scattered electric and magnetic fields respectively. The total fields are the sum of the corresponding incident and scattered fields. The material properties $\{\epsilon, \mu, \sigma, \sigma_m\}$ are not constant and their values in free space differ from those in a dielectric. To take the boundary conditions into account, we have to average these quantities at the dielectric interface, leading to $\{\epsilon_{av}, \mu_{av}, \sigma_{av}, \sigma_{mav}\}$. The incident field represents a monochromatic plane wave illumination from the far field.

3. Discrete Equations

The Yee algorithm is a low operation count solution method for Ampère's and Faraday's law that is implemented on two mutually orthogonal meshes. A primal tetrahedral mesh is generated using a Delaunay method. The Voronoi diagram associated with this primal mesh is used to define a dual mesh. Each Voronoi face is a perpendicular bisector of the corresponding Delaunay edge and each Delaunay face is a perpendicular bisector of the corresponding Voronoi edge. N_e^D and N_e^V edges form the primal Delaunay and the dual Voronoi mesh respectively. For the scheme to be second order, the unknowns are located at the midpoints of these edges. The unknown at the node on the i^{th} Delaunay edge corresponds to the projection, $D_{scat,i}$, of the scattered electric field onto the direction of the edge. The unknown at the node on the j^{th} Voronoi edge corresponds to the projection, $B_{scat,j}$, of the scattered magnetic field onto the direction of the edge. The discretization of Ampère's and Faraday's law leads to the equations:

$$D_{scat,i}^{n+1} = \left(I + \frac{\Delta t \bar{\sigma}_\epsilon}{2} \right)^{-1} \left(\left(I - \frac{\Delta t \bar{\sigma}_\epsilon}{2} \right) \mathbf{D}_{scat,i}^n + \frac{\Delta t}{A_i^V} \left[\sum_{k=1}^{M_i^V} H_{scat,j_{ik}}^{n+0.5} l_{j_{ik}}^V - A_i^V (\bar{\sigma}_{av} \mathbf{E}_{inc,i})_i - A_i^V \left((\bar{\epsilon}_{av} - \bar{\epsilon}_0) \frac{\partial}{\partial t} \mathbf{E}_{inc,i} \right)_i \right] \right) \quad (3)$$

$$B_{scat,j}^{n+0.5} = \left(I + \frac{\Delta t \bar{\sigma}_m}{2} \right)^{-1} \left(\left(I - \frac{\Delta t \bar{\sigma}_m}{2} \right) \mathbf{B}_{scat,j}^{n-0.5} + \frac{\Delta t}{A_j^D} \left[- \sum_{k=1}^{M_j^D} E_{scat,i_{jk}}^{n+0.5} l_{i_{jk}}^D - A_j^D (\bar{\sigma}_m \mathbf{H}_{inc,j})_j - A_j^D \left((\bar{\mu}_{av} - \bar{\mu}_0) \frac{\partial}{\partial t} \mathbf{H}_{inc,j} \right)_j \right] \right) \quad (4)$$

Here, Δt is the time step, the superscript n denotes an evaluation at time level $n\Delta t$, l_i^D represents the length of the i^{th} Delaunay edge and A_i^V corresponds to the Voronoi face spanned by the Voronoi edges surrounding Delaunay edge i . Similarly, l_j^V represents the length of the j^{th} Delaunay edge and A_j^D corresponds to the Delaunay face spanned by the Delaunay edges surrounding Voronoi edge j . The numbers $j_{i,k}, k = 1, \dots, M_i^V$ refers to the M_i^V edges of the Voronoi face corresponding to the i^{th} Delaunay edge, as illustrated in Figure 1. Similarly, the numbers $i_{j,k}, k = 1, \dots, M_j^D$, refers to the the M_j^D edges of the Delaunay face corresponding to the j^{th} Voronoi edge, as illustrated in Figure 2

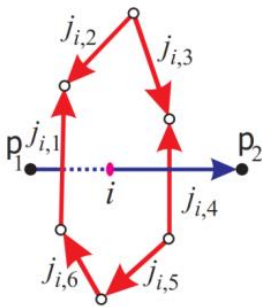


Figure 1

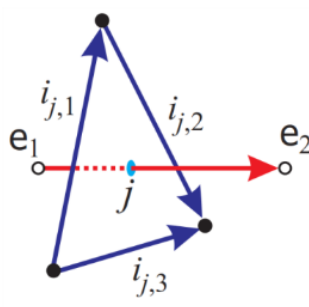
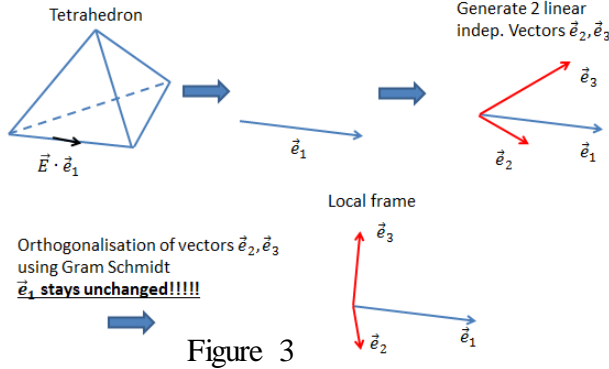


Figure 2

3. Updating Scheme

For simplicity, we restrict ourselves to the updating scheme for a lossless dielectric material $\{\bar{\sigma}, \bar{\sigma}_m = 0\}$. If we consider conducting Dielectric materials $\{\bar{\sigma}, \bar{\sigma}_m \neq 0\}$, we use the same methodology but two additional steps are required. By using the integral formulation of Maxwell's equations we do not update the displacement field vector \mathbf{D}_{scat} but it's projection $D_{scat,i} = \mathbf{D}_{scat} \cdot \mathbf{e}_i$ to a Delaunay edge \mathbf{e}_i . In the case of an isotropic material, the electric permittivity and magnetic permeability are scalars like the projections and updating the fields does only involve scalar multiplication between the field projections and material property scalars. In the anisotropic case in the integrals of Ampère's and Faraday's law's we have the matrix vector multiplication between material tensors $\{\bar{\sigma}, \bar{\epsilon}, \bar{\sigma}_m, \bar{\mu}\}$ and the fields $(\mathbf{D}_{scat}, \mathbf{B}_{scat})$. To deal with the matrix vector



multiplication we first create two linear independent vectors for each Delaunay and Voronoi edge. Using the Gram Schmidt orthonormalization procedure we orthonormalize those three vectors with respect to each other, as depicted in Figure 3.

The first vector to which two linear independent vectors are added remains unchanged during the whole process. Each set of three orthogonal vectors represents one local coordinate system. We have as many local systems then as Delaunay and Voronoi edges.

Unfortunately, we have no direct access to the exact field vectors, but we can reconstruct an approximated field vector for each local coordinate system using the field projections of the surrounding Delaunay or Voronoi edges. Those through averaging obtained field vectors will now be projected to the two especially for this purpose created orthogonal vectors forming a local frame. The first vector of each subset (which remained unchanged during the orthonormalization procedure) can be immediately updated through the projection equation we also use in the isotropic case. For this projection, no error due to the field averaging is induced.

The material tensors are expressed in the global reference frame formed by the orthonormal vectors $\mathbf{i}, \mathbf{j}, \mathbf{k}$. Three orthonormalized vectors $\mathbf{i}', \mathbf{j}', \mathbf{k}'$ we created before form the basis of each local coordinate system. The transformation matrix which transforms a vector or an operator like a matrix from a global to local frame is the Jacobian matrix $\bar{\mathbf{J}}$:

$$\bar{\mathbf{J}} = \begin{pmatrix} \partial x' / \partial x & \partial x' / \partial y & \partial x' / \partial z \\ \partial y' / \partial x & \partial y' / \partial y & \partial y' / \partial z \\ \partial z' / \partial x & \partial z' / \partial y & \partial z' / \partial z \end{pmatrix} \quad \bar{\mathbf{J}}_R = \begin{pmatrix} \mathbf{i}' \cdot \mathbf{i} & \mathbf{i}' \cdot \mathbf{j} & \mathbf{i}' \cdot \mathbf{k} \\ \mathbf{j}' \cdot \mathbf{i} & \mathbf{j}' \cdot \mathbf{j} & \mathbf{j}' \cdot \mathbf{k} \\ \mathbf{k}' \cdot \mathbf{i} & \mathbf{k}' \cdot \mathbf{j} & \mathbf{k}' \cdot \mathbf{k} \end{pmatrix}$$

Due to the orthogonality of the basis vectors of both, the local and global system, the Jacobian becomes a rotation matrix $\bar{\mathbf{J}}_R$ which can be calculated using the dot product of the global and local coordinate system vectors. The material property tensor transforms according to $\bar{\mathbf{a}}' = \frac{\bar{\mathbf{J}} \bar{\mathbf{a}} \bar{\mathbf{J}}^T}{\det(\bar{\mathbf{J}})}$ to $\bar{\mathbf{a}} = \bar{\sigma}, \bar{\epsilon}, \bar{\sigma}_m$ or $\bar{\mu}$, where "det" denotes the determinant. When we construct a local orthonormal system, some systems may be left or right handed. This results in a determinant $\det(\bar{\mathbf{J}}) = \pm 1$. This is not a concern for us, because we only use the additional vectors as a support for storing information. Therefore, we use the absolute value of the determinant $|\det(\bar{\mathbf{J}})|$. To finally pass from the displacement field projection \mathbf{D} to the electric field projection \mathbf{E} we use the constitutive equation $\mathbf{E} = \bar{\epsilon}^{-1} \mathbf{D}$. But we do not need to perform a full matrix vector multiplication. As we are only interested in the projection and because supplementary information is stored in the transformation matrix, $E_{scat} = \bar{\epsilon}_{11}^{-1} D_{scat} + \bar{\epsilon}_{12}^{-1} (\mathbf{D}_{scat} \cdot \mathbf{e}_2) + \bar{\epsilon}_{13}^{-1} (\mathbf{D}_{scat} \cdot \mathbf{e}_3)$ is sufficient for updating the electric field projections. The same procedure is applied to the Voronoi mesh for updating the magnetic field projections H_{scat} .

4. Numerical Results

Figure 4 shows the Bistatic RCS for a biaxial permittivity and electric conductivity tensor. We compare our results (co-volume) with those obtained from DDscat [4], an open source scattering program based upon the discrete dipole approximation[5].

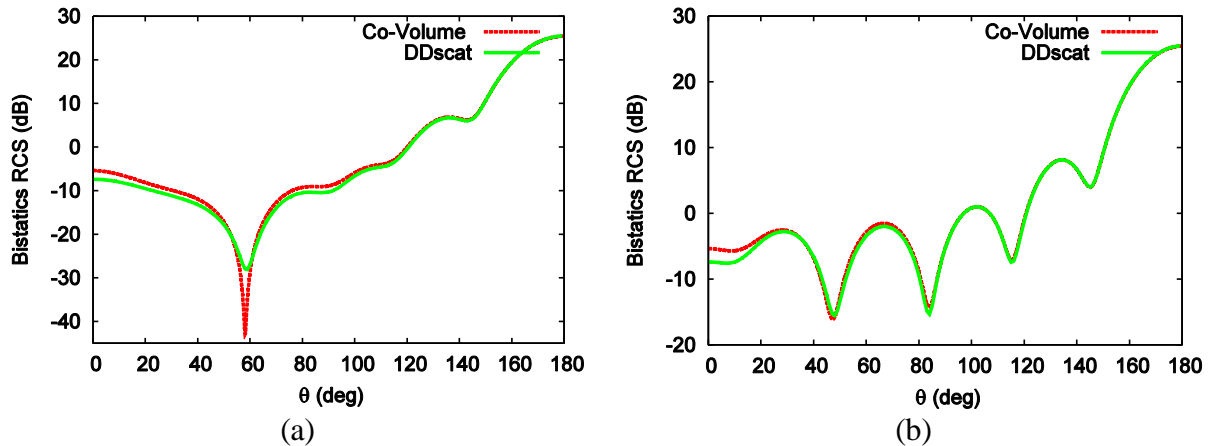


Figure 4. Scattering by an electrically anisotropic lossy dielectric sphere of electric length 2λ : (a) RCS distribution in the plane $\varphi = 0$ and (b) in the plane $\varphi = \pi/2$

5. Conclusion

A Yee algorithm procedure is used on an appropriately generated unstructured mesh to model electromagnetic scattering of electrically and magnetically anisotropic and conducting dielectric materials. Our results have been successfully validated using the discrete dipole approximation. The generalization from isotropic to anisotropic materials allows us now to accurately model anisotropic objects of complex geometry.

Acknowledgements

A.Gansen gratefully acknowledges the financial support provided by the National Research Fund, Luxembourg

References

- [1] K. Yee, "Numerical solution of initial boundary value problems involving Maxwell's equations in isotropic media," *IEEE Transactions on Antennas and Propagation*, no. 14, pp. 302-307, 1966.
- [2] Z. Xie, O. Hassan and K. Morgan, "Tailoring unstructured meshes for use with a 3D time domain co-volume algorithm for computational electromagnetics," *International Journal for Numerical Methods in Engineering*, no. 87, pp. 48-65, 2011.
- [3] A.Gansen, M.El hachemi, S.Belouettar, O.Hassan and K.Morgan, 3D leap-frog scheme for electromagnetic scattering by dielectric media using unstructured meshes, "*Proceeding of the 22nd UK Conference of the Association for Computational Mechanics in Engineering* " 2-4 April 2014, University of Exeter, pp-45-48,2014
- [4] B. T. Draine and P. J. Flatau, "Discrete dipole approximation for scattering calculations", *Journal of the Optical Society of America. A*, 11, 1491-1499, 1994
- [5] Yu. Eremin. The Method of Discrete Sources in Electromagnetic Scattering by Axially Symmetric Structures. *J. Commun. Techn. Electron.* 45, S269-S280 (2000).

Computation of resonant modes in cavities with a Discontinuous Galerkin time domain approach

M. Dawson, R. Sevilla, O. Hassan and K. Morgan

Zienkiewicz Centre for Computational Engineering, College of Engineering, Swansea University,
Swansea, Wales, UK SA2 8PP

{743587,R.Sevilla,O.Hassan,K.Morgan}@swansea.ac.uk

ABSTRACT

We present a method of obtaining frequency domain quantities of an electromagnetic resonator, such as the frequency spectrum, quality factors, resonant frequencies and the associated mode shapes, using a parallelised Discontinuous Galerkin solver with explicit time marching. The method is validated using a 2D free-space cavity with analytically known resonant frequencies. The relative error in resonant frequency is quantified and we demonstrate a faster convergence of error, using the filter diagonalisation method (FDM), than with the traditional fast Fourier transform (FFT). The implementation of material dispersion in the solver is validated using a 2D dispersive cavity with known analytical solution.

Key Words: *Finite Element, Discontinuous Galerkin, Electromagnetics, Resonant Cavities, Time Domain*

1. Introduction

Recent advances in manufacturing techniques, such as electron beam lithography, make it possible to manufacture resonant cavities on the scale of the wavelength of light. These nanoresonators, key components in nanolasers, can have many desirable qualities such as well defined resonant frequencies and high quality factors [1]. However, the typical scale and the geometric complexity introduce several challenges for numerical simulation.

The behaviour of these resonators is described by Maxwell's equations of classical electromagnetics. For dispersive materials, an auxiliary ordinary differential equation based on the Drude models [2] is coupled to the Maxwell system. Frequency domain solvers are traditionally employed to find the resonant frequencies and associated modes, but as the scale and geometric complexity of the devices increase, the large eigenvalue system that must be solved becomes computationally prohibitive.

We propose to use the Discontinuous Galerkin (DG) method with explicit time marching, which only requires solving a block diagonal system of equations for each timestep [3]. The frequency spectrum, resonant frequencies and quality factors can then be recovered by a Fourier transform of the time domain solution.

2. DG solution of the transient Maxwell's equations in dispersive media

Maxwell's equations of classical electromagnetics and the auxiliary ordinary differential equation required for dispersive media can be written in linear, dimensionless, conservation form as

$$\frac{\partial \mathbf{U}}{\partial t} + \sum_{k=1}^{nsd} \frac{\partial \mathbf{F}_k(\mathbf{U})}{\partial x_k} = \mathbf{S}(\mathbf{U}), \quad (1)$$

where nsd denotes the number of spatial dimensions. The vector of unknowns, \mathbf{U} , the flux vectors, \mathbf{F}_k , and the source \mathbf{S} are given by

$$\mathbf{U}_1 = \begin{pmatrix} \epsilon E_1 \\ \epsilon E_2 \\ \epsilon E_3 \\ \mu H_1 \\ \mu H_2 \\ \mu H_3 \\ J_1 \\ J_2 \\ J_3 \end{pmatrix}, \quad \mathbf{F}_1 = \begin{pmatrix} 0 \\ H_3 \\ -H_2 \\ 0 \\ -E_3 \\ E_2 \\ 0 \\ 0 \\ 0 \end{pmatrix}, \quad \mathbf{F}_2 = \begin{pmatrix} -H_3 \\ 0 \\ H_1 \\ E_3 \\ 0 \\ -E_1 \\ 0 \\ 0 \\ 0 \end{pmatrix}, \quad \mathbf{F}_3 = \begin{pmatrix} H_2 \\ -H_1 \\ 0 \\ -E_2 \\ E_1 \\ 0 \\ 0 \\ 0 \\ 0 \end{pmatrix}, \quad \mathbf{S} = \begin{pmatrix} 0 \\ 0 \\ 0 \\ 0 \\ 0 \\ 0 \\ \omega^2 E_1 - \gamma J_1 \\ \omega^2 E_2 - \gamma J_2 \\ \omega^2 E_3 - \gamma J_3 \end{pmatrix},$$

where E_k , H_k and J_k are the k th spatial components of the dimensionless intensity vectors of electric field, magnetic field and the polarisation current respectively. The material parameters ϵ , μ , ω and γ are the electric permittivity, magnetic permeability, plasma frequency and electron damping coefficient respectively.

We discretise the computational domain Ω on an unstructured mesh. The DG weak formulation [4] of (1) on an element Ω_e can then be written as

$$\int_{\Omega_e} \mathbf{W} \frac{\partial \mathbf{U}_e}{\partial t} d\Omega + \int_{\Omega_e} \mathbf{W} \cdot \left(\sum_k \frac{\partial \mathbf{F}_k(\mathbf{U}_e)}{\partial x_k} - \mathbf{S}(\mathbf{U}_e) \right) d\Omega + \int_{\partial\Omega_e} \mathbf{W} \cdot \mathbf{A}_n^- [[\mathbf{U}_e]] d\Gamma_e = 0,$$

where \mathbf{U}_e denotes the solution vector restricted to the element Ω_e , \mathbf{W} is a vector of test functions and $[[\mathbf{U}_e]] = \mathbf{U}_e - \mathbf{U}_{out}$ denotes the jump of the solution across the element boundary Γ_e . The boundary term, derived after introducing the numerical flux on the boundary and using a flux-splitting technique, results in

$$\mathbf{A}_n^- [[\mathbf{U}_e]] = \frac{1}{2} \begin{pmatrix} -\mathbf{n} \times [[\mathbf{H}]] + \mathbf{n} \times (\mathbf{n} \times [[\mathbf{E}]]) \\ \mathbf{n} \times [[\mathbf{E}]] + \mathbf{n} \times (\mathbf{n} \times [[\mathbf{H}]]) \\ \mathbf{0}_3 \end{pmatrix},$$

where \mathbf{n} is the outward unit normal of the element and $\mathbf{0}_3$ is a zero vector of length 3. After introducing the approximation of the solution and using a Galerkin formulation, the following system of ordinary differential equations is obtained,

$$\mathbf{M} \frac{d\mathbf{U}}{dt} + \mathbf{R}(\mathbf{U}) = \mathbf{0},$$

where \mathbf{U} is the vector of nodal values, \mathbf{M} is the block diagonal mass matrix and $\mathbf{R}(\mathbf{U})$ is the residual vector. The system of ordinary differential equations is advanced in time using a fourth-order explicit Runge-Kutta method.

3. Computation of resonant frequencies

The engineering quantities of interest in cavities are usually the resonant frequencies, associated modes and quality factors. In order to obtain these quantities using a time domain solver, the electromagnetic field is first excited by introducing an initial condition or a source in the domain (Figure 1(a)). As the solution is advanced in time, its value is monitored at each timestep for a given period of time, T (Figure 1(b)). Using the fast Fourier transform, or more sophisticated techniques, we can then obtain the frequency spectrum (Figure 1(c)) from the monitored solution. The resonant frequencies of the cavity can be obtained from the locations of peaks in the frequency spectrum by curve-fitting and the quality factors from the width of the peaks. Mode shapes can be obtained by running the time domain simulation with the resonant frequency as an input.

The error in frequency is inversely proportional to T , and the highest frequency is inversely proportional to the simulation timestep. The main limitation of the proposed approach is therefore the need for longer periods in order to minimise the error in the obtained resonant frequencies. To overcome this issue we considered the filter diagonalisation method [5] (FDM) which gives a much better accuracy than FFT in a significantly shorter time period.

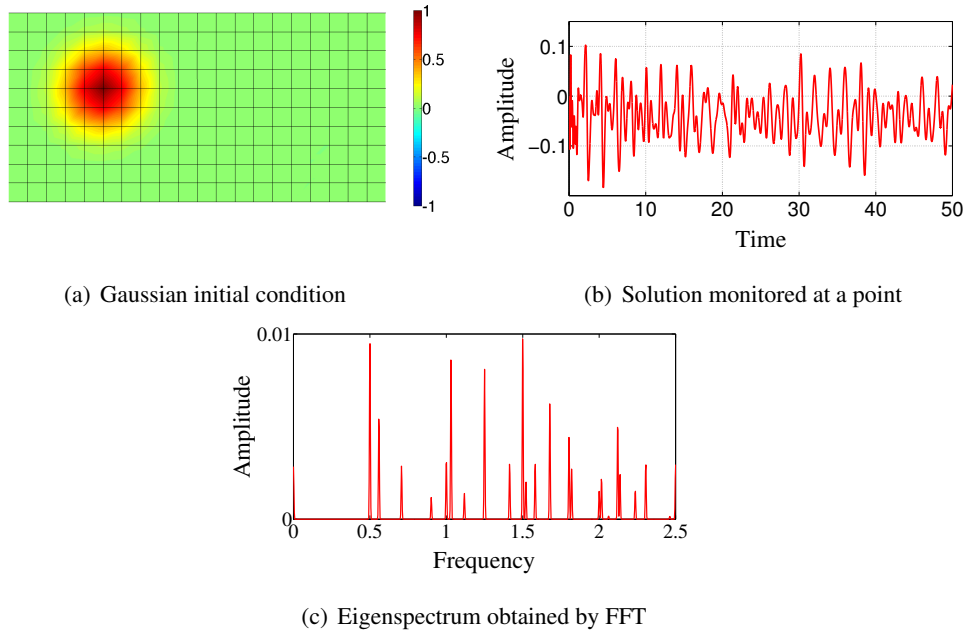


Figure 1: Steps required to find the frequency spectrum and resonant frequencies shown for a 2D rectangular cavity.

To further improve the performance of the proposed approach, the relative ease of parallelisation of the DG method is exploited to achieve the long periods required in reasonable computational time. The solver has been parallelised using MPI and the implementation and performance has been validated using two- and three-dimensional test cases.

4. Numerical Results

The first example presented is a rectangular 2D non-dispersive free-space cavity ($\epsilon = \mu = 1, \omega = \gamma = 0$) surrounded by a perfect electric conductor (PEC) with a width twice its length. Analytical expressions for the resonant frequencies of this cavity are known [6]. Figure 2(a) shows the relative error in the resonant frequencies converging as expected with T . The final value is the error due to the spatial discretisation of the domain, which decreases with mesh refinement. The error using FDM can be seen to converge almost an order of magnitude quicker than FFT, as Figure 2(b) shows.

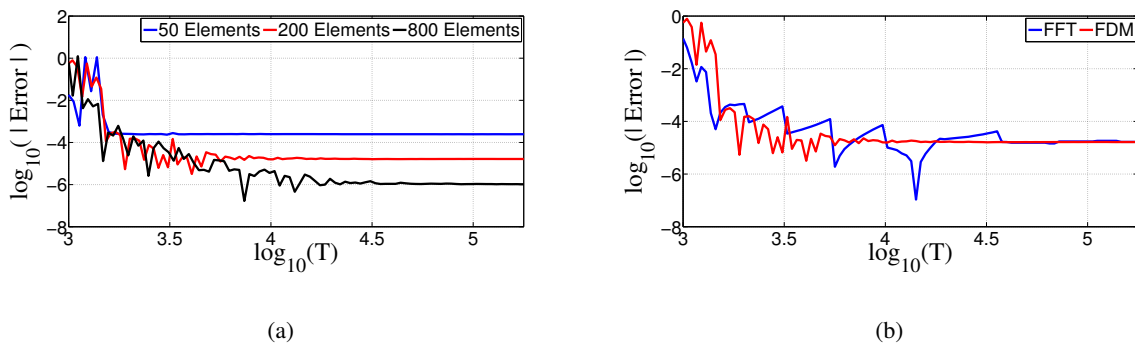


Figure 2: (a) Convergence of the relative error in calculated resonant frequencies with increasing period T for three different meshes in a free space cavity. (b) Comparison of convergence with period obtained with FDM and FFT.

The second example presented is a dispersive cavity with an additional source term added to the right hand side of Maxwell's equations ((1)) to ensure that the problem has an exact known solution. The same 2D rectangular cavity as the previous example was considered filled with a gold medium ($\epsilon = 1, \sigma = 1, \omega = 6.7433, \gamma = 0.0799$). Snapshots in time of the solutions obtained for the electric intensity vectors are shown in Figure 3.

Optimal convergence (i.e. a rate of $p + 1$) was achieved in the $\mathcal{L}^2(\Omega)$ norm of the relative error in the solution as shown in Figure 4 for component E_1 .

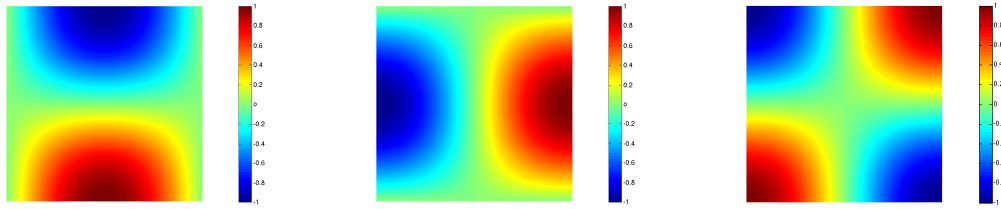


Figure 3: Left to right: Components E_1 , E_2 and E_3 of the solution obtained for a rectangular cavity with a dispersive material and a volumetric source.

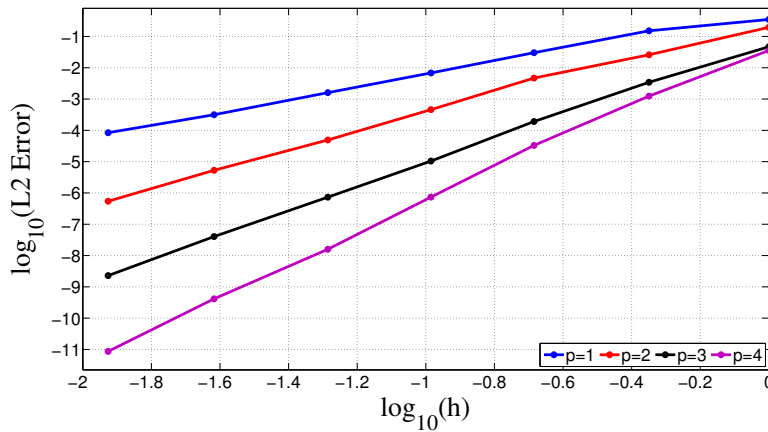


Figure 4: h -convergence of the $\mathcal{L}^2(\Omega)$ norm of the relative error in E_1 for a cavity filled with dispersive material with an additional source term.

5. Conclusions

A method has been presented for obtaining frequency spectrum, resonant frequencies, mode shapes and quality factors for resonant cavities using a parallelised Discontinuous Galerkin time domain electromagnetic solver. Excellent agreement with analytical values has been observed for the resonant frequencies of a 2D free-space resonant cavity, and the convergence of the solution with the time period has been presented. The dispersive media implementation has been validated with the expected h -convergence of the $\mathcal{L}^2(\Omega)$ norm of the relative error.

Acknowledgements

The authors gratefully acknowledge the financial support provided by the Sêr Cymru National Research Network in Advanced Engineering and Materials

References

- [1] Kurt Busch, Michael König, and Jens Niegemann. Discontinuous Galerkin methods in nanophotonics. *Laser & Photonics Reviews*, 5(6):773–809, 2011.
- [2] A. Taflov. *Computational Electrodynamics: The Finite-difference Time-domain Method*. Antennas and Propagation Library. Artech House, 1995.
- [3] Ruben Sevilla, Oubay Hassan, and Kenneth Morgan. The use of hybrid meshes to improve the efficiency of a discontinuous galerkin method for the solution of maxwells equations. *Computers & Structures*, 137:2–13, 2014.
- [4] Jan S Hesthaven and Tim Warburton. *Nodal discontinuous Galerkin methods: algorithms, analysis, and applications*, volume 54. Springer Science & Business Media, 2007.
- [5] Vladimir A. Mandelshtam and Howard S. Taylor. Harmonic inversion of time signals and its applications. *The Journal of Chemical Physics*, 107(17):6756–6769, 1997.
- [6] David M Pozar. *Microwave Engineering, 4th Edition*. John Wiley & Sons, 2011.

WAVE PROPAGATION 2

SOLVING THE MAGNETIC INDUCTION TOMOGRAPHY INVERSE PROBLEM USING HP-FINITE ELEMENTS

*Ross M. Kynch, †Paul D. Ledger

College of Engineering, Swansea University, Swansea, SA2 8PP

*r.m.kynch@swansea.ac.uk, †p.d.ledger@swansea.ac.uk

ABSTRACT

We investigate the impact of applying high-order *hp*-finite elements to the Magnetic Induction Tomography (MIT) inverse problem. By simulating the process of measurement in MIT, we consider the associated inverse problem and, in the talk, will consider the effect on the recovery of electromagnetic material parameters. We focus on the formulation for the conductivity for use in industrial and medical imaging applications such as detecting metallic objects or imaging of cerebral stroke.

Key Words: *hp*-finite elements; Magnetic Induction Tomography; Inverse Problems

1. Introduction

Magnetic Induction Tomography (MIT) [1] is a non-invasive imaging technique where the goal is to recover the electromagnetic material parameters of a body or object from non-local measurements of the electromagnetic fields. An MIT system is set up with an array of excitation and sensor coils, a schematic of which can be seen in Figure 1a. By passing a current through each exciter coil in turn, a series of background magnetic fields are generated. These magnetic fields generate eddy currents when they interact with conducting bodies causing the field to be perturbed. The perturbed magnetic fields are measured as voltages by the sensor coils. As regions of conductivity are of interest in an industrial or clinical setting (e.g. detection of metallic objects or cerebral stroke), the goal is to identify them from input currents and the measured voltages. This requires the solution of an ill-posed non-linear inverse problem.

Standard inversion techniques for the MIT problem involve linearising the inverse problem by a sensitivity analysis [2]. In order to evaluate the sensitivity of the voltages to changes in material parameters, the solution of the forward problem is required. It has been common to make use of low-order computational schemes for the solution of the forward problem [3, 2], however, we investigate the use of high-order *hp*-finite elements.

hp-Finite element methods approximate the solution of a partial differential equation (PDE) on a mesh using high-order polynomials, allowing derivatives to be captured more accurately. The method results in exponential convergence of the solution with increasing polynomial degree for smooth functions and, by combining with mesh refinement, for piecewise analytic functions with singularities [4]. We aim to demonstrate that the ability to accurately capture the solution and its derivatives for the forward problem leads to an improved reconstruction.

2. Methods

2.1. Forward Problem

To solve the inverse problem we require a forward solver to predict the measurements for a given geometry, frequency, material distribution and applied current. The field equations for the electromagnetic problem are Maxwell's equations. Neglecting the displacement currents, we consider the \mathbf{A} -based eddy current approximation of the time-harmonic Maxwell's equations in some domain Ω

$$\nabla \times \frac{1}{\mu_r} \nabla \times \mathbf{A} + \kappa \mathbf{A} = \mu_0 \mathbf{J}_s \quad \text{in } \Omega, \quad (1)$$

where \mathbf{A} is such that $\mathbf{E} = -i\omega\mathbf{A}$, \mathbf{E} is the electric field and ω is the angular frequency. The material parameters are $0 < \mu(\mathbf{x}) < \infty$, the magnetic permeability, $\mu_0 = 4\pi \times 10^{-7} \text{Hm}^{-1}$ and $0 \leq \sigma(\mathbf{x}) \leq \infty$, the conductivity, with $\mu_r(\mathbf{x}) = \frac{\mu(\mathbf{x})}{\mu_0} \geq 1$ and $\kappa(\mathbf{x}) = i\omega\mu_0\sigma(\mathbf{x})$. The current sources are represented by \mathbf{J}_s , the current density. In the case that $\sigma = 0$ the system becomes singular so we regularise the equation by setting $\kappa = \omega\mu_0\sigma_{\text{reg}}$, with σ_{reg} a small regularisation parameter.

Boundary conditions for this equation are of the form

$$\mathbf{n} \times \mathbf{A} = \mathbf{f} \text{ on } \Gamma_D, \quad \mathbf{n} \times \nabla \times \mathbf{A} = \mathbf{f} \text{ on } \Gamma_N, \quad (2)$$

where \mathbf{n} is the outward normal $\partial\Omega = \Gamma_D \cup \Gamma_N$, $\Gamma_D \cap \Gamma_N = \emptyset$ and Γ_D and Γ_N are Dirichlet and Neumann boundaries, respectively.

We solve these equations numerically using an edge-based curl-conforming hp -finite element method, making use of the implementation contained in the deal.II [5] open-source hp -finite element library. The linear system resulting from the discretisation is split into blocks associated with low and higher order basis functions and solved using a preconditioned GMRES iterative solver. The block preconditioner is composed of a sparse direct LU factorisation of the low-order blocks and a sparse incomplete LU (ILU) factorisation on the higher-order blocks.

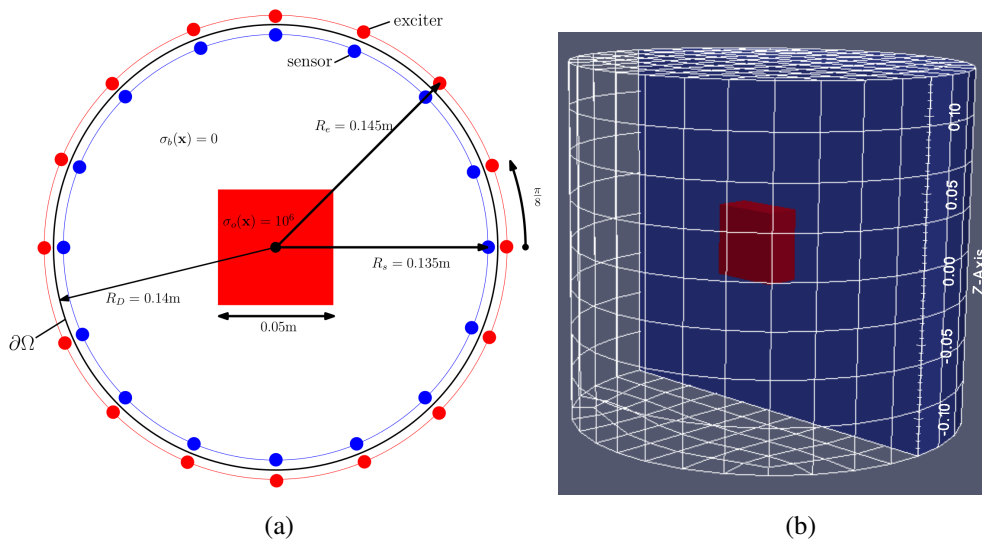


Figure 1: Diagram showing (a) The MK1 [3] array of exciter and sensor coils with a highly conducting cube inside, (b) the coarse mesh, M1, with the cube present.

2.2. Simulated Measurements

We approximate the presence of an exciting coil as a dipole source, applying Dirichlet conditions on the whole boundary based on the representation

$$\mathbf{n} \times \mathbf{A} \approx \mathbf{n} \times \mathbf{A}_0(\mathbf{r}) = \frac{\mu_0}{4\pi r^3} \mathbf{n} \times (\mathbf{m} \times \mathbf{r}) \quad \text{on } \Gamma_D, \quad (3)$$

with \mathbf{m} the dipole moment of the coil and \mathbf{r} the radial vector from its centre, r being its length.

Following the hp -finite element solution for $\mathbf{A}_{hp} \approx \mathbf{A}$, assuming the coil has zero width, the simulated measurements of the voltages induced in the i^{th} sensor coil can be approximated by

$$V_i = \oint_{L_i} \mathbf{E} \cdot \boldsymbol{\tau} dL \approx -i\omega \oint_{L_i} \mathbf{A}_{hp} \cdot \boldsymbol{\tau} dL, \quad (4)$$

where $\boldsymbol{\tau}$ is the tangent to the coil and L_i is the surface of the i^{th} coil. By illuminating each exciter in turn and simulating the resulting voltages in each of the sensors a set voltage measurements, V^S , are obtained.

2.3. Inverse Problem

The goal of the inverse problem is to recover the material parameter distribution given a set of measurements. In the current work we focus on the recovery of σ and only consider $\mu = \mu_0$. Given a set of coil excitation and sensor measurements, V^M , and a representation of $\sigma(\mathbf{x})$ through a series of coefficients we look for the set of coefficients that minimise the functional

$$G(\sigma) = \frac{1}{2} \|V^M - V^S(\sigma)\|_0^2 + \frac{\alpha^2}{2} \|R(\sigma - \sigma^b)\|_0^2, \quad (5)$$

where the regularisation parameter α and regularisation matrix R are present in order to overcome the ill-posed nature of the inverse problem and $\|\cdot\|_0$ denotes the Euclidean norm. For the representation of $\sigma(\mathbf{x})$ we use a voxel-based approach, introducing N voxels, C_i , we have

$$\sigma(\mathbf{x}) = \sum_{i=1}^N B_i(\mathbf{x}) \sigma_i, \quad B_i(\mathbf{x}) = \begin{cases} 1 & \text{if } \mathbf{x} \in C_i \\ 0 & \text{otherwise.} \end{cases} \quad (6)$$

A sensitivity analysis [2] of the system yields the following for a given voxel C_j to a given coil combination $i = a + (b - 1)N_s$ as

$$J_{ij}(\sigma) = \int_{C_j} \mathbf{E}^a(\sigma) \cdot \mathbf{E}^b(\sigma) dV \approx -\omega^2 \int_{C_j} \mathbf{A}^a(\sigma) \cdot \mathbf{A}^b(\sigma) dV, \quad (7)$$

where $b = 1, \dots, N_e$ is the exciter coil index and $a = 1, \dots, N_s$ is the sensor coil index. Here the N_e is the number of excitation coils and N_s is the number of sensor coils.

To solve the inverse problem, we employ a regularised Gauss-Newton iterative scheme. For real-valued J , V^M , V^S , the update [2] for at step n is given by

$$\sigma^{[n+1]} = \sigma^{[n]} + \delta\sigma^{[n]}, \quad \delta\sigma^{[n]} = -\left(J_n^T J_n + \alpha^2 R^T R\right)^{-1} \left(J_n^T (V^S(\sigma_n) - V^M) + \alpha^2 R^T R\right), \quad (8)$$

which is iterated until a desired tolerance is reached or no further reduction in the functional is achieved.

3. Results and Discussion

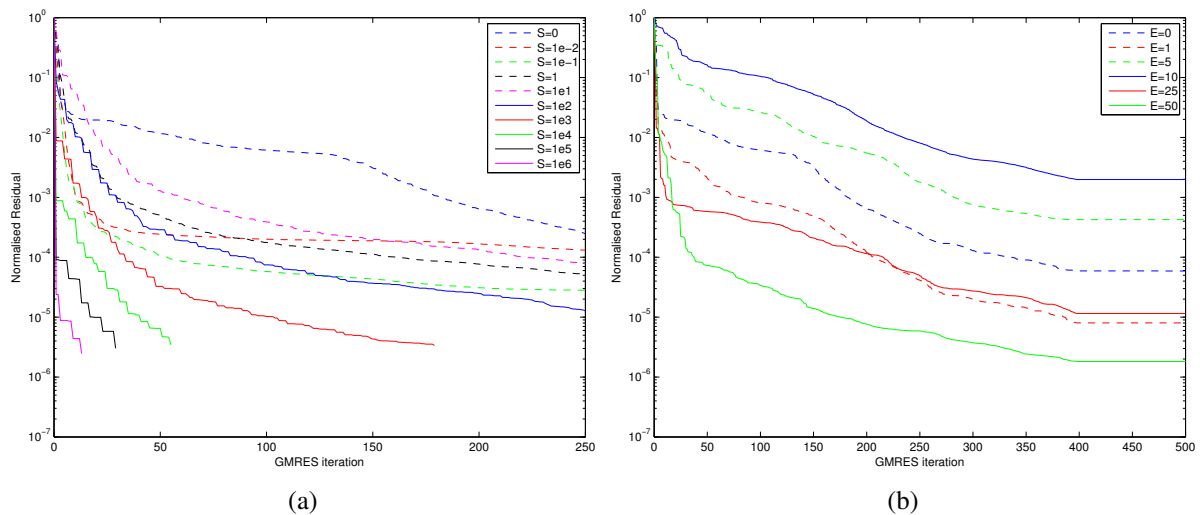


Figure 2: Normalised preconditioned residual at each GMRES iteration for (a) diagonal strengthening, S , and (b) number of extra off-diagonals, E , for the ILU block preconditioner. This is the hp -FEM solution of the forward problem of a single coil illumination from Figure 1 at $p = 2$ on mesh M2.

We consider the test problem shown in Figure 1 on a coarse mesh ($M1$, 768 hexahedral elements) and a finer mesh ($M2$, 2717 hexahedral elements) with $\omega = 2\pi \times 10^6$ rad/s and investigate the performance of the iterative solver for the forward problem and the simulated voltages resulting from the solution for higher order elements with $p = 0, 1, 2, 3$. Through experimentation the effectiveness of the sparse ILU-decomposition has been found to be greatly improved by diagonal strengthening.

Figure 2a shows the effect of increasing the diagonal strengthening of the ILU factorisation for $p = 2$. There is a noticeable improvement in the convergence rate compared to no strengthening and this becomes more dramatic as the value of S is increased to 10^6 . Figure 2b shows the effect of increasing the off-diagonals included in the ILU factorisation, closer approximating the LU factorisation of the block. The initial convergence rate improves for some particular values and there is a clear improvement by $E = 50$, although not as stark as through using diagonal strengthening. The use of additional off-diagonals also comes with a performance impact, so we choose to disable it.

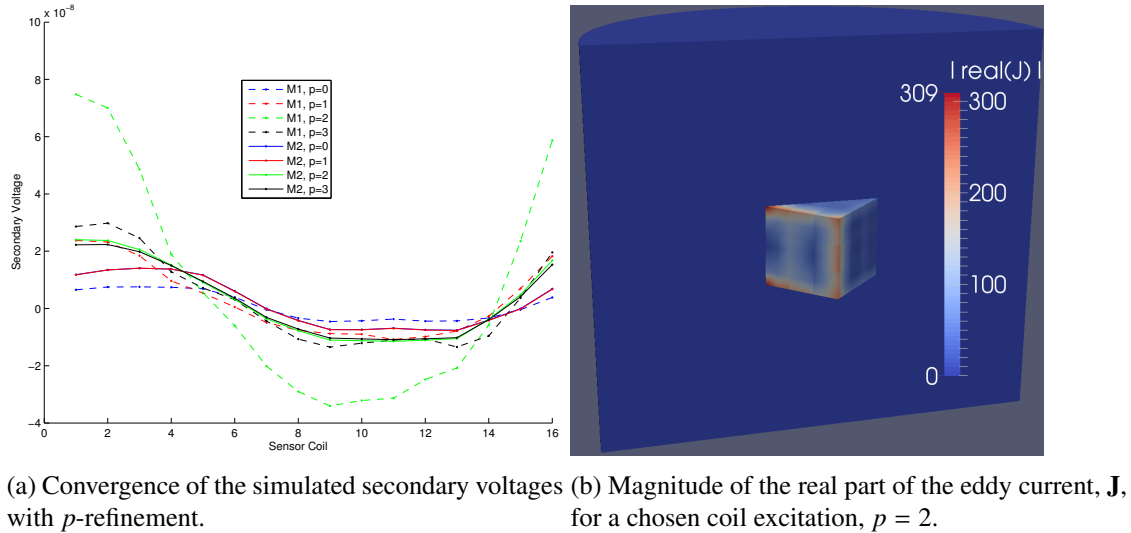


Figure 3

The convergence with p -refinement on M1 and M2, for a particular coil excitation, are shown in Figure 3a and the eddy currents are shown in Figure 3b. The results for other excitations are similar. The combination of mesh refinement and polynomial enrichment is required in order to accurately capture the voltages, with the coarse mesh unconverted even at $p = 3$ whereas the finer mesh shows agreement between $p = 2$ and $p = 3$. This demonstrates the suitability of hp -finite elements for the solution of the forward problem, where accurately measuring the simulated voltages is important in accurately predicting the value of the functional given in (5).

In the talk, we shall present results for the solution of the inverse problem based on these simulated measurements using the Gauss-Newton inversion method detailed in Section 2.3.

Acknowledgements

The authors would like to express their gratitude to the Engineering and Physical Sciences Research Council (EPSRC) for funding this research via grant EP/K023950/1.

References

- [1] H. Griffiths. Magnetic induction tomography. *Measurement Science and Technology*, 12(8), 1126-1131, 2001.
- [2] M. Soleimani, W. R. B. Lionheart. Absolute conductivity reconstruction in magnetic induction tomography using a nonlinear method. *IEEE Transactions on Medical Imaging*, 25(12), 1521-1530. 2006
- [3] M. Zolgharni, P. D. Ledger, H. Griffiths. Forward modelling of magnetic induction tomography: a sensitivity study for detecting haemorrhagic cerebral stroke. *Medical & Biological Engineering & Computing*, 47(12), 1301-1313, 2009.
- [4] P. D. Ledger, S. Zaglmayr. hp -Finite element simulation of three-dimensional eddy current problems on multiply connected domains. *Computer Methods in Applied Mechanics and Engineering*, 199(49), 3386-3401, 2010.
- [5] W. Bangerth, R. Hartmann, G. Kanschat. deal.II a general-purpose object-oriented finite element library. *ACM Transactions on Mathematical Software*. 33(4), 24, 2007.

Assessment of polynomial and non-polynomial based high order FEM for the solution of Helmholtz problems at high frequency

*K. Christodoulou¹, M.S. Mohamed¹, O. Laghrouche¹ and J. Trevelyan²

¹Institute for Infrastructure & Environment, Heriot-Watt University, Edinburgh EH14 4AS, UK

²School of Engineering and Computing Sciences, Durham University, Durham DH1 3LE, UK

*kc328@hw.ac.uk

ABSTRACT

This paper deals with the numerical solution of Helmholtz wave problems. High-order finite elements (p -FEM) based on Lagrange interpolating polynomials are used to solve a two-dimensional problem at high frequencies. The Lagrange basis functions are defined on different nodal grid distributions, an equi-spaced grid and the Chebyshev-Gauss-Lobatto grid. The high-order elements are then compared with elements enriched by plane waves (PUFEM). The performance of both methods is considered in terms of accuracy, number of degrees of freedom per wavelength, and conditioning. It is shown that p -FEM with careful nodal distribution can potentially give similar accuracy to the PUFEM but requires more degrees of freedom per wavelength.

Key Words: Helmholtz equation; Finite element method; Lagrange polynomials; Partition of unity finite element method

1. Introduction

Numerical solutions to the Helmholtz problems depend significantly on the wave number k . Specifically, the accuracy of the finite element solution using piecewise linear elements (polynomials of order 1) deteriorates with increasing wave number, even if the number of elements per wavelength is kept constant [1]. This is due to the *pollution* error.

Many techniques were developed to overcome this issue, either by reducing the pollution term [2] or via increasing the efficiency by incorporating analytical solutions into the FE-solution space. One of the latter techniques is called PUFEM [5]. The PUFEM has been applied to a range of diffraction problems in two and three dimensions [3].

In this paper, we compare the performance of high order finite elements to those of enriched elements. The accuracy of both methods is determined by using the relative error in the L_2 norm. This paper is organized as follows: In section 2, the formulation of both methods is described. Numerical results that are used to assess the performance of these methods are presented in section 3 and thereafter we give our conclusions.

2. Mathematical Formulation

The problem of a horizontal plane wave scattered by a rigid circular cylinder is considered in a finite domain $\Omega \subset \mathbb{R}^2$ with smooth boundary Γ . We are interested in the solution ϕ which satisfies the 2D Helmholtz equation and the Robin boundary conditions

$$\nabla^2 \phi + k^2 \phi = 0 \quad \text{in } \Omega, \quad (1)$$

$$\nabla \phi \cdot \underline{\mathbf{n}} + ik\phi = g \quad \text{on } \Gamma. \quad (2)$$

The coefficient $k = \omega/c$ is the wave number, g is the prescribed boundary condition and $\underline{\mathbf{n}}$ denotes the outward normal defined on the line boundary Γ .

Multiplying equation (1) by a weight function $W(x, y)$ and integrating by parts over the domain Ω we obtain the weak formulation of the problem

$$\int_{\Omega} (-\nabla W \cdot \nabla \phi + k^2 W \phi) d\Omega + \int_{\Gamma} W \nabla \phi \cdot \underline{\mathbf{n}} d\Gamma = 0. \quad (3)$$

Replacing the normal derivative of the function ϕ by its expression deduced from (2), the system of equations to solve is then

$$\int_{\Omega} (\nabla W \cdot \nabla \phi - k^2 W \phi) d\Omega + ik \int_{\Gamma} W \phi d\Gamma = \int_{\Gamma} W g d\Gamma. \quad (4)$$

The computational domain Ω is meshed into n -noded elements. The solution ϕ is approximated over each element via polynomial functions N_j and among their linear combination such that

$$\phi_h = \sum_{j=1}^n N_j \phi_j. \quad (5)$$

In this work, high-order finite elements (p -FEM) based on Lagrange polynomial basis functions are used to solve the considered problem. The Lagrange polynomials are defined on two different nodal grid distributions, an equi-spaced grid (EQ) and the Chebyshev-Gauss-Lobatto grid (CGL). They are given respectively by the following schemes:

$$\xi_i^{EQ} = \frac{2(i-1)-p}{p} \quad \text{and} \quad \xi_i^{CGL} = -\cos\left(\frac{(i-1)\pi}{p}\right), \quad (6)$$

where p is the order of the polynomial element.

The PUFEM is based on the standard weak formulation of FEM and its numerical implementation can be easily adapted to any mesh. The finite element approximation (5) is enriched by solutions of the Helmholtz differential equation. They are in the form of plane waves. At each node of the meshed domain, the wave potential is expanded by a set of plane waves propagating in different directions. The PUFEM approximation is then given by

$$\phi_h = \sum_{j=1}^n \sum_{l=1}^m N_j e^{ik \xi_l \cdot \mathbf{r}} A_j^l, \quad (7)$$

where A_j^l are the plane wave amplitudes and the new unknowns of the problem, \mathbf{r} is the position vector and $\xi_l = (\cos \alpha_l, \sin \alpha_l)$ with $\alpha_l = 2\pi l/m$, $l = 1, 2, \dots, m$, are the plane wave directions attached to node j .

3. Numerical Results

An incident plane wave of unit amplitude is diffracted by a rigid cylinder of unit radius and then radiates away to infinity. The scattered wave $\phi(x, y)$ which satisfies the two dimensional Helmholtz equation is approximated on a square domain $\Omega \in [1, 2]^2$. This problem has an analytical solution expressed as a series of Hankel functions [3]. The analytical solution is imposed on the boundary Γ through the Robin boundary condition given in expression (2). It is also used to assess the performance of approximation ϕ_h by calculating the relative error in the L_2 norm. Finally, the parameter $\tau = \lambda \sqrt{\text{totdof}/\text{area}(\Omega)}$, gives the number of degrees of freedom per wavelength (DOF/λ) for any considered case. Note that *totdof* is the total number of degrees of freedom.

3.1. FEM: Equi-spaced versus Chebyshev Gauss Lobatto nodal distribution

The problem stated above is first solved with the finite element method. The considered wave number is taken to be $k = 2\pi$ which corresponds to a wavelength of $\lambda = 1$. The computational domain is divided into 100 uniform square n -noded elements. The Lagrange polynomial interpolation at each element is analyzed on two different nodal distributions, EQ and CGL. Figure 1 shows the results obtained from this study. The relative error in L_2 -norm is plotted against the polynomial degree of the shape functions, p . As can be seen from the graph, both nodal distributions give almost the same accuracy for polynomials up to and including the 5th order. However, as p increases, the error obtained by using the EQ-grid

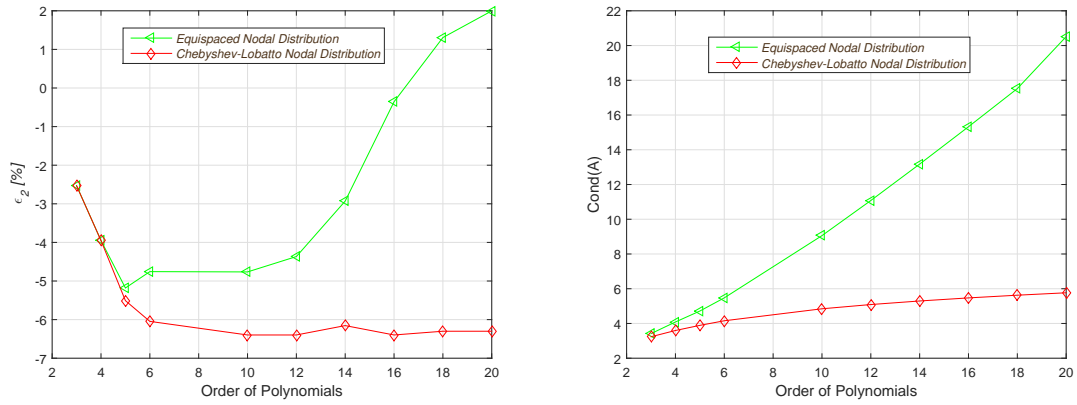


Figure 1: Relative error [%] in L_2 norm (left) and conditioning (right) for the case $hk = \pi/5$ with $k = 2\pi$. The polynomial degree of the shape functions is increased from $p=3$ to 20.

increases. In contrast, the CGL-grid appears to improve the accuracy with p and provides errors of magnitude up to $10^{-6}\%$. Once the CGL-grid solution reaches a certain level of accuracy, the error stagnates even if we keep increasing the order of the polynomial functions. Further, for $p=20$, the CGL-grid gives an error of $9.3 \times 10^{-6}\%$ while the EQ-grid gives almost a 100% error. These results indicate that high order polynomials with uniform mesh distribution do not provide accurate computations. In this study, the conditioning $cond(A)$ of the final system matrix is also analyzed for both nodal distributions. As shown in Figure 1, the conditioning for the EQ-grid increases with p resulting in very high condition values at high polynomial orders. On the other hand, the condition values obtained from the CGL-grid remain very low even for high polynomial orders. Therefore, the EQ-grid is more sensitive for ill-conditioning and consequently it affects the accuracy of the method. From this study it can be concluded that the finite element solution is significantly affected by the nodal distribution and the EQ-grid cannot be recommended because of the ill-conditioning.

3.2. FEM vs. PUFEM

In this study, the performance of high order polynomials based only on the Chebyshev-Gauss Lobatto nodal distribution is investigated at relatively high frequency. It is compared to PUFEM on the basis of accuracy, number of degrees of freedom per wavelength and conditioning. The simulations are performed for the wave numbers $k = 40\pi$ and $k = 100\pi$. The error of the FEM and the PUFEM is plotted against the total number of degrees of freedom. In the case of the FEM, the *total dof* increases by refining the mesh grid. For the PUFEM, the number of elements is kept constant so that the *total dof* increases by adding more approximating plane waves into the solution space. The results are illustrated in Figure reffig3. As expected, the error obtained by the enriched method decreases as the number of plane waves increases. Similarly, the p -FEM exhibits better accuracy on a fine mesh grid. Although, the numerical results for both methods show that the error decreases up to a certain level and then it remains practically unchanged. The minimum error we can reach with both methods deteriorates as the wave number k increases. For instance, at $k = 40\pi$ we get an approximate error of magnitude less than $10^{-4}\%$ whereas the same accuracy seems not to be achievable for $k = 100\pi$. Furthermore, it can be seen that the p -FEM gives slightly better accuracy in comparison to the PUFEM for both wave problems. It is also noticeable that higher order polynomials improve significantly the convergence rate of the p -FEM solution. At $k = 100\pi$, polynomials of order 50 can provide 0.01% error with $\tau \approx 4$ while polynomials of order 10 can provide the same error with $\tau \approx 6$. On the other hand, the PUFEM provides the same error with only $\tau \approx 1.5$ and therefore the number of unknown variables is greatly reduced. The condition number for both formulations is also analyzed for the same wave numbers. It is obvious that the enriched finite element method suffers from ill-conditioning when the number of approximating plane waves increases whereas the condition number of the p -FEM remain unchanged with p .

4. Conclusions

In this work, solutions to wave problems governed by the Helmholtz equation are approximated either by high order finite elements (p -FEM) or by elements enriched with plane waves (PUFEM). The results are compared to those obtained from the analytical solution of the problem through an L_2 -norm

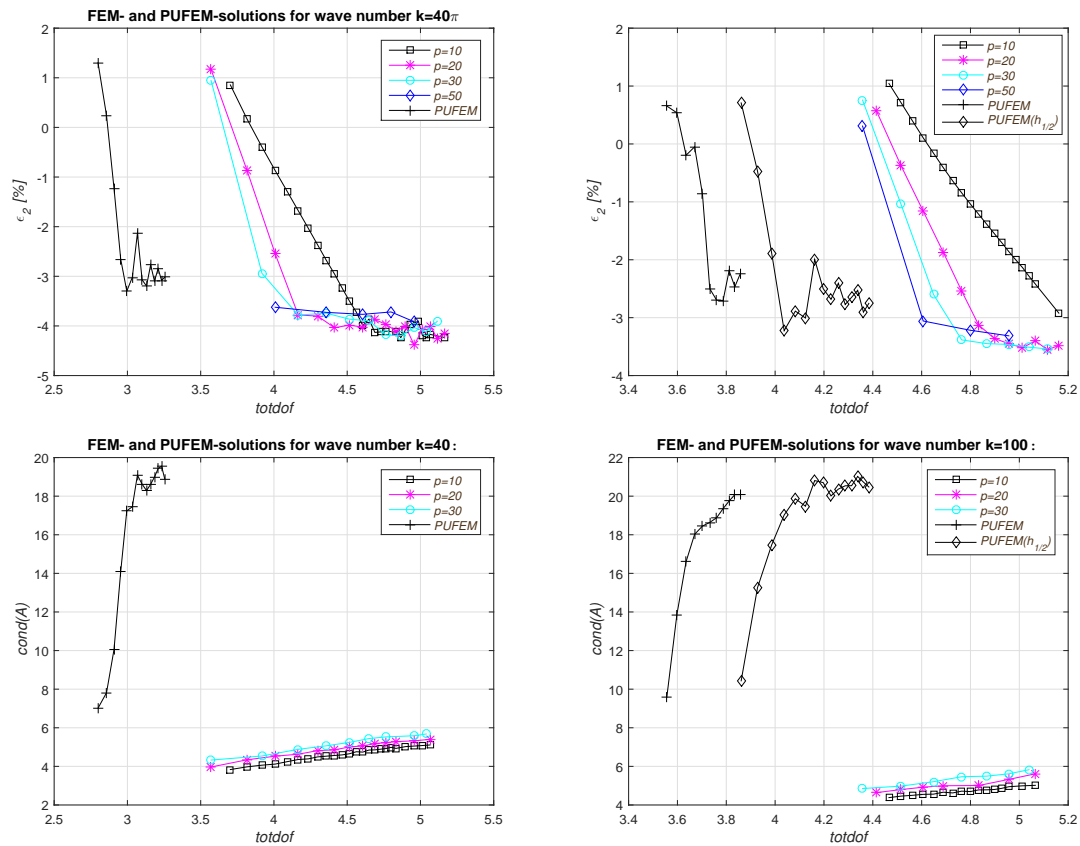


Figure 2: Relative error [%] vs. *totdof* for $k = 40\pi$ (top left), Relative error [%] vs. *totdof* for $k = 100\pi$ (top right), Conditioning vs. *totdof* for $k = 40\pi$ (bottom left), Conditioning vs. *totdof* for $k = 100\pi$ (bottom right).

error. Numerical experiments show that finite element solutions are strongly affected by the nodal points distribution. In fact, polynomial interpolations defined on Chebyshev-Gauss Lobatto nodal distribution provide much better accuracy with low conditioning in comparison to polynomial interpolation solutions on uniform distribution. Moreover, the performance of nonuniform polynomial elements is compared to the PUFEM. It is shown that the PUFEM provides high quality results with only few degrees of freedom per wavelength and consequently the number of parameters in the whole problem is significantly reduced. However, the method suffers from ill-conditioning. On the other hand, the p -FEM can potentially give similar results if high order polynomial elements are used with nonuniform mesh grids but require more degrees of freedom per wavelength.

References

- [1] A. Bayliss, C.I. Goldstein, E. Turkel. On accuracy conditions for the numerical computation of waves. *Jour. Comp. Phys.* 59.3, 396-404, 1985.
- [2] L.L.Thompson, P.M. Pinsky. A Galerkin least-squares finite element method for the two-dimensional Helmholtz equation. *Int. Jour. Num. Meth. Eng.* 38.3, 371-397, 1995.
- [3] O. Laghrouche, P. Bettess, R.J. Astley. Modelling of short wave diffraction problems using approximating systems of plane waves. *Int. Jour. Num. Meth. Eng.* 54.10, 1501-1533, 2002.
- [4] D. Schmicker, S. Duczek, S. Liefold, U. Gabbert. Wave propagation analysis using high-order finite element methods: spurious oscillations excited by internal element eigenfrequencies. *Tech. Mech.*, 34.2, 51-71, 2014.
- [5] J.M. Melenk, I. Babuška. The partition of unity finite element method: basic theory and applications. *Comp. Methods Appl. Mech. and Engrg.* 139.1, 289-314, 1996.

Enriched finite elements for numerical solution of Electromagnetic waves in the time domain

*M. Drolia¹, M. S. Mohamed¹, O. Laghrouche¹, M. Seaid², and J. Trevelyan²

¹Institute for Infrastructure and Environment, Heriot Watt University, Edinburgh EH14 4AS, UK

²School of Engineering and Computing Sciences, Durham University, Durham DH1 3LE, UK

*md272@hw.ac.uk

ABSTRACT

This paper proposes a novel scheme for the solution of Maxwell equations [1] in the time domain. A discretization scheme in time is developed to render implicit solution of system of equations possible. The scheme allows for calculation of the field values at different time slices in an iterative fashion. This facilitates us to tackle problems whose solutions have harmonic or even more general dependency on time.

The spatial grid is partitioned into finite number of elements with intrinsic shape functions to form the bases of solution. Furthermore, the finite elements are enriched with plane wave functions. This significantly reduces the number of nodes required to discretize the geometry, without compromising on the accuracy or allowed tolerance in the errors, as compared to that of classical FEM. Also, this considerably reduces the computational costs, viz. memory and processing time. Parametric studies, presented herewith, confirm the robustness and efficiency of the proposed method.

The numerical scheme can thus be further developed for solution of problems where analytical solutions cannot be developed, or even when the solution cannot be categorized as time-harmonic in nature.

Key Words: Maxwell Equations; Finite Element; Partition of Unity; Time Domain; Wave Equations

1. Transverse Electric Mode of propagation

Let Ω be a unit square defined on a 2D Euclidean space, with its four edges as the boundary Γ . The boundary value problem be defined as follows

$$\frac{\partial^2 E}{\partial t^2} - c^2 \nabla^2 E = f(t, x, y); \quad \text{on } \Omega \quad (1a)$$

$$\frac{\partial E}{\partial \hat{\mathbf{v}}} + hE = g(t, x, y); \quad \text{on } \Gamma \quad (1b)$$

$$E^0 = U_0 \quad (1c)$$

$$\frac{\partial E^0}{\partial t} = V_0 \quad (1d)$$

where E is the magnitude of the transverse electric field in the direction $\hat{\mathbf{z}}$ perpendicular to the Euclidean plane. The above equation can be approximated using finite element and finite difference schemes for numerical solution. Let's discretize the time derivative in the following way (in order to facilitate the development of time-dependent formulations [2] as seen in analyses for transient response [3] or diffusion problems [4])

$$\frac{\partial^2 E^n}{\partial t^2} = \frac{E^n - 2E^{n-1} + E^{n-2}}{\Delta t^2} \quad (2)$$

Where the superscript n stands for the value of the field at the time instance $t = n\Delta t$. Substituting in (1a) gives

$$\begin{aligned} \nabla^2 E^n &= \frac{E^n - 2E^{n-1} + E^{n-2}}{c^2 \Delta t^2} - \frac{1}{c^2} f(t, x, y) \\ \Rightarrow E^n - (c^2 \Delta t^2) \nabla^2 E^n &= 2E^{n-1} - E^{n-2} + (\Delta t^2) f(t, x, y) \end{aligned} \quad (3)$$

The equation (3) can be used to obtain a weak form which can be further solved over a finite number of elements in space as a linear system of equations. Let u be a test function multiplied to (3)

$$u(E^n - (c^2 \Delta t^2) \nabla^2 E^n) = u(2E^{n-1} - E^{n-2} + (\Delta t^2) f(t, x, y)) \quad (4)$$

Integrating the left and right hand sides, over the domain Ω with boundary Γ , and applying the divergence theorem we get

$$\int_{\Omega} u E^n d\Omega + (c^2 \Delta t^2) \left\{ \int_{\Omega} \nabla u \cdot \nabla E^n d\Omega - \int_{\Gamma} u \hat{\mathbf{v}} \cdot \nabla E^n d\Gamma \right\} = \int_{\Omega} u (2E^{n-1} - E^{n-2} + (\Delta t^2) f(t, x, y)) d\Omega \quad (5)$$

Where $\hat{\mathbf{v}}$ is the normal unit vector to Γ . From (1b) and (5) we get the solvable weak form

$$\int_{\Omega} u E^n d\Omega + (c^2 \Delta t^2) \int_{\Omega} \nabla u \cdot \nabla E^n d\Omega + (c^2 \Delta t^2) \int_{\Gamma} u (h E^n) d\Gamma = \int_{\Omega} u (2E^{n-1} - E^{n-2} + (\Delta t^2) f(t, x, y)) d\Omega + (c^2 \Delta t^2) \int_{\Gamma} u g(t_n, x, y) d\Gamma \quad (6)$$

This equation (6) can be used to solve for E^n for the given set of boundary and initial conditions. The equation can then be iterated over n to obtain subsequent values of the fields for consecutive time steps.

This paper validates the proposed method against a problem where the solution is a cylindrical wave such that

$$E = e^{i(kr - \omega t + \varphi)} \quad (7)$$

where k is the wave number, ω angular frequency, φ phase shift, r length of the position vector, e the natural exponent and i the imaginary number. Then the above constant c becomes the phase velocity defined such as $c = \frac{\omega}{k}$ and $f(t, x, y) = 0$ while the function $g(t, x, y)$ is defined on each domain edge according to the relevant normal direction.

The initial conditions are defined by

$$U_0 = e^{i(kr + \varphi)} \quad (8a)$$

$$V_0 = e^{i(kr + \varphi)} (-i\omega) \quad (8b)$$

To solve the weak form (6) using the finite element method we mesh the domain into a set of elements where the field E over each element is approximated in terms of a set of nodal values E_i and nodal shape functions N_i such as

$$E = \sum_{i=1}^n E_i N_i \quad (9)$$

Using the partition of unity [5] property one may further express the nodal values of the potential E_i as a combination of Q plane waves [6] such that

$$E = \sum_{i=1}^n \sum_{q=1}^Q A_i^q N_i e^{i(kx \cos \alpha_q + ky \sin \alpha_q + \varphi_q)} \quad (10)$$

where φ_q and α_q are the phase and the angle of the q th plane wave respectively. Now by solving the linear system resulting from the above discrete representation we get the amplitudes A_i^q of the plane waves which is the q th plane wave contribution at the node i .

2. Error analysis

In this paper we present results from 2 sets of studies, with the aim to check the behaviour of the proposed PUFEM for different analysis parameters, and to compare the method with FEM in the time domain for a given wave problem. The angular frequency ω of the progressive wave (being captured) was fixed (at 1). The data represented herein are solely numeric in nature, which have been used for qualitative analysis. The domain considered for analyses was (as discussed in the previous section) a unit square, with its vertices at points (1, 1), (2, 1), (2, 2), (1, 2). Linear (square) elements were used to mesh the geometry.

However, the number of nodes in each direction (m), and hence the number of elements, varied for the two sets of experiments studied.

For investigation of the role of problem parameters (like step size in time) on the numerical error for the field-enriched FEM in the time domain, 4×4 elements were used, i.e. we had 5 nodes in either of the two directions (fig 1(c)). Three different values for the step-size in time were used, viz. $\Delta t = 0.001, 0.005,$ and 0.009 . The values of λ (wavelength) studied were $1/4, 1/6$ and $1/9$. Thus we had $3 \times 3 = 9$ cases in total. The degrees of freedom per wavelength (τ), the number of plane waves used (Q) for a given wavelength(λ) and the number of nodes in each direction (m), were related by the equation (11), however for the purpose of this study Q was also forced to be an even integer with 2 as its minimum value.

$$\tau = \lambda m \sqrt{Q} \Rightarrow Q = \left(\frac{\tau}{\lambda m} \right)^2 \quad (11)$$

Thus, the values of λ, τ, Q corresponding to the three wavelengths studied were computed to be $(1/4, 4.3, 12)$, $(1/6, 4.08, 24)$, and $(1/9, 3.04, 30)$ respectively. The 9 cases were run on a computer (each for a total time = 1) and figure(1) below shows a snapshot.

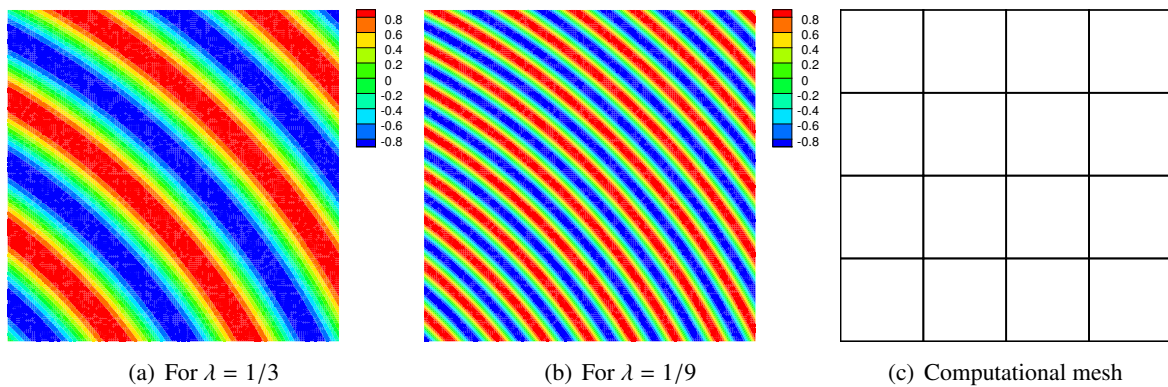


Figure 1: Real part of the numerical solution for E , for largest and smallest wavelengths considered

The relative errors (i.e. L^2 error percentage) obtained were plotted on a semilog graph as shown in figure 2(a). It can be observed that the error in all cases is below 2%. Also, for a given λ , a decrease in time step Δt recorded a lower error. The largest λ (blue lines) had the least number of plane waves for enrichment, and resulted in maximum error recorded (for any Δt category) as compared to that for smaller wavelengths. For any given Δt the smaller wavelengths (red and black lines) showed higher rate of increase in error for initial iterations as compared to that observed for the largest λ . For later iterations in time, the rates for all wavelengths behaved very similarly. It can be inferred that the error contributed by the step size Δt in time dominated the spatial error in the cases studied.

For comparison of the suggested PUFEM with classical FEM for the given problem, a further paramet-

Table 1: : Parameters for PUFEM vs. FEM

Type	Δt	λ	m	Q	τ
PUFEM1	10^{-4}	$1/3$	5	10	5.27
PUFEM2	10^{-4}	$1/3$	5	8	4.71
FEM	10^{-4}	$1/3$	31	n/a	10.33

ric study was conducted. Table 1 shows the values of the parameters studied for each method. The τ for FEM was calculated as $\tau = \lambda m$. The parameters were so chosen in order to get the range of errors in both methods comparable to each other in the first few iterations, to have a fair ground for comparison. The errors were computed for 10,000 iterations in time for each method (resulting in a total time = 1). The results obtained were plotted on a semilog graph as shown in figure 2(b).

In all the three cases, the error was always below 2%. For FEM (black line), the initial iterations (\approx till 4000) show rate of increase of error comparable to that of the other two cases. However, we see a considerable hike in the later iterations. Similar hike is observed in case of PUFEM1 and PUFEM2, however, the errors are lower than that observed in FEM.

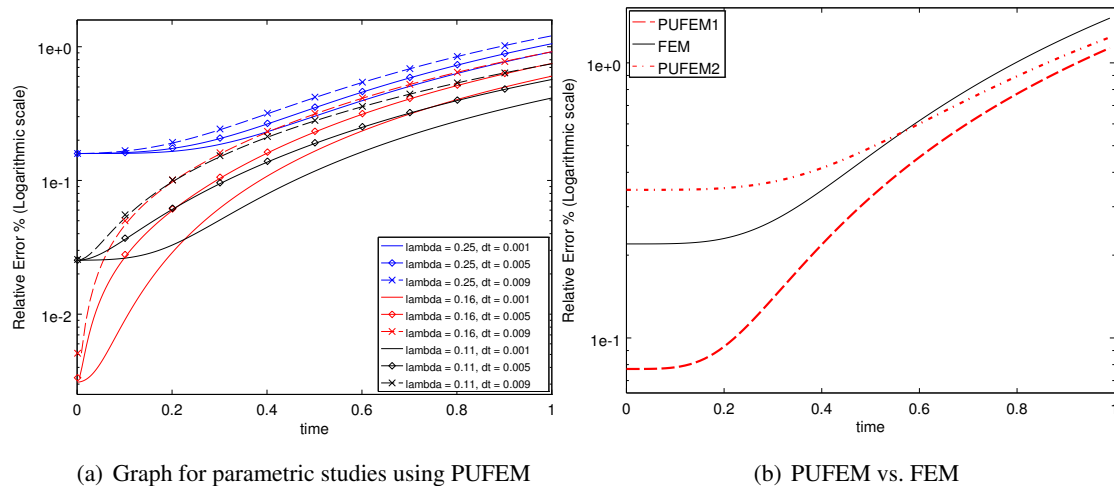


Figure 2: Plots of relative errors observed in analysis

3. Conclusions

The parametric studies on the suggested PUFEM (fig. 2(a)) clearly show that for a given wavelength under test, the error in analysis increases with increasing discrete step size. This is expected as the coarser time step worsens the linear approximation of the (second order accurate) time derivative. Further, for a fixed time step (Δt), a reduction in the wavelength under study (with other parameters being constant) should have led to higher errors. However, the number of plane waves used for enrichment was increased with decreasing wavelength, in an attempt to minimize the change in τ . This led to a considerable reduction in errors due to higher enrichment. Hence, it would be fair to conclude that the error due to discretization in time contributed as the dominant part of error in the analyses with higher plane waves for enrichment.

Comparison of the errors observed for PUFEM with that for FEM (fig. 2(b)), suggest that the relative errors are smaller as compared to that observed in the latter for large iterations in time. However, there is scope for further study to investigate this behaviour.

References

- [1] J.C. Maxwell, "A dynamical theory of the electromagnetic field," *Philosophical Transactions of the Royal Society of London*, vol. 155, pp. 459-512, 1865.
- [2] Mohamed M.S., Seaid M., Trevelyan J. and Laghrouche O. (2014), An enriched finite element model with q-refinement for radiative boundary layers in glass cooling. *Journal of Computational Physics*, doi: <http://dx.doi.org/10.1016/j.jcp.2013.11.005>
- [3] Mohamed M.S., Seaid M., Trevelyan J. and Laghrouche O. (2014), Time-independent hybrid enrichment for finite element solution of transient conduction-radiation in diffusive grey media. *Journal of Computational Physics*, doi: <http://dx.doi.org/10.1016/j.jcp.2013.05.030>
- [4] Mohamed M.S., Seaid M., Trevelyan J. and Laghrouche O. (2013), A partition of unity FEM for time-dependent diffusion problems using multiple enrichment functions. *International Journal for Numerical Methods in Engineering*, 93: 245265. doi: 10.1002/nme.4383
- [5] Melenk JM, Babuška I. The partition of unity finite element method: basic theory and applications. *Computer Methods in Applied Mechanics and Engineering* 1996; 139:289314.
- [6] Laghrouche O., Bettess P. and Astley R. J. (2002), Modelling of short wave diffraction problems using approximating systems of plane waves. *International Journal for Numerical Methods in Engineering*, 54: 15011533. doi: 10.1002/nme.478

A black-box fast multipole method for accelerated isogeometric boundary element analysis with T-splines

Robert N. Simpson^{1}, Michael A. Scott², Jon Trevelyan³

¹School of Engineering, University of Glasgow, Glasgow G12 8QQ

²Department of Civil and Environmental Engineering, Brigham Young University,
Provo, Utah 84602, USA

³School of Engineering and Computing Sciences, Durham University, South Road, Durham, DH1 3LE

*robert.simpson.2@glasgow.ac.uk

ABSTRACT

We outline the use of a black-box fast multipole method (FMM) originally conceived for N-body problems in the context of boundary element analysis using T-spline discretisations to achieve $O(N)$ scaling. The algorithm is based on an octree subdivision of space in which we outline the necessary criteria to terminate octree subdivision. In the spirit of isogeometric analysis, we use a discretisation based on computational geometry taking the form of T-splines. To verify the implementation we compare the scaling behaviour of the proposed FMM approach against a direct LU solver in which an improvement from $O(N^2)$ to $O(N)$ is clearly demonstrated in solution runtime. The approach is applied to geometries obtained directly from Computer Aided Design software using Bézier extraction providing a fast and highly efficient tool for conceptual design. The current study is based on three-dimensional Laplace problems.

Key Words: *fast-multipole method; isogeometric analysis; boundary element method; T-splines*

1. Introduction

It is well-known that a straightforward application of the boundary element method (BEM) leads to dense matrices whose construction scales as $O(N^2)$ in both runtime and memory. Coupled with direct solvers which scale as $O(N^3)$ this asymptotic behaviour can be a severely debilitating feature for three-dimensional problems and an appropriate method that accelerates the solution runtime and which compresses the system matrices must be used. Many such methods have been developed over the past few decades and all rely on some form of approximation of far-field effects. One of the most commonly used acceleration methods is the fast multipole method (FMM) which was originally developed for N-body problems [1]. Other approaches include Adaptive Cross Approximation (ACA), H-matrices and Wavelets.

From an implementation standpoint the FMM can lead to substantial code rewrites to allow for different kernels. This prevents the use of object-oriented code designs that allow for efficient code reuse. One approach to overcome this limitation is to use an algebraic method such as ACA that achieves $O(N \log N)$ behaviour. In the present study we favour the FMM approach to achieve $O(N)$ scaling and implement a 'black-box' approach that allows trivial kernel interchange. In this way, highly optimised FMM code that has been developed over several years for N-body problems can be applied to BEM analysis code for a variety of engineering applications.

The contribution of the present study is to unite advanced computer-aided geometric design (CAGD) discretisations with black-box FMM technology that allows boundary element analysis to be performed on CAGD geometries that achieves $O(N)$ scaling. By making use of CAGD discretisations to represent both the geometry and analysis fields the task of meshing is circumvented entirely which is highly desirable in the context of engineering design. The present approach falls under the umbrella of isogeometric analysis.

The present paper is structured as follows: we first briefly outline the black-box FMM; we then describe the machinery that allows the black-box FMM to accelerate boundary element analysis with T-splines discretisations; and finally, we demonstrate numerically the $O(N)$ asymptotic behaviour of the approach for Laplace problems.

2. Black box fast multipole method

The implementation used in the present study is based heavily on the work of Darve et al. [3] and therefore only a brief summary of the method is given.

Fast multipole methods were originally developed to overcome the intractable computational complexity of N -body problems when solved by direct means. Such problems can be expressed as

$$f(\mathbf{x}_i) = \sum_{j=1}^{N_s} K(\mathbf{x}_i, \mathbf{y}_j) \sigma_j \quad i = 1, 2, \dots, N_f \quad (1)$$

where $f(\mathbf{x}_i)$ is the desired force or field, $K(\mathbf{x}, \mathbf{y})$ is a problem specific kernel, $\{\sigma_j\}_{j=1}^{N_s}$ is a set of charges, $\{\mathbf{x}_i\}_{i=1}^{N_f}$ a set of field points and $\{\mathbf{y}_j\}_{j=1}^{N_s}$ a set of source points. In the case $N_s = N_f = N$ and (1) is applied directly, the computation time scales as $O(N^2)$ which necessitates acceleration methods for large problems. Many variants of the FMM exist, but all are based on the premise that Eq. (1) can be split into a near-field and far-field component as

$$f(\mathbf{x}) = f_{near}(\mathbf{x}) + f_{far}(\mathbf{x}) + \epsilon(\mathbf{x}) \quad (2)$$

in which f_{near} and f_{far} are the near and far-field terms respectively and ϵ is an error term. In general, the FMM approach is based on the following requirements:

1. **Prescribed tolerance:** a tolerance ϵ is prescribed to determine the number of terms retained in far-field expansions. These may be based on e.g. spherical harmonics or polynomials.
2. **Subdivision of space:** a hierarchical subdivision of space is constructed consisting of m levels indexed by $k = 0, 1, \dots, m$. Octree subdivision is commonly used for three-dimensional problems.
3. **Upwards pass:** far-field expansions are computed for each cell at the lowest level m of the tree. Far field expansions for cells in level $m - 1$ and higher are computed from expansions in lower levels through a Moment-to-Moment (M2M) translation operator.
4. **Downwards pass:** working down the tree, local expansions are formed for each cell. These are calculated through a Moment-to-Local (M2L) operator for cells in the interaction list and a Local-to-Local (L2L) operator applied to the cell's parent cell. See [2] for a thorough definition of FMM terms including well-separated, near-neighbours and the interaction list of a cell.
5. **Evaluation:** working at the lowest level of the tree, the FMM approximation of $f(\mathbf{x}_i)$ is computed by evaluating the relevant cell's local expansion to compute the far-field approximation. The near-field components are evaluated directly by summing over all near-neighbours.

In the case of the black-box algorithm of [3], far-field expansions are based on Chebyshev interpolation and M2L operators are constructed through reduced rank operators calculated by Singular Value Decomposition (SVD). A particularly beneficial feature of this approach is its ability to handle arbitrary kernels in contrast to conventional FMM implementations.

3. Black-box FMM for isogeometric BE analysis

We first assume that the surface geometry is defined through a set of four-dimensional control points $\{\mathbf{P}_A\}_{A=1}^n$ and associated T-spline basis functions $\{R_A\}_{A=1}^n$ as defined in [4]. We adopt the isogeometric approach in which both the geometry and analysis fields are discretised using the T-spline basis which is obtained directly from Computer Aided Design software. Efficient Bézier extraction algorithms [6] can be used to provide fast T-spline evaluation routines. Assuming appropriate boundary conditions are defined over the surface of the domain, we wish to accelerate the solution of the system of equations

$$\mathbf{Ax} = \mathbf{b} \quad (3)$$

where \mathbf{A} is a dense matrix of boundary integral terms, \mathbf{x} is a vector of unknown coefficients and \mathbf{b} is a vector obtained by multiplying boundary integral terms with nodal boundary condition values. Further details for constructing this system of equations can be found in [5].

The black-box FMM accelerates the computation of (3) by rapidly evaluating the matrix-vector product $[\mathbf{A}]\{\mathbf{x}\}$ in conjunction with an appropriate iterative solver such as GMRES. Prior to calling the iterative solver, the following data structures must be defined:

1. **Field points** $\{\mathbf{x}_i\}_{i=1}^{N_f}$: these are directly equivalent to collocation points in a conventional BE formulation.
2. **Source points** $\{\mathbf{y}_j\}_{j=1}^{N_s}$: these correspond to the physical coordinates for all quadrature points over all elements on the surface.
3. **Charges** $\{\sigma\}_{j=1}^{N_s}$: these are computed from the interpolated boundary conditions/current solution, quadrature weights and jacobian determinants. For the double-layer kernel, normal components are also included.

It should be noted that the FMM notation used above in which source points are equivalent to quadrature points and field points are equivalent to collocation points is the opposite to that normally used in BEM formulations.

Employing a GMRES iterative solver, the solution process proceeds as follows:

1. **Octree initialisation:** Construct an octree division of space that bounds the problem domain in physical space. The largest boundary element must be contained within the union of a cell and its nearest neighbours (criteria for terminating subdivision).
2. **Precomputation:** Assign the pre-computed sets of field points, source points and charges to the black-box FMM algorithm. Construct a preconditioning matrix for the GMRES solver from diagonal components of the matrix \mathbf{A} . Assign an initial guess for the solution.
3. **FMM evaluation:** Compute the components of the matrix-vector product $[\mathbf{A}]\{\mathbf{x}\}$ for all field (collocation) points. On the first iteration, compute the components of the vector $\{\mathbf{b}\}$ by looping over all field points.
4. **Update solution:** Compute the residual and update the current solution. Update the set of charges with the updated solution.
5. **Convergence check:** Loop through 3-4 until the residual falls below a prescribed tolerance.

4. Results

To evaluate the asymptotic behaviour of the proposed approach a Laplace problem posed over a torus geometry was solved with increasingly refined discretisations. In the present study we adopt cubic T-splines and apply uniform h-refinement. By employing a known smooth analytical solution to Laplace's equation, nodal boundary condition values were generated by performing an L_2 projection of the known function onto the T-spline basis. Specifically, the function $\phi = x$ was prescribed with a solution $\partial\phi/\partial n = n_x$ using the notation $\mathbf{n} = (n_x, n_y, n_z)$ to denote the outward pointing normal. The geometry parameterisation contained no degeneracies.

A timing comparison was made with an equivalent BE formulation using an LU (direct) solver. The $O(N)$ and $O(N^2)$ asymptotic behaviour can be seen clearly in Fig. 1. For large, three-dimensional problems the need for an accelerated approach is evident.

To demonstrate the ability of the approach to handle non-smooth geometries we performed the same experiment with a geometry containing non-smooth normals. An example octree for this geometry along with the corresponding numerical solution is shown in Fig. 2. The same $O(N)$ asymptotic behaviour was observed for this geometry.

5. Conclusion

We have demonstrated the use of a black-box FMM to accelerate boundary element analysis using T-spline discretisations to achieve $O(N)$ scaling behaviour. The use of T-splines to discretise both the geometry and analysis fields precludes mesh generation and paves the way for integrated design and analysis software that will offer substantial efficiency savings for industrial conceptual design studies. By adopting a black-box approach the method can be easily extended to other kernels that model e.g. Stokes flow, elasticity and low frequency acoustic/electromagnetics.

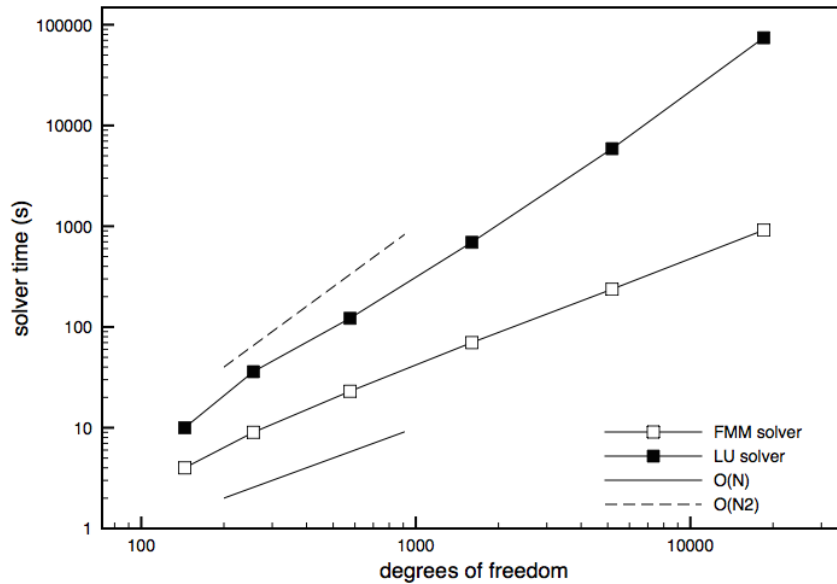


Figure 1: Torus study: solution runtime comparison of LU and FMM solvers.

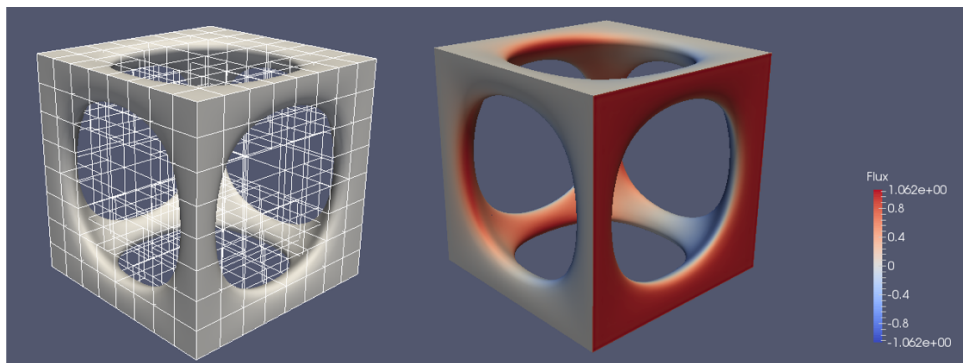


Figure 2: Non-smooth geometry: octree subdivision of space and example numerical solution.

Acknowledgements

We gratefully acknowledge the assistance of Ruoxi Wang and Eric Darve in guiding the implementation of the present work.

References

- [1] L. Greengard, V. Rokhlin, A fast algorithm for particle summations, *Journal of Computational Physics* 73, 325–348, 1987.
- [2] R. Beatson, L. Greengard, A short course on fast multipole methods, *Wavelets, Multilevel Methods and Elliptic PDEs*, 1–37, 1997.
- [3] W. Fong, E. Darve, The black-box fast multipole method. *Journal of Computational Physics* 228 (23), 8712–8725, 2009.
- [4] X. Li, M. A. Scott, T. W. Sederberg, Analysis-suitable T-splines: characterization, refineability, and approximation, *Mathematical Models and Methods in Applied Sciences* 24 (6), 1141–1164, 2014.
- [5] M. A. Scott, R. N. Simpson, J. A. Evans, S. Lipton, S. P. A. Bordas, T. J. R. Hughes, T. W. Sederberg, Isogeometric boundary element analysis using unstructured T-splines, *Computer Methods in Applied Mechanics and Engineering* 254 197–221, 2013.
- [6] M. A. Scott, M. J. Borden, C. V. Verhoosel, T. W. Sederberg, T.J. R. Hughes, Isogeometric Finite Element Data Structures based on Bézier Extraction of T-splines. *International Journal for Numerical Methods in Engineering*, 88, 126–156, 2011.

LIST OF AUTHORS

- Adam Philo, 187, 451
Akbar Javadi, 61, 87, 219
Alex Gansen, 469
Ali Dogru, 303
Alireza Ahangar-Asr, 87
Alireza Jalali, 209, 227
Amit Das, 349
Andre Massing, 169
Andrew Evans, 349
Ansam Qsymah, 327
Anthony Jefferson, 133, 281
Antonio J. Gil, 123, 159, 165, 173, 181, 245, 393, 407
Asaad Faramarzi, 79
Behrooz Tafazzolimoghaddam, 101
Ben J. Evans, 317
Benedict D. Rogers, 115
Bhushan Karihaloo, 191
Borek Patzak, 375
Bruce Jones, 177
Cameron Pleydell-Pearce, 397
Carl Ollivier-Gooch, 209, 227
Carlo Sansour, 415
Charles Augarde, 411
Charles Mortished, 363
Chenfeng Li, 421, 429
Chengyuan Wang, 151, 339
Chennakesava Kadapa, 137
Chris J. Sutcliffe, 187
Chris Pearce, 93, 267, 273, 403
Christopher Leonardi, 177
Chuansan Ma, 133
Chun Hean Lee, 119, 165, 393, 407
Costy Kodsí, 273
Cris Arnold, 75, 119
Darong Jin, 123
David Bould, 75, 397
David James, 57
David Jones, 231
David Moxey, 213
David Naumann, 317
David T. Gethin, 119
David Worsley, 439
Desmond Andrew Brennan, 439
Diane Gardner, 133
Diane McBride, 237
Dirk Ekelschot, 213
Djordje Peric, 137
Dominic Reeve, 195
E. Enticknap, 397
Elia Gironacci, 255, 433
Erik Burman, 169
Euan Richardson, 141
Farzaneh Hafezi, 237
Fawzi Belblidia, 57, 75, 119, 461
Firas Badry, 191

Gabriel Hattori, 277, 285
 Gede Pringgana, 115
 Giorgio Greto, 393
 Graham McShane, 313
 Guilio Alfano, 335
 H Alicia Kim, 313
 Hamed Haddad Khodaparast, 321
 Hamid Bahai, 147, 335
 Harshinie Karunarathna, 195
 Hassan Al-Budairi, 267
 Hector U. Levatti, 119
 Heiko Gimperlein, 443
 Hichem Boulechfar, 455
 Hocine Matallah, 83
 Hossein Madani, 147
 Ian Cameron, 461
 Ian Mabbett, 439
 Ian Masters, 249
 Ibrahim A. Alatawi, 277, 285
 Igor Sazonov, 65, 129
 J. Cullen, 397
 Jan Novak, 375
 Jan Wissink, 147
 Jason Joannou, 187
 Javier Bonet, 165, 173, 181, 393, 407
 Jennifer Thompson, 309
 Jibran Haider, 407
 Joao Duro, 313
 Joaquim Peiró, 205, 213
 Joaquín Navarro-Zafra, 101, 263
 Johann Sienz, 57, 75, 83, 119, 187, 199, 309, 363, 451, 461
 John Cherry, 187, 451
 John Williams, 177
 Jon Elvins, 439
 Jon Trevelyan, 277, 285, 483, 487, 491
 José Luis Curiel-Sosa, 101, 263
 Juan Carlos García Orden, 447
 Juergen Eckermann, 57
 Julien Vignollet, 155, 353
 Justin Prince, 205
 K.Adi Navaneetha Kumari, 381
 Karin de Borst, 105, 141
 Kenneth Morgan, 231, 241, 295, 469, 473
 Kenny W. Q. Low, 199
 Konstantinos Christodoulou, 483
 Konstantinos Krestenitis, 53
 Kulchamai Thienkarochanakul, 61
 Lee Cunningham, 357
 Lee Margetts, 327
 Lee S. Cunningham, 115
 Lintao Zhang, 461
 Lucas Franceschi, 291
 Luis Saucedo-Mora, 259
 Lukasz Kaczmarczyk, 93, 267, 273, 403
 Luke Rees, 299
 M S Mohamed, 487
 Mahfoud Djeddar, 455
 Mahkame Sharbatdar, 209, 227
 Mai Abdul Latif, 223
 Maimouna Al Manthari, 111
 Mar Giralt, 465

Mark Cross, 237
 Mark Dawson, 473
 Martin Horak, 375
 Marton Huszar, 75
 María Del Carmen Serna Moreno, 263
 Matthew Profit, 371
 Mayank Drolia, 487
 Michael Cortis, 403
 Michael Edwards, 303
 Michael Hicks, 425
 Michael I. Friswell, 65
 Michael Scott, 491
 Michael Weberstadt, 245
 Min Wang, 151
 Mohaddeseh Mousavi Nezhad, 255, 433
 Mohamed Benamer, 429
 Mohamed El Hachemi, 469
 Mohammad Rezania, 255, 433
 Mohammed Hjjaj, 415
 Mohammed Hussain, 219
 Mohammed Seaid, 487
 Moirangthem Dinachandra, 367
 Moura Mehravar, 79
 Mt Rahmati, 335
 Muhammad Iqbal, 443
 Muhannad Aldosary, 429
 Nicholas P. Lavery, 187, 397, 439, 451
 Nick Croft, 83, 237, 249, 349
 Nick Owen, 71
 Nidal Hilal, 241
 Omar Laghrouche, 443, 483, 487
 Ouahid Harireche, 79
 Oubay Hassan, 231, 241, 295, 299, 309, 465, 469, 473
 Patrick Wlodarski, 75
 Paul D. Ledger, 123, 159, 479
 Perumal Nithiarasu, 111, 129
 Peter Benzie, 363
 Peter Betsch, 447
 Peter Theobald, 313
 Philip Vardon, 425
 Pooya Mahmoodi, 65, 71
 Quentin J. Fisher, 255
 Raid Daud, 357
 Rajesh S. Ransing, 65
 Rajneesh Sharma, 327
 Raju Sethuraman, 367, 381, 389
 Ramaseshan Kannan, 345
 Raoul van Loon, 199
 Remi Caudoux, 105
 René de Borst, 155, 353
 Reza Naseri-Karim-Vand, 219
 Richard Evans, 129
 Rob Ellis, 237
 Robert Lark, 133
 Robert Simpson, 491
 Rogelio Ortigosa, 165, 173
 Roman Poya, 181
 Ross Kynch, 479
 Rubén Sevilla, 245, 291, 299, 465, 473
 Sam Rolland, 199, 237, 309
 Scott Bagwell, 159

Sean Walton, 295
Sergio Conde Martin, 447
Shadi Mohamed, 443, 483
Shahid Manzoor, 303
Shahid Mehmood, 119
Shahin Mehraban, 397
Shaoqing Cui, 421
Shirin Yekrangian, 97
Shivani Srivastava, 389
Simon Annan, 71
Sivakumar Kulasegaram, 191, 393
Sondipon Adhikari, 321, 385
Soo-Hyeong Kim, 241
Spencer Sherwin, 213
Stefan May, 155, 353
Stephen G. R. Brown, 187, 397, 451
Stephen Hardy, 83
Stephen Hendry, 345
Sudip Dey, 321
Sue Alston, 75
Susanne Claus, 169
Tanmoy Mukhopadhyay, 321, 385
Tareq Al-Shaalan, 303
Thomas James Marrow, 259
Thomas Lake, 249
Tien Long Nguyen, 415
Tim Charlton, 411
Tomasz Koziara, 53
Violeta Moloney, 195
Waled Alnaas, 281
Wenjun Tan, 371
William Coombs, 411
William G. Charles, 65
Wulf Dettmer, 137
Yajun Li, 425
Yao Xiao, 339
Yong Wang, 357
Yun Tian Feng, 151, 223, 331, 339, 371
Zahur Ullah, 93
Zhangjian Wu, 97
Zheng Cui, 331
Zhenjun Yang, 327